Probing Power-Absorbing Structures at Near-Infrared Wavelengths using Energy Absorption Interferometry

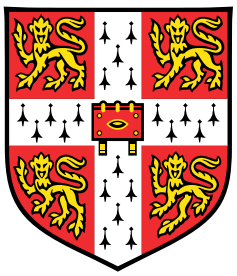

Dan Moinard

Department of Physics
University of Cambridge

This dissertation is submitted for the degree of
Doctor of Philosophy

Gonville and Caius College

September 2019

Declaration

This dissertation is the result of my own work and includes nothing which is the outcome of work done in collaboration except as declared in the Preface and specified in the text. It is not substantially the same as any that I have submitted, or, is being concurrently submitted for a degree or diploma or other qualification at the University of Cambridge or any other University or similar institution except as declared in the Preface and specified in the text. I further state that no substantial part of my dissertation has already been submitted, or, is being concurrently submitted for any such degree, diploma or other qualification at the University of Cambridge or any other University or similar institution except as declared in the Preface and specified in the text. The thesis is not to exceed, without prior permission of the Degree Committee, 60,000 words, including summary/abstract, tables, footnotes and appendices, but excluding table of contents, photographs, diagrams, figure captions, list of figures/diagrams, list of abbreviations/acronyms, bibliography and acknowledgements.

Dan Moinard
September 2019

Acknowledgements

I was recently asked by a new graduate to describe my experience working towards a PhD. The best metaphor I could find was that of a roller-coaster, as an exhilarating yet terrifying journey with many lows and memorable highs. Before moving on to new personal adventures, I want to use this opportunity to acknowledge the very long list of people who were along for the ride: you have made this work possible and my time in the Quantum Sensors group most enjoyable.

First and foremost, I am deeply indebted to Prof. Stafford Withington, for trusting me to successfully complete this amazing project and sharing his wisdom along the way. The guidance he provided in countless conversations and meetings was invaluable, and taught me more about physics and problem-solving than I can express. I am thankful for his numerous contributions, among many others in the development and theoretical description of our phase-correction scheme, and for his attentive proof-reading of this manuscript.

The support provided by Dr. Christopher Thomas on this work cannot be overstated, nor my appreciation for his assistance and patience. In particular, I am very grateful for his decisive contribution in elaborating the method to estimate the number of modes in amplitude-only datasets, as well as the study of reconstruction schemes to deal with missing diagonal bands in experimental datasets.

The informal meetings I had the pleasure to share with Dr. David J. Goldie have always been most gratifying; many thanks as well for sharing my pain on days when our respective experimental systems had decided to be “useless”. I want to send particularly warm thanks to Dennis Molloy, who participated in numerous hour-long debates about the design and manufacture of experimental components, and David Sawford, whose advice in LabView programming and building the data acquisition system was particularly constructive. My sincere thanks also to Michael Crane, for stimulating conversations and second opinions, and Dr. Dorota Glowacka, for her amiability and generosity.

I also extend my heartfelt gratitude to all of my student colleagues in the Quantum Sensors group; starting with my seniors, Djelal, Rachel, Tejas and Isa, for welcoming me in the team and introducing me to the Cavendish Canteen and the Financial Times. I wish the best of luck and lots of success to those next in line to submit a QS-stamped dissertation:

Rebecca, Jonah, Emily, Tess, Songyuan and Kunal; thank you for your friendship, and keep the Maxwell coffee machine flowing! A warm shout-out also to those who visited the group, Ben, Andrea and Vincent, and those who will shortly return for longer periods of time, Bram and Denis.

My family definitely deserves sincere thanks for their continued support and advice: my mother Friederike who introduced me to mathematics, my father Yves for inspiring to "shall" every day, and my brother Alex, whose regular banter and legendary mug have been much more effective than Caius' Gate of Humility. I sincerely appreciate their perseverance with my best attempts to describe my work, and assure my Austrian family that I was no more successful in my explanations to my French family: ich habe endlich das Licht gefunden! Last but by no means least, I am forever grateful to Marige, whose love and kindness supported me through thick and thin, and pushed me to give my best every day. I am a better man for it, and could not be happier to share my next adventures with you.

Finally, I acknowledge the Science and Technology Facilities Council for funding my studentship, as well as the Quantum Sensors group for financial support, and the Cambridge NanoDTC and Gonville and Caius College for additional contributions.

Abstract

Energy Absorption Interferometry was recently proposed as an interferometric technique capable of fully characterizing the optical response of single-mode, few-mode and multi-mode power-absorbing structures, such as near-infrared detectors. A detector's output can be written as the full spatial contraction of the external field correlation tensor and detector response correlation tensor representing their respective spatial coherence states; EAI recovers the latter, solely using power measurements. EAI is essentially a generalization of holography, and allows the reconstruction of the individual degrees of freedom through which the device under test can absorb energy, including their relative sensitivities and spatial forms. The natural modes of the detector response are intimately related to its optical coupling mechanisms and the underlying solid-state phenomena responsible for power absorption: their study therefore has direct applications in improving current infrared detector technology. In particular, device properties dependent on its geometry and material are directly obtained, such as the absorber's spatial coherence length. EAI yields an experimental procedure where the system under test is excited with two external coherent sources, and the fringe in the total power dissipated is measured as the relative phase between the sources is varied. Iterating for multiple source positions, the fringes' complex amplitudes allow the two-point detector response function to be retrieved: this correlation function can then be decomposed into a set of natural modes.

In this thesis, we demonstrate the application of EAI at near-infrared wavelengths. We describe the theoretical basis of EAI and numerically investigate its feasibility at infrared wavelengths. We present for the first time the design of a room-temperature, fiber-based, 1550 nm-wavelength experiment and its performance. We report the first measurement of the complex-valued DRF of fiber-coupled photodetectors, with single-mode, few-mode and multi-mode behaviors; this includes extending the experimental system to suppress environmental phase drift in optical fibers. We recover the natural modes of the devices under test, and compare their spatial forms to numerical simulations. Finally, we discuss the application of EAI to many-body structures as varied as spin systems and energy-harvesting absorbers, and its extension to measure quantum correlation functions using a pair of probes creating generalized forces.

Table of contents

List of figures

List of tables

Chapter 1

Introduction

1.1 Characterizing Power-Absorbing Structures

1.1.1 Natural Modes and their Measurement

Power-absorbing structures whose optical response exhibit few-mode behavior are of prime importance in a large number of fields. In the telecommunications industry, significant effort is placed in optimally coupling the signal transmitted by optical fibers into high-speed photodiodes, including using few-mode fibers where each mode constitutes a data channel [1]. CCD and CMOS cameras with ever smaller pixels are used in a large number of applications [2], from medical imaging [3, 4] to astronomy [5] and Earth observation [6]. Energy harvesting, using photovoltaic cells to generate electricity from sunlight or antenna arrays to extract energy from radio waves in the environment, would be significantly improved by accurately measuring the degrees of freedom through which these systems absorb optical power [7]. Muller cells in the retina of animal and human eyes are expected to be few-mode, based on geometrical arguments [8]: precisely measuring their optical response would allow the confirmation of this hypothesis, and provide a deeper comprehension of vision mechanisms.

The understanding, engineering and practical use of such power-absorbing structures requires methods to measure the number of natural modes present and their respective spatial and polarimetric forms. In the context of power-absorbing structures such as detectors, modes are the set of fully-coherent field patterns through which the system can incoherently absorb energy [9]. These modes are mutually orthogonal with respect to some inner product, typically defined as the spatial integral of the product of fields. Precisely measuring a device's reception modes is critical to exploring its photon absorption mechanisms, to produce an optimal coupling to its environment including the reduction of optical noise, to perform

optimization of its power absorber's design, and to engineer it as part of a larger optical system [10, 11].

The optical response of such devices greatly influences other key performance characteristics, including the responsivity spectrum, the output rise time, noise metrics such as the Noise-Equivalent Power measuring the device's sensitivity, and the gain pattern of the device, among many others [12, 13]. While well-established measurement methods are available for these characteristics, even if they differ depending on the type of device and operating wavelength considered [14], standardized characterization methods to recover the number and forms of the natural modes of a device of interest are singularly limited.

1.1.2 Motivation and Thesis Objectives

Measurement schemes exist for coherent systems such as antennas, whose response is defined by a single mode, generally at radio wavelengths: radiometric techniques are broadly used to measure the spatial pattern of the reception mode [15, 16]. Analogous characterization methods are used to study incoherent systems including bolometers, whose response is composed of a very large number of modes, generally at optical wavelengths [14]. For power-absorbing structures whose optical behavior falls between these two limiting cases, understanding the number of natural modes present and their spatial forms is much more complex and current characterization methods are unsatisfactory. The results presented in this dissertation directly address these issues by answering the two following questions:

- What is the appropriate theoretical description of the optical response of power-absorbing structures, including those with few-mode behavior?
- Is it possible to experimentally characterize their full optical response using only power measurements, including to recover their natural modes?

In this thesis, we conclusively answer both questions by developing and demonstrating a powerful interferometric technique called Energy Absorption Interferometry. Although the emphasis in this dissertation is placed on fiber-coupled photodetectors at infrared wavelengths, the theoretical framework and experimental techniques presented are applicable much more broadly, both in terms of detector technologies and of operating wavelengths.

1.1.3 Existing Methods

Many fields and applications would profit from an experimental method capable of measuring the reception modes of few-mode power-absorbing structures; however, few such schemes

exist, most of which utilize optical fibers. One example is the measurement of coupling efficiencies between optical fiber modes and superconducting detectors [17]. In the context of optical fibers, modes are the eigensolutions of Maxwell's equations in the propagating medium, i.e. the fiber core, and are called Linearly Polarized (LP) modes [18]. In this scheme, the fundamental LP mode is generated by a laser source and illuminates spatial light modulators used to produce phase holograms: the expected high-order LP modes of fibers are artificially created, and then projected onto a power detector. This method effectively measures the sensitivity of the detector to each incident LP mode, but does not directly allow the reconstruction of the natural modes of the detector.

Polarization and spatial modes of optical fibers are also particularly important in temperature and strain sensors. Fiber characteristics such as the temperature and strain dependences of their stimulated Brillouin scattering parameters can be measured by leveraging high-order LP modes produced by spatial light modulators [19]. A complex measurement system involving pulsed pump and probe laser signals, optical circulators, a 3 km-long test fiber, and a 6×6 set of coherent receivers is required, with significant assumptions made about their respective optical behavior.

It is also possible to produce a second-order LP mode by applying pressure periodically along a fiber, using a mechanical grating: periodic alternations of the fiber's refractive index appear due to the photo-elastic effect, producing a coupling of the fundamental LP mode into the second-order LP mode [20]. In this technique, the produced signal is interfered with a reference first-order mode to obtain the conversion efficiency.

It is important to note that these characterization methods use artificially generated optical fiber modes, in effect probing the fibers' optical behavior with a selected basis set of field patterns, rather than the fibers' natural modes. Additionally, the techniques discussed are not able to measure the natural modes of the detectors used.

1.2 Detector Technology

1.2.1 Near-Infrared Detectors based on Semiconductors

Having described the various methods that are currently available to characterize the optical response of near-infrared detectors, as well as their limitations, it is important to consider the variety of technologies to which they are applicable. We start with semiconductor-based detectors, which are generally suitable for optical and near-infrared operating wavelengths.

Charge Coupled Devices (CCD) are currently a technological reference for a large range of applications, from astronomical detectors to Earth observation and medical imaging, due

to their well-understood physics, very large megapixel arrays, and the experience from their use at room-temperature [2, 21]. However in semiconductor detectors including CCDs, single-photon avalanche photodiodes (SPADs) and photomultiplier tubes (PMTs), strong charge multiplication and similar amplification mechanisms are necessary: these lead to high noise levels and dark-count rates of order 100 kHz, even when the operating temperatures are decreased to 200-250 K to reduce thermal noise contributions [22]. CCDs also have a low time resolution, of the order of a tens of milliseconds.

Whereas CCD pixels are passive, active-pixel sensors such as Complementary Metal-Oxide-Semiconductor (CMOS) sensors have pixels each built from a photodetector and an active amplifier [23]. CMOS sensors are generally less expensive than CCD cameras and generally display lower cross-coupling between saturated pixels and their neighbors, a phenomenon known as blooming. Their pixel sidelength is as small as 1.7 µm, i.e. a large fraction of their operating 400-900 nm wavelengths [24].

At near-infrared wavelengths, the semiconductor-based technology of choice is InGaAs PIN-junction photodiodes, particularly in telecommunications [25]: they feature high speeds up to a few GHz, high sensitivities and large wavelength range from 800 nm to 1700 nm. Their physical size ranges from 0.1 mm to 2 mm, such that they are generally considered to be fully incoherent detectors. The same InGaAs architecture is also used in line and area image sensors, which can contain several hundreds to hundreds of thousands of pixels respectively, with applications in spectrometry and scientific cameras for microscopy. The choice of their pixel size, in the 20-200 µm range, largely depends on applications, which include spectroscopy and optical imaging [26].

1.2.2 Near-Infrared Detectors based on Superconductors

Infrared detectors based on superconducting materials exhibit superior sensitivity and intrinsic energy-resolving capabilities, with important applications applications in astronomy [27] and in quantum communications [22]. Superconducting Tunnel Junctions (STJs) are historically the first superconducting detector still currently in use. STJs are composed of a thin insulating barrier between two superconducting layers, through which quasiparticles created by photon absorption events can tunnel: tunnelling events generate current pulses, proportional to the photon energy. STJs have to be operated well below the superconductor's critical temperature T_c to avoid dark currents from thermally excited quasiparticles, and must be voltage-biased. Multiplexing STJs to simplify their readout is notoriously difficult.

Transition-Edge Sensors (TESs) are microcalorimeters made of a superconducting film generally less than 10 nm thick, balanced thermally at its superconductivity transition: heat from an absorbed photon creates a very sharp resistivity increase. TESs are voltage-biased

for balance at their optimal operating point, through an electro-thermal feedback caused by the Joule heating of the bias current. The feedback also implies a reduction in the pulse recovery time constant and an improved linearity of the device. SQUID multiplexing schemes have been demonstrated successfully [28], but require complex cryogenic electronics. Moreover, TESs have intricate fabrication procedures because they are required stand on fragile suspended membranes for precise thermal coupling, which is a major drawback for potential space-based applications. Optical fiber coupling to TESs has been successfully shown to increase their total coupling efficiency [29].

Superconducting Nanowire Single-Photon Detectors (SNSPDs / Nanowires) are thin superconducting wires biased precisely below their critical current density, such that an incoming photon creates a normal-state hotspot. Because the nanowires are thin, normal hotspots disappear very quickly and their recovery time is extremely short, typically a few nanoseconds: this makes them very interesting for quantum information applications where high count rates are important. However, SNSPDs are single-photon detectors, so parallel-SNSPD arrays are required for photon-counting. Moreover, nanowire detector efficiencies are currently low, rarely above 10%. While the optical response of SNSPDs are expected to be single-moded, there has recently been interest in coupling with few-mode fibers [17].

Kinetic Inductance Detectors (KIDs) are thin superconducting film resonant circuits with extremely high quality-factors, coupled in whole arrays to a single transmission line [30]. Quality-factors above 10^6 [31] imply that KIDs only affect a small frequency-window around their resonance frequency, such that they can be passively frequency-multiplexed and read out independently using room-temperature electronics. Experimental results indicate that antenna-coupled KIDs are likely few-moded, due to spurious modes appearing from the interaction between bridge structures and the substrate [32].

1.2.3 Optical Fibers

Having discussed the use of optical fibers in many applications and highlighted their importance at optical and infrared wavelengths, it is beneficial to describe their characteristics and different types, which will inform their extensive use throughout this thesis. Optical fibers are manufactured from two transparent, concentric silica glass cylinders [33], an inner core and an outer cladding, whose refractive indices are carefully selected to provide total internal reflection to transmitted optical power. Optical fibers therefore act as waveguides, with a maximum input angle defined by the core and cladding refractive indices. Choosing low-loss materials, attenuations as low as 0.2 dB/km are routinely obtained in optical fibers suitable for transmission at optical and infrared wavelengths; this characteristic in particular makes optical fibers the technology of choice in telecommunications.

The number of transmission modes supported by optical fibers depends on the refractive indices of the core and cladding layers, as well as the core radius, which can range from several microns to tens of microns; the most widely used diameter for fiber claddings is 125 µm. Optical fibers are generally classified by the number of modes supported:

- Single-mode fibers support only the fundamental LP mode; they are used for single-channel long-distance communication [1], high-precision strain, temperature, pressure, and rotation measurements [34], as well as for chemical and biological sensors [35].
- Multi-mode fibers support hundreds of modes, which allows them to carry very high powers, such as for laser welding; other applications include extrinsic temperature or electromagnetic sensors, for instance in environments with large magnetic fields where metallic wires are unsuitable [36].
- Few-mode fibers are generally understood to support between 2 and 6 modes; this property is widely exploited in multi-channel communication using mode division multiplexing [37], in few-mode amplifiers via active rare-earth doped fibers [38], and in applications requiring low nonlinearities [1].

Additionally, multi-core fibers have been developed to bundle several single-mode fibers, where each constitutes data channel using multiple-input multiple-output digital signal processing [1]. In recent years, fibers based on photonic crystals have been introduced in high-power applications and for the development of mode-locked fiber lasers. A large number of unique properties are achievable by design, including nonlinearities used in supercontinuum generation [39].

1.2.4 Theoretical and Numerical Investigations

Beyond these practical applications, a better understanding of the behavior of few-mode systems is also required in theoretical investigations. Given the reception pattern of a detector, propagating the beampattern from the detector surface back through an optical system is only possible for a single-moded optical response, using Maxwell's equations or for highly multi-mode responses using ray optics [40]. For intermediate systems with few-mode behavior, the full state of coherence of the detector response is required [41]. Commercial electromagnetic modelling packages are very accurate in the same extreme cases, but are similarly ill-suited to partially coherent behavior. This is particularly relevant to telescopes used in astronomy, for instance to maximize the telescope's throughput, a metric for the quality of its optical response [42, 43]. In antenna engineering, the reception pattern of an antenna is often considered to be identical to its transmission pattern, based on the reciprocity theorem;

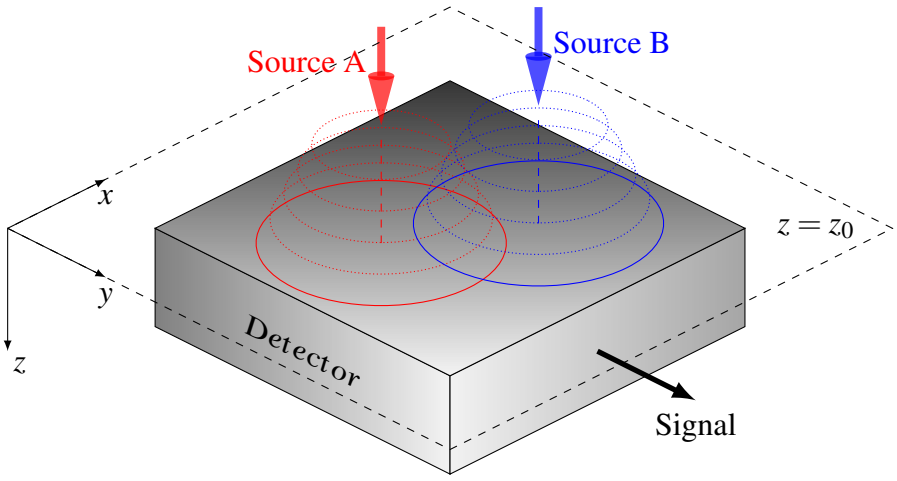

Fig. 1.1 Schematical representation of the detector volume illuminated by an incident field produced by two sources, on the detector surface $z = z_0$.

however, proving reciprocity is difficult in few-mode systems, for instance in the presence of evanescent waves [44, 45]. Similar investigations have been performed for blackbodies made of a polar material, whose emission spectra exhibit temporal coherence caused by thermally excited surface waves [46].

Additionally, as high-precision instrumentation progresses and noise contributions and systematics are reduced, more accurate theoretical frameworks and expressions for power absorption become necessary. Using formulae suitable for the single-mode or extremely highly multi-mode extreme cases is insufficient for few-mode systems. For instance, bolometric detectors used in the investigation of the polarization pattern of the Cosmic Microwave Background require careful design to avoid polarization contamination [47, 48]. Similarly, the optical response of CCD arrays in spectrographs for exoplanet detection needs to be known very accurately to produce high-sensitivity radial velocity measurements: this includes the effective position of the CCD pixels [49] and the effect of colored noise [50].

1.3 Measuring Optical States of Coherence

1.3.1 Energy Absorption Interferometry

Energy-Absorption Interferometry (EAI) is an interferometric technique capable of fully characterizing the optical response of single-mode, few-mode and multi-mode detectors [51]. Its principle is illustrated in Figure 1.1: two phase-locked sources illuminate the device under test, and we measure the fringe in its output as the relative phase between the two sources is modulated. The complex fringe amplitude recorded contains information about the optical

response of the device under test. It has been shown that the power absorbed by a detector can be written as the full spatial contraction of the coherence tensors respectively describing the external field and of the detector response: EAI recovers the latter, named Detector Response Function (DRF) [52]. If a sufficiently large number of source position pairs are sampled, the complex-valued DRF can be totally reconstructed, producing a full characterization of the detector response's state of coherence. It can be shown that the required number of scanned positions is finite, such that the accrual of information from fringes' complex amplitudes leads to a convergence towards the true DRF of the device under test.

It is important here to note that both the states of coherence of the incident field and the detector response are completely general. EAI is therefore applicable to all power detectors, of any mode number, for any source and detector bandwidths, with sources under both pulsed and continuous-wave operation, and for both near-field and far-field measurements. EAI can be interpreted as a generalization of holography: the measured DRF is effectively the state of coherence of the external field to which the device under test is maximally sensitive. Diagonalizing the measured DRF produces the natural modes of the detector response [53], yielding the number and spatial forms of the individual degrees of freedom through which the device under test incoherently absorbs power. EAI therefore successfully fulfills the goal stated in Section 1.1.2.

1.3.2 Aperture Synthesis Interferometry: EAI in Reverse

Just as EAI measures the state of coherence of the optical response of the device under test, it is possible to use two coherent detectors illuminated by an external field to recover the state of coherence of its optical response. Aperture Synthesis Interferometry (ASI) is an interferometric method used in astronomy, in which the signals from a system of telescopes are combined to obtain images whose resolution is equal to that of a virtual detector as large as the system considered [54]. In the case of a system of two telescopes, a signal from the source will be detected by the two detectors with a phase delay, whose magnitude is proportional to their projected spatial separation as seen from the source, called the baseline. For a system of n telescopes, $(n^2-n)/2$ baselines are available simultaneously. For a given baseline, an interferometer measures a fringe as the angle between the source and the normal baseline is varied as the Earth rotates: the complex fringe amplitude is the Fourier component of the source field for the corresponding baseline. Long baselines measure the smallscale structure of the source field, but fringe washout prohibits largescale structure from being recovered; the opposite applies to short baselines, due to the resolution limit. Repeating this procedure for many different baselines, the Fourier transform may be inverted to find the source brightness distribution. A fully filled aperture is effectively synthesized when

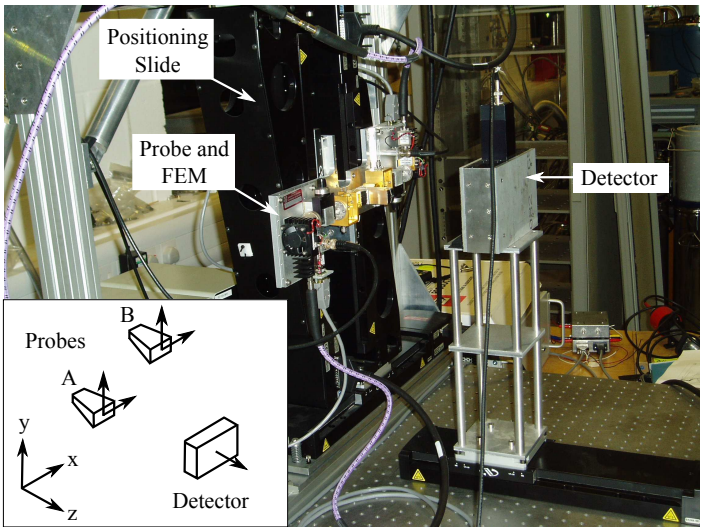

Fig. 1.2 Labeled photograph of the EAI experimental system for the study of submillimeter-wavelength power detectors; reproduced from [58].

the number of baselines is sufficiently large, even if the Fourier Transform is not fully sampled: non-linear deconvolution algorithms, such as maximum entropy methods [55], produce high-resolution reconstructions for relatively sparse sets of baselines. In effect, ASI produces the measurement of the astrophysical source's state of coherence, using two or more phase-locked detectors.

ASI was historically first realized in the 1950s at radio wavelengths, where the amplitude and phase of the incoming signal are measured electronically by each telescope [56]. The same method is unfeasible at optical and infrared wavelengths: the signals need to be interfered optically instead, which limits the baselines to distances covered by optical fibers [57]. The development of techniques such as closure-phase mapping and self-calibration in the 1990s have largely removed these constraints, as well as increased the telescope sensitivities by suppressing atmospheric phase fluctuations and wavefront aberrations.

1.3.3 EAI at Submillimeter Wavelengths

A proof-of-concept EAI experiment was implemented by Thomas et. al [59, 58], for the study of submillimeter-wavelength power detectors, and is presented in Figure 1.2. The goal of this study was to characterize the full optical behavior of multi-mode power detectors at submillimeter wavelength, using a THz power meter that had its front window reduced to a 15 mm $\times$ 15 mm square aperture, in order to synthesize the behavior of a spatially-incoherent planar absorber. The targeted frequency range was from 195 GHz to 270 GHz (equivalently, from 1.54 mm to 1.11 mm), such that the input aperture of the power meter had a side length

between 10 and 14 wavelengths. Two signal generation systems were used to generate the illuminating field with a pair of waveguide probes, both driven in the fundamental Transverse Electric TE_{01} mode [60]. Phase modulation was produced by locking the signal generators together, with the probe frequencies differing by 8 Hz. Each probe was mounted on a two-dimensional motorized scanning system.

The experimental system was successful in recovering the DRF of the device under test, for sources scanned over a uniformly sampled line, although the work undertaken with this prototype did not include a full development of the technique. The measured DRF was decomposed to obtain the spatial forms and sensitivity spectrum of approximately 15 detector modes. In particular, the modes' amplitude and phase patterns were found to be in good agreement with the forms expected for the detector's square aperture. As we will discuss in this dissertation, the choice of the operating wavelength dictates many design considerations for an EAI experimental system. The work presented in this manuscript will therefore have significant differences with the proof-of-concept experiment at submillimeter wavelengths.

1.4 Thesis Outline

The primary goal of this thesis is to demonstrate, develop and investigate the characteristics of EAI at near-infrared wavelengths, through its application to fiber-coupled photodetectors with a wide variety of modal behaviors. This objective entails exploring the technique's feasibility at infrared wavelengths using such fiber-coupled detectors, designing and constructing an experimental system and data analysis procedure to carry out these studies, and performing EAI measurements on a range of devices with single-mode, few-mode and multi-mode behaviors in order to ultimately recover their natural modes. The main topics of this dissertation are divided into chapters as follows:

- Chapter 1 introduces Energy Absorption Interferometry and the scientific motivations behind its development.

- Chapter 2 derives the theory underlying EAI based on writing the power absorbed by an optical detector as the full contraction of the two-point correlation functions characterizing the incident field and the detector response, describes how the DRF can be experimentally measured from fringes in the detector output as the relative phase between two illuminating sources is varied, and explains how this DRF can be written in terms of the so-called natural modes, individually fully-coherent field patterns through which the device under test absorbs optical power.

- Chapter 3 reports on numerical simulations of EAI produced using assumed circularly symmetric DRFs, built from linear superpositions of Linearly Polarized or Laguerre-Gaussian modes (respectively, of transmission in a fiber core and of free-space laser light propagation), studies the effect of changes of representations between the various bases at play, and investigates the efficiency of scanning strategies that could be relevant in experimental settings.

- Chapter 4 describes the design of the experimental system, from qualitative choices (such as the 1550 nm wavelength for its importance in applications, and a fully fiber-based architecture) to quantitative requirements (including the necessary scanning range and resolution, the laser source's power as a tradeoff between high signal-to-noise ratio and operability simplicity, and how interchangeable optical fiber lengths coupled to the photodetector recording the fringes acts as a mode filter).

- Chapter 5 explains the choice of specific components fulfilling our experimental design requirements, the construction and testing of the experimental system, as well as noise measurements characterized by spectra and Allan Variance computations, and the first measurement of fringes in the detector output.

- Chapter 6 details the experimental method for measuring the amplitude pattern of the DRF as sources are scanned over one-dimensional grids, presents the control and data analysis software implemented, reports on the first such measurement of the DRF of single-, few- and multi-mode devices, and derives a bound on the number of modes that can be obtained solely from the DRF amplitude patterns.

- Chapter 7 describes several possible phase correction methods, argues for the implementation of a particular technique based on adding a reference channel close to the device under test, illustrates its effects using numerical simulations including a study of the eigenspectrum and eigenvectors obtained with a phase-corrected DRF.

- Chapter 8 describes the choice and characterization of additional elements to implement this phase correction scheme, studies the performance enhancement obtained in terms of the fringe phase coherence time, performs EAI studies of single-, few- and multi-mode devices using either a two-fiber phase correction system with 10 mm separation or a fiber array with 125 µm separation.

- Chapter 9 discusses a reconstruction method for the missing diagonal band in measured DRFs, caused by the finite size of sources, and its application to simulated and

experimental data; reconstructed DRFs are diagonalized to obtain their natural modes and the corresponding sensitivity spectrum.

- Chapter 10 summarizes the achievements attained during our studies, and discusses the future outlook based on our investigations, including additional experiments possible with our current system, with further system extensions, and with a cryogenic analogue for low-temperature detector, as well as potential applications of EAI to pairs of probes acting through generalized forces.

Chapter 2

Theoretical Description of Power-Absorbing Detectors

2.1 Introduction

While existing methods and models for describing detectors, such as those discussed in Chapter 1, are dependent on the devices' particular nature including their geometry, we seek a general framework to deal with detectors having any modal behavior. Such a general description was first proven by Withington and Saklatvala [61, 52]. The starting point for their framework is the assumption that the output P of any detector should scale as the square of the incoming field amplitude. Regardless of their specific forms, it was shown that the optical response of the absorbing structure and the incident radiation are fully characterized by two-point correlation functions. They are represented as dyadic functions, second-order tensors used to deal with multilinear algebra, and can also be viewed respectively as the states of coherence of the detector's optical response and the external field. Moreover, the detector output can be written as the full contraction of these two dyadic functions. This result also provides a framework for numerically computing the power absorbed by a detector from a partially coherent field, based on their parametrization, namely the assumed model for their optical response.

The first goal of this chapter is to summarize the model derived by Withington and Saklatvala. The second will be to use this formalism to obtain an experimental method for reconstructing the two-point correlation function describing the detector's optical response, called the Detector Response Function (DRF), and its decomposition into natural modes, defined as the set of mutually orthogonal field patterns through which the detector absorbs power. This experimental technique will be referred to as Energy-Absorption Interferometry

(EAI). The results in this chapter will be used throughout this thesis: the following chapters will deal with numerical studies, the design of an experimental system and experimental characterization of a set of infrared power detectors, all of which will make direct references to the equations and concepts derived in this chapter.

Section 2.2 will review the essential elements of EAI theory, introducing both notation and concepts: most of this section will be a condensation of the successive articles published on the topic, leaving out the details of some topics that will be referred to qualitatively. In Section 2.3, we derive an alternative formulation for these results. We first prove rigorously that the incident field and detector response correlation functions can be decomposed in terms of their respective modes. We then show that the power absorbed in the detector can be written as the weighted sum of projections of these sets of modes onto one another, which we refer to as a coupled-mode model. Section 2.4 discusses the choice of two coherent, phase-locked sources to generate the incident field. In particular, choosing fully-coherent quasi-monochromatic sources, we obtain a powerful experimental method to measure the DRF. Placing the two sources at fixed positions, partial information about the DRF can be extracted from the fringes in the detector output as the relative phase between sources is varied; repeating over a number of source positions, the entire DRF can be recovered. In Section 2.5, we will transform previous results into a discretized formulation based on matrices rather than continuous-variable dyadics, in order to make them usable for computational studies and experimental data analysis. Section 2.6 will make important remarks about experimental considerations. These include how one can recover the DRF from a set of measurements of the detector output and how to assess whether enough data was acquired to successfully reconstruct the DRF. The retrieval of other quantities of interest will be discussed, such as the characteristic distance inside the detector volume over which correlations in the detector response are observed, also called the absorbing structure's coherence length.

2.2 Characterization of Detectors

2.2.1 Assumptions

We start by summarizing our assumptions about the properties of the incident field and the detector operation:

1. **The detector response is quadratic in the electromagnetic field.** This assumption, discussed in Section 2.1, means that, if the incoming field amplitude is scaled by some

factor $\lambda \in \mathbb{R}$, then the output P detector should scale as $|\lambda|^2$. Stated mathematically,

$$\boldsymbol{E}(\boldsymbol{r},t) \to \lambda \boldsymbol{E}(\boldsymbol{r},t) \;\; \forall \boldsymbol{r} \in \mathbb{R}^2, t \in \mathbb{R} \implies P \to |\lambda|^2 P, \tag{2.1}$$

where $\boldsymbol{r}$ is the transverse position on the reference surface through which we consider the incident power flow. Note that this operation is a multiplication by a scalar, and leaves the spatio-temporal state of coherence of the incident field unaltered.

2. **The detector output is proportional to the power absorbed in the device.** A well-defined sub-volume of the detector is sensitive to the incoming radiation and absorbs a fraction of it according to its optical response, as described in the first assumption. In other words, the detector output is linear in the power absorbed, and in turn in the incident optical power. For this reason, we may use the terms "absorbed power" and "detector output" nearly interchangeably, with the important caveat that these values have different units, respectively of power and of the measured quantity, such as a voltage or current.

3. **The incoming field has finite bandwidth.** The range of radiation frequencies considered ω satisfies $\omega \in [\omega_l; \omega_h]$, where $\omega_{l/h}$ respectively denote the lowest and highest signal frequencies. We remark that this is not a strict requirement, and Withington and Saklatvala demonstrated a more general theory applicable to detectors of all bandwidths [61]. We choose to apply the finite bandwidth assumption here as it offers useful simplifications, and because the practical applications considered in the rest of this dissertation fulfill this condition.

4. **The duration of measurement of the detector output is finite.** Again, this assumption is in line with realistic situations, where the instantaneous detector output is not generally measurable. We further remark that, because real detectors operate with finite response time, the true time-domain response function of detectors is most often time-integrated. The detector output is also independent of absolute time.

5. **A constraint on the detector output bandwidth ω_p is placed by the incident radiation frequency.** The spectral domain description of external radiation is often based on analytical signals, the use of which here is only valid if the following two conditions are fulfilled: $\omega_h < 3\omega_l$ and $\omega_p < \omega_h - \omega_l$, where $\omega_{l/h}$ are defined as in the assumption 3. In the case of long-term averaging, i.e. integration of signal over a duration much longer than these characteristic times, the conditions above can be replaced by $\omega_p < 2\omega_l$. As the detector output corresponds to the square of the incident signal's

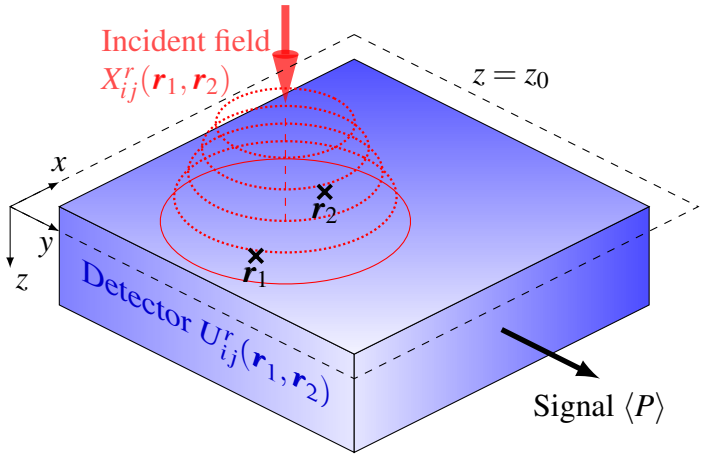

Fig. 2.1 Schematical representation of the detector volume, whose optical response is characterized by the two-point correlation tensor $U^r_{ij}(\boldsymbol{r}_1,\boldsymbol{r}_2)$, illuminated by an incident field, characterized by the corresponding dyadic $X^r_{ij}(\boldsymbol{r}_1,\boldsymbol{r}_2)$, at two points $\boldsymbol{r}_1$ and $\boldsymbol{r}_1$ on the detector surface $z = z_0$.

envelope function, this condition prohibits the detection of spectral components above $2\omega_l$ directly in the output.

6. **The incoming field has time-invariant statistics.** In most signals of interest, such as detecting thermal power at infrared wavelengths, electromagnetic sources are assumed to be temporally stationary. The formalism can be extended to non-stationary statistics, suitable for describing pulsed illuminating fields, but will not be done so here.

2.2.2 Generic Model of a Linear Detector

We first consider a standard result of linear systems theory [62], in order to introduce the necessary notation for the following derivation. The response $y(t)$ of a system with impulse response function $h(t,t_1)$ to a time-dependent excitation $x(t_1)$ is given by

$$y(t) = \int_{-\infty}^{+\infty} dt_1 h(t,t_1) x(t_1), \tag{2.2}$$

where the impulse response function h statisfies causality, i.e. $h(t,t_1) = 0$ for $t < t_1$. The response of the system at time t is written in Equation (2.2) as the weighted integral of the excitation over all times.

We need to extend this form to deal with the output of a device that measures power, and must therefore be quadratic in the incoming field. In stricter terms, the ratio of the detector output to the integrated Poynting flux must depend only on the form of the incoming field, rather than its magnitude. This implies that the detector output must be linear in

the correlation function $E_i^r(\boldsymbol{r}_1,t_1)E_j^r(\boldsymbol{r}_2,t_2)$, with $E_i^r(\boldsymbol{r},t)$ denoting the i^{th} component of the external field vector $\bar{\boldsymbol{E}}^r(\boldsymbol{r},t)$, where the ^{r} superscripts indicate that the fields are real-valued [61]. We extend Equation (2.2) to describe the output of any linear power detector in terms of generic real external fields $\boldsymbol{E}^r(\boldsymbol{r},t)$ and a detector bilinear response function $U_{ij}^r(t;\boldsymbol{r}_1,t_1;\boldsymbol{r}_2,t_2)$ at observation time t:

$$P(t)=\sum_{i,j}\iint_{\mathscr{S}^2}d^2\boldsymbol{r}_1d^2\boldsymbol{r}_2\iint_{-\infty}^{+\infty}dt_1dt_2U_{ij}^r(t;\boldsymbol{r}_1,t_1;\boldsymbol{r}_2,t_2)E_i^r(\boldsymbol{r}_1,t_1)E_j^r(\boldsymbol{r}_2,t_2), \tag{2.3}$$

where $\boldsymbol{r}_i$ with $i\in\{1,2\}$ stands for the transverse distance from the origin in some reference plane $\mathscr{S}$. Note here that the integration surface $\mathscr{S}$ can be chosen as convenient, for instance the detector plane or some intermediate plane to which the external field and detector response patterns are propagated. Figure 2.1 illustrates this configuration with the the incident field and detector response specified at two points $\boldsymbol{r}_1$ and $\boldsymbol{r}_2$ of the detector surface, defined by the constant $z=z_0$ plane. In the general case where the external fields are stochastic, we need to take the ensemble average of fields and obtain

$$\langle P(t)\rangle=\sum_{i,j}\iint_{\mathscr{S}^2}d^2\boldsymbol{r}_1d^2\boldsymbol{r}_2\iint_{-\infty}^{+\infty}dt_1dt_2U_{ij}^r(t;\boldsymbol{r}_1,t_1;\boldsymbol{r}_2,t_2)X_{ij}^r(\boldsymbol{r}_1,t_1;\boldsymbol{r}_2,t_2), \tag{2.4}$$

where we have defined $X_{ij}^r(\boldsymbol{r}_1,t_1;\boldsymbol{r}_2,t_2)=\langle E_i^r(\boldsymbol{r}_1,t_1)E_j^r(\boldsymbol{r}_2,t_2)\rangle$.

The fields $E_i^r(\boldsymbol{r},t)$ with finite duration and bandwidth, as stated in Assumptions 3 and 4 in Section 2.2.1, have the Fourier Transform definition in the frequency domain

$$E_i^r(\boldsymbol{r},t)=\frac{1}{2\pi}\int_{-\infty}^{+\infty}d\omega E_i^r(\boldsymbol{r},\omega)\exp(-i\omega t). \tag{2.5}$$

This leads to the transformation of the tensor X_{ij}^r,

$$X_{ij}^r(\boldsymbol{r}_1,t_1;\boldsymbol{r}_2,t_2)=\frac{1}{(2\pi)^2}\iint_{-\infty}^{+\infty}d\omega_1d\omega_2X_{ij}^r(\boldsymbol{r}_1,\omega_1;\boldsymbol{r}_2,\omega_2)\exp(-i\omega_1t_1)\exp(+i\omega_2t_2), \tag{2.6}$$

where $X_{ij}^r(\boldsymbol{r}_1,\omega_1;\boldsymbol{r}_2,\omega_2)=\langle E_i^r(\boldsymbol{r}_1,\omega_1)E_j^{r*}(\boldsymbol{r}_2,\omega_2)\rangle$. We can similarly transform the tensor U_{ij}^r representing the detector response:

$$U_{ij}^r(t;\boldsymbol{r}_1,t_1;\boldsymbol{r}_2,t_2)=\frac{1}{(2\pi)^2}\iint_{-\infty}^{+\infty}d\omega_1d\omega_2U_{ij}^r(t;\boldsymbol{r}_1,\omega_1;\boldsymbol{r}_2,\omega_2)\exp(-i\omega_1t_1)\exp(+i\omega_2t_2). \tag{2.7}$$

We substitute the forms in Equations (2.6) and (2.7) into Equation (2.4), evaluate the integrals with respect to times t_1 and t_2, and obtain

$$\langle P(t)\rangle = \frac{1}{(2\pi)^2}\sum_{i,j}\iint_{\mathscr{S}} d^2\boldsymbol{r}_1 d^2\boldsymbol{r}_2 \iint_{-\infty}^{+\infty} d\omega_1 d\omega_2 U_{ij}^{r*}(t;\boldsymbol{r}_1,\omega_1;\boldsymbol{r}_2,\omega_2) X_{ij}^{r}(\boldsymbol{r}_1,\omega_1;\boldsymbol{r}_2,\omega_2). \tag{2.8}$$

Because $E_i^r(\boldsymbol{r},t)$ is real-valued, $E_i^r(\boldsymbol{r},\omega)$ is Hermitian, i.e. $E_i^r(\boldsymbol{r},-\omega) = E_i^{r*}(\boldsymbol{r},\omega)$. This also implies that X_{ij}^r is Hermitian as well. By noting that $\langle P(t)\rangle$ in Equation (2.8) is real, it must be that U_{ij}^{r*} is also Hermitian. Therefore, we can split both integrals with respect to angular frequencies ω_1 and ω_2 in Equation (2.8), with

$$\begin{aligned}&\iint_{-\infty}^{0} d\omega_1 d\omega_2 U_{ij}^{r*}(t;\boldsymbol{r}_1,\omega_1;\boldsymbol{r}_2,\omega_2) X_{ij}^{r}(\boldsymbol{r}_1,\omega_1;\boldsymbol{r}_2,\omega_2)\\ &\quad= \left(\iint_{0}^{+\infty} d\omega_1 d\omega_2 U_{ij}^{r*}(t;\boldsymbol{r}_1,\omega_1;\boldsymbol{r}_2,\omega_2) X_{ij}^{r}(\boldsymbol{r}_1,\omega_1;\boldsymbol{r}_2,\omega_2)\right)^*.\end{aligned} \tag{2.9}$$

But because the integral is real and both field correlation tensors in the integrand are Hermitian, the equality holds even without the complex conjugation. Therefore, we obtain

$$\langle P(t)\rangle = \frac{2}{(2\pi)^2}\sum_{i,j}\iint_{\mathscr{S}^2} d^2\boldsymbol{r}_1 d^2\boldsymbol{r}_2 \iint_{0}^{+\infty} d\omega_1 d\omega_2 U_{ij}^{*}(t;\boldsymbol{r}_1,\omega_1;\boldsymbol{r}_2,\omega_2) X_{ij}(\boldsymbol{r}_1,\omega_1;\boldsymbol{r}_2,\omega_2), \tag{2.10}$$

where the ^{r} superscripts can be suppressed by recognizing that we can now equivalently work with complex analytic fields, instead of real fields, defined as

$$E_i(\boldsymbol{r},\omega) = \begin{cases} E_i^r(\boldsymbol{r},\omega) & ,\ \omega \geq 0 \\ 0 & ,\ \omega < 0. \end{cases} \tag{2.11}$$

Analytical signals arise in optics when time-domain signals are reconstructed only from their positive-frequency spectrum. The use of analytical signals is valid only as long as Assumption 5 in Section 2.2.1 is fulfilled. As the detector response and external field correlation functions U_{ij} and X_{ij} are second-order tensors, we can simplify our notation by using their dyadic representations [63]. Recalling the dyadic property $\sum_{i,j} A_{ji}^* B_{ij} = \overline{\overline{\mathbf{A}}}^{\dagger} \cdot\cdot\, \overline{\overline{\mathbf{B}}}$, where † denotes the conjugate transpose operator, Equation (2.10) becomes

$$\langle P(t)\rangle = \frac{2}{(2\pi)^2}\iint_{\mathscr{S}^2} d^2\boldsymbol{r}_1 d^2\boldsymbol{r}_2 \iint_{-\infty}^{+\infty} d\omega_1 d\omega_2 \overline{\overline{\mathbf{U}}}^{\dagger}(t;\boldsymbol{r}_1,\omega_1;\boldsymbol{r}_2,\omega_2) \cdot\cdot\, \overline{\overline{\mathbf{X}}}(\boldsymbol{r}_1,\omega_1;\boldsymbol{r}_2,\omega_2). \tag{2.12}$$

Assume now that the incoming fields are statistically stationary. This violates the finite duration assumption (Assumption 4) in general, but since we only record the detector output for a finite amount of time in practice, we continue without loss of generality:

$$\begin{aligned}\overline{\overline{\mathbf{X}}}(\boldsymbol{r}_1,\omega_1;\boldsymbol{r}_2,\omega_2) &= \iint_{-\infty}^{+\infty} dt_1 dt_2 \overline{\overline{\mathbf{X}}}(\boldsymbol{r}_1,0;\boldsymbol{r}_2,t_2-t_1)\exp(+i\omega_1 t_1)\exp(-i\omega_2 t_2)\\ &= 2\pi\delta(\omega_1-\omega_2)\int_{-\infty}^{+\infty} du \overline{\overline{\mathbf{X}}}(\boldsymbol{r}_1,0;\boldsymbol{r}_2,u)\exp(-i\omega_2 u)\\ &= 2\pi\delta(\omega_1-\omega_2)\overline{\overline{\mathbf{X}}}(\boldsymbol{r}_1,\boldsymbol{r}_2,\omega_2). \end{aligned} \tag{2.13}$$

Substituting into (2.12), we obtain

$$\langle P(t)\rangle = \frac{1}{\pi}\iint_{\mathscr{S}^2} d^2\boldsymbol{r}_1 d^2\boldsymbol{r}_2 \int_0^{+\infty} d\omega\, \overline{\overline{\mathbf{U}}}^{\dagger}(t;\boldsymbol{r}_1,\omega;\boldsymbol{r}_2,\omega)\cdot\cdot\overline{\overline{\mathbf{X}}}(\boldsymbol{r}_1,\boldsymbol{r}_2,\omega). \tag{2.14}$$

We can directly introduce the finite measurement duration, using some temporal filtering function $h(t)$, such as a top-hat function for an ideal finite-duration measurement, and write the integrated detector output P as follows:

$$\begin{aligned}\langle P\rangle &= \int_{-\infty}^{+\infty} dt h(t)\langle P(t)\rangle\\ &= \frac{1}{\pi}\iint_{\mathscr{S}^2} d^2\boldsymbol{r}_1 d^2\boldsymbol{r}_2 \int_0^{+\infty} d\omega \left(\int_{-\infty}^{+\infty} dt h(t)\overline{\overline{\mathbf{U}}}^{\dagger}(t;\boldsymbol{r}_1,\omega;\boldsymbol{r}_2,\omega)\right)\cdot\cdot\overline{\overline{\mathbf{X}}}(\boldsymbol{r}_1,\boldsymbol{r}_2,\omega)\\ &= \frac{1}{\pi}\iint_{\mathscr{S}^2} d^2\boldsymbol{r}_1 d^2\boldsymbol{r}_2 \int_0^{+\infty} d\omega \overline{\overline{\mathbf{V}}}^{\dagger}(\boldsymbol{r}_1,\boldsymbol{r}_2,\omega)\cdot\cdot\overline{\overline{\mathbf{X}}}(\boldsymbol{r}_1,\boldsymbol{r}_2,\omega), \end{aligned} \tag{2.15}$$

where we have defined the time-integrated response function as

$$\overline{\overline{\mathbf{V}}}(\boldsymbol{r}_1,\boldsymbol{r}_2,\omega) := \int_{-\infty}^{+\infty} dt h(t)\overline{\overline{\mathbf{U}}}(t;\boldsymbol{r}_1,\omega;\boldsymbol{r}_2,\omega). \tag{2.16}$$

Note that, instead of taking the time-integrated output, we could have considered the time-averaged output, by inserting a factor of $1/\int_{-\infty}^{+\infty} dt h(t)$. However, this factor can just as well be included in the definition of $\overline{\overline{\mathbf{V}}}$, such that the formalism is identical.

For single-frequency sources, the frequency-domain ω-dependence can be discarded (or more generally, integrated into the definitions of the dyadics). In order to indicate explicitly that the detector response and external field only contain a single frequency ω_0, we relabel

their dyadics as

$$\overline{\overline{\mathbf{D}}}(\boldsymbol{r}_1,\boldsymbol{r}_2) := \overline{\overline{\mathbf{X}}}(\boldsymbol{r}_1,\boldsymbol{r}_2,\omega=\omega_0) \tag{2.17}$$

$$\overline{\overline{\mathbf{E}}}(\boldsymbol{r}_1,\boldsymbol{r}_2) := \overline{\overline{\mathbf{V}}}(\boldsymbol{r}_1,\boldsymbol{r}_2,\omega=\omega_0). \tag{2.18}$$

We then obtain

$$\langle P\rangle = \iint_{\mathscr{S}^2} d^2\boldsymbol{r}_1 d^2\boldsymbol{r}_2 \overline{\overline{\mathbf{D}}}^{\dagger}(\boldsymbol{r}_1,\boldsymbol{r}_2)\cdot\cdot\overline{\overline{\mathbf{E}}}(\boldsymbol{r}_1,\boldsymbol{r}_2), \tag{2.19}$$

where we have used the relabeled detector response and external field dyadics $\overline{\overline{\mathbf{D}}}$ and $\overline{\overline{\mathbf{E}}}$. Equation (2.19) allows us to write the output of a (potentially partially-coherent) detector illuminated by a temporally stationary external field as the full contraction of two dyadics; $\overline{\overline{\mathbf{E}}}(\boldsymbol{r}_1,\boldsymbol{r}_2)$ represents the state of spatial coherence of the incident field, and $\overline{\overline{\mathbf{D}}}(\boldsymbol{r}_1,\boldsymbol{r}_2)$ represents the state of coherence of the detector response. As such, the latter will be referred to as the Detector Response Function (DRF) throughout this manuscript. The DRF can also be interpreted as the state of coherence of the incident field to which the detector is maximally sensitive; in other words, for a given incident intensity, the power absorbed is maximal when $\overline{\overline{\mathbf{D}}} \propto \overline{\overline{\mathbf{E}}}$. We can also understand the full contraction in Equation (2.19) as the inner product between the two dyadics in the vector space of complex, bilinear, three-dimensional vector fields, as projected on the reference surface $\mathscr{S}$. This inner product is then maximal when the two dyadics are parallel in this vector space. It is important here to recall that we have only made one supposition about the detector response, namely that it is linear with incoming electromagnetic radiation. No assumptions have been made about the nature of its absorption mechanisms, such as the creation of an electron-hole pair in the depletion region of a PIN photodiode or the breaking of superconducting Cooper Pairs in a Kinetic Inductance Detector; nor about its geometry or type, for instance whether the absorptive region of the detector is a thin film structure or a bulk volume of material.

Note that the form in Equation (2.19) is cast in a position-dependent representation, but wavevector and directional forms are analogous. In particular, in the far-field limit, we can view the problem in the Fourier domain by using transverse wave-vectors $\boldsymbol{k}$:

$$\overline{\overline{\mathbf{D}}}(\boldsymbol{r}_1,\boldsymbol{r}_2) = \frac{1}{(2\pi)^2}\iint_{-\infty}^{+\infty} d^2\boldsymbol{k}_1 d^2\boldsymbol{k}_2 \overline{\overline{\mathbf{D}}}(\boldsymbol{k}_1,\boldsymbol{k}_2)\exp(i\boldsymbol{k}_2.\boldsymbol{r}_2)\exp(-i\boldsymbol{k}_1.\boldsymbol{r}_1) \tag{2.20}$$

$$\overline{\overline{\mathbf{E}}}(\boldsymbol{r}_1,\boldsymbol{r}_2) = \frac{1}{(2\pi)^2}\iint_{-\infty}^{+\infty} d^2\boldsymbol{k}_1 d^2\boldsymbol{k}_2 \overline{\overline{\mathbf{E}}}(\boldsymbol{k}_1,\boldsymbol{k}_2)\exp(i\boldsymbol{k}_2.\boldsymbol{r}_2)\exp(-i\boldsymbol{k}_1.\boldsymbol{r}_1). \tag{2.21}$$

Moreover, we can use unit vectors of direction of propagation $\hat{\boldsymbol{\Omega}} = \sin(\theta)\cos(\phi)\hat{\boldsymbol{x}} + \sin(\theta)\sin(\phi)\hat{\boldsymbol{y}} + \cos(\theta)\hat{\boldsymbol{z}}$ rather than transverse wave-vectors $\boldsymbol{k} = -2\pi\omega/c(\hat{\boldsymbol{x}}\hat{\boldsymbol{x}} + \hat{\boldsymbol{y}}\hat{\boldsymbol{y}})\cdot\hat{\boldsymbol{\Omega}}$, where c is the speed

of light in a vacuum, such that

$$\langle P \rangle = \iint_{\mathscr{S}^2} d\hat{\boldsymbol{\Omega}}_1 d\hat{\boldsymbol{\Omega}}_2 \, \overline{\overline{\mathbf{D}}}^{\dagger}(\hat{\boldsymbol{\Omega}}_1, \hat{\boldsymbol{\Omega}}_2) \cdot\cdot \overline{\overline{\mathbf{E}}}(\hat{\boldsymbol{\Omega}}_1, \hat{\boldsymbol{\Omega}}_2), \tag{2.22}$$

where all constant factors are inserted into the definition of $\overline{\overline{\mathbf{D}}}$ and $\overline{\overline{\mathbf{E}}}$.

2.3 Coupled-Mode Formulation

2.3.1 Mercer's Theorem

In Chapter 1, we discussed the concept of modes by addressing the terms "single-mode", "few-mode" and "multi-mode" that are often present in the literature. Our definition of modes was then as an orthonormal basis for describing a general state of coherence, and we noted that the concept would be applied to both the incoming field correlation function and the detector response function. Here, we provide a formal mathematical description of the origin and properties of these modes. Representing partially coherent field as coherent-mode sums was first introduced by Wolf [40, 41]. Note that we consider only traveling waves for the incident field such that it does not possess an evanescent component, although this generalization has been accomplished [64].

Using the notation in Equation (2.19), we recall that the field correlation dyadic is written in terms of the external analytical fields as $\overline{\overline{\mathbf{E}}}(\boldsymbol{r}_1, \boldsymbol{r}_2) = \langle \boldsymbol{E}(\boldsymbol{r}_1)\boldsymbol{E}(\boldsymbol{r}_2)\rangle$. We assume nothing about the fields $\boldsymbol{E}(\boldsymbol{r})$, which could be partially coherent. Hence we wish to expand $\overline{\overline{\mathbf{E}}}$ as an incoherent superposition of a set of fully spatially coherent fields $\boldsymbol{U}_m(\boldsymbol{r})$, known as the coherent or natural modes of the field, defined by the eigenvalue equation

$$\beta_m \boldsymbol{U}_m(\boldsymbol{r}_1) = \int_{\mathscr{S}} d^2\boldsymbol{r}_2 \overline{\overline{\mathbf{E}}}(\boldsymbol{r_1}, \boldsymbol{r_2}) \cdot \boldsymbol{U}_m(\boldsymbol{r}_2) \tag{2.23}$$

$$\iff \beta_m \delta_{mn} = \iint_{\mathscr{S}^2} d^2\boldsymbol{r}_1 d^2\boldsymbol{r}_2 \boldsymbol{U}_n^*(\boldsymbol{r}_1) \cdot \overline{\overline{\mathbf{E}}}(\boldsymbol{r}_1, \boldsymbol{r}_2) \cdot \boldsymbol{U}_m(\boldsymbol{r}_2), \tag{2.24}$$

where

$$\int_{\mathscr{S}} d^2\boldsymbol{r} \boldsymbol{U}_m^*(\boldsymbol{r}) \cdot \boldsymbol{U}_n(\boldsymbol{r}) = \delta_{mn} \qquad \forall m, n. \tag{2.25}$$

It is now important to investigate how these modes are related to the detector and field correlation dyadics. They appear naturally in this context in Mercer's Theorem, which is stated as follows [65]:

Theorem 1 (Mercer's Theorem)**.** *Let A be the integral operator on $L_2[a,b]$, with a,b finite,*

$$y(s) = \int_a^b R(s,t)x(t)dt, \quad a \leq t \leq b,$$

corresponding to a real-valued function R that is continuous, symmetric, and non-negative definite. Let $\{e_n,\ n = 1,2,\ldots\}$ be an orthonormal basis for the space spanned by the eigenvectors corresponding to the nonzero (hence positive) eigenvalues of A. If the basis is taken so that e_n is an eigenvector corresponding to the eigenvalue λ_n, then

$$R(s,t) = \sum_{n=1}^{\infty} \lambda_n e_n(s)\, e_n(t)$$

where the series converges absolutely, converges to $R(s,t)$ uniformly in both variables, and also converges to $R(s,t) \in L_2([a,b] \times [a,b])$.

Theorem 1 proves that dyadics such as the correlation functions discussed admit such a decomposition, in a way that is analogous to matrix diagonalization. The eigenfunctions and eigenvalues are precisely those defined by Equation (2.24). Note that Theorem 1 is a special case of the Hilbert-Schmidt decomposition: in the latter, the dyadic function is separated over two distinct inner product spaces [66]. The Hilbert-Schmidt decomposition is then the dyadic analogue of the Singular Value Decomposition for matrices.

We can notice several properties of the correlation dyadic $\overline{\overline{\mathbf{E}}}(\boldsymbol{r}_1,\boldsymbol{r}_2)$, the first of which is Hermicity, by definition using the exchange symmetry of the fields $\boldsymbol{E}(\boldsymbol{r})$:

$$\overline{\overline{\mathbf{E}}}^{\dagger}(\boldsymbol{r}_1,\boldsymbol{r}_2) = \overline{\overline{\mathbf{E}}}(\boldsymbol{r}_2,\boldsymbol{r}_1). \tag{2.26}$$

We also know that $\overline{\overline{\mathbf{E}}}(\boldsymbol{r}_1,\boldsymbol{r}_2)$ is continuous with respect to $\boldsymbol{r}_1$ and $\boldsymbol{r}_2$, which implies that

$$\iint d^2\boldsymbol{r}_1 d^2\boldsymbol{r}_2 \bar{\bar{\mathbf{I}}} \cdot \cdot \overline{\overline{\mathbf{E}}}(\boldsymbol{r}_1,\boldsymbol{r}_2) \leq \infty \tag{2.27}$$

We further remark that, for any modulus-squared integrable function $\boldsymbol{f}(\boldsymbol{r}) \in L^2[a,b]$,

$$\langle \left| \int d^2\boldsymbol{r} \boldsymbol{f}^*(\boldsymbol{r}) \cdot \mathbf{E}(\boldsymbol{r}) \right|^2 \rangle \geq 0, \tag{2.28}$$

in the Hilbert space of complex vector functions, subject to the following definition of the inner product $\circ$:

$$\boldsymbol{f}(\boldsymbol{r}) \circ \boldsymbol{g}(\boldsymbol{r}) = \int d^2\boldsymbol{r} \boldsymbol{f}^*(\boldsymbol{r}) \cdot \boldsymbol{g}(\boldsymbol{r}). \tag{2.29}$$

Rearranging Equation (2.28), we obtain that

$$\iint d^2\boldsymbol{r}_1 d^2\boldsymbol{r}_2 \boldsymbol{f}^*(\boldsymbol{r}_1)\cdot\overline{\overline{\mathbf{E}}}(\boldsymbol{r}_1,\boldsymbol{r}_2)\cdot\boldsymbol{f}(\boldsymbol{r}_2)\geq 0. \tag{2.30}$$

$\overline{\overline{\mathbf{E}}}(\boldsymbol{r}_1,\boldsymbol{r}_2)$ therefore fulfills all of the properties of a Hermitian, positive semi-definite Hilbert-Schmidt operator.

The detector response dyadic $\overline{\overline{\mathbf{D}}}(\boldsymbol{r}_1,\boldsymbol{r}_2)$ can be shown to have the same properties. Using the Hermicity of $\overline{\overline{\mathbf{E}}}(\boldsymbol{r}_1,\boldsymbol{r}_2)$ and noting that the absorbed power in Equation (2.19) is real, it follows that $\overline{\overline{\mathbf{D}}}(\boldsymbol{r}_1,\boldsymbol{r}_2)$ is also Hermitian:

$$\overline{\overline{\mathbf{D}}}^{\dagger}(\boldsymbol{r}_1,\boldsymbol{r}_2)=\overline{\overline{\mathbf{D}}}(\boldsymbol{r}_2,\boldsymbol{r}_1). \tag{2.31}$$

In [53], Saklatvala proved the continuity of the detector output, by arguing that the change in detector output arising from an infinitesimal change in the incident field could not be discontinuous, which requires that

$$\iint d^2\boldsymbol{r}_1 d^2\boldsymbol{r}_2 \bar{\bar{\mathbf{I}}}\cdot\cdot\overline{\overline{\mathbf{D}}}(\boldsymbol{r}_1,\boldsymbol{r}_2)\leq\infty. \tag{2.32}$$

Finally, following the properties of modulus-squared integrable functions as in Equation (2.28), we can set $\boldsymbol{f}(\boldsymbol{r})=\mathbf{E}(\boldsymbol{r})$. Because the detected power in Equation (2.19) is non-negative, it is required that

$$\iint d^2\boldsymbol{r}_1 d^2\boldsymbol{r}_2 \boldsymbol{f}^*(\boldsymbol{r}_1)\cdot\overline{\overline{\mathbf{D}}}(\boldsymbol{r}_1,\boldsymbol{r}_2)\cdot\boldsymbol{f}(\boldsymbol{r}_2)\geq 0. \tag{2.33}$$

Applying Mercer's Theorem to the incident radiation and detector response dyadics, they can be written in diagonalized form, as follows:

$$\overline{\overline{\mathbf{E}}}(\boldsymbol{r}_1,\boldsymbol{r}_2)=\sum_n \beta_n \boldsymbol{U}_n(\boldsymbol{r}_1)\boldsymbol{U}_n^*(\boldsymbol{r}_2) \tag{2.34}$$

$$\overline{\overline{\mathbf{D}}}(\boldsymbol{r}_1,\boldsymbol{r}_2)=\sum_m \alpha_m \boldsymbol{R}_m(\boldsymbol{r}_1)\boldsymbol{R}_m^*(\boldsymbol{r}_2), \tag{2.35}$$

where $\boldsymbol{U}_n$ is defined as previously in Equation (2.24), and $\boldsymbol{R}_m$ is recognized as the m^{th} natural mode of the detector's reception pattern. The complex coefficients β_n and α_n in these decompositions are respectively the occupancy of the n^{th} field mode and the sensitivity of the m^{th} detector mode. We have effectively decomposed the tensors representing the states of coherence of the incident field and detector response into a weighted sum of outer products of waveforms on a two-dimensional surface. The field modes in Equation (2.34) correspond

to the field patterns incident on the surface of interest $\mathscr{S}$, for instance the detector surface; the detector modes in Equation (2.35) are the propagating field patterns to which the detector is sensitive.

Mandel and Wolf also provide a formal demonstration that the modes are indeed fully coherent in the spatial (and space-frequency) domain [9]. By taking the Fourier Transform of the wave equation on the time-dependent external field dyadic $\overline{\overline{\mathbf{E}}}$, it can be shown that it satisfies the two Helmholtz equations:

$$\nabla_1 \overline{\overline{\mathbf{E}}}(\boldsymbol{r}_1, \boldsymbol{r}_2) + k^2 \overline{\overline{\mathbf{E}}}(\boldsymbol{r}_1, \boldsymbol{r}_2) = 0 \tag{2.36}$$

$$\nabla_2 \overline{\overline{\mathbf{E}}}(\boldsymbol{r}_1, \boldsymbol{r}_2) + k^2 \overline{\overline{\mathbf{E}}}(\boldsymbol{r}_1, \boldsymbol{r}_2) = 0. \tag{2.37}$$

where $k = 2\pi\omega/c$ is the wavenumber associated with the frequency ω, and $\nabla_{1/2}$ denote the vector differential operator along $\boldsymbol{r}_{1/2}$ respectively. Defining $\overline{\overline{\mathbf{E}}}^{(n)}(\boldsymbol{r}_1, \boldsymbol{r}_2) = \boldsymbol{U}_n(\boldsymbol{r}_1)\boldsymbol{U}_n^*(\boldsymbol{r}_2)$, it is proven that $\overline{\overline{\mathbf{E}}}^{(n)}$ also satisfies the two Helmholtz equations:

$$\nabla_1 \overline{\overline{\mathbf{E}}}^{(n)}(\boldsymbol{r}_1, \boldsymbol{r}_2) + k^2 \overline{\overline{\mathbf{E}}}^{(n)}(\boldsymbol{r}_1, \boldsymbol{r}_2) = 0 \tag{2.38}$$

$$\nabla_2 \overline{\overline{\mathbf{E}}}^{(n)}(\boldsymbol{r}_1, \boldsymbol{r}_2) + k^2 \overline{\overline{\mathbf{E}}}^{(n)}(\boldsymbol{r}_1, \boldsymbol{r}_2) = 0. \tag{2.39}$$

This implies that $\overline{\overline{\mathbf{E}}}^{(n)}$ represents a mode of the field, and therefore that Equations (2.34) and (2.35) describe the field and detector response correlation functions as a weighted superposition of fully-coherent modes.

2.3.2 Coupling Field and Detector Modes

Substituting the two dyadic decompositions in Equations (2.34) and (2.35) into Equation (2.19) describing the detector output as the contraction of these two dyadics, and using the Hermicity of $\overline{\overline{\mathbf{D}}}$, $\overline{\overline{\mathbf{D}}}^{\dagger}(\boldsymbol{r}_1, \boldsymbol{r}_2) = \overline{\overline{\mathbf{D}}}(\boldsymbol{r}_2, \boldsymbol{r}_1)$, we obtain

$$\begin{aligned}
\langle P \rangle &= \iint_{\mathscr{S}^2} d^2\boldsymbol{r}_1 d^2\boldsymbol{r}_2 \left(\sum_m \alpha_m \boldsymbol{R}_m(\boldsymbol{r}_2) \boldsymbol{R}_m^*(\boldsymbol{r}_1) \right) \cdot\cdot \left(\sum_n \beta_n \boldsymbol{U}_n(\boldsymbol{r}_1) \boldsymbol{U}_n^*(\boldsymbol{r}_2) \right) \\
&= \sum_{m,n} \alpha_m \beta_n \left(\int_{\mathscr{S}} d^2\boldsymbol{r}_1 \boldsymbol{R}_m^*(\boldsymbol{r}_1) \cdot \boldsymbol{U}_n(\boldsymbol{r}_1) \right) \left(\int_{\mathscr{S}} d^2\boldsymbol{r}_2 \boldsymbol{R}_m(\boldsymbol{r}_2) \cdot \boldsymbol{U}_n^*(\boldsymbol{r}_2) \right) \\
&= \sum_{m,n} \alpha_m \beta_n |S_{mn}|^2,
\end{aligned} \tag{2.40}$$

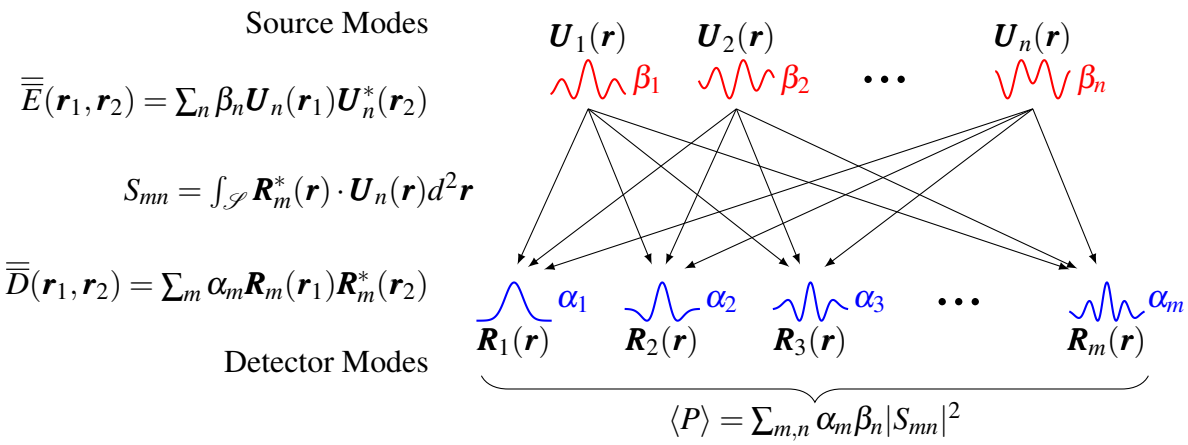

Fig. 2.2 Schematic representation of the coupled-mode formulation.

where

$$S_{mn} = \int_{\mathscr{S}} d^2\boldsymbol{r} \boldsymbol{R}_m^*(\boldsymbol{r}) \cdot \boldsymbol{U}_n(\boldsymbol{r}) \tag{2.41}$$

is the overlap between natural mode m of the detector and natural mode n of the field. Equation (2.40) then expresses the power absorbed by the detector as a weighted sum of overlap integrals of field and detector modes; the sum is over all field and detector mode combinations and the weighting is given by the product of the relevant field mode occupancy and detector mode sensitivity. The overlap integral defined by Equation (2.41) can be understood as the complex coupling coefficients of the natural modes of the external field with those of the detector response. Figure 2.2 depicts the coupled-mode model schematically. In other words, the coupled-mode formulation allows us to substitute the propagation of two-point correlation functions for the propagation of sets of fully coherent fields.

Equation (2.40) also provides an expression for the minimum number of degrees of freedom required to reconstruct the detector output. In particular, if the incident field is single-moded, the detector output and detector response will have the same number of degrees of freedom, namely the number of terms in the decomposition of Equation (2.35).

2.3.3 Fully Coherent Detector

We now consider the two extreme cases, fully coherent and fully incoherent detectors, discussed in Section 1.1. Here, we consider the former, whose coherence tensor can be decomposed using Mercer's Theorem with only one mode and corresponding eigenvalue:

$$\overline{\overline{\mathbf{D}}}(\boldsymbol{r}_1,\boldsymbol{r}_2) = \alpha \boldsymbol{R}(\boldsymbol{r}_1)\boldsymbol{R}^*(\boldsymbol{r}_2). \tag{2.42}$$

Substituting in Equation (2.19), the detector output becomes

$$\langle P \rangle = \alpha \left| \int_{\mathscr{S}} d^2 \boldsymbol{r} \boldsymbol{R}(\boldsymbol{r}) \cdot \boldsymbol{E}(\boldsymbol{r}) \right|^2 . \tag{2.43}$$

This corresponds to the standard form describing single-mode systems, as is found for instance in the literature on antennas [60].

2.3.4 Fully Incoherent Detector

At the other extreme, we consider the response of a fully incoherent detector. Its response tensor is

$$\overline{\overline{\mathbf{D}}}(\boldsymbol{r}_1, \boldsymbol{r}_2) = \delta(\boldsymbol{r}_1, \boldsymbol{r}_2) \lambda(\boldsymbol{r}_1), \tag{2.44}$$

where $\lambda(\boldsymbol{r})$ denotes the position-dependent sensitivity of the detector response. We can then write the detector output as

$$\langle P \rangle = \int_{\mathscr{S}} d^2 \boldsymbol{r} \lambda(\boldsymbol{r}) I(\boldsymbol{r}) \tag{2.45}$$

where $I(\boldsymbol{r}) = |E(\boldsymbol{r})|^2$ describes the position-dependent intensity of the external radiation of complex amplitude $E(\boldsymbol{r})$. This is again in agreement with the standard form describing a fully incoherent system such as bolometers, where the power absorbed is the surface-integrated product of the incident intensity with the absorber sensitivity.

It is important here to emphasize that, because detectors are in general neither fully coherent nor incoherent, the full expressions described in this chapter are necessary to describe the full range of modal behaviors. This illustrates the importance of the coupled-mode model.

2.4 Two Phase-Locked Sources Configuration

We now have two formulations at our disposal to express the power absorbed by a generic detector in terms of the incident field and the detector's optical response. It is important here to note that we have made no assumption regarding the physical origin of the incident field. We can therefore investigate the case where the external field is generated by two sources; we suppose only that they are phase-locked and individually fully-coherent, but make no assumption regarding their origin or specific spatial forms.

Consider N positions in space to which each source can be moved, with corresponding non-orthogonal vector field set $\mathbb{E} = \{\boldsymbol{e}_n(\boldsymbol{r}), \forall n \in \{1, ..., N\}\}$, where $\boldsymbol{e}_n(\boldsymbol{r})$ is the field produced by a source at position $\boldsymbol{r}_n$ as measured at the point $\boldsymbol{r}$ of the surface $\mathscr{S}$. The configuration is

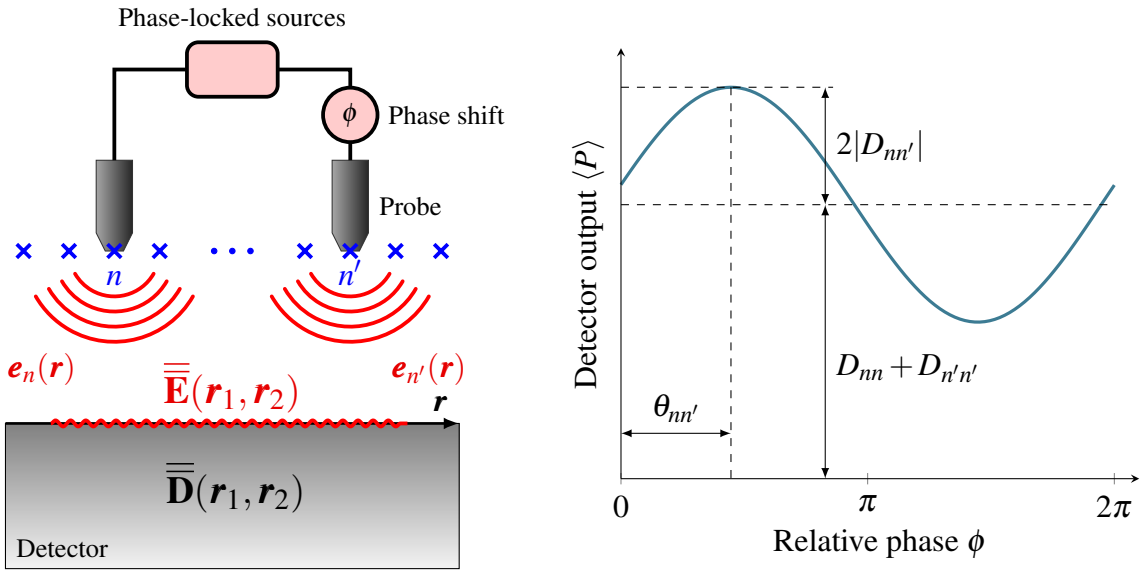

(a) Experimental configuration

(b) Fringe pattern

Fig. 2.3 Configuration for an EAI experiment using two coherent, phase-locked sources; rotation of their relative phase yields a fringe pattern in the detector output.

summarized in Figure 2.3. The elements of $\overline{\overline{\mathbf{D}}}(\boldsymbol{r}_1,\boldsymbol{r}_2)$ in the basis $\mathbb{E}$ are

$$D_{nn'} = \iint_{\mathscr{S}^2} d^2\boldsymbol{r}_1 d^2\boldsymbol{r}_2 \boldsymbol{e}_n^*(\boldsymbol{r}_1)\cdot\overline{\overline{\mathbf{D}}}(\boldsymbol{r}_1,\boldsymbol{r}_2)\cdot\boldsymbol{e}_{n'}(\boldsymbol{r}_2). \tag{2.46}$$

Because the elements of the set $\mathbb{E}$ are not necessarily mutually orthogonal, we reconstruct $\overline{\overline{\mathbf{D}}}(\boldsymbol{r}_1,\boldsymbol{r}_2)$ via

$$\overline{\overline{\mathbf{D}}}(\boldsymbol{r}_1,\boldsymbol{r}_2) \approx \sum_{n,n'} D_{nn'}\tilde{\boldsymbol{e}}_n(\boldsymbol{r}_1)\tilde{\boldsymbol{e}}_{n'}^*(\boldsymbol{r}_2), \tag{2.47}$$

where $\tilde{\mathbb{E}} = \{\tilde{\boldsymbol{e}}_n(\boldsymbol{r}), \forall n \in \{1,...,N\}\}$ is the dual set of $\mathbb{E}$ [67]. The utilization of the dual vectors $\tilde{\boldsymbol{e}}_n(\boldsymbol{r})$ is necessary because we do not know whether the basis $\mathbb{E}$ is undercomplete, perfectly complete or overcomplete. Moreover, Equation (2.47) is an equality only if the basis $\mathbb{E}$, and hence its dual $\tilde{\mathbb{E}}$, is complete or overcomplete. By column-wise concatenating the vectors $\boldsymbol{e}_n(\boldsymbol{r})$ into a matrix $\mathbf{E}$, the completeness of the basis $\mathbb{E}$ can be assessed by considering the so-called "frame" matrix, defined as

$$\mathbf{S} = \mathbf{E}\mathbf{E}^\dagger = \sum_{k=1}^{N} \boldsymbol{e}_k \boldsymbol{e}_k^\dagger, \tag{2.48}$$

which is the sum of all outer products of the vectors of the basis $\mathbb{E}$ with their respective conjugate transpose. Because $\mathbf{S}$ is not generally invertible, we consider its pseudoinverse

$\tilde{\mathbf{S}}^{-1}$, which can be obtained by minimizing the residual $\varepsilon = \|\tilde{\mathbf{S}}^{-1}\mathbf{S} - \mathbf{I}\|$, where $\mathbf{I}$ denotes the identity matrix. The property $\tilde{\mathbf{S}}^{-1} = \mathbf{S}^{-1}$ only holds when $\mathbf{S}$ is invertible. The dual basis vectors $\tilde{\boldsymbol{e}}_n(\boldsymbol{r})$ can then be defined as

$$\tilde{\boldsymbol{e}}_n(\boldsymbol{r}) = \tilde{\mathbf{S}}^{-1}\boldsymbol{e}_n(\boldsymbol{r}). \tag{2.49}$$

We can note that the duals defined in this way only satisfy the orthogonality condition

$$\int_{\mathscr{S}} d^2\boldsymbol{r}\, \tilde{\boldsymbol{e}}_m^*(\boldsymbol{r})\boldsymbol{e}_n(\boldsymbol{r}) = \int_{\mathscr{S}} d^2\boldsymbol{r}\, \tilde{\boldsymbol{e}}_m(\boldsymbol{r})\boldsymbol{e}_n^*(\boldsymbol{r}) = \delta_{mn} \tag{2.50}$$

if the basis $\mathbb{E}$ is linearly independent. It is also important to remark that the dimensionality of the matrix of singular values $\mathbf{S}$ will be set by some sampling of the reference surface $\mathscr{S}$, which will be discussed in Section 2.5; up to now, this dimensionality has been assumed to be infinite, such that the sampling of the reference surface can be considered continuous.

Then, assuming two sources are respectively at positions labeled n and n', we can write the total field $\boldsymbol{E}(\boldsymbol{r})$ as

$$\boldsymbol{E}(\boldsymbol{r}) = \boldsymbol{e}_n(\boldsymbol{r}) + \boldsymbol{e}_{n'}(\boldsymbol{r})e^{i\phi}, \tag{2.51}$$

where ϕ is the relative phase of the sources. The correlation dyadic can then be written as

$$\begin{aligned}\overline{\overline{\mathbf{E}}}(\boldsymbol{r_1},\boldsymbol{r_2}) =& \{\boldsymbol{e}_n(\boldsymbol{r}_1) + \boldsymbol{e}_{n'}(\boldsymbol{r}_1)e^{i\phi}\} \times \{\boldsymbol{e}_n(\boldsymbol{r}_2) + \boldsymbol{e}_{n'}(\boldsymbol{r}_2)e^{i\phi}\}^* \\ =& \boldsymbol{e}_n(\boldsymbol{r}_1)\boldsymbol{e}_n^*(\boldsymbol{r}_2) + \boldsymbol{e}_n(\boldsymbol{r}_1)\boldsymbol{e}_{n'}^*(\boldsymbol{r}_2)e^{-i\phi} + \boldsymbol{e}_{n'}(\boldsymbol{r}_1)\boldsymbol{e}_n^*(\boldsymbol{r}_2)e^{i\phi} + \boldsymbol{e}_{n'}(\boldsymbol{r}_1)\boldsymbol{e}_{n'}^*(\boldsymbol{r}_2).\end{aligned} \tag{2.52}$$

Substituting into Equation (2.19),

$$\begin{aligned}\langle P\rangle = \iint_{\mathscr{S}^2} d^2\boldsymbol{r}_1 d^2\boldsymbol{r}_2 \Big(\sum_{m,m'} D_{mm'}\tilde{\boldsymbol{e}}_m(\boldsymbol{r}_1)\tilde{\boldsymbol{e}}_{m'}^*(\boldsymbol{r}_2)\Big)^\dagger \cdot\cdot \Big(&\boldsymbol{e}_n(\boldsymbol{r}_1)\boldsymbol{e}_n^*(\boldsymbol{r}_2) + \boldsymbol{e}_n(\boldsymbol{r}_1)\boldsymbol{e}_{n'}^*(\boldsymbol{r}_2)e^{-i\phi} \\ &+ \boldsymbol{e}_{n'}(\boldsymbol{r}_1)\boldsymbol{e}_n^*(\boldsymbol{r}_2)e^{i\phi} + \boldsymbol{e}_{n'}(\boldsymbol{r}_1)\boldsymbol{e}_{n'}^*(\boldsymbol{r}_2)\Big).\end{aligned} \tag{2.53}$$

Using the dyadic property $(\boldsymbol{ab})\cdot\cdot(\boldsymbol{cd}) = (\boldsymbol{a}\cdot\boldsymbol{d})(\boldsymbol{b}\cdot\boldsymbol{c})$,

$$\begin{aligned}\langle P\rangle = \iint_{\mathscr{S}^2} d^2\boldsymbol{r}_1 d^2\boldsymbol{r}_2 \sum_{m,m'} \Big(&D_{mm'}^*\tilde{\boldsymbol{e}}_{m'}(\boldsymbol{r}_2)\boldsymbol{e}_n^*(\boldsymbol{r}_2)\tilde{\boldsymbol{e}}_m^*(\boldsymbol{r}_1)\boldsymbol{e}_n(\boldsymbol{r}_1) \\ &+ D_{mm'}^*\tilde{\boldsymbol{e}}_{m'}(\boldsymbol{r}_2)\boldsymbol{e}_{n'}^*(\boldsymbol{r}_2)\tilde{\boldsymbol{e}}_m^*(\boldsymbol{r}_1)\boldsymbol{e}_n(\boldsymbol{r}_1)e^{-i\phi} \\ &+ D_{mm'}^*\tilde{\boldsymbol{e}}_{m'}(\boldsymbol{r}_2)\boldsymbol{e}_n^*(\boldsymbol{r}_2)\tilde{\boldsymbol{e}}_m^*(\boldsymbol{r}_1)\boldsymbol{e}_{n'}(\boldsymbol{r}_1)e^{i\phi} \\ &+ D_{mm'}^*\tilde{\boldsymbol{e}}_{m'}(\boldsymbol{r}_2)\boldsymbol{e}_{n'}^*(\boldsymbol{r}_2)\tilde{\boldsymbol{e}}_m^*(\boldsymbol{r}_1)\boldsymbol{e}_{n'}(\boldsymbol{r}_1)\Big).\end{aligned} \tag{2.54}$$

Using the definition of dual vectors $\int_{\mathscr{S}} d^2\boldsymbol{r}\, \tilde{\boldsymbol{e}}_m^*(\boldsymbol{r})\boldsymbol{e}_n(\boldsymbol{r}) = \int_{\mathscr{S}} d^2\boldsymbol{r}\, \tilde{\boldsymbol{e}}_m(\boldsymbol{r})\boldsymbol{e}_n^*(\boldsymbol{r}) = \delta_{mn}$, and the Hermicity of $\overline{\overline{\mathbf{D}}}$ such that $D^*_{mm'} = D_{m'm}$, we obtain

$$\begin{aligned}
\langle P\rangle &= \sum_{m,m'} \left(D_{m'm}\delta_{nm}\delta_{nm'} + D_{m'm}\delta_{nm}\delta_{n'm'} + D_{m'm}\delta_{n'm}\delta_{nm'} + D_{m'm}\delta_{n'm}\delta_{n'm'}\right) \\
&= D_{nn} + D_{n'n}e^{-i\phi} + D_{nn'}e^{i\phi} + D_{n'n'} \\
&= D_{nn} + D_{n'n'} + 2\Re\{D_{nn'}e^{i\phi}\} \\
&= D_{nn} + D_{n'n'} + 2|D_{nn'}|\cos(\phi + \theta_{nn'}),
\end{aligned} \tag{2.55}$$

where $|D_{nn'}|$ and $\theta_{nn'}$ are the magnitude and phase of $D_{nn'}$ respectively. The last term is proportional to $\cos(\phi)$: by varying the phase difference ϕ, we obtain fringes in the detector output, as illustrated in Figure 2.3. The amplitude, phase and constant offset of the fringe respectively correspond to $|D_{nn'}|$, $\theta_{nn'}$ and $D_{nn} + D_{n'n'}$: measuring a fringe allows us to extract information concerning the detector response function $\overline{\overline{\mathbf{D}}}$. Equation (2.55) expresses the detector output $\langle P\rangle$ as the sum of the two single-source terms and the cross-source contributions. While $D_{nn'}$ is a complex quantity and is therefore not strictly defined as a measurable, it still possesses the unit of the detector output.

It is important here to reflect on the importance of Equation (2.55), as it provides a powerful experimental method for reconstructing the detector response function. By illuminating some power detector whose optical response, as described by its state of coherence, is unknown using two coherent, phase-locked sources, we can measure fringes in the measured detector output as the relative phase between the sources is varied. These fringes contain information about the detector response function, which can be fully recovered by repeating the fringe measurements over a number of source position pairs. This experimental method is called Energy-Absorption Interferometry (EAI). Moreover, from the theory developed in Section 2.3, we know that the detector response function can be decomposed into its natural modes. EAI therefore allows us to determine the spatial forms of the individual degrees of freedom through which the detector structure absorbs external power.

It is also important to remember that the fringe measurements are performed with monochromatic sources at a single frequency. As opposed to other less powerful characterization methods such as those discussed in Chapter 1, sweeping the sources' frequency is not required. Just the opposite, by repeating a full set of measurements for various radiation frequencies, EAI experiments could obtain the frequency-dependent behavior of the detector response function as well.

While the following sections will in part discuss how repeating fringe measurements over a sufficiently large number of source position pairs guarantees that we are able to retrieve the

full DRF, we can already link this topic to Aperture Synthesis Interferometry (ASI), which we described in Chapter 1. In the context of ASI, one wishes to retrieve the state of coherence of the incoming radiation, and can generally describe the incident field in terms of plane waves. The separation between the telescopes used sets the (spatial) Fourier frequency of the fringe in the signal, also called the baseline. In EAI, assuming that the two sources produce plane waves at the surface of the detector, we can analogously think of the separation between the two sources as setting the baseline for the reconstruction of the DRF. By repeating fringe measurements for multiple source position pairs, we measure the DRF with an increasing number of baselines.

2.5 Matrix Formulation

In order to obtain a formulation suitable for computational studies and experimental data analysis, we turn to a notation based on matrices rather than dyadics. This implies discretizing the detector surface $\mathscr{S}$ into J points, using an appropriate sampling convention, such that the field $\boldsymbol{e}_n(\boldsymbol{r})$ produced by a source at position n becomes the vector $\mathsf{e}_n \in \mathbb{C}^J$. Concatenating these column-wise, we obtain a matrix of source fields $\mathsf{E} \in \mathbb{C}^{J\times N}$, such that the n^{th} column of E corresponds to e_n. We can then write the decomposition of the detector response function $\overline{\overline{\mathbf{D}}}(\boldsymbol{r}_1,\boldsymbol{r}_2)$ into the dual vectors of fields generated by sources at the N allowed positions, Equation (2.47), as

$$\mathsf{M} = \tilde{\mathsf{E}}\mathsf{D}\tilde{\mathsf{E}}^{\dagger}, \tag{2.56}$$

where the n^{th} column of $\tilde{\mathsf{E}}$ corresponds to $\tilde{\mathsf{e}}_n$, the discretized version of the dual vector $\tilde{\boldsymbol{e}}_n(\boldsymbol{r})$, in which any $\boldsymbol{r}$ dependence is omitted since it is already included in the definition of the source position n, and the components of the measurement matrix D are given by $D_{nn'}$, related to the power measurements by Equation (2.55).

Considering two coherent, phase-locked sources at positions m and m', with phase difference ϕ, as in Section 2.4, we obtain the following form for the detector output as a function of the relative phase ϕ between the sources:

$$\begin{aligned} P_{nn'} &= \sum_{m,m'} D_{mm'} \left[\mathsf{e}_m + \mathsf{e}_{m'}e^{i\phi}\right]^{\dagger} \tilde{\mathsf{e}}_n\tilde{\mathsf{e}}_{n'}^{\dagger} \left[\mathsf{e}_m + \mathsf{e}_{m'}e^{i\phi}\right] \\ &= \sum_{m,m'} D_{mm'} \left[\mathsf{e}_m^{\dagger} + \mathsf{e}_{m'}^{\dagger}e^{-i\phi}\right] \tilde{\mathsf{e}}_n\tilde{\mathsf{e}}_{n'}^{\dagger} \left[\mathsf{e}_m + \mathsf{e}_{m'}e^{i\phi}\right] \\ &= D_{nn} + D_{n'n'} + 2|D_{nn'}|\cos(\phi + \theta_{nn'}), \end{aligned} \tag{2.57}$$

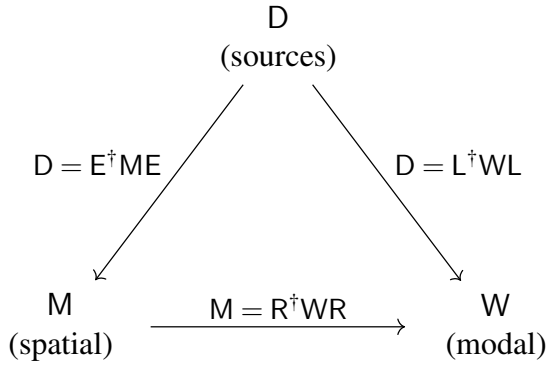

Fig. 2.4 Schematical illustration of the relations between the spatial, source-numbered and modal representations of the DRF; the basis of each matrix is stated in parentheses.

using $\mathsf{e}_m\tilde{\mathsf{e}}_n^\dagger = \tilde{\mathsf{e}}_m\mathsf{e}_n^\dagger = \delta_{mn}$. This reveals the general form for the response matrix in basis of source fields:

$$\mathsf{D} = \mathsf{E}^\dagger\mathsf{M}\mathsf{E}. \tag{2.58}$$

Note that Equation (2.58) corresponds to an embedding of the detector's response to the field in the detector plane, M, into the detector's response to sources some distance away from the detector, D. This operation can be seen as a filtering of the measured DRF from the domain of M, indexed by the sampled positions on the reference surface, into the domain of D, indexed by the scanned source positions. Similarly, Equation (2.56) describes a deconvolution from the domain of D into the domain of M.

In general experimental cases, we may actually not wish to use the transformation in Equation (2.56). Indeed, the matrices D and M can both be diagonalized, to retrieve the eigenvectors and eigenvalues of the detector response function in their respective bases:

$$\mathsf{D} = \mathsf{L}^\dagger\mathsf{W}\mathsf{L} \tag{2.59}$$

$$\mathsf{M} = \mathsf{R}^\dagger\mathsf{W}\mathsf{R}, \tag{2.60}$$

where W is the diagonal matrix of eigenvalues, containing the relative sensitivities of the DRF to the modes appearing column-wise in L (for their representation in the basis of source fields) and R (for their representation in the spatial basis). Columns of R correspond to the modes $\boldsymbol{R}(\boldsymbol{r})$ in Equation (2.35), discretized over the reference surface using the same sampling convention as chosen above to construct the matrix E. Elements of the matrix L are the overlap integrals of the detector modes in the spatial basis with the incident external fields at the chosen set of source positions; they are given by $\mathsf{L}_{mn} = \int_{\mathscr{S}} d^2\boldsymbol{r}\boldsymbol{R}_m(\boldsymbol{r}) \cdot \boldsymbol{e}_n(\boldsymbol{r})$. The matrix $\mathsf{L}' = \mathsf{R}\mathsf{E}$, which appears when substituting Equation (2.60) into Equation (2.59), converges

towards the integral form above as the number of sample points J over the integration surface becomes infinite. Figure 2.4 depicts the relationships between the three bases discussed, namely the basis of source positions, the basis of sampled spatial points on the detector surface, and the basis of eigenmodes. The transformations between the former two are described by Equations (2.56) and (2.58), while their respective transformations into the modal basis are given by the diagonalizations in Equations (2.59) and (2.60).

Substituting Equation (2.58) into Equation (2.56), we obtain the measured response matrix M' in terms of the actual response matrix M:

$$\mathsf{M}' = \tilde{\mathsf{E}}\mathsf{E}^\dagger \mathsf{M} \mathsf{E} \tilde{\mathsf{E}}^\dagger. \tag{2.61}$$

If the measurement set $\mathbb{E}$ is complete or overcomplete, i.e. if dual vectors $\tilde{\mathsf{e}}_n$ are contained in the columns of $\tilde{\mathsf{E}}$, then by definition $\mathsf{E}^\dagger\tilde{\mathsf{E}} = \mathsf{I} = \tilde{\mathsf{E}}^\dagger\mathsf{E}$. In that case, $\mathsf{M}' = \mathsf{M}$: we can completely retrieve the response matrix from the measured matrix. In the opposite case, where the measurement source fields do not completely span the fields to which the power detector is sensitive, we use Singular Value Decomposition (SVD) to compute the pseudo-inverse matrices:

$$\mathsf{E} = \mathsf{U}\Sigma\mathsf{V}^\dagger \tag{2.62}$$

$$\implies \tilde{\mathsf{E}} = \mathsf{U}\Sigma^{-1}\mathsf{V}^\dagger, \tag{2.63}$$

where $\mathsf{U} \in \mathbb{C}^{J\times J}$ and $\mathsf{V} \in \mathbb{C}^{N\times N}$ are unitary matrices whose columns correspond to the left-singular and right-singular vectors respectively, and $\Sigma \in \mathbb{C}^{J\times N}$ is a positive semidefinite diagonal matrix containing the singular values of E. We then obtain:

$$\mathsf{E}\tilde{\mathsf{E}}^\dagger = \mathsf{U}\Sigma\Sigma^{-1}\mathsf{U}^\dagger \tag{2.64}$$

$$\mathsf{E}^\dagger\tilde{\mathsf{E}} = \mathsf{V}\Sigma^{-1}\Sigma\mathsf{V}^\dagger. \tag{2.65}$$

Equation (2.64) corresponds to the projection of the natural modes onto measurement space, followed by the application of a diagonal filter, and the reconstruction of the measured modes. Information is lost in the imperfect filtering step if $\Sigma\Sigma^{-1}$ is not the identity matrix.

It is important to note that multiplication by $\mathsf{E}\tilde{\mathsf{E}}^\dagger$ is very different from applying $\mathsf{E}\mathsf{E}^\dagger$, which corresponds to mappings between the source and detector planes, with some information loss if the set of vectors $\{\mathsf{e}_n\}$ does not span the space of the matrix onto which $\mathsf{E}\mathsf{E}^\dagger$ is applied. We can also remark that $\mathsf{E}\mathsf{E}^\dagger \in \mathbb{C}^{N\times N}$ is the discretized version of the frame matrix

defined in Equation (2.48). Using Equation (2.62), it can be re-written as

$$\mathbf{S} = \mathsf{U}\Sigma\Sigma^{\dagger}\mathsf{U}^{\dagger}. \tag{2.66}$$

The frame matrix measures the completeness of the basis set $\mathbb{E}$ over the J sampled points on the reference surface $\mathscr{S}$, as the number of nonzero singular values in the frame matrix corresponds to the number of degrees of freedom representable in the basis $\mathbb{E}$ [68]. Similarly, we can define the Gram matrix $\mathbf{T} \in \mathbb{C}^{J\times J}$ as

$$\mathbf{T} = \mathbf{E}^{\dagger}\mathbf{E} = \sum_{k=1}^{N} \boldsymbol{e}_k^{\dagger}\boldsymbol{e}_k. \tag{2.67}$$

Using Equation (2.62) as for the frame matrix, the discretized Gram matrix can be re-written as

$$\mathbf{T} = \mathsf{V}\Sigma^{\dagger}\Sigma\mathsf{V}^{\dagger}. \tag{2.68}$$

and provides a measure of the basis set's linear dependence. Berry et al. proved that the number of non-zero singular values is equal to the number of linearly independent vectors in the basis [67]. Note that the diagonal matrices $\Sigma\Sigma^{\dagger} \in \mathbb{R}^{J\times J}$ and $\Sigma^{\dagger}\Sigma \in \mathbb{R}^{N\times N}$ have components $|\Sigma_{ii}|^2$ for $i \in \{1,2,...,\min(N,J)\}$ and zero otherwise.

2.6 Experimental Considerations

2.6.1 Populating the Detector Response Matrix

Equation (2.57) gives interesting insights into possible experimental procedures to populate the response matrix D. In particular, D can be populated using measurements for two different values of the relative phase between sources, ϕ. The simplest form is obtained when $\phi \in \{0, \pi/2\}$; we can then split measurement data into three types:

$$\begin{cases} P^0_{nn} = D_{nn} \\ P^c_{nn'} = D_{nn} + D_{n'n'} + 2\Re\{D_{nn'}e^{i0}\} \\ P^s_{nn'} = D_{nn} + D_{n'n'} + 2\Re\{D_{nn'}e^{i\pi/2}\} \end{cases}$$
$$\implies \begin{cases} P^0_{nn} = D_{nn} \\ P^c_{nn'} = D_{nn} + D_{n'n'} + 2\Re\{D_{nn'}\} \\ P^s_{nn'} = D_{nn} + D_{n'n'} - 2\Im\{D_{nn'}\}, \end{cases} \tag{2.69}$$

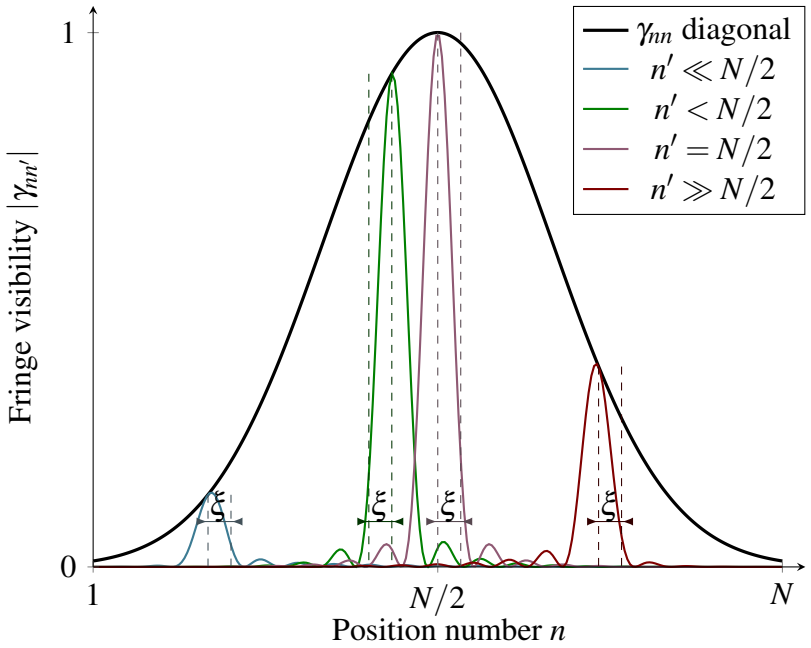

Fig. 2.5 Graphical illustration of plots obtained by moving along various rows of a measured detector response function D; the black envelope is the matrix diagonal, corresponding to the single-source power elements; the width of the enclosed structures is recognized as the coherence length ξ.

where the first line corresponds to single-source measurements. This can be rearranged to obtain the elements of D in terms of the measurements:

$$\begin{cases} D_{nn} = P^0_{nn} \\ \Re\{D_{nn'}\} = (P^c_{nn'} - P^0_{nn} - P^0_{n'n'})/2 \\ \Im\{D_{nn'}\} = -(P^s_{nn'} - P^0_{nn} - P^0_{n'n'})/2. \end{cases} \tag{2.70}$$

Note that this is only the method that requires the minimum theoretical number of required measurements. As will be discussed in much more detail in following chapters, when performing fringe measurements in experiments, we will in practice use different phase modulation schemes to extract the amplitude and phase of the $D_{nn'}$ elements.

2.6.2 Coherence Lengths and Other Quantities of Interest

While we have only considered the measured detector response until now, other associated quantities are of significant interest. In particular, the complex fringe visibility $\gamma_{nn'}$, also called the Michelson visibility in the context of classical optics, is defined as the ratio of the amplitude of the fringe pattern over the sum of individual sources' powers. It measures the

contrast of interference phenomena [69], and is related to the elements of D as follows:

$$\gamma_{nn'} = \frac{2D_{nn'}}{D_{nn} + D_{n'n'}}. \tag{2.71}$$

It is possible to plot $\gamma_{nn'}$ by moving along the n^{th} row of D, which reveals the transverse coherence length graphically. For a given source position, the other source can be scanned to obtain the two-source correlation function, which goes to 0 as the distance between the sources is increased. Choosing an appropriate cutoff, the two-source correlation gives the coherence length explicitly. Figure 2.5 is an illustration of this scheme. It shows how, for various positions of the second source n', plots of $|\gamma_{nn'}|$ as a function of the first source position n fit under the plot of the normalized single-source beampattern. In particular, their widths are all identical and, choosing a uniform cutoff at a certain percentage of the maximum value, can be used to graphically infer the transverse coherence length ξ.

We can also apply another normalization to the DRF, to obtain the complex fringe coherence defined as

$$\Gamma_{nn'} = \frac{D_{nn'}}{\sqrt{D_{nn} D_{n'n'}}}. \tag{2.72}$$

The starting observation is that Equation (2.57) has integrated the source intensities into the definition of $\boldsymbol{E}(\boldsymbol{r})$ and $\overline{\overline{\mathbf{E}}}(\boldsymbol{r}_1, \boldsymbol{r}_2)$ because they were assumed to be identical. In practice, this assumption will be difficult to achieve, and we must consider the case where the sources' amplitudes are different. The total external field can be re-written as

$$\boldsymbol{E}(\boldsymbol{r}) = E_n \hat{\boldsymbol{e}}_n(\boldsymbol{r} - \boldsymbol{r}_n) + e^{i\phi} E_{n'} \hat{\boldsymbol{e}}_{n'}(\boldsymbol{r} - \boldsymbol{r}_{n'}), \tag{2.73}$$

where $\hat{\boldsymbol{e}}_n$ is the unit vector for the external field generated by the source at position n. Using the definition of the external field dyadic, it becomes

$$\begin{aligned}
\overline{\overline{\mathbf{E}}}(\boldsymbol{r_1}, \boldsymbol{r_2}) &= |E_n|^2 \hat{\boldsymbol{e}}_n(\boldsymbol{r}_1 - \boldsymbol{r}_n) \hat{\boldsymbol{e}}_n^*(\boldsymbol{r}_2 - \boldsymbol{r}_n) && (2.74)\\
&+ E_n E_{n'}^* e^{-i\phi} \hat{\boldsymbol{e}}_n(\boldsymbol{r}_1 - \boldsymbol{r}_n) \hat{\boldsymbol{e}}_{n'}^*(\boldsymbol{r}_2 - \boldsymbol{r}_n) && (2.75)\\
&+ E_n^* E_{n'} e^{+i\phi} \hat{\boldsymbol{e}}_{n'}(\boldsymbol{r}_1 - \boldsymbol{r}_n) \hat{\boldsymbol{e}}_n^*(\boldsymbol{r}_2 - \boldsymbol{r}_n) && (2.76)\\
&+ |E_{n'}|^2 \hat{\boldsymbol{e}}_{n'}(\boldsymbol{r}_1 - \boldsymbol{r}_{n'}) \hat{\boldsymbol{e}}_{n'}^*(\boldsymbol{r}_2 - \boldsymbol{r}_{n'}) && (2.77)\\
& && (2.78)
\end{aligned}$$

We then obtain

$$P = |E_n|^2 \tilde{D}_{nn} + |E_{n'}|^2 \tilde{D}_{n'n'} + 2\Re\left[E_n^* E_{n'} \tilde{D}_{nn'} e^{i\phi}\right]. \tag{2.79}$$

where

$$\tilde{D}_{nn'} = \iint_{\mathscr{S}^2} d^2\boldsymbol{r}_1 d^2\boldsymbol{r}_2 \hat{\boldsymbol{e}}_n^*(\boldsymbol{r}_1 - \boldsymbol{r}_n) \cdot \overline{\overline{\mathbf{D}}}(\boldsymbol{r}_1, \boldsymbol{r}_2) \cdot \hat{\boldsymbol{e}}_n(\boldsymbol{r}_2 - \boldsymbol{r}_{n'}). \tag{2.80}$$

$\tilde{D}_{nn'}$ is related to the definition of $D_{nn'}$ in Equation (2.46) by $D_{nn'} = |E_n E_{n'}| \tilde{D}_{nn'}$. We therefore obtain that the coherence function $\Gamma_{nn'}$ can be re-written as

$$\Gamma_{nn'} = \frac{\tilde{D}_{nn'}}{\sqrt{\tilde{D}_{nn}\tilde{D}_{n'n'}}} = \tilde{D}_{nn'}, \tag{2.81}$$

as $\tilde{D}_{nn} = 1$ by definition. This clearly shows that $\Gamma_{nn'}$ corresponds to the fringe amplitude that would be obtained for identical sources producing unit response in the detector output. Note also that the width of the structure observable in fringe visibility plots, such as in Figure 2.5, will be identical when plotting the fringe coherence function. The latter however corrects the effect of the source intensities, which is particularly important if they are unequal, as we may expect in experimental configurations.

2.6.3 Convergence

Because the number of natural modes in the detector response is typically unknown, it is important to have a method for analyzing the number of measurements required [59]. The number of measurements required goes as $\mathscr{O}(N^2)$, because we need to fill in the matrix $\mathsf{M} \in \mathbb{C}^{N\times N}$; on the other hand, the amount of information required to reconstruct the modes in the system goes at most as $\mathscr{O}(mN)$, because the information required grows as the number of modes m and the number of eigenvalues of a $N \times N$ matrix. Therefore, any data analysis algorithm will eventually converge, when a complete set of measurement fields is attained: the measured detector response then matches the actual response, and the detector's modes can be recovered.

While this guarantees convergence, additional issues such as the choice of source scanning strategies and impact of noise make monitoring the accrual of experimental data more difficult. However, techniques for real-time analysis are available, even with incomplete data and an undercomplete set of basis vectors. Using incremental SVD (iSVD) on successive matrices constructed from data acquired [70], it is possible to iteratively check whether a sufficient number of measurements has been performed to successfully reconstruct the detector response function. The iSVD technique will converge when there is sufficient information to find all degrees of freedom, i.e. the detector's natural modes. It also has the advantage of being able to deal with missing and untrusted values, contrary to standard SVD algorithms [71].

2.7 Conclusion

We have summarized the derivation of a model showing that a linear power detector's output can be expressed as the full contraction of two tensor fields, respectively corresponding to the states of coherence of the detector's response function and of the external electric field. We have further introduced the notion of natural modes, for both the optical field and the detector reception pattern, corresponding to the set of independent field modes through which the field transmits power and the detector absorbs power. While the natural modes of the field and detector are based on their physical properties only, the problem to be solved can also be cast in a large number of representations, for instance spatially-dependent or angular-dependent. Physically motivated bases can also be chosen, such as Hermite-Gaussian functions [72] or Laguerre-Gaussian functions [73, 74].

We have also seen how the detector response function, and its (possibly partially coherent) decomposition in the basis of the detector's natural modes, can be fully reconstructed from a finite number of power measurements. This formalism yields an elegant experimental method, called Energy-Absorption Interferometry: at various location pairs attained by some scanning system, power measurements of the field emitted by two coherent, phase-locked sources reveals the full information of the detector response function. This method was demonstrated successfully in a proof-of-concept experiment at submillimeter wavelength [58]. In the next chapter, we will use the theory developed here to numerically investigate model infrared systems. In Chapter 4, we will examine the design of an experimental system at infrared wavelength, while the following chapters will deal with the system's performance and its utilisation to perform EAI on infrared detector systems with various modal behaviors.

The EAI theory is valid for a very large number of situations, far beyond those allowed by the assumptions made in Section 2.2.1. For instance, it should be noted that the EAI theory applies to all electromagnetic radiation. Ongoing work deals with the case of electromagnetic excitation of sets of magnetic dipoles, including the emergence of long-range order [75]. A further extension, to quantum correlation functions and incident fields generated by two (potentially different) generalized forces, has been proven by Withington [51]. Furthermore, it was shown by Withington and Saklatvala that EAI could reveal the link between fluctuations in the field and in the detector response [53], as well as be used for the study of quantum states of light, photon-number statistics and correlations between detectors in a single array [61].

Chapter 3

Simulating EAI on Infrared Detectors

3.1 Introduction

The Energy-Absorption Interferometry theory developed in Chapter 2 is used in this chapter to create a numerical simulation framework for the investigation of the optical response of near-infrared detectors. The main goal is to study simulated single-mode, few-mode and multi-mode systems based on realistic assumptions, and find differentiating features in their simulated DRFs. This constitutes the first numerical demonstration of EAI at near-infrared wavelengths, and will have particular importance when considering experimentally measured DRFs, particularly in Chapters 6 and 8. Their comparison will provide an additional practical confirmation of EAI's power and versatility.

More generally, we want to root our numerical investigations in physical rationales. For instance, we choose a 1550 nm operating wavelength for the sources, as it is a key wavelength in near-infrared technology, particularly in the telecommunications community; its significance will be explored again when designing an EAI experimental system, in Chapter 4. Much discussion in Chapter 2 revolved around the use of physically motivated modal bases, such as the Laguerre-Gaussian (LG) modes describing the propagation of circularly symmetric beams in free-space and Linearly Polarized (LP) modes for radiation transmission in optical fibers: we also wish to investigate optical responses built from these mode sets. These observations, among others, will be directly applicable to designing and operating an experimental system to demonstrate EAI on near-infrared detectors, from Chapter 4 onwards.

The recovery of the DRF's natural modes via its diagonalization is not explored in this chapter, as it is technically straightforward for simulated DRFs that are effectively noiseless and devoid of measurement imperfections, but rather in Chapter 9 in the context of experimentally measured DRFs. Instead, we here report on a broad study of the requirements

placed on source scanning strategies to recover the system's modes, in a more general and powerful scheme. This examination will echo discussions from Chapter 2 regarding the completeness of the set of scanned source positions.

In Section 3.2, we create a powerful and versatile numerical simulation framework, allowing us to compute the DRF of a large variety of systems; significant computational simplifications are introduced, including to reduce the scheme's algorithmic complexity. Section 3.3 presents the first simulations of DRFs for infrared detectors, modelling both the detector's response and the sources' beams as field from point-like antenna structures. In Sections 3.4 and 3.5, the finite-sized sources are modeled as generating Gaussian beams, and the detector response is built from the incoherent sums of LG and LP modes, respectively. Qualitative features of single-mode, few-mode and multi-mode systems are explored, and the comparison yields differentiating structures for LG-based and LP-based systems. Section 3.6 discusses a functional form for the detector's response that is not based on modes, but rather on a finite-coherence response. In particular, we explore the interplay between three characteristic lengths: the 1550 nm operating wavelength, the absorber sidelength and its coherence length. In Section 3.7, we study the importance of scanning strategies for the source positions. This produces significant insight into how information is accrued as the sources are scanned over various sampling schemes, such as Cartesian and polar grids. Furthermore, it reveals how the dynamic range of the experimental system, an important metric of its performance measuring the range between the largest and smallest recoverable eigenvalues, influences the convergence of the scanned source fields towards a complete set.

3.2 Implementing a Numerical Simulation Framework

3.2.1 General EAI Framework

An important first and non-trivial step is to choose a representation for the DRF datasets obtained from the simulated fringes' complex amplitudes, given a set of sampled positions over which each source is scanned. In Chapter 2, we discussed the DRF's elements D_{mn} as denoted by the indices m and n of the positions at which the first and second sources are placed. We differentiate between the functional form $\overline{\overline{\mathbf{D}}}(\mathbf{r}_i, \mathbf{r}_j)$ of the DRF in the spatial basis, which we substitute into Equation (2.19) and here call the assumed DRF, and the matrix of computed DRF elements D_{mn} in the basis of sampled source positions, which we here call the simulated DRF.

While the experimental method derived in Chapter 2, and which will be implemented in Chapters 4 and 5, is fully capable of performing two-source scans over two-dimensional

sampling grids, a large part of this manuscript is dedicated to one-dimensional sampling grids. As such, the matrix D_{mn} can be represented as a matrix, with row and column indices respectively corresponding to the two sources' positions along the sampled line. To preempt experimental considerations in later chapters, we label the two sources R and L. Without loss of generality, the uniformly sampled line is taken along the x-axis; the positions of the sources are then denoted x_R and x_L. The visibility and coherence matrices, defined in Equations (2.71) and (2.72), then follow the same indexing convention.

3.2.2 Simplifications for Computation

We recall that the DRF elements D_{mn} in the basis of source positions are given by

$$D_{mn} = \iint_{\mathscr{S}^2} \boldsymbol{e}_m^*(\boldsymbol{r}_1) \cdot \overline{\overline{\mathbf{D}}}(\boldsymbol{r}_1, \boldsymbol{r}_2) \cdot \boldsymbol{e}_n(\boldsymbol{r}_2) d^2\boldsymbol{r}_1 d^2\boldsymbol{r}_2, \tag{3.1}$$

where $\boldsymbol{e}_m(\boldsymbol{r})$ is the field produce at a point $\boldsymbol{r}$ on the reference surface by a source placed at the position labeled m. Performing the double-integral described in Equation (3.1) is computationally intensive, as it involves numerical integration of multi-dimensional complex-valued functions. Additionally, the number of two-source position pairs grows as the square of the single-source sampled positions. It is therefore important to investigate what simplifications can be applied to reduce the computational complexity of a brute force algorithm, in which each DRF element is simulated independently. We remark that symmetry arguments on the radially symmetric source beams are not applicable as their origins are generally displaced with respect to the detector's on-axis position.

Using a functional form for the detector's optical response written as an incoherent sum, such as the Hilbert-Schmidt form of the DRF given in Equation (2.35),

$$\overline{\overline{\mathbf{D}}}(\boldsymbol{r}_1, \boldsymbol{r}_2) = \sum_k \alpha_k \boldsymbol{R}_k(\boldsymbol{r}_1) \boldsymbol{R}_k^*(\boldsymbol{r}_2), \tag{3.2}$$

the simulated DRF measurement elements D_{mn} defined in Equation (2.46) can then be written as

$$D_{mn} = \sum_k \alpha_k \iint_{\mathscr{S}^2} d^2\boldsymbol{r}_1 d^2\boldsymbol{r}_2 \; \boldsymbol{e}_m^*(\boldsymbol{r}_1) \cdot \left(\boldsymbol{R}_k(\boldsymbol{r}_1) \boldsymbol{R}_k^*(\boldsymbol{r}_2)\right) \cdot \boldsymbol{e}_n(\boldsymbol{r}_2). \tag{3.3}$$

Importantly, we can thus simulate and store the response of each mode separately, and later add each with a chosen sensitivity factor, rather than simulating the system's total response at one time, which has the same total computational duration and does not allow tuning of each mode's sensitivity. Wherever possible, we have therefore used this simplification.

For spatially-separated forms of the detector response, such as in Equation (3.3), we obtain

$$D_{mn} = \sum_k \alpha_k \left(\int_{\mathscr{S}} d^2\boldsymbol{r}_1 \; \boldsymbol{e}_m^*(\boldsymbol{r}_1) \cdot \boldsymbol{R}_k(\boldsymbol{r}_1) \right) \left(\int_{\mathscr{S}} d^2\boldsymbol{r}_2 \; \boldsymbol{R}_k^*(\boldsymbol{r}_2)) \cdot \boldsymbol{e}_n(\boldsymbol{r}_2) \right), \tag{3.4}$$

where the two integrals are complex conjugates. It is therefore only necessary to compute one integral for each source position, concatenate these values as a vector, and compute its outer product with its conjugate transpose, to obtain all D_{mn} elements. Considering N positions to which every source is scanned, this simplification reduces the algorithmic complexity from $\mathscr{O}(N^2)$ to $\mathscr{O}(N)$.

We note however that, in order to reproduce the conditions of experimental measurements, we can use the simulated DRF to produce fringe patterns at every position pair (m,n) and extract the fringe parameters from the fringes. For instance, the detector output $P(\phi)$ as a function of the relative phase between the probes ϕ can be computed as

$$P(\phi) = D_{mm} + D_{nn} + 2\Re\{D_{mn} e^{i\phi}\}. \tag{3.5}$$

This allowed us to investigate the effect of methods of extracting the fringe amplitude, phase and offset, for instance with least-squares fitting of a sinusoid. These three parameters can also be extracted from the Fast Fourier Transform (FFT) of such simulated detector output measurements, respectively by selecting the amplitude and phase of the element corresponding to the relative phase modulation frequency, and the first element corresponding to the DC term of the Fourier Series. Both the fitting and FFT methods were implemented and applied to emulated fringes using the DRF elements D_{mn} simulated using the methods described in this section. We found that the fringe parameters were very accurately retrieved in both cases, providing solid benchmarks for their use to recover the fringe parameters of experimental DRFs, for which the elements D_{mn} are not directly accessible.

Additionally, this capability allows the exploration of the accuracy of the extracted fringe amplitude and phase for various sampling rates and measurement durations. More generally, this form also provides a natural way of inserting noise contributions into the simulated detector output measurements and studying their effect on the extracted fringe parameters. These opportunities will be further discussed in Chapter 10.

3.3 Point-Like Sources and Detectors

3.3.1 Theory

In order to perform simulations, we need to choose the nature of the sources and of the detector. In practice, this means selecting models for the fields produced, physically by the sources and virtually as reception patterns by the detector system. The simplest model available is that of point-like sources and detector. It is characterized by an infinitesimal physical size and an azimuthally uniform radiation transmission or reception pattern. We use the standard formula for the field produced by an electric dipole oscillating in time with dipole moment p_0 along the $\hat{\mathbf{z}}$ direction and an angular frequency ω, related to the wavenumber $k = \omega/c$ where c is the speed of light [76]:

$$\mathbf{E} = \frac{1}{4\pi\varepsilon_0}\left\{\frac{k^2}{r}(\hat{\mathbf{r}}\times\mathbf{p})\times\hat{\mathbf{r}} + \left(\frac{1}{r^3} - \frac{ik}{r^2}\right)(3\hat{\mathbf{r}}\,[\hat{\mathbf{r}}\cdot\mathbf{p}] - \mathbf{p})\right\} e^{i(kr-\omega t)}. \tag{3.6}$$

In the far-field, i.e. for $kr \gg 1$:

$$\begin{aligned}\mathbf{E} &= -\frac{\omega^2\mu_0 p_0}{4\pi}\sin(\theta)\left(\hat{\phi}\times\hat{\mathbf{r}}\right)\frac{e^{i(kr-\omega t)}}{r} \\ &= -\frac{\omega^2\mu_0 p_0}{4\pi}\sin(\theta)\frac{e^{i(kr-\omega t)}}{r}\hat{\theta}.\end{aligned} \tag{3.7}$$

3.3.2 Implementation

Using the far-field expression for a point-like source from Equation (3.7), we can define its field at a position $\boldsymbol{r}$ on the detector surface when the source is at the sampled position with index n as:

$$\boldsymbol{e}_n(\boldsymbol{r}) = \mathbf{E}(\boldsymbol{r} - \boldsymbol{r}_n). \tag{3.8}$$

While Equation (3.7) can also be used for the assumed DRF of a point-like detector, the problem can be significantly simplified by considering a reference surface $\mathscr{S}$ containing the detector position $\boldsymbol{r}_d$. In that case, the assumed DRF reduces to

$$\overline{\overline{\mathbf{D}}}(\boldsymbol{r}_1, \boldsymbol{r}_2) = \begin{cases}\delta(\boldsymbol{r}_1 - \boldsymbol{r}_2) & \boldsymbol{r}_1, \boldsymbol{r}_2 = \boldsymbol{r}_d \\ 0 & \text{otherwise,}\end{cases} \tag{3.9}$$

where a proportionality constant can be introduced to account for non-unity response. We then obtain the following form for the measured DRF elements, from Equation (2.46):

$$D_{mn} = \iint_{\mathscr{S}^2} \boldsymbol{e}_m^*(\boldsymbol{r}_1) \cdot \overline{\overline{\mathbf{D}}}(\boldsymbol{r}_1, \boldsymbol{r}_2) \cdot \boldsymbol{e}_n(\boldsymbol{r}_2) d^2\boldsymbol{r}_1 d^2\boldsymbol{r}_2 \tag{3.10}$$

$$= \int_{\mathscr{S}} \boldsymbol{e}_m^*(\boldsymbol{r}) \cdot \boldsymbol{e}_n(\boldsymbol{r}) d^2\boldsymbol{r}$$

$$= \boldsymbol{e}_m^*(\boldsymbol{r}_d) \cdot \boldsymbol{e}_n(\boldsymbol{r}_d). \tag{3.11}$$

In practice, we used the simplification discussed in Section 3.2.2: a vector was constructed, whose n^{th} element is $\boldsymbol{e}_n(\boldsymbol{r}_d)$, and the outer product with its conjugate transpose was computed to obtain all matrix elements D_{mn} simultaneously.

3.3.3 Results and Discussion

Figure 3.1 presents the simulated DRF for the sources labeled R and L scanned over 151 positions on a uniformly sampled line segment along the x-axis, $x \in [-15; 15]$ mm, at a normal distance $z = 100$ mm of the detector, whose on-axis position is $x = 0$ mm. We observe a slowly-varying amplitude pattern in Figure 3.1a, and a quickly-varying phase pattern in Figure 3.1b, both of which have symmetries along the center row and column, as well as the diagonal and antidiagonal.

The simulated DRF phase pattern shown in Figure 3.1b can be shown to correspond to a fast-wrapping phase, caused by the geometric phase contribution of the point-like sources' fields. Using a much finer step size, equal to 1 µm, we computed the DRF phase pattern for $x_L = 0$ and $x_R = 0$, i.e. respectively the central row and column of the DRF matrix: Figure 3.2 shows these phase-unwrapped patterns, whose peak-to-peak magnitude over the scanning range is approximately 4 500 rad and whose form is in line with the spherical phase due to the displacement of sources off-axis.

3.4 Laguerre-Gaussian Modes

3.4.1 Theory

Many experimental systems use a laser for radiation generation, and fiber-coupled detectors as a convenient way of restricting the number of modes that enter the power-absorbing structure. It is therefore important to investigate detector responses built from the basis describing such systems, known as the Laguerre-Gaussian (LG) modes. LG modes are the modes for free-space propagation of radially symmetric beams, solutions of the Helmholtz

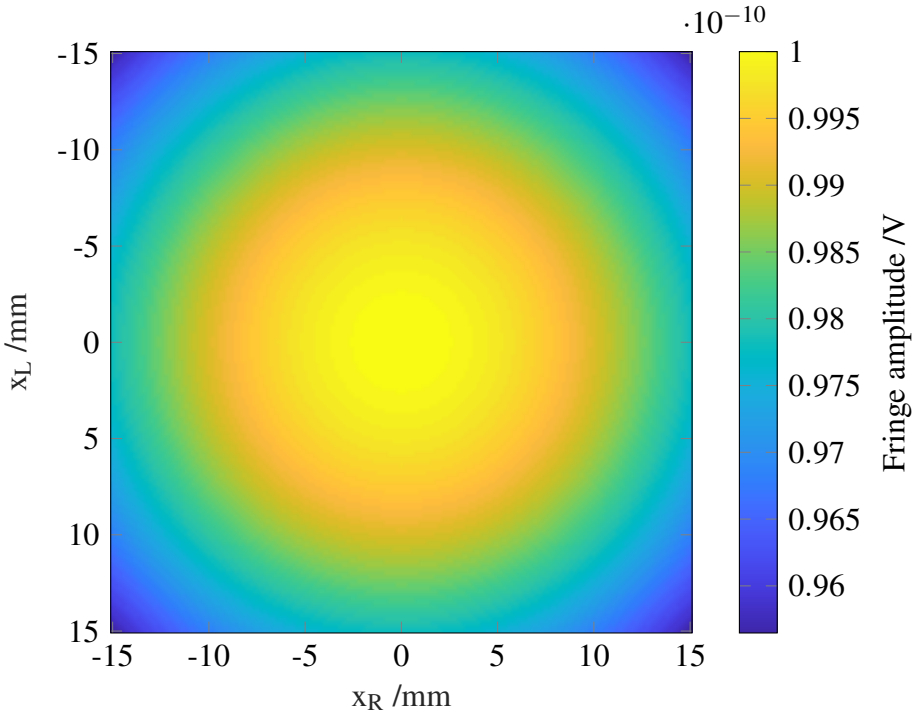

(a) DRF amplitude

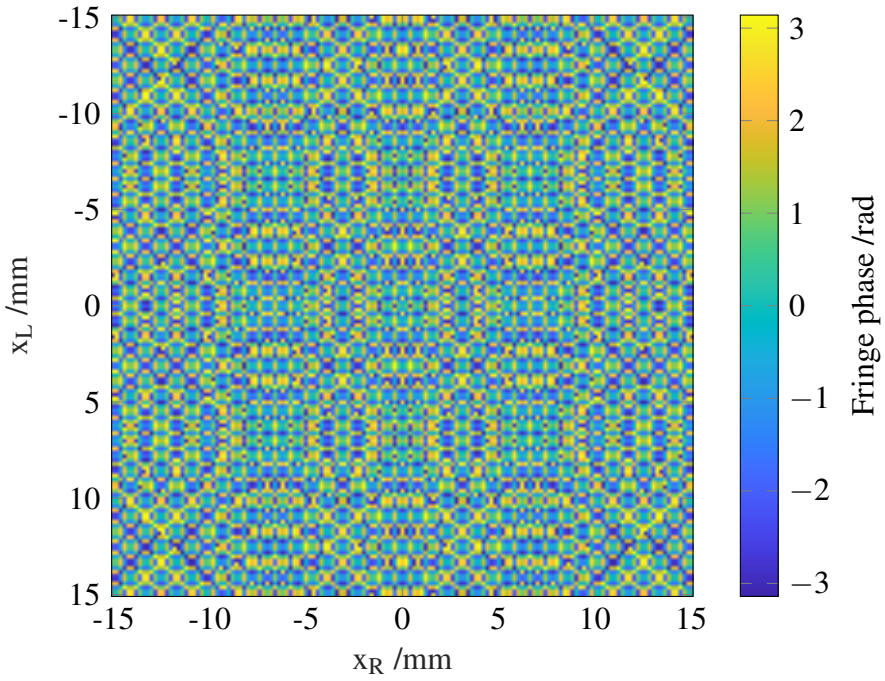

(b) DRF phase

Fig. 3.1 Simulated DRF assuming point-like sources and detector.

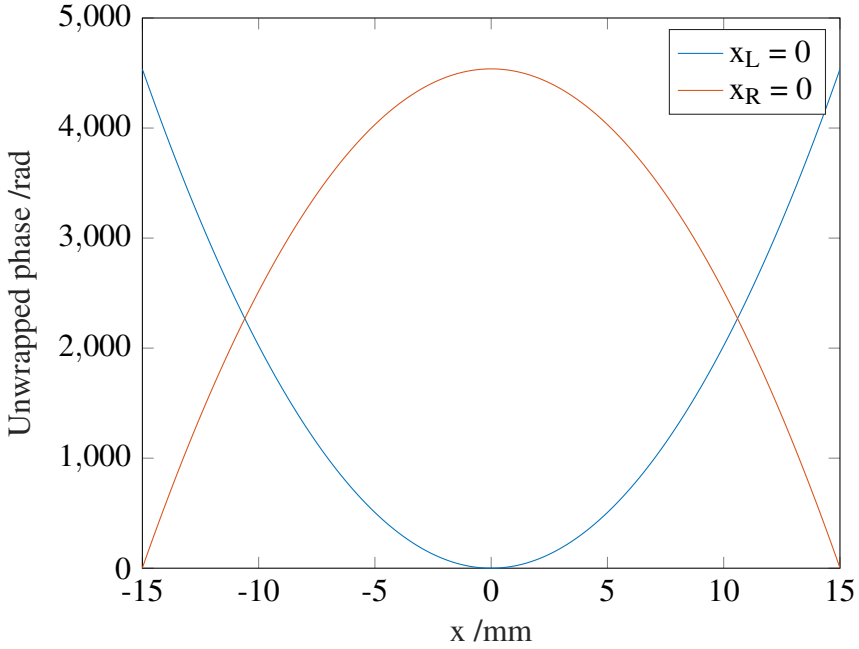

Fig. 3.2 Unwrapped phase patterns of the simulated DRF assuming a point-like detector and two sources, labeled R and L, for $x_R = 0$ and $x_L = 0$.

equation in the paraxial approximation, i.e. for small angles $\varphi \leq 10°$ such that $\sin(\varphi) \approx \phi$ [77]. The complex amplitude of an LG mode with radial index $p \geq 0$ and azimuthal index l, as measured at an on-axis distance z and a transverse position (r, φ) in cylindrical coordinates, is given by [73, 74]:

$$LG_{pl}(r,\varphi,z) = \frac{C_{pl}^{LG}}{w(z)} \left(\frac{r\sqrt{2}}{w(z)}\right)^{|l|} \exp\left(\frac{-r^2}{w^2(z)}\right) L_p^{|l|}\left(\frac{2r^2}{w^2(z)}\right) \times \exp\left(-ik\frac{r^2}{2R(z)} + il\varphi - ikz + i\psi(z)\right). \tag{3.12}$$

where we denote:

- $C_{pl}^{LG} = p!\sqrt{\frac{2}{\pi p!(|l|+p)!}} = \sqrt{\frac{2p!}{\pi(|l|+p)!}}$: normalization constant;
- $w(z) = w_0\sqrt{1+(z/z_R)^2}$: beam spot size at a distance z along the focus of the beam, defined as 1/e-amplitude radius;
- $w_0 = w(z=0)$: waist size;

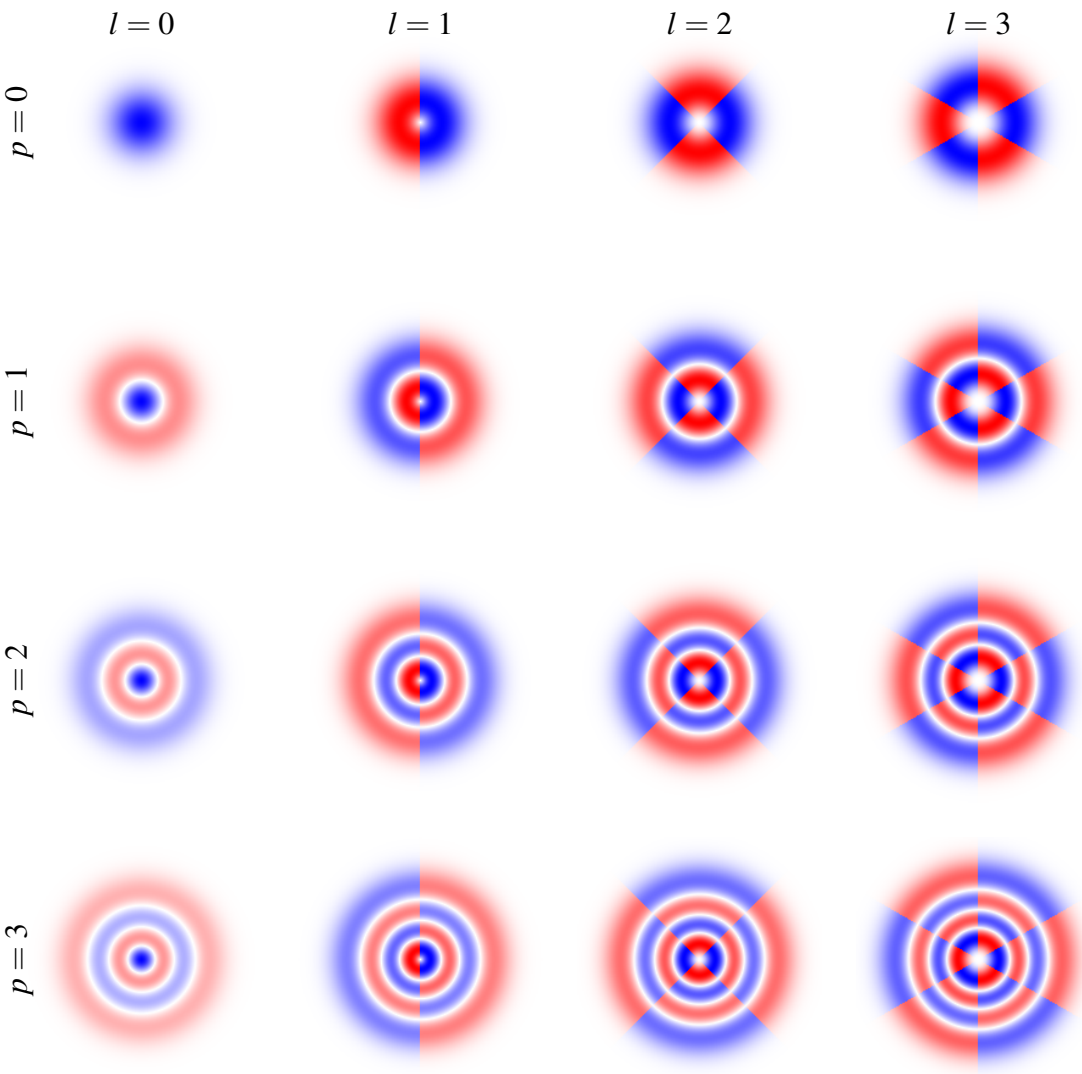

Fig. 3.3 Spatial forms of the low-order LG_{pl} modes, for $p, l \leq 3$; the opacity is proportional to the mode's amplitude, and the blue and red colors respectively correspond to the positive and negative sign of the phase.

- $z_R = \pi w_0^2/\lambda$: Rayleigh length, generally considered as the boundary between the near-field and far-field regimes, for which the beam spot size $w(z = z_R) = \sqrt{2}w_0$ and the on-axis intensity is twice the peak intensity at $z = 0$;
- $R(z) = z(1 + (z_R/z)^2)$: radius of curvature of the wavefront;
- $L_p^l(r)$: generalized Laguerre polynomial;
- $\psi(z) = (N + 1)\tan^{-1}(z/z_R)$: Gouy phase shift, which accounts for an increase of effective wavelength near the beam waist;

- $N = |l| + 2p$: combined mode number.

In the case of fibers, the waist size w_0 is equal to half of the mode field diameter (MFD), typically specified as a characteristic of the fiber by the manufacturer. The analogue description for beams with two orthogonal symmetry axes are Hermite-Gaussian modes, i.e. rectangular beams for which the Helmholtz equation is separable along the Cartesian x and y axes [72].

Figure 3.3 illustrates the spatial forms of low-order LG_{pl} modes, for $p, l \leq 3$: the increasing number of roots of the generalized Laguerre polynomials are visible along the radius, while the increasing number of phase changes corresponds to the larger azimuthal index l. Note that the width of LG modes increases with both p and l indices; indeed, the beam width of high-order LG modes is approximately $w_0\sqrt{2p+l+1}$ [78].

While the functional form in Equation (3.12) describes the LG modes, these are only valid in the paraxial approximation. In order to better deal with sources illuminating a detector at larger angles, it is necessary to generalize the parabolic wavefront into a spherical wavefront. In practice, we replace the phase contribution $\frac{r^2}{2R(z)}$ by $\sqrt{R(z)^2 + r^2} - R(z)$.

3.4.2 Implementation

The simulation algorithm follows a number of steps:

1. Values for the source and detector beam waists are selected, and the indices of LG modes of interest are chosen;

2. The vector of single-source, single-point power contributions is computed by performing a two-dimensional integral of the product of the source beam (projected LG mode) with the detector response (LG mode) over the integration surface;

3. The outer product of this vector with its conjugate transpose is computed to obtain the single-mode simulated DRF;

4. Steps 2 and 3 are repeated for each LG mode;

5. Multi-mode DRFs are assembled from the sum of single-mode DRFs, weighted by selected sensitivities.

For the two-dimensional integration step, absolute and relative tolerances must be selected for Matlab's numerical integrator: we selected 10^{-10} and 10^{-6} respectively. Computing the DRF by taking the outer product of a vector whose elements have these accuracy characteristics, we obtain DRF elements with 10^{-20} absolute and 10^{-12} relative accuracy respectively.

3.4.3 Single-Mode Systems

We used this simulation procedure with the same source scanning configuration as Section 3.3: the sources labeled R and L are scanned over $x_R, x_L \in \{-15, -14.8, \ldots, 15\}$ mm, at a normal distance $z = 100$ mm of the detector, whose on-axis position is $x = 0$ mm. The simulated DRF amplitude in Figure 3.4a has a distinctive Gaussian-like shape. The DRF phase pattern presented in Figure 3.4b includes a large contribution from the geometric phase of the sources, similar to that observed in the case of point-like sources and detectors in Figure 3.1b. At this time, we do not wish to remove this contribution: the phase pattern contains important information and it is non-trivial to prove that an operation removing the geometric phase term allows the simulated DRF's modes and sensitivity spectrum to be recovered properly. This topic will be revisited in Chapter 7, in the context of experimental datasets.

Figure 3.5 presents the DRF's visibility and coherence patterns, as defined by Equations (2.71) and (2.72); their respective phase patterns are identical to that of the complex DRF amplitude, and therefore not shown again. The visibility's diagonal cross shape is caused by the sum of single-source contributions in the denominator and reaches a maximum value of 1 along the diagonal and antidiagonal; this corresponds to measuring a fringe in the detector output whose peak-to-peak amplitude is equal to the sum of single-source powers. The DRF coherence is constant and equal to 1, within the computational precision. This behavior is characteristic of single-mode systems.

The same simulation procedure can be repeated for detector responses built from LG modes other than the fundamental LG_{00}. Figure 3.6 presents the single-mode DRF obtained assuming that the detector response has functional forms based on either the LG_{01}, LG_{10} or LG_{11} mode. For the LG_{01} and LG_{11} modes, we observe a four-fold symmetry associated with the $l = 1$ azimuthal index; while the fine structure in the phase patterns is dominated by the geometric phase contribution, we clearly observe different symmetries compared to the LG_{00} and LG_{10} cases. For cases where $p = 1$, secondary amplitude maxima are visible, separated from each other (and the global maximum, in the case of LG_{10}) by zero-amplitude lines along x_R and x_L. These simulated DRFs differ from the assumed LG modes used to model the detector's response, shown in Figure 3.3. Indeed, the simulated DRFs in Figure 3.6 are the projections of LG modes from the spatial basis on the detector surface into the basis of sampled source positions, subject to the chosen model for the source fields, as was discussed in Section 2.5.

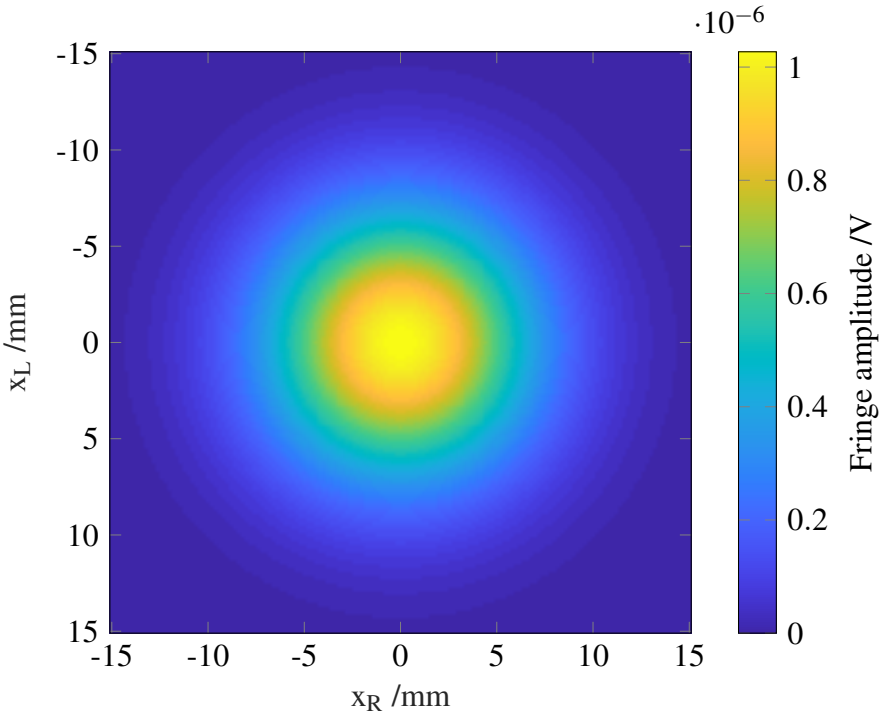

(a) DRF amplitude

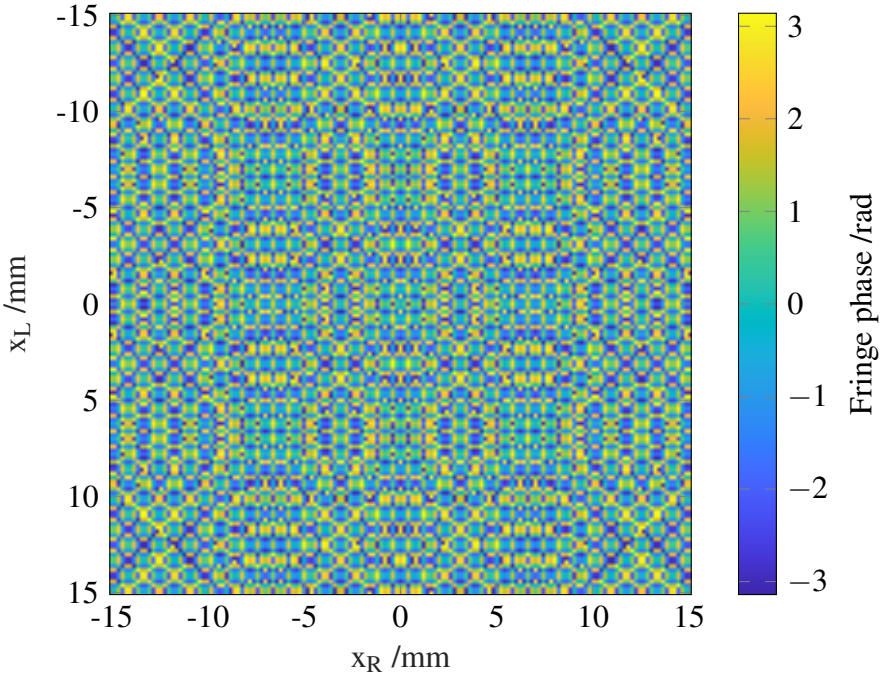

(b) DRF phase

Fig. 3.4 Simulated single-mode DRF, built from the LG_{00} mode.

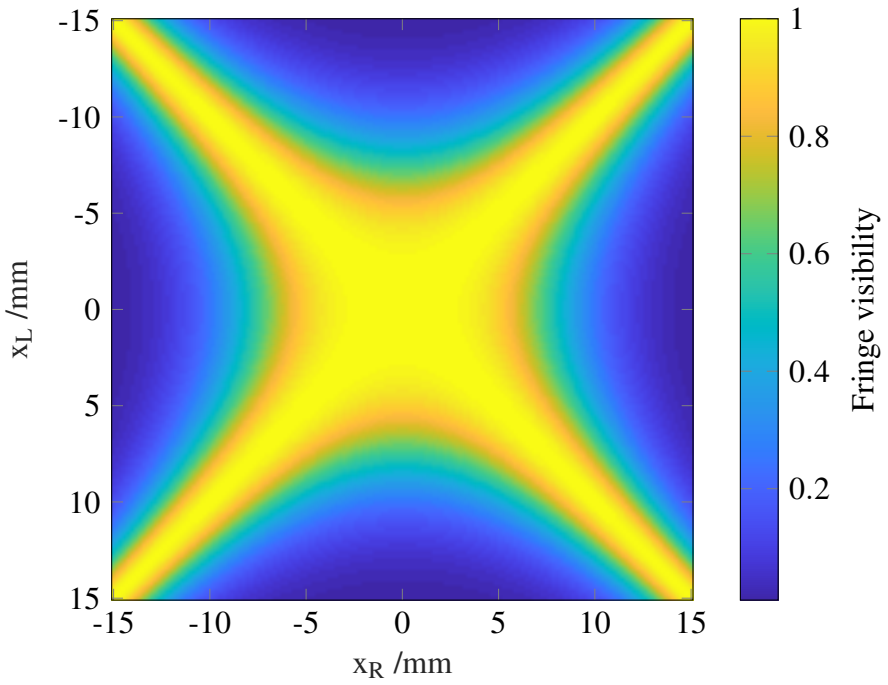

(a) DRF visibility amplitude

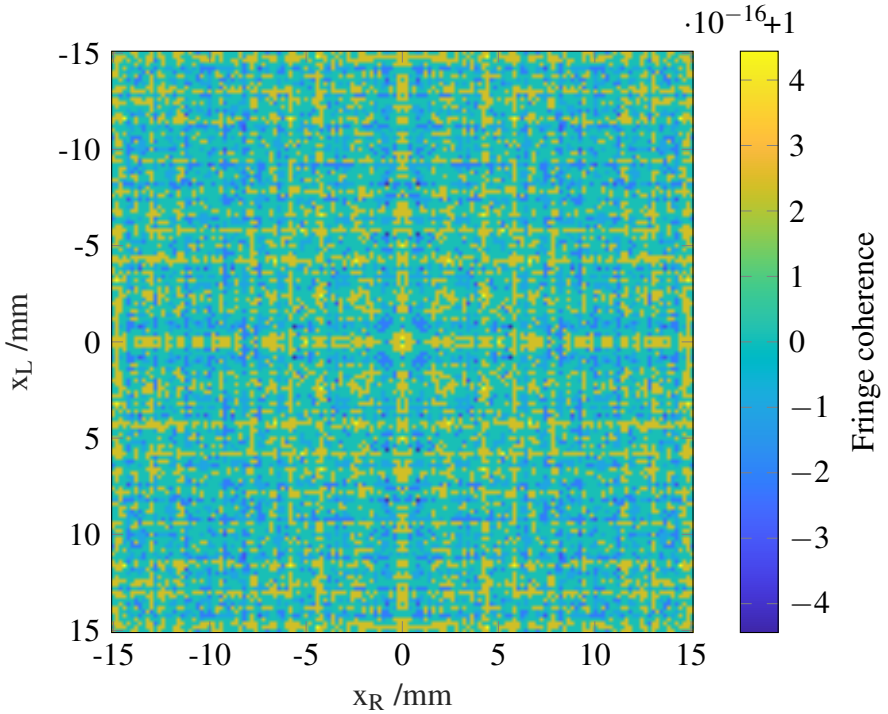

(b) DRF coherence amplitude, relative to a constant pattern with value 1.

Fig. 3.5 Simulated single-mode DRF, built from the LG_{00} mode.

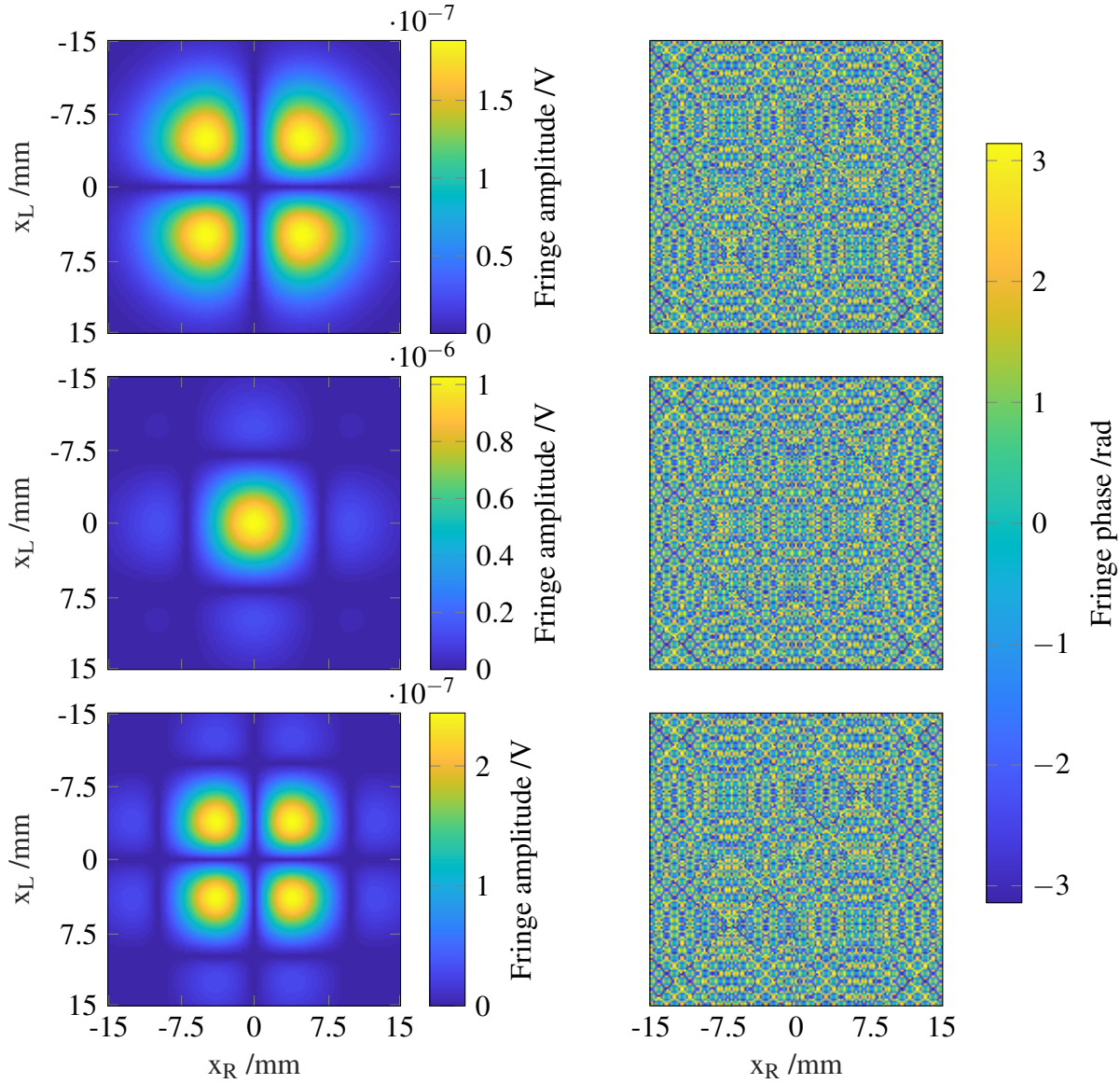

Fig. 3.6 Simulated single-mode DRF amplitude (left column) and phase (right column) patterns, respectively built from the LG_{01}, LG_{10} and LG_{11} modes.

3.4.4 Few-Mode Systems

Figure 3.7 presents the simulated DRF amplitude and phase patterns, obtained by building the detector response as an incoherent sum of the LG_{00} and LG_{01} modes, i.e. the two lowest order LG modes. We observe a primary maximum at the on-axis position, with decreases along the main diagonal. Along the antidiagonal, the DRF amplitude decreases rapidly, reaches a zero-amplitude point before increasing monotonically towards a secondary maximum approximately at $x_{R/L} = \pm 7\,\mathrm{mm}$. This behavior is symmetric along the main

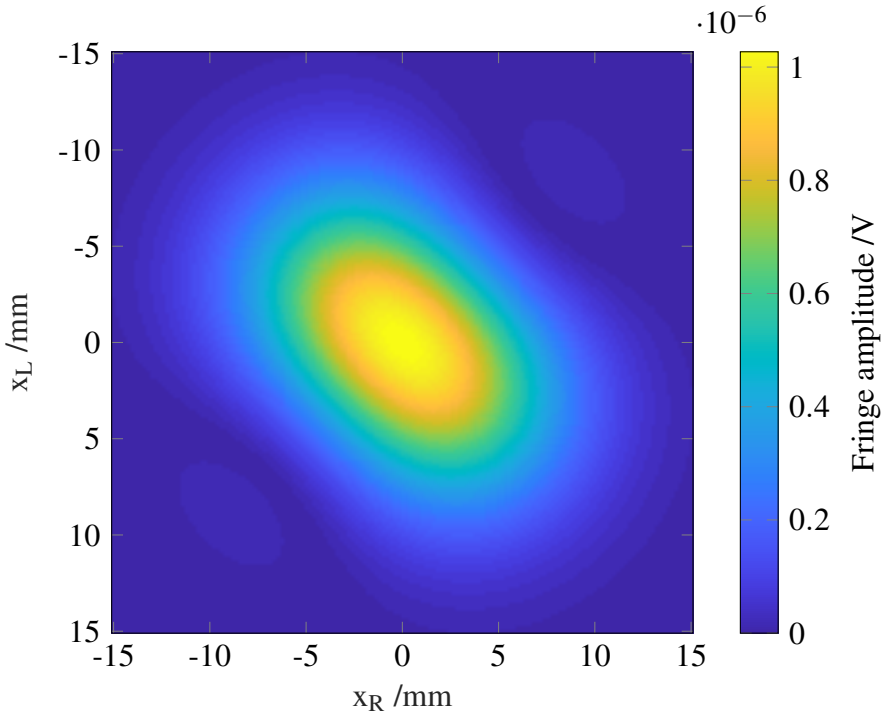

(a) DRF amplitude

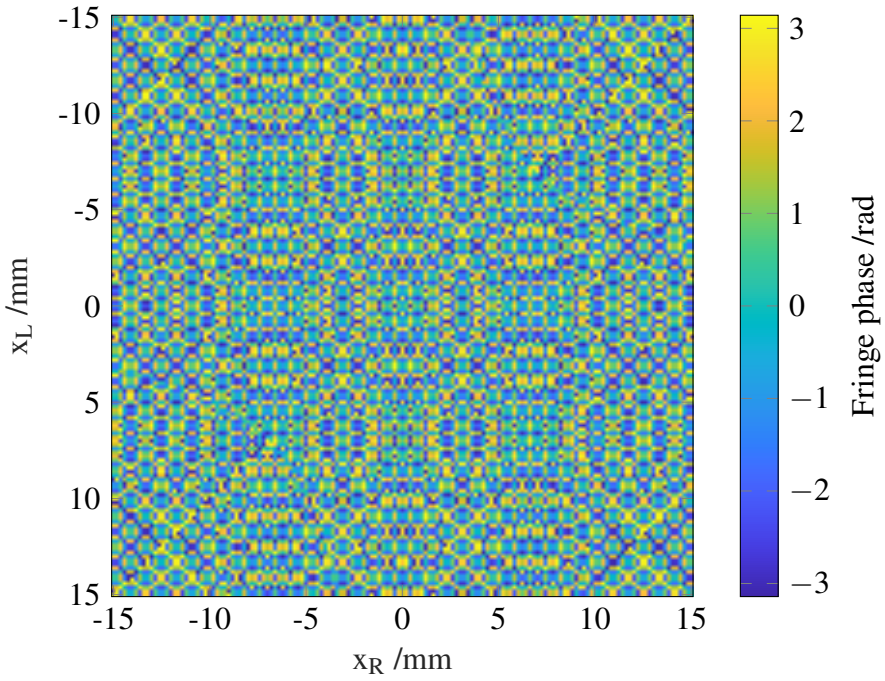

(b) DRF phase

Fig. 3.7 Simulated two-mode DRF, built from the LG_{00} and LG_{01} modes.

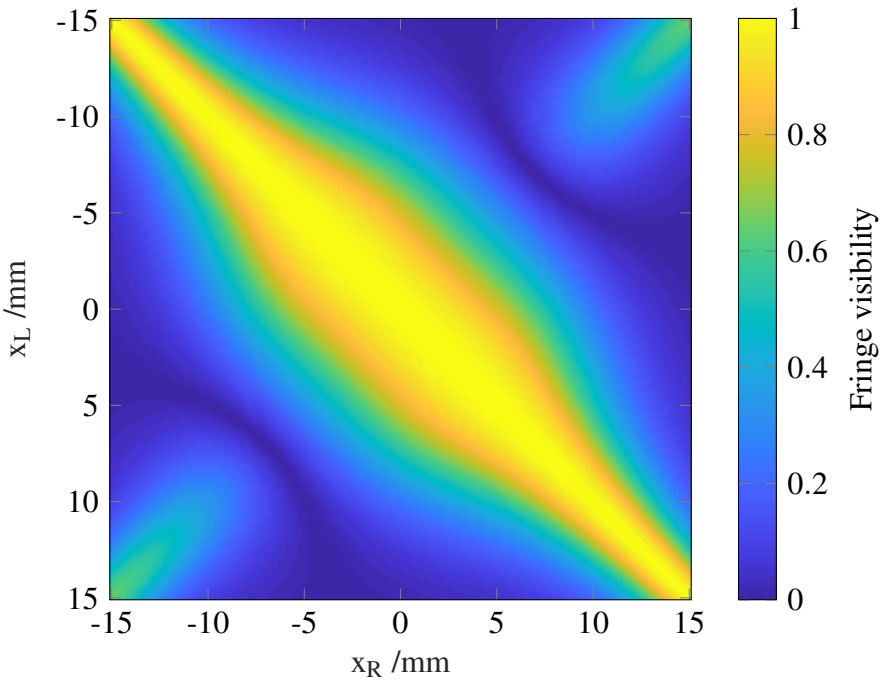

(a) DRF visibility amplitude

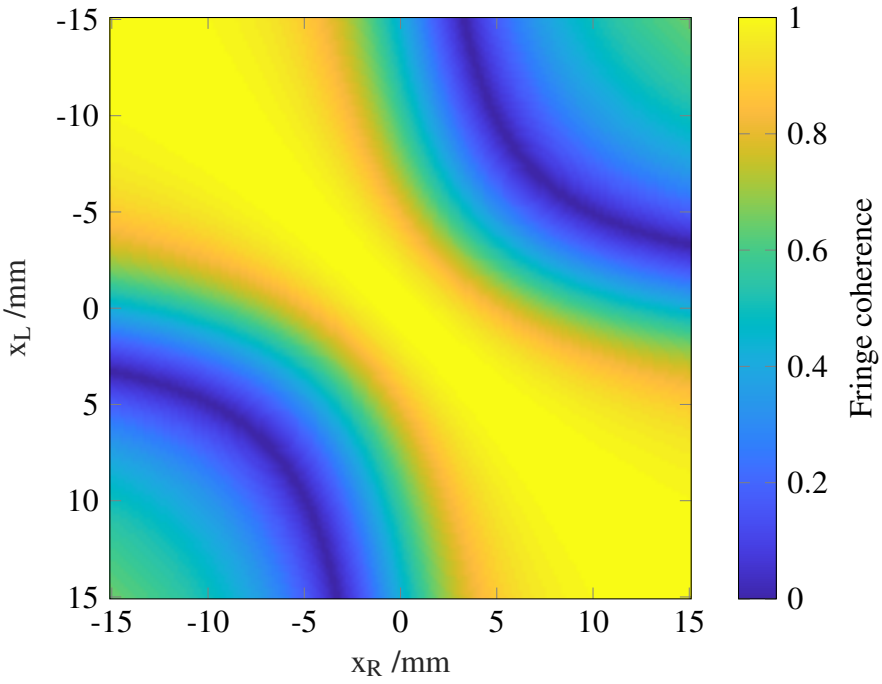

(b) DRF coherence amplitude

Fig. 3.8 Simulated two-mode DRF, built from the LG_{00} and LG_{01} modes.

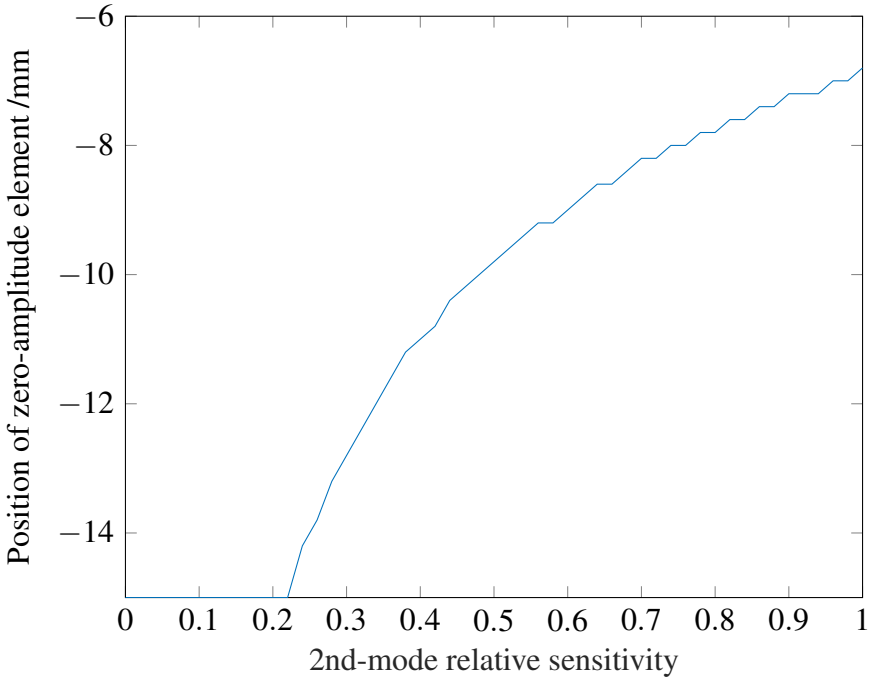

Fig. 3.9 Position along the antidiagonal $x_R = -x_L$ for which the fringe amplitude is zero, in a two-mode simulated system built from the LG_{00} and LG_{01} modes with varying relative sensitivity of the second mode; a value of -15 mm indicates that the zero-amplitude line is outside of the scanning range considered.

diagonal. The simulated DRF's visibility and coherence patterns shown in Figure 3.8 clearly display a zero-amplitude line in the antidiagonal corners, separating the pattern's global maximum from the local maxima. Both patterns have value 1 along the diagonal, with structure appearing rapidly as the sources are moved to unequal positions.

In general systems, the two lowest-order modes do not necessarily have equal sensitivities. We studied the effect of changing the relative sensitivities of the two-modes by decreasing that of the second mode, and found that the position of the zero-amplitude line recedes towards the antidiagonal corners. For the chosen scanning configuration, the zero-amplitude lines disappears from the scanning range when the ratio of sensitivities falls below 0.24. In Figure 3.9, we show the off-axis position corresponding of the antidiagonal element closest with value nearest zero, as a function of the relative sensitivity of the second mode. If instead we keep the ratio of mode sensitivities fixed, i.e. vary their absolute values by a unique factor, we observe that the position for which the fringe amplitude is zero remains constant. In other words, the zero-amplitude line's position with respect to the antidiagonal corners is dependent only on the ratio of the two modes' sensitivities, not their absolute values.

3.4.5 Multi-Mode Systems

An important subtlety in the case of multi-mode systems is the choice of the sequence in which high-order LG modes appear; indeed, we were unable to find a definitive ordering of LG modes in the literature, i.e. a list of index pairs from lowest to highest order. We choose to use as a proxy the ordering of Linearly Polarized (LP) modes, describing radiation transmission in optical fibers, which will be investigated in Section 3.5. The order of appearance is related to the roots of the Bessel function of the first kind J_l, with the order l equal to the azimuthal index defined in Equation (3.12):

- For azimuthal index $l = 0$, we consider the $p-1^{\text{th}}$ root J_1 for the the p^{th} mode;
- For azimuthal indices $l > 0$, we consider the p^{th} root J_{l-1} for the the p^{th} mode;
- The n^{th} LG mode has the l and p indices of the mode with n^{th} largest corresponding Bessel function root.

We remark that this order approximately corresponds to the order of increasing LG mode width, illustrated in Figure 3.3.

By generating a large enough number of Bessel function roots, we can sequentially find the index pairs of the LG modes up to an arbitrarily large order. In Figure 3.10, we show the simulated DRF amplitude and phase patterns of a system built from the 121 lowest-order LG modes. The amplitude pattern displays structure with smaller width than in the few-mode case, with zero-amplitude lines between local maxima; the latter decrease with the distance from the on-axis position. The phase pattern retains many of the symmetries observed in single-mode and few-mode systems, indicating that the geometric phase remains the dominating contribution. Differences between the multi-mode DRF phase pattern in Figure 3.10b and those of single-mode and few-mode systems are noticeable; we hypothesize that these are linked to the zero-amplitude boundaries between local amplitude maxima, and will study this in Chapter 8.

We also investigated highly multi-mode DRFs obtained from the incoherent sum of single-mode DRFs using non-uniform sensitivities, rather than equal sensitivities. An unambiguous order must be chosen for the application of these weights to the collection of single-mode DRFs: for simplicity, we can choose the order in which they were computed. Figure 3.11 presents the DRF amplitude pattern of the incoherent sum of the same 121 modes as Figure 3.10, but with sensitivities set by the opposite of an "S"-shaped function; we choose the opposite of the logistic function, defined as

$$f(x) = 1 - \frac{L}{1 + e^{-k(x-x_0)}} \tag{3.13}$$

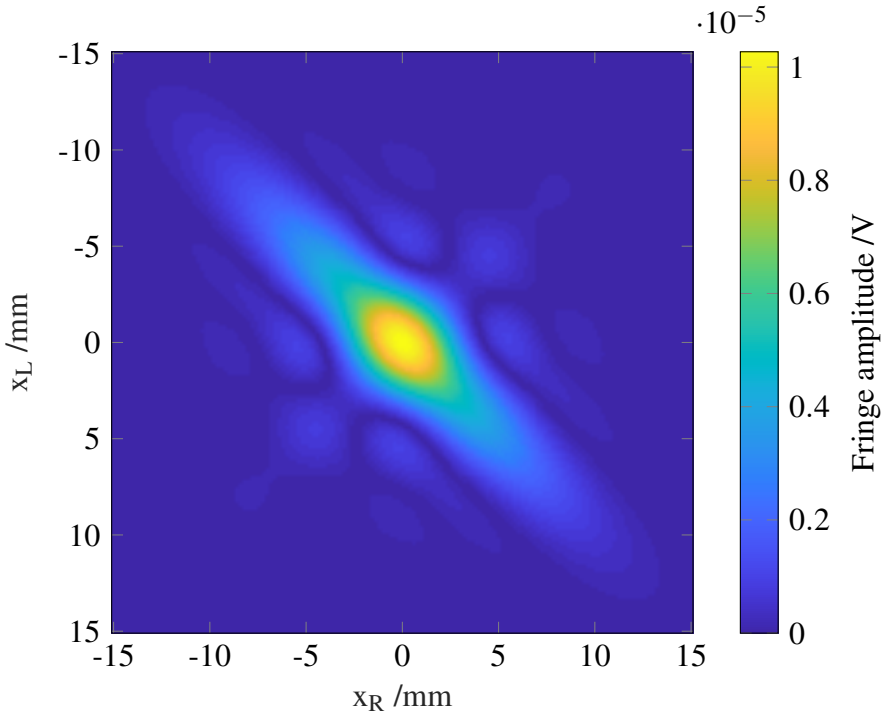

(a) DRF amplitude

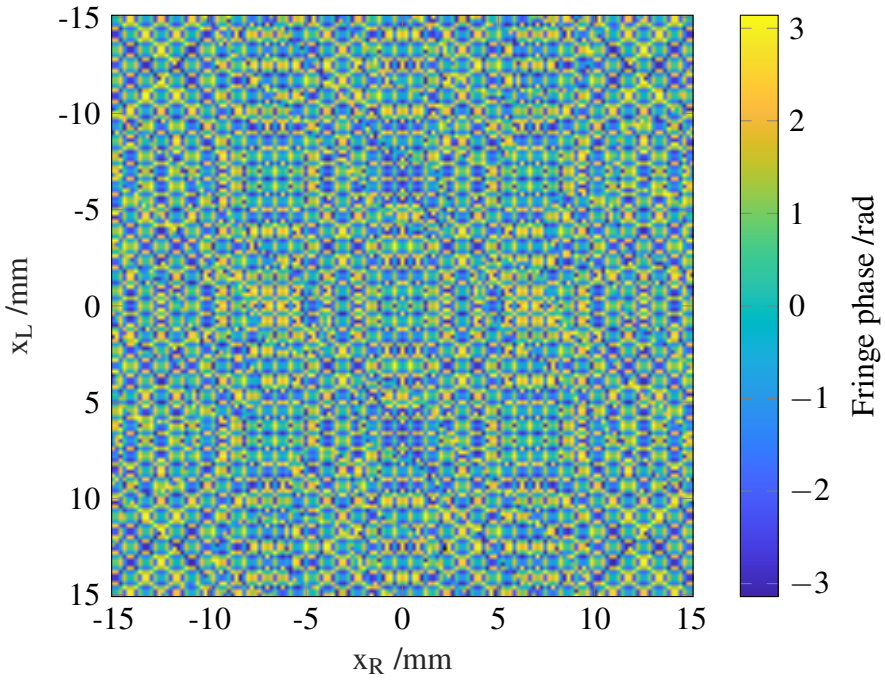

(b) DRF phase

Fig. 3.10 Simulated multi-mode DRF, built from the 121 first LG modes using equal sensitivities.

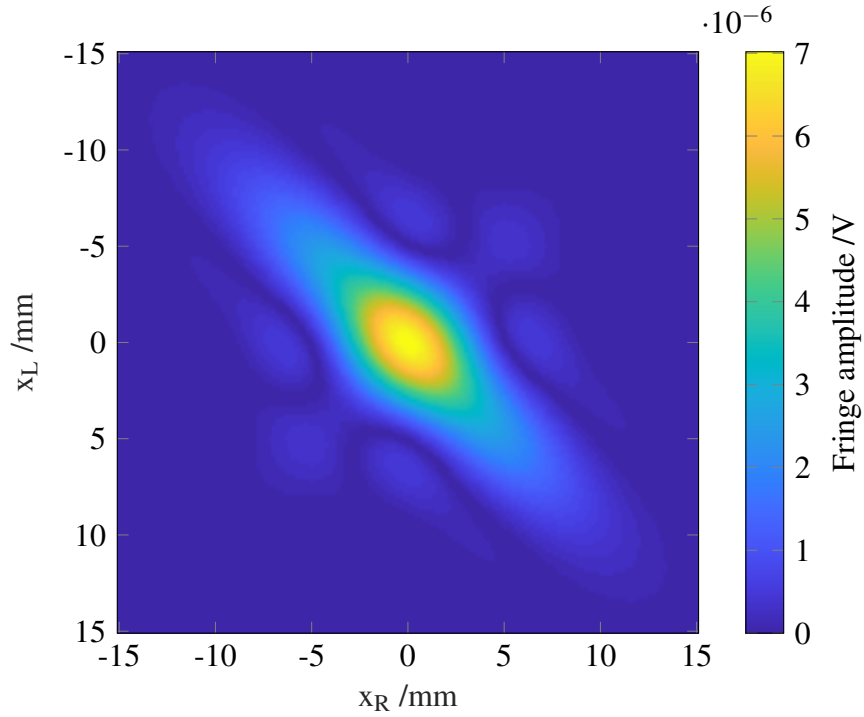

(a) DRF amplitude

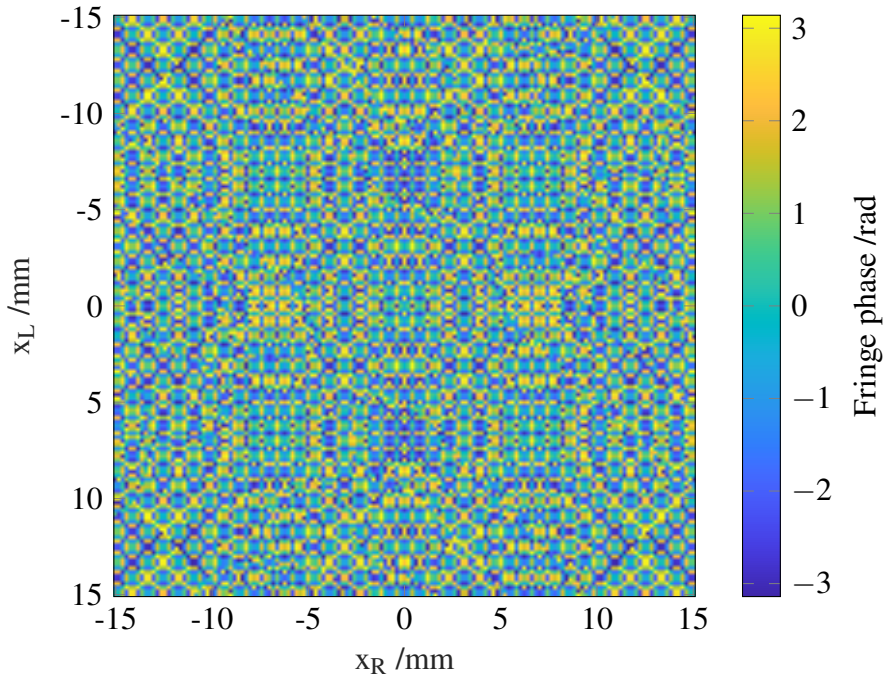

(b) DRF phase

Fig. 3.11 Simulated multi-mode DRF, built from the 121 first LG modes using a tapered sensitivity spectrum defined by the logistic function in Equation (3.13) with $L = 1$, $k = 0.1$ and $x_0 = 60$.

where x_0 is the sigmoid's midpoint, L is the curve's maximum value, and k is the logistic growth rate or steepness of the curve; we selected $L = 1$, $k = 0.1$ and $x_0 = 60$. We observe that the amplitude structure is wider in the case of the tapered sensitivity spectrum, and that the global and local maxima are decreased; the phase pattern remains largely unchanged.

In all of the results above, the detector beam waist was assumed to be 5 µm, in line with the MFD of single-mode and few-mode fibers measured by manufacturers. However, this argument is less applicable for multi-mode fibers, whose MFDs are measured for their total beampattern: the beam waist of their first mode cannot be inferred from their MFD, because the width of LG modes increases with their order, as we had seen in Figure 3.3. To investigate the effect of changing the beam width, we repeat the simulation procedure assuming a detector beam waist of 25 µm, instead of 5 µm. The simulated DRF, presented in Figure 3.12, displays the same qualitative features as Figure 3.10 but seemingly zoomed out; in particular, the phase pattern appears to wrap more rapidly, while retaining its symmetries. Using sensitivities set by the logistic curve with width $k = 0.1$ and midpoint $x_0 = 60$ instead of uniform sensitivities, as for Figure 3.11, has the same qualitative effect: the amplitude structure has reduced widths and a lower maximum, while the amplitude pattern is largely identical.

3.5 Linearly Polarized Modes

3.5.1 Theory

In keeping with basing the selection of a modal basis for the assumed DRF on physical intuition, such as the properties of the detector system, we may ask whether the optical behavior of fiber-coupled detectors is determined by LG modes, from the free-space propagation of the virtual detector beampattern, or by LP modes, from the radiation transmission inside the fiber. Indeed, both of these sets of modes must come into play in the total system. It is therefore important to investigate assumed DRFs built from LP modes, analogously to Section 3.4.

LP modes arise when considering the complex electric field $E(r,\phi)$ in an optical fiber, a radially symmetric medium; its propagation is determined by the wave equation

$$\frac{\partial^2 E}{\partial r^2} + \frac{1}{r}\frac{\partial E}{\partial r} + \frac{1}{r^2}\frac{\partial^2 E}{\partial \phi^2} + \beta E = 0, \tag{3.14}$$

with β denoting the imaginary part of the propagation constant in the medium. Solving Equation (3.14) relies on the radial symmetry of the medium, where its refractive index is

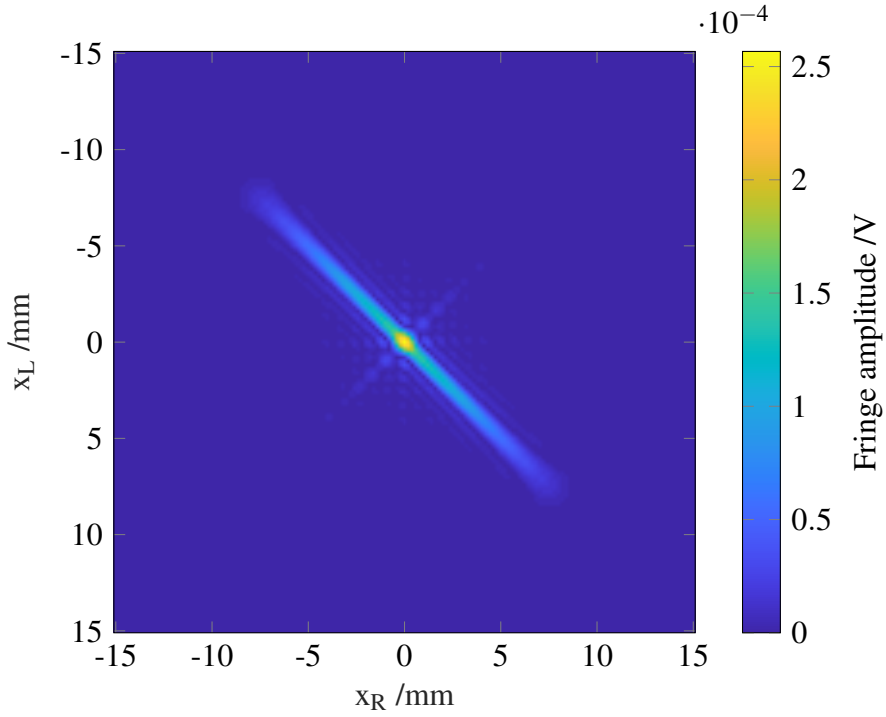

(a) DRF amplitude

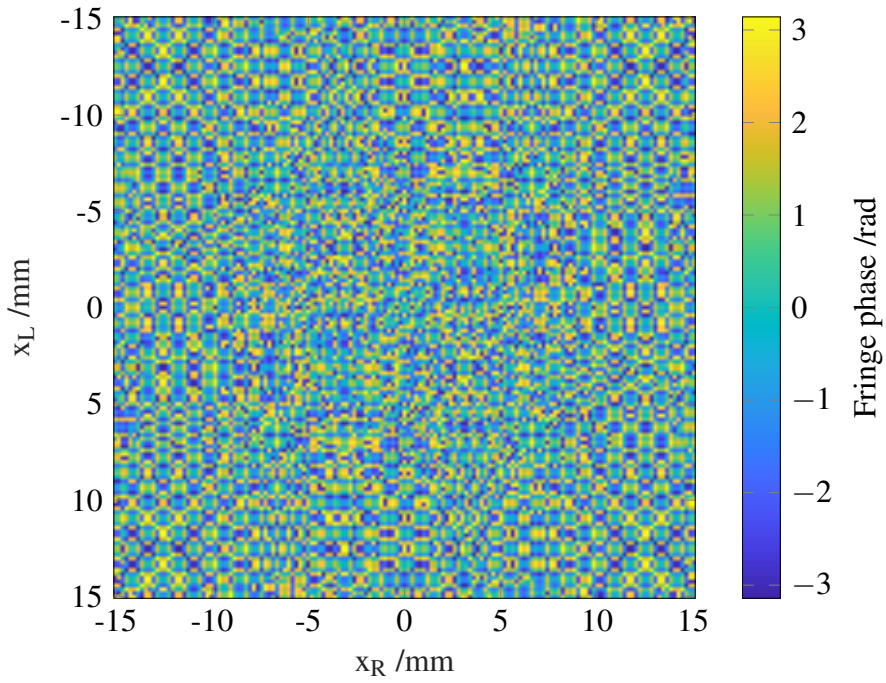

(b) DRF phase

Fig. 3.12 Simulated multi-mode DRF, built from the 121 first LG modes with 25 µm width, using equal sensitivities.

dependent only on the radius r: an ansatz $E(r,\phi) = E_{lm}(r)e^{il\phi}$ is introduced, where $l \geq 0$ and $m \geq 1$ are integer indices respectively denoting the angular dependence and the ordering number of the mode for the corresponding l-value. Simplifications are obtained for two-layer "step-index" fibers: when the refractive indices of the concentric core and cladding are almost identical, the weak guidance limit is used [18]. Equation (3.14) for an optical fiber of core radius a then has the solutions

$$\mathrm{LP}_{lm}(r,\phi) = N_{lm}e^{il\phi}\begin{cases}\dfrac{J_l(\nu_{lm}r/a)}{J_l(\nu_{lm})} & \text{for } r < a\\[2ex] \dfrac{K_l(\mu_{lm}r/a)}{K_l(\mu_{lm})} & \text{for } r \geq a\end{cases} \tag{3.15}$$

where J_l and K_l are respectively the Bessel functions of the first and second kind, of order l, and ν_{lm} and μ_{lm} are respectively the normalized propagation constants of the core and cladding [79].

The propagation constants are found by solving the eigenvalue equation:

$$\nu\frac{J_{l+1}(\nu)}{J_l(\nu)} = \mu\frac{K_{l+1}(\mu)}{K_l(\mu)} \tag{3.16}$$

subject to

$$\nu^2 + \mu^2 = V^2, \tag{3.17}$$

where

$$V = \frac{2\pi}{\lambda}NA\ a \tag{3.18}$$

is the fiber's V-number, set by the operating wavelength λ, the fiber core radius a and its numerical aperture NA, a dimensionless characteristic of the maximum angle at which the fiber accepts radiation. The V-number is a dimensionless quantity loosely interpreted as a normalized optical frequency and related to the number of modes supported by the fiber; this will be discussed further in Chapter 4. Equations (3.16) and (3.17) are solved numerically for the V-number of interest. For each value of l, there may be one or more (ν,μ) pair satisfying the eigenvalue equation (3.16); in the latter case, they can be ordered by increasing ν, giving rise to the second index m. In practice, we subtract the left- and right-hand sides of Equation (3.16) and use (3.17) to obtain

$$\nu\frac{J_{l+1}(\nu)}{J_l(\nu)} - \sqrt{V^2-\nu^2}\frac{K_{l+1}(\sqrt{V^2-\nu^2})}{K_l(\sqrt{V^2-\nu^2})} = 0. \tag{3.19}$$

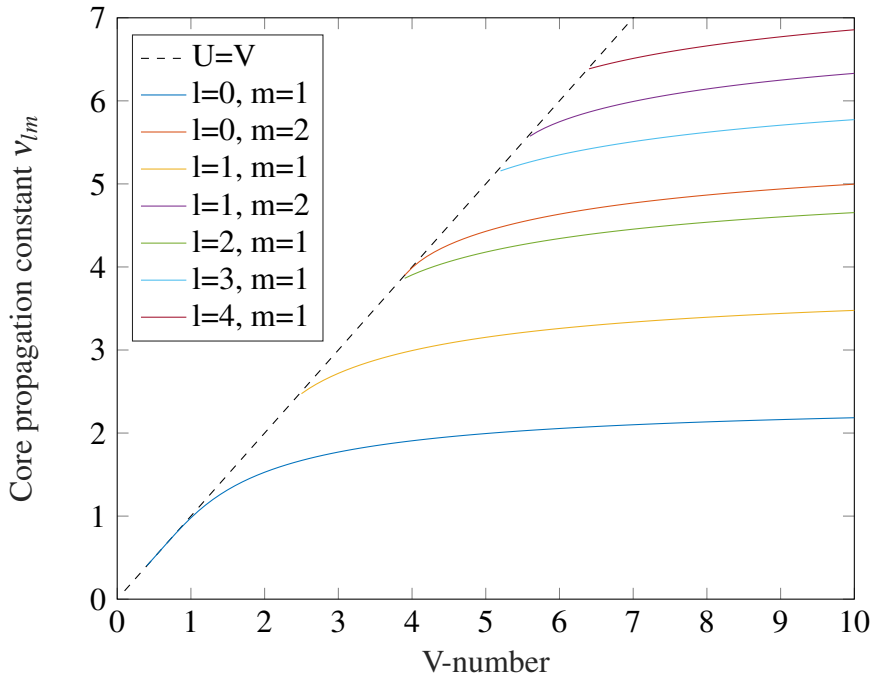

Fig. 3.13 Propagation constant of low-order LP modes, as function of the fiber's assumed V-number V, displaying the appearance of higher-order modes for increasing $V \in [0;10]$.

Here, we consider only step-index fibers, rather than graded-index. While the latter often have superior performance (such as lower loss when bent), step-index are the simplest case to evaluate because their behavior is well understood theoretically, the most readily available commercially, and therefore the most likely to be used in the future experiment that will be discussed in the next chapters.

3.5.2 Implementation

We first verified our ability to properly solve the eigenvalue equation (3.16), by numerically solving Equation (3.19) for various order indices l. In Figure 3.13, we show the computed values of the propagation constant of low-order LP modes in the fiber core, as the fiber V-number is varied. This result is found to be in exact agreement with the literature [18]. As V is increased, solutions become available for larger values of the order index l. The values of V for which each mode appears is equal to the corresponding root of the Bessel function of the first kind, found in Section 3.4.5. We also demonstrated our ability to correctly compute the corresponding cladding propagation constants [18]. Together, these were used to obtain the spatial forms of the 10 lowest-order LP modes, presented in Figure 3.14. Note that,

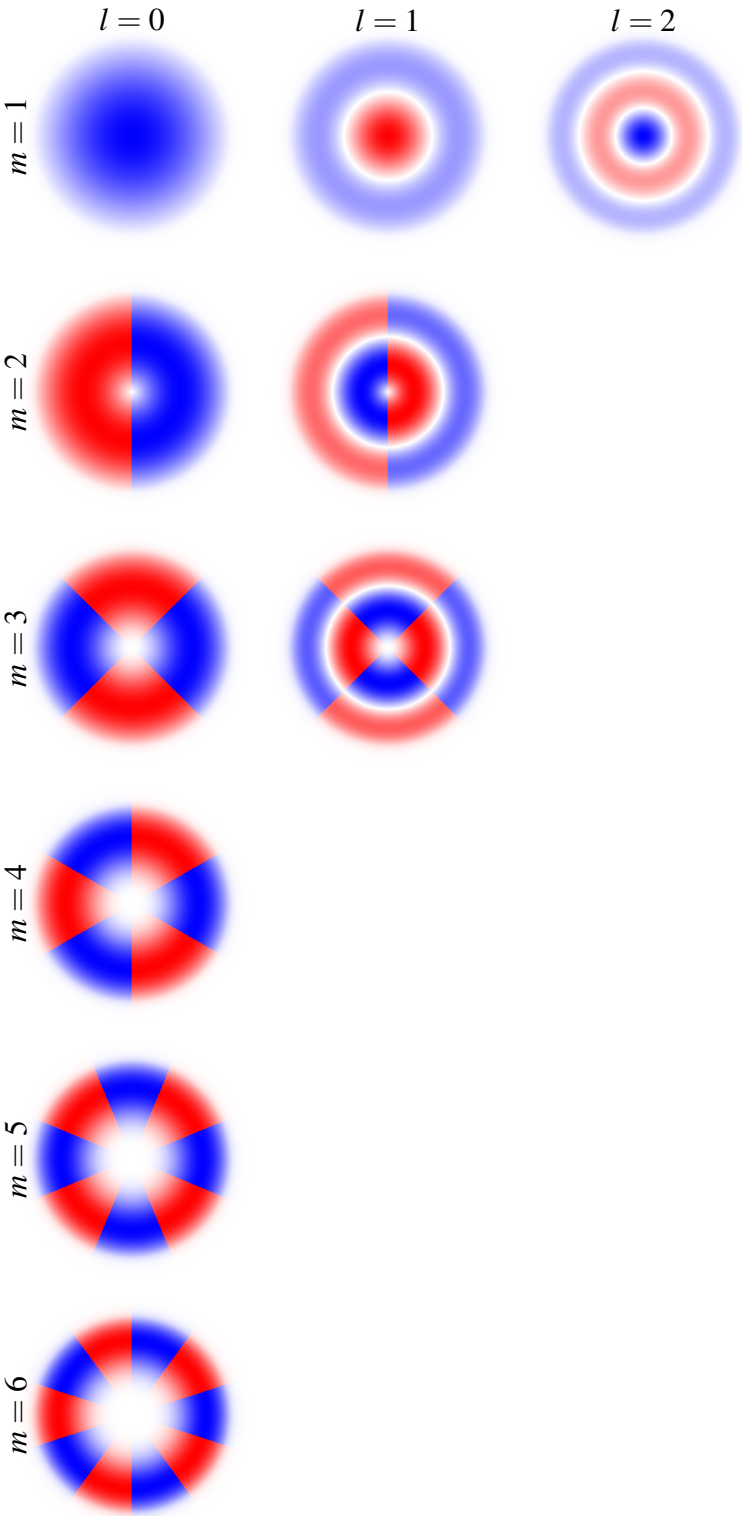

Fig. 3.14 Spatial forms of the 10 lowest order LP modes, arranged by their azimuthal index l and order index m; the opacity is proportional to the mode's amplitude, and the blue and red colors respectively correspond to the positive and negative sign of the phase.

contrary to LG modes, the width of LP modes is similar for all indices because it is related to the core radius a.

Using this capability, the simulation algorithm has the following steps:

1. Values of the fiber core radius a and its numerical aperture NA are selected, and the fiber's V-number V is computed using Equation (3.18);

2. Equation (3.19) is solved to obtain the propagation constants of all modes present;

3. The vector of single-source, single-point power contributions is computed by performing a two-dimensional integral of the product of the source beam (projected LG mode) with the detector response (LP mode) over the integration surface;

4. The outer product of this vector with its conjugate transpose is computed to obtain the single-mode simulated DRF;

5. Steps 3 and 4 are repeated for each LP mode;

6. Multi-mode DRFs are assembled from the sum of single-mode DRFs, weighted by user-selected sensitivities.

We note that the source beam is still modeled using projected LG modes, rather than LP modes because (i) we know that the free-space behavior is described by LG modes, and (ii) we do not have a way of propagating LP modes in free-space. As for Laguerre-Gaussian modes in Section 3.4, we computed the DRF of each LP mode individually.

3.5.3 Single-Mode Systems

The same source scanning configuration as Sections 3.3 and 3.4 is used: the sources labeled R and L are scanned over $x_R, x_L \in \{-15, -14.8, \ldots, 15\}$ mm, at a normal distance $z = 100$ mm of the detector, whose on-axis position is $x = 0$ mm. We proceeded using the core radius $a = 4.1$ µm and the numerical aperture NA $= 0.14$, to simulate the behavior of a single-mode optical fiber with these characterstics. The simulated DRF, presented in Figure 3.15, has a clear resemblance with the single-mode DRF assuming LG modes: its amplitude pattern is Gaussian-like, while its phase pattern is nearly identical and dominated by the geometric phase contribution observed in Section 3.3.3. Similarly, the DRF visibility and coherence have the same qualitative features as those observed with a single-mode system based on LG modes, in Section 3.4.3.

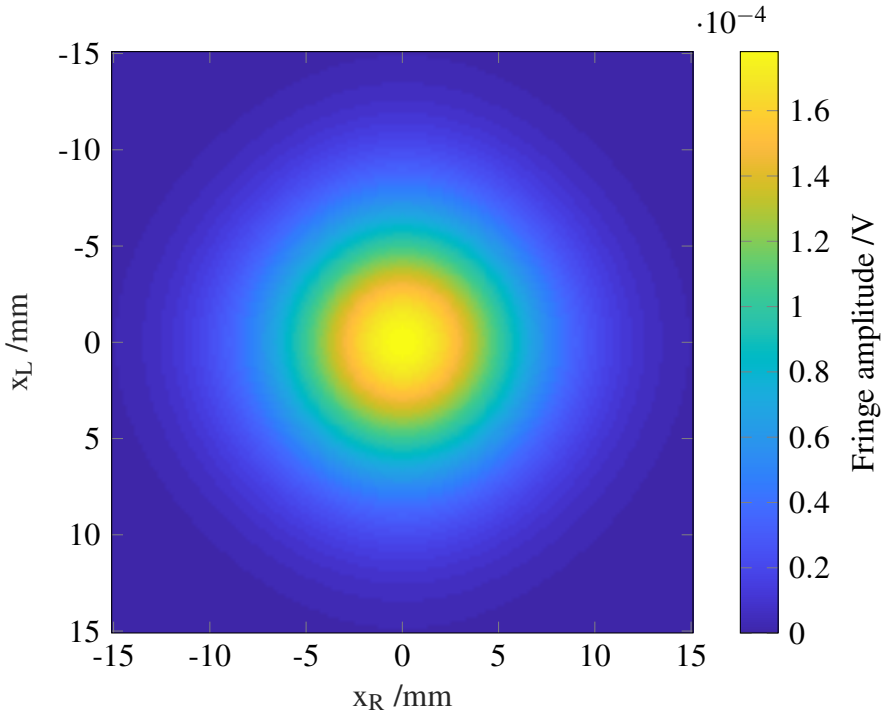

(a) DRF amplitude

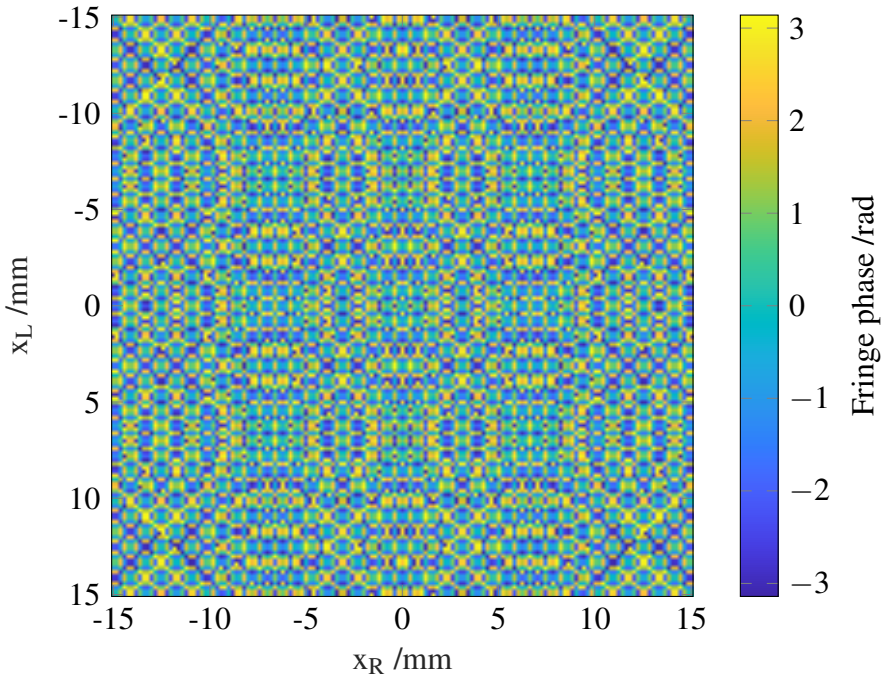

(b) DRF phase

Fig. 3.15 Simulated single-mode DRF, built from the fundamental LP_{10} mode.

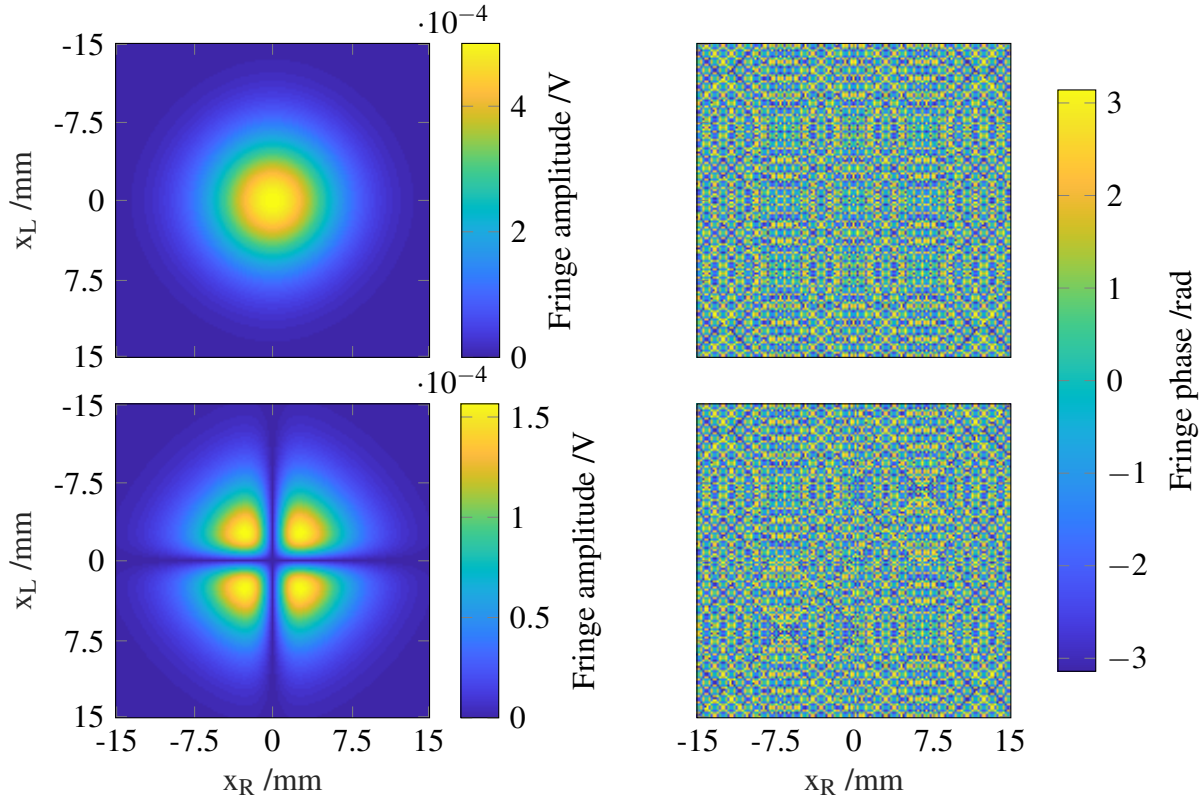

Fig. 3.16 Simulated single-mode DRF amplitude (left column) and phase (right column) patterns, respectively built from the LP_{10} and LP_{11} modes, with $a = 5.5\,\mu m$ and $NA = 0.12$.

3.5.4 Few-Mode Systems

The same simulation procedure is repeated using the core radius $a = 11\,\mu m$ and the numerical aperture $NA = 0.12$, characteristics typical of an optical fiber whose behavior is two-moded at $\lambda = 1550\,nm$ operating wavelength. In Figure 3.16, we present the amplitude and phase patterns of the two modes' individual responses, which are in line with our qualitative expectations: the LP_{10} mode's DRF has a Gaussian-like amplitude and a phase pattern similar to the single-mode's due to the geometric phase, while the LP_{11} mode's DRF has four-fold symmetry from the $e^{il\phi}$ term and zero amplitude at $x_R = x_L = 0$ due to the J_1 term.

For low-order modes, the $LG_{p,l}$ mode has a functional form that most resembles the $LP_{l,p+1}$ mode. For example, Figures 3.3 and 3.14 show that the LG_{00} and LP_{01}, LG_{10} and LP_{02}, LG_{01} and LP_{11}, and LG_{02} and LP_{21} modes are qualitatively similar, both in their amplitudes' radial symmetry and the angular phase factor. These pairs can indeed be coupled to each other with very high fractional efficiencies, provided that the LG modes' width is adjusted to that of the corresponding LP mode. For instance, it is possible to generate a specific LG mode using a spatial light modulator and project it onto a correlation

filter emulating an LP mode: the coupling efficiency is then measured experimentally [80]. However, for the purpose of confirming whether the optical response of a more general system, such as a fiber-coupled detector, is set by LG or LP modes as mentioned in Section 3.5.1, we require another method; EAI is a strong candidate. Its success in an experimental setting may depend on the impact of noise in the measured datasets, as well as imperfections in the experimental apparatus and uncertainties in the detector system, including the typical 5% manufacturing precision of optical fiber core sizes.

We investigated the two-mode system built from the incoherent sum of the LP_{10} and LG_{11} modes presented in Figure 3.16. In Figure 3.17, we present its amplitude and phase patterns; the former has an oval shape that is slightly concave along the antidiagonal, with opposite local maxima separated from the on-axis maximum by a zero-amplitude line. When applying a relative sensitivity coefficient to the LP_{11} mode, the position of the zero-amplitude lines moves towards the antidiagonal corners as the coefficient is decreased, similarly to what we had observed with LG modes.

We notice that the two-mode LG-based system has a concave zero-amplitude line near each antidiagonal corners, while the two-mode LP-based system's is convex. This is clearly observable in the DRF visibility and coherence patterns, presented in Figure 3.18. We were unable to resolve theoretically the question of whether LG or LP modes are appropriate as modes for the assumed DRF of a fiber-coupled detector system. This open question will be settled experimentally, in Section 6.5.2.

3.5.5 Multi-Mode Systems

The same simulation procedure is repeated using the core radius $a = 25\,\mu\text{m}$ and the numerical aperture $\text{NA} = 0.22$, characteristics typical of an optical fiber with multi-mode behavior at $\lambda = 1550\,\text{nm}$ operating wavelength. Figure 3.19 presents the simulated amplitude and phase patterns of the first four LP modes, namely LP_{10}, LP_{11}, LP_{12} and LP_{20} modes. Contrary to the low-order modes in the two-mode system shown in Figure 3.16, we observe secondary maxima in the amplitude patterns for these four first modes. Local maxima were observed in LG modes with radial index $p \geq 1$, shown in Figure 3.6, but to a much lesser degree. The presence of multiple local maxima with large amplitude in Figure 3.19 is indicative of a highly multi-mode system.

In Figure 3.20, we observe that the amplitude and phase patterns of the multi-mode DRF obtained from the incoherent sum of the 68 first LP modes is qualitatively similar to the multi-mode DRF obtained from LG modes, presented in Figure 3.20. The DRF amplitude decreases rapidly off-axis, albeit more gradually along the diagonal and antidiagonal, and displays local maxima that are separated by zero-amplitude lines. As observed previously,

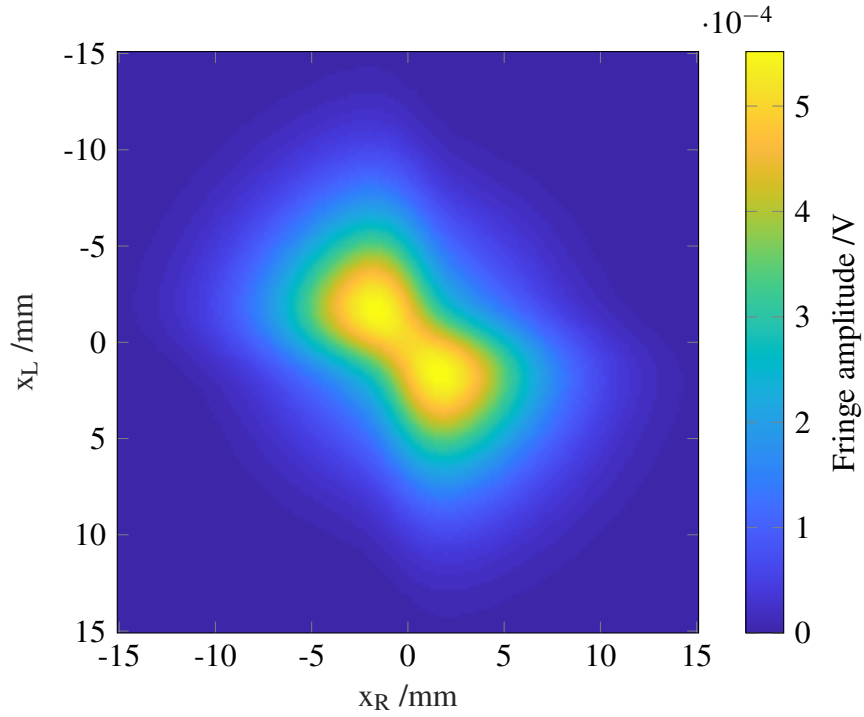

(a) DRF amplitude

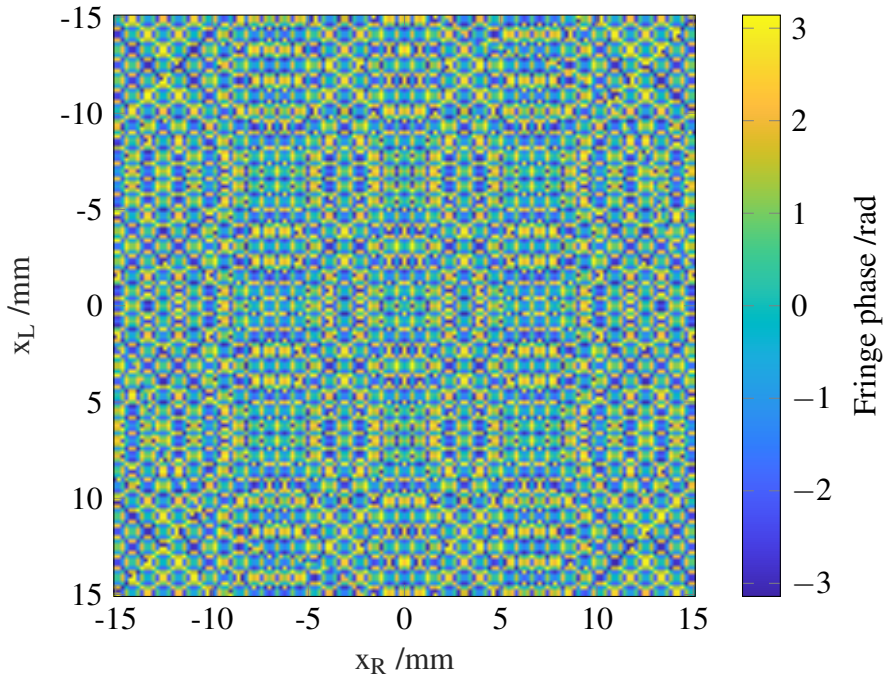

(b) DRF phase

Fig. 3.17 Simulated two-mode DRF, built from the LG_{00} and LG_{01} modes.

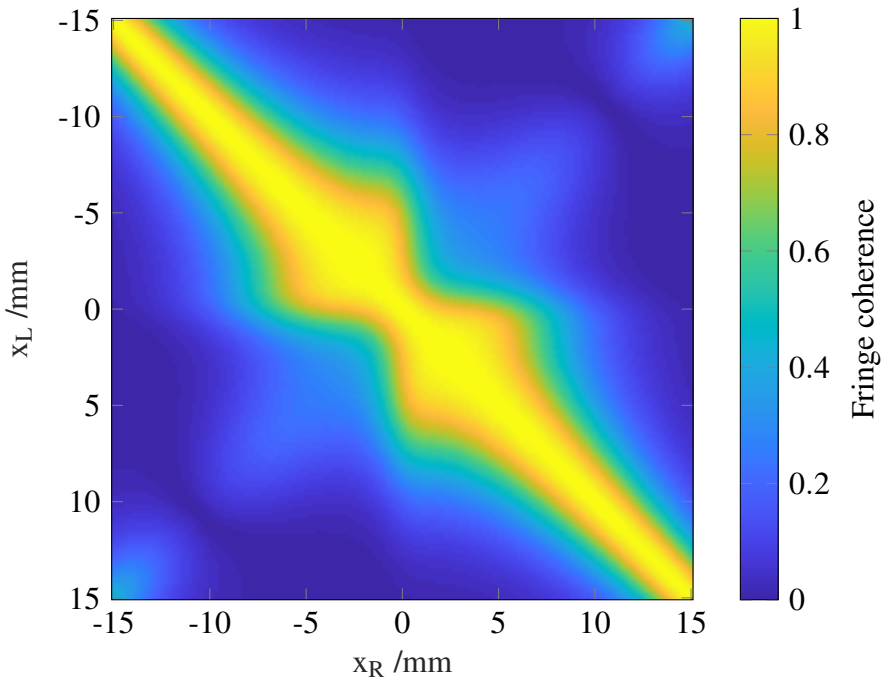

(a) DRF visibility amplitude

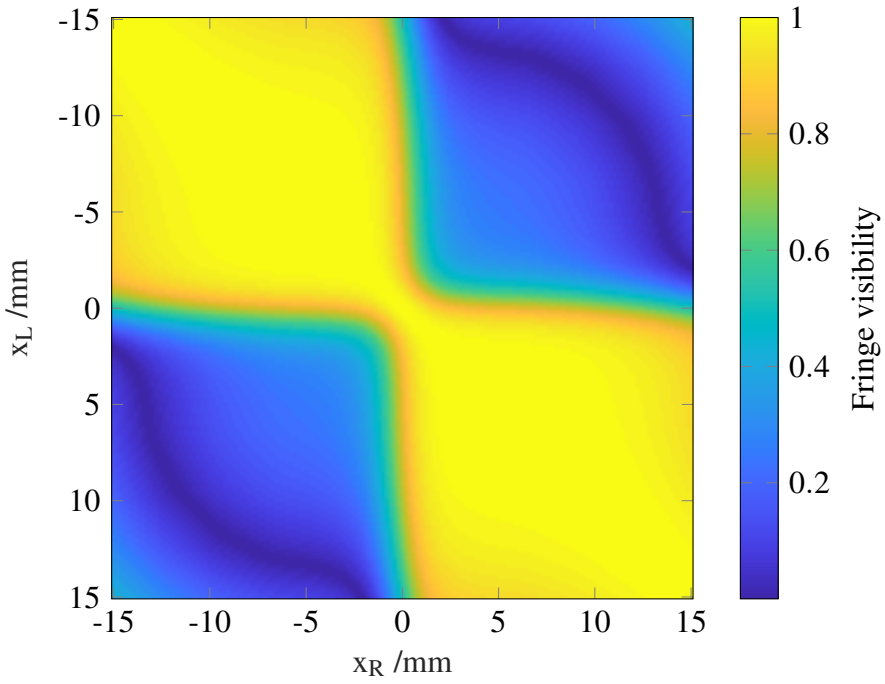

(b) DRF coherence amplitude

Fig. 3.18 Simulated two-mode DRF, built from the LP_{10} and LG_{11} modes.

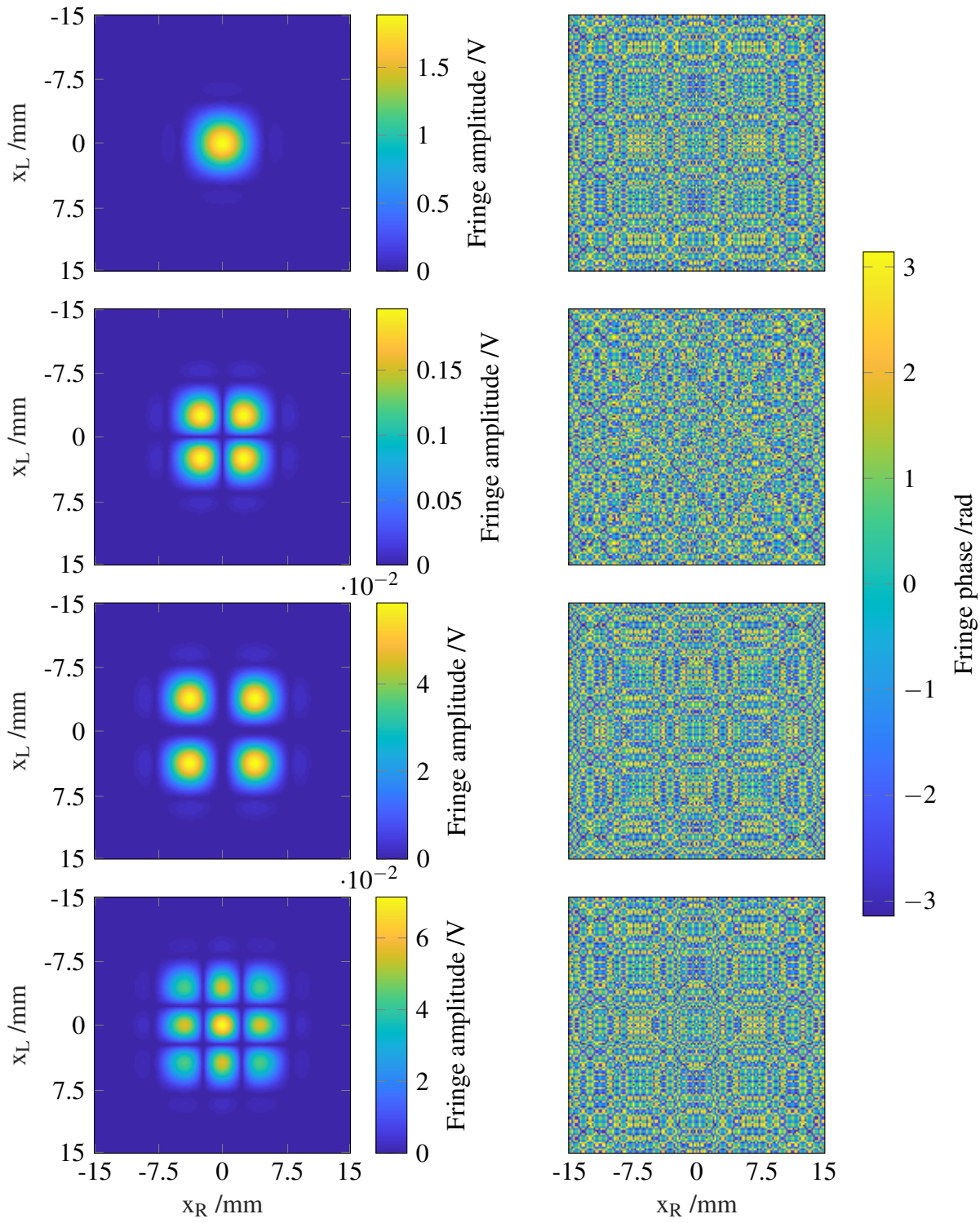

Fig. 3.19 Simulated single-mode DRF amplitude (left column) and phase (right column) patterns, respectively built from the LP_{10}, LP_{11}, LP_{12} and LP_{20} modes, with $a = 25\,\mu m$ and $NA = 0.22$.

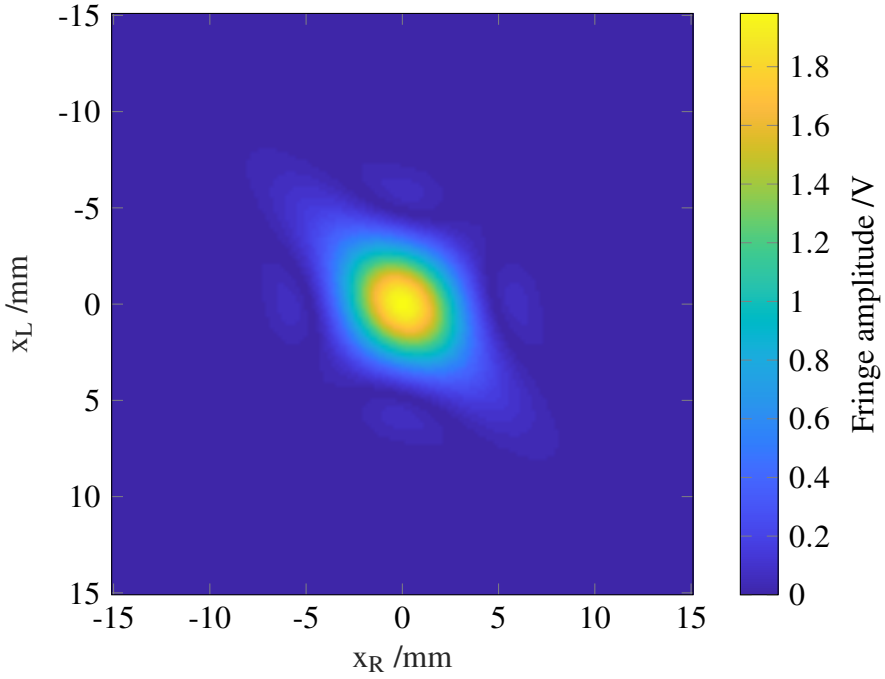

(a) DRF amplitude

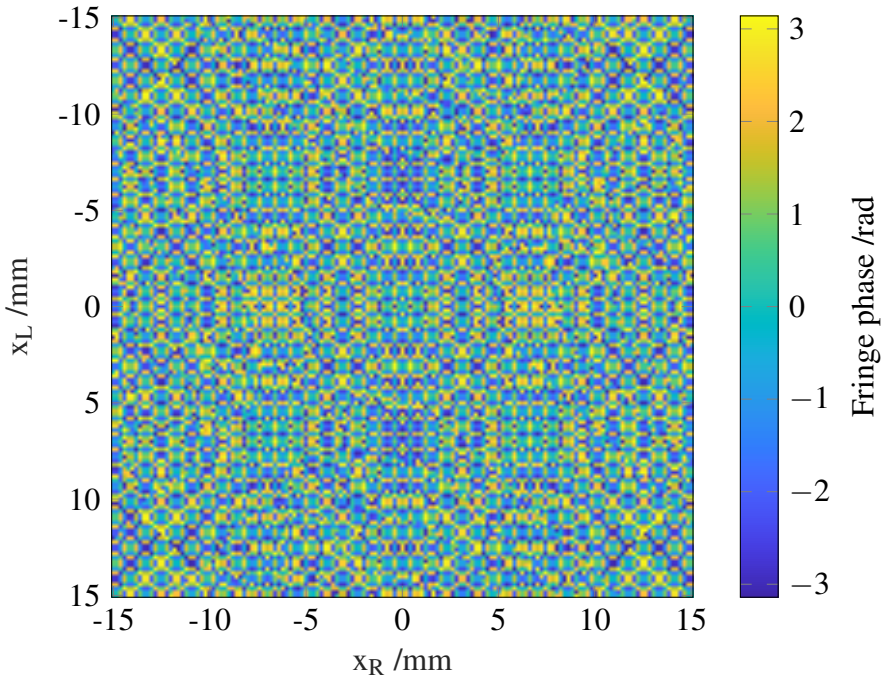

(b) DRF phase

Fig. 3.20 Simulated multi-mode DRF, built from the first 68 LP modes.

DRF visibility and coherence patterns have similar structure, with generally higher contrast due to the normalization procedure used.

Contrary to the ambiguity we faced when simulating multi-mode systems using LG modes, LP modes are generated with the selected core radius a, which is always provided by fiber manufacturers. We note that the multi-mode system simulated in Figure 3.20 qualitatively resembles that simulated from LG modes with 5 µm width, rather than with 25 µm width.

We again used the logistic function defined in Equation (3.13) to produce a tapered sensitivity spectrum; with $k = 0.2$ and $x_0 = 35$, its median has half-maximum sensitivity and its smallest sensitivities remain non-negligible. These sensitivities were applied to the individual modes' DRFs in the order that they were simulated. This operation produces similar effects to the case with LG-based DRFs: the DRF amplitude is generally decreased, including the local maxima, whose positions are displaced slightly away from the main diagonal.

3.6 Non-Modal DRF: Coherence Lengths

3.6.1 Theory

While choosing a modal basis can allow us to base our assumed DRF's functional form on physical arguments, it is not a necessary step. Indeed, any two-point two-dimensional function can be used as the assumed DRF. Non-separable forms will require a full four-dimensional integral to be computed, but this is not prohibitive conceptually, only perhaps in terms of computational resources.

In particular, we can model the detector as a square absorbing structure of sidelength w with finite coherence length L, whose detector response is given by

$$\overline{\overline{\mathbf{D}}}(\mathbf{r}_1, \mathbf{r}_2) = \begin{cases} \exp\left(-\frac{\|\mathbf{r}_1 - \mathbf{r}_2\|}{L}\right) & \|\mathbf{r}_1\|, \|\mathbf{r}_2\| \leq w/2 \\ 0 & \text{otherwise} \end{cases}, \tag{3.20}$$

where $\|\cdot\|$ denotes the vector's ℓ^2-norm, i.e. its Euclidean length [81]. A proportionality constant could be added to Equation (3.20) to account for a non-unity response at the origin or for a normalization of the DRF, but is ignored here without loss of generality. In the limit where the coherence length L is infinite, the assumed DRF reduces Equation (3.20) to a constant equal to 1 over the absorber's surface.

3.6.2 Implementation

In the general case where $L < \infty$, a practical implementation cannot use the simplifications discussed in Section 3.2.2, because the assumed DRF is not separated between the two spatial coordinates. We therefore need to explicitly perform the four-dimensional integral defined in Equation (3.1), for which dedicated Matlab functions are available [82], at every position pair. To reduce the computational load, we can note that the sources' configuration has two symmetries: the exchange of sources, i.e. along the DRF matrix diagonal, and right-left symmetry of the scanning range, i.e. along the matrix antidiagonal. We therefore only need to compute the positions in one of the four DRF quadrants defined by the diagonal and antidiagonal lines. The full DRF is then obtained using appropriate symmetries, including the corresponding complex conjugation operations. Without loss of generality, we select the north quadrant.

For $L = \infty$, the assumed DRF's functional form is separable, such that we can apply the simplifications discussed in Section 3.2.2. Because the method's algorithmic complexity in the number of source positions N is $\mathcal{O}(N^2)$, we increased the step size from 200 µm to 400 µm: the sources labeled R and L are scanned over $x_R, x_L \in \{-15, -14.6, \ldots, 15\}$ mm. We note that the numerical results obtained are identical without these simplifications, confirming that these hold.

Absolute and relative tolerances must be selected for the four-dimensional numerical integration: we specified 10^{-6} and 10^{-3} respectively. However, we found that the simulated DRF was identical when selecting 10^{-8} and 10^{-5} absolute and relative tolerances, and some elements were different for 10^{-10} and 10^{-7}: the effective accuracy of the numerical integrator is therefore better than the former, even when weaker tolerances are specified in the algorithm. This feature of the algorithm's behavior was expected [82].

3.6.3 Infinite Coherence

We first performed simulations in the case of a detector whose response has infinite coherence length, $L = \infty$. Figure 3.21 presents the simulated DRFs for square detectors with sidelength $w \in \{4, 10, 20, 40\}$ µm. The DRF amplitude pattern in the cases with $w = 20$ µm and $w = 40$ µm have local maxima along x_R and x_L, and regularly spaced zero-amplitude lines. The phase pattern has structure with similar boundaries, indicating that the DRF amplitude and phase are intimately linked. On the other hand, the $w = 4$ µm and $w = 10$ µm cases both have Gaussian-like amplitude patterns, and display identical phase patterns.

An important verification for our simulation scheme is to perform the same procedure with $\overline{\overline{\mathbf{D}}}(\mathbf{r}_1, \mathbf{r}_2) = 1$, and compare the simulated DRFs obtained for various integration areas

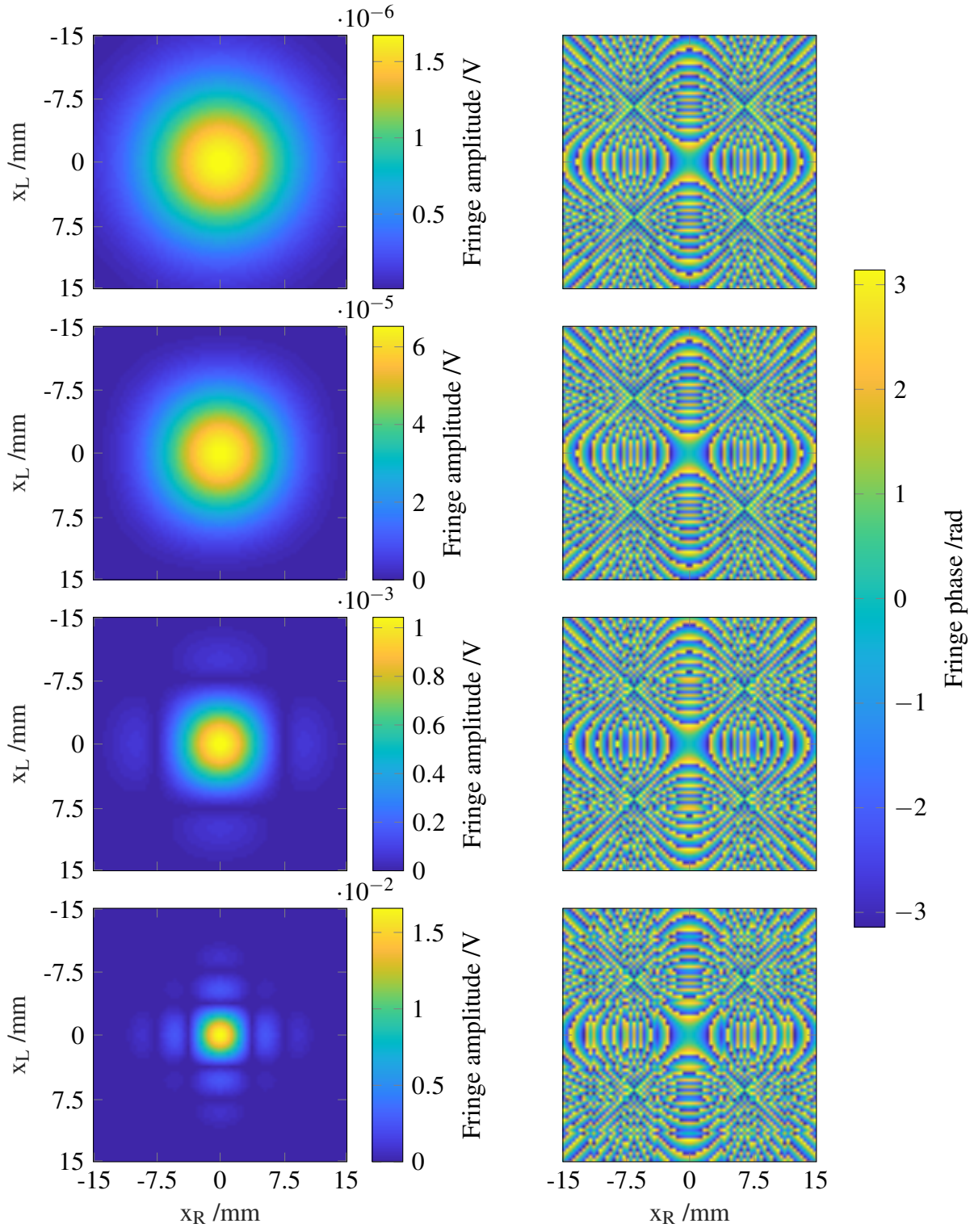

Fig. 3.21 Simulated DRF amplitude (left column) and phase (right column) patterns, assuming infinite coherence length $L = \infty$ and detector sidelength $w \in \{4, 10, 20, 40\}$ µm respectively.

to the corresponding DRFs simulated with $L = \infty$. We indeed find that the two configurations produce identical DRFs, within the accuracy limits of the numerical integrator. Additionally, we simulated DRFs using the mode-based method described in Sections 3.4 and 3.5 with a single mode of amplitude 1 throughout the integration surface, and again found it to match the case of a detector with infinite coherence length.

3.6.4 Finite Coherence

We then proceeded with simulations assuming a DRF functional form described by Equation (3.20), with $L < \infty$. We chose a set of coherence lengths $L \in \{2, 5, 20\}$ µm, and repeated each with detector sidelength $w \in \{4, 10, 20, 40\}$ µm. The amplitude patterns of the resulting 12 simulated DRFs are presented in Figure 3.22. The structure is Gaussian-like for small w values and increasingly diagonal for large w/L ratios, i.e. when the coherence length is significantly shorter than the detector sidelength. The on-axis maximum of DRFs increases with w, which is expected as a larger detector will absorb more of the incident power, and is consistently smallest for $L = 5$ because it is the transition between the $w \approx \lambda$ and $w \gg \lambda$ regimes. We found the corresponding DRF phase patterns to be less instructive and largely dominated by the geometric phase contribution, which is difficult to interpret due to the larger scanning step size used.

In order to further verify the results obtained in Section 3.6.3, we repeated this procedure with very large values of the coherence length $L \in \{2\,000, 10\,000, 100\,000\}$ µm. The simulated DRFs are identical to those obtained with $L = \infty$ within the integration precision selected.

3.7 Sampling Requirements and Strategies

3.7.1 Metrics for Mode Recovery

Having simulated DRFs for a large number of systems, it is crucial to investigate whether their natural modes can be recovered. Their recovery using a diagonalization method will be discussed in Chapter 9 in the context of experimentally measured DRFs. A more general study is presented here, to explore the number and locations of source positions required to successfully recover a given number of the detector's natural modes.

Several choices are required: a sampling strategy for the sources, a model for their generated beam and a set of modes for the detector's reception pattern. We considered sources producing an LG_{00} beam and LG modes for the optical response of the detector, which is placed at a normal distance $z = 100\,\text{mm}$ of the source plane, i.e. in the same

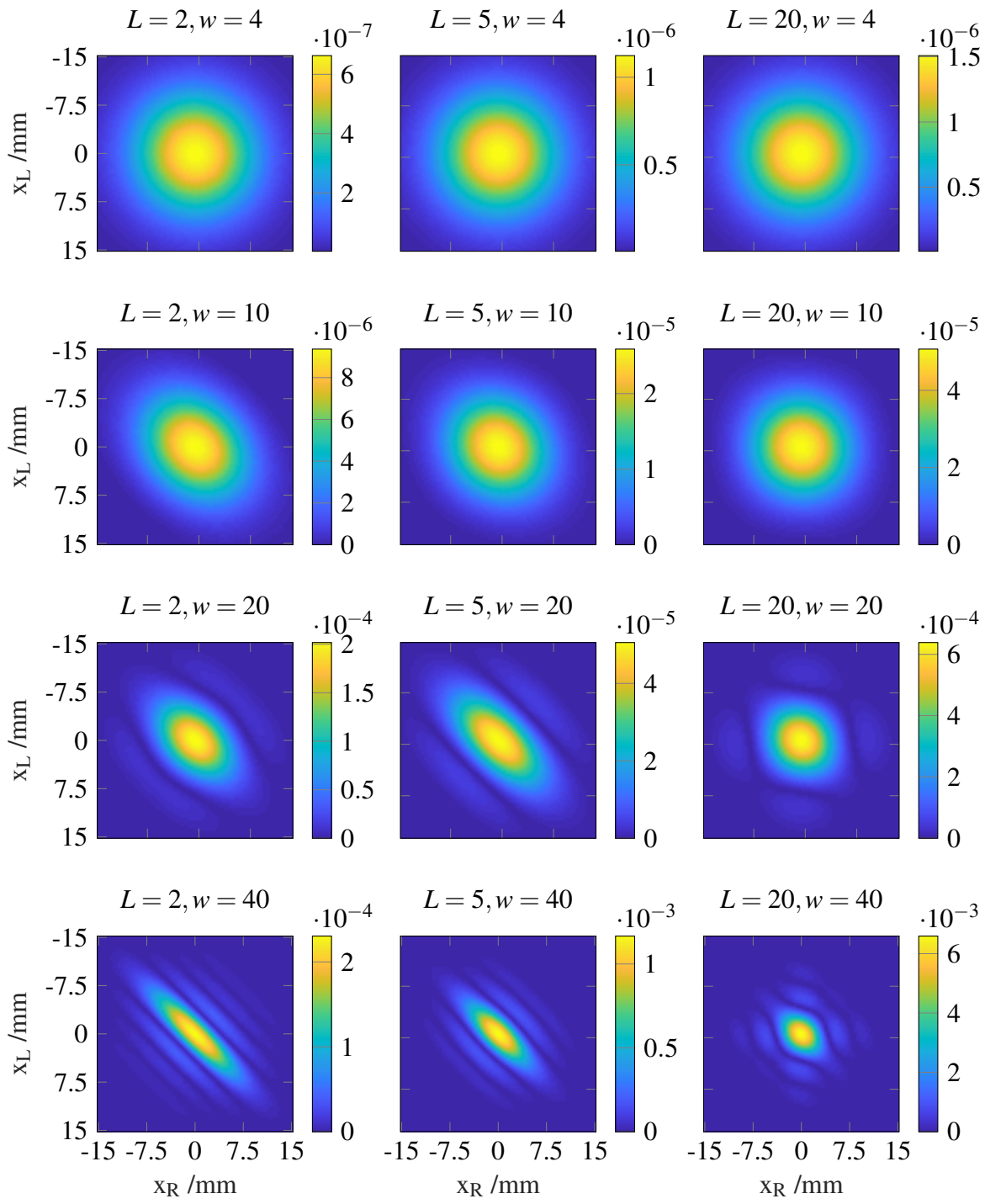

Fig. 3.22 Simulated DRF amplitude patterns, assuming infinite coherence length $L \in \{2, 5, 20\}$ µm (columns) and detector sidelength $w \in \{4, 10, 20, 40\}$ µm (rows) respectively.

configuration as Section 3.4. Given a source sampling strategy, the matrix of single-source beam overlaps with each detector response mode can be computed as

$$L_{ij} = \int_{\mathscr{S}} d^2\mathbf{r}\, \mathbf{R}_i(\mathbf{r}) \cdot \mathbf{E}_j^*(\mathbf{r}), \tag{3.21}$$

where $\mathscr{S}$ is the chosen integration surface, i is the index of the assumed detector mode $\mathbf{R}_i(\mathbf{r})$ in the selected basis set, i.e. LG modes, and j is the index of the source position in the scanning set. The matrix L defined by Equation (3.21) was introduced in Chapter 2 as containing in each of its columns the eigenvectors of the DRF in the basis of source positions, if these eigenvectors are the chosen basis set. An important metric to consider is the condition number of the matrix L, defined as the ratio of the largest to smallest singular values of the matrix's Singular Value Decomposition (SVD) [83]. Effectively, the condition number measures the dynamic range required for an experimental system to accurately retrieve all of the modes present in the detection system, given the set of sampled positions over which the sources are scanned. The dynamic range is defined as the ratio of largest and smallest signals recordable by an experimental system: generally, the former is set by a saturation signal of one of the experiment's components, and the latter is determined by the measurement system's noise floor [84].

In practice, each element L_{ij} is computed independently by performing the two-dimensional numerical simulation. The j^{th} column of L corresponds to the j^{th} sampled position: the condition number of any matrix built from a subset of columns of L can then be computed to study the dependence of the mode reconstruction efficiency on the corresponding subset of source positions sampled. In particular, concatenating columns of L into increasingly large submatrices emulates the accrual of information as the source is scanned over the sampled positions. The dependence on the number of modes of interest can be studied analogously by selecting the corresponding rows of L. For a given submatrix, a smaller condition number indicates a lower required dynamic range and lower vulnerability to noise, and is therefore preferable; the best case of is a condition number of 1, where all singular values are equal.

Because the numerical simulations' accuracy is essentially perfect, given that we can set an arbitrarily small machine precision, the distribution of singular values is also of great interest. For instance, the number of singular values λ larger than a fraction of the largest singular value λ_{max} provides a metric for the number of modes recovered given a fixed experimental dynamic range. The best case corresponds to all considered modes being recoverable for the largest possible fraction of λ_{max}.

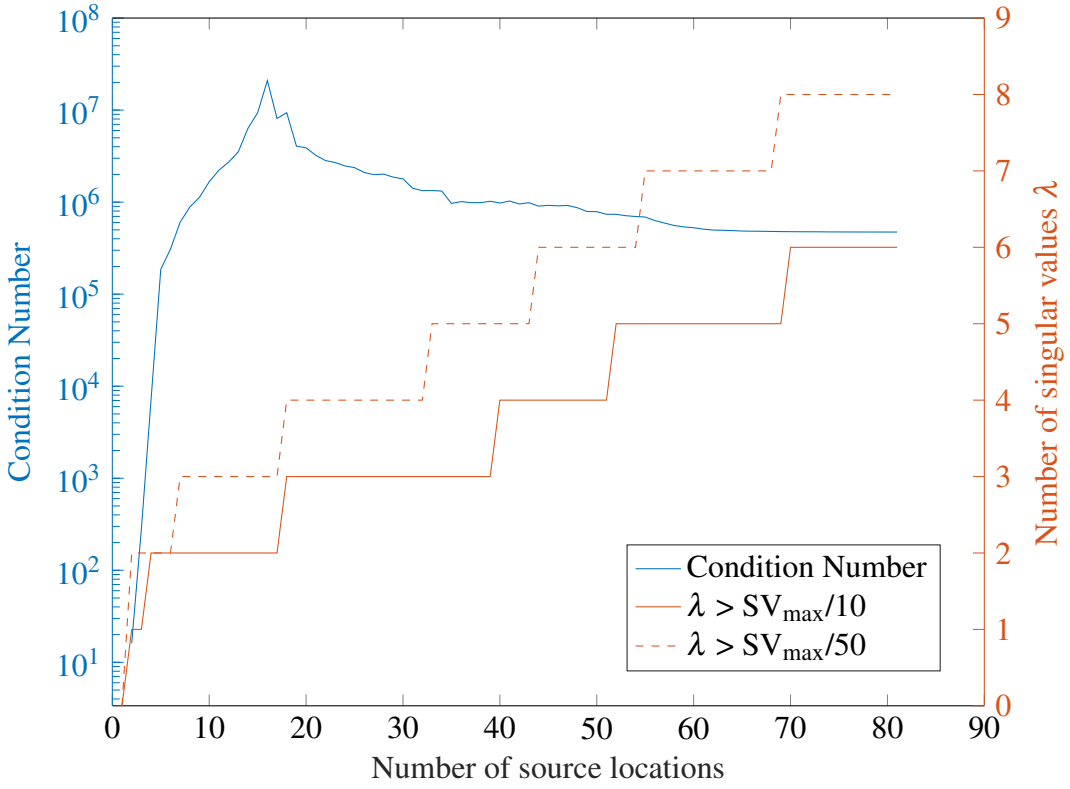

Fig. 3.23 Evolution of the L matrix's condition number and singular values λ such that $\lambda > \lambda_{\max}/10$ and $\lambda > \lambda_{\max}/50$, as a single source is scanned over the uniformly sampled line segment $x \in \{-20, -19.5, \ldots, 20\}$ mm.

3.7.2 Cartesian Grid Sampling Strategies

We start by considering 81 positions uniformly sampled over a line segment, with coordinates $x \in \{-20, -19.5, \ldots, 20\}$ mm. The L matrix is computed using Equation (3.21) for each position and using the 16 LG modes with indices $p, l \leq 3$. For each submatrix width, the condition number is computed as well as its SVD. Figure 3.23 presents the condition number as the number of sampled positions increases, and the number of singular values λ that are larger than $\lambda_{\max}/10$ and $\lambda_{\max}/50$, where $\lambda_{\max}$ is the largest singular value. The condition number appears to converge towards a minimum of 4×10^5 as positions are added; on the other hand, the number of modes recovered with a dynamic range of 10 or 50 continues to increase. We note that the modes recovered here would be those in the projected basis of one-dimensional source positions, as discussed in Section 3.4.3; we expect to recover a lower number of modes than the 16 LG modes considered, because of a degeneracy in their symmetries.

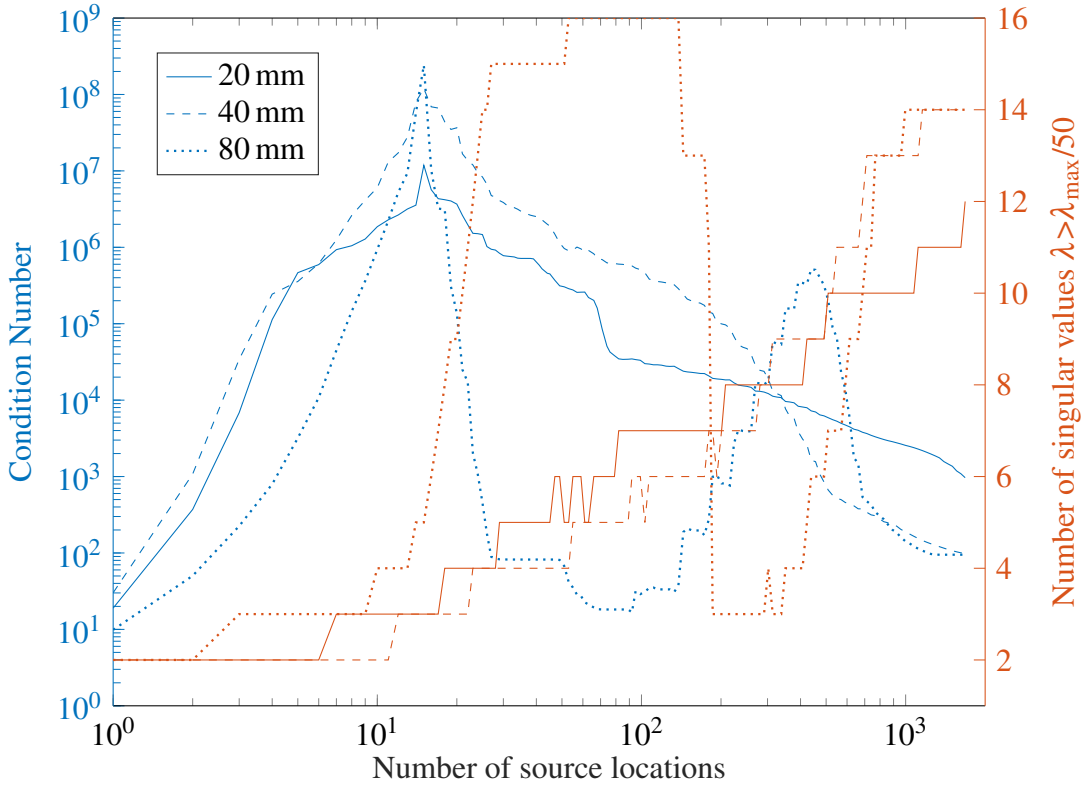

Fig. 3.24 Evolution of the L matrix's condition number and singular values λ such that $\lambda > \lambda_{\max}/10$ and $\lambda > \lambda_{\max}/50$, as a single source is scanned over the uniformly sampled line segments of length 20 mm, 40 mm and 80 mm.

While a large portion of this dissertation will consider one-dimensional scanning strategies, it is important to explore two-dimensional sampling as well. The conclusions obtained below are identical in both cases. Scanning over Cartesian grids, the source positions are taken in the order of increasing y values, then increasing x values; we call this ordering "column-by-column". Figure 3.24 explores the effect of scaling the scanning range and step size between neighboring positions: 41 points are sampled along both the x and y axes for scanning ranges of 20 mm, 40 mm or 80 mm. The case with 20 mm scanning range is found to be inferior: the much larger condition number for more than 600 sampled positions reflects the scanning strategy's inability to include information from far off-axis positions. We notice that the case with 80 mm scanning range displays a clear minimum between 50 and 100 sampled points, followed by a local maximum and a subsequent monotonic decrease. We understand the first minimum to be a feature of the sampled subset of positions, which are very far off-axis: a distorted basis is recovered for this subset of sampled positions, before converging to the correct basis as additional positions are sampled.

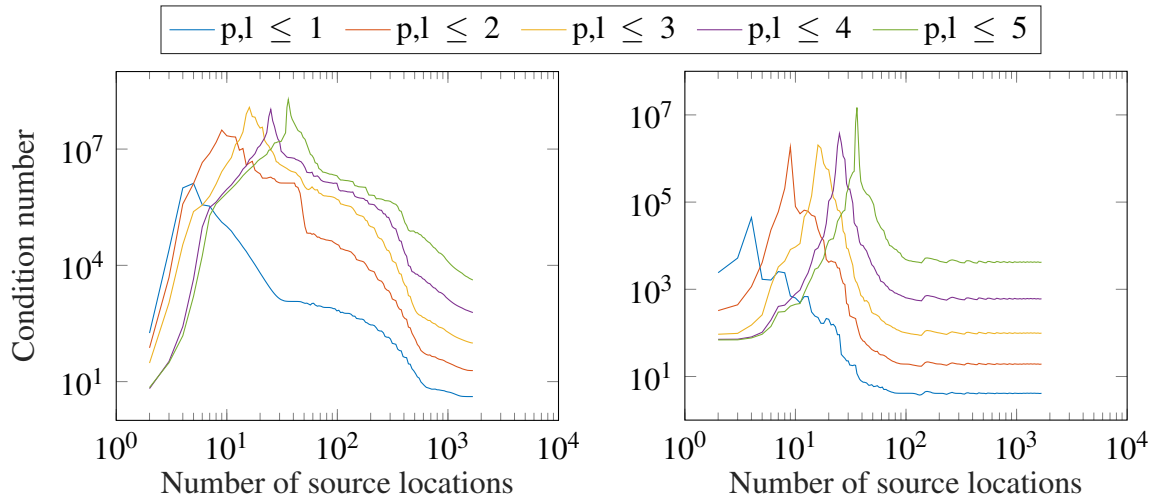

(a) Column-wise strategy

(b) Modulo 17 strategy

Fig. 3.25 Condition number of the matrix L for various numbers of modes to be recovered; the Cartesian grid is either scanned column-wise, i.e. with increasing y values then increasing x values, or modulo 17, i.e. selecting every 17^{th} position in the original order.

3.7.3 Mode Number and Scanning Order

We can also consider how the number of modes we wish to retrieve affects the condition number of the L matrix. The L matrix is computed for the 36 LG modes with indices $p, l \leq 5$, with sources scanned on a Cartesian grid of 41×41 points uniformly sampled over the range $x, y \in \{-20, -19, \ldots, 20\}$ mm. In Figure 3.25a, we present the condition number when selecting only the LG modes with $p, l \leq 2, 3, 4$ and 5: as the number of modes to recover increases, the maximum condition number is greater and reached for larger numbers of sampled positions.

The same procedure can be repeated, but changing the order in which the positions are sampled, to explore the effect of position ordering on the convergence towards the condition number obtained when the entire sampling grid is scanned. Every 17^{th} position of the original column-by-column order is selected, looping around at the end of the grid until all positions are sampled. We refer to this ordering as "modulo 17". Figure 3.25b shows the condition number using this order: while the position of the maximum is identical to the column-by-column order, its value is significantly reduced and the condition number then decreases much more rapidly as sampled positions are added. Similar results are obtained when selecting the sampled positions in a random order. Using a random or pseudo-random order, such as the modulo 17 order, information about the DRF modes is accrued much more rapidly than by scanning the source column-by-column.

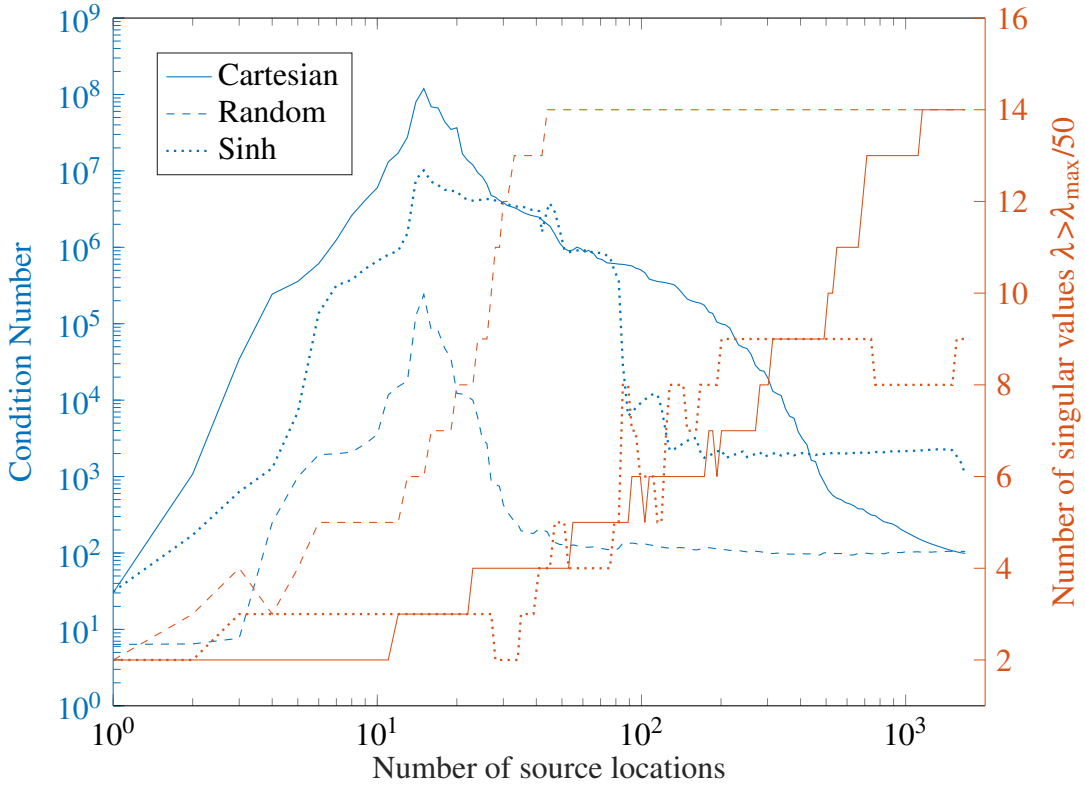

Fig. 3.26 Comparison of the evolution of the L matrix's condition number and singular values λ such that $\lambda > \lambda_{max}/50$, for scanning strategies with identical ranges using a uniform Cartesian grid, two-dimensional random samples and a Cartesian grid with hyperbolic sine step size.

3.7.4 Comparing Sampling Strategies

We explored different grid patterns, choosing 41×41 positions over a given range $x, y \in \{-20, -19, \ldots, 20\}$ mm: (i) Cartesian with step size 1 mm, (ii) random points over this two-dimensional area, and (iii) Cartesian with step size set by the hyperbolic sine function of appropriate range. Figure 3.26 compares these three scenarios, as positions are added in the order that they appear in L, i.e. without random or modulo ordering. The random sampling strategy has faster convergence to the condition number minimum of 200, and qualitatively similar to random reordering of the Cartesian grid.

As the assumed detector response is based on the circularly-symmetric LG modes, we also explored whether scanning sources on a polar grids was more efficient than on Cartesian grids. In order to properly compare with our previous results, we chose appropriate radial and angular step sizes to obtain 41×41 sampled positions, with both the radial and angular directions uniformly sampled with 41 points. We found that the condition number of the

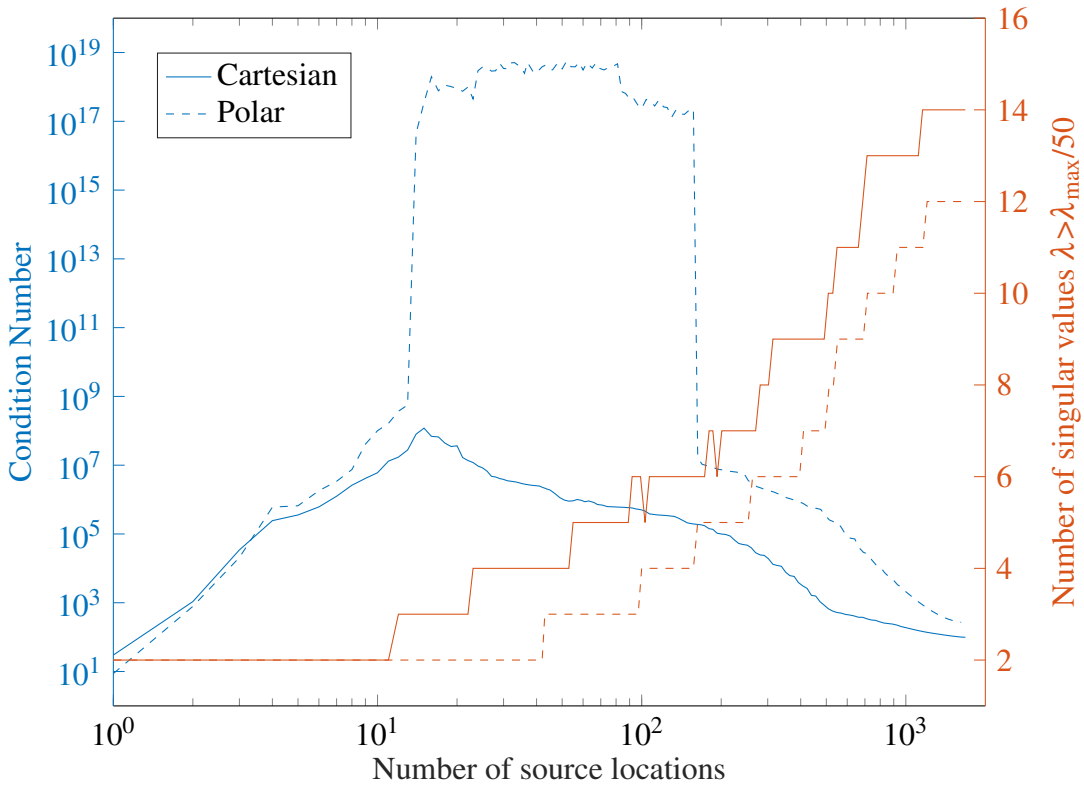

Fig. 3.27 Comparison of the evolution of the L matrix's condition number and singular values λ such that $\lambda > \lambda_{max}/50$, for scanning strategies using Cartesian and polar grids with identical ranges.

L matrix was considerably improved by discarding the repeated $r = 0$ positions. This case, with radial sampling $r \in \{-20, -19, \ldots, 20\}$ and angular sampling $\theta \in \{0, \pi/40, \ldots, \pi\}$ is compared in Figure 3.27 to the case of a Cartesian grid with similar range (previously presented in Figure 3.26). We observe that the Cartesian grid strategy has a lower condition number and higher number of singular values $\lambda > \lambda_{max}/50$, for any number of source positions selected. The same conclusion is reached when changing the radial sampling range or when trading resolution between the radial and angular components, for instance choosing 81 samples along the radial direction and 21 along the angular direction. Considering a different order of the polar grid, we obtain a slight improvement when ordering by increasing x and a large improvement with random ordering, similarly to the case of a Cartesian grid.

In the context of experimental procedures, these observations indicate that randomness in either the sampled positions or the order of regularly sampled positions allows the rapid accrual of information in order to accurately recover the DRF modes. On the other hand, randomness in either the sampling strategy or order implies much longer displacements between consecutive positions, both in terms of distance and displacement durations, whereas

the column-wise scanning of a Cartesian grid is arguably optimal. We should also recall that this time penalty will apply to each of the sources scanned to measure the DRF elements. This trade-off would be best investigated in the context of experimental measurements, where the effect of finite signal-to-noise ratio may also be revealed.

3.8 Conclusion

We have performed a large variety of numerical simulations to investigate how EAI allows us to measure the optical response of the device under test, regardless of its assumed functional form. By generating an illuminating field using two phase-locked sources, we have reconstructed the DRF of the modeled detector, under a large variety of conditions. In particular, we have studied cases where sources and detectors are either point-like or have finite size.

Many of the simulations performed and explored in this chapter are highly informative for the experimental EAI system that will constitute the basis for the rest of this dissertation. In particular, its design will be greatly helped by the scanning ranges investigated in this chapter, while the scanning strategies examined in Section 3.7 could contribute to optimizing its operation. We have paid particular attention to the simulated DRFs which we may expect from fiber-coupled systems. A large fraction of our simulated DRFs assume Laguerre-Gaussian modes, but we have also taken care to explore the Linearly Polarized modes that theoretically characterize optical power transmission in optical fibers, as well as a non-modal functional form based on a finite-sized absorber with finite or infinite coherence length. More generally, the simulation framework implemented in this chapter can take any one-dimensional or two-dimensional, two-position functional form as an input for the assumed DRF, demonstrating its versatility.

While the next step is to design an experimental system to perform EAI on infrared detector systems, the results obtained in this chapter give valuable insights into the expected behavior of single-mode, few-mode and multi-mode systems. In particular, we have investigated the case of two-source one-dimensional scans and chosen a matrix representation for the simulated complex fringe amplitude, which is directly applicable to experimental data as well. Additionally, we have implemented a numerical simulation method that artificially creates fringes as the relative phase between sources is varied. This has allowed us to recreate the dataflow expected from an experimental system, with an FFT-based extraction technique for the recorded fringe's amplitude, phase and offset parameters.

Chapter 4

Designing an Infrared EAI Experiment

4.1 Introduction

We present the design of an EAI experimental system for the characterization of detectors at infrared wavelengths. As described in Chapter 2, we can obtain all of the information about a detector's state of coherence by measuring the fringes in the output as we modulate the relative phase between two phase-locked electromagnetic sources. The central goal for the experimental system is to perform EAI in order to find the electromagnetic modes through which optical power is coupled into detectors with a wide range of modal behaviors.

Starting from the theory described in Chapter 2, various basic technical capabilities are required. These can be summarized in the form of the block diagram shown in Figure 4.1. First of all, we need some electromagnetic radiation generator: it is clear that the experimental method can be simplified by considering the case of identical, individually highly-coherent phase-locked sources with a well-defined polarization. We then need some way of manipulating the emitted radiation, in particular creating two arms whose optical power output and polarization are as identical as possible, and whose relative phase can be controlled. Post-measurement analysis can be greatly simplified if we have well-known source beam patterns; we must therefore ensure that we can precisely ascertain the form of the beams illuminating the device under test as well as the positions of the probes. Some scanning system, preferably motorized and computer-programmable, is necessary to move the two sources precisely to relevant position pairs. A power-absorbing structure must be chosen to produce an output that displays fringes as the relative phase between the sources is varied, with appropriate characteristics such as a sufficient signal-to-noise ratio (SNR). Finally, we need a way of acquiring this signal data and storing it in a computer-readable format for post-measurement analysis. Fulfilling all of these requirements amounts to a significant technical challenge, which we start undertaking with a blank slate at the conceptual

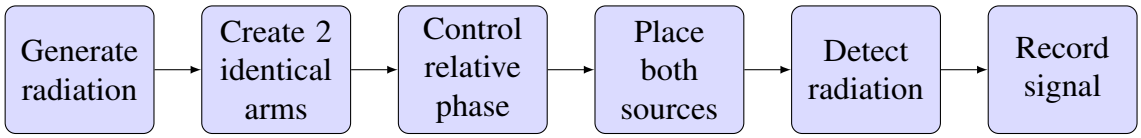

Fig. 4.1 Block diagram illustrating the required successive steps of the experimental system.

level. The goal of this chapter is therefore to prove the feasibility of an EAI experiment at near-infrared wavelengths, and converge towards a design that will allow us to perform such experiments to characterize a wide range of devices.

In this chapter, we will describe the different elements that we considered in the design of the EAI experiment. In Section 4.2, we will present design choices for the experiment's general architecture, including the decision towards a fully fiber-based system. Section 4.3 will cover the quantitative study of a wide number of topics: (i) optical sources and the required coherence length, losses in optical components and required power, (ii) mechanical design, minimum sampling, minimum and maximum distance, (iii) gaussian beam propagation, diffraction of gaussian beams through apertures and effective numerical apertures, (iv) power detection, restriction of the number of detector modes, and signal conversion and amplification, and (v) numerical cases, illustrating typical experimental values. Section 4.4 will summarize safety issues and how they have been dealt with throughout the design phase of this EAI experiment. In Section 4.5, we will briefly reflect on the differences between our near-infrared experimental architecture and the system built by Thomas et al. for the study of power detectors at submillimeter and microwave frequencies [58]. In particular, we will discuss how the difference of operating wavelength range implies significant contrasts in design choices.

4.2 General Architecture Choices

In this section, we qualitatively argue for specific choices regarding the overall architecture of the experiment. Quantitative investigations of many of these topics will be conducted in Section 4.3. The general requirements listed in Section 4.1 and illustrated in Figure 4.1 can be fulfilled as follows:

- **Generating infrared radiation.** An electromagnetic radiation generator is needed, with a well-defined polarization and high enough spatial coherence to allow the coherent illumination of the detector surface with two distinct probes. A narrow-linewidth laser that can be considered quasi-monochromatic corresponds ideally.

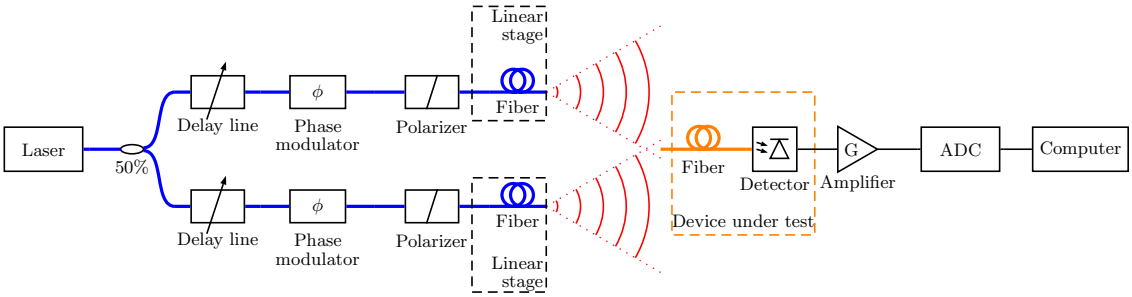

Fig. 4.2 Block diagram of the proposed EAI experimental system; blue lines denote polarization-maintaining fibers, the orange line represents the interchangeable optical fiber length coupled to the highly multi-mode detector, and black full lines denote electrical connections.

- **Creating two identical arms.** We then require a method for producing two probes that are individually highly coherent. While this could be obtained using two locked lasers, a simpler solution is to use a 50%-50% beamsplitter to obtain two equal beams that are intrinsically phase-locked and have the same polarization.

- **Controlling the probes' properties.** Delay lines can be used to adjust the path lengths of each arm, while phase modulators are able to accurately control the relative phase difference. Depending on the application, ascertaining the shape of the source beam patterns may be necessary; in a fiber-based system, it is possible to use shaped-tip fiber assemblies or to add pinholes at the exit of the probe fibers.

- **Placing the two probes.** We must find a method to reliably position the probes for long periods of time, as even sub-micron movements will correspond to displacements of large fractions of a wavelength. Moreover, a motorized and computer-programmable scanning system is required, in order to place the two probes precisely at large numbers of chosen position pairs.

- **Detecting radiation.** The modal behavior of the device under test will depend on the characteristics of the photodetector, but also on any optics in the optical path. In order to demonstrate the technique, a photodetector is used to absorb optical power; an output amplifier is required in order to obtain high SNR. It is possible to choose a fiber-coupled detector, where the optical fiber would act as a mode filter and determine the modal behavior of the fiber-plus-photodetector system. We also note that, while a photodetector is our choice of power-absorbing structure, other power detectors could be used, such as an energy-harvesting antenna or a solar cell.

- **Recording the signal.** A method of acquiring the detector output signal and transforming it into computer-readable data is required. An Analog-to-Digital Converter (ADC) with sufficient bandwidth connected to a computer is an appropriate option.

More generally, it is important at this point to choose whether the four first bullet-pointed items will be realized using a free-space or fiber-based system. We opted for the latter, using a fiber-coupled laser fed into a fused-fiber beamsplitter and fiber-coupled delay lines and phase modulators. The main reason is the ease of use of optical fibers: significantly more precise positioning possibilities are available by simply placing the open end of an optical fiber on a positioning stage, rather than resorting to an elaborate set of mirrors to channel a collimated beam. A corollary of this choice is the intrinsically safer operation of the system, which will be the topic of Section 4.4. All of these design choices are summarized as a block diagram in Figure 4.2.

Another critical choice is the operating wavelength. Our decision towards the wavelength $\lambda = 1550\,\text{nm}$ is primarily motivated by its importance as a standard wavelength in the communications industry, and the wide availability of a large range of products for all components including lasers and optical fibers. Demonstrating EAI at this wavelength will therefore allow many direct applications on widely used technology.

4.3 Design Topics

4.3.1 Optical Radiation Generator

Lasers are the ideal choice to obtain narrow-linewidth highly-coherent radiation. In the context of this experiment, their radiation coherence length Δx must be far greater than the differential optical path length to the device being tested, with

$$\Delta x \approx \frac{c}{\Delta \nu} \approx \frac{\lambda^2}{\Delta \lambda}, \tag{4.1}$$

where λ is the central wavelength, and $\Delta\lambda$ and $\Delta\nu$ are respectively the radiation linewidth in units of length and frequency [85]. At $\lambda = 1550\,\text{nm}$, we have the following equivalence: $\Delta x = 1\,\text{m} \iff \Delta\lambda = 2.4\,\text{pm} \iff \Delta\nu = 300\,\text{MHz}$. Because the maximum optical path length will be at most of the order of meters, a laser with $\Delta\nu < 1\,\text{MHz}$ is sufficient.

We also wish to keep a well-defined polarization from the laser through the beamsplitter, delay line, phase modulator, and up to the probe tips. We therefore need to use polarization-maintaining fibers and components without polarization-dependent loss or polarization cross-coupling. In order to further ensure that a single polarization is selected, a polarizer

Component	Typical insertion loss (dB)
Beamsplitter (input to single output)	3.6 ± 0.2
Delay line	1.5 ± 0.3
Phase modulator	3.2 ± 0.5
Fiber connection (with index-matching gel)	0.5 ± 0.1
Propagation in optical fiber ($\approx$6m)	< 0.01

Table 4.1 Table of power losses for the successive components and steps of the experimental system.

can be introduced at the end of the optical system; phase modulators with a built-in polarizer are also available.

In order to choose the power output of the laser, which can range from a few milliwatts to several watts, it is necessary to know the ratio between the power at the laser output and at the probe tips. This ratio corresponds to the optical power loss in the system up to the probes and comes mainly from insertion loss in the different components of the fiber circuit. Typical experimental values are listed in Table 4.1.

Summing these contributions, and assuming 3 connectors are on the path of each source (beamsplitter to delay line, delay line to phase modulator, phase modulator to source fiber), the expected total loss is approximately 10 dB, i.e. a reduction by a factor 10: a laser with optical power output 50 mW implies two fiber sources of 5 mW each.

4.3.2 Mechanical Considerations

In order to find constraints on scanning ranges and accuracy, we must first compute the minimum sampling of the detector beam pattern. Using the Nyquist-Shannon sampling theorem [86, 87], the step size Δx between source positions is such that

$$\Delta x \leq \frac{1}{2C}, \tag{4.2}$$

where C is determined by the larger of three lengths:

- The source radiation's center wavelength λ;
- The physical size of the source, its diameter d_{source};
- The spot size of detector beam pattern $s(z)$ at an on-axis distance z from the source plane.

The comparison of these three lengths is summarized in Figure 4.3. Using $\lambda = 1550$ nm, the wavelength is always much smaller than the other two quantities in any reasonable

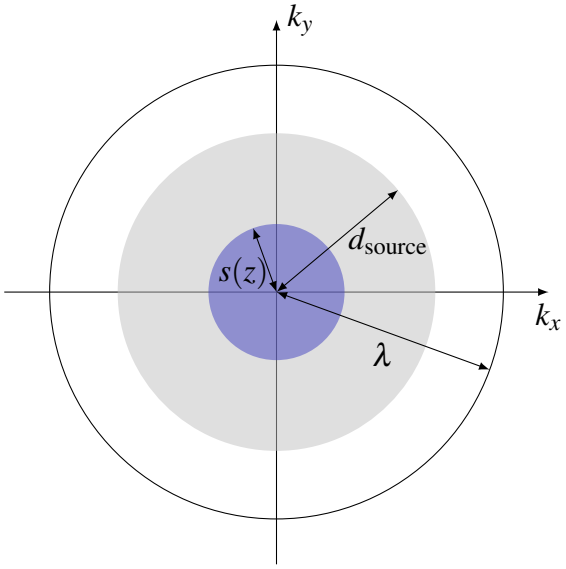

Fig. 4.3 Diagram of concentric limits placed on the maximum measurable two-dimensional wavevector.

experimental system. Moreover, because we will only consider diverging beams in the far-field regime, we conclude that $d < s(z)$; therefore

$$\Delta x \leq \frac{s(z)}{4\pi}. \tag{4.3}$$

This implies a very powerful result: taking $s(z) = N\Delta x$, we see that we can sample successfully if we take N identical steps over the detector spot size, with

$$\frac{s(z)}{N} \leq \frac{s(z)}{4\pi} \iff N \geq 4\pi \approx 13. \tag{4.4}$$

Assume that $s(z)$ is entirely due to the divergence angle θ of the beam coming out of the detector fiber, also called its acceptance angle. It is related to another key quantity in optics, its numerical aperture, by $\text{NA}_{\text{detector}} = \sin(\theta)$. Then, we have a spot size

$$s(z) = 2z\tan(\theta) + s(0) = 2z\tan(\sin^{-1}(\text{NA}_{\text{detector}})) + d_{\text{detector}}. \tag{4.5}$$

Therefore, the largest acceptable step size of the sources is

$$\Delta x^{max} = \frac{2z\tan(\sin^{-1}(\text{NA}_{\text{detector}})) + d_{\text{detector}}}{4\pi}. \tag{4.6}$$

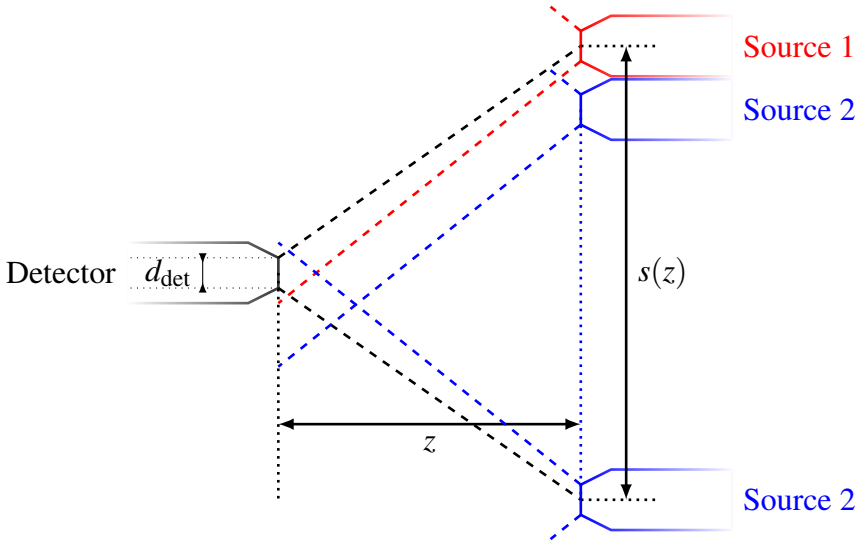

Fig. 4.4 Top-view diagram of the experimental system's optics, showing the extreme case of source 1 at one end of the detector beam pattern while source 2 is scanned over its width $s(z)$; beam sizes of detector, source 1 and source 2 are black, red and blue respectively.

As Equation (4.6) does not define any requirement on the distance z, we now wish to compute the optimal distance between the sources and the detector. There are additional constraints to be taken into account:

- The divergence angle of the sources must be larger than the acceptance angle of the detector fiber,
- The information loss due to the minimal distance between the sources, at best approximately 250 µm, must be as small as possible,
- The power coupled into the detector must allow sufficient SNR.

Consider the beam sizes in the far-field and compute using numerical apertures, i.e. using the 1% power cone, as in Figure 4.4. The first contraint simply requires

$$\text{NA}_{\text{detector}} \leq \text{NA}_{\text{source}}. \tag{4.7}$$

The second constraint requires that the spot size of the source be larger than the spot size of the detector (at a given distance z) plus the assumed physical size of each source, 250 µm:

$$\begin{aligned}
&s_{\text{detector}}(z) + 250\,\mu\text{m} \leq s_{\text{source}}(z) \\
&\iff 2z\tan(\sin^{-1}(\text{NA}_{\text{detector}})) + d_{\text{detector}} + 250\,\mu\text{m} \leq 2z\tan(\sin^{-1}(\text{NA}_{\text{source}})) + d_{\text{source}} \\
&\iff 250\,\mu\text{m} + (d_{\text{detector}} - d_{\text{source}}) \leq 2z\left(\tan(\sin^{-1}(\text{NA}_{\text{source}})) - \tan(\sin^{-1}(\text{NA}_{\text{detector}}))\right) \\
&\iff 250\,\mu\text{m} + (d_{\text{detector}} - d_{\text{source}}) \leq 2z\left(\tan(\sin^{-1}(\text{NA}_{\text{source}})) - \tan(\sin^{-1}(\text{NA}_{\text{detector}}))\right) \\
&\iff \frac{250\,\mu\text{m} + (d_{\text{detector}} - d_{\text{source}})}{2\left(\tan(\sin^{-1}(\text{NA}_{\text{source}})) - \tan(\sin^{-1}(\text{NA}_{\text{detector}}))\right)} \leq z. \qquad (4.8)
\end{aligned}$$

Lastly, we can obtain a maximum distance by requiring the detector SNR to be sufficiently high. This is critically dependent on the behavior of the source beams, as we will discuss in Section 4.3.4.

4.3.3 Source Beams and Optical Coupling

We consider a monochromatic beam with wavelength λ exiting a single-mode fiber. Its beam pattern is Gaussian, namely that of the fiber's fundamental Laguerre-Gaussian mode LG_{00} [88]. As in Chapter 3, we assume that we operate under the paraxial approximation, which holds for any angular divergence $\theta_{\text{div}} < 0.5$ rad. We compute the width of the gaussian beam, i.e. its half-radius in a plane normal to the propagation direction, at distance z from the fiber exit:

$$w(z) = \left[1 + \left(\frac{\lambda z}{\pi w_0^2}\right)^2\right]^{1/2}, \qquad (4.9)$$

where w_0 is half the mode field diameter MFD, defined as the diameter at which the power density is reduced to e^{-2} of its maximum value. We recall the definition of the Rayleigh length z_R, which defines the limit between near- and far-field regimes:

$$z_R = \frac{\pi w_0^2}{\lambda}; \qquad (4.10)$$

it corresponds to half of the confocal parameter in optics [89]. In the near-field case where $z \ll z_R$, the beam is considered to be well-collimated. In the far field case where $z \gg z_R$, the beam width grows linearly with z: the beam has a divergence angle θ_{div} such that

$$n\sin(\theta_{\text{div}}) \approx \frac{\lambda}{\pi w_0} = \frac{w_0}{z_R}, \qquad (4.11)$$

where n is the refractive index of the medium outside the fiber, with $n_{air} \approx 1$. The numerical aperture stated by manufacturers is typically obtained by measuring the far-field 1% power level; the ratio of the e^{-2}-power to 1%-power radii is 1.51742. Therefore, the equivalent numerical aperture of step-index fibers $\mathrm{NA}_{\mathrm{eq}}$ can be obtained by

$$\mathrm{NA}_{\mathrm{eq}} = \sin\left(\tan^{-1}\left(1.51742\frac{w(z)}{z}\right)\right). \tag{4.12}$$

Note that this equation gives satisfactory results only for step-index fibers, as opposed to graded index fibers, including power-law index profiles often used in multi-mode fibers. In general, in the far-field case, all computations of $w(z)$ should be made using the mode field diameter provided by the manufacturer. Furthermore, we obtain the intensity I, i.e. surface power density, in a beam with total propagating power P_{tot} at a distance z from the fiber exit and a distance r orthogonal to the propagation axis as

$$I(z,r) = P_{tot}\frac{2}{\pi w(z)^2}\exp\left[-2\left(\frac{r}{w(z)}\right)^2\right]. \tag{4.13}$$

Because the beam pattern of laser light exiting an optical fiber is highly dependent on the fiber's properties, such as whether the core-cladding interface has a step-index or graded-index profile, we need to prepare a correction method to produce a beam of known form. More generally, various applications may require control over the beam form, for instance through the use of shaped-tip optical fibers, such as conical or spherical assemblies [90]. Using flat-faced optical fibers, a possible waveform control method is to use the beam diffracted through an aperture of easily measurable size. While this option was ultimately shelved because the selected fiber system produced a clean beam, we derive the relevant analytical formulae here to underline the range of extensions to our experimental system. Taking $A(x',y')$ to be the amplitude of the field at coordinates (x',y') in the aperture plane, the amplitude of the diffracted beam pattern at distance z is

$$U(x,y,z) = \iint\limits_{Aperture} A(x',y')\exp\left(\frac{-ik(xx'+yy')}{z}\right)dx'\,dy', \tag{4.14}$$

where $k = 2\pi/\lambda$. For a circularly symmetric aperture and incoming beam, this reduces to

$$U(r,z) = N\int_0^a \rho A(\rho)J_0\left(\frac{k}{z}\rho r\right)d\rho, \tag{4.15}$$

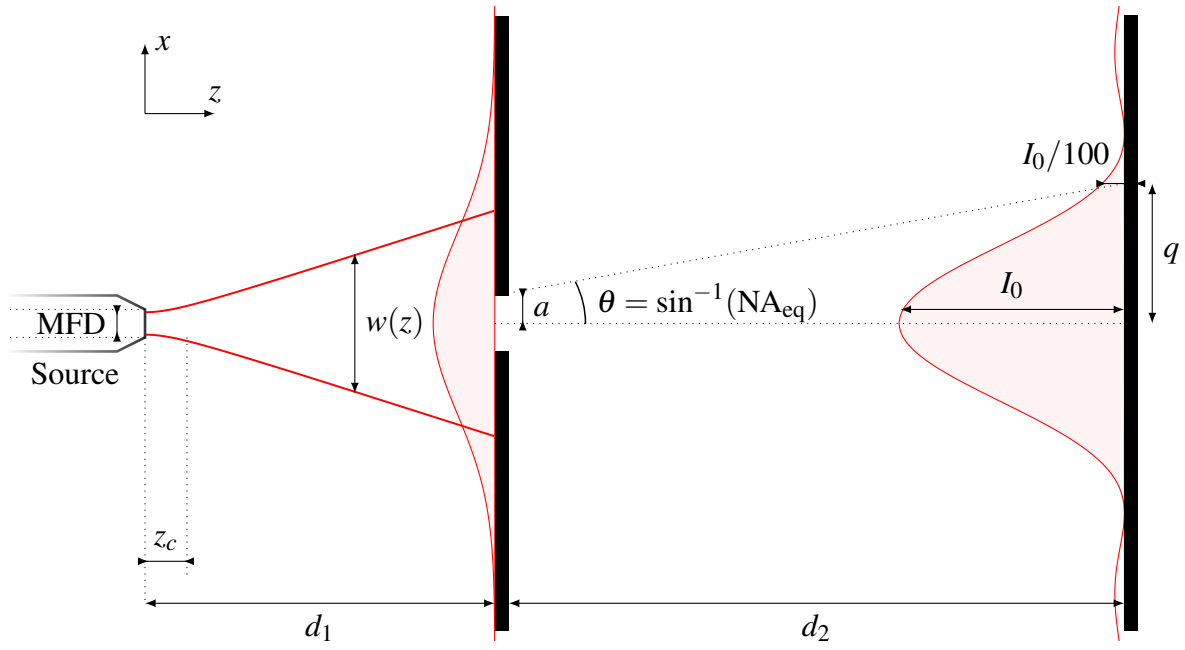

Fig. 4.5 Diagram of experimental system for sources: laser light exits a fiber with given mode field diameter MFD, diverges as a gaussian beam with full width $w(z)$ at distance z from fiber exit, before hitting the aperture plane at distance d_1; light passing through the aperture of radius a is diffracted, leading to a well-defined beam pattern on the detector plane at distance d_2 from the aperture plane, with maximum intensity I_0 and 1%-power level radius q, corresponding to a diffraction angle θ.

where a is the aperture radius and N is a normalization factor such that the total power at distance z is equal to the total power passing through the aperture:

$$N^2 = \int_0^a 2\pi\rho A(\rho)^2 d\rho \Big/ \int_0^\infty 2\pi r \left(\int_0^a \rho A(\rho) J_0\left(\frac{k}{d}\rho r\right) d\rho \right)^2 dr, \tag{4.16}$$

for any distance $z = d > 0$. The power density pattern is obtained by taking the square of the amplitude: $I(r,z) = [U(r,z)]^2$.

For an input Gaussian beam with finite width, we replace $A(\rho)$ by a Gaussian amplitude and integrate numerically. In particular, when considering the light from a fiber,

$$A(\rho) = \sqrt{Pd(z = d_1, \rho)} = \sqrt{\frac{2P_{tot}}{\pi w(d_1)^2}} \exp\left[-\left(\frac{\rho}{w(d_1)} \right)^2 \right], \tag{4.17}$$

where d_1 is the fixed distance between the fiber end and the aperture. The general beam intensity pattern is then given by

$$I(r,z) = \frac{2P_{tot}}{\pi w_0^2} \frac{\int_0^a 2\pi\rho \exp(-2\frac{\rho^2}{w(d)^2})\, d\rho}{\int_0^\infty 2\pi\rho' \left(\int_0^a \rho \exp\left(-\frac{\rho^2}{w(d)^2}\right) J_0\left(k\rho\rho'\right) d\rho\right)^2 d\rho'} \times \left(\int_0^a \rho \exp\left(-\frac{\rho^2}{w(d)^2}\right) J_0\left(\frac{k}{z}\rho r\right) d\rho\right)^2. \tag{4.18}$$

The configuration is summarized in Figure 4.5, with radiation from an open-ended fiber being diffracted through a circular aperture onto a plane normal to the propagation direction at a fixed distance d_2. Using Equation (4.18), we can numerically find the radius r such that $I(r, z = d_2) = 0$, or the radius q such that $I(q, z = d_2) = I(0, d_2)/100$ to compute the equivalent numerical aperture NA_{eq} as

$$\mathrm{NA}_{eq} = \sin\left(\tan^{-1}\left(\frac{q-a}{z}\right)\right). \tag{4.19}$$

The 1%-power radius q will also provide an appropriate metric for discussing the required signal-to-noise ratio in Section 4.3.4.

4.3.4 Detection

While semiconductor photodetectors are expected to be highly multi-mode, we wish to control the number of degrees of freedom in the context of this experimental demonstration, to obtain a detector system that has single-mode, few-mode or multi-mode behavior. By coupling the detector to a length of optical fiber, the latter acts as a mode filter and we obtain a mode reconstruction problem with a limited number of modes. Using an optical fiber for the demonstration introduces two advantages: (i) fibers can be selected and interchanged to obtain the modal constraints desired, and (ii) we can estimate the number of modes of step-index fibers, with the same computation giving a lower bound to the number of modes for a few-mode fibers and an accurate estimate for multi-mode fibers.

First, we define a fiber's V-value as

$$V = \frac{2\pi}{\lambda} a.\mathrm{NA}, \tag{4.20}$$

where λ is the operating wavelength, a is the fiber core radius and NA its numerical aperture [11]. If a fiber has $V < 2.405$, it is single-mode at that wavelength. For highly multi-mode

fibers, the number of modes N can be approximated by

$$N = \frac{A\Omega}{\lambda^2}, \tag{4.21}$$

where A is the fiber core area and Ω is the fiber beam pattern's solid angle, taken as a cone with half-angle θ such that NA=sin(θ). Then, with $A = \pi a^2$ and $\Omega = 2\pi[1 - cos(\theta)] = 2\pi[1 - \sqrt{1 - \mathrm{NA}^2}] \approx \pi \mathrm{NA}^2$, we obtain

$$N \approx \frac{\pi a^2 \times \pi \mathrm{NA}^2}{\lambda^2} = \frac{V^2}{4}. \tag{4.22}$$

It should be noted that fibers labeled as single-mode, but with a second-mode cutoff wavelength slightly higher than the operation wavelength, can be used as few-moded fibers. Setting $V = 2.405$ in Equation (4.20), we can obtain the second-mode cutoff wavelength λ_0 for fibers of known radius a and numerical aperture NA, as would be typical for commercial fibers characterized by manufacturers. For instance, a fiber with second-mode cutoff wavelength $\lambda_0 = 1700\,\mathrm{nm}$ is expected to behave as a two-moded fiber at $\lambda = 1550\,\mathrm{nm}$ [19]. This can be approximately tested in Equations (4.20) and (4.22), using $V = 2.405$ at $\lambda_0 = 1700\,\mathrm{nm}$; then, $V(\lambda = 1550\,\mathrm{nm}) = 2.405 \times 1700/1550 \approx 2.64$, and $N \approx 1.74 \sim 2$.

It is important to note that V is also related to the MFD and beam waist; in step-index fibers, their relationship is given by

$$\frac{w_0}{a} = 0.65 + \frac{1.619}{V^{3/2}} + \frac{2.879}{V^6}, \tag{4.23}$$

where a is the fiber core radius as defined in Equation (4.20) [91]. In the case of multi-mode fibers, Equation (4.23) applies to the fundamental mode. A modified form,

$$\frac{w_0}{a} = 0.634 + \frac{1.619}{V^{3/2}} + \frac{2.879}{V^6} - \frac{1.561}{V^7}, \tag{4.24}$$

has an accuracy of better than 1% above $V = 1.5$, which corresponds to all of the cases considered here [92]. Equation (4.24) has further importance as it is most closely related to the commonly used far-field definition of the MFD in circularly symmetric fibers, the so-called "Petermann II mode field diameter definition" [93],

$$\mathrm{MFD} = \frac{\lambda}{\pi} \sqrt{\frac{2\int_0^{\pi/2} I(\theta) \sin\theta \cos\theta d\theta}{\int_0^{\pi/2} I(\theta) \sin^3\theta \cos\theta d\theta}}. \tag{4.25}$$

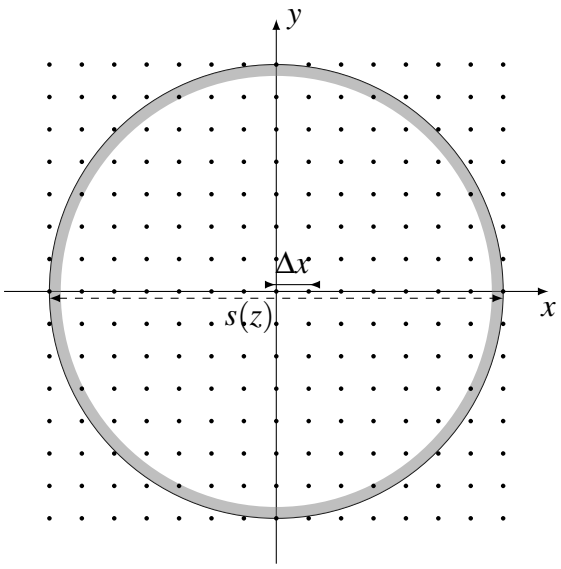

Fig. 4.6 Diagram showing the proportion of 2-D locations inside 5% of the 1% power-level radius, taking $\Delta x = s(z)/14$, i.e. 15 sample points for each movement axis.

Commercially available photodetectors generally have outputs that take the form of current sources. Typical responsivities are 1 A/W, such that 1 nW of optical power produces a 1 nA current signal: such small currents need to be amplified before being read out as a voltage by a computer through an analog-to-digital converter. Several different noise specifications are used to characterize an amplifier, two of which are particularly important for our design:

- Input noise current density: measured at a given bandwidth and is a good estimation for any bandwidth chosen manually below the upper cut-off frequency;
- Integrated input noise current: corresponds to RMS noise at bandwidth equal to upper cut-off frequency; it is typically much larger than the input noise current density times that bandwidth.

We must choose a post-detection measurement bandwidth. By the sampling theorem, the sampling steps in phase-space must be at least half of the 2π rad periods. If we want to have one visibility measurement per second, with the fringe measurement taking 10ms to minimize errors linked to source movements, and 10 optical power measurements to create the visibility plot, then the required bandwidth is 1 kHz.

For an input noise current density of 30 fA/$\sqrt{\text{Hz}}$, a 1 kHz bandwidth implies a noise of 1 pA, corresponding to a 1 pW optical power required for a unit SNR. Note that we want a high SNR even in the case of a single source at a location on the detector's 1% power-level

radius, where the power incident on the detector will be minimal; for an SNR of 10, we require $P(r = s(d_2)) > 10\,\text{pW}$. When measuring fringes for a fixed pair of source positions, the cases where both sources couple minimal power into the detector fiber will be quite rare, corresponding to having both sources on the detector's 1% power ring. If considering a circle with radius equal to 7 Δx steps as in Figure 4.6, this corresponds to at most 26 positions out of 150, which implies less than 4% of all 2-sources 2-D position pairs.

4.3.5 Numerical Cases

Having listed the main constraints and requirements for the design of the experiment, the goal in this section is to create a table of realistic scenarios. We now proceed through an entire computation of the different parameters for which equations were established in previous sections, in order to produce the first column of Table 4.2. In all of these scenarios, we assume that the source optical fiber has a mode field diameter MFD$= 10\,\mu\text{m}$ with total power output is 5 mW, at wavelength $\lambda = 1550\,\text{nm}$.

In the first scenario, we assume a pinhole with aperture radius $a = 2\,\mu\text{m}$ and that the source optical fiber is glued directly on the pinhole plate, meaning that $d_1 = 0\,\text{mm}$. This configuration is that in which the Gaussian beam is the most collimated, equivalently the least spread-out; its spot width is the mode field diameter. We first compute the power through the pinhole aperture, P_0, obtained by numerically integrating the source intensity over the aperture; in this scenario, $P_0 = 1.37\,\text{mW}$. We can also obtain a figure for the flatness of the incoming beam at the pinhole aperture by considering the ratio of intensities at the edge and center of the aperture is $I(r = a, z = 0)/I(r = 0, z = 0) = 0.726$. If the distance between the detector plane and the aperture plane is assumed to be $d_2 = 10\,\text{mm}$, then the equivalent numerical aperture of the beam diffracted through the pinhole is $\text{NA}_{eq} = 0.395$, corresponding to an acceptance angle of $\theta = 23.3°$ and implying a 1% power radius $q = 2.15\,\text{mm}$ on the detector plane $z = d_2$.

Further assuming that the detector fiber has core radius $a_d = 4.5\,\mu\text{m}$, the power incident on its core is obtained by numerical integration. When the detector fiber is aligned with the pinhole, the incident power on the core surface is 5.63 nW. Moreover, assuming this detector fiber has a numerical aperture of $\text{NA}_d = 0.13$, if the source center sits on the detector's 1% power ring, the power incident on its core is 4.05 nW. With these dimensions, the detector fiber has a Rayleigh length $z_R = 36.6\,\mu\text{m}$.

We can use Section 4.3.2 to compute the minimum distance between the aperture plane and the detector plane $z^{min} = 427\,\mu\text{m}$: this is much smaller than the 10 mm chosen. Then, we compute the maximum acceptable step size: $\Delta x^{max} = 209\,\mu\text{m}$. Finally, Equation (4.22)

Experimental parameter	Symbol	Value				
Aperture radius	a (μm)	2	2	4	2	2.5
Fiber-aperture distance	d_1 (mm)	0	0	0	0	0.015
Aperture-detector normal distance	d_2 (mm)	10	50	50	50	50
Detector radius	a_d (μm)	4.5	4.5	4.5	25	4.5
Detector numerical aperture	NA_d	0.13	0.13	0.13	0.22	0.13
Power through aperture	P_0 (mW)	1.37	1.37	3.61	1.37	1.84
Aperture edge/center intensity	$I(a)/I(0)$	0.726	0.726	0.278	0.726	0.631
Equivalent numerical aperture	NA_{eq}	0.395	0.395	0.223	0.395	0.328
Source 1% power radius	q (mm)	4.30	21.5	11.5	21.5	17.3
Max power on detector	$P(r=0)$ (nW)	5.63	0.182	1.86	5.63	0.382
Min power on detector	$P(r=s(d_2)/2)$	4.05	0.138	0.619	2.34	0.246
Detector Rayleigh length	z_d (μm)	36.6	36.6	36.6	534	36.6
Minimum distance	z^{min} (mm)	0.427	0.427	1.29	0.724	0.589
Maximum step size at d_2	Δx^{max} (mm)	0.209	1.04	1.04	1.80	1.04
Mode number estimate	N_{modes}	1	1	1	125	1

Table 4.2 Given experimental parameters (top), the values (bottom) are computed assuming the presence of a pinhole at a distance d_1 from the source, with power at output of fiber $P_{tot} = 5$ mW and fiber MFD$= 2w_0 = 10$ μm, at wavelength $\lambda = 1550$ nm; i.e. source Rayleigh length $z_R = 50.7$ μm.

provides an estimate for the number of modes of the detector system: $N = 1$ given the detector fiber dimensions in this scenario.

The same procedure was used to compute the elements of Table 4.2, with the top five parameters stating fixed experimentally-achievable values, and the items below stating the corresponding computed values. In Table 4.3, similar inputs are used to compute the design parameters, in the case where no pinhole is used and the source beam propagates in free-space without diffraction. Together, these scenarios demonstrate the feasibility of carrying out an EAI experiment at infrared wavelengths using a laser source of relatively low power, for which constraining safety measures are not unduly restrictive.

4.4 Safety Considerations

In parallel to considering the constraints for the design of the experiment, we must ensure that it fulfills important safety requirements. Rather than approaching this topic as a limitation on the capabilities of the system, the trade-off between gains in SNR from higher optical powers and the necessary safety precautions while operating the experimental system drives its design. For instance, it is important that the range of optical powers available is sufficient

Experimental parameter	Symbol	Value			
Aperture-detector normal distance	d_2 (mm)	10	50	50	100
Detector radius	a_d (μm)	4.5	4.5	25	4.5
Detector numerical aperture	NA_d	0.13	0.13	0.22	0.13
Source 1% power radius	q (mm)	1.50	7.49	7.49	15.0
Equivalent numerical aperture	NA_{eq}	0.10	0.10	0.10	0.10
Max power on detector	$P(r=0)$ (nW)	208	8.32	25.7	2.08
Min power on detector	$P(r=s(d_2)/2)$	6.00	0.243	0.007	0.061
Detector Rayleigh length	z_d (μm)	36.6	36.6	534	36.6
Minimum distance	z^{min} (mm)	3.99	3.99	1.18	3.99
Maximum step size at d_2	Δx^{max} (mm)	0.209	1.04	1.80	2.09
Mode number estimate	N_{modes}	1	1	125	1

Table 4.3 Given experimental parameters (top), the values (bottom) are computed assuming the absence of a pinhole, with power at output of fiber $P_{tot} = 5$ mW and fiber MFD$= 2w_0 =$ 10 μm, at wavelength $\lambda = 1550$ nm; i.e. source Rayleigh length $z_R = 50.7$ μm.

to characterize a wide range of infrared detectors, but also that the experiment can easily and safely be run by a non-technical expert, in order to make it attractive for a large number of applications.

The main hazard is the use of laser radiation, in particular in the free-space section between the open-ended optical fiber probes and the fiber-coupled detector. Because diffraction through an aperture never leads to a power density larger than in the non-diffracted case, we only consider the safety of the beam exiting the source fibers. However, it should be noted that, for positions where the non-diffracted beam is considered dangerous, the diffracted beam may be dangerous at larger angles.

The main risk is associated with damage to the human eye. The Maximum Permissible Exposure (MPE) is the widely recognized safety metric, and is defined as the radiation intensity above which the human eye becomes damaged. For a laser of 1550 nm wavelength, the MPE is 1000 W/m^2 [94], so we compute the minimum distance at which the power density drops below this value, for a given total power output and fiber properties. Note that this assumes that the laser input fills the acceptance angle of the optical fiber to which it is coupled: if the laser input is focused into the optical fiber at an angle smaller than the acceptance angle, the output light exits the fiber with roughly the same angle. In practice, fiber-coupled laser sources are designed to fill the acceptance angle of the output fiber.

The computation based on the MPE also assumes a uniform power density over the eye's cross-section, modeled as a 3.5 mm diameter aperture; we therefore choose the center power density, in order to get an upper bound. Using a fiber with MFD$=$ 10 μm, we obtain the safe distances as a function of the laser output power in Table 4.4. For instance, for a 60 mW laser,

Laser output power (mW)	10	20	30	40	50	60	80	100
Safe distance (mm)	25.6	36.2	44.3	51.1	57.2	62.6	72.3	80.9

Table 4.4 Table of safe viewing distance upper bounds versus laser output powers, for a typical single-mode fiber MFD$=10\,\mu$m

the MPE is reached at a distance of 63 mm. Personal protective equipment is also available as a final safety measure; protective glasses are rated with an optical density, defined as the base-10 logarithm of the attenuation factor through the glasses. A typical optical density of commercially available protective glasses for infrared radiation is 4; using the example of a 60 mW laser, the safe distance decreases to 0.6 mm.

4.5 Comparison of Designs at Infrared and Submillimeter Wavelengths

Having overcome significant challenges in completing the design of an EAI experiment for the study of near-infrared detectors, it is interesting to reflect on the differences with the experimental system demonstrated at submillimeter wavelengths by Thomas et al. [59], which was briefly described in Chapter 1. While some similarities are expected for systems that are built to achieve the same goal, the difference in wavelength range implies a considerable contrast in the design choices made and the technologies chosen:

- In the submillimeter wavelength experiment, an electrical signal was produced by the phase-locked synthesizers, a temporal phase modulation was applied, and then fed to the probes to produce an electromagnetic field. At infrared wavelength, there is no analogue where the signal provided to the sources is identical in nature to the signal generated by the synthesizer. Instead, an optical signal must first be generated, modulated and transmitted to the probe tips.

- At optical and infrared frequencies, frequency multipliers are not readily available, particularly for a $\times 24$ frequency multiplication; moreover, frequency multiplication or division is generally impractical as it requires elaborate up- or down-conversion techniques. It is far more advisable here to look for a signal generator that intrinsically provides the desired infrared wavelength, as well as a well-defined polarization.

- As a source is moved relative to the detector, the spherical phase of the beam changes. The phase shift induced by moving a source is important for displacements larger than a fraction of a wavelength. At infrared wavelengths, this corresponds to sub-micron

displacements, even for small off-axis distances. More generally, the fringe phase will wrap quickly for consecutive source positions. This also implies stringent requirements on the positional stability of the infrared probes over time.

- An important limitation of the submillimeter experimental system was the slow response time of the device under test. At infrared wavelength, readily available detectors have far greater bandwidth, in the MHz to GHz range, in part due to technological advances for uses in optical fiber telecommunication. The readout scheme is therefore greatly simplified.

4.6 Conclusion

We have completed the design of a room-temperature EAI experiment to fully characterize the optical behavior of infrared detectors, and have studied all necessary specifications and performance parameters needed to fulfill the requirements set out in Section 4.1. In other words, we have demonstrated the feasibility of a fiber-based experimental system to perform EAI at near-infrared wavelengths, using commercially available components; the realization of this system will be the topic of Chapter 5. Figure 4.2 summarizes the proposed experimental system, and convincingly responds to the required steps illustrated in Figure 4.1. A narrow-linewidth generates high-coherence radiation, which is coupled into a polarization-maintaining optical fiber and a 50%-50% split ratio beamsplitter. Phase modulators provide accurate control of the relative phase between the two arms, while delay lines and polarizers ensure that the high coherence and polarization are preserved throughout the fiber lengths. A system of motorized linear stages places each of the open-ended fibers, which constitute the probes. An amplified photodetector provides a signal linear in the input power through an interchangeable optical fiber, which acts as a modal filter for the system under test. The analog signal is converted into a digital signal and recorded by a computerized system.

Further to the design of the experiment, we realized a search for commercially available components. The choice of operating at $\lambda = 1550\,\text{nm}$ was greatly beneficial for the range of components available, and multiple options were considered for critical components, such as the laser source and motorized stages. The decisions were made on the basis of component performance and flexibility; for instance, some motorized stages models have a sufficient acceleration to allow raster scans to be envisioned without large time penalties for starting and stopping the scan movement. In the next chapter, we will discuss the specific components chosen to fulfill the design requirements listed in this chapter, and in particular the choice and performance of commercially-available components. Additionally, we will describe some

additional custom parts required, including fiber holders for sources, which we designed and manufactured.

While the design described in this chapter fulfils the requirements listed in Section 4.1, its potential goes far beyond the application we have chosen, and many extensions of the current system are possible. The most obvious one is the straightforward adaptation of the architecture to optical wavelengths, where a large majority of components are also available with similar specifications. The current room-temperature experiment design can also be upgraded easily and is attractive in many other contexts, some of which will be discussed in Chapter 10. In particular, it constitutes an important step forward towards a potential future objective of applying EAI to the study of low-temperature detectors. These could include cooled CCD arrays or even superconducting detectors such as those mentioned in Chapter 1, in particular KIDs. Such an investigation would require a cryogenic version of the experimental system, in which optical fibers could be run down into a cryostat and their open ends could be positioned with cryo-compatible piezoelectric stages. While some of the required technologies would differ, a significant fraction of the design considerations discussed in the context of our room-temperature experiment could be directly leveraged.

Chapter 5

Construction and Characterization of the Experimental System

5.1 Introduction

Having fully investigated the design of an EAI experiment at infrared wavelengths in Chapter 4, we now turn to the construction of the system we have described and its characterization. We have chosen an all-fiber design and the operating wavelength of $\lambda = 1550\,\text{nm}$, both of which are crucial in terms of the technologies available and the potential applications for our EAI technique. The goal of this chapter is to demonstrate that the experimental system was successfully constructed, using a combination of commercially available and custom-made components, and that its performance is well within the specifications we had set out in Chapter 4. In particular, this will bring us to attempt the measurement of fringes in the detector output as the relative phase between the sources is modulated. This alone corresponds to an important milestone towards performing EAI on infrared devices, as the measurement of the DRF characterizing their optical response is based on the extraction of the parameters of the measured fringes.

In Section 5.2, we introduce the choice of specific components to complete the design presented in Chapter 4. In particular, we discuss the components' specifications that will be of importance for the assembly of the experimental system. Sections 5.3 and 5.4 will describe the construction of the experimental system, naturally splitting the topic between the generation of the external field and the creation of the detector system. More specifically, in Section 5.3 , we will discuss the half of the experimental system that deals with the sources, from the laser source up to the open-end optical fibers that serve as the probes for the EAI experiment. In Section 5.4, we will then discuss the second half that deals with the detector,

in other words the fiber-coupled detector system that constitutes the device under test, and the signal treatment and data acquisition system. This includes the first measurement of a fringe in the detector output as the phase between the sources is rotated, for sources in fixed positions set manually. In Section 5.5, we continue by performing calibration measurements, in two key areas: the detector output linearity with the incoming optical power and the phase modulation linearity with input voltage from the waveform generator. These are critical to building confidence in the experimental system and setting up standard procedures for future measurements. In Section 5.6, we proceed with a full characterization of the performance of the detection system. This includes its noise characteristics and its optimal measurement time, which is found using a metric called the Allan Variance, to be discussed in detail. An important additional measurement is that of the settling time of the system after source displacements, necessary to appropriately delay the start of fringe measurements and obtain bias-free, high-SNR fringe complex amplitude values.

5.2 Experiment Components

In order to fufill the design requirements listed in Chapter 4, the following components were chosen:

- **Laser source:** PurePhotonics PPCL300 laser source has a 1550 nm center wavelength and achieves a 10 kHz linewidth corresponding to a 30 000 m coherence length, much larger than the few meters strictly required. It produces a tunable output power between 6 dBm and 18 dBm (4 mW to 63 mW), allowing us to perform important calibration measurements in Section 5.5. Its output is an angled FC/APC female connector, compatible with the polarization-maintaining fiber used in the experimental system.

- **Beamsplitter:** Thorlabs PMC1550-50B-APC beamsplitter is built from fused polarization-maintaining optical fiber with a 1550 nm center wavelength and ± 15 nm bandwidth. It has one input and two outputs, a 50%-50% split ratio with precision within 0.3 dB (i.e 7%), and a 55 dB directivity that prohibits reflections at output connectors from travelling in the opposite direction into the laser source. Its 18 dB Polarization Extinction Ratio ensures that cross-coupling between polarization modes is minimized, and its FC/APC connectors provide polarization alignment with connected components.

- **Phase modulators:** Two Thorlabs LN65S fiber-coupled phase modulators were customized with polarization-maintaining fibers and narrow-key FC/APC connectors and each include a 40 dB polarizer aligned with the slow polarization axis: this ensures a well-defined polarization at their respective outputs. Phase modulation is obtained

by feeding a low-voltage $[-10\,\mathrm{V}, +10\,\mathrm{V}]$ signal with frequency up to 10 GHz, much larger than our expected target fringe frequency.

- **Motorized stages:** Two sets of three Zaber X-LSM050A-E03 were chosen. Each set of stages includes an adapter plates to create three-axis sets. Each linear stage has a 50 mm travel range, with 4 µm absolute accuracy and 1 µm unidirectional repeatability, significantly smaller than our projected step size during scans. An integrated controller and motor encoder are included, providing communication capability with a computer and protection against slipping and stalling.

- **Manual stage:** We selected a Thorlabs PT3A/M manual stage for precise placement of the device under test. Thorlabs DM12 differential micrometers produce a 25 mm travel range, and include a 0.5 µm fine tuning resolution that allowed us to verify the presence of standing waves with a precision smaller than a wavelength.

- **Detector:** Thorlabs DET01CFC InGaAs photodetector is operated under -12 V reverse bias to obtain peak performance that includes a 4.5 fW/Hz$^{1/2}$ NEP and 1.2 GHz bandwidth; these performances exceed those of the rest of the measurement system, ensuring that these two metrics are not limited by the photodetector. The fiber-coupled optical input uses a female flat-faced FC/PC connector, the industry standard.

- **Amplifier:** LaserComponents DLPCA-200 is a low-noise transimpedance amplifier that produces a large voltage signal from the current input from the photodetector. It has a variable gain setting, from 10^3 V/A to 10^9 V/A gain over 7 settings; these have corresponding bandwidths, from 500 kHz to 1 kHz, and NEP, from 20pA/Hz1/2 to 4.3 fA/Hz$^{1/2}$. An extra $\times 100$ voltage gain is available in high-gain mode.

- **ADC:** National Instruments PCIe-6321 has a 250 kS/s maximum sampling rate, cumulative over all analog inputs. Digital inputs are available for operations such as triggering. The ADC is provided with a LabVIEW driver and library, which was used to control measurements of the detector output. The ADC's output uses National Instrument's proprietary 68-pin SHC68-68-EPM cable, for which we required a custom-built adapter to BNC cables, described in Section 5.4.2.

- **Fiber connections:** Thorlabs ADAFCB3 mating sleeves were used to couple optical fibers with FC/APC connectors, guarantee their polarization alignment, and are mountable on the optical table.

Figure 5.1 shows a top-down view of the optical table used for the experiment, which includes the listed components as well as custom components, the fabrication of which will

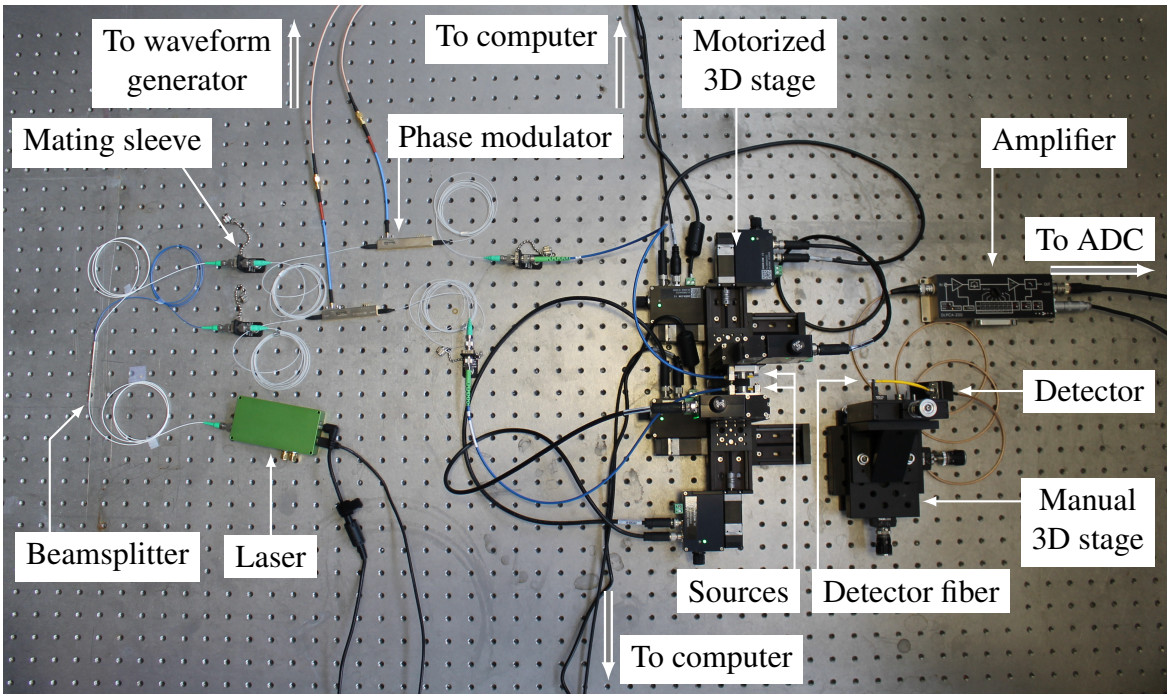

Fig. 5.1 Labelled top-view photograph of the experimental system.

be discussed in detail in this chapter. The fiber-based components, namely the beamsplitter and phase modulators, were installed in plastic trays to protect them from accidental damage and minimize any environmental perturbations such as mechanical vibrations.

5.3 Source System

5.3.1 Requirements

In this section, we discuss the construction of the part of the experimental system that creates the two phase-locked probes necessary to an EAI experiment. This corresponds to the system from the laser source up to the open-end optical fibers, mounted on the motorized stages for scanning. There are several key requirements that this section will address:

- The motorized scanning stages must communicate with the computer and be controllable;
- The two open-ended optical fibers that constitute the probes must be secured to their respective motorized stage sets, with adequate stress relief, while minimizing their physical sizes and the distance between the fiber cores;

- The polarization axis at the connection with the laser and phase modulation system must be aligned;
- The polarization axis at the output of the source fibers must be set such that they are parallel;
- The motorized scanning system must maximize the useful scanning range;
- Complex scanning instructions must be generated;
- Given a set of scanning instructions, an independent method must verify whether these are safe, i.e. that they do not lead to a collision between the probes.

Many other requirements, such as the details of how to produce the phase modulation, are also necessary but require a functional detection system. These will be discussed in Section 5.5.

5.3.2 Motorized Stages' Performance

Communication between the control computer and the motorized stages was achieved straightforwardly by configuring the computer's USB ports. The stages of each three-axis set were daisy-chained to use a single communication channel. A manufacturer-provided computer console was used for manual stage-level positioning instructions and movement settings, including the acceleration and deceleration used at the beginning and end of each movement, as well as the maximum travel velocity. In practice, each motorized stage's position is given by a distance relative to its "home", defined in the stage's hardware by a magnetic Hall sensor. The stages' positions are provided in units of microsteps, abbreviated µsteps; the conversion to metric units is 1 µstep = 0.047625 µm. In other words, the 50.8 mm scanning range corresponds to 1 066 700 µsteps, which will be important when considering simultaneous scans of the two sources, a topic discussed in Section 5.3.5. The computer console also includes a function that returns the stages' positions as read by the rotary quadrature encoder on their motor, with a resolution of 8 µstep. This provides a way to verify each stage's position during multi-displacement scans, as will be presented in Chapter 6.

An important verification was that the positioning repeatability of each individual stage was in agreement with the manufacturer's specifications. These measurements were performed using a dial gauge, measuring the relative distance of the stage's travelling plate to the gauge along the direction of movement, as the motorized stage was repeatedly scanned back and forth to a target position. The dial gauge used has a resolution of 1/10 000" = 2.5 µm. We tested each of the scanning stages individually, and found that the repeatability

was within a fraction of the dial gauge's resolution, in line with the specification stated by the manufacturer of within 1 μm.

Three motorized stages were mounted together to create a three-axis set, using the mounting holes in the stage plates and a custom adapter plate produced by the stages' manufacturer. These sets were mounted with right-left symmetry, i.e. symmetrical about the plane $x = 0$; in this configuration, the probes are closest when both stages are at their maximal x positions. The two x-axis stages were mounted such that their structures are almost touching, with a sub-centimeter gap. The mounting holes have a small tolerance, equal to a few degrees; orthogonality between the motorized stages was ensured by carefully mounting them with a set square. More generally, this tolerance also allowed us to relax the strict orthogonality and carefully adjust the mounting angle between the three stages of each set, in order to align the propagation of the source beams with one another and the detector, in Section 6.3.2. Once the three-stage axis sets were mounted together, we reiterated these repeatability measurement for both horizontal stages, as these bear loads from the other stages mounted on them. Again measuring the position of the stage plate relative to the dial gauge for repeated movements back and forth to a target position, we found that the stages' movements have sub-micron repeatability.

It is important here to make a few remarks about the symmetry of the scanning system. We will denote the right and left sources as viewed in the direction of the source beams, i.e. towards the detector. We note that, under the current configuration, it is not possible to exchange the positions of the two sources: the right source is always to the right of the left source and vice versa. This implies that right-left symmetry of the source system assumes that the sources are identical, i.e. that they have identical power output, beam pattern and beam direction, as well as perfect positioning. When scanning the two sources over all position pairs, as will be discussed in Chapter 6, we only considered position pairs where the right source position along the x-axis, x_R, is smaller than the left source position along the x-axis, x_L. This reduced by a factor 2 the number of position pairs to which the sources were scanned, and thus the duration of such measurement sets.

5.3.3 Mounting the Probes

We elected to use two open-ended source fibers that will constitute the probes in our EAI experiment. The first key item to consider is the holder system to mount each of them onto their respective motorized stages' plates. These holders are particularly important, as their design determined the minimum distance between the probes, which in turn set a limit on the number of sampled position pairs that could actually be physically achieved without a collision between the probes. The main requirements were to find a way of reliably securing

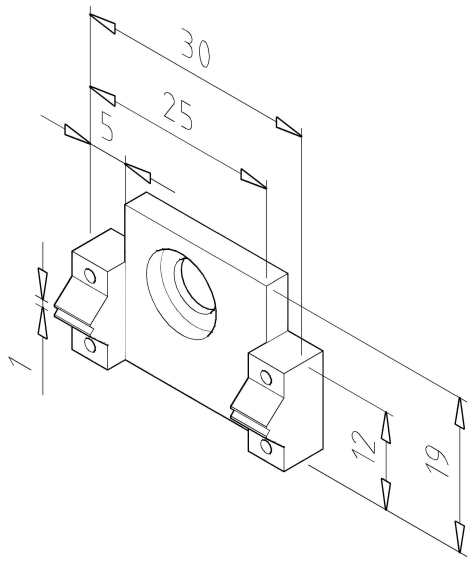

Fig. 5.2 Schematical drawing of a fiber holder; values are in millimeters.

an open-ended optical fiber to the motorized stages' structure, and to bring the optical fiber cores as close as possible to each other. We therefore wished to reduce the physical size of the mounting structure; in practice, this must be achieved for three of the top, bottom, left and right sides, in order to bring the probes as close as possible to each other horizontally and vertically. Figure 5.2 shows the schematical design of one fiber holder: two "v"-shaped grooves along tapered structures of an aluminum block, into which a small hollow cylindrical ferrule can be glued, with the optical fiber epoxied inside. By doing so, the minimum distance between two such probes placed vertically or horizontally with respect to each other is set by the size of the ferrule itself. We chose aluminum as the fabrication material chiefly for its manufacturing simplicity and its low thermal expansion coefficient. The holder structure could then be mounted onto a motorized stage's travelling plate using a single screw, allowing vertical alignment as will be discussed in Section 6.3.2.

The next step was the choice of the fiber to be mounted on these fiber holders. In order to keep the polarization axis at the connectorized end known, we chose a Thorlabs P3-1550PM-FC-2 polarization-maintaining fiber patch cable with FC/APC connectors, compatible with the optical fiber used in the system and particularly for the pigtails of the phase modulators they are directly connected to. The 2 m-long patch cable was cut in two equal parts, straightforwardly with a cable cutter. We then obtained two identical lengths with the slow polarization axis aligned to the connector key. For each fiber length obtained, we then needed to secure the open end of the fiber on the motorized stage with a set polarization. To reach this goal, we followed part of standard instructions for connectorizing fibers [95]. We

removed approximately 60 mm of the patch cable's external plastic tubing, and 20 mm of its kevlar mesh and internal plastic tubing. The 250 µm diameter fiber was then stripped of its coating layer using a specialized stripping tool, down to the cladding-core, circular, concentric bilayer with 125 µm diameter. We chose a cylindrical ceramic ferrule for securing the fiber, with 127 µm bore size (i.e. inner diameter) and 1.25 mm outer diameter. Stainless steel ferrules were also available but rejected, because they are mostly designed for applications in optogenetics; while their bore size is specified analogously to ceramic ferrules, the inner diameter is larger for most of the ferrule length for increased contact with the bonding agent, which is not relevant to our application. Ferrules with 2.5 mm outer diameters exist as well, but these defeat the explicit goal we had of reducing the physical size of the probes.

The ferrule were first cleaned in an ultrasound bath of isopropyl alcohol for 3 minutes, and dried using compressed air. In order to adhere the stripped optical fiber to the ferrule's internal surface, we chose a two-component epoxy with a 30-minute pot life, i.e. duration over which the mixture is malleable enough to work, and a relatively low viscosity of 1 800 mPa.s, compared to 4 000 mPa.s to 20 000 mPa.s for most other commercial epoxies. The advantage of these two properties is that this type of epoxy is among the easiest to work with during the most delicate step of this fabrication process, fitting a 125 µm-diameter stripped optical fiber inside a ferrule with 127 µm bore size. As the optical fiber was slid through the ferrule, a small bead of epoxy formed at the outer tip of the ferrule: this was necessary for the following polishing steps. The curing time for the chosen epoxy at 25°C is 24 hours. After this waiting period, a piece of heat-shrink tubing was applied around the back of the ferrule and the inner plastic tubing of the patch cable, to reinforce the main weak point that is the stripped fiber epoxied at the back end of the ferrule. We needed to leave a minimum length of 5 mm of ferrule without heat-shrink tubing, out of the 6.4 mm total ferrule length, in order to properly place the ferrule in the aluminum holder v-groove.

The final step is to polish the optical fiber at the tip of the ferrule. We start off by cutting the protruding optical fiber with a ruby fiber scribe at the top of the epoxy bead. This is necessary to avoid the fiber snapping off with the epoxy blob, which would damage the optical fiber inside the ferrule. The main tools for the polishing step are a set of 5 sheets of lapping film, with decreasing grain sizes (30, 6, 3, 1, 0.02 µm grit), and the custom aluminum holder. The small holes on either side of both v-grooves are used to temporarily mount clamping brackets, which secure the ferrule and fiber tubing in their respective v-grooves. We set the optical fiber and ferrule in the two v-grooves of the holder with the bracket, such that the ferrule sticks out by approximately 1 mm, as shown in Figure 5.3. A purpose-made polishing disc would generally be used, but the smallest hole for securing the connector ferrule is 2.5 mm, rather than 1.25 mm in our case; given the fragility of our setup, we have

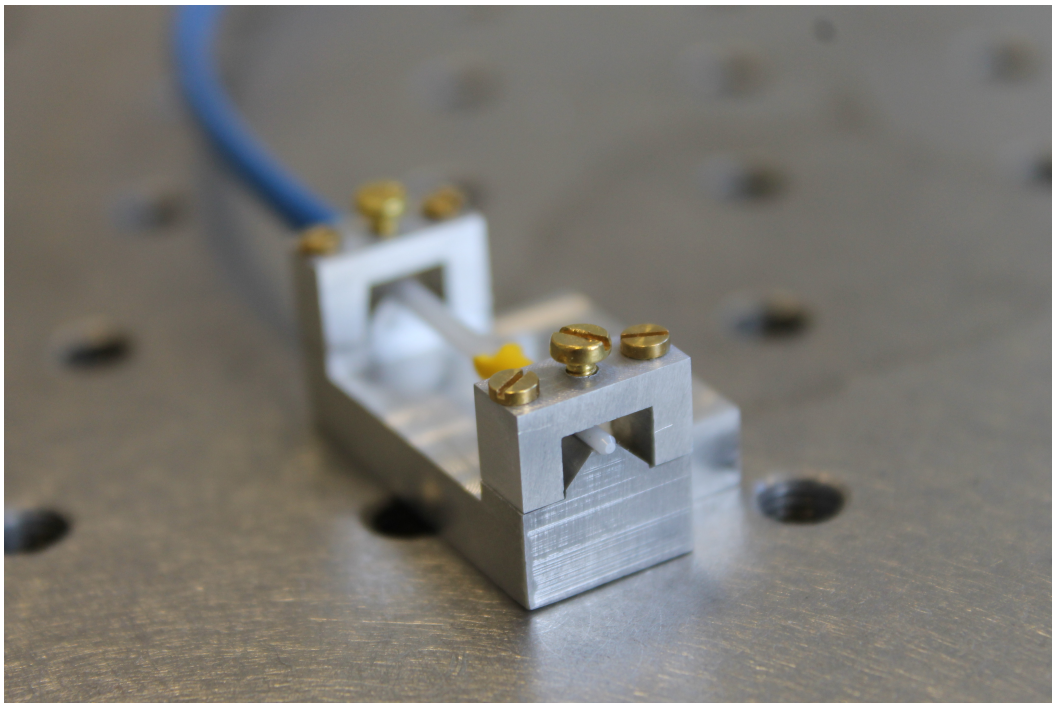

Fig. 5.3 The open end of a polarization-maintaining optical fiber is epoxied in the ceramic ferrule, and secured in the custom fiber holder's two v-groove structures with brackets, prior to polishing.

found it best to use the custom aluminum holder. Once secured in this way, the ferrule and optical fiber setup is moved across the 30 µm grit polishing sheet; starting with no downward pressure, increasing force is applied until the epoxy bead is gradually removed. Our experience showed that the figure-eight motion widely recommended indeed provides the best results, and that adding a drop of water prevents excessive friction between the ferrule surface and the polishing sheets, which could damage the fiber. Note also that the epoxy chosen has a dark blue color; it is therefore simple to inspect the ferrule by eye to verify whether this polishing action has removed the epoxy bead entirely. The same process is repeated four more times, with polishing films of decreasing grain size. For the two final grit sizes, we found it most helpful to look at the polished face under a microscope, in order to directly assess the polish achieved: for instance, when using the 1 µm grit film, viewing under the microscope at 200× magnification clearly showed whether small scratches from the previous 3 µm grit film remained. This was particularly important for the final polishing step, using the 0.02 µm grit film, which removed any visible grooves from the polished face.

Once the optical fiber had been properly polished, we viewed it under the microscope at 200× magnification. When the fiber is properly polished, the stress members of the panda-type polarization-maintaining fiber are visible as off-axis circles in the cladding layer,

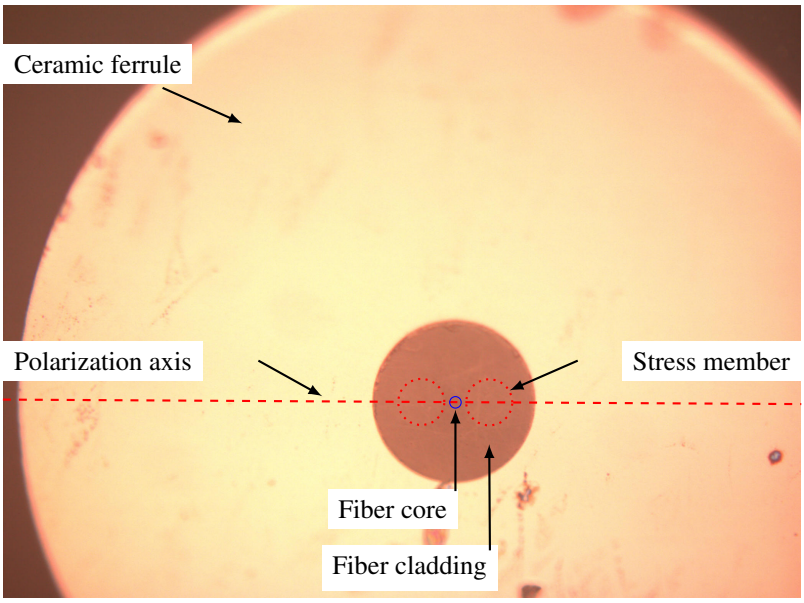

Fig. 5.4 Ferrule tip with polished fiber, viewed under a microscope with 200× magnification; the blue circle denotes the optical fiber core, the red dotted circles outline the stress members of the panda-style polarization-maintaning fiber, and the red dashed line passes through the centers of the three circles and represents the slow polarization axis of the fiber.

on opposite sides of the fiber core. Figure 5.4 shows the view through the microscope at 200× magnification: the slow polarization axis is defined by the line between the centers of the stress members, which also crosses the center of the fiber core, shown as a red line in the figure. By slightly loosening the clamping screws on the ferrule and plastic tubing, we were able to accurately rotate the ensemble, and thus the polarization axis, with respect to the fixed holder and clamp system. Under a lower magnification, we placed the holder such that the v-groove axis is accurately known. Once the desired polarization axis had been achieved, the ferrule and plastic tubing were again solidly clamped with the bracket screws. We chose to align the stress members with the holder v-groove. Setting the v-groove length normal to the detector surface, this implies that the slow polarization axis was aligned horizontally along the orthogonal direction, i.e. along the x scanning axis, and the fast polarization axis was aligned vertically.

After setting the polarization axis, we permanently fixed it by gluing the ferrule into the holder's v-groove. We carefully applied superglue into front and back v-grooves, using a single drop of superglue at the end of a thin pointed tip, such as a needle or cocktail stick. Gravity and capillarity ensured that the superglue ran down the entirety of the v-groove and correctly filled the volume between the aluminum holder and ceramic ferrule surfaces. For the front v-groove in particular, we found it critical to pour the superglue from the top, near

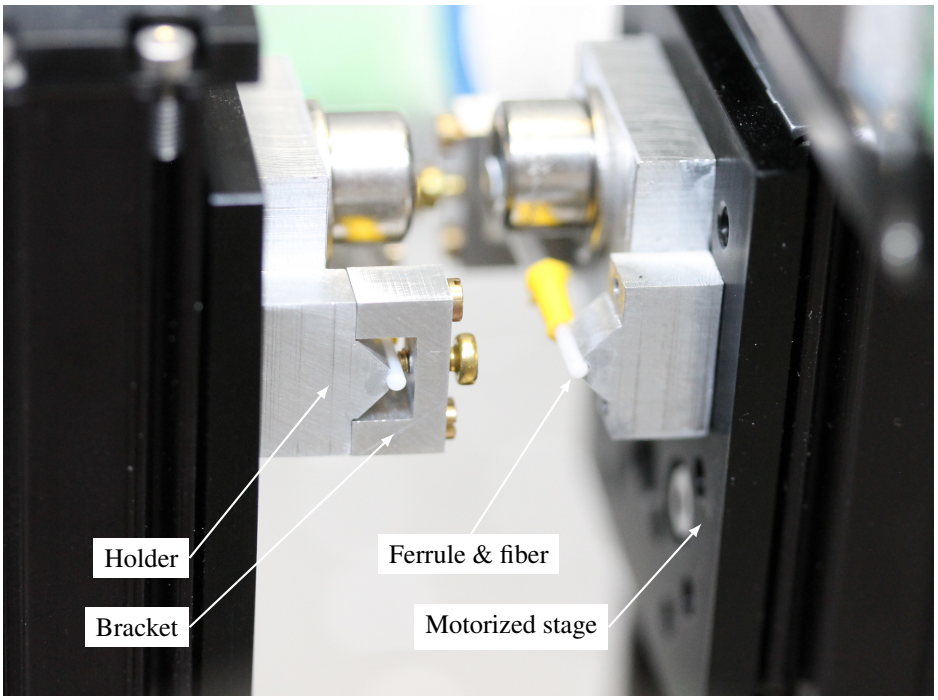

Fig. 5.5 Labelled probes mounted on the motorized stages.

the polished face, so that gravity pulls glue down into v-groove, away from polished surface. Note also that, even after polishing, the tip of the ferrule had enough of a tapered geometry to avoid the superglue flowing up the taper onto the polished surface. The curing time for the chosen superglue is 24 hours, after which the clamps were unscrewed and the ferrule safely released. The same procedure was applied to both open-ended fibers.

Figure 5.5 is a picture of the arrangement in its near-final configuration. On the right side, the left source fiber is epoxied in the white ceramic ferrule, which is glued to the aluminum holder. The yellow heat-shrink tubing wraps around the back end of the ferrule and the front end of the patch cable's optically transparent inner plastic tubing. On the left side, the same system is still held by the clamping bracket used for the polarization alignment and gluing steps of the manufacturing process. This bracket was removed when performing EAI experiments, such that the two probes approached one another up to contact of the ceramic ferrules. Overall, this process was found to be highly effective and repeatable.

5.3.4 Maximizing the Scanning Range

Having manufactured the probes, we turned to the means by which the sources were scanned. In the configuration with two sets of three axes described in Section 5.3.2, the sources could be brought close enough that they collide. However, this could only be achieved for

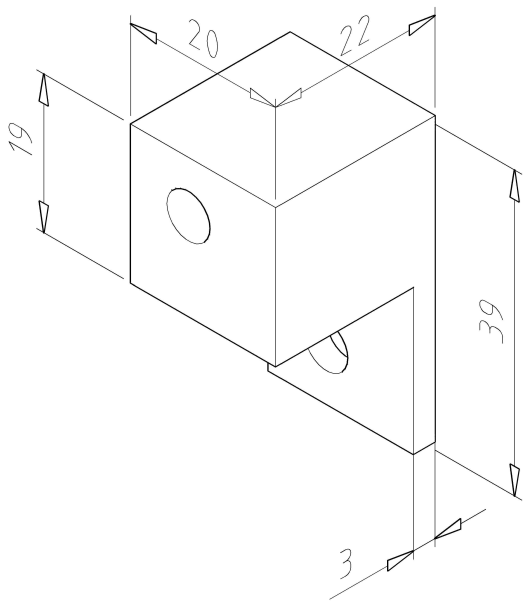

Fig. 5.6 Schematical drawing of an extender for the fiber holder; values are in millimeters.

a very limited range of (x_R, x_L) values, where x_R and x_L denote the right and left sources' position along their respective x scanning axes, following the convention discussed in Section 5.3.2. Instead, one of the goals stated in Section 5.3.1 was to maximize the useful scanning range, in other words, the range of (x_R, x_L) for which the probes are minimally distant. We note that, because the motorized stage system has x-axis symmetry, increasing x_R and x_L values mean scanning the right and left probes towards the left and right, respectively, i.e. towards one another. In practice, the probes should ideally be infinitesimally close to touching when $x_R + x_L = 1\,066\,700$ µsteps. In that case, the probes would nearly collide for both $(x_R, x_L) = (1\,066\,700\,\text{steps}, 0)$ and $(x_R, x_L) = (0, 1\,066\,700\,\text{steps})$, i.e. when either of the sources is at the home position and the other is at its maximal x position.

In order to achieve such a configuration while keeping the system symmetry, we chose to add extending structures to each of the y-axis plates. The total extension length along the x-axis needed to be 44 ± 1 mm. In order to preserve symmetry, we chose to add one extender on each y-axis plate with 22 mm in length.

In practice, the extender was designed as an L-shaped structure, as shown in Figure 5.6, with the shorter side resting vertically against the y-axis plate and the longer side providing the extension along the x-axis. A mounting hole was included at the bottom of the vertical side for securing to motorized stage and vertical alignment, as will be discussed in Section 6.3.2, and another on the arm's vertical face to mount the fiber holder. Two additional properties of aluminum are here also advantageous: the aluminum structure is rigid, such

that bending of the large section with respect to the mounting screw can be neglected, and has low density, therefore avoiding any complicating considerations regarding the load on the motorized stage system. Lastly, the motorized stages' structures were made of aluminum as well, so the entire system has a unique thermal expansion coefficient. We manufactured these extending structures with a precision within 10 µm; this includes the overall dimensions of the manufactured pieces, as well as the placement of the screw holes. We can therefore assume spatial positioning symmetry of the sources on the right and left motorized stage sets. This was partially verified during specific calibration procedures, which will be described in Chapter 6.

Using these extenders, the sources can come into contact when the sum of the right and left stage plates' x-axis positions is $x_R + x_L = 1\,062\,000$ µsteps, very close to the maximal range of 1 066 700 µsteps targeted. The source radius was measured as 1.19 mm, corresponding to 25 000 µsteps. We remark that this is larger than the radius of the ceramic ferrule used, 0.625 mm or 13 000 µsteps: the probe size is limited by the heatshrink tubing used to connect the optical patch cable's plastic tubing and the ceramic ferrule, and therefore has a larger radius than the latter.

5.3.5 Scanning Instructions

While moving the probes to chosen positions is feasible using the manufacturer's proprietary console, this method requires manual input and is unsuitable for scanning the sources as rapidly as possible over a large number of position pairs in an automated manner. A library of LabVIEW commands is available to control the motorized stages, corresponding to the commands and settings entered manually via the manufacturer's console. In particular, commands for movements of a chosen stage and of given magnitude, in relative or absolute terms, are available. It is therefore possible to instruct the motorized stages to move through a series of coordinate vectors, for instance for the four left and right, horizontal and vertical axes (i.e x and y axes, respectively), by using one vector as movement instructions for each iteration of a `for` loop.

Rather than providing the movement instruction set through a table filled manually, we decided to generate text files readable by our LabVIEW program, where each line corresponds to one set of target coordinates, in either absolute or relative terms. We wrote a Matlab script that generates such a file in the appropriate format, given a two-dimensional array of absolute coordinates to which we wish to move the stages. From these coordinates, our algorithm creates a list of two-source position pairs, removing those that are not achievable due to the physical size of the probes, based on the measurements performed in Section 5.3.4. We

considered scanning instructions for the x- and y-axis stages of the left and right motorized stage sets, but adding the two z-axis stages is straightforward.

Once we had a method for generating scanning instructions for the probes, we needed to ensure that the probes did not collide during their movements. This was particularly important as our EAI experimental method requires us to bring the sources as close as possible, while contact between the probes is strictly forbidden. We therefore also included a method to generate only "safe" scanning instructions, to avoid the unlikely scenario where the two motorized stage sets' movements do not start simultaneously. In practice, this was implemented by splitting each 4-stage displacement instruction into 3 separate movements: moving x-axis stages in the negative direction first, then proceeding with y-axis movements, and finally with positive x-axis movements. The idea is that the first movement type takes the sources away from the other horizontally, the axis along which the collision paths are most likely. An additional option was added so that, if the probes' start or end y values are close, the "safe" mode is automatically triggered and an extra 50 000 µsteps movement is added in both the negative and positive x directions for this displacement's set of three movement instructions.

More generally, avoiding potential collisions during the scanning of the motorized stages has required us to write a second Matlab script to check whether a collision occurs given a set of scanning instructions, irrespective of their generation method. Here, we chose to work in absolute coordinates, but conversion from relative coordinates is straightforward. This algorithm verifies whether the two sources ever come to within a probe diameter of one another. The radius of a single probe was set as 25 000 µsteps in the program, in line with the measurement described in Section 5.3.4.

While this can be done straightforwardly by checking the distance between the sources for each two-dimensional position pair, such a method does not check for collisions along the movement course. Figure 5.7 illustrates such an example, showing the case of the right probe performing a vertical movement (i.e. with no horizontal component), colliding with a stationary left probe parked at the same horizontal position; in this case, the start and end points of the probe pair are allowed. Figure 5.8 describes an illustrative case where both sources move: the right source's movement intersects the left source's, even though their start and end positions do not violate the minimal distance condition. The method we implemented to extend our checks to such cases was to repeatedly verify that the minimal distance between probes is respected after a small displacement δr, in units of µsteps, until the final position of this movement is reached. This procedure is repeated for every movement in the instruction set. δr can be chosen by the user, as small as $\delta r = 1$ µsteps. We used $\delta r = 50$ µsteps, as a trade-off between precision and computational efficiency. The movements are reproduced in

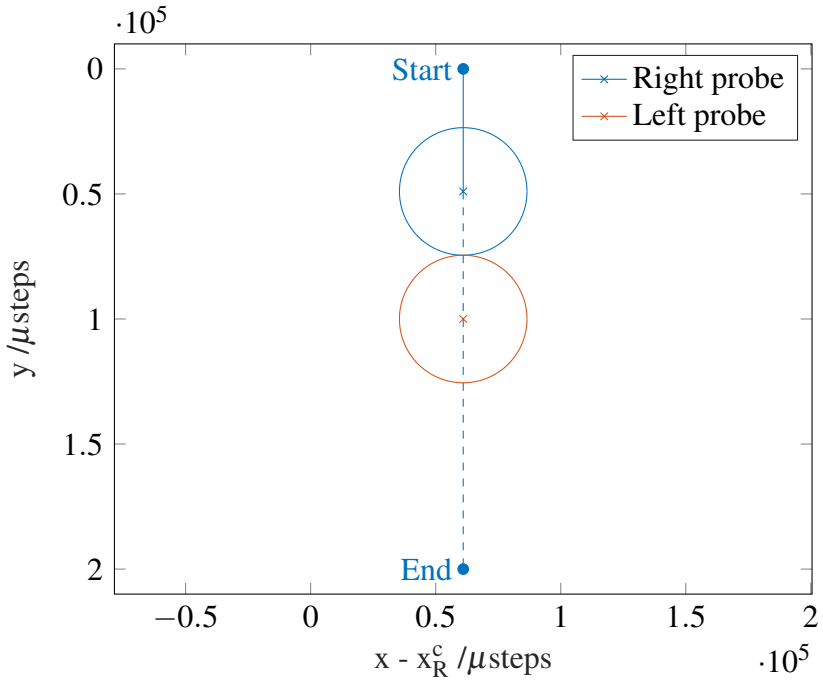

Fig. 5.7 Single-source vertical movement causing a collision, even though start and end positions are not prohibited.

this algorithm as in practice, with the x- and y-axis components of the movement for each probe independently stopping as soon as their target value is reached.

There are two main limitations of this method. The first is that it assumes that the source movements are at constant speed, equal for both sources; this is realistic as long as the settings for the acceleration and maximum speed for the sources are identical. A possible issue occurs in the case of a slip or stall of one of the sources; this has however never been observed, and is unlikely in the current configuration as the loads on the stages are well within the manufacturer's specifications. A second limitation is that the movements of the two sources are assumed to start at the same time. In practice, this is the case to within a fraction of a second; issues would arise if the LabVIEW script for controlling the stages failed between sending a movement order to one source's stages and the other's. This is solved by the "safe" path provisions in the scanning instruction generation method described in this section, but does limit the generality of the collision checking algorithm.

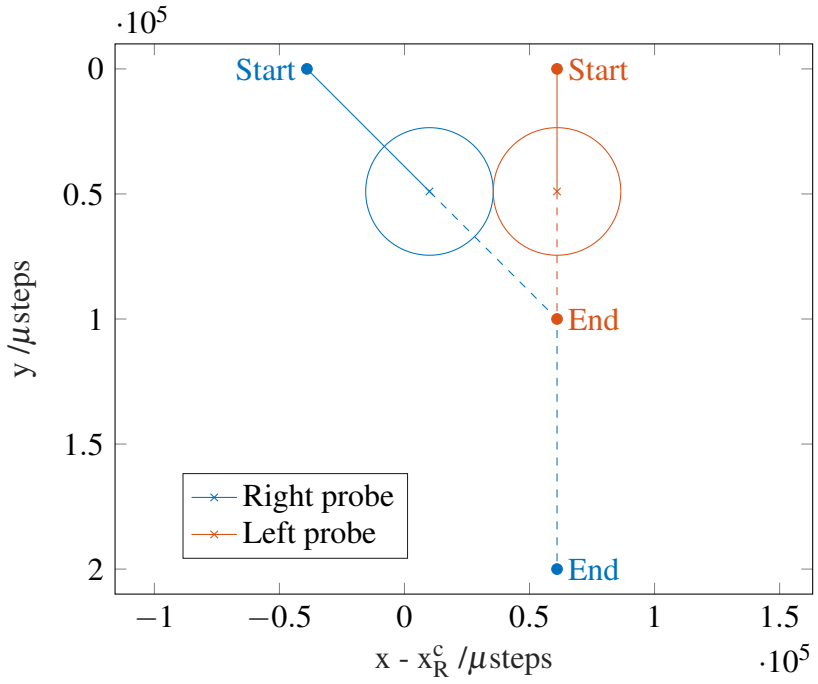

Fig. 5.8 Two-source diagonal movement causing a collision, even though start and end positions are not prohibited.

5.4 Detection System

5.4.1 Requirements

We now list the required basic capabilities for the detection system of our experimental apparatus:

- The amplified photodetector must produce a measurable signal in response to optical detection;
- Appropriate connectorized optical fibers must be prepared for coupling to the photodetector;
- Optical power from the laser source must couple into the detector fiber and detected by the photodetector.

In this section, as in the rest of this chapter, we will restrict ourselves to the study of the detection system with the sources either placed at fixed position pairs, or moving to this target position pair. Investigations with the sources being scanned over multiple positions across the detector surface, as well as the software infrastructure to perform this, will be discussed in Chapter 6.

5.4.2 Analog-to-Digital Converter

The first step in the construction of the detection system was to connect our signal recording device, a National Instruments PCIe-6321 analog-to-digital converter, to the computer that controls the entire experiment, from the data logging to the laser output power and scanning of the motorized stages. In practice, the ADC was plugged into the computer's PCIe port; communication was achieved straightforwardly using the driver and the set of LabVIEW functions provided.

The input/output connector on the back of the ADC board is a 68-pin proprietary connector. We therefore manufactured a custom BNC board, with two female BNC connectors and a female connector for the ADC cable. We connected all necessary pins to BNC cables: one BNC carrying the detector output signal to an analog input for measurement recording and one BNC carrying a synchronization signal to ensure that measurements are triggered precisely with respect to the modulation signal.

An important verification was the correct retrieval of synthesized fringes. In practice, we used an Agilent 33220A waveform generator to produce a sinusoidal waveform with known properties, connected it with a BNC cable directly into the analog input of the ADC, and recorded the signal. We verified that the amplitude and phase of the measured fringes were as expected by recording a time series of the ADC's analog input, performing a Discrete Fourier Transform and extracting the amplitude and phase of the DFT's component corresponding to the modulation frequency. For a measurement of $N_{\text{samples}} = 2\,\text{MS}$ at $f_{\text{sampling}} = 250\,\text{kS/s}$ sampling frequency and $f_{\text{modulation}} = 2.5\,\text{kHz}$ modulation frequency, we selected the component with index

$$i_{\text{DFT}} = N_{\text{samples}} f_{\text{modulation}} / f_{\text{sampling}} + 1, \tag{5.1}$$

equal to 20,001 in this example; the addition of 1 comes from the labelling of the DFT's DC component as index 1. The extracted complex fringe amplitude and phase were found to be in excellent agreement with the synthesized sinusoidal signal; deviations were smaller than 0.1%. We also verified that there was no measurable cross-coupling between the analog and digital inputs, by recording the former connected to a shorted BNC cable while feeding the waveform generator's synchronization signal into the latter.

5.4.3 Detector Fiber Fabrication

The photodetector we have chosen is not free-space coupled, but rather has a female FC/PC connector with a glass ball lens, for coupling to a connectorized optical fiber. The latter acts

as a mode filter and sets the modal behavior of our device under test, which corresponds to the fiber-coupled detector. We argued that, because the optical fiber coupled to the photodetector would in general not be polarization-maintaining, we wanted its length to be as short as possible in order to avoid any effect of cross-coupling between the two polarization modes. Such short optical fiber lengths are only obtainable by cutting commercially available bare fibers, and it was necessary to connectorize them for use in our system.

The fabrication procedure for connectorizing these lengths of fiber is similar to the process described in Section 5.3.3, except for the tools used in the polishing step. One end of the fiber needed to be mated with a male FC/PC connector to be compatible with the photodetector's connector, while the other end needed to be mounted in an appropriate structure to be held; as in Section 5.3.3, we chose a ceramic ferrule with 127 μm bore size to fit stripped optical fibers, but with a 2.5 mm outer diameter compatible with commercially available clamping structures.

The main weak point of the construction is at the contact between the back of the ferrule and the optical fiber, as this is the boundary between the stripped and unstripped portions of the fiber. In order to strengthen this region, an additional drop of epoxy was added to the concave tapered end of the ferrule. This polishing procedure was repeated for connectorizing the other end of the optical fiber length with an FC/PC connector. The fabrication was somewhat less delicate, as the fragile section of optical fiber at the back end of the connector ferrule was reinforced by pushing the 0.9 mm plastic tubing into the connector and sliding a strain relief boot over it. We then followed the polishing procedure set out in Section 5.3.3. For both the FC/PC detector and the large-diameter ferrule, a custom holder was not necessary for the polishing steps. Instead, we used a polishing disc with a 2.5 mm-diameter hole, in which the ceramic ferrules can be secured for the polishing procedure, with a clamping screw tightened onto the ferrule.

The holder for the ferrule is built from a plastic clamp, which is slitted into two arms with a circular void region of diameter 2.5 mm, obtained from semi-circular holes in each of the arms. The latter can be tightened with a single screw close to their common base. Figure 5.9 shows the experimental arrangement with a bare single-mode fiber coupled to the DET01CFC photodetector with an FC/PC connector and secured to the manual stage using a plastic clamp to firmly hold the ferrule.

5.4.4 First Fringes

At this point, we attempted the recording of fringes in the detector output as the relative phase between the two arms of the experiment is modulated. Although all tests of the experimental system had yet to be performed, the ability to record fringes would open the possibility of

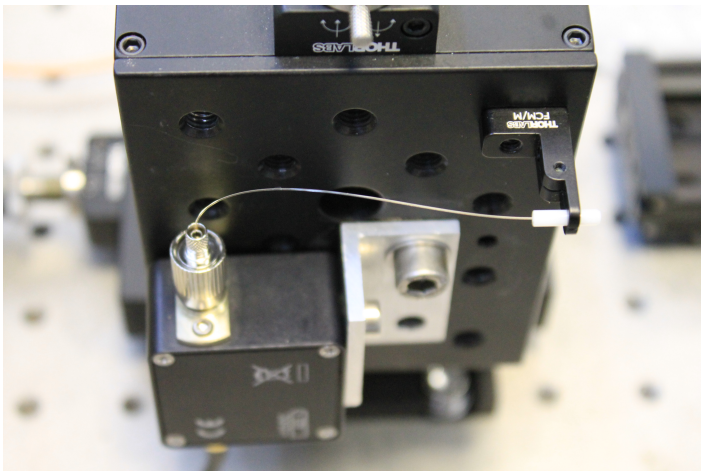

Fig. 5.9 Fiber-coupled detector mounted on the manual stage, with open-ended fiber epoxied in the ferrule and held in a clamp.

more sensitive calibration procedures, as we will discuss in Sections 5.5 and 5.6. We found the on-axis position of each source rudimentarily by manually scanning their respective x-axis stage and identifying the position for which the detector output is maximal. A more precise approach will be developed in Section 6.3.2. The two probes were placed as close as possible to their respective measured on-axis position, without making contact, at a distance of approximately 100 mm to the detector.

Each phase modulators was connected in turn to a signal generator, for which we selected an Agilent 33220A function waveform generator. There are five key settings for the input waveform:

- the waveform type: among several options (such as a sinusoidal, square or pulse shape), we chose the linear ramp waveform, as it corresponds to a continuous linear waveform if the appropriate voltage range is chosen;
- the peak-to-peak voltage: selected with a resolution of 0.1 mV, we first chose twice the phase modulator manufacturer's stated $V_\pi = 4$ V DC voltage corresponding to a constant π rad phase shift, before performing a calibration procedure in Section 5.5.2;
- the waveform symmetry: selected as a percentage, we chose 0% symmetry in order to have only an increasing voltage in seesaw form, such that the phase modulation wraps around at V_π to $V_{-\pi} = -V_\pi$;
- the constant voltage offset: selected with a resolution of 0.01 mV, we chose 0 V in order to obtain a waveform that is symmetric in time about 0 V, which corresponds to $\Delta\phi = 0$ rad phase shift;

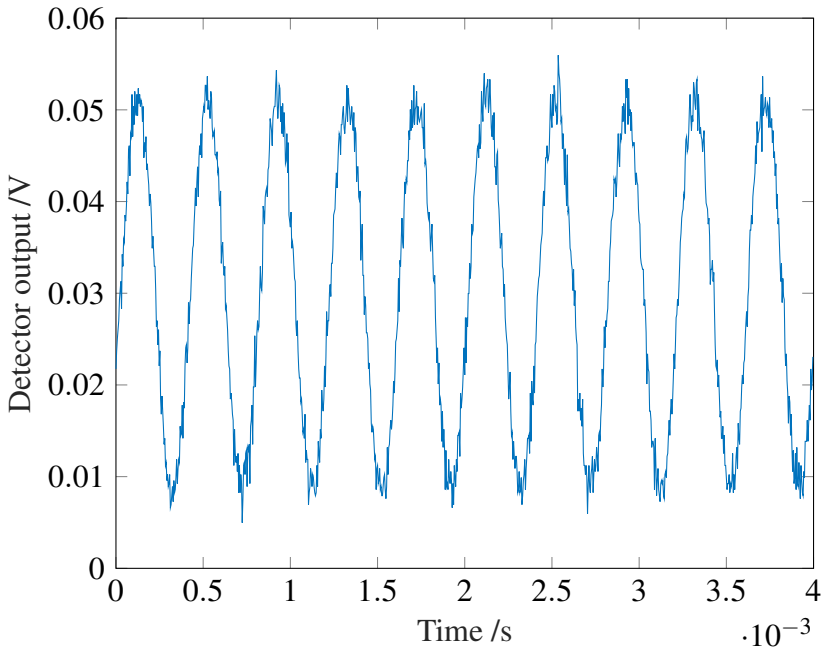

Fig. 5.10 First experimental measured fringe, at 2.5 kHz modulation frequency.

- the frequency: selected with a resolution of 0.1 µHz, we first chose 2.5 kHz to sample 100 points per fringe period using the maximum 250 kS/s sampling frequency on the ADC.

With the system in this configuration and the sources placed as close as possible to their on-axis position, we turned on the laser source, modulated the relative phase between the arms of the experiment and recorded the detector output, amplified with a gain factor of $G = 10^7$ V/A. We observed a fringe pattern precisely at the modulation frequency selected. Figure 5.10 shows our first successful measurement of fringes in the detector output as the sources' relative phase is varied. It is important to remark here that the observation of fringes at this point is already an important achievement. Indeed, even before proceeding with the careful calibration of the experimental system, we were able to record fringes in the detector output as the relative phase between the two arms of the experiment is rotated, with the sources placed in fixed positions. This is a critical milestone in the objectives we outlined in Chapter 1, and following the experimental system's design started at the early conceptual stage in Chapter 4.

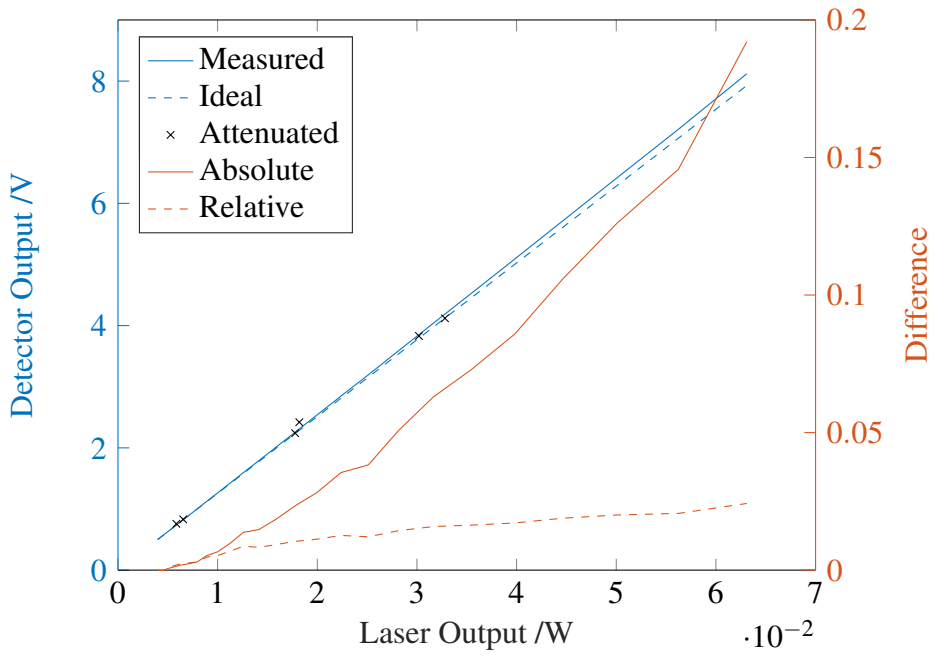

Fig. 5.11 Calibration of detector linearity, with comparison between the measured detector output voltage and the ideal linear behavior as the laser power output is changed (lines), and when calibrated attenutors are added at fixed laser power output (crosses).

5.5 Calibration Measurements

5.5.1 Detector Linearity

In Chapter 2, we emphasized the importance of a fundamental assumption for our derivation of EAI theory, that the detector output is quadratic in the incoming field, i.e. linear in the incident power. It was worth at this point verifying whether this assumption holds in practice for the chosen photodetector.

To begin, we connected the laser source directly to the left source fiber, and placed the left probe directly opposite the bare Thorlabs DET01CFC detector (i.e. with no coupled fiber), at a distance of approximately 80 mm. The detector output was not amplified, but rather fed directly to a calibrated Keithley 196 System DMM voltmeter. The distance between the source and detector was chosen specifically such that the minimal 6 dBm power setting (equal to 4 mW) for the laser output produced a 0.500 V signal at the detector's output. This was necessary to avoid running into the detector's maximum voltage output of 10 V at the highest laser output power; starting from a 0.500 V signal at 6 dBm optical power, we expected the signal at 18 dBm optical power to be 7.92 V. The laser power output was increased in 0.5 dBm increments from 6 dBm until the maximum setting of 18 dBm (equal to 63 mW),

and the detector output voltage was measured for each successive setting. Figure 5.11 shows the relationship between these measured voltages and the laser output power for which they are obtained; it is extremely close to proportional, with an error reaching at most 2% for the highest power values. We observed small fluctuations in the detector output of the order of $\pm 2\%$, which are the dominant noise contribution for the measured voltage. We therefore conclude that the detector output signal is indeed proportional to the laser power output.

These measurements require the assumption that the laser power reading on the computer-control console is correct. To avoid this assumption, we used six fixed optical fiber attenuators, with attenuations of 2.84 dB, 3.20 dB, 5.40 dB, 5.50 dB, 9.84 dB and 10.32 dB, calibrated by the manufacturer with 0.01 dB precision. The detector output voltage measured for each of these attenuators inserted in our system, with the laser power output held constant at its 18 dBm setting, are shown as black crosses in Figure 5.11. The limiting precision of this measurement procedure is the repeatability of adding the attenuator to the fiber system: depending on the force applied when joining the attenuator's FC/APC connectors to the rest of the system, respectively a female mating sleeve connector and a male patch cable connector, the detector output can be modified by up to 2%. Nevertheless, the results obtained with this second measurement procedure confirm those produced with the first, independently of the laser's power reading on the computer console, showing that the detector output is indeed linear in the incident optical power.

5.5.2 Phase Modulation

As discussed in Section 5.4.4, modulation of the relative phase between the sources is obtained by driving either (or potentially both) of the phase modulators using a time-dependent voltage output of an Agilent 33220A waveform generator. The chosen waveform is a linear ramp, with 0% waveform symmetry, and 0 V DC offset; the modulation frequency was selected to be 2.5 kHz, such that recording the signal with the ADC's maximum sampling frequency of 250 kS/s implies 100 datapoints per fringe period, which simplifies the extraction of fringe parameters in post-measurement analysis. We had left unanswered the question of the appropriate value for the peak-to-peak amplitude necessary to obtain a precise phase modulation from $-\pi$ rad to π rad. The next step was therefore to calibrate the two phase modulators independently. In practice, this meant finding the peak-to-peak voltage of the linear ramp input signal for which a full 2π phase rotation is achieved. Assuming that the center of this voltage range is taken to be 0 V, i.e. choosing a 0 V constant offset in the waveform generator settings, the maximum input voltage would then be V_π. In Section 5.4.4, this value was taken to be 4 V, as stated by the manufacturer. We placed the two sources close to the detector axis and modulated their relative phase at 2.5 kHz, as in Section 5.4.4.

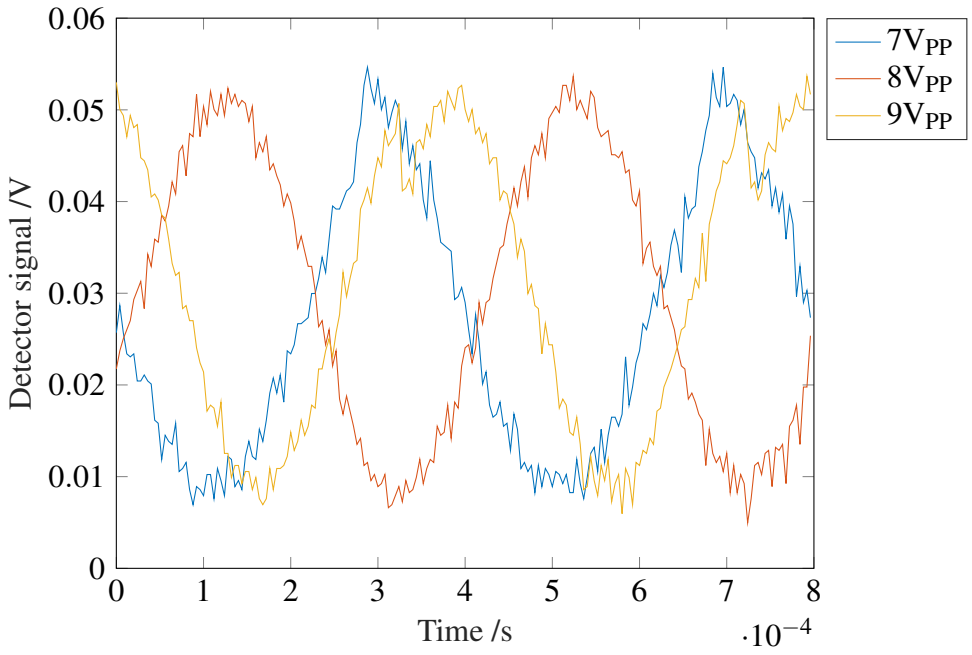

Fig. 5.12 Measured fringe in the detector output as the right phase modulator is fed a linear ramp waveform of various peak-to-peak voltages; the photodetector is coupled to free-space.

The shape of the measured fringe in the detector output provides a first-order indication of the phase modulation achieved with the input peak-to-peak amplitude selected, as shown in Figure 5.12. Discontinuities in the fringe correspond to an inaccurate input voltage setting: a discontinuity before the full sinusoid is completed indicates that V_π is larger than the maximum voltage setting selected, while a discontinuity after a full sinusoid and a fraction of the next implies that V_π is smaller than the maximum voltage setting. From Figure 5.12, we see that V_π is neither 7 V nor 9 V; 8 V is likely the appropriate value, but the signal-to-noise ratio (SNR) is too low for this determination to be confident.

The optimal way of achieving this was by using a beamcombiner, to combine the outputs of the phase modulators and use the photodetector on either of the beamcombiner outputs. In practice, the optical power obtained in this manner saturated the detector unless a fixed attenuator was used: we therefore added a 3.20 dB attenuator at the chosen beamcombiner output, and set the optical power of the laser source to the minimum 6 dBm setting. The fringes in the detector output as the relative phase of between the system's arms is modulated were observed with an SNR in excess of 2 000. In Figure 5.13, we show the fringes observed for various amplitudes of the input linear ramp waveform to the right phase modulator. We observe discontinuities for all peak-to-peak amplitudes, but these are clearly minimized for 7.85 V: we therefore consider the phase modulator has $2V_\pi = 7.85$ V at 2.5 kHz modulation

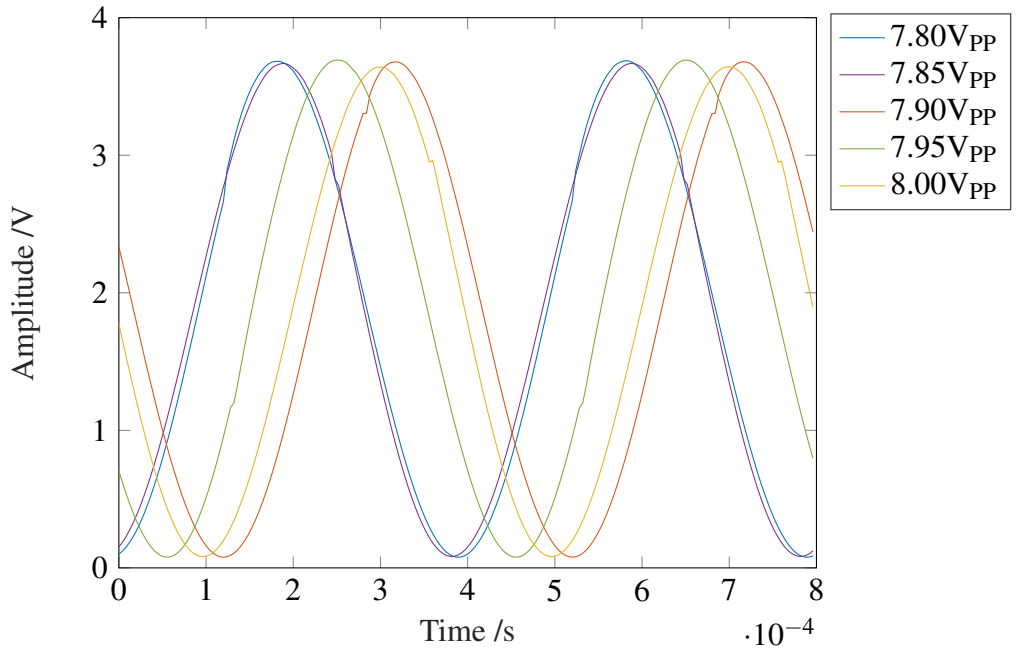

Fig. 5.13 Measured fringe in the detector output as the right phase modulator is fed a linear ramp waveform of various peak-to-peak voltages; the photodetector is coupled to the beamcoupler's output.

frequency. The same procedure was repeated by modulating the left phase modulator, and we find that $2V_\pi = 8.1$ V.

5.6 System Noise Characteristics

5.6.1 Vibration and Stage Settling

Before studying more traditional noise properties such as optical noise for one or two fixed sources illuminating the detector system, we considered sources of transient noise in the system. There are two main causes: vibrations of the entire experimental system through the optical table, and the settling of the motorized stages after their scanning movements. In order to measure these noise sources, we proceeded with two types of tests. The first consisted in measuring variations in the detector output signal with a single-source illuminating the fiber-coupled detector; the second consisted in measuring the fringe amplitude and phase variations when two sources are illuminating the device under test with their relative phase modulated. It is important to note that the second is generally more sensitive, because the fringe is an interferometric phenomenon, much more dependent on the precise positioning

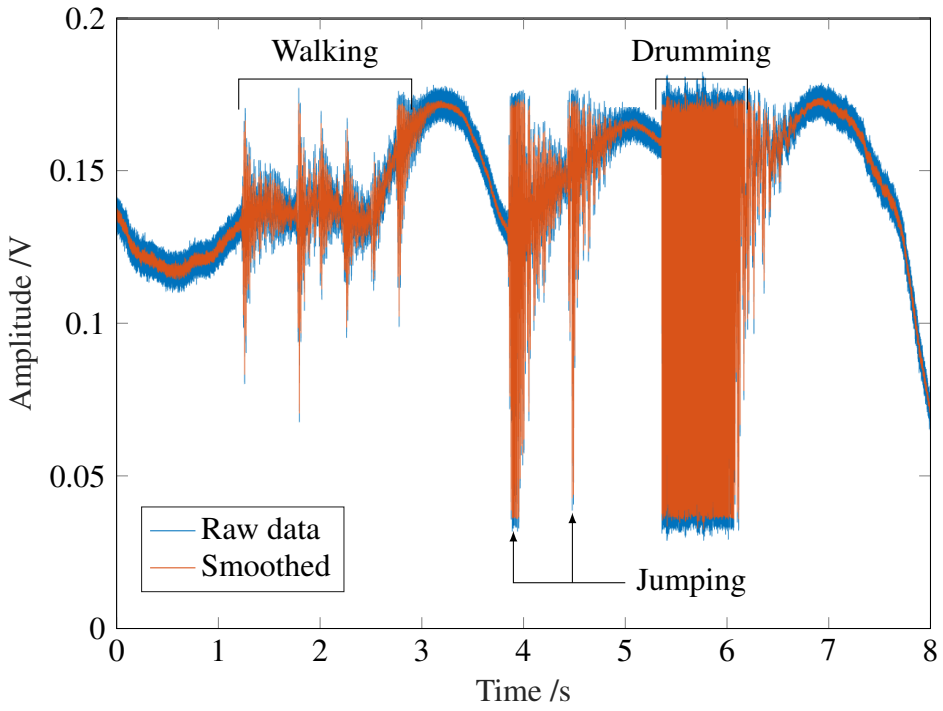

(a) Detector output

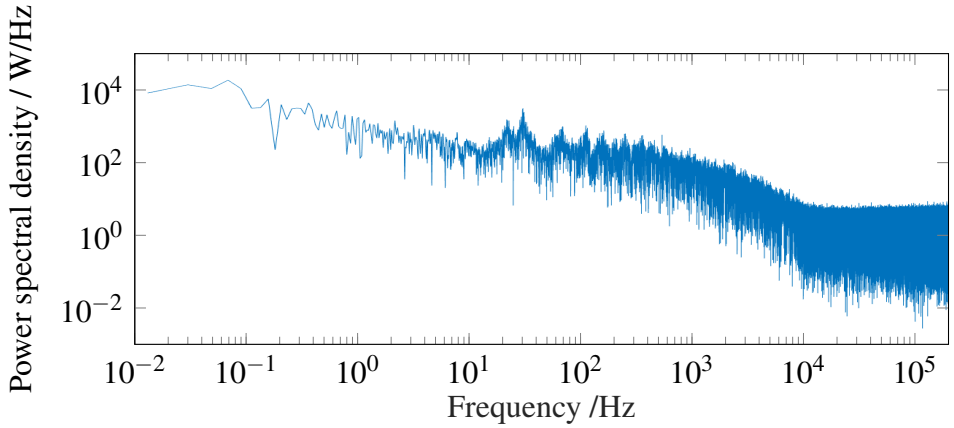

(b) Power spectrum

Fig. 5.14 Measured detector output and power spectrum, with two sources illuminating it at fixed positions while environmental disturbances are applied, displaying a settling time of 0.5 s and vibration frequencies of 62 Hz and 80 Hz.

of the sources than the slowly-varying amplitude of a single source beam projected on the detector surface.

A first key measurement was the assessment of the effect of environmental vibrations on the measured detector output. The goal is to simulate extreme environmental perturbations caused by human activity around the experimental system; in practice, this means vibrations

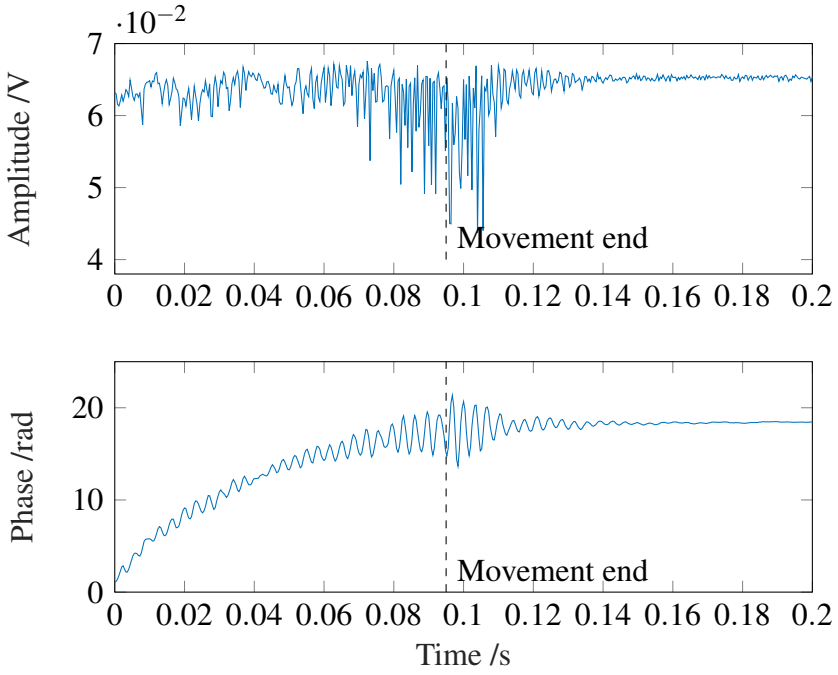

Fig. 5.15 Extracted fringe amplitude and unwrapped phase as the left source is scanned to its target position, displaying a settling period with a 0.03 s timescale.

in the optical table, which were produced by purposefully hitting table in qualitatively reproducible ways. Using the same configuration as in Section 5.4.4, over an 8 s duration, we measured the detector output at 250 kS/s sampling frequency as the sources were placed as close as possible to their on-axis position, while successively walking around the optical table, jumping twice next to it, and lightly drumming the table corner farthest from the sources. Figure 5.14a shows the detector output without modulation of the probes' relative phase: the voltage measured is severely disturbed by the environmental perturbations, in particular direct contact with the optical table. It is therefore crucial to ensure that the immediate surrounding of the experimental system is free of such mechanical vibrations during sets of fringe measurements. Studying the spectrum of perturbed periods indicated in Figure 5.14b, we observed two distinct peaks at 62 Hz and 80 Hz: we believe these correspond to the frequencies of the vibrational modes of the stage systems or of the optical table. We also remark that, repeating these measurements when using the beamcoupler discussed in Section 5.5.2 instead of the free-space section, similar perturbations were observed in the detector output, albeit with smaller magnitude. This indicates that perturbations of the optical fibers contributes at least partially to the variations observed in the detector output.

The second key measurement performed was the investigation of vibrations in the sources' arrangement after they are moved, in order to assess the precautions needed under the normal

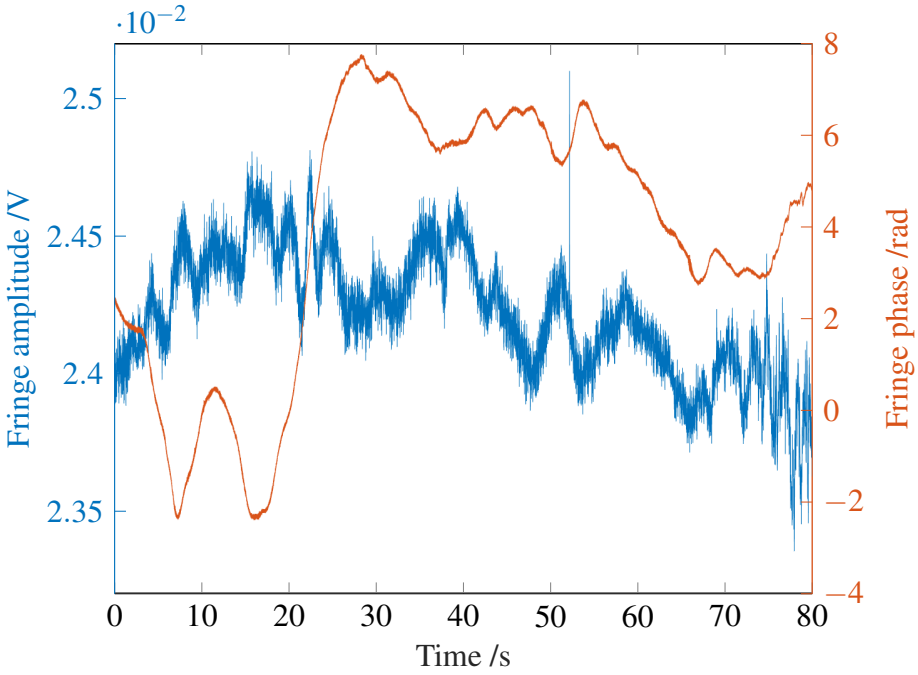

Fig. 5.16 Extracted fringe amplitude and phase, displaying large phase drift.

utilization of the motorized stages. In practice, we measured the settling time of the source system after displacing the stages. This was done by starting a long measurement, which we chose again to last 8 s at a sampling rate of 250 kS/s, as the stages were scanned to their target position, which we selected as identical to the study of environmental perturbations and to Section 5.4.4. The fringe amplitude and phase were extracted for 0.4 ms blocks, corresponding to 100 samples or equivalently 1 fringe period. In Figure 5.15, we show the extracted fringe amplitude and phase as the left source is moved to its target position, with the right source already placed at its own. Large variations were observed while the source is scanned, as expected, followed by a transient oscillatory period once the movement had stopped, with a timescale of 0.03 s. In subsequent measurements, it was therefore important to add a delay between the end of the stages' movements and the start of the detector output's measurement; we chose a 0.5 s delay, implemented in the LabVIEW code described in Section 6.2.1.

5.6.2 Fringe Phase Drift and Amplitude Noise

An important observation made during both of these measurements is the temporal evolution of the detector signal, when the two sources are held in fixed positions and their relative phase is not modulated, as in Figure 5.14. At this point, we did not attempt to characterize this

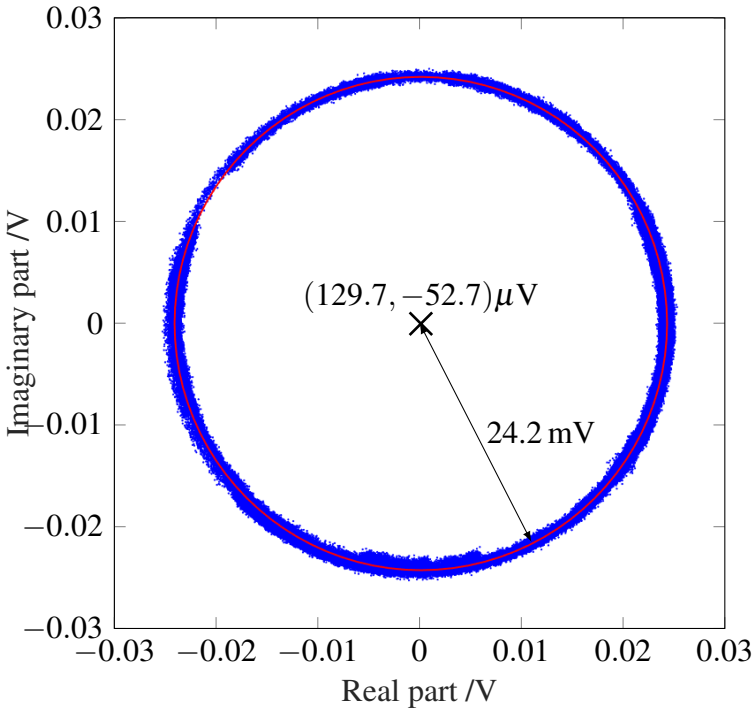

Fig. 5.17 Extracted fringe real and imaginary parts, fitted with a circle.

phenomenon any further than observing that the signal's evolution is slow and continuous, seems random, and is bounded by the maximum and minimum signal values obtained in fringe measurements as the relative phase is modulated. This implies that the detector output time variations are a true phase drift, caused by a temporal variability in the relative phase shift between the two sources, rather than an additional signal from some other origin. When performing a continuous measurement of the fringe in the detector output over long time periods, with the sources held in fixed positions and the relative phase modulated as described in Section 5.6.1, we observed that the extracted fringe phase drifts in a similar fashion. This is shown in Figure 5.16 for an 80 s measurement at 250 kS/s sampling frequency, which will use as an example dataset throughout this subsection. This topic will be discussed in greater detail in Chapter 7. In the meantime, we conclude that fringe phase measurements are valid over timescales shorter than 1 s; beyond this, only the fringe amplitude measurements can be considered accurate.

While we elected not to study further the nature of the observed fringe phase drift, it was important to investigate whether it contributes to noise in the fringe amplitude. A first measure of the relationship between the fringe amplitude and phase was to study the shape of the extracted fringe real and imaginary parts in the Argand plane. By using a circle fitting procedure, we found that the representation of the complex fringe amplitude in the Argand

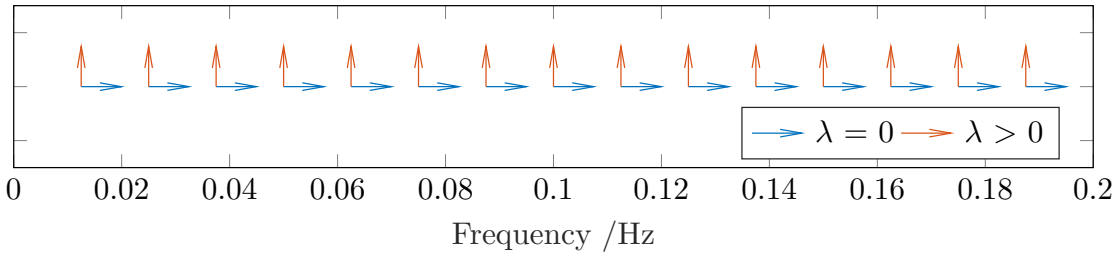

Fig. 5.18 Eigenvectors of the amplitude-phase spectral covariance matrices for the 15 lowest frequencies; the corresponding eigenvalues λ are zero and positive. Components of vectors along the horizontal and vertical axes denote fringe amplitude and phase contributions, respectively.

plane is a perfect circle. In Figure 5.17, we show the extracted fringe amplitude and phase for our reference dataset, for which the fitted circle has a radius of 24.2 mV, in line with the fringe amplitude extracted via our FFT-based method described in Section 5.4.2, and a center with coordinates (129.7 µV, -52.7 µV). The small off-origin displacement of the circle's center can be fully attributed to noise and asymmetry in the distribution of datapoints around the circular shape.

A second metric to consider, given that the phase drift is slow, is the eigenvectors for the low-frequency elements of the cross-spectrum between the extracted fringe amplitude and phase. In practice, this is done by computing the 2×2 covariance matrices for the amplitude and phase spectra and cross-spectrum elements at each frequency, and operating an eigenvalue decomposition on each. We found that one of the eigenvalues is always zero, within the machine precision used for the eigenvalue decomposition, while the other is positive. The corresponding eigenvectors are directed precisely along the axes corresponding to the amplitude and phase contributions, respectively. This is shown in Figure 5.18 for the 15 lowest frequency elements of our example dataset. We also note that the spectrum obtained from the non-zero eigenvalues is almost identical to the phase spectrum, further indicating that the fringe amplitude and phase evolutions are not related.

It is also interesting at this point to consider the fringe visibility, which we defined in Chapter 2 as $\gamma_{mn} = D_{mn}/(D_{mm} + D_{nn})$ where D_{mn} is the complex fringe amplitude, for sources placed at positions m and n. This quantity is of crucial interest, particularly in fringe measurements as the two sources are scanned, discussed in Chapter 6. For a single set of position indices m and n, the fringe visibility γ can be extracted from one fringe measurement as

$$\gamma = \frac{V_{\max} - V_{\min}}{V_{\max} + V_{\min}}, \tag{5.2}$$

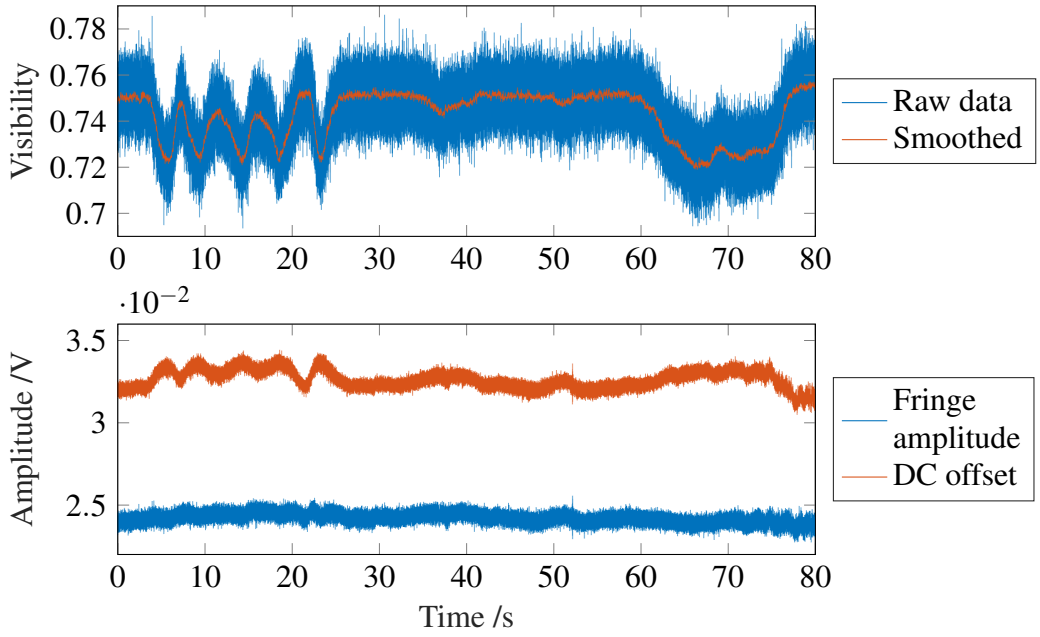

Fig. 5.19 Extracted fringe visibility, and comparison with the extracted fringe amplitude and DC offset.

where $V_{\max}$ and $V_{\min}$ are the maximum and minimum recorded voltages in the detector output. The fringe visibility corresponds to the ratio of the fringe amplitude, $(V_{\max} - V_{\min})/2$, to the fringe DC offset, $(V_{\max} + V_{\min})/2$. In Figure 5.19, we observe oscillations in our example dataset's fringe visibility that are qualitatively similar to those measured in the fringe phase. When separating the fringe amplitude and offset, we found that it is indeed the fringe offset that fluctuates by up to 6%, rather than the fringe amplitude. In conclusion, the fringe amplitude stability was demonstrated to be independent of the phase drift observed.

5.6.3 Electrical and Optical Noise Characteristics

Returning to more standard noise characteristics, we investigated the spectra of measured datasets, under various experimental conditions. These include, for instance, the noise of an ADC input connected to a 50 Ω termination, a shorted input to the amplifier with a chosen amplification setting, and the optical power detected by the photodetector illuminated by one or two sources. We first considered the second example, with the transimpedance amplifier input shorted and its gain setting selected as $G = 10^7$ V/A without additional filtering, recorded by our ADC with the maximal [-10 V,+10 V] input range setting. A 10 s measurement of its output was performed, at a sampling rate of 200 kS/s: the results presented in Figure 5.20 show a nearly flat spectral density, characteristic of white noise, with small peaks at 50 Hz and its odd multiples, indicative of a mains hum of limited amplitude. These

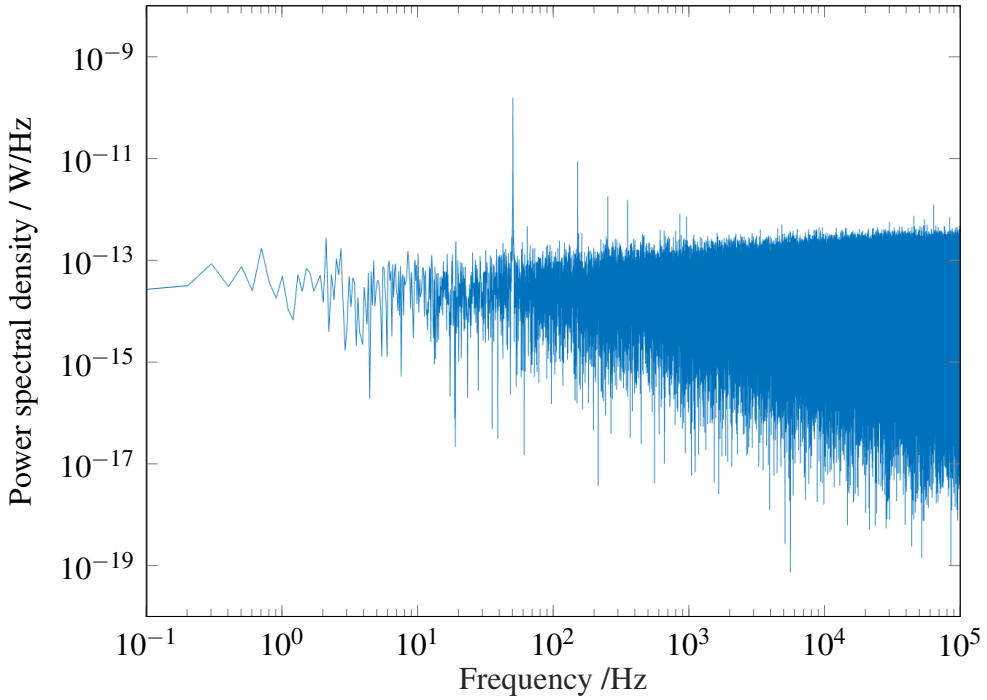

Fig. 5.20 Power spectral density of the transimpedance amplifier at $G = 10^7$ gain setting, with shorted input.

characteristics, and the 100 fW/Hz power spectral density, are in line with the manufacturer specifications.

Secondly, we returned to the reference dataset used in Section 5.6.2, and computed its power spectrum. In Figure 5.21, we observe very sharp peaks for the 2.5 kHz modulation frequency and its harmonics. The width of the fundamental tone is approximately 2 Hz, and its amplitude is several orders of magnitude larger than the nearest noise tones, indicating we obtain a very high SNR in our fringe parameter extraction method. The mains hum at 50 Hz is also noticeable, as well as a small peak at 100 Hz: we believe that this tone corresponds to power from the laboratory's ceiling lights. Both of these signals are sufficiently small compared to the phase modulation signal that they can effectively be neglected in future fringe measurements. We also notice a significant peak of larger width at 888 Hz, as well as its harmonics: this corresponds to the frequency of the laser source's stabilization system. We verified that these peaks indeed disappear when this active stabilization is turned off, in the laser's computer console; in other measurements, it remained turned on, as our primary goal was stability and repeatability over long periods of time, up to several hours in Chapter 6.

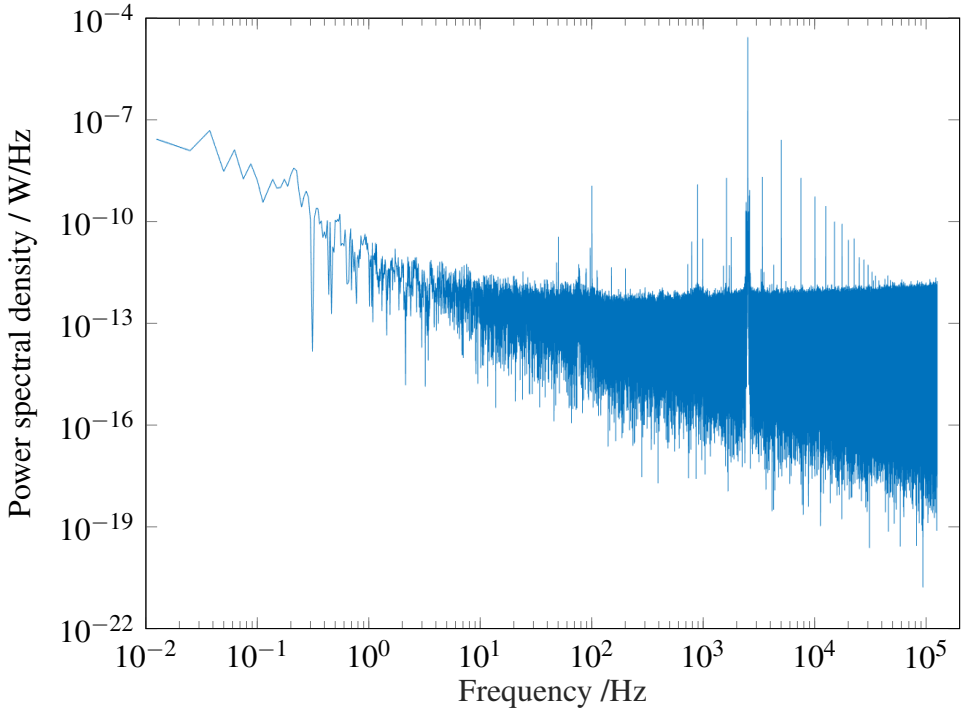

Fig. 5.21 Power spectral density of the measured fringe, displaying high peaks at the 2.5 kHz modulation frequency and its harmonics.

5.6.4 Allan Variance

In order to go beyond the noise spectra presented in Section 5.6.3, we turn to an additional quantity called the Allan Variance. Computing the Allan Variance of a sufficiently long time series measured under constant experimental settings produces important insights into the stability, and indeed the instability mechanisms, of the apparatus used. In particular, the integration time for which the Allan Variance is minimized corresponds to the system's optimal measurement duration, the so-called Allan stability time. Historically, the concept of Allan Variance was developed to study the statistics of clock pairs, including the frequency stability of atomic clocks, and of gyroscopes. In the context of astronomical instruments, Allan Variance has been used to find the characteristic timescales of noise and drift, which can be compensated for instance by using the reference signal from a known calibrator [96].

In practice, Allan Variance can be viewed as the statistical variance of the difference between the signal of interest and some reference signal, dependent on the duration of the measurement integration [97]. This is why the Allan Variance is sometimes also know as the "two-sample variance", and is a special case of the M-sample variance [98]. When such a reference signal is not available, the Allan Variance can be redefined in terms of the signal of

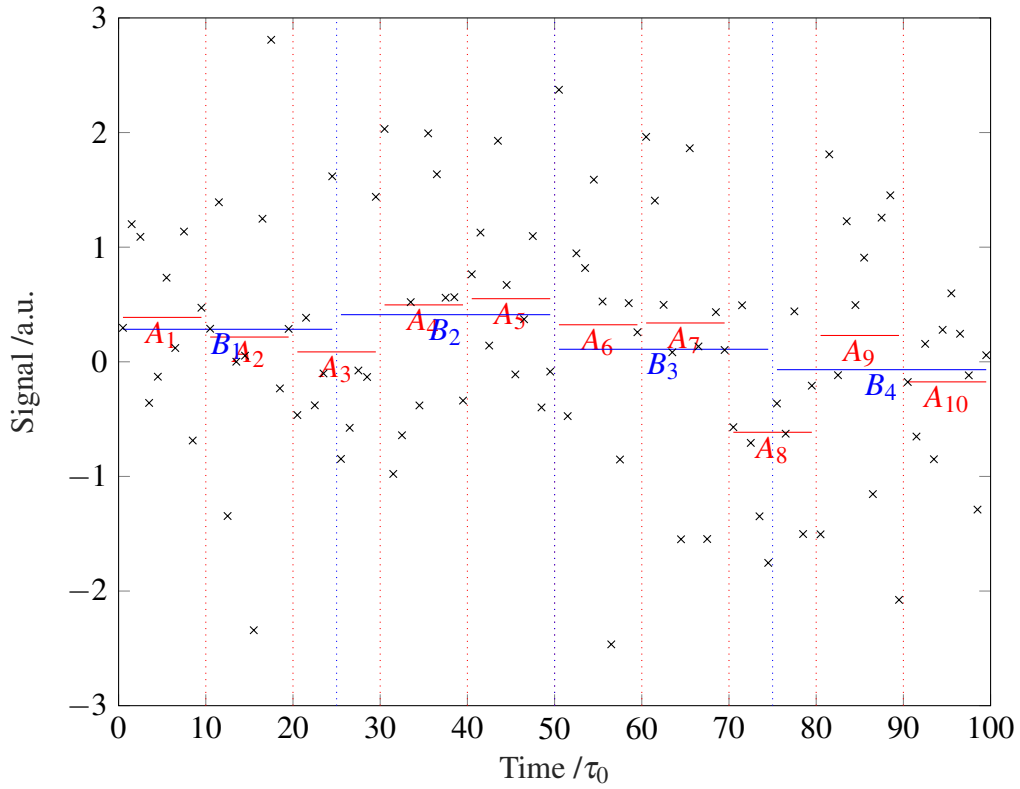

Fig. 5.22 Schematic of two Allan Variance computations with 100 data points, for integration times equal to $10\tau_0$ (red) and $25\tau_0$ (blue).

interest and itself shifted by the integration period; the computation then uses the difference of consecutive time-integrated datapoints. This is the case we will consider here.

We consider a time-domain signal x_i, discretely sampled at intervals $\tau_0 = 1/f_0$, defined as the inverse of the sampling frequency f_0; $i \in \{1,...,N\}$ is the sample label, where $N\tau_0$ is the total measurement duration. In practice, the sampling period τ_0 is set by the user for the measurement device used such as an ADC: the data we have access to is inherently discrete. We compute the average signal value for groups of m samples, with duration $\tau = m\tau_0$, which corresponds to the effective averaging time (proportional to the integration time, used in other derivations):

$$y_K(\tau) = \frac{1}{\tau} \sum_{j=K}^{K+m-1} x_j \tag{5.3}$$

where K is the index of the first sample in the averaged cluster. Assuming we choose m to be a divisor of N, we can then create N/m such clusters without overlap. The Allan variance as

a function of the cluster duration τ is defined as:

$$\sigma_A^2(\tau) = \frac{1}{2}\langle (y_{K+m} - y_K)^2 \rangle, \tag{5.4}$$

where $\langle\rangle$ denotes the ensemble average over all clusters. Expanding the ensemble average, the Allan variance is computed as mean square difference between consecutive clusters:

$$\sigma_A^2(\tau) = \frac{1}{2(\frac{N}{m}-1)} \sum_{i=0}^{\frac{N}{m}-2} \left(y_{m(i+1)+1} - y_{mi+1}\right)^2. \tag{5.5}$$

Computationally, it is often advantageous to consider the integrated signal S_i from the first to the i^{th} sample,

$$S_i = \sum_{j=1}^{i} x_j. \tag{5.6}$$

The τ-average signal $y_K(\tau)$ is related to the total integrated signal S_i by

$$y_K(\tau) = \frac{S_{K+m} - S_K}{\tau}. \tag{5.7}$$

The Allan variance is then computed as

$$\sigma_A^2(\tau) = \frac{1}{2\tau^2(\frac{N}{m}-1)} \sum_{i=0}^{\frac{N}{m}-2} \left(S_{n(i+2)} - 2S_{n(i+1)} + S_{ni}\right)^2. \tag{5.8}$$

Figure 5.22 provides an example of the computation of the Allan Variance of a dataset of 100 points, for two cluster durations of $10\tau_0$ and $25\tau_0$. The 100 data points can be subdivided into 10 or 4 non-overlapping clusters of 10 or 25 data points, respectively, and averaged to obtain the time-averaged signal A_i with $i \in \{1,...,10\}$ and B_j with $j \in \{1,...,4\}$. The Allan Variance for each integration time is then the variance of the arrays A and B. We remark that some sources use the Allan deviation $\sigma_A(\tau)$, square root of Allan Variance $\sigma_A^2(\tau)$, rather than the latter [99].

A second option for the computation of the Allan variance of a dataset is based on the same method to cluster samples, but the summation over differences of sample clusters is different. Instead of summing over clusters starting at multiples of the integration time τ, we can sum over clusters starting at multiples of the sampling period τ_0. The Allan variance is then defined as

$$\sigma_A^2(\tau) = \frac{1}{2\tau^2(N-2m)} \sum_{k=1}^{N-2m} \left(S_{k+2m} - 2S_{k+m} + S_k\right)^2, \tag{5.9}$$

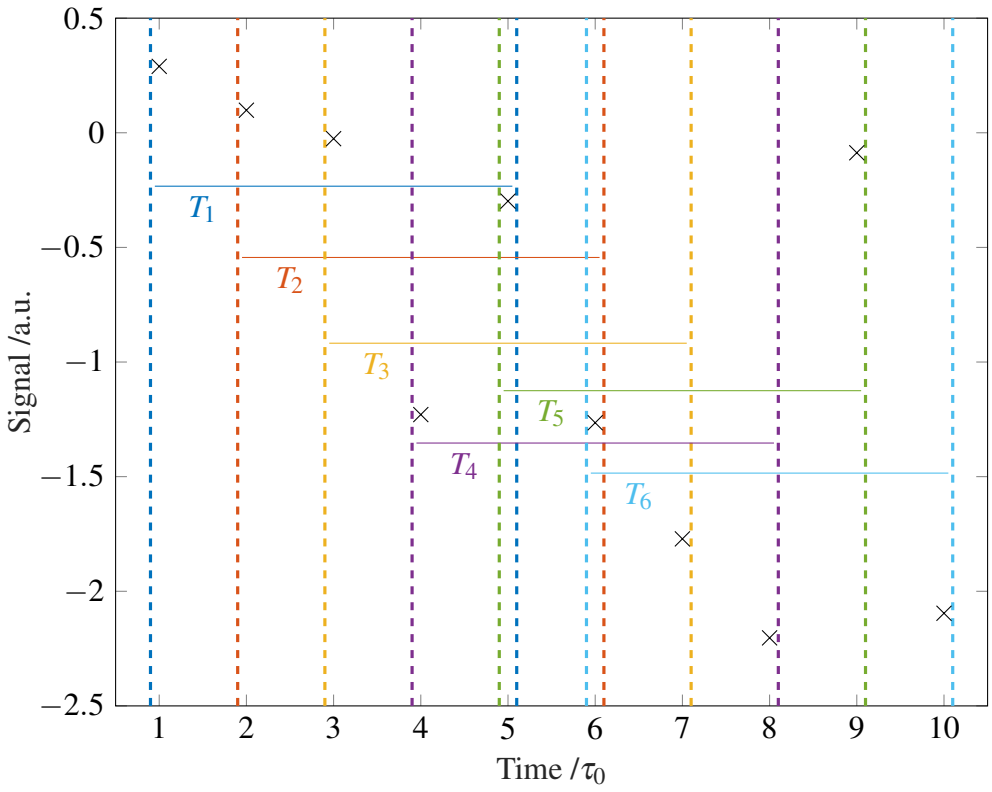

Fig. 5.23 Schematic of an Allan Variance computation using the overlap method, with 10 data points, for integration time equal to $5\tau_0$.

where the prefactor is adjusted to account for the new number of summed terms. This new computation method therefore has clusters that overlap, and we refer to this version as "overlapping". In practice, this provides a greater density of integration times, as we are no longer limited to multiples of τ, and leads to lower error on the computed Allan variance.

Figure 5.23 illustrates the computation of the Allan Variance of a set of 10 data points, for integration time equal to $5\tau_0$, i.e. over 5 data points. The successive integration clusters are simply displaced by the sampling period τ_0, i.e. one data point. Using this overlapping method, the Allan Variance is computed as the variance of the data integrated over 6 clusters. Using the simple method instead, the Allan Variance would have been computed as the variance of the data integrated over only 2 clusters. Considering this example with 10 data points, the maximum integration time with the overlapping method is $9\tau_0$ (with two clusters), and the minimum integration time of $2\tau_0$ has 9 clusters. Using the simple method, the maximum integration time is $5\tau_0$ (with two clusters), and the minimum integration time of $2\tau_0$ has 5 clusters.

Once we have computed the Allan variance for several integration times τ, we can find the value of τ which minimizes the Allan variance. This value is the so-called Allan

Noise mechanism	Allan Variance feature
Quantization noise	Constant slope, coefficient -2
White noise, random walk (angle)	Constant slope, coefficient -1
Correlated noise	Single local peak
Single frequency (e.g. 50 Hz noise)	Repeated peaks of decreasing amplitude
Bias instability, 1/f noise	Constant slope, coefficient 0
Rate random walk	Constant slope, coefficient +1
Rate ramp, drift noise	Constant slope, coefficient +2

Table 5.1 Noise mechanisms and their corresponding features in Allan Variance plots with logarithmic scales

stability time, denoted T_A, and effectively provides the optimal measurement duration under the experimental configuration chosen. We can also produce a plot of the Allan variance computed using the various integration times τ. The minimum on this plot is the Allan stability time. Such a figure provides significant additional information: using a logarithmic scale on both axes, it displays regions of fixed slope, the coefficient of which corresponds to a specific noise source. Some of the typical observed slope coefficients and features, and their corresponding instability mechanism are listed in Table 5.1. In effect, this allows us to understand which noise mechanism is dominant for a chosen measurement duration, and provides a powerful tool for understanding the behavior of an experimental system.

We produced a Matlab implementation that includes a choice of between the simple and overlapping methods, and a generation method of the integration time vector optimizing the number of durations. This method can be used on large datasets, for instance measuring the noise of an ADC input connected to a 50 Ω terminator, a shorted input to the amplifier with a chosen amplification setting, or the optical power detected by a photodetector. Figure 5.24 shows an example of this second case, where we measured the output of the transimpedance amplifier with $G = 10^6$ V/A gain setting and a shorted input, during 40 000 s or 11 hours. The Allan Variance was computed for integration times from 2 ms to 16 000 s, and fitted using a polynomial functional form. We observe three distinct regions, with slope coefficients -1, 0 and approximately 2: these are understood to be contributions respectively from white noise, flicker or 1/f noise, and drift noise [100].

We also wish to understand our system under the precise settings of used in experimental fringe measurements, and to compute the Allan Variance of extracted fringe amplitude and phase datasets. We used the extracted amplitude and phase of the FFT component corresponding to the phase modulation frequency for a window with size equal to the chosen integration time as datapoints. These were then fed into our Allan Variance computation algorithm as previously. Figure 5.25 shows the Allan Variance of the fringe amplitude

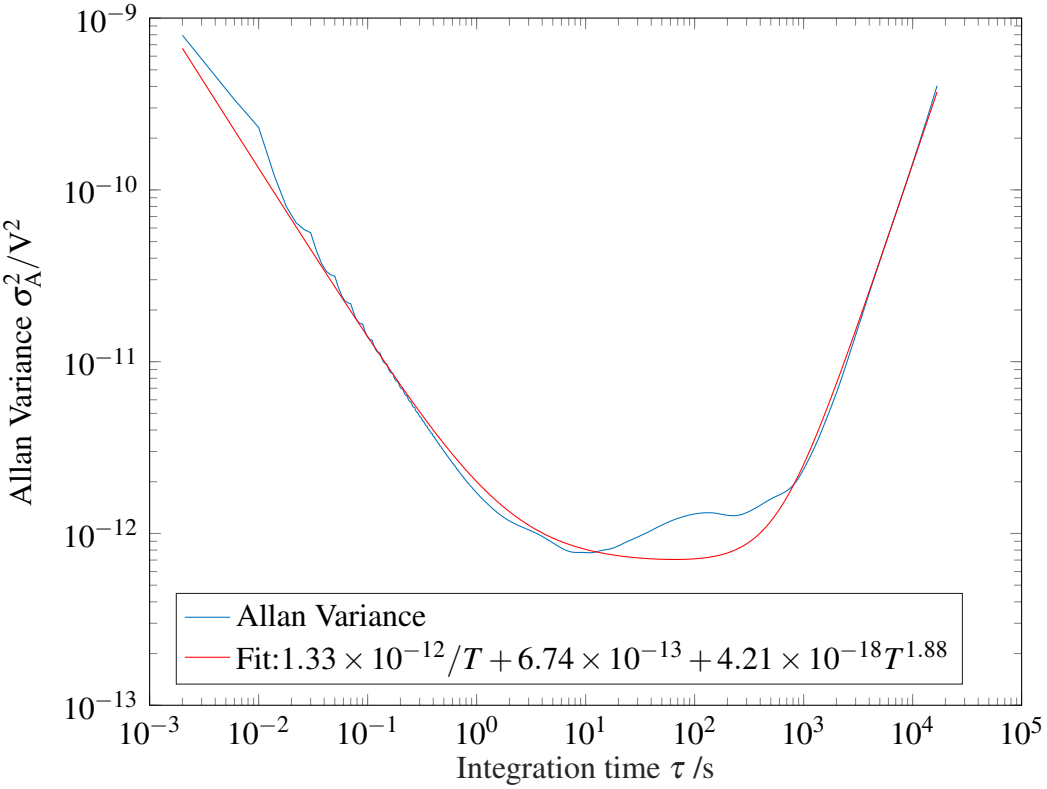

Fig. 5.24 Allan variance as a function of the integration time τ, for a 20 MS measurement of the transimpedance amplifier output with $G = 10^6$ V/A gain setting, at 500 S/s sampling rate.

extracted in 0.4 ms blocks for two measurements, performed before and after the phase modulation calibration (using $2V\pi = 8.0$ V and 8.1 V respectively) and the fabrication of an improved ADC-to-BNC adapter card. The Allan stability times were measured to be 0.15 s and 0.3 s respectively, at Allan variance values equal to 1.05×10^{-7} V^2 and 2×10^{-8} V^2. This proves that our work on the experimental system indeed improved its performance. In particular, the optimal measurement duration was significantly improved to approximately 0.3 s: this parameter was used for fringe measurements during scans, as described in Chapters 6 and 8.

5.7 Conclusion

We have described the construction and characterization of our EAI experimental system at infrared wavelength. The main outcomes from this chapter are that our experimental system has been successfully built, including custom parts designed to optimize the potential capabilities of the system, and that its performance has been characterized. These tests have

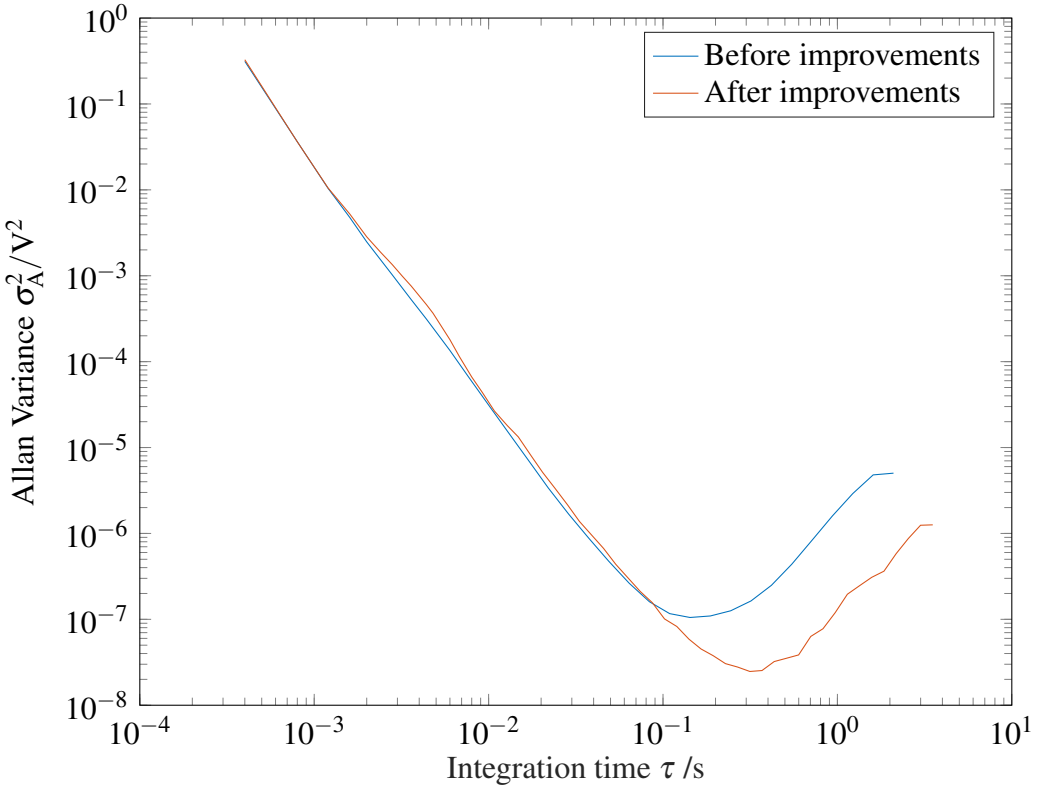

Fig. 5.25 Allan variance of the extracted fringe amplitude as a function of the integration time τ, for fringe measurements before and after the phase modulation calibration and the fabrication of an improved ADC-to-BNC adapter card.

confirmed that our system's capabilities fulfill the requirements we had set out in Chapter 4. In particular, we have demonstrated that fringes in the detector output as the relative phase between the probes is modulated can be observed with high signal to noise ratio, and their amplitude and phase can be extracted using a simple FFT-based method. In and of itself, this is already an important achievement, as such fringe measurements underpin the entire EAI experimental technique. Furthermore, we have developed tools that will be critical to performing future experiments. A significant amount of time and attention was devoted to writing various programs for generating scanning instructions following user-declared scanning strategies, checking that it is safe to proceed by avoiding any trajectories in which the finite-sized probes would collide, and performing simple measurements of the detector output.

At this point, a large portion of the infrastructure required for the realization of an EAI experiment on the chosen fiber-coupled infrared detector is in place and has been tested extensively. Along the way, several parameters with particular importance for the methodology of future experiments have been chosen. The settling timescale of the sources

was measured to be 0.03 s, and we have chosen a 0.5 s delay between the end of the motorized stages' movements and the start of the recording of the detector output by the ADC. The optimal measurement time, as characterized by the minimum of the Allan Variance as a function of integration time, was found to be 0.3 s. To preserve a workable multiple number of points acquired per fringe period, we have chosen that the measurement time would be set to 0.2 s; at 2.5 kHz modulation frequency, this corresponds to 500 fringes per measurement. These tools and measured optimal parameters will be used directly in Chapter 6 when performing EAI on fiber-coupled detectors.

Furthermore, we have identified an important limitation of the current experimental system: the presence of a drift in the relative phase between the two arms of the experiment. This was observed as a slow, continuous and seemingly random temporal drift in the fringe phase measured in the detector output. The main implication is that the fringe coherence time of our system is only a few seconds, much too small to measure the fringe phase reliably as the sources are scanned over a large number of positions, which would take several minutes to several hours. The next chapter will therefore be devoted to measurements of the detector response function's amplitude pattern. Appropriate extensions to the experimental system to correct for this phase drift will be discussed in Chapter 7, and full measurements of the fringes' amplitude and phase will be presented in Chapter 8.

Chapter 6

Amplitude-Sensitive Experimental Characterization

6.1 Introduction

Fringes in the detector output as the relative phase between the probes is modulated were recorded in Chapter 5, proving the capability of our experimental apparatus to measure such coherent phenomena. In particular, these were used as sensitive tools to characterize important parts of the experimental system itself. In this chapter, we extend these newly developed tools in order to perform EAI on, and to characterize the optical response of, the device under test, i.e. the system created by coupling a length of optical fiber to the chosen InGaAs biased photodetector. The EAI theory derived in Chapter 2 had indicated an experimental method for measuring the Detector Response Function (DRF) which fully characterizes the optical behavior of the device under test, by extracting the properties of the fringes recorded for multiple pairs of positions of the sources illuminating the detector surface. In this chapter, we perform these measurement sets and extract the amplitude of the recorded fringes to obtain the characteristic DRF features of single-mode, few-mode and multi-mode devices. Another main objective is the comparison of the DRF structure observed in experimentally measured DRFs with those of simulated DRFs presented in Chapter 3. In order to gain a deeper understanding of the relationship between these DRF features and the number of optical reception modes of the device under test, we also seek quantitative methods to estimate the latter using only the measured DRF amplitude. Particular care is required to clarify how the modes' sensitivity eigenspectrum is reduced to a single metric.

Section 6.2 describes the experimental method for obtaining the detector output amplitude as one source is scanned over a one-dimensional position grid. This method is then extended

to perform measurements of the fringe in the detector output as the relative phase between sources is modulated, with the two sources scanned over all pairs of positions on a similar one-dimensional grid. In Section 6.3, we apply the method for single-source scans to a system constructed from the photodetector and a short length of optical fiber; we describe the issues with this arrangement and how longer optical fiber cables solve these. Additionally, we perform final calibration procedures, including the angular alignment of source beams. Section 6.4 presents the application of this method to obtain the first experimental measurement of the DRF amplitude of a large variety of infrared systems. In Section 6.5, we discuss these results, including the distinctive characteristics of patterns obtained with single-mode, few-mode and multi-mode devices, as well as compare them to the simulated DRFs obtained in Chapter 3. In Section 6.6, we derive bounds on the number of modes present in the system under test: an upper bound on the number of modes that have quasi-constant relative magnitude and a lower bound on the total number of modes. These bounds can be computed using only the amplitude component of the measured fringes, and an algorithm is implemented to apply this theory to our experimental datasets.

6.2 Experimental Method and Verifications

6.2.1 Control and Measurement Software

While we have previously discussed the generation of scanning instruction sets in Section 5.3.5, it is important at this point to describe the LabVIEW software that used these instructions to control the motorized stages, as well as perform and synchronize the measurement of the detector output. In part, we built on the simple software used in Chapter 5 to record single-shot measurements of noise characteristics and fringes. The LabVIEW code we implemented has several core capabilities:

- **Initialize all systems.** The computer communication to each set of three motorized stages is initialized, and the x- and y-axis stages of the right and left scanning systems, labeled R and L, are sent to their home positions, i.e. $x_R = x_L = y_R = y_L = 0\,\mu$steps, to ensure the proper starting position for the scanning procedures. This is a far off-axis position where no optical power is coupled from either of the sources into the detector. We found that individually instructing each axis is more reliable than using the "home all" function, which is unsuitable. Some additional properties must be set, including whether the movement instructions are displacements in relative or absolute terms, i.e. with respect to the current position of the stage or to its home, respectively; the

former is chosen by default. Computer communication with the ADC is initialized, the measurement channels are set, and the sampling number and rate are selected.

- **Move sources to given position list.** The table of scanning instructions, generated with our Matlab script described in Section 5.3.5, is read; alternatively, manual entries into a LabVIEW table are available. The first 4 elements in each row correspond to relative displacement instructions (with an option to change to absolute positions) for the right x- and y-axis, and left x- and y-axis; the row is split into single elements and fed to each stage, which start their movement immediately.

- **Synchronize movements and measurements.** We use the error messages from the motorized stages' idle signal as inputs for a case structure containing the measurement commands, which forces the program to wait for all variables to be provided, i.e. until all stages are indeed idle. Once all stage movements are complete, a 0.5 s delay time is executed to allow the stages to settle, as decided in Section 5.6.1. Additionally, the voltage and position measurements are not triggered if a fifth component in source position list exists and is equal to 0, as this is used to indicate the first two of three-displacement instructions in the "safe" generation mode, discussed in Section 5.3.5, to avoid source collisions during complex displacement patterns.

- **Synchronize measurement and phase modulation.** The synchronization output of the waveform generator is connected to one of the ADC's digital inputs. Its rising edge serves as a digital trigger for starting a measurement of the voltage inputs to the ADC; this ensure that every measurement in a set begins at the same relative phase shift.

- **Measure ADC input voltage with given sampling rate and sample number.** The appropriate sub-VI provided by the ADC manufacturer's library is called: triggered by the rising slope of the selected digital input, it measures the voltage input to the selected ADC pins for the chosen sampling duration and frequency.

- **Save measurements.** The raw waveform data is saved as a single file for each fringe measurement; at the end of the measurement run, the table of extracted complex fringe parameters is saved in a separate file.

- **Real-time fringe parameter extraction.** In parallel with the recording of the raw voltage input waveforms, we extract the complex fringe amplitude at the modulation frequency, by selecting the corresponding FFT element, as defined by Equation (5.1). For future computational simplicity, the complex amplitude is transformed into its magnitude and argument, as well as its real and imaginary components. An array is

created with these 4 parameters and the DC component, extracted from the first FFT element, and appended to a Matlab-compatible file for further off-line analysis.

- **Measure source positions.** Simultaneous to the voltage measurement, the motorized stages' positions as given by their respective motor encoders are measured. The four position values, in units of µsteps, are concatenated into an array (in the same order as stages in the instruction list), which is appended as a line to a purpose-made file.

6.2.2 Method: Single-Source Scans

We used the Thorlabs DET01CFC photodetector, with its current output signal amplified by the LaserComponents DLPCA-200 transimpedance amplifier. While the amplifier has the capability of providing a bias voltage to the photodiode between -10 V and +10 V, we chose to operate the photodetector with a 12 V reverse bias to obtain best performance. The $G = 10^7$ V/A amplifier gain setting was selected, providing a 50 kHz bandwidth, with low-noise mode (i.e. no additional $\times 100$ voltage gain), full-bandwidth mode rather than 10 Hz ultra-low-noise mode as the latter would be insufficient for kHz-frequency fringes, and DC coupling rather than AC coupling as we wanted to record the DC component of the signal to study the fringe visibility as the sources are scanned. The transimpedance amplifier also allows a constant voltage offset to be added to the output, in the range between -0.1 V and +0.1 V; we use this to nullify the DC voltage measured when the sources are very far off-axis and no optical power is coupled into the photodetector, and caused by contributions from the amplifier noise and an imperfect DC offsetting of the ADC, specified by the manufacturer up to 2.2 mV.

The transimpedance amplifier output was connected to the appropriate ADC pin using a custom-made adapter card, described and tested in Chapter 5. The measurement performed at each source position is 0.25 s long, recording 500 S at 2 kS/s sampling frequency. The laser source's output power was set to its maximum value of 18 dBm (i.e. 63 mW) to obtain maximal SNR. Its "dither" mode was selected to provide long-term frequency and power stability, at the expense of a noise peak at 888 Hz, as discussed in Chapter 5.

The next step was to choose the properties of the sampled source positions, in order to produce appropriate scanning instructions. At a distance between the source and detector planes of 105.0 mm, we found the position range for which the recorded amplitude is non-zero to be approximately 500 000 µsteps (i.e. 25 mm). We chose an scanning range of 600 000 µsteps, with a step size of 2 000 µsteps. While precise calibration of the two-dimensional on-axis positions of each source will be performed in Section 6.3.2, approximate values were obtained by manually scanning each source across the detector and finding the

position for which the amplitude is maximized, as was done in Section 5.4.4. These were used to set the center of the scanning range. Two such sets of scanning instructions were then generated, one for each of the sources. Performing this measurement set produced 301 detector output amplitude values and the source positions at which they were recorded.

6.2.3 Method: Two-Source Scans

Measuring the DRF involves performing a measurement of the fringe in the detector output at each position pair of the sources. In practice, we considered scanning strategies for the sources over one-dimensional, uniformly sampled grids with fixed scanning range; our method can however be applied to general two-source, two-dimensional scanning strategies. In order to ensure that our measurements maximized the recorded information for the selected scanning range, we chose to center each stage's sampled grid on their respective on-axis postions, as for single-source scans. The scanning range was again selected to be 600 000 µsteps. The step size, i.e. the distance between neighboring positions to which the sources are scanned, can be chosen between the sampled source positions, for the given range of 600 000 µsteps held fixed. For simplicity, the step size is chosen to be a divisor of the scanning range. In practice, we will use a step sizes of 4 000 µsteps, or alternatively of 10 000 µsteps for comparative studies discussed in Section 6.6.5. Given alignment properties and physical size of probes, some position pairs are not achievable; these details will be described in Section 6.3.2. Scanning instructions are generated using the method described in Section 5.3.5, and checked for any mistakes with our collision verification script.

For each fringe measurement performed at given source position pairs, we used the same photodetector and amplifier configuration as in the single-source scans. The laser output power was also set to 18 dBm, again in "dither" mode for maximal temporal stability, and each measurement consisted in recording 50 kS at 250 kS/s sampling frequency; this 0.2 s measurement duration is in line with the optimal duration obtained from our Allan Variance analysis in Chapter 5. In order to produce a modulation of the relative phase between the sources, we fed the left phase modulator with a ramp voltage waveform using the Agilent 33220A signal generator, with 0% symmetry, 2.5 kHz frequency, and 8.1 V peak-to-peak amplitude, and 0 V constant offset; these settings are based on the calibration performed in Section 5.5.2.

It is important at this point to remark that the duration of a measurement set is quadratic in the number of positions to which each source is scanned, i.e. inversely quadratic in the step size. For a resolution of 4 000 µsteps, fringe measurements are performed at 10 011 position pairs and the entire measurement set lasts 4 hours; for a resolution of 10 000 µsteps, the

scanning lasts 1 hour with 1 653 measurements; for a resolution of 20 000 µsteps, scanning lasts approximately 16 minutes with 435 measurements.

The extracted fringe data produced by the measurement procedure corresponds to the parameters of the complex fringe amplitude D_{mn} for right and left sources at positions m and n, respectively. We implemented a method to transform the recorded table of fringe parameters into matrix form, to obtain a lower triangular matrix; the elements in the center diagonal band are missing, the width of which is set by the number of positions that cannot be attained because of the physical size of the probes. This technique provides the desired representation of the DRF amplitude, an important milestone in the characterization of the optical response of infrared detectors. In addition, we discussed in Chapter 2 two related quantities:

- The fringe visibility, defined as

$$\gamma_{mn} = \frac{2D_{mn}}{D_{mm} + D_{nn}}, \tag{6.1}$$

  is the fringe amplitude normalized by the fringe's DC offset.

- The fringe coherence, defined as

$$\Gamma_{mn} = \frac{D_{mn}}{\sqrt{D_{mm} D_{nn}}}, \tag{6.2}$$

  is the fringe amplitude normalized by the single-source beampattern amplitudes.

These two quantities, along with the complex fringe amplitude, can be represented as matrices and visualized as image or surface plots, as will be presented in Section 6.4.

We can however also perform other scanning strategies, each of which corresponds to a subset of the full two-source one-dimensional strategy. Keeping the same set of positions along a uniform one-dimensional grid, these include the following cases:

- The sources are scanned in opposite directions, symmetrically about their centers: this corresponds to the counter diagonal of the matrix;

- The sources are scanned at a fixed distance from each other: this corresponds to the n^{th} diagonal of the matrix, where n is the distance between the sources in units of the chosen step size;

- The left source remains fixed while the right source is scanned: this corresponds to a row of the matrix;

- The right source remains fixed while the left source is scanned: this corresponds to a column of the matrix.

In practice, the latter two cases can be achieved by generating scanning instructions to move the second source to a fixed positions and instruct movements of 0 µsteps. In Section 2.6.2, we had discussed the use of such scanning strategies: the width of the fringe amplitude structure as one source is scanned while the other remains fixed provides a measurement of the DRF's coherence length. In addition, comparing the geometric mean of the single-source beampatterns with these one-dimensional slices of fringe amplitude matrix is expected to give an estimate of the number of modes composing the DRF; this topic will be investigated in Section 6.6.

6.3 Verifications and Alignment

6.3.1 Suppressing Cladding Modes

In Chapter 5, we first measured optical radiation by placing one of the probes at the approximate on-axis position relative to the detector. Fringes in the detector output as the relative phase between the probes was varied, with the two sources placed as close as possible to each other and to their respective on-axis positions. In this section, we wish to expand on these results with two key capabilities: the measurement of the detector beampattern as a single source is scanned across the detector, and the accurate determination of the on-axis position of each source.

Scanning a single source while the other is left at a far off-axis position, and recording the detector output for each sampled position as described in Section 6.2.2, we measure the single-source beampattern of the detector response. The beampatterns obtained have irregular shapes, particularly for sampled positions near the on-axis position, where the amplitude of the recorded signal is greater than half of the beampattern's amplitude. Figure 6.1 shows one such example, obtained with a short, 20 cm-long single-mode non-polarization maintaing fiber, and scanning the right source only. The observed beampattern shape disagrees with the numerical simulations we had performed in Chapter 3, as highlighted in Figure 6.1 by the least-squares fit of a Gaussian functional form of the recorded amplitude $A(x)$,

$$A(x) = a\ \exp\left(-\frac{(x-b)^2}{2c^2}\right), \tag{6.3}$$

where x is the off-axis position, and a, b and c are respectively the maximum beampattern amplitude, its center and its width.

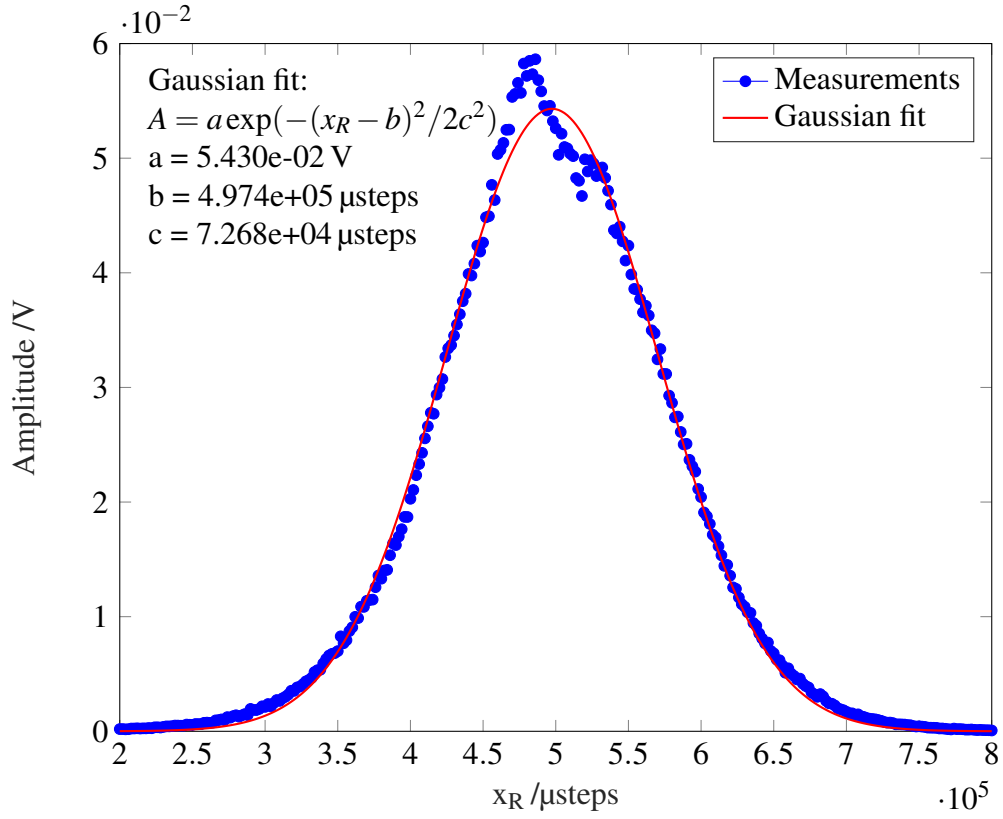

Fig. 6.1 Beampattern measurement using the right source, displaying cladding mode contributions; the fitted parameters a, b and c are the maximum amplitude, center and width of the Gaussian functional form described in Equation (6.3).

The irregularities in its shape are reminiscent of those caused by standing waves [101]. However, after careful minimization of reflective areas that could potentially contribute, by adding optically scattering "wet-and-dry" paper on these surfaces, we obtained no noticeable improvement. To test this hypothesis further, we used the manual stage that the detector system is mounted on and varied the distance between the detector and source planes with a precision of 0.25 µm. Figure 6.2 shows the results of 8 consecutive beampattern measurements, between which the detector was repeatedly moved forward by 0.25 µm, and moved back to its original position for the final measurement. We find that the beampattern shape shows little dependence to the chosen source-to-detector distance; instead, the beampattern shape seems to vary with time, over timescales of several minutes. For instance, the 8 measurement runs presented in Figure 6.2 were performed over 30 minutes.

The cause of this behavior was found to be cladding modes, transmission modes for the incident optical power inside the optical fiber's large cladding layer that is concentric with the core. While these modes have large loss coefficients of several dB/m, they still

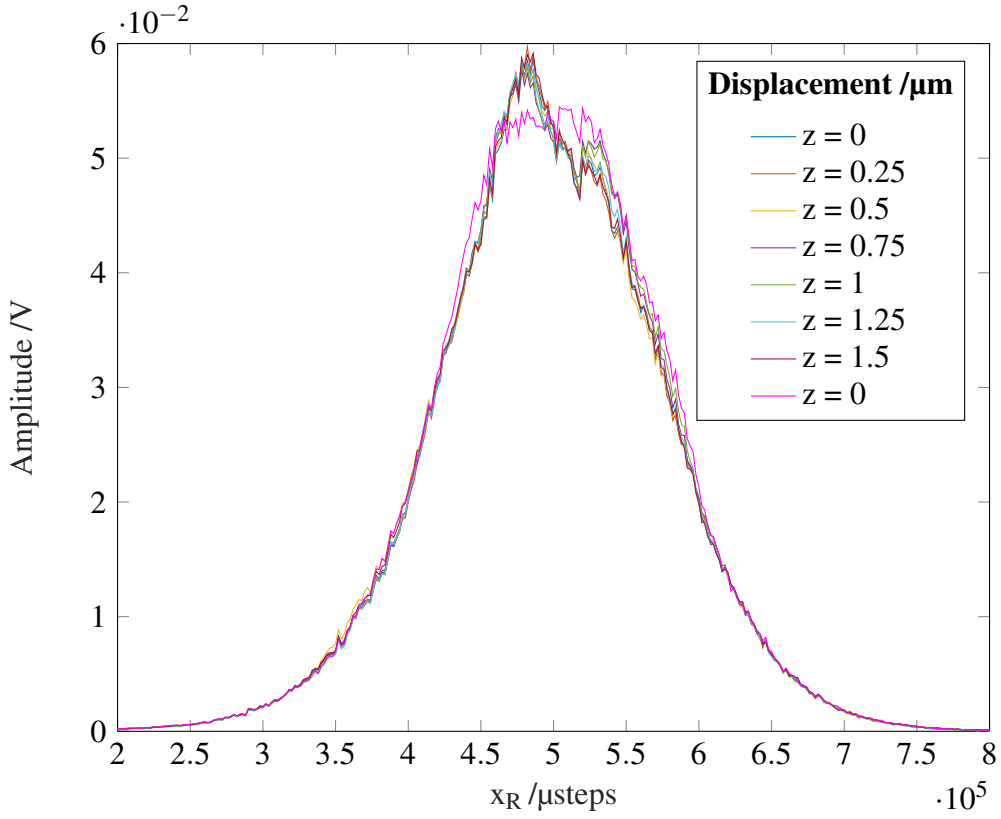

Fig. 6.2 Comparison of 8 consecutive beampattern measurements using the right source, with small displacements of the detector position.

transmit enough power to be significant at the fiber-coupled detector input, when using short optical fibers. The characteristic fiber length for cladding modes to become suppressed depends on the fiber type and geometry, and is several tens of centimeters for single-mode step-index fibers [102]. Incoming radiation always couples into the optical fiber's cladding as well as the core, because these have very similar refractive indices. However, while the radiation coupled into the fiber's core is transmitted with minimal loss due to total internal reflection for incident angles smaller than the critical angle, as discussed in Section 1.2.3, transmission in the fiber's cladding is very lossy. The main loss mechanism is transmission through the cladding-coating boundary, as the coating material is specifically chosen with a high refractive index for this purpose. That process is illustrated in Figure 6.3, in the context of cladding modes, of radiation incident at an angle larger than the fiber's critical angle, and of radiation incident on an improperly polished fiber core region.

In practice, the radiation transmitted in cladding modes is considered negligible versus the power transmitted in the fiber core for fiber lengths greater than 1 m. On the contrary, in

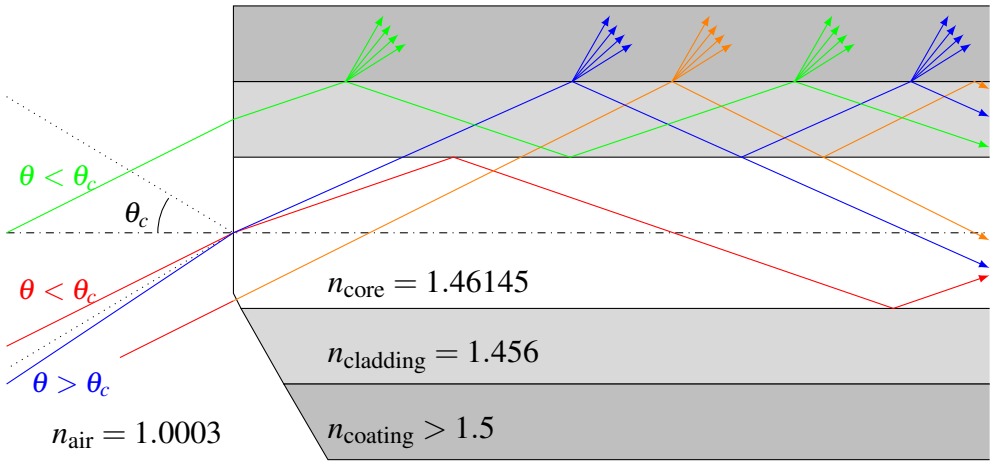

Fig. 6.3 Transmission in an optical fiber of incoming radiation with incident angle θ smaller than its critical angle θ_c via core modes (red) and cladding modes (green); the former display total internal reflection at the core-cladding surface, while the latter are largely scattered at the cladding-coating surface due to uneven surfaces and refractive index choices. The same mechanism produces large losses for radiation incident on the fiber core with incident angle $\theta > \theta_c$ (blue), as well as for radiation incident on imperfections in the fiber's core (orange). The refractive index values indicated are representative for single-mode fibers.

optical fibers of lengths below 20 cm, such as those we connectorized in Section 5.4.3, power transmission in cladding modes cannot be neglected.

The intuitive solution to the problem of cladding modes is to use a longer piece of optical fiber to couple the incoming radiation into the photodetector. This was done straightforwardly with a commercially available optical fiber patch cable of appropriate length. We chose a 2 m-long connectorized polarization-maintaining patch cable. Its connector ferrule is also a 2.5 mm ceramic ferrule, and was therefore fitted into the holder without any change. Figure 6.4 presents the detector beampattern measurement performed with this optical patch cable, and otherwise unchanged settings compared to Figure 6.1: the beampattern shape no longer has irregularities, and is in excellent agreement with the Gaussian least-squares fit. The same measurement procedure was repeated with the 2 m-long Thorlabs 1550BHP single-mode (non-polarization-maintaining) optical fiber patch cable. The beampattern obtained as a single source is scanned across the detector again has a Gaussian shape, and is very well fitted by a Gaussian functional form. This confirms that the irregular beampattern shapes, such as presented in Figure 6.1, were indeed caused by cladding modes and not influenced by the presence or absence of polarization-maintaining properties.

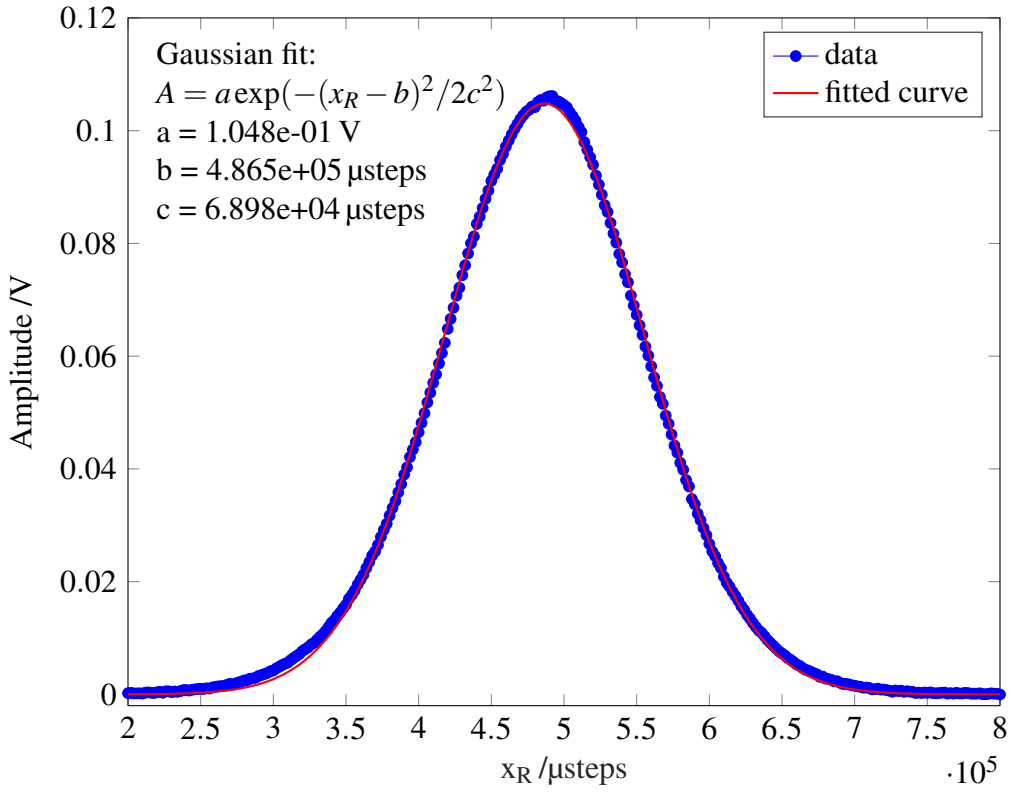

Fig. 6.4 Beampattern measurement using the right source, displaying no cladding mode contributions, contrary to Figure 6.1; the fitted parameters a, b and c are the maximum amplitude, center and width of the Gaussian functional form described in Equation (6.3).

6.3.2 Source Alignment

Now that we are able to reproducibly measure single-source beampatterns of the detector response, we can perform a final key calibration procedure, in addition to those performed in Chapter 5: the sources' alignment, i.e. the angle of their respective beam's direction relative to the target direction, that of the detector fiber's virtual beam. In order to obtain a measure of the misalignment angle of each source, we can perform single-source beampattern measurements at two different distances between the source and detector planes. Using the least-squares fitting procedure on the measured beampattern, as presented in Section 6.3.1, with the Gaussian functional form defined in Equation (6.3) produces a fitting value for the source position corresponding to the center of the beampattern, i.e. when the source is on-axis with the detector fiber. As illustrated in Figure 6.5, we can deduce the following relationship between the horizontal misalignment angle θ_x and the measured values of the

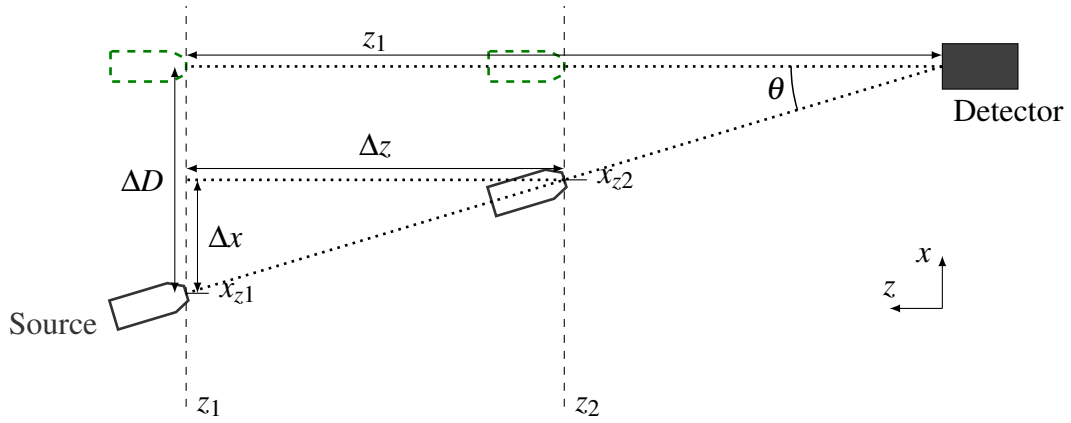

Fig. 6.5 Schematic drawing of the alignment procedure for the source direction; the green dashed polygons represent the on-axis positions of the source when it is perfectly aligned with the detector axis.

beampattern centers obtained for scans at distances z_1 and z_2:

$$\tan(\theta_x) = \frac{\Delta x}{\Delta z} = \frac{\Delta D}{z_1}, \tag{6.4}$$

where $\Delta x = x_{z2} - x_{z1}$ is the difference between the fitted beampattern centers for measurements at distance z_2 and z_1, $\Delta z = z_2 - z_1$ is the difference of distances between the source and detector planes for the two measurement sets, and ΔD is the distance along the x-axis at $z = z_1$ between the current fitted beampattern center x_{z1} and the ideal center position. The same holds for the vertical misalignment angle θ_y, using vertical single-source scans.

In practice, the distance z_1 between the source and detector planes is defined when the sources' z-axis motorized stage are at their minimal position; we measure $z_1 = 105.0\,\text{mm}$. In order to obtain maximally sensitive estimates of the misalignment angle θ, we choose z_2 to be as close as possible to the $z_1/2$ as possible. As the stages' scanning range is 50.8 mm, we choose $\Delta z = 50.8\,\text{mm}$ and obtain $z_2 = 54.2\,\text{mm}$.

One-dimensional or two-dimensional scans can be used to obtain the beampattern centers along either or both x and y, respectively. In practice, a one-dimensional scan with 301 sampled positions lasts 3 minutes, while a two-dimensional scan with 31×31 sampled positions lasts 9 minutes. We choose to use two-dimensional scans, and perform the alignment of each source along the x- and y-axis simultaneously, rather than consecutively.

The calibration procedure starts with a first set of measurements at z_1 and z_2; this provides a value for the current misalignment θ, as well as a total spatial displacement ΔD at distance z_1. To change the horizontal alignment, a rotation of the vertical stage structure with respect to the horizontal stage's plate can be applied; for vertical alignment, we can rotate the

extender arm structure with respect to the vertical stage plate. The beampattern measurement is reiterated at z_1 to compute an updated ΔD, and small angular adjustments are repeated until the fitted center of the beampattern has been displaced by ΔD. A final beampattern measurement at z_2 confirms that the source alignment is correct.

A number of assumptions are made for this calibration procedure to hold. First, small rotation adjustments are made by rotating the fiber about its tip; while this is not quite correct as we rotate either the vertical stage's structure, onto which the source's extender arm and holder are mounted, or the extender arm itself, the approximation is sufficiently accurate for small angles. More generally, the final measurement of alignment does not depend on the angular adjustment method. We also suppose that the least-squares fit of the measured single-source beampattern with a Gaussian fit is perfectly accurate; as the beampatterns observed have nearly Gaussian shapes and the fitting procedure employed has an arbitrarily small accuracy threshold, this assumption holds broadly. Finally, we assume that the set of scanned positions are perfectly orthogonal to the detector's virtual beam direction, and that the motorized stages place the sources at their target positions with perfect accuracy; given the motorized stages' accuracy of within 4 µm, i.e. a small fraction of the chosen 100 µm step size, stated by the manufacturer and tested in Chapter 5, this assumption holds.

We perform this alignment procedure for both the left and right sources. After several iterations, we obtain near-perfect alignment of the sources; the main limitations to this procedure are the precision with which small correcting rotations can be applied, and sub-degree rotations occurring when tightening the mounting screws. For the right source, the two-dimensional beampattern scan results, and their least-squares fit with a two-dimensional Gaussian function, are shown in Figure 6.6. The measured center positions are $(x_R^c, y_R^c) = (4.868 \times 10^5, 4.032 \times 10^5)$ µsteps at $z_1 = 105.0$ mm, and $(x_R^c, y_R^c) = (4.892 \times 10^5, 4.103 \times 10^5)$ µsteps at $z_2 = 54.2$ mm. This implies 2.2 mrad horizontal and 6.7 mrad vertical misalignments, respectively. For the left source, the center positions are measured to be $(x_L^c, y_L^c) = (6.021 \times 10^5, 3.994 \times 10^5)$ µsteps at $z_1 = 105.0$ mm, and $(x_L^c, y_L^c) = (6.044 \times 10^5, 4.115 \times 10^5)$ µsteps at $z_2 = 54.2$ mm; this implies 2.2 mrad horizontal and 11 mrad vertical misalignments, respectively. The fitted Gaussian center values at $z = 105.0$ mm steps are considered to be the on-axis positions of each of the sources, and used as the two-dimensional center positions (x_R^c, y_R^c) and (x_L^c, y_L^c) to generate well-centered scanning instructions, using the methods described in Section 6.2. We note that, by symmetry of the right and left motorized stages' mounting configuration, discussed in Section 5.3.2, these residual misalignments mean that the source beams are very slightly converging towards the detector. This in turn implies that more source position pairs are attainable without collision, equivalent to 10 000 µsteps. On the other hand, the y-axis directions are identical

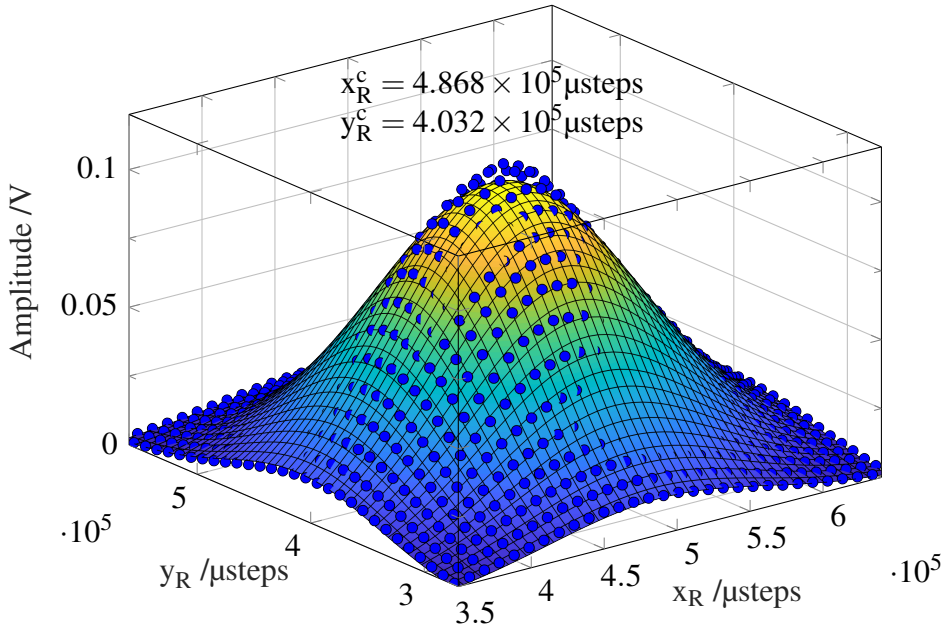

(a) $z = 105.0\,\text{mm}$

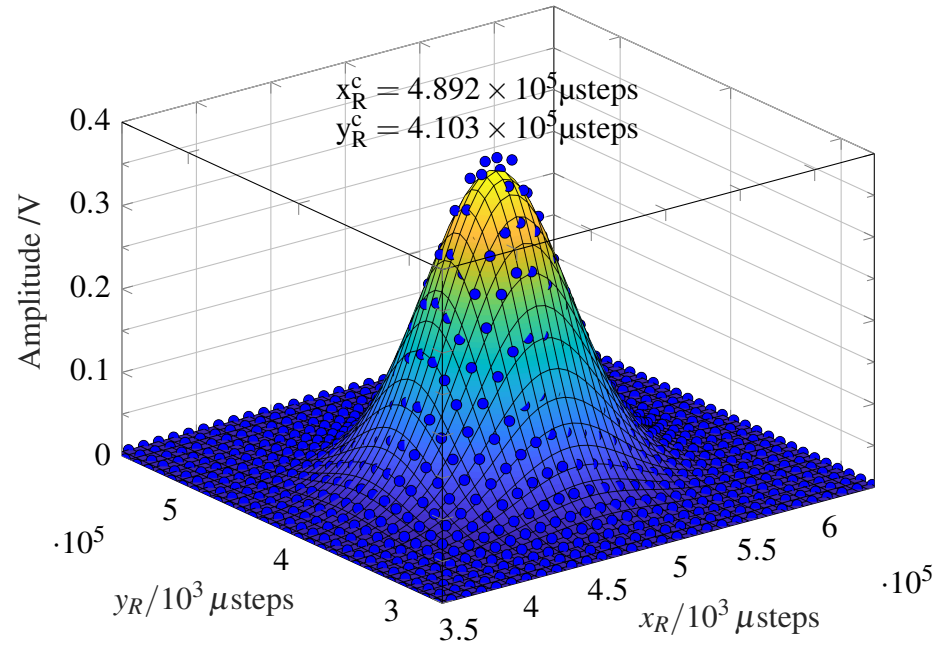

(b) $z = 54.2\,\text{mm}$

Fig. 6.6 Right source beampattern measurements at different distances between the source and detector planes, with two-dimensional Gaussian least-squares fit; center positions (x_R^c, y_R^c) are extracted.

Fiber name	Core diameter	Numerical aperture	Mode number	Cutoff wavelength	Polarization maintaining	Section
1550BHP	9 µm	0.13	1	1400 nm	No	6.4.1
PM1550-XP	8.5 µm	0.125	1	1380 nm	Yes	
SM2000	11 µm	0.12	2	1750 nm	No	6.4.2
P1-23Z	9 µm	0.19	2	2300 nm	No	
P1-32F	9 µm	0.26	4	3200 nm	No	
FG050LGA	50 µm	0.22	125	N/A	No	6.4.3

Table 6.1 Properties of the various 2 m-long optical fiber patch cables used as interchangeable mode filters for the photodetector, for operating wavelength $\lambda = 1550$ nm.

for the two motorized stage systems; the residual misalignments are therefore approximately aligned with respect to each other.

6.4 Experimental Results

6.4.1 Single-Mode

Following our investigation of cladding modes in 20 cm-long optical fibers in Section 6.3.1, we elected to use 2 m-long optical patch cables for coupling to our photodetector. We recall that the modal behavior of the optical fiber determines that of the device under test, i.e. the photodetector and optical fiber system. Table 6.1 summarizes the various optical fiber patch cables that were used for performing EAI, as presented in this section, including their properties and expected number of modes.

We begin by considering the case of coupling the detector to the Thorlabs PM1550-XP single-mode, polarization maintaining optical fiber patch cable. We performed a beampattern measurement for each source, as described in Section 6.2.2, and a two-source scan measuring fringes in the detector output, as described in Section 6.2.3. In Figure 6.8a, we observe that the fringe amplitude pattern is nearly circular. We recall that the true measured data is in the lower triangle of the depicted matrix; the upper triangle is the transpose of the former, which assumes symmetry of the DRF under the exchange of sources. Figure 6.8b presents the corresponding fringe coherence matrix, which is constant. The upper triangle of the fringe coherence matrix is different from the lower triangle matrix because this assumption does not strictly hold: the complex DRF amplitude is divided by the outer product of the two entire single-source scans, which is not precisely symmetric under exchange of sources, i.e. about the matrix's main diagonal. In effect, this means that we use pairs of single-source optical power measurements at position pairs that are not reached during the two-source

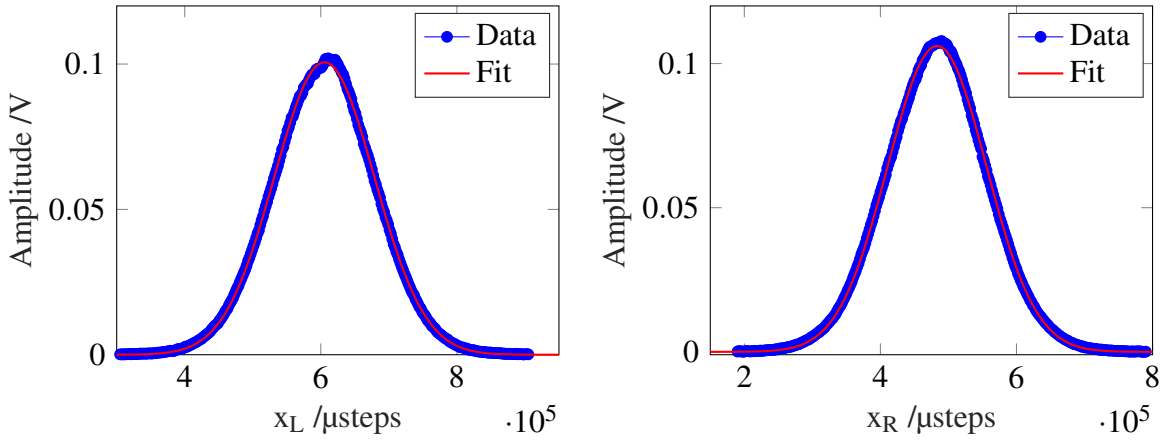

(a) Left source

(b) Right source

Fig. 6.7 Left and right source beampattern measurements obtained with the PM1550-XP fiber-coupled system, with one-dimensional Gaussian least-squares fit.

fringe measurements. We also note that the near-constant value of the fringe coherence matrix is approximately 0.9. This is close to the value of 1 expected from our simulations in Chapter 3, shown in Figure 3.5b; this discrepancy will be addressed in Section 6.5.2. The center diagonal, filled with the element-wise product of the single-source beampatterns, is equal to 1 by construction.

The same measurement procedure was repeated with the photodetector coupled to the Thorlabs 1550BHP single-mode optical fiber patch cable. In Figure 6.9a, we observe that the fringe amplitude pattern is nearly circular. Figure 6.9b shows that the fringe coherence is constant with the source positions, and has a value approximately equal to 0.9. The results obtained are qualitatively similar to those presented with the PM1550-XP polarization-maintaining fiber. This confirms that our concern that a long length fiber without polarization-maintaining properties may lead to loss of coherence, which had led us to manufacture shorter lengths of optical fibers in Section 5.3.3 and test them in Section 6.3.1, was unfounded.

6.4.2 Few-Mode

In Figure 6.10a, we observe that the fringe amplitude pattern obtained with the SM2000 fiber-coupled system, which we expect to be two-moded, has a slightly oval shape, as well as a nearly circular, concave line of zero-amplitude near the anti-diagonal corners. Note that the asymmetry between the top-left and lower-right portions of the central fringe amplitude peak is caused by the asymmetry and non-Gaussian shape of the single-source beampatterns, which is expected for few-mode systems in the presence of experimental imperfections. Figure 6.10b presents the corresponding fringe coherence matrix, with a qualitatively similar

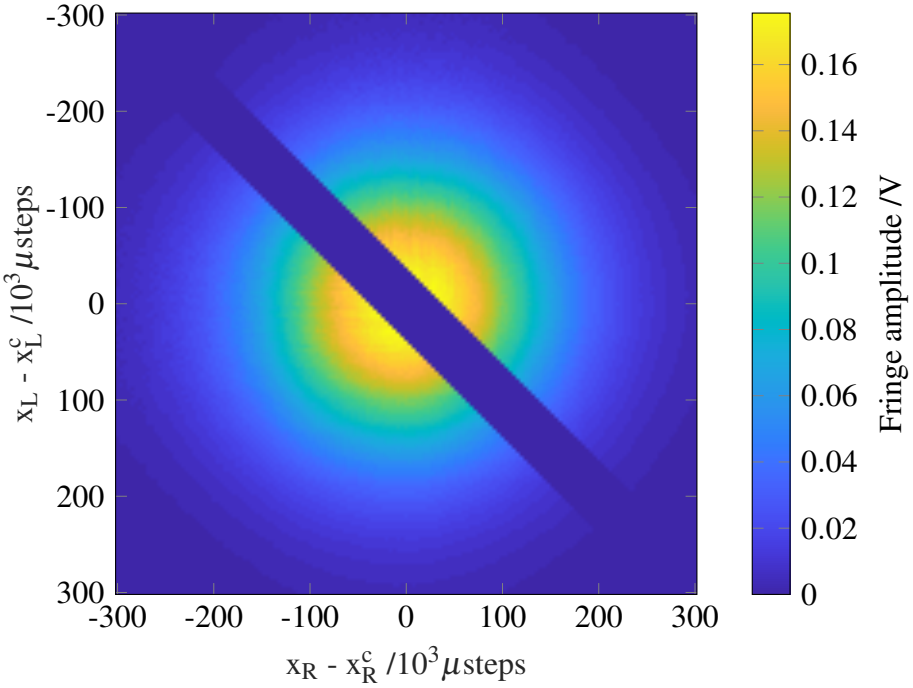

(a) Fringe amplitude

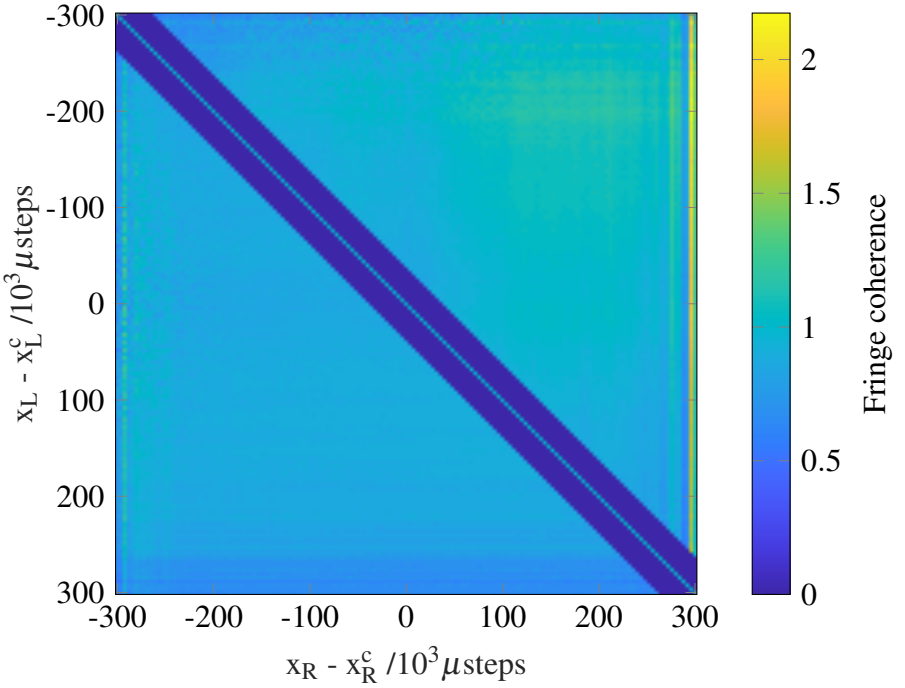

(b) Fringe coherence

Fig. 6.8 Measured DRF fringe amplitude and coherence for the PM1550-XP fiber-coupled system.

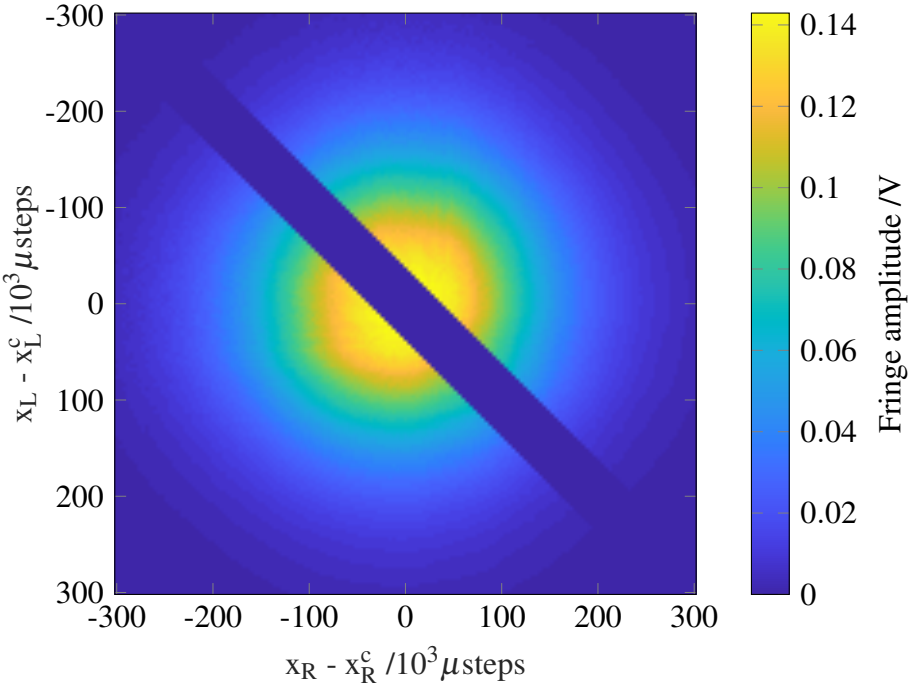

(a) Fringe amplitude

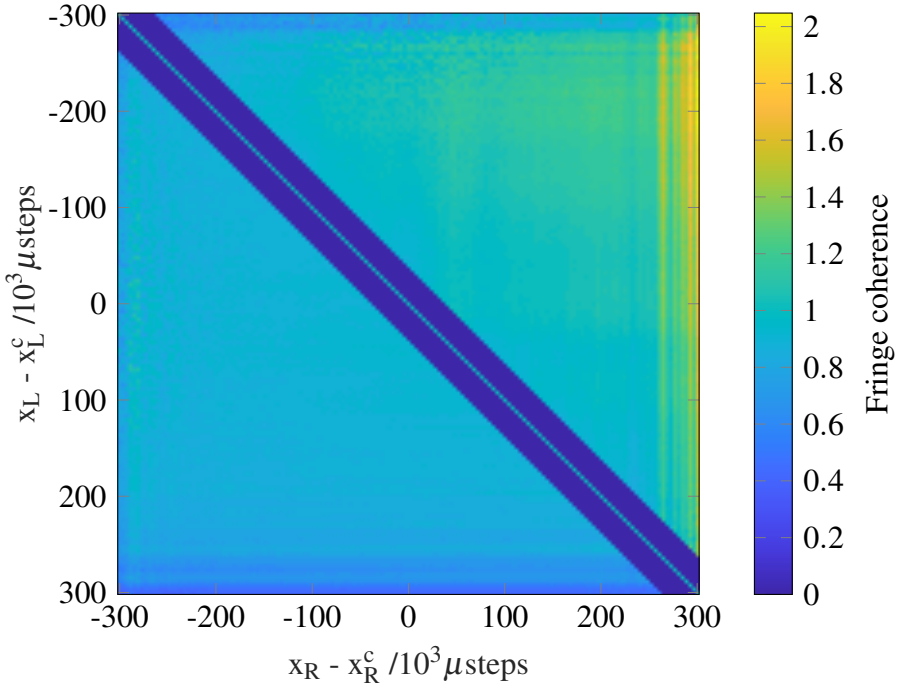

(b) Fringe coherence

Fig. 6.9 Measured DRF fringe amplitude and coherence for the 1550BHP fiber-coupled system.

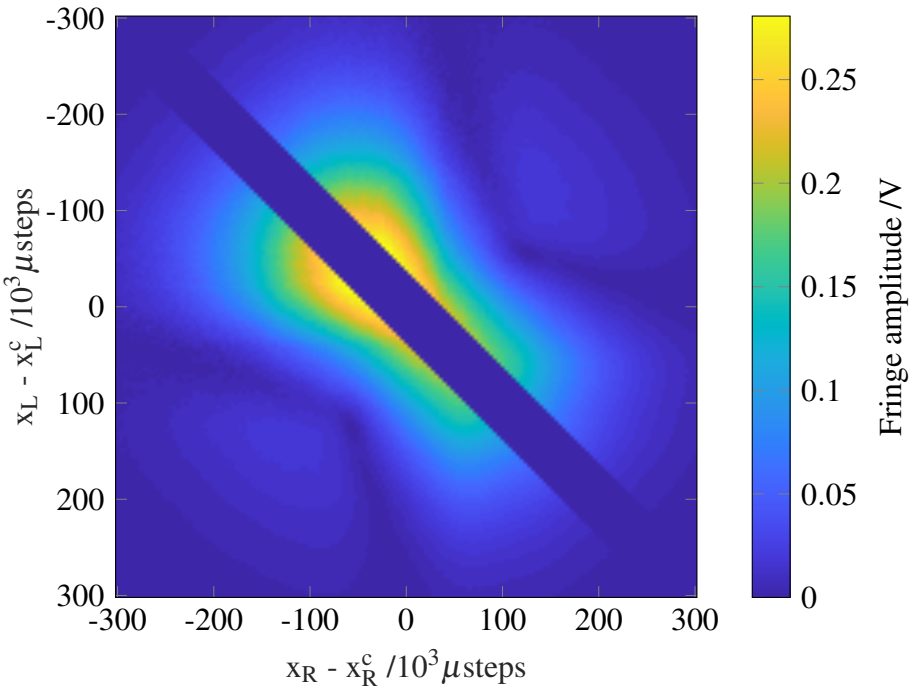

(a) Fringe amplitude

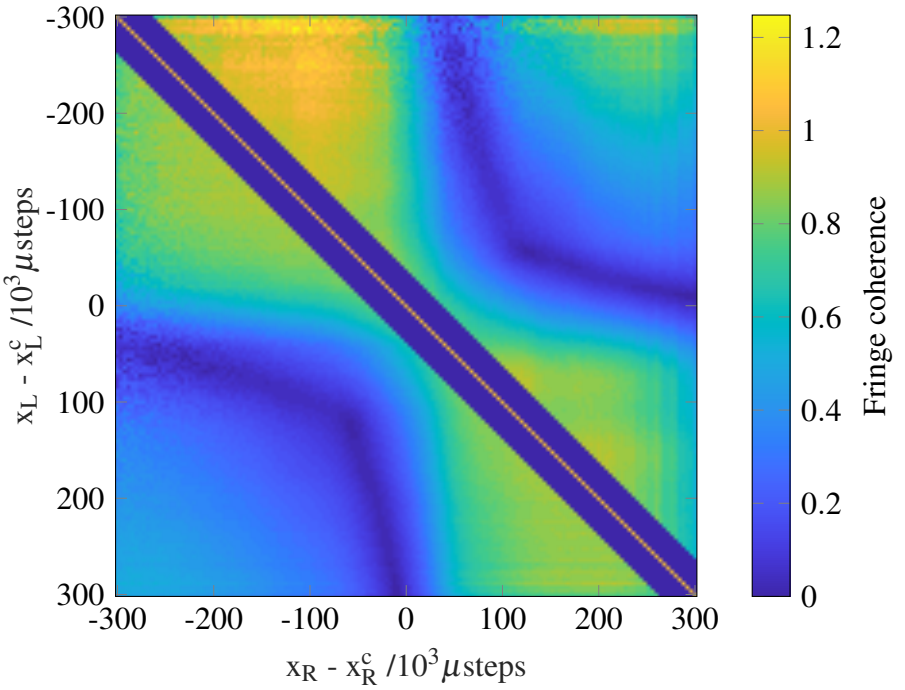

(b) Fringe coherence

Fig. 6.10 Measured DRF fringe amplitude and coherence for the SM2000 fiber-coupled system.

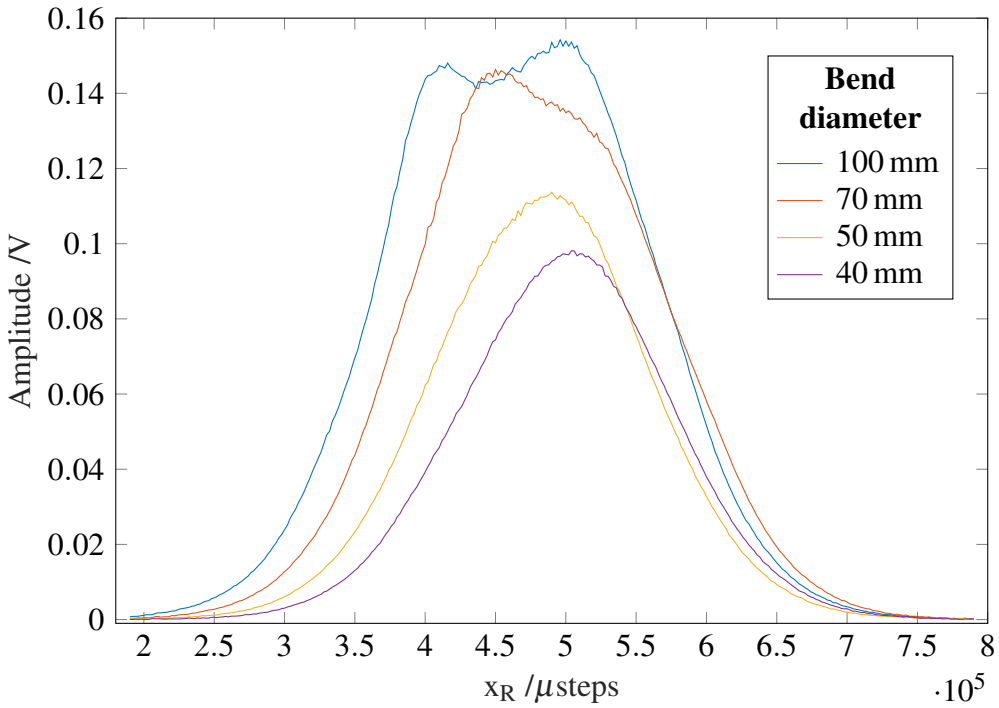

Fig. 6.11 Detector beampattern measured with right source, for various bend diameters of detector fiber.

pattern. The contrast of the line for which the fringe coherence is equal to zero is even greater than the corresponding zero-amplitude line. The coherence increases to 0.6 at the antidiagonal corners, and approaches 1 towards the center diagonal; the fringe coherence pattern is approximately symmetric about the antidiagonal, indicating that the asymmetry in the fringe amplitude pattern was indeed caused by the asymmetry of the single-source measurements.

We repeat the measurement procedure with the detector fiber wrapped around cylinders of decreasing diameter. By applying decreasingly small bend diameters to the optical fiber around the chosen mandrel, we expect to produce the effect of a mode scrambler [103]. Figure 6.11 presents detector beampatterns as the right source is scanned, for various bend diameters: as the bend diameter is decreased, the beampattern shape becomes Gaussian and its maximum amplitude decreases, indicating that less optical power is coupled into the detector. We also observe an increase of the beampattern center: this is likely caused by a combination of some tension on the optical fiber, very slightly changing its alignment angle, the right source's small but non-zero misalignment angle, and the decreasing influence of the second mode. The latter phenomenon is most clearly seen in the fringe coherence matrix obtained for a two-source scan with a 40 mm bend diameter: its pattern is constant, with a

value approximately 0.85, in line with the single-mode behavior presented in Section 6.4.1. Moreover, the fringe amplitude pattern is circular and does not display a zero-amplitude line, when applying a 40 mm bend diameter to the SM2000 fiber. We therefore conclude that wrapping the two-mode SM2000 fiber around a mandrel of small diameter suppresses the system's second mode, and produces a single-mode system.

Repeating the same measurement procedure with the P1-23Z fiber-coupled system, Figures 6.12a and 6.12b show that the fringe amplitude and coherence structures are generally similar to the case of the SM2000-coupled system. However, it appears that the fringe amplitude structure observed here is a slightly zoomed-in version of the one observed with the SM2000 fiber; this is most noticeable with the zero-amplitude lines, which are closer to the antidiagonal corners. This is surprising given that the P1-23Z-coupled system's second mode is expected to have a greater sensitivity, given that the operating wavelength, $\lambda = 1550\,\text{nm}$, is further from the second mode's cutoff wavelength, $\lambda_c = 2300\,\text{nm}$, instead of $\lambda_c = 1700\,\text{nm}$ for the SM2000 optical fiber. Our understanding is that this phenomenon stems from the difference of numerical aperture, which is equal to 0.12 for the SM2000 optical fiber and 0.19 for the P1-23Z optical fiber. In general, a larger numerical aperture corresponds to a larger acceptance angle for the incoming radiation. However, in our configuration, the sources' numerical aperture of 0.13 are the limiting factor, and the additional portion of the acceptance cone when using the P1-23Z optical fiber is never reached. Instead considering the virtual beam emitted by the detector system, a larger numerical aperture implies a larger virtual spot size. Because our scanning range and the distance between the source and detector planes remain fixed, we effectively sample a smaller fraction of the virtual detector beam cone. This qualitatively explains why the fringe amplitude pattern obtained for systems with larger numerical apertures seems focused on the center fraction of the fringe amplitude pattern obtained for systems with smaller numerical apertures, assuming their modal behavior is approximately similar.

Figure 6.13a presents the P1-32F fiber-coupled system's amplitude pattern, an oval center peak with large width and no zero-amplitude lines in the antidiagonal corners. In Figure 6.13b, we observe that the fringe coherence pattern has a somewhat diagonal shape. However, its slightly concave curvature is reminiscent of that observed for the SM2000- and P1-23Z-coupled systems: it seems that the observed fringe amplitude structure is further zoomed-in on the center portion of the fringe amplitude pattern recorded with the SM2000 fiber. This further confirms our earlier hypothesis that choosing a fiber with a larger numerical aperture, 0.26 in the case of the P1-32F optical fiber, implies a larger virtual detector spot size, for which we only scan the center region when keeping the scanning range fixed.

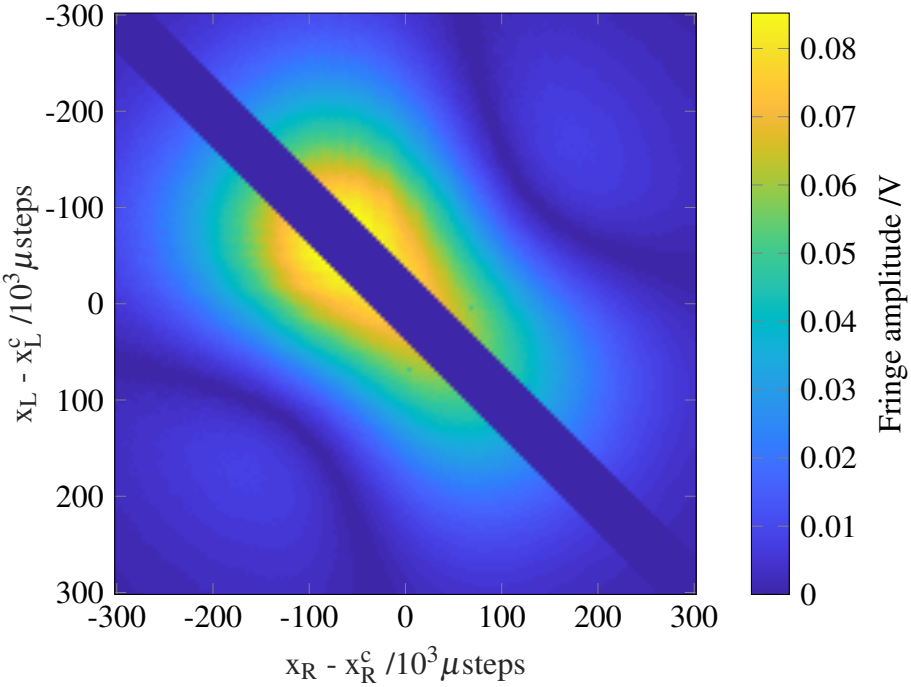

(a) Fringe amplitude

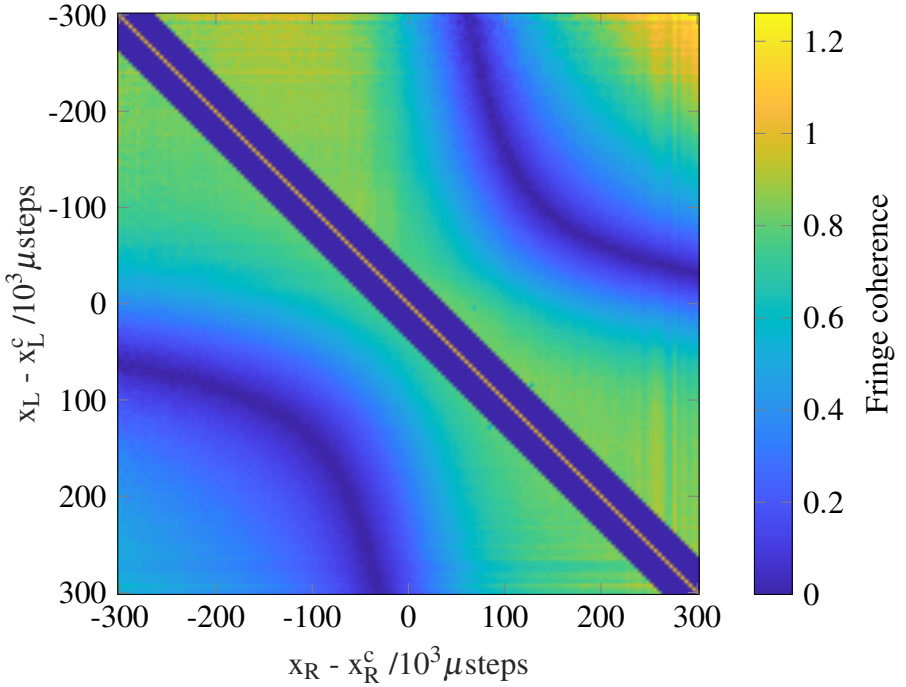

(b) Fringe coherence

Fig. 6.12 Measured DRF fringe amplitude and coherence for the P1-23Z fiber-coupled system.

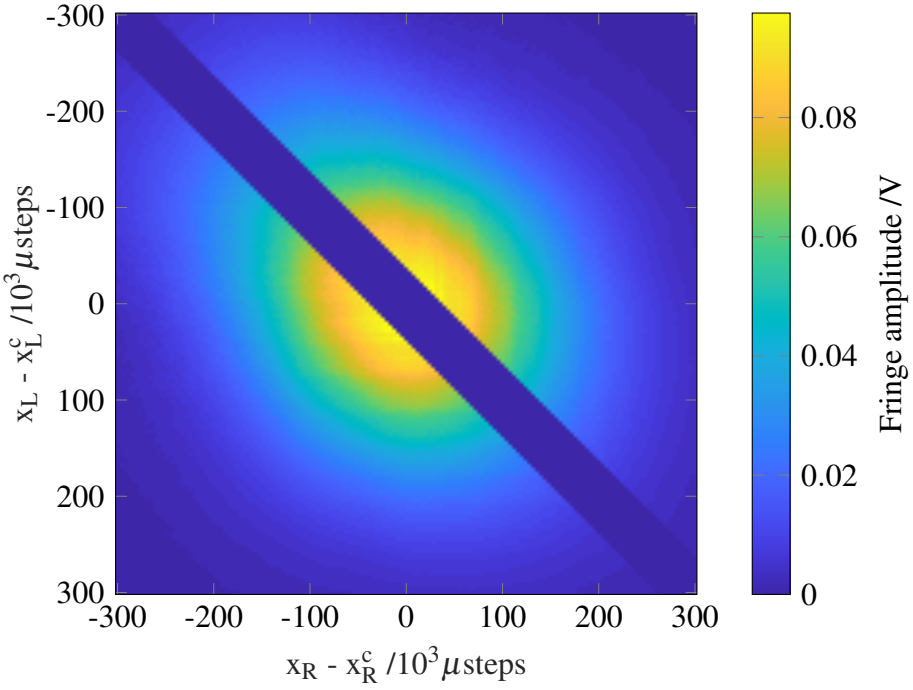

(a) Fringe amplitude

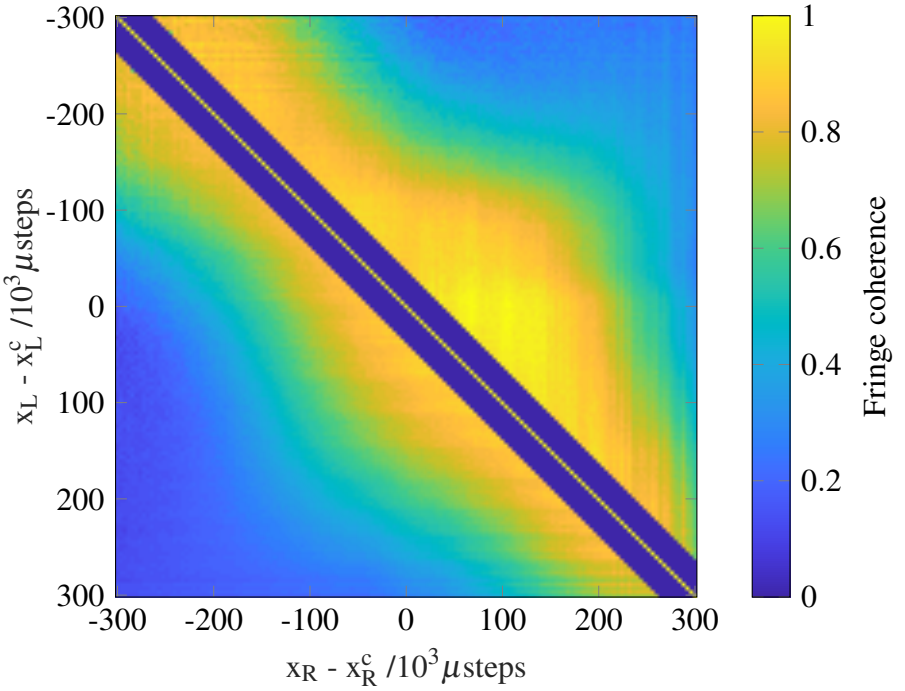

(b) Fringe coherence

Fig. 6.13 Measured DRF fringe amplitude and coherence for the P1-32F fiber-coupled system.

6.4.3 Multi-Mode

We now turn to the case of highly multi-mode systems. We first investigate the coupling of the photodetector to a multi-mode fiber, with an expected 125 modes. In Figure 6.14a, we observe that the fringe amplitude pattern has a strong diagonal structure, of decreasing amplitude moving along the anti-diagonal, i.e. for greater distance between the sources, and moving along the diagonal, i.e. for greater off-axis distances. The structure width is much smaller than in the case of few-mode systems, and the experimental system's capability to reproducibly measure such fine features is a testament to its multi-hour time stability. Figure 6.14b presents the corresponding fringe coherence matrix, which clearly displays a similarly diagonal structure, but with constant magnitude along the diagonals. This diagonal pattern means that the fringe coherence is dependent only on the distance between the sources, but independent of the distance of the sources to their on-axis positions.

The same experimental procedure can be repeated with no optical fiber coupled to the photodetector, and instead illuminating its open female FC/PC connector. As we do not couple the highly multi-mode detector to any optical fiber that would act as a mode filter, we expect the number of modes present in the detector-only system to be maximal, and set by the photodetector properties itself. Using Equation (4.21), we can estimate the number of modes of the bare photodetector from its dimensions, a 0.12 mm diameter and a 0.21 rad acceptance angle (effectively set by the dimensions of the female FC/PC connector, a cylinder 12 mm in length and 2.5 mm in diameter), would indicate 650 modes in two-dimensional scans. However, the ball lens in front of the photodiode as well as the acceptance angle of the detector system require a more complex analysis to obtain a more reliable estimate. Note that the FC/PC connector only limits the acceptance angle in the open-detector case, as the radiation is directly incident on the connector; when using a fiber-coupled system, the optical fiber transmits the incident beam such that the radiation is coupled onto the photodiode from the fiber's output tip, at a few millimeters from it.

Regardless of the mode estimate accuracy, it is interesting to repeat the measurement set using the detector-only system. In Figure 6.15a, we observe that the fringe amplitude pattern displays a clear diagonal structure with small width, a clear indicator of highly multi-mode behavior. Nearest to the center diagonal, the fringe amplitude displays three distinct peaks: we understand the two side peaks to be caused by reflection of the incident beams in the FC/PC connector for small position ranges, i.e. for appropriate solid angles. The fringe coherence matrix, presented in Figure 6.15b, also displays this diagonal structure. As for the FG050LGA-coupled system, the fringe coherence value is constant along the diagonals. However, the maximal fringe coherence is much smaller, approximately 0.06 rather than 0.2. The width of the diagonal structure is also smaller: considering the fringe amplitude for fixed

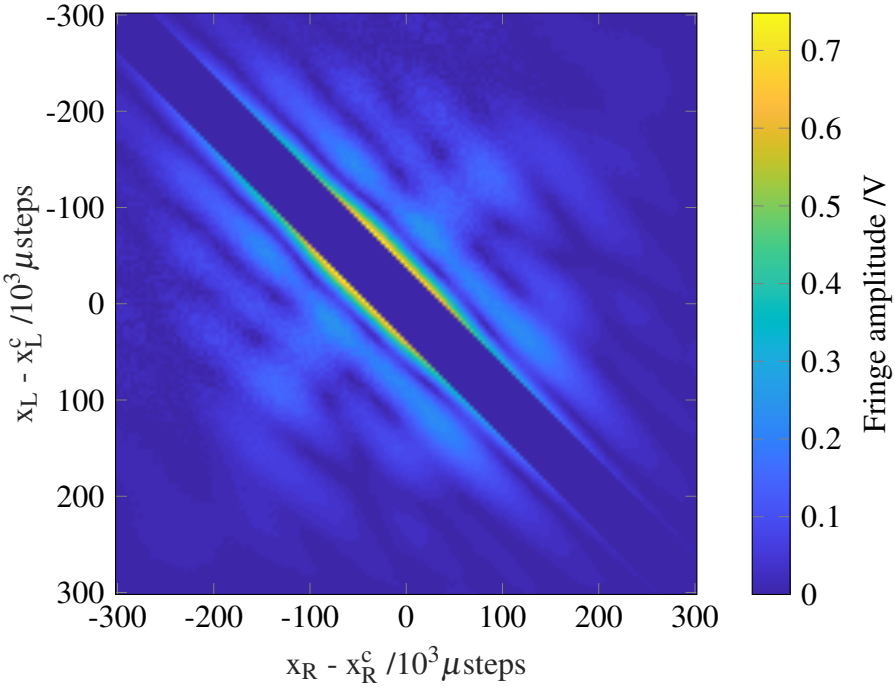

(a) Fringe amplitude

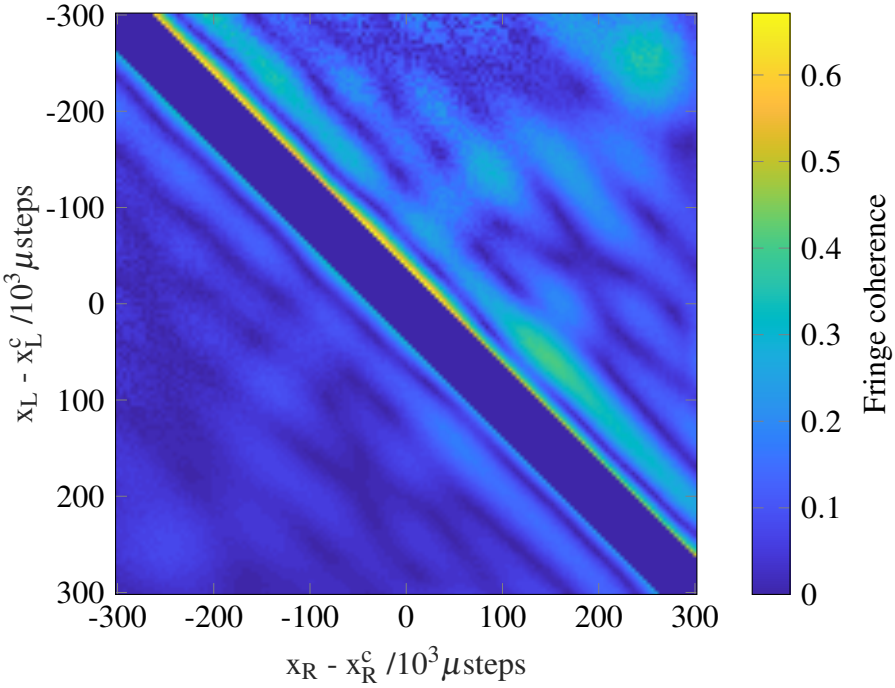

(b) Fringe coherence

Fig. 6.14 Measured DRF fringe amplitude and coherence for the FG050LGA fiber-coupled system.

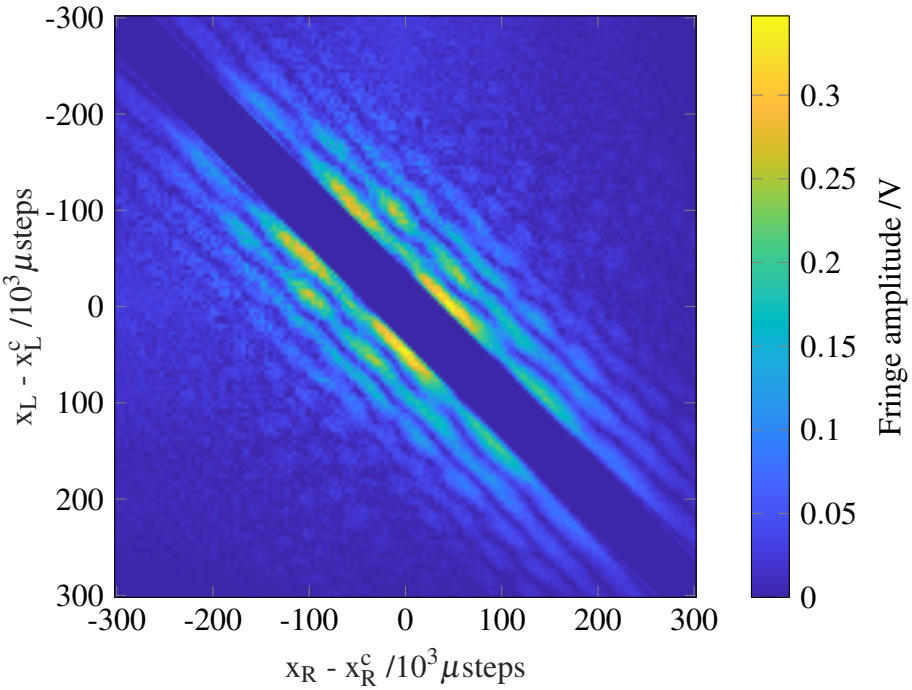

(a) Fringe amplitude

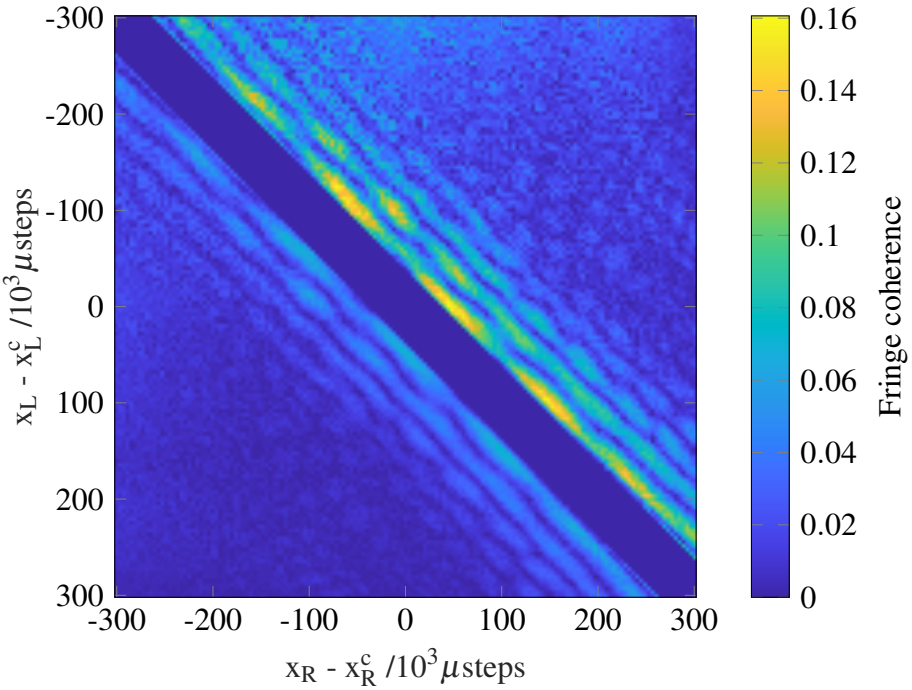

(b) Fringe coherence

Fig. 6.15 Measured DRF fringe amplitude and coherence for the detector-only system.

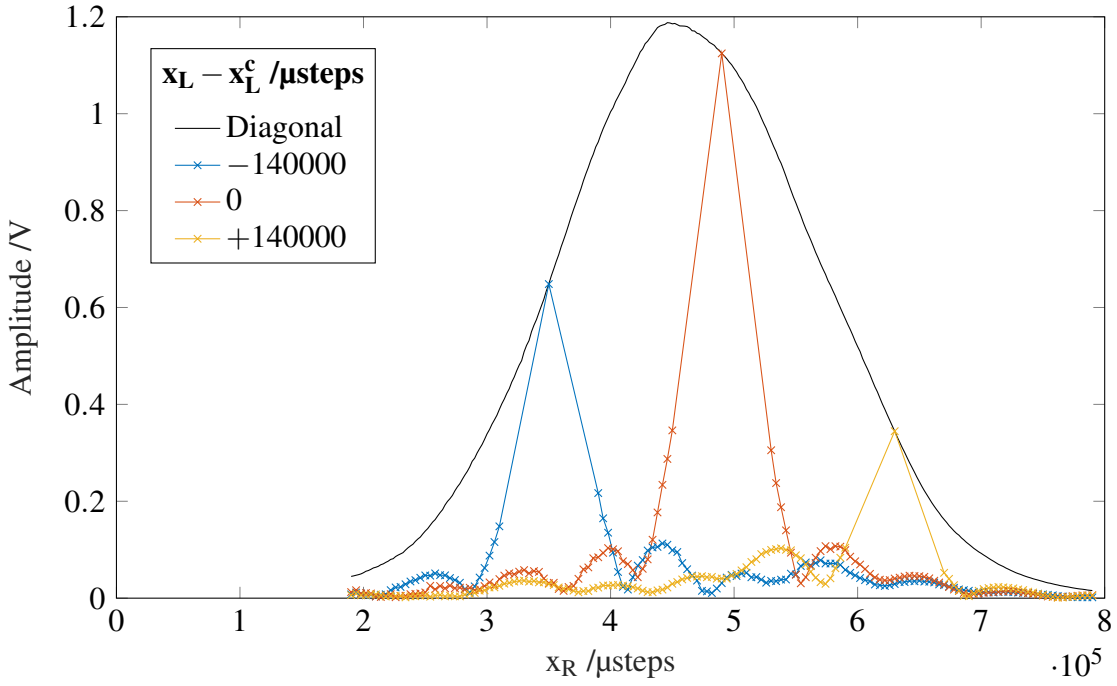

(a) FG050LGA-coupled system

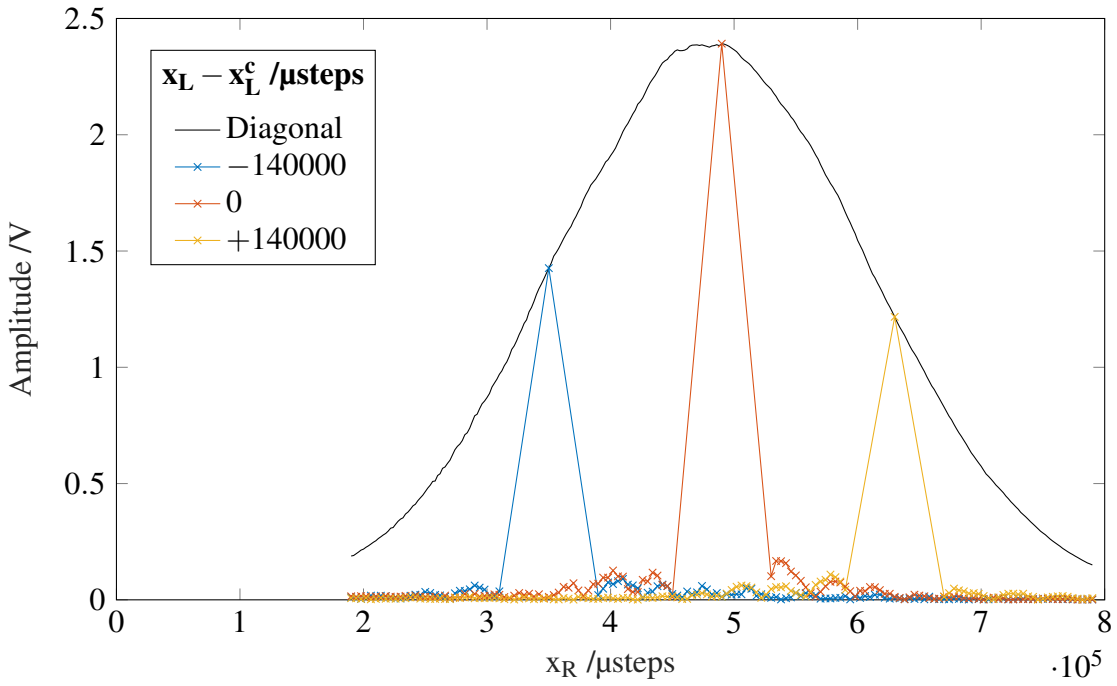

(b) Bare detector system

Fig. 6.16 Measured DRF fringe amplitude for fixed x_L values and along the DRF diagonal, for the FG050LGA-coupled and bare detector systems.

x_L values as in Figure 6.16, the coherence length is estimated to be 50 000 µsteps with the FG050LGA-coupled system in Figure 6.16a, compared to 20 000 µsteps for the bare detector in Figure 6.16b. These observations indicate a greater number of reception modes present in the detector-only system.

6.5 Discussion of Experimental Results

6.5.1 Qualitative Differences Between Modal Behaviors

It is helpful at this point to summarize the achievements attained, starting from a well-calibrated system and the successful observation of fringes with high SNR for sources in fixed positions. We have implemented a standardized experimental method to allow us to repeat fringe measurements for a large number of position pairs over which the sources are scanned. The resulting fringe amplitude datasets, represented as matrices with indices corresponding to the left and right source positions, display characteristic patterns depending on the number of modes present in the response of the device under test. We also remark that these results prove a critical hypothesis we had made during the design of our experimental system, in Chapter 4: coupling a highly multi-moded photodetector to a length of optical fiber creates a system whose modal behavior is determined by the fiber.

We can summarize the differences between systems coupled to single-mode, few-mode and multi-mode fibers:

- **Single-mode systems:** The fringe amplitude pattern is circular and has decreasing magnitude with off-center distance and source-to-source distance, reaching small but non-zero magnitudes at the extremes of the scanning range; the fringe coherence is nearly constant, with a value approximately equal to 0.9; we observed no significant difference between polarization-maintaining and other single-mode optical fibers.

- **Few-mode systems:** The fringe amplitude pattern has a main peak with a slightly oval shape, with decreasing magnitude to a zero amplitude line curved around the antidiagonal corners of the scanning range, and a minor peak beyond; the fringe coherence is quasi-constant near the center diagonal, with a zero-magnitude line similar to the fringe amplitude, and increases again to values approximately equal to 0.5 at the antidiagonal corners; the specific behavior is highly dependent on the coupled fiber's properties.

- **Multi-mode systems:** The fringe amplitude pattern has a diagonal structure, with consecutive peaks and zero-amplitude lines along the anti-diagonal; the fringe coherence

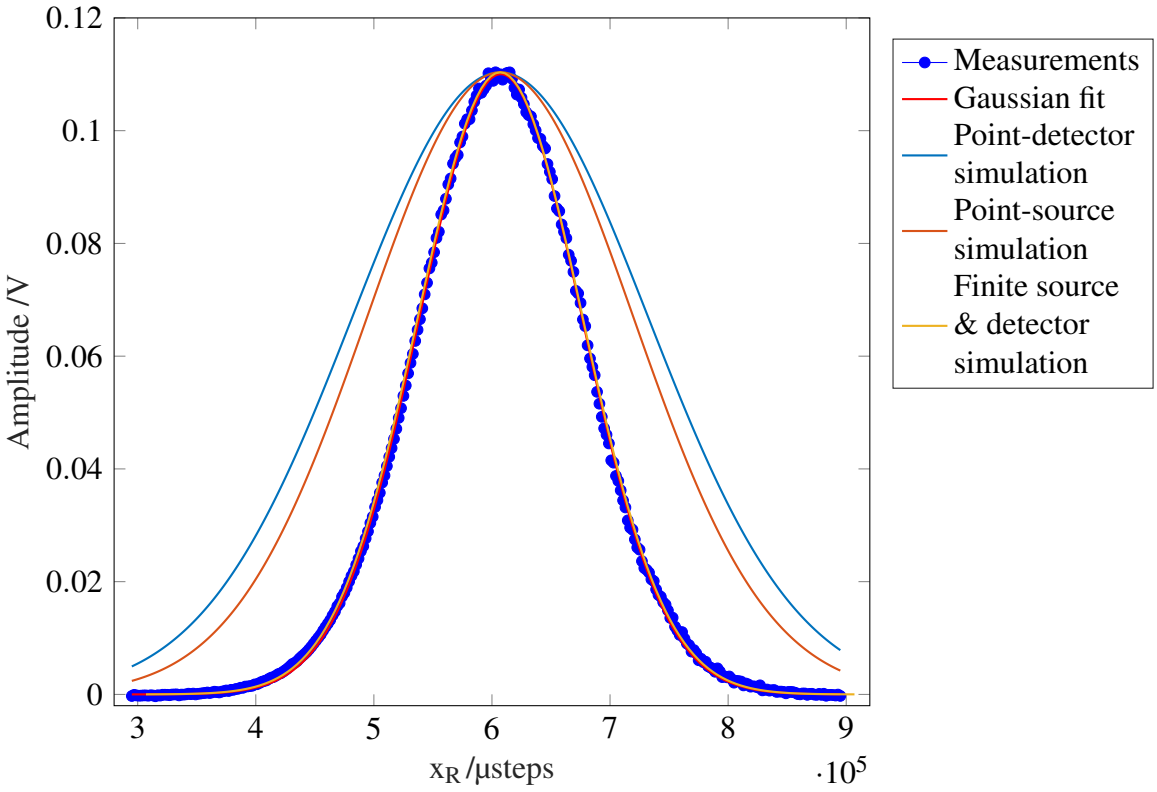

Fig. 6.17 Detector beampattern measured with right source, compared to simulations and least-square fit results.

is constant along the diagonals, and both the fringe visibility and coherence have much lower values than for lower-moded systems.

For all systems, we successfully measured the coherence length of the DRF from the width of the fringe amplitude structure. In Section 2.6.2, we had discussed a hypothesis that the number of modes is approximately equal to the ratio of the coherence length to the width of a single-source beampattern. This qualitative hypothesis is indeed observed in experimental datasets, and needs to be confirmed by a quantitative investigation: this will be discussed in Section 6.6.

6.5.2 Comparison with Simulations

It is instructive at this point to compare the wide variety of results obtained experimentally with the simulations performed in Chapter 3. We can start by investigating whether the shape and width of the single-source beampattern measurements corresponds to the results of simulations. There is however some ambiguity about how to accurately simulate this

configuration, where the distance between source and detector planes is assumed to be 105 mm, and the simulated sources are placed at the experimentally sampled positions:

- With a single-mode source of output beam radius $w_{0s} = 4.5\,\mu\text{m}$ and point-like detector;
- With a point-like source and a single-mode detector with beam radius $w_{0d} = 5\,\mu\text{m}$;
- With a single-mode source of output beam radius $w_{0s} = 5\,\mu\text{m}$ and a single-mode detector with beam radius $w_{0d} = 5\,\mu\text{m}$.

Figure 6.17 shows the comparison of the experimental dataset obtained by scanning the left source across the PM1550-XP fiber-coupled detector, its least-squares fit using a Gaussian functional form, and the results of these three simulations. We find that the first two simulated beampatterns, assuming either point-like sources or detector, have much larger width. On the other hand, the simulated beampattern assuming finite-sized sources and detector is in excellent agreement with the experimental data, and almost identical to the best least-squares fit. This indicates that the simulation framework described in Chapter 3 produces an accurate representation of experimental behavior.

For single-mode systems, the circular shape of the fringe amplitude and the quasi-constant pattern of the fringe coherence are in excellent agreement with simulations presented in Chapter 3. However, the value of the near-constant fringe coherence is experimentally found to be approximately 0.9, rather than the value of 1 expected from our numerical investigations. We believe that two main mechanisms contribute to lowering the fringe coherence value:

- Source misalignment: In an angular representation as was described by Equation (2.22), slightly misaligned sources imply not being able to scan the full two-dimensional two-position hypercone, thus never reaching the fully constructive and destructive interference between the sources that is required to obtain a unit fringe coherence.
- Polarization misalignment: The polarization alignment of the source beams was performed in Section 5.3.3 with a precision of a few degrees. A misalignment of this magnitude would imply imperfect coherence phenomena and reduce the fringe visibility and coherence.

Neither of these mechanisms is a fundamental defect of the EAI method, but rather features of any experimental system: there are opportunities for improvement, through alignment with higher sensitivity or calibration procedures.

At this point, it is also interesting to answer a question we had asked in Section 3.5.4: whether modes that compose the DRFs of fiber-coupled detectors are Linearly Polarized

(LP) modes, corresponding to the propagation modes inside an optical fiber, or Laguerre-Gaussian (LG) modes, describing the modes of circularly-symmetric beams in free-space. We had observed that the zero-amplitude line of a simulated two-mode system, near the antidiagonal corners of the measured DRF matrix, was concave for LG modes and convex for LP modes. We see in Section 6.4.2, using the zero-amplitude lines of the two-moded systems investigated, that the experimental behavior corresponds to the case of LG modes. It will be important to confirm these results using the DRF phase patterns, which will be discussed further in Chapter 8.

Using LG modes, we had also investigated in Section 3.4.4 the impact of changing the relative sensitivities of the modes, in the case of a two-moded DRF. In particular, we observed that the zero-amplitude line recedes towards the anti-diagonal corner as the ratio of the sensitivities of the first to the second mode increases, until it disappears from the matrix obtained for the chosen scanning range. This qualitative behavior is observed between the SM2000- and P1-23Z-coupled systems, and in some respects with the P1-32F-coupled system, although its behavior is further complicated by the effects of its large numerical aperture.

For multi-mode systems, the experimentally measured DRFs are qualitatively similar to the simulated DRFs presented in Chapter 3: the fringe amplitude structure has clear diagonal patterns, of width comparable to that of the simulated 121-moded system shown in Figure 3.11a. In particular, the latter displays a structure along the anti-diagonal with several consecutive minor peaks, resembling the patterns seen in Figure 6.14. We hypothesize that the strong diagonal pattern with small structure width observed in Figure 6.15 may require simulations with much larger numbers of modes.

6.6 Mode-Number Bounds

6.6.1 Theory

The results presented in Section 6.4 have enabled us to clearly differentiate between single-mode, few-mode and multi-mode regimes; we wish to go beyond this qualitative understanding and obtain a quantitative metric for the number of modes present in the system. Although the goal of EAI is to measure the eigenvalue spectrum of a DRF using the methods described in Chapter 2, it is beneficial to obtain the number of modes of the device under test without explicitly calculating the spectrum. In this section, we therefore derive and apply a technique to obtain a bound on the number of modes present in the system using only the measured DRF amplitudes. The starting hypothesis is that the number of modes is related to the number

of coherence lengths that can fit under a beampattern, which we had discussed in Section 2.6.2.

For now, we consider only two-source scans over one-dimensional sampling grids for co-aligned polarization, corresponding to our experimental configuration, barring imperfections in the system. In the reduced dimensionality problem, we can express the power absorbed in the detector analogously to Equation (2.19), as

$$P = \iint D(x,x')E(x,x')\,dxdx' \tag{6.5}$$

where $D(x,x')$ is the detector response function, $E(x,x')$ is the single-polarization incident field correlation function

$$E(x,x') = \langle E(x)E^*(x')\rangle, \tag{6.6}$$

and the integrals are taken over the domain of the sweep on the source plane. We approximate the sources as ideal point-like sources using delta-functions, and obtain the incident field at position x on the source plane:

$$E(x) = |E_1|\delta(x-x_1) + |E_2|e^{i\phi}\delta(x-x_2), \tag{6.7}$$

where $|E_1|$ and $|E_2|$ are the magnitudes of the two sources, labeled 1 and 2 and placed at positions x_1 and x_2 respectively. The output for a single source configuration (characterized by a set of values of x_1, x_2 and the relative phase between the sources ϕ) is then

$$P(x_1,x_2,\phi) = |E_1|^2D(x_1,x_1) + |E_2|^2D(x_2,x_2) + 2|E_1||E_2||D(x_1,x_2)|\cos(\phi + \mathrm{Arg}[D(x_1,x_2)]). \tag{6.8}$$

In Section 6.4, we effectively measured three functions: the single-source scans

$$f_{11}(x_1) = |E_1|^2D(x_1,x_1) \tag{6.9}$$

and

$$f_{22}(x_2) = |E_2|^2D(x_2,x_2), \tag{6.10}$$

along with the fringe amplitude

$$f_{12}(x_1,x_2) = 2|E_1||E_2||D(x_1,x_2)|. \tag{6.11}$$

We can then ask how we can use the measured function to estimate the number of reception modes of the system. We recall from Equation (2.35) that the detector response

function admits a decomposition

$$D(x_1,x_2) = \sum_{m=1}^{\infty} \lambda'_m U_m(x_1) U_m^*(x_2). \tag{6.12}$$

where the mode sensitivities λ'_m, which we will refer to as singular values, are real and positive and satisfy the orthogonality property

$$\int U_m^*(x) U_n(x)\, dx = \delta_{mn}. \tag{6.13}$$

In practice, only some finite subset of the singular values will be non-zero. Let N denote the number of modes with non-zero singular value and denote this set by $\{\lambda_m\}$, then we can simplify Equation (6.12) to

$$D(x_1,x_2) = \sum_{m=1}^{N} \lambda_m U_m(x_1) U_m^*(x_2), \tag{6.14}$$

with $\lambda_m > 0$, for all $m \in \{1,...,N\}$.

It is possible to obtain several sums over the singular values by integrating the detector response response function. Integrating Equation (6.9) over x_1, using Equation (6.14) to substitute for $D(x_1,x_1)$ and then using Equation (6.13), we find

$$\int f_{11}(x_1)\, dx_1 = |E_1|^2 \sum_{n=1}^{N} \lambda_n. \tag{6.15}$$

Repeating the process for $f_{22}(x_2)$, we have

$$\int f_{22}(x_2)\, dx_2 = |E_2|^2 \sum_{n=1}^{N} \lambda_n. \tag{6.16}$$

Now consider integrating $|f_{12}(x_1,x_2)|^2$ over both x_1 and x_2,

$$\iint |f_{12}(x_1,x_2)|^2\, dx_1 dx_2 = 4|E_1|^2|E_2|^2 \iint \Big| \sum_{m=1}^{N} \lambda_m U_m(x_1) U_m^*(x_2) \Big|^2 dx_1 dx_2. \tag{6.17}$$

The integral evaluates as

$$\begin{aligned}
&\iint \Big| \sum_{m=1}^{N} \lambda_m U_m(x_1) U_m^*(x_2) \Big|^2 dx_1 dx_2 \\
&= \sum_{m=1}^{N} \sum_{n=1}^{N} \iint \lambda_m \lambda_n^* U_m(x_1) U_n^*(x_1) U_m^*(x_2) U_n(x_2) dx_1 dx_2 \\
&= \sum_{m=1}^{N} \sum_{n=1}^{N} \lambda_m \lambda_n^* \delta_{mn} \\
&= \sum_{n=1}^{N} |\lambda_n|^2,
\end{aligned} \tag{6.18}$$

giving

$$\iint |f_{12}(x_1,x_2)|^2 dx_1 dx_2 = 4|E_1|^2 |E_2|^2 \sum_{n=1}^{N} \lambda_n^2. \tag{6.19}$$

Equations (6.17), (6.15) and (6.16) taken together imply

$$\frac{4\left(\int f_{11}(x_1)\,dx_1\right)\left(\int f_{22}(x_2)\,dx_2\right)}{\iint |f_{12}(x_1,x_2)|^2\,dx_1 dx_2} = \frac{\left(\sum_{n=1}^{N} \lambda_n\right)^2}{\sum_{n=1}^{N} \lambda_n^2}. \tag{6.20}$$

Notice that as formulated the source amplitude factors E_1 and E_2 drop-out; this ratio can be calculated without worrying about calibrating the amplitude of the sources.

A bound can be put on the value of Equation (6.20) by using the Chebyshev sum inequality [104]:

$$N \sum_{m=1}^{N} \lambda_m^2 \geq \Big(\sum_{n=1}^{N} \lambda_n \Big)^2, \tag{6.21}$$

which is the restricted case of Chebyshev's sum inequality for two series with equal terms. Combining Equations (6.21) and (6.20), we obtain the inequality

$$N \geq \frac{4 \int f_{11}(x_1)\,dx_1 \int f_{22}(x_2)\,dx_2}{\iint |f_{12}(x_1,x_2)|^2\,dx_1 dx_2}, \tag{6.22}$$

which provides an upper bound on the total number of modes N that have non-zero sensitivities.

As an alternative to N as measure of the number of modes, we can define an effective number of modes N_{eff}. Let $\lambda_{\max}$ be the largest λ_m. We define N_{eff} by

$$N_{\text{eff}} = \frac{\sum_{m=1}^{N} \lambda_m}{\lambda_{\max}}. \tag{6.23}$$

Physically, N_{eff} corresponds to the number of modes that would be required to absorb the same amount of power from an isotropic, spatially-incoherent, field (i.e. blackbody) as the actual mode structure of the detector if all the mode singular values where equal to $\lambda_{\max}$. Define a new set of values $\{\varepsilon_m\}$ by

$$\lambda_m = \lambda_{\max}\varepsilon_m. \tag{6.24}$$

By definition of $\lambda_{\max}$, we must have $0 < \varepsilon_m \leq 1$ for all m. The following inequality holds,

$$\sum_{m=1}^{N} \varepsilon_m^2 \leq \sum_{m=1}^{N} \varepsilon_m. \tag{6.25}$$

Multiplying both sides of Equation (6.25) by $\lambda_{\max}^2$ and using Equations (6.24) and (6.23) to simplify, we find

$$\sum_{m=1}^{M} \lambda_m^2 \leq \lambda_{\max}^2 N_{\text{eff}}, \tag{6.26}$$

then dividing both sides by the square of $\sum \lambda_m$ yields

$$\frac{\sum_{m=1}^{M} \lambda_m^2}{(\sum_{m=1}^{M} \lambda_m)^2} \leq \frac{1}{N_{\text{eff}}}. \tag{6.27}$$

Combining this inequality with Equation (6.20), we find

$$N_{\text{eff}} \leq \frac{4\int f_{11}(x_1)\,dx_1 \int f_{22}(x_2)\,dx_2}{\iint |f_{12}(x_1,x_2)|^2\,dx_1 dx_2}, \tag{6.28}$$

which provides a lower bound on the effective number of modes N_{eff}.

In summary, we have shown

$$N_{\text{eff}} \leq \frac{4\int f_{11}(x_1)\,dx_1 \int f_{22}(x_2)\,dx_2}{\iint |f_{12}(x_1,x_2)|^2\,dx_1 dx_2} \leq N, \tag{6.29}$$

where N is the number of modes in the singular-value decomposition of $D(x_1,x_2)$ with non-zero singular values and N_{eff} is an effective number of modes defined by

$$N_{\text{eff}} = \frac{\sum_{m=1}^{N} \lambda_m}{\lambda_{\max}}, \tag{6.30}$$

where $\lambda_{\max}$ is the largest member of $\{\lambda_m\}$. Thus we can use the ratio of the integrals to provide both an upper bound for N_{eff} and a lower bound for N.

The difference between N_{eff} and N essentially provides a measure of the spread of values within the set of singular values $\{\lambda_m\}$. To illustrate this, we first consider the case where all the λ_m are similar in value, i.e. $\lambda_m \approx \lambda_{\max}$ for all m. Then

$$N_{\text{eff}} = \frac{\sum_{m=1}^{N} \lambda_m}{\lambda_{\max}} \approx \frac{\lambda_{\max} \sum_{m=1}^{N} 1}{\lambda_{\max}} = N. \tag{6.31}$$

Therefore, low spread in singular values, i.e. when $(\lambda_{\max} - \lambda_{\min}) \ll \lambda_{\max}$, results in $N_{\text{eff}} \approx N$. Now consider the opposite limit, where one eigenvalue dominates over the others. Now we have

$$N_{\text{eff}} = \frac{\sum_{m=1}^{N} \lambda_m}{\lambda_{\max}} \approx \frac{\lambda_{\max}}{\lambda_{\max}} = 1, \tag{6.32}$$

indicating high spread, i.e. when $(\lambda_{\max} - \lambda_{\min}) \approx \lambda_{\max}$, gives low values of N_{eff}. As a result, we expect the integral ratio to give a very good measure of the number of modes when all of the modes are equally responsive, e.g. as expected for an optically large, uniform, absorber or for a very small absorber with unpolarized response. However, the estimate number of modes (as measured by the equality) will be be larger for intermediate systems where a few modes are excited with a range of singular values.

Finally, it is worth making a brief comment about the effect of experimental noise on this measure. The results have been derived assuming no noise. The presence of noise in the measurements effectively adds degrees of freedom to the measured detector response function and so will tend to increase N, assuming the noise has been made Hermitian, as will be the case in experimental datasets where we assume symmetry under the exchange of the sources. However, provided the signal-to-noise ratio is high, it will have little effect on N_{eff}. Therefore, we expect the estimated number of modes to be pulled up slightly by the presence of noise.

6.6.2 Example: Absorber with Finite Coherence Length

As an example, we consider a detector response function with some finite coherence length L over a region of size w, as given by

$$D(x_1, x_2) = \begin{cases} \alpha e^{-|x_2 - x_1|/L} & |x_1|, |x_2| \leq w/2 \\ 0 & \text{otherwise,} \end{cases} \tag{6.33}$$

where α is the appropriate normalization constant. This is the one-dimensional version of the finite-coherence DRF discussed in Section 3.6. Then for equal source amplitudes

$E_1 = E_2 = 1$, we have

$$\int f_{11}(x_1)\,dx_1 = \int f_{22}(x_2)\,dx_2 = \alpha \int_{-w/2}^{+w/2} dx = \alpha w \tag{6.34}$$

and

$$\begin{aligned}
\iint |f_{12}(x_1,x_2)|^2\,dx_1 dx_2 &= 4\alpha^2 \iint e^{-2|x_2-x_1|/L}\,dx_1 dx_2 \\
&= 8\alpha^2 \int_{-w/2}^{+w/2} \int_{-w/2}^{x_2} e^{-2(x_2-x_1)/L}\,dx_1 dx_2 \\
&= 8\alpha^2 \int_{-w/2}^{+w/2} e^{-2x_2/L} \int_{-w/2}^{x_2} e^{+2x_1/L}\,dx_1 dx_2 \\
&= 4\alpha^2 wL \left[1 + \frac{L}{2w}\left(e^{-2w/L} - 1\right)\right].
\end{aligned} \tag{6.35}$$

Applying Equation (6.29), we find

$$N_{\text{eff}} \leq \frac{w}{L}\left[1 + \frac{L}{2w}\left(e^{-2w/L} - 1\right)\right]^{-1} \leq N. \tag{6.36}$$

For $w/L \gg 1$, where the absorber size is much larger than the coherence length, we can approximate this result by

$$N_{\text{eff}} \leq \frac{w}{L} \leq N, \tag{6.37}$$

as we might have expected from physical reasoning about degrees of freedom. Now let

$$g(x) = x\left[1 + \frac{1}{2x}\left(e^{-2x} - 1\right)\right]^{-1} \tag{6.38}$$

which is simply the value of the integral ratio with $x = w/L$. For small $x = w/L$, we have

$$\begin{aligned}
g(x) &\approx x\left[1 + \frac{1}{2x}\left(1 - 2x + 2x^2 - \frac{4}{3}x^3 - 1\right)\right]^{-1} \\
&= x\left[x - \frac{2}{3}x^2\right]^{-1} \\
&\approx 1 + \frac{2}{3}x,
\end{aligned} \tag{6.39}$$

giving

$$N_{\text{eff}} \leq 1 + \frac{2w}{3L} \leq N. \tag{6.40}$$

This is what we expect, as there will always be at least one mode present however small the absorber is made.

6.6.3 Example: Positive-Definite Hermitian Matrices

This analysis maps over to the singular-value decomposition of Hermitian matrices. Let H be a Hermitian matrix, then Equation (6.29) becomes

$$N_{\text{eff}} \leq \frac{(\text{Tr}[H])^2}{\sum_{m,n} |H_{mn}|^2} \leq N, \tag{6.41}$$

where Tr[] denotes the trace of the matrix and the sum is taken over all matrix elements. We have implemented a program that generates a Hermitian matrix with a known number of non-zero singular values and then calculates N, N_{eff} and the central ratio in Equation (6.41), which we will refer to as the test-value. Repeating this algorithm for a wide variety of Hermitian matrices, it becomes evident that the test value tends to fall near to

$$\frac{(\text{Tr}[H])^2}{\sum_{m,n} |H_{mn}|^2} \approx \frac{N + N_{\text{eff}}}{2}. \tag{6.42}$$

This is an extremely useful observation, as it tells us the test value tends not favour one or other of N or N_{eff}, which should also map over to Equation (6.29). This is not guaranteed by the equality and gives us an extra piece of information. For example, we know

$$N_{\text{eff}} \geq 1. \tag{6.43}$$

Then taking Equation (6.42) as an equality, we have

$$\frac{(\text{Tr}[H])^2}{\sum_{m,n} |H_{mn}|^2} \geq \frac{N+1}{2} \quad \Longrightarrow \quad N \leq \frac{2(\text{Tr}[H])^2}{\sum_{m,n} |H_{mn}|^2} - 1. \tag{6.44}$$

Whereas Equation (6.29) provided a lower bound on N, this provides an approximate upper bound, which is informative in its own right but is also extremely useful when we try to calculate modal decompositions on full amplitude and phase data.

6.6.4 Application to Discrete Datasets

In this section, we briefly consider the details of how the method can be applied to DRF amplitudes obtained for discretely scanned sources, as would be relevant to simulated and experimental datasets. The integrals over the single source scans are easily treated numerically and we will concentrate on evaluating the integral over both coordinates of the detector response function. Throughout we will assume the absolute positions of the sources are known source that the sources can be put on the same grid of points $\{x_m\}$ in space.

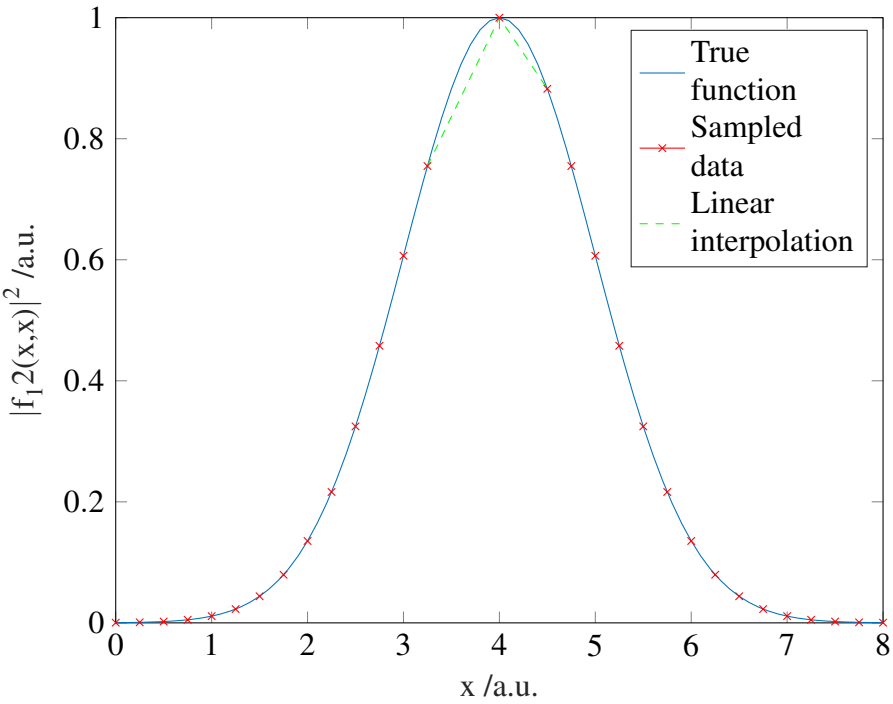

Fig. 6.18 Illustration of the linear interpolation for missing elements of a fringe amplitude pattern, for a fixed source position x'.

If we represent the sampled detector response as a matrix, as in Section 6.4, the problem is that we do not have access to the elements in a band along the diagonal due to restrictions on how closely the sources can be placed together. As a start, the single source scans can be used to fill in the on-diagonal elements. What we want for the integral is the quantity

$$|f_{12}(x,x)|^2 = 4|E_1|^2|E_2|^2|D(x,x)|^2. \tag{6.45}$$

However, given the single source scans are

$$f_{nn}(x) = |E_n|^2 D(x,x), \tag{6.46}$$

where $n \in \{1,2\}$ represents the source label, we have

$$|f_{12}(x,x)|^2 = 4|f_{11}(x)||f_{22}(x)|. \tag{6.47}$$

However, this still leaves some diagonals unfilled.

To see how to address this problem, we first consider the set of intermediate integrals of the form

$$I(x) = \int |f_{12}(x,x')|^2 \, dx' \tag{6.48}$$

that we must evaluate. The function to be integrated is illustrated in Fig. 6.18; the blue line shows the true function and the red crosses the sampled data as taken from the corresponding row of the matrix of fringe amplitudes, with the diagonal elements filled in using Equation (6.47). As can be seen, the problem is we are missing some data for small values of $|x-x'|$. The simple approach is to approximate the data in the gap by linear interpolation, represented by the green dotted line in Figure 6.18, which can be done automatically by using the trapezium rule with non-uniform node spacing for the numerical integration step [105]. The final integral can then be calculated using

$$\iint |f_{12}(x,x')|^2 \, dx dx' = \int I(x) \, dx, \tag{6.49}$$

where again the trapezium rule can be used to calculate the integral. This should provide a reasonable approximation to the integral, which can be improved by moving the sources back to widen the response pattern, at the expense of signal-to-noise ratio,

6.6.5 Application to Experimental Datasets

We then sought to apply to experimental results this method for placing bounds on the number of modes through which the device under test can absorb power. The algorithm described in Section 6.6.4 was implemented straightforwardly to accept the measured DRF matrices obtained in Section 6.4, where the unknown elements are excluded from the computation.

In Table 6.2, we summarize the results obtained by applying the algorithm to our various experimental datasets, part of which are presented in Section 6.4. The bound values obtained are consistent with our expectations: they are just above 1 for single-mode fibers, including few-mode fibers that are rolled on a mode scrambler; they are slightly larger than 2 for few-mode fibers expected to be 2-moded, and slightly below for the P1-32F which seemed to have smaller relative sensitivity; they are approximately equal to 8 for multi-mode systems. This observation for multi-mode devices may seem far from the expected 125 modes; however, this estimation was obtained assuming two-dimensional scans. As we are performing scans over a one-dimensional sampling grid, we are implicitly projecting all modes onto this restricted basis, where many of the modes are degenerate. The expected number of modes for one-dimensional scan is 11, such that the bound obtained with our method is quite accurate. The remaining discrepancy can be explained by the use of the single-source scan to fill the

Fiber name	Section	Configuration	Theoretical mode number	Computed bound
1550BHP	6.4.1		1	1.10
PM1550-XP	6.4.1		1	1.21
SM2000	6.4.2	>100 mm bend diameter	2	2.43
		>100 mm bend diameter vertical scan		2.08
		40 mm bend diameter		1.22
		40 mm bend diameter vertical scan		1.29
P1-23Z	6.4.2		2	1.83
P1-32F	6.4.2		4	1.53
FG050LGA	6.4.3	Step size 10 000 µsteps	11	7.91
		Step size 4 000 µsteps		7.87
Bare detector	6.4.3	Step size 10 000 µsteps	N/A	11.20
		Step size 4 000 µsteps		11.25

Table 6.2 Properties of the various 2 m-long optical fiber patch cables used as interchangeable mode filters for the photodetector, and their corresponding computed mode number bound; the experimental configuration is as described in Section 6.4, including the scanning step size of 4 000 µsteps, unless stated otherwise.

diagonal elements, which produces an artificially large fringe amplitude peak for multi-mode systems where the fringe amplitude structure is expected to have small widths, visible in Figure 6.16. This would increase the denominator in Equation (6.29), and decrease the computed bound. The results obtained for vertical scans, rather than horizontal, are identical; this is understood as the circular symmetry of the device under test's optical response.

Finally, the experimental procedure utilized in Section 6.4 was repeated using the photodetector without any coupled optical fiber length. The estimated number of modes obtained with the bound derived in Section 6.6.1 is approximately 11, higher even than with the multi-mode fiber. In Section 6.4.3, we had crudely estimated its modal behavior to contain 650 modes in two dimensions, hence approximately 25 for one-dimensional scans.

6.6.6 Entropy

In order to investigate the significance of the number of modes as defined by the quantities N and N_{eff}, we wish to compare them to other metrics related to the sensitivity eigenspectrum.

We can define an entropy-like measure S for the detector response function $D(x,x')$ by

$$S\left[D(x,x')\right] = -\sum_{m=1}^{N} p_m \ln p_m, \tag{6.50}$$

where

$$p_m = \frac{\lambda_m}{\sum_{n=1}^{N} \lambda_n} \tag{6.51}$$

are the normalized singular values for all $m \in \{1,...,N\}$, the latter being defined by Equation (6.14), satisfying the property

$$\sum_{n=1}^{N} p_n = 1. \tag{6.52}$$

As we have defined it, this "entropy" can be seen to have the same mathematical form as the Von-Neumann entropy of the density matrix in quantum mechanics, or the Shannon entropy in information theory [106]. As such, S as defined perhaps provides the best measure of the degrees of freedom of the detector response function, although we cannot calculate it in the first instance without phase data. However, we can put bounds on S and show that our measure of the mode number calculated from purely amplitude data must provide a rough estimate of S.

Since Equation (6.50) has the same mathematical form as the Shannon entropy, it is maximised when $p_1 = p_2 = \cdots = p_N$, or equivalently when the singular values λ_m are all equal. Explicitly, we must maximise S with respect to variations in the set of normalized singular values $\{p_m\}$ subject to Equation (6.52). To do so, we maximise the auxiliary function

$$L(p_1, p_2, \ldots, p_N) = S(p_1, p_2, \ldots, p_N) + \alpha \sum_{m=1}^{N} p_m, \tag{6.53}$$

where α is a Lagrange multiplier. At the stationary points of L, we have

$$\partial_{p_k} L(p_1, p_2, \ldots, p_N) = -\ln p_k - 1 + \alpha = 0 \tag{6.54}$$

for all $k \in \{1,...,N\}$. Equation (6.54) has one solution:

$$p_k = e^{\alpha - 1} \tag{6.55}$$

for any k. This corresponds to all λ_m equal to some constant κ and $S = \ln N$. To prove this is indeed a maximum, we differentiate Equation (6.54) again to yield the Hessian

$$\frac{\partial^2 L}{\partial p_j \partial p_k} = -\frac{\delta_{jk}}{p_k}, \tag{6.56}$$

which is negative definite as required. Hence we have shown

$$\exp(S) \leq N, \tag{6.57}$$

under all condition.

Using the definitions of ε_m and N_{eff} from previously, we may write

$$\begin{aligned} \exp(S) &= \exp\left(-\sum_{m=1}^{N} p_m \ln p_m\right) \\ &= \exp\left(-\sum_{m=1}^{N} \frac{\varepsilon_m}{N_{\text{eff}}} \ln \frac{\varepsilon_m}{N_{\text{eff}}}\right) \\ &= N_{\text{eff}} \exp\left(-\frac{1}{N_{\text{eff}}} \sum_{m=1}^{N} \varepsilon_m \ln \varepsilon_m\right). \end{aligned} \tag{6.58}$$

By definition, $0 < \varepsilon_m \leq 1$, which implies

$$-\varepsilon_m \ln \varepsilon_m > 0; \tag{6.59}$$

hence

$$-\sum_{m=1}^{N} \varepsilon_m \ln \varepsilon_m > 0. \tag{6.60}$$

The exponential term in Equation (6.58) is therefore always greater than unity and so

$$e^S \geq N_{\text{eff}}. \tag{6.61}$$

Combining Equations (6.57) and (6.61) yields

$$N_{\text{eff}} \leq \exp(S) \leq N, \tag{6.62}$$

which suggests the exponential of the entropy provides a measure of the modes in the same way as the measure calculated from only the amplitude data, in Equation (6.29). This is perhaps not unsurprising, as the entropy in thermodynamics is related to the logarithm of

the number of microstates available to the system that give the same measured macroscopic parameters; equivalent, very loosely, to the degrees of freedom of the system.

6.7 Conclusion

We have demonstrated that the near-infrared experimental system designed in Chapter 4 and constructed in Chapter 5 is capable of performing EAI on fiber-coupled infrared detectors with a large range of modal behaviors. Measurement of fringes in the detector output as the relative phase between the sources is modulated, first successfully presented in Chapter 5, was implemented in a standardized manner, for sources scanned over larger numbers of position pairs along a uniformly sampled one-dimensional grid. Using this method, we reported the first measurement of the DRF amplitude of near-infrared detectors.

We found that the extracted DRF amplitude, represented as a matrix in terms of the right and left source positions, and its corresponding coherence matrix, i.e. its amplitude corrected with the amplitudes of the single-source beampatterns at the corresponding positions, have patterns that are characteristic of single-mode, few-mode and multi-mode behaviors. This was achieved by creating a standard measurement set and experimental method, in which we first performed the single-source beampattern measurements of the right and left sources individually, and then measured the fringe in the detector output as we rotated the relative phase of the sources placed at all available position pairs. Multiple devices were investigated in this manner, with single-mode, few-mode and multi-mode behavior. For instance, we used our EAI method to show how tightly wrapping a few-mode optical fiber around a mandrel decreased the sensitivity of high-order modes until they have disappeared, experimentally proving the function of mode scramblers.

In addition, we demonstrated a method to estimate the number of modes present in a DRF using only the amplitude of its components, rather than its amplitude and phase; the measurement of the latter will be the subject of Chapters 7 and 8. The algorithmic implementation is able to deal with missing data, which appears in DRF amplitude matrices as an empty diagonal band. The resulting estimate provides a lower bound for the total number of modes in the optical response of the device under test and an upper bound for the number of modes that have approximately unit relative sensitivity. We found that applying this method to experimentally measured DRF quantitatively confirms our qualitative observations: the estimate for single-mode devices is approximately 1 and it increases approximately as the square root of the expected number of modes, as we are projecting the two-dimensional space of modes onto the one-dimensional space of scanned source positions.

A limitation of our existing experimental method is the presence of the missing data in the central diagonal band, which is expected to contain the most information characterizing the DRF. However, this is not a fundamental flaw of either EAI or the experimental system, but rather the result of a trade-off of far-field operation, between signal-to-noise ratio and angular resolution. Importantly, this has not impeded our qualitative and quantitative investigations of devices over a wide range of modal behaviors: the assessment of this limitation is indeed only possible because the experimental system's performance has exceeded our expectations in many other regards. In order to move beyond amplitude-only measurements of DRF elements, and to achieve the full characterization of the devices' optical response, the next step is to introduce a scheme to accurately measure the DRF phase.

Chapter 7

Phase-Sensitive Characterization: Theory and Design

7.1 Introduction

In Chapter 5, we observed experimentally that the extracted fringe phase measured with sources placed at fixed positions drifts over time. Figure 7.1 presents a typical example of this phenomenon, illustrating how a fringe drifts over a total measurement time of 8 seconds, corresponding to 20 000 periods of the 0.4 ms-long phase modulation period, at the selected 2.5 kHz phase modulation frequency. The total drift is approximately π rad over 8 seconds, which is typical of the phase drift observed with our experimental system. It is important to note that the evolution of the fringe phase is seemingly random and always smooth (i.e. without discontinuities), in the absence of extreme disturbances such as mechanical vibrations applied to the optical table.

This drift is consistent with environmental fluctuations affecting the optical fibers, leading to a slowly-varying differential phase between the two arms of the interferometer. For single-mode optical fibers, the expected phase shifts due to temperature fluctuations are approximately 100 rad/K/m [107]; those caused by pressure fluctuations are approximately 2 rad/Pa/m [108]; finally, those caused by strain fluctuations are estimated to be 10 rad/m [109]. In our experimental system, such mechanisms would need to apply to the differential temperature, pressure or strain variations between the interferometer's arms. Recalling that each arm is approximately 4 m long, the differential variations in temperature, pressure or strain expected in a laboratory environment have the appropriate order of magnitude to explain the observed phase drift between the two sources. For instance, a phase drift rate of

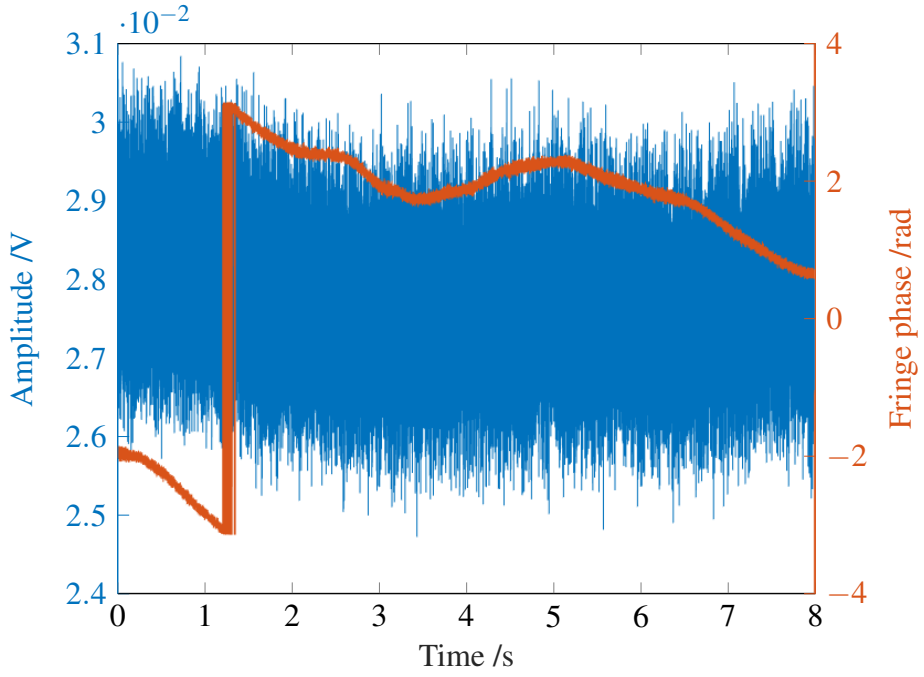

Fig. 7.1 Extracted fringe amplitude (blue) and phase (orange) for a 2 MS measurement at 250 kS/s sampling rate, with 2.5kHz phase modulation frequency; each point corresponds to the extracted fringe amplitude and phase (in blue and orange, respectively) for one 0.4 ms-long phase modulation period.

0.4 rad/s as observed in Figure 7.1 could be explained by a differential temperature variation of 1 mK over 1 s.

We also remark that such a large phase drift means that the measured fringe phase can be considered roughly 1 s. This is insufficient to produce DRF phase patterns corresponding to the DRF amplitude patterns measured in Chapter 6, as the two sources are scanned over large numbers of positions, taking an appreciable amount of time. Another concern is differential phase drifts occurring in the fibers as the interferometer's arms are moved. The required fringe phase stability is ideally several hours; even the minimum duration of fringe scan measurements, approximately 15 minutes obtained with a large step size of 20 000 µsteps, requires an additional phase correction method to be implemented.

In order to theoretically investigate methods that would allow us to experimentally correct the phase drift observed, the first goal set out for this chapter is to describe two classes of proposed solutions to this issue, based respectively on implementing a fiber-based system at the phase modulators' outputs and on adding a "reference" fiber-coupled detector near the device under test. We will argue why the latter extension to the experimental system was chosen over the former. A second objective is to investigate the effects of the phase correction scheme on the expected experimental results using numerical simulations. Additionally, we

seek to describe potential further improvements to the experimental system, in particular by reducing the distance between the reference detector and the device under test.

In Section 7.2, we discuss several potential phase correction methods based on analyzing the Lissajous figures obtained from two signals, either from time-domain splitting of the device under test's output or from the signal of additional photodetectors, fed by the split optical power output of the phase modulators. While these options were ultimately rejected, this discussion highlights the versatility of our experimental system and the potential for applications of EAI far beyond the study of near-infrared photodetectors. Section 7.3 describes a phase correction method based on measuring fringes in the output of a reference detector placed near the device under test, and subtracting the former's extracted fringe phase from the latter's. The reference detector is effectively used as a phase reference channel, and the plane of constant phase is moved from the plane of sources to the surface of this second channel. In particular, if the spatial distance between the reference and the device under test is reduced, the residual geometric phase is significantly diminished. In Section 7.4, we used the numerical framework built in Chapter 3 to accurately investigate the effect of the phase correction scheme using a reference channel. In particular, we prove that this technique does not affect the sensitivities of the reconstructed modes nor their amplitude patterns, rather only their phase patterns. Assuming that the DRF elements can be simulated numerically or measured experimentally, the numerical investigations demonstrate that phase-corrected DRFs contain a very large amount of information.

7.2 Fiber-based Correction Schemes

7.2.1 Introduction

In an EAI experiment, the phase-shift of the fringe must be measured against the relative phase between the sources. In a system with high phase-stability, it is sufficient to plot against the set value ψ of the phase modulator. However, in an unstable system the actual phase shift is $\psi + \Delta\phi(t)$, where $\Delta\phi(t)$ is a colored noise term. In general, the goal is to modify the current experimental system such that the optical power measured is related to $\cos(\psi + \Delta\phi(t))$ and/or $\sin(\psi + \Delta\phi(t))$. With ψ set by the phase modulator, $\Delta\phi(t)$ can be retrieved. If only ψ is known, the stability time of the phase may make comparing the phase of fringes within a sweep extremely difficult, or may even prevent the phase being measured at all. This had been observed in Chapter 6.

In this section, we propose several methods to measure the phase drift term $\Delta\phi(t)$, using fiber-based extensions of the experimental system at the outputs of the phase modulators.

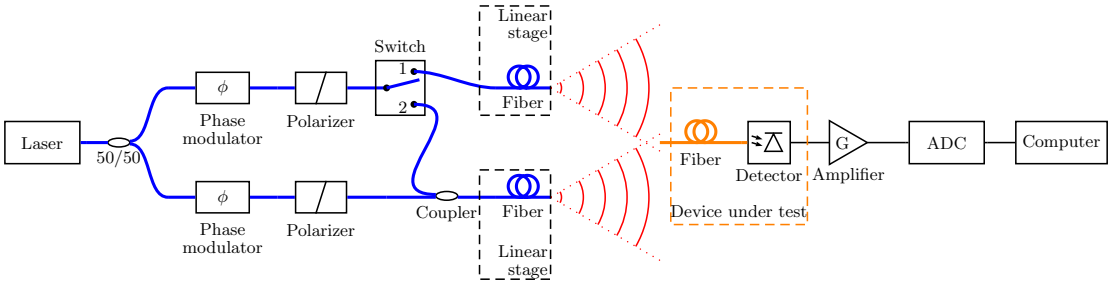

Fig. 7.2 Proposed experimental arrangement, using an optical switch and a beamcoupler to create a two-probe and a single-probe operation configurations.

Our objective is then to correct for the differential phase drift between the two arms of the experiment caused by environmental fluctuations on the fiber lengths between the beamsplitter and the outputs of the phase modulator pigtails.

7.2.2 Optical Switch

A first solution, illustrated in Figure 7.2, uses a single-pole double-throw optical switch to connect the outputs of the two phase modulators, labeled 1 and 2 in the figure, either to the two open-ended fiber probes as previously, or to a single probe. This experimental arrangement assumes that such optical switches are available; commercial components exist with lifetimes of the order of 10^9 cycles, and switching speeds approximately 1 ms, much smaller than the stability time of the phase drift. A beamcoupler is also needed, in order to combine the optical power into one of the probes, in the latter configuration. A 2x2 beamcoupler would be appropriate, using a beam dump on the tap output. The beamcouplers are built by fusing two fibers together, and the transfer of power from one fiber to another is obtained by evanescent wave coupling. The coupled signal has its phase shifted by $\pi/2$, with respect to the transmitted signal [110]. For instance, if the input signals are $\pi/2$ out of phase, then one output will have zero power (complete destructive interference) and the other will have the sum of input powers (complete constructive interference).

The usefulness of this method assumes that the major source of phase-drift is prior to the switch. It will not work, for example, if the switch or beamcoupler introduce significant drift, or there is significant drift in the differential path between the sources and the detector. In the following analysis, we will assume the phase shifts in the switch box and from propagation are time-independent.

In operation, the switch changes the system between two configurations. In the first, the two signals (un-shifted and shifted) drive separate probes, i.e. the normal experimental configuration. In the second, both signals are routed through the same probe to provide a

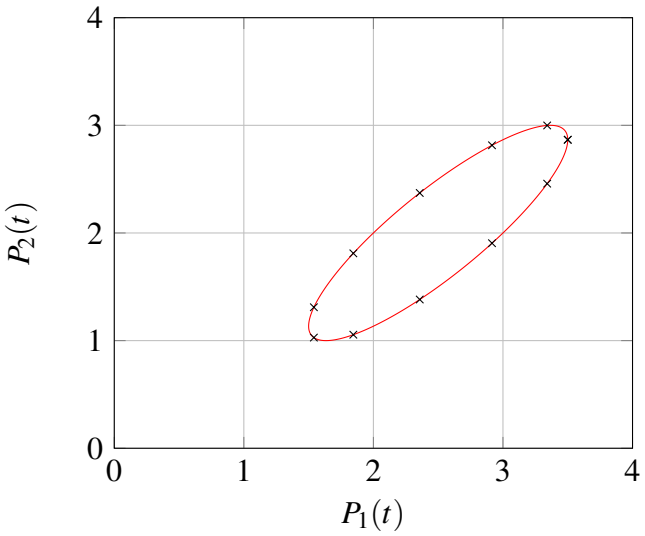

Fig. 7.3 Lissajous figure obtained from the near-simultaneous measurements in the two-source configuration P_1 and the re-routed single-source configuration P_2, as the relative phase ψ between the two arms of the system is rotated.

phase reference. In the first configuration, the measured fringe is

$$\begin{aligned} P_1(t) = {} & D_{AA}G_A^2G_{A1}^2E_1^2 + D_{BB}G_B^2G_{B2}^2E_2^2 \\ & + 2|D_{AB}|G_AG_BG_{A1}G_{B2}E_1E_2\cos\left(\psi(t)+\Delta\phi(t)+\phi_{BA}+\phi_B-\phi_A+\phi_{B2}-\phi_{A1}\right). \end{aligned} \tag{7.1}$$

Here the D_{mn} are the elements of the detector response matrix for the sources labeled A and B at positions m and n respectively, with ϕ_{BA} the phase of the fringe. E_1 and E_2 are the amplitudes of the input signals. G_A is the amplitude gain on propagation from emitter to detector and G_{A1} the gain along the path through the switch box from port 1 to emitter A, with ϕ_A and ϕ_{A1} the phase-shifts along the same paths. G_B, G_{B2}, ϕ_B and ϕ_{B2} are the equivalent quantities for the second path. In the second configuration, the measured fringe is

$$\begin{aligned} P_2(t) = {} & D_{AA}G_A^2G_{A1}^2E_1^2 + D_{AA}G_A^2G_{A2}^2E_2^2 \\ & + 2|D_{AA}|G_A^2G_{A1}G_{A2}E_1E_2\cos\left(\psi(t)+\Delta\phi(t)+\phi_{A2}-\phi_{A1}\right). \end{aligned} \tag{7.2}$$

Assume we can switch between the two configurations within a time δt. On an (x,y)-axis, we plot the set of points

$$(x_n,y_n) = (P_1(t_n),P_2(t_n+\delta t)), \tag{7.3}$$

where t_n denotes the time of the n^{th} sample. Provided we switch sufficiently quickly that $\psi(t+\delta t)+\Delta\phi(t+\delta t)\approx\psi(t)+\Delta\phi(t)$, the points should trace out a Lissajous figure as ψ is slowly varied with t [111], or even if $\Delta\phi$ is left to drift. This is illustrated in Figure 7.3.

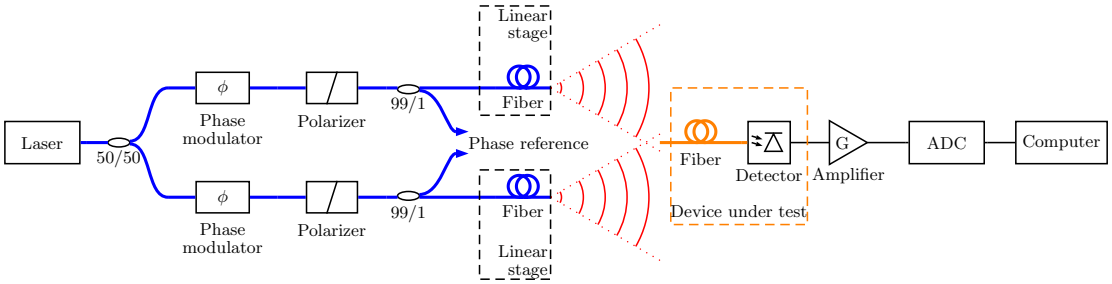

Fig. 7.4 Proposed extension to the experimental system, with 99%-1% beamcouplers added to create a phase reference.

By fitting an ellipse to the figure and noting the direction of rotation with increasing ψ, it is possible to extract the phase shift θ between the oscillations in the two directions, which from (7.1) and (7.2) is

$$\theta \approx \phi_{BA} + \phi_B - \phi_A + \phi_{B2} - \phi_{A2}. \tag{7.4}$$

This allows measurement of the phase shift of the fringe, comprising the detector response and the path difference between the sources. The additional term $\phi_{B2} - \phi_{A2}$ is constant within our assumptions. The attraction of fitting an ellipse to the Lissajous figure is we do not have to assign a phase to each point before fitting, which is why we can deal with drifts.

7.2.3 Beamcoupler-based Methods

The methods presented in this section are discussed as if we were looking to measure the relative phase difference between the two arms of the experiment, at the output of the phase modulators. We therefore disregard the free-space section, i.e. (i) the 50 cm polarization-maintaining optical fibers whose respective outputs are mounted on the motorized stages, (ii) the air over the source-to-detector distance, and (iii) the optical fiber connected to the detector. In order to use these methods in parallel with the normal operation of the EAI experiment, we suggest inserting 20 dB beamsplitters at the output of the phase modulators, as illustrated in Figure 7.4. The 1% of redirected optical power is used to create the phase reference channel, following one of three schemes below. For simplicity, we assume that the power redirected from each arm is equal to $P_0/2$.

I. 2x2 beamcoupler

A first solution based on a standard fiber-based Mach-Zehnder interferometer [113] is illustrated in Figure 7.5. A 2x2 beamcoupler is used to recombine the arms of the interferometer.

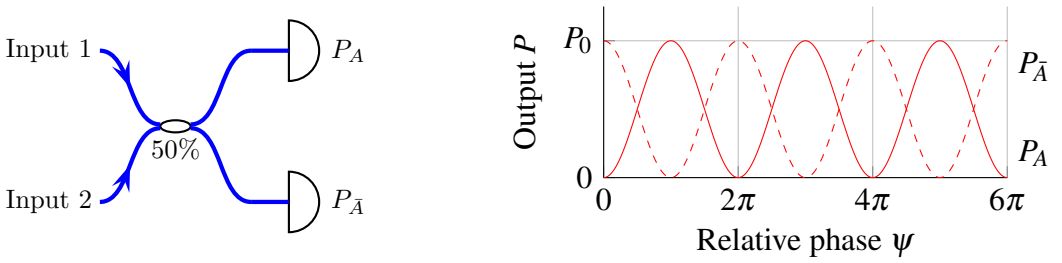

(a) Experimental arrangement (b) Detector output

Fig. 7.5 Phase reference system with one 2x2 output coupler, a fiber-optic Mach-Zehnder interferometer; adapted from [112].

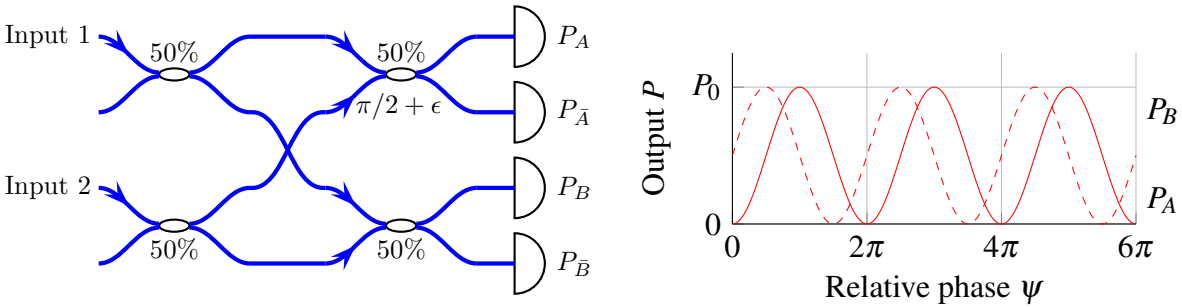

(a) Experimental arrangement (b) Detector output

Fig. 7.6 Phase reference system with four 2x2 output couplers; adapted from [112].

Its outputs are then given by

$$P_{A,\bar{A}} = \frac{P_0}{2}[1 \mp \cos(\psi + \Delta\phi(t))]. \tag{7.5}$$

As the two outputs are π out of phase, we can avoid uncertainties linked to low signal by measuring the two outputs simultaneously. For instance, we may consider $\Delta P = P_{\bar{A}} - P_A = 2\cos(\psi + \Delta\phi(t))$. Note however that the sensitivity of this setup is still dependent on the relative phase $\psi + \Delta\phi(t)$, and maximal when $P_{A,\bar{A}} = P_0/2$. The main drawback here is that we do not measure $\psi + \Delta\phi(t)$ directly, but rather only its cosine.

II. Four 2x2 beamcoupler set

In order to obtain an instantaneous measurement of the relative phase between the two arms of the experiment, we need to utilize more elaborate methods. A first possibility based on four 2x2 beamcouplers is illustrated in Figure 7.6, and is referred to as a Passive Quadrature Demodulator [112]. This method is based on an output coupler matrix, constructed with

four 2x2 beamcouplers: the two arms of the experiment are each connected to one input of two couplers, whose outputs are then crossed into the inputs of two additional couplers. The outputs of one of the final couplers, called A, are then simply that of a Mach-Zehnder interferometer:

$$P_{A,\bar{A}} = \frac{P_0}{2}[1 \mp \cos(\psi + \Delta\phi(t))]. \tag{7.6}$$

The outputs of the other final coupler, called B, can be shown to have the form

$$\begin{aligned} P_{B,\bar{B}} &= \frac{P_0}{2}[1 \mp \cos(\psi + \Delta\phi(t) + \eta_{AB})] \\ &= \frac{P_0}{2}[1 \pm \sin(\psi + \Delta\phi(t) + \varepsilon)], \end{aligned} \tag{7.7}$$

where we have used the differential phase shift η_{AB} to define the phase shift error ε as

$$\begin{aligned} \eta_{AB} &= \frac{2\pi n \Delta l}{\lambda} = (2N+1)\frac{\pi}{2} + \varepsilon \\ \implies \varepsilon &= \frac{2\pi n \Delta l}{\lambda} - (2N+1)\frac{\pi}{2}, \end{aligned} \tag{7.8}$$

and $\Delta l = (l_{13} - l_{23}) - (l_{14} - l_{24})$ is the differential pathlength of the coupler matrix.

Consider then the difference between the outputs of each of the two final couplers:

$$\begin{aligned} \Delta P_A &= P_A - P_{\bar{A}} = -P_0 \cos(\psi + \Delta\phi(t)) \\ \Delta P_B &= P_B - P_{\bar{B}} = P_0 \sin(\psi + \Delta\phi(t) + \varepsilon). \end{aligned} \tag{7.9}$$

Approaches are suggested in the literature to obtain only the slowly-varying $\Delta\phi(t)$, including a variety using Lissajous patterns [34]. It remains however that this technique is complicated by the appearance of the extra phase contribution ε, which may itself be subject to drift caused by temperature or pressure variations within the coupler matrix.

III. 3x3 beamcoupler

Another system, based on the Mach-Zehnder interferometer architecture with a 3x3 output beamcoupler, avoids these complications. The experimental apparatus, illustrated in Figure 7.7, is significantly simpler than the 2x2 coupler matrix, and provides an elegant way of retrieving the relative phase difference of interest [114].

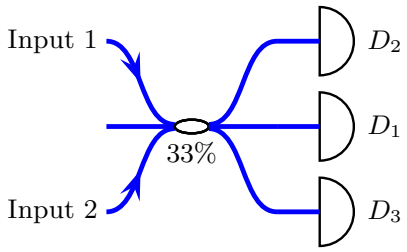

Fig. 7.7 Optical system with a 3x3 output coupler; adapted from [114].

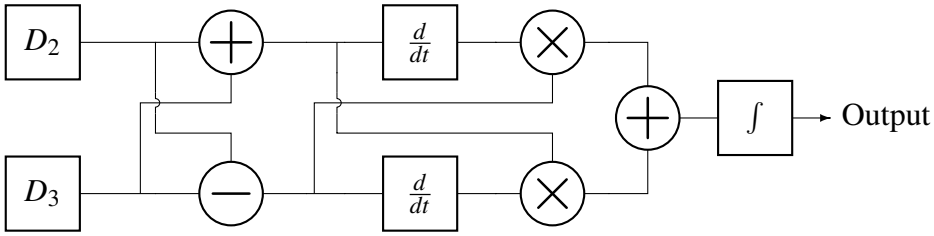

Fig. 7.8 Electronic system to process the output of the 3x3 output coupler apparatus; adapted from [114].

This technique is based on the ability to obtain two optical outputs, X and Y, with a $\pi/2$ phase difference:

$$\begin{aligned} X &= A\cos(\theta) \\ Y &= B\sin(\theta), \end{aligned} \tag{7.10}$$

where A and B are constants, and θ denotes the relative phase between the two input arms of the interferometer, which we wish to measure. Then, we can apply the following functional operation:

$$\begin{aligned} Z &= X\frac{\partial Y}{\partial t} - \frac{\partial X}{\partial t}Y \\ &= AB\frac{\partial \theta}{\partial t}[\cos^2(\theta) + \sin^2(\theta)] \\ &= AB\frac{\partial \theta}{\partial t} \\ \Longrightarrow Z' &= \int Z dt = AB\theta. \end{aligned} \tag{7.11}$$

This produces a value that is directly proportional to θ.

In order to obtain forms similar to X and Y in Equation (7.10), we can use a 3x3 beamcoupler with the arms of the interferometer connected to inputs 2 and 3. The outputs of the 3x3 coupler, P_i with $i \in \{I, II, III\}$, are given by

$$\begin{aligned} P_I &= -B_2[1+\cos(\theta)] \\ P_{II,III} &= B_1 + B_2\cos(\theta) \pm B_3\sin(\theta), \end{aligned} \tag{7.12}$$

where $B_i, i \in \{1,2,3\}$, are constants dependent only on the coupling coefficients of the coupler [115]. We then consider the sum and difference of $P_{II,III}$,

$$\begin{aligned} P^+ &= P_{II} + P_{III} = 2[B_1 + B_2\cos(\theta)] \\ P^- &= P_{II} - P_{III} = 2B_3\sin(\theta). \end{aligned} \tag{7.13}$$

IV. Processing

Processing these signals as suggested above, we obtain

$$\begin{aligned} D &= P^+\frac{\partial P^-}{\partial t} - \frac{\partial P^+}{\partial t}P^- \\ &= 4B_1B_3\frac{\partial\theta}{\partial t}\cos(\theta) + 4B_2B_3\frac{\partial\theta}{\partial t} \end{aligned} \tag{7.14}$$

$$E = \int D dt = 4B_1B_3\sin(\theta) + 4B_2B_3\theta. \tag{7.15}$$

As B_1 is simply the DC component of $P_{II,III}$, we may introduce an offset to set $B_1 = 0$. Then,

$$\begin{aligned} D &= 4B_2B_3\frac{\partial\theta}{\partial t} \\ \implies E &= \int D dt = 4B_2B_3\theta. \end{aligned} \tag{7.16}$$

An important advantage of this scheme is the absence of additional phase drift in the measurement section, unlike in the 2x2 coupler matrix case for instance. This simplifies the direct recovery of the relative phase shift $\theta = \psi + \Delta\phi(t)$. The processing step detailed in Equation (7.11) can be obtained in software or using electronic hardware, as described in Figure 7.8.

An alternative way of retrieving the relative phase shift θ is to use the Lissajous figures described by the two channels' voltage outputs [30]. It assumes that the two outputs voltages

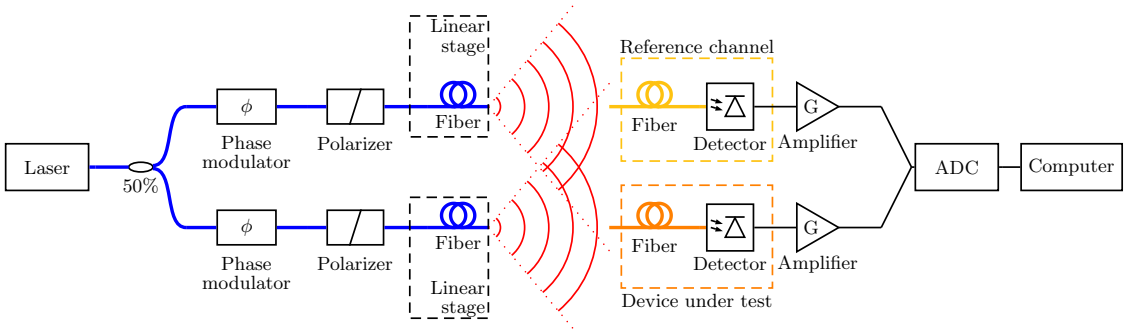

Fig. 7.9 Schematic drawing of extended experimental system, with a reference channel constructed using a reference fiber and amplified detector (yellow).

of an IQ mixer can be measured as

$$\begin{aligned} I &= I_0 + A_I \cos(\theta) \\ Q &= Q_0 + A_Q \cos(\theta + \gamma). \end{aligned} \tag{7.17}$$

Comparing with Equation (7.13), we expect to obtain $I_0 = 2B_1, Q_0 = 0, A_I = 2B_2, A_Q = 2B_3, \gamma = \pi/2$. For a non-ideal IQ mixer, these two outputs produce an ellipse, centered at (I_0, Q_0). As we modulate the phase using the phase shifter to obtain fringes from the device under test, we also produce the required θ-sweep to trace the ellipse. Fitting this ellipse to extract the half long axis a, half short axis b, and the orientation angle Φ, we can retrieve the mixer parameters as

$$\begin{aligned} A_I &= \sqrt{a^2 \cos^2\Phi + b^2 \sin^2\Phi} \\ A_Q &= \sqrt{a^2 \sin^2\Phi + b^2 \cos^2\Phi} \\ \gamma &= \arctan\frac{b\sin\Phi}{a\cos\Phi} + \arctan\frac{b\cos\Phi}{a\sin\Phi} - \pi. \end{aligned} \tag{7.18}$$

7.3 Reference Channel

7.3.1 Experimental Scheme

While the methods described in Section 7.2 correct for phase drifts caused by environmental variations in the optical fiber system up to the output of the phase modulators, they require long additional optical fiber systems to be added, in which phase drifts could appear as well. Moreover, none addresses a second key phenomenon: the fast wrapping of the fringe phase pattern as either or both of the sources are scanned. Indeed, as the 1550 nm wavelength

is significantly smaller than path length differences of the spherical wavefront between successive positions to which each of the sources is scanned, we expect the phase of the fringes recorded in the detector output to vary quickly, up to several radians for consecutive position pairs such that it wraps on the $[0, 2\pi]$ rad range. This had been observed in Chapter 3 in the form of irregular phase patterns, which were explained as a fast-wrapping phase pattern aliased by the relatively large spatial resolution used in the simulations, i.e. step size between neighboring sampled source positions.

Instead of modifying the section of the experiment producing and controlling the sources, a second class of phase correction methods can be obtained through the addition of a second detector system near the device under test, i.e. by modifying the section of the experiment dealing with signal detection. The experimental arrangement is schematized in Figure 7.9. The outputs of these two detector systems then constitute two channels: the "signal" channel is the device under test, including the interchangeable fiber, and the "reference" channel provides the simultaneous phase reference. In practice, the two channels' optical fibers are held at constant displacement throughout fringe measurements over scanned source positions and are coupled to independent detectors. Subtracting the fringe phase extracted in the reference channel from the signal channel's produces a corrected fringe phase, whose pattern can be presented and analyzed in the same way that we did with the fringe amplitude patterns in Chapter 6. The scheme should also take out to some extent imperfections in the FFT used to extract the fringe parameters, as long as the data sets are collected simultaneously, for instance on two inputs of the same ADC; additionally, the phase noise in the laser source is removed, out to the bandwidth determined by the sampling and FFT.

An important advantage of this method is that it does not require any change to the optical configuration for the sources. As the channels operate independently, each can be checked on its own against the results obtained before the system extension, presented in Chapter 6. This arrangement provides a total correction of the phase drift for mechanisms affecting the fiber system from the laser source up to the source fibers' open ends, as well as significant correction of air refractive index fluctuations on the optical path between probe tips and detector fiber surfaces, because the signal and reference channel beams essentially share the same volume of space. A second crucial advantage is to move the constant-phase plane from the source tips to the reference detector fiber input. In practice, the fringe phase wraps much less rapidly as the sources are scanned towards and away from the on-axis position, as an intrinsic effect of the scheme. Additionally, as the scanning plane is moved closer to the source, the reference wavefront automatically adjusts. The phase correction method also decreases the effect of imperfections in the scanning plane, and sampling points used; for example, if the scanning plane is tilted or varies from one scan to the next.

In addition to element-wise subtracting the reference and signal channels' extracted fringe phases, numerous analysis methods are possible. For instance, we could look at the correlations between the two recorded phases, or produce Lissajous figures on the basis of the recorded outputs and analyze them as suggested in Section 7.2.3. Regarding the diagonalization of the corrected-phase DRF to obtain its modes, if the individual modes of the device under test have significantly different phase centres, these would show up through the radii of curvature left over after a common reference phase front had been subtracted. This phase correction method also has the potential to be extended further. For instance, three reference fibers could be used to define a plane against which the positions of the pixels in a photodetector array could be measured.

A few limitations to this scheme should be noted. The reference beam must have an appreciable response over the region for which the device under test has an appreciable response. Assuming that the beam width of the sources are the limiting factor, as is the case in our experimental system and was discussed in Chapter 6, this requires the signal and reference channels to be spatially close. Note however that we could also expand the reference beam to have a wide angle, say using a lens or an optical fiber with a shaped tip [90]; this avenue will be discussed further in Chapter 10. A second limitation may appear when the SNR of the reference is low: the phase of the reference would rotate over a full 2π rad, and it would not be helpful to subtract it off. Additional precautions, such as placing an SNR-dependent coefficient on the subtracted phase, may be necessary in experimental realizations of this scheme.

7.3.2 Simulated DRF Corrected Phase

Considering only the fringe phase and discarding its amplitude, a simulation framework can be created for the study of geometric phase factors. For simplicity, we model the detectors and sources as point-like objects with spherical phasefronts, as we had done in Section 3.3. Assuming a point-like detector, its DRF can be written as $\overline{\overline{\mathbf{D}}}(\boldsymbol{r}_1, \boldsymbol{r}_2) = \delta(\boldsymbol{r}_1 - \boldsymbol{r}_2)$, where $\boldsymbol{r}_1$ and $\boldsymbol{r}_2$ are positions on the chosen reference surface. For point-like detectors, we can also choose the reference surface to be the detector surface: $\mathscr{S} = \boldsymbol{r}_d$. A point-like source with spherical phasefront at the sampled position labeled n produces a field $\boldsymbol{e}_n(\boldsymbol{r}) \propto \exp[i\boldsymbol{k} \cdot (\boldsymbol{r}_n - \boldsymbol{r})]$, where $\boldsymbol{k}$ is the source beam wavevector, as defined in Chapter 2.

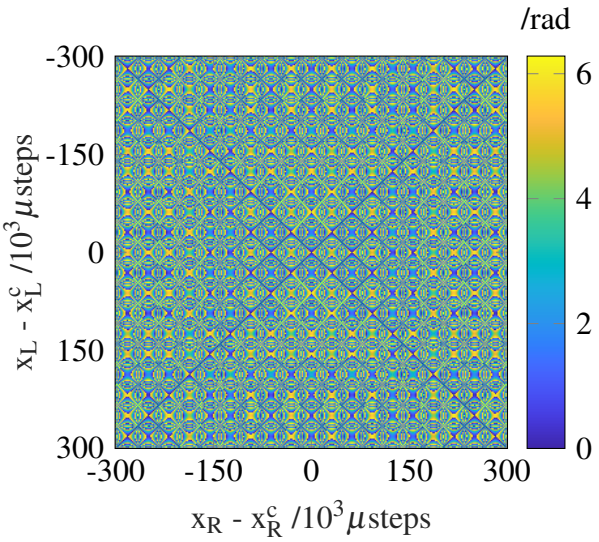

(a) Single detector case; placed opposite center of scanning range

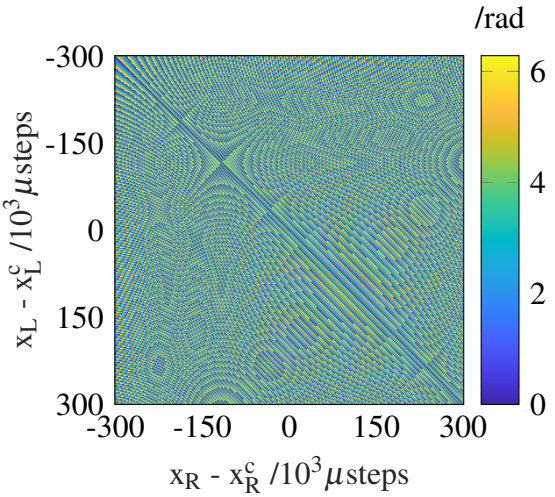

(b) Difference of two measured fringe phases; second detector placed 10 mm right of the first

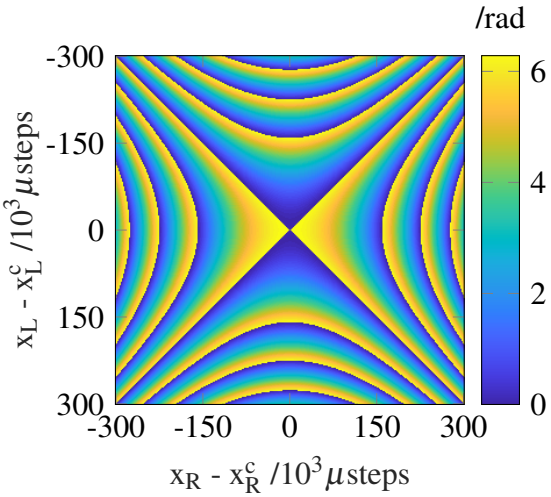

(c) Difference of two measured fringe phases; second detector placed 10 mm above the first

Fig. 7.10 Simulated fringe phase for various detection systems, as a function of sources' positions; the sources are scanned horizontally over a 30 mm range opposite detectors placed at a distance $z = 100$ mm.

We then obtain the following form for the measured DRF elements, from Equation (2.46):

$$D_{mn} \propto \iint_{\mathscr{S}^2} \boldsymbol{e}_m^*(\boldsymbol{r}_1) \cdot \overline{\overline{\mathbf{D}}}(\boldsymbol{r}_1, \boldsymbol{r}_2) \cdot \boldsymbol{e}_n(\boldsymbol{r}_2) d^2\boldsymbol{r}_1 d^2\boldsymbol{r}_2 \tag{7.19}$$

$$\propto \int_{\mathscr{S}} \boldsymbol{e}_m^*(\boldsymbol{r}) \cdot \boldsymbol{e}_n(\boldsymbol{r}) d^2\boldsymbol{r}$$

$$\propto \boldsymbol{e}_m^*(\boldsymbol{r}_d) \cdot \boldsymbol{e}_n(\boldsymbol{r}_d)$$

$$\propto \exp[i\boldsymbol{k} \cdot (\boldsymbol{r}_n - \boldsymbol{r}_d) - i\boldsymbol{k} \cdot (\boldsymbol{r}_m - \boldsymbol{r}_d)]. \tag{7.20}$$

While obtaining the fringe amplitude requires a full projection of the source beam, we are only interested in the fringe phase, more specifically the difference of measured phases between two detectors, labeled A and B:

$$\begin{aligned}\phi_{AB} &= arg(D^A_{mn}) - arg(D^B_{mn}) \qquad (7.21)\\ &= [\boldsymbol{k}\cdot(\boldsymbol{r}_n-\boldsymbol{r}_A)-\boldsymbol{k}\cdot(\boldsymbol{r}_m-\boldsymbol{r}_A)]-[\boldsymbol{k}\cdot(\boldsymbol{r}_n-\boldsymbol{r}_B)-\boldsymbol{k}\cdot(\boldsymbol{r}_m-\boldsymbol{r}_B)]\\ &= [k|\boldsymbol{r}_n-\boldsymbol{r}_A|-k|\boldsymbol{r}_m-\boldsymbol{r}_A|]-[k|\boldsymbol{r}_n-\boldsymbol{r}_B|-k|\boldsymbol{r}_m-\boldsymbol{r}_B|] \qquad (7.22)\end{aligned}$$

as $\boldsymbol{k}$ and $\boldsymbol{r}_n-\boldsymbol{r}_d$, for $d\in\{A,B\}$ are always colinear in point-like objects.

In Figure 7.10, we show the results of numerical simulations obtained using this simplified framework, where the source-to-detector distance is set to 100 mm and the sources are scanned over the position pairs $(x_R,x_L)\in\{-15\,\text{mm},-14.8\,\text{mm},...,15\,\text{mm}\}^2$, with $y_R=y_L=z_R=z_L=0\,\text{mm}$. Note that these values are specifically chosen to replicate the configuration of the experimental system. Two notable exceptions are that the source-to-detector distance is 105 mm in practice, and the sources are scanned from -300 000 µsteps to +300 000 µsteps, i.e. from -14.3 mm to +14.3 mm. These differences nearly cancel each other out, as the ratio of the experimental to numerical distances, $105/100=1.05$, is nearly equal to the ratio of the experimental to numerical scanning ranges, $15/14.3=1.049$. Figure 7.10a presents the simulated fringe phase measured by one on-axis detector, with no phase correction, displaying a very complex structure associated with aliased fast-wrapping phase contributions as the sources are scanned off-axis; the same configuration was simulated without simplifying assumptions in Chapter 3. Figure 7.10b presents the difference between this DRF phase and that obtained with a reference placed at $(x,y)=(10,0)$ mm, i.e. offset along the x-axis with respect to the signal channel. The corrected DRF phase pattern is evidently altered, but still varies very fast between neighboring source position pairs. On the other hand, the DRF phase pattern obtained with a reference channel placed at $(x,y)=(0,10)$ mm, i.e. displaced by the same magnitude along the y-axis with respect to the signal channel, varies much more slowly, as shown in Figure 7.10c. We note that, simulating a second detector at the same position as the first, we effectively correct the device under test's phase with itself and obtain a constant phase pattern. This corresponds to a change of the constant-phase plane from the source plane to the surface of the reference detector.

A crucial result is that the phase correction method is most effective when the two detectors positions are offset in the direction orthogonal to the scanning direction. Under the experimental scanning configuration used in Chapter 6, where the sources were scanned over a horizontal one-dimensional grid, we would need to place the two detectors vertically with respect to each other. More complex cases can be simulated using the framework built in

Chapter 3, for instance to deal with few-mode and multi-mode detector responses, and will be discussed in Section 7.4.

7.3.3 Effect of Phase-Correction on Eigenmodes and Eigenspectrum

It is crucial to investigate theoretically whether this two-detector phase correction scheme will influence, or perhaps even limit, our ability to successfully perform EAI, i.e. to measure the device under test's true DRF and its decomposition into the system's natural modes. Suppose that we have a single-mode reference detector (RD) whose amplitude pattern is as least as extensive as the amplitude pattern of the primary device under test (DUT). We can measure the response matrix of the RD, R, at that same time as response matrix D of the DUT itself without any loss of time or source power.

Suppose that the correlation matrices of both detectors are measured on a point-by-point basis as the sources are scanned over sampled position pairs. For an ideal measurement system, the elements of the two matrices are D_{ij} and R_{ij}. Suppose, however, that the system has poor phase stability; then we actually measure

$$\begin{aligned} D_{ij}^{m} &= D_{ij} e^{-i\Delta_{ij}} \\ R_{ij}^{m} &= R_{ij} e^{-i\Delta_{ij}}. \end{aligned} \tag{7.23}$$

The phase error is the same on both measurements because we are assuming that the outputs of the DUT and RD can be read out on a differential timescale that is much smaller than the phase coherence time of the test system.

Because the RD is single mode, it has the decomposition

$$\begin{aligned} \mathsf{R} &= r\mathsf{r}\mathsf{r}^{\dagger} \\ R_{ij} &= r r_i r_j e^{i(\phi_i - \phi_j)} \\ R_{ij}^{m} &= r r_i r_j e^{i(\phi_i - \phi_j)} e^{-\Delta_{ij}}, \end{aligned} \tag{7.24}$$

where r is the eigenvalue, and r is the column eigenvector of the reference detector, where $r_i \exp[i\phi_i]$ is the field pattern of the mode.

We can divide each element of R_{ij}^{m} by its modulus to obtain its phase,

$$R_{ij}^{p} = e^{i(\phi_i - \phi_j)} e^{-\Delta_{ij}}, \tag{7.25}$$

and then we form the corrected-phase DRF elements,

$$\begin{aligned} D^c_{ij} &= D^m_{ij} R^{p*}_{ij} \\ &= D_{ij} e^{-i(\phi_i - \phi_j)} \\ &= e^{-i\phi_i} D_{ij} e^{+i\phi_j}. \end{aligned} \tag{7.26}$$

In other words we subtract the phase of the RD on an element by element basis. The last line is

$$\mathsf{D}^c = \Phi^\dagger \mathsf{D} \Phi, \tag{7.27}$$

where Φ is a diagonal matrix containing the phases of the beam pattern of the RD. We note that

$$\begin{aligned} \Phi\Phi^\dagger &= \mathsf{I} \\ \Phi^\dagger\Phi &= \mathsf{I}; \end{aligned} \tag{7.28}$$

in other words, the transformation is unitary, complete, and orthogonal.

Now the response matrix of the DUT can be diagonalized:

$$\begin{aligned} \mathsf{D}^c &= \Phi^\dagger \mathsf{U} \Sigma \mathsf{U}^\dagger \Phi \\ &= \mathsf{W} \Sigma \mathsf{W}^\dagger, \end{aligned} \tag{7.29}$$

where Σ is a diagonal matrix whose elements are the sensitivities corresponding to the eigenvectors of the corrected response matrix, contained in the columns of

$$\mathsf{W} = \Phi^\dagger \mathsf{U}. \tag{7.30}$$

Then, the recovered modes of the phase-corrected DRF are related to the recovered modes of the uncorrected DRF by

$$\mathsf{d}^c_i = \mathsf{d}_i e^{-\phi_i}. \tag{7.31}$$

The recovered modes have the phase response, at the sample points, of the RD subtracted, but otherwise they remain the same; importantly, the spectrum of eigenvalues remains the same. Any structure in the phase fronts of the individual modes of the DUT remain the same; we have simply subtracted off the single-mode reference phase. In antenna engineering, when displaying the beam patterns of antennas, the phase front would usually be subtracted off

anyway, because it does not have any intrinsic interest, and indeed varies with the distance of the observation point to the antenna [60]. This general analysis method could be used to reveal various aspects of the scheme; for example, we may ask what happens if the reference detector is few-mode.

7.4 Study of Simulated Phase-Corrected DRFs

7.4.1 Single-Mode Phase-Corrected DRFs

Having chosen a phase correction method, it is important to investigate numerically the effects of this technique and the phase patterns of the DRFs to be measured experimentally, in Chapter 8. For this study, it is possible to use the simulation framework built in Chapter 3. We recall that it relies on projecting the beams of two sources built from the fundamental Laguerre-Gaussian mode, LG_{00}, onto the detector surface whose reception pattern is defined by the incoherent sum of individually fully-coherent modes, each of which is a two-point function built from the outer product of single-point functions such as Laguerre-Gaussian modes, LG_{pl}, where p and l are the radial and azimuthal indices respectively, as described in Section 3.4.1. The projection of the incident field onto the detector response provides a single element of the DRF matrix in the basis of source position indices. This calculation procedure is then repeated over all position pairs of a pre-defined sampling grid; depending on the configuration, simplifying assumptions can be made to reduce the problem and speed up the computation.

We start with the case of a single-mode DRF built from the LG_{00} mode, where we correct fringe phase with itself, i.e. use the signal channel as its own reference channel: we obtain a constant phase pattern, with value equal to 0 rad. Although this operation seems trivial, the result clearly indicates that this procedure moves the constant-phase surface from the plane of sources to the detector surface. In Section 7.3.3, we had also proved theoretically that the eigenspectrum of DRFs, i.e. their representation in the modal basis, with and without the phase correction are identical. It is important at this point to verify this phenomenon with the simulated single-mode DRF phase. We diagonalized the simulated DRF without and with the phase correction; in this configuration, this corresponds to diagonalizing the simulated DRF's complex amplitude and its amplitude only, respectively. We found that the eigenspectrum is identical within the machine computational precision, as shown in Figure 7.11. Figure 7.12 compares the spatial forms of the first mode, the only one with non-negligible eigenvalue, in the case without and with prior phase correction: their amplitudes are identical, while their phases are respectively quickly varying and constant, as expected. These observations are in

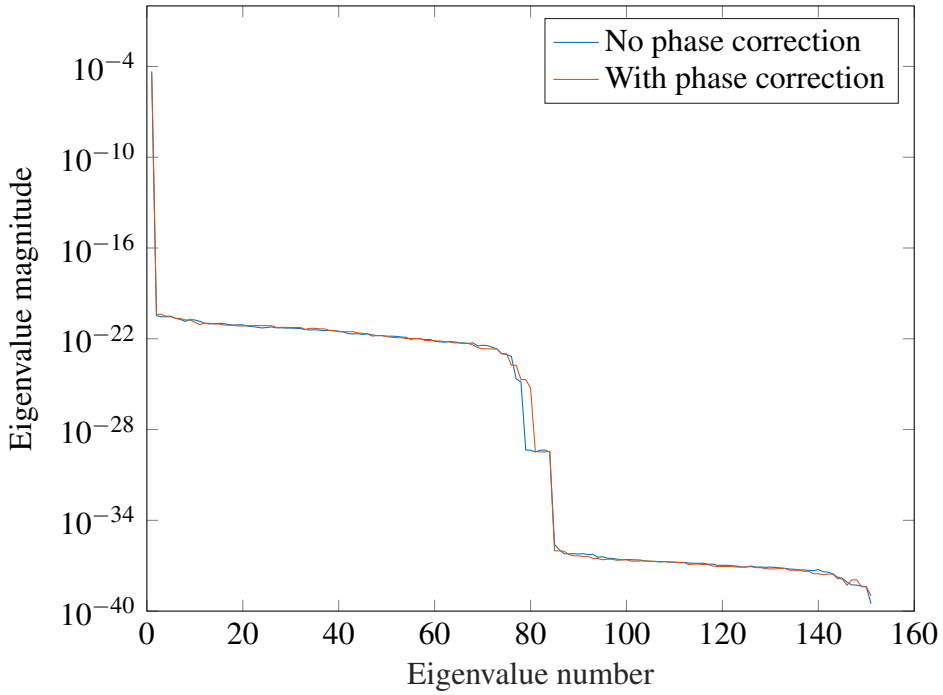

Fig. 7.11 Comparison of the eigenspectrum of simulated single-mode DRFs, built from the LG_{00} mode, without and with phase correction. The single large eigenvalue corresponding to the simulated mode is identical; the two plateaus respectively correspond to the eigenvalues of modes from the finite computation precision of the DRF, and to the finite precision of the eigenvalue decomposition procedure.

agreement with our theoretical investigations of our phase correction scheme. We note that the eigenmode's phase in the case with no correction is an aliased fast-wrapping phase.

We repeated these numerical simulations with the center of the detector surfaces placed at different positions, in particular slightly displaced along the y-axis, which was found to be the preferred option in Section 7.3.2. We then used the phase of this displaced single-mode DRF to correct the phase of the on-axis single-mode DRF; this procedure is identical to the one described in Section 7.3.2, except that we do not work within the simplified framework where assumed that the sources and detectors were point-like. Using the same configuration as in Figure 7.10c, where the signal detector is on-axis with the origin while the reference is displaced to $y = 10\,\text{mm}$, we show in Figure 7.13 that the corrected fringe phase pattern is almost identical. This indicates that the simplifying assumptions used in Section 7.3.2 that the sources and detectors are point-like are broadly valid.

Our investigation of the effect of the phase correction scheme on the eigenmodes obtained was repeated in the case of a reference channel placed at a different position shown in Figure 7.13. Again, we found that the eigenspectra obtained in the uncorrected and corrected

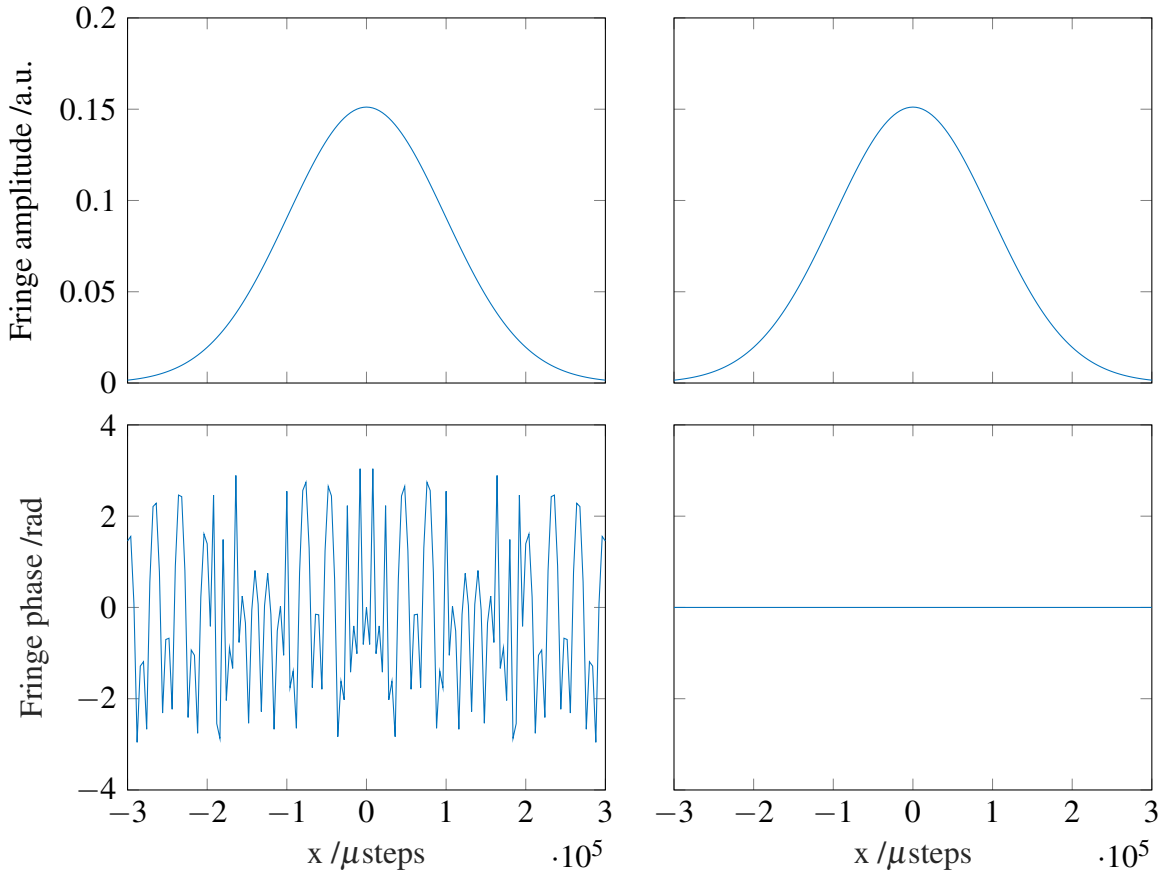

Fig. 7.12 Comparison of the first eigenmode of simulated single-mode DRFs, built from the LG_{00} mode, without and with phase correction.

phase cases are identical within the machine's computational precision. The first eigenmode, the only one with non-negligible eigenvalue, obtained from the cases without and with phase correction have identical amplitude patterns. Their phase patterns are compared in Figure 7.14: the phase for the former case is identical to Figure 7.12, displaying an aliased fast-wrapping phase pattern, while the latter case is varying much more slowly. In this configuration, the geometric phase factor is significantly, albeit not entirely, eliminated by the phase correction scheme. Again, these results are in line with our expectations from the theory derived in Section 7.3.3.

7.4.2 Few-Mode Phase-Corrected DRFs

In the case of investigating the behavior of few-mode and multi-mode devices, we may ask whether we would still use a reference channel with single mode behavior. Our intuition is that the single-mode behavior of the reference guarantees a constant phase on the reference

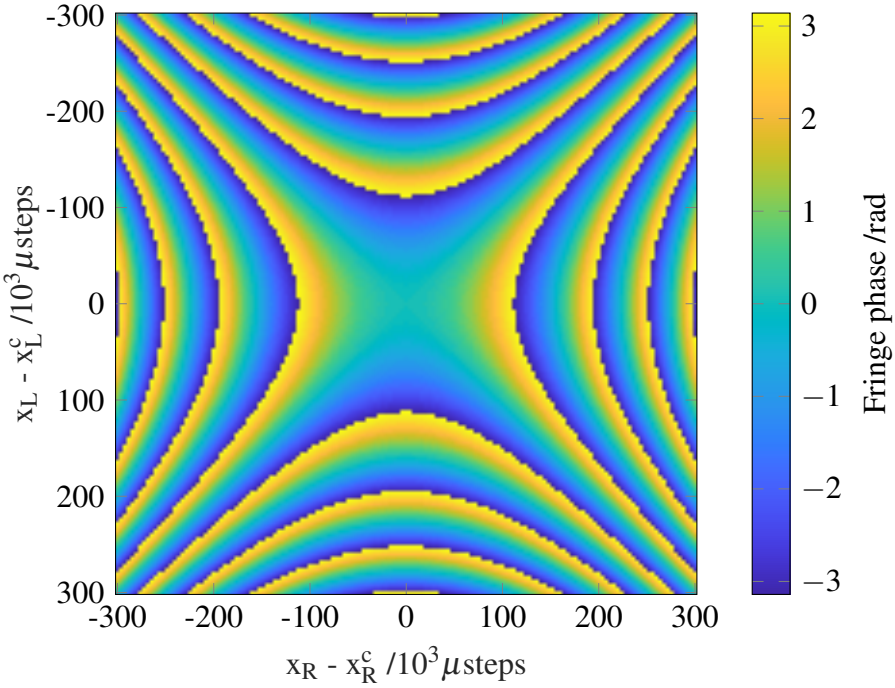

Fig. 7.13 Simulated fringe phase for a single-mode system, built from the LG_{00} mode, corrected with the phase of a single-mode system, built from the LG_{00} mode, displaced at $y = 10\,\text{mm}$.

plane, namely the surface of the reference channel. This result is obtained straightforwardly from the DRFs that were simulated for each individual mode, as was described in Chapter 3.

We began with the case of a two-mode simulated DRF, assuming a 10 µm mode field diameter to simulate individual LG modes, similarly to Section 3.4. The simplest configuration is to use the corresponding fundamental mode's phase to correct the few-mode system's phase. As shown in Figure 7.15, we observe that the simulated DRF phase is separated into several regions, each of which is constant within the 10^{-11} rad computation precision. The phase difference between neighboring regions is π rad. The lines where the x_R- and x_L-gradients of the signal channel fringe amplitude are equal to zero, as represented in Figure 7.15: the circular lines in the anti-diagonal corners correspond perfectly with the boundary of the phase-reversal between constant phase regions. This is a clear characteristic of few-mode behavior. It is important here to note that we use the x_R- and x_L-gradients are proxies for finding the zero-amplitude lines, which correspond to where both gradients are zero simultaneously. This observation holds when varying the relative sensitivities of the two modes, which displaces the zero-amplitude line towards the anti-diagonal corners, eventually taking it out of the considered scanning range; this is in agreement with the results obtained with the amplitude of simulated DRFs, in Figure 3.9.

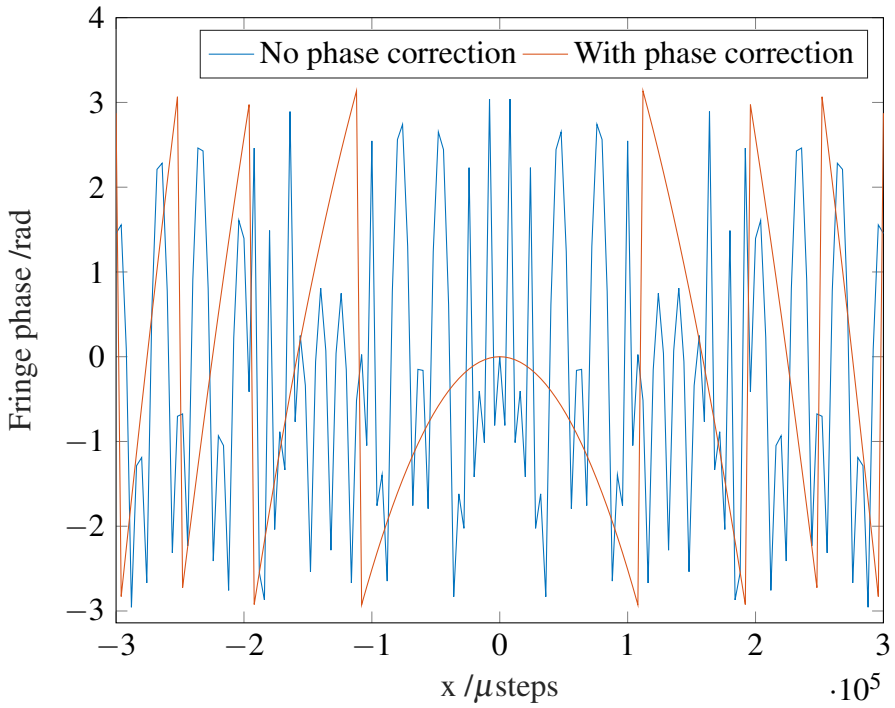

Fig. 7.14 Comparison of the first eigenmode of simulated single-mode DRFs, built from the LG_{00} mode, without and with phase correction by a reference channel placed at $y = 10\,\text{mm}$.

Figure 7.16 shows the DRF's eigenspectrum in the uncorrected and corrected cases, which are identical within the machine's computation precision and both show that two modes dominate. We note that the two largest eigenvalues are not identical, by approximately a factor 4, contrary to the equal sensitivities used in the LG_{00} and LG_{01} modes' incoherent addition to create the simulated DRF. This difference is caused by unequal power coupling from the incident field into each of the modes, such that the normalization of the recovered eigenmodes induces a difference in the recovered sensitivities. Figure 7.17 presents the comparison of the second eigenmode of the uncorrected and corrected DRF decompositions. Their amplitude patterns are again equal; while the uncorrected DRF's seconde mode has a phase pattern displaying aliased wrapping, the corrected DRF's is symmetric about $x = 0$, similarly to the second mode in the spatial basis used to simulate the DRF.

We also investigated cases where the signal and reference detectors have different positions along the y-axis. In Figure 7.18a, we present the fringe phase pattern of a two-mode system at $y = 0\,\text{mm}$ corrected with the fringe phase of a single-mode reference system placed at $y = 1\,\text{mm}$. In Figure 7.18b, the fringe phase pattern has a small anti-symmetric component about the antidiagonal; it is qualitatively similar to the phase pattern observed in Figure 7.10c, with a smaller magnitude due to a reduced distance between the signal and reference

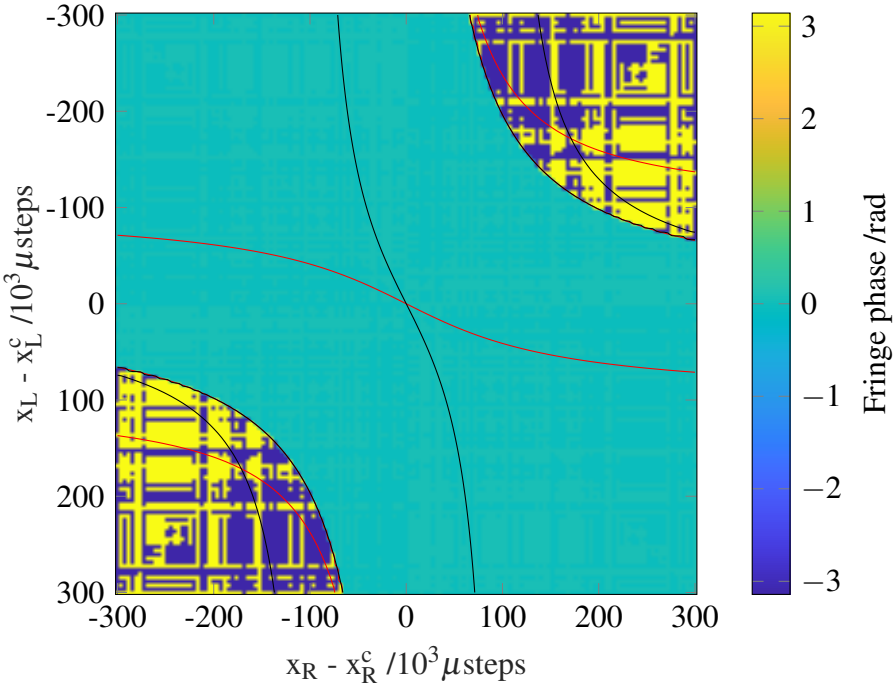

Fig. 7.15 Simulated fringe phase for an on-axis two-mode system, built from the LG_{00} and LG_{01} modes, corrected with the phase of a single-mode system at the same location, built from the LG00 mode; the structure observed in the anti-diagonal corner regions are caused by the 10^{-11} rad computation precision. The black and red lines correspond to the zeros in the x_R- and x_L-gradients of the signal channel fringe amplitude, respectively.

channel positions (1 mm instead of 10 mm). We note that the fringe amplitude pattern in the former case has a zero-amplitude line corresponding to the phase-reversal boundary. In the latter case, however, the fringe amplitude pattern does not present a zero-amplitude line. This highlights the fact that the fringe phase correction moves the phase reference plane from the source plane to the surface of the reference detector, but does not influence the DRF phase pattern which is solely defined by the signal channel's modal behavior.

We repeated these investigations with the signal and reference channels placed symmetrically about $y = 0$, which cancels out the phase contribution due to the differential path lengths, such as observed in Figure 7.18. While the corrected DRF phase patterns are qualitatively similar, we notice that the boundary between the phase-reversed regions is less sharp when the distance between the channels is increased. Figure 7.19 shows this phenomenon for simulated fringe phase patterns of a two-mode system, corrected with the phase of a single-mode system, placed symmetrically about $y = 0$.

Figure 7.20 presents the DRF phase of a four-mode system, built from the LG_{00}, LG_{01}, LG_{10} and LG_{11} modes with equal sensitivities, corrected with the phase of a single-mode

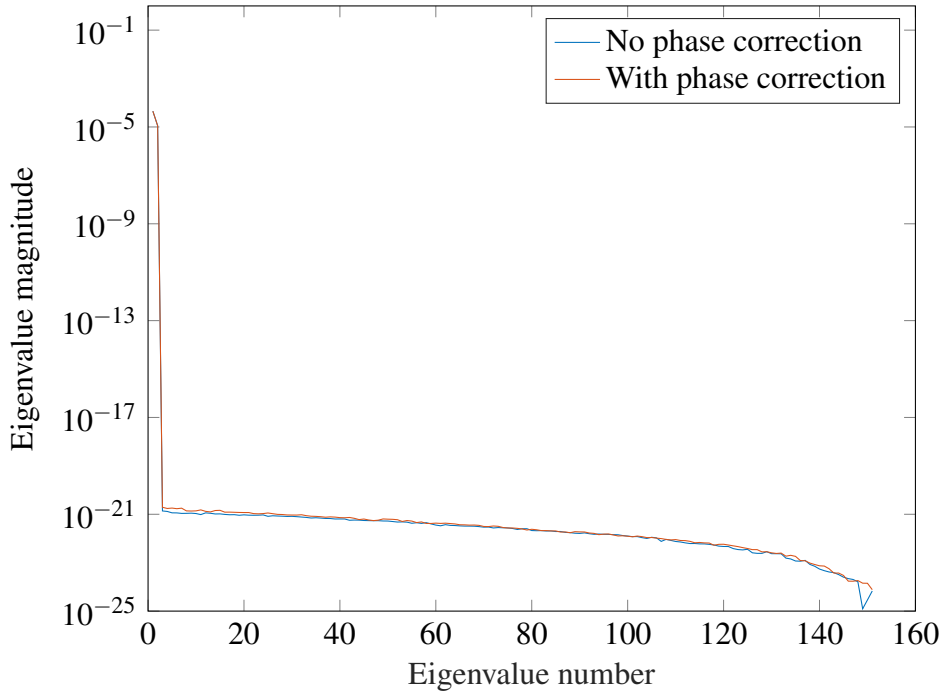

Fig. 7.16 Comparison of the eigenspectrum of simulated single-mode DRFs, built from the LG_{00} and LG_{01} modes, without and with phase correction.

reference at the same on-axis position. The zero-magnitude lines of the DRF amplitude pattern again correspond to the boundaries between the constant regions of the DRF phase.

We also investigated the case where the phase correction is performed using a few-moded reference channel system. As in the single-mode case, if the modal behavior and positions of the signal and reference channels are identical, the corrected fringe phase pattern is constant, with a value of zero. In Figure 7.21, we present the DRF phase of a simulated four-moded signal channel corrected with the phase of a two-moded reference channel. The DRF phase pattern obtained is the difference of the four-moded case shown in Figure 7.20 and the two-moded case shown in Figure 7.15. The structure observed becomes more complex to interpret, and the DRF amplitude's zero-magnitude lines no longer correspond to all of the phase reversals observed, as additional modal behavior is introduced. A key result is that we should always prefer using a single-mode reference channel system to perform our phase correction scheme.

7.4.3 Multi-Mode Phase-Corrected DRFs

Using this insight, we pursued our investigation of the phase correction scheme on multi-mode systems. Figure 7.22 presents the DRF phase of a 121-mode system, whose DRF

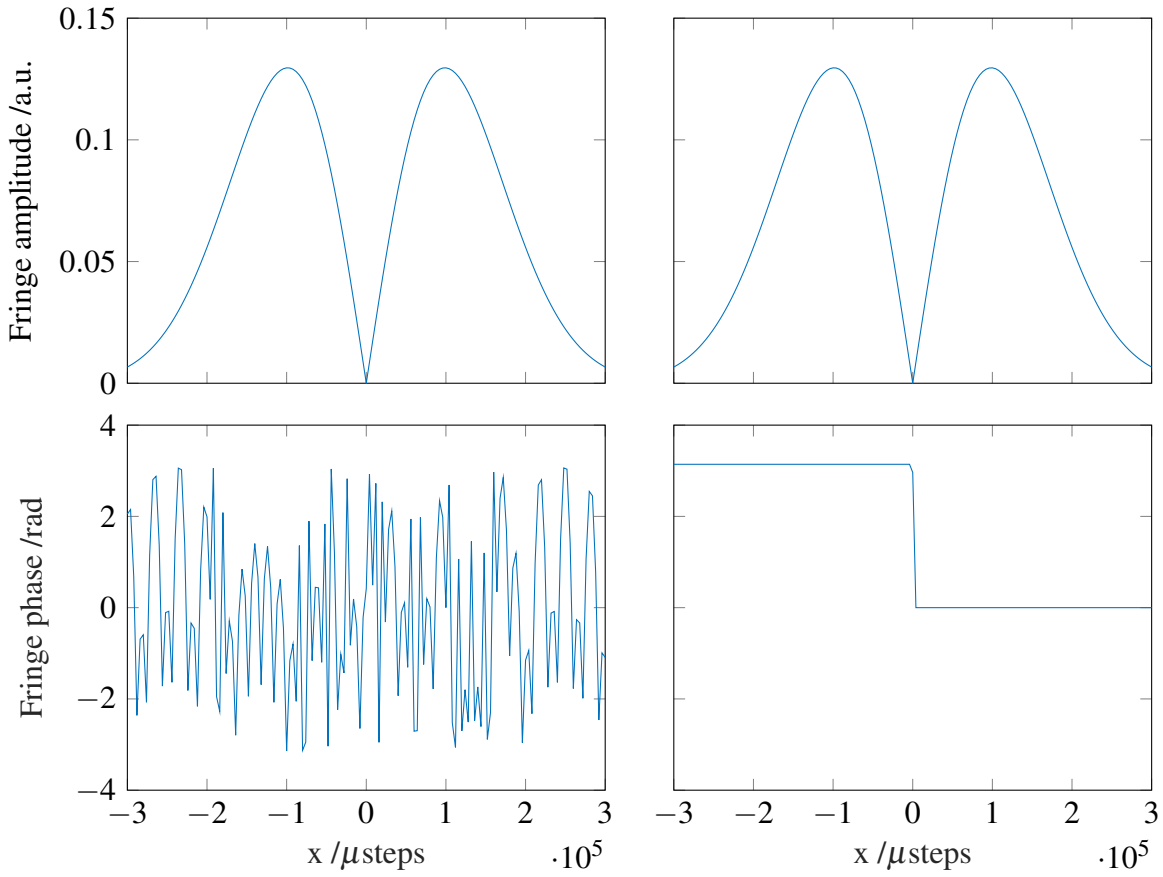

Fig. 7.17 Comparison of the second eigenmode of simulated single-mode DRFs, built from the LG_{00} and LG_{01} modes, without and with phase correction.

amplitude and uncorrected phase had been presented in Figure 3.11, corrected with the DRF phase of a single-mode system placed at the same on-axis position; Figures 7.22a and 7.22b show different sensitivities applied to this set of 121 modes, respectively uniform and following a logistic function with center index 60 and 0.1 inverse width, i.e. the 40 first modes have relative sensitivities larger than 0.9 and the first 60 modes have relative sensitivities larger than 0.5. Both cases display a large number of regions with constant phase; the phase difference between neighboring regions is π rad. As for few-mode systems, the corresponding DRF amplitude pattern's zero-magnitude lines correspond precisely to the π rad transitions between near-constant phase regions. In the case with non-uniform sensitivities, the smaller number of phase structures, each with larger width, implies a lower modedness of the DRF, accounting for the small sensitivities applied to high-order modes.

We diagonalized the 121-moded DRF with equal sensitivities, whose corrected phase is presented in Figure 7.22a, with and without the phase correction step. Figure 7.23 compares their eigenspectrums, which are identical as expected: this confirms our theoretical result

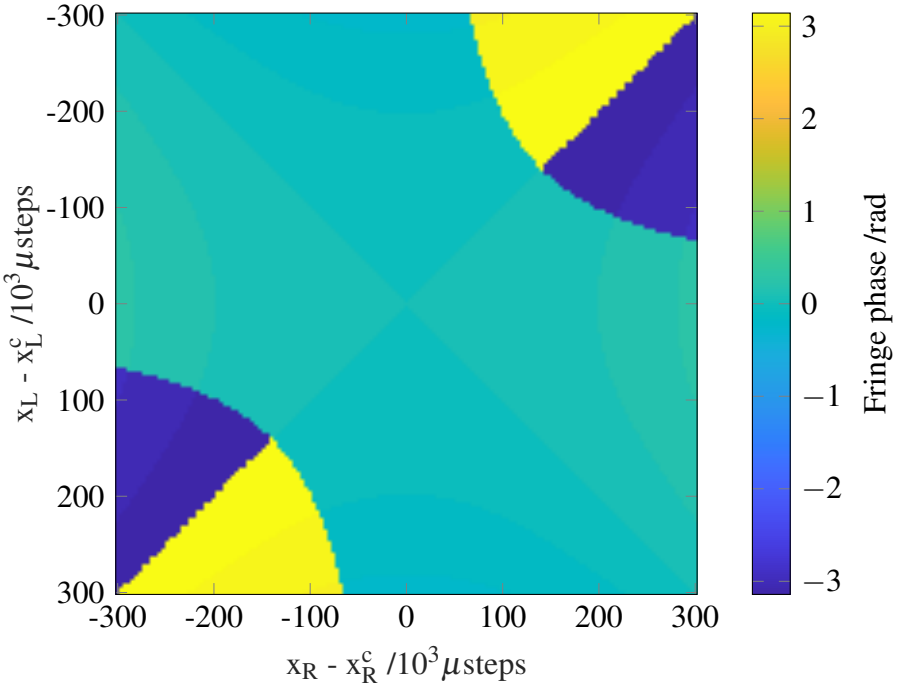

(a) Signal at $y = 0$ mm, reference at $y = 1$ mm

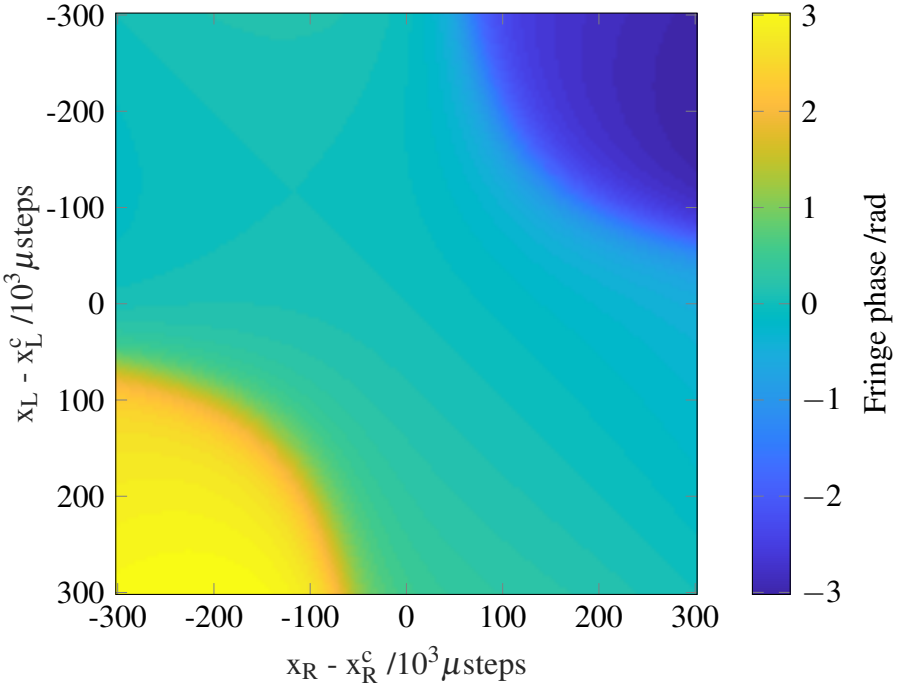

(b) Signal at $y = 1$ mm, reference at $y = 0$ mm

Fig. 7.18 Simulated fringe phase for a two-mode system, built from the LG_{00} and LG_{01} modes, corrected with the phase of a single-mode system, built from the LG_{00} mode.

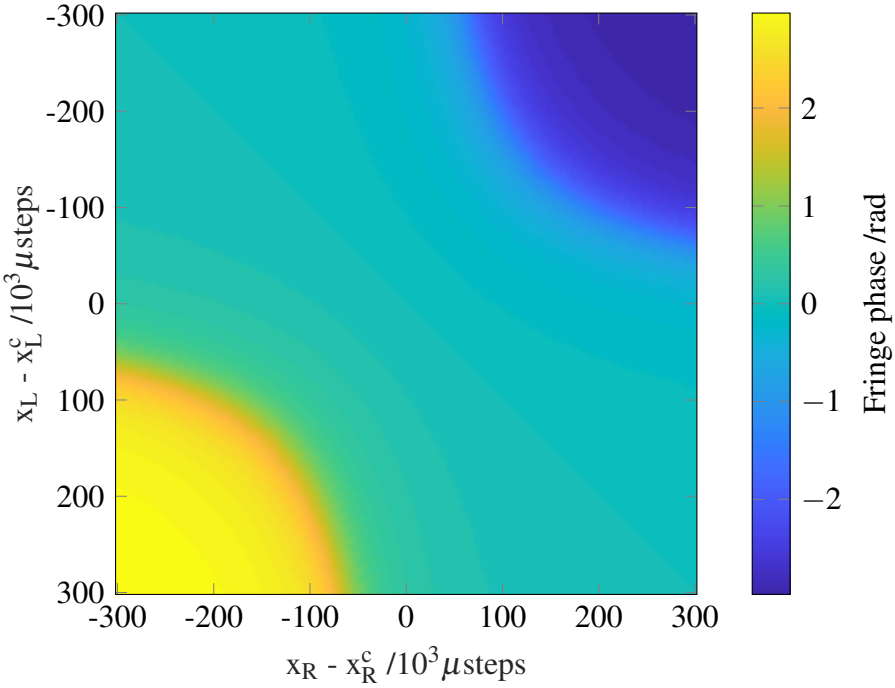

(a) Signal and reference at $y = \pm 1$ mm

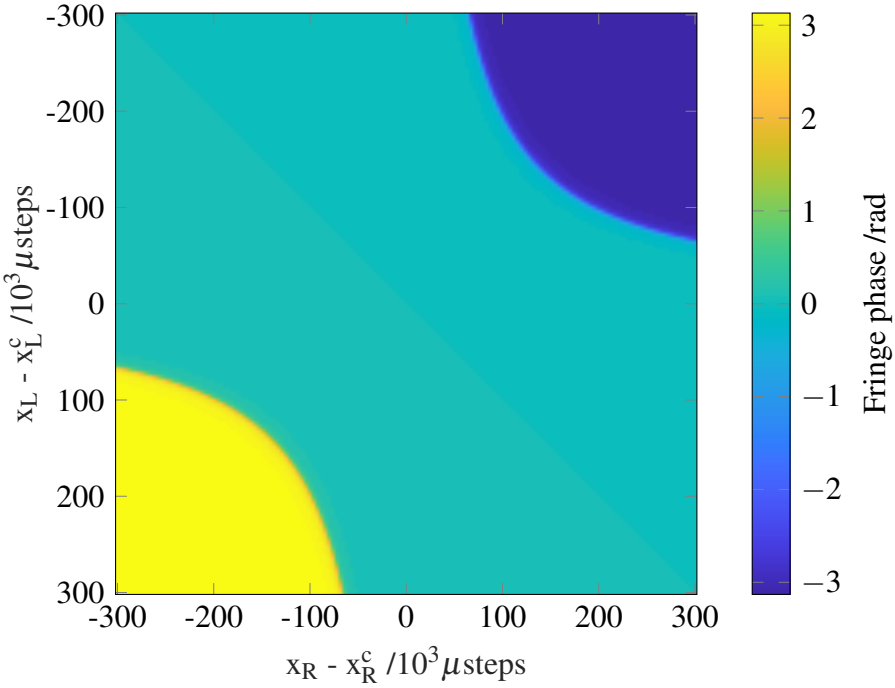

(b) Signal and reference at $y = \pm 0.125$ mm

Fig. 7.19 Simulated fringe phase for a two-mode system, built from the LG_{00} and LG_{01} modes, corrected with the phase of a single-mode system, built from the LG_{00} mode.

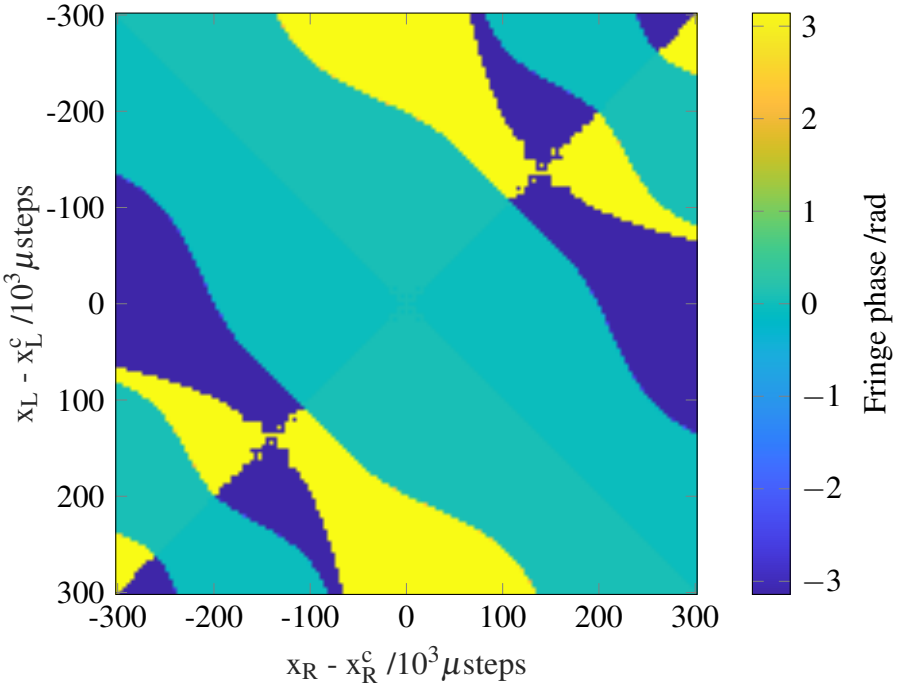

Fig. 7.20 Simulated fringe phase for a four-mode system, built from the LG_{00}, LG_{01}, LG_{10} and LG_{11} modes, corrected with the phase of a single-mode system, built from the LG_{00} mode.

from Section 7.3.3 for multi-mode systems. However, we observe that the spectrum does not have 121 large eigenvalues. As in the few-mode DRF case, this is partly due to the normalization of the eigenmodes; however, in the multi-mode DRF case, many of the modes are degenerate when projected onto the basis of two-source one-dimensional sample positions, reducing the apparent number of modes in the system. In 7.24, we present the amplitude and phase patterns of the eigenmode with largest eigenvalue, in the cases of the DRF with uncorrected and corrected phase. The amplitude patterns are identical, but not Gaussian as in the decomposition of the single-mode and few-mode systems' DRFs, rather presenting several local peaks symmetric about the on-axis maximum. In the corrected DRF's first eigenmode, the phase jumps by π rad at every successive zero in the amplitude; this behavior is not clear in the uncorrected DRF's first eigenmode, as it is hidden by the aliased fast-wrapping phase. These observations hold for all eigenmodes with large corresponding eigenvalues, while the eigenmodes with small eigenvalues correspond to artifacts from the finite precision of the DRF computation.

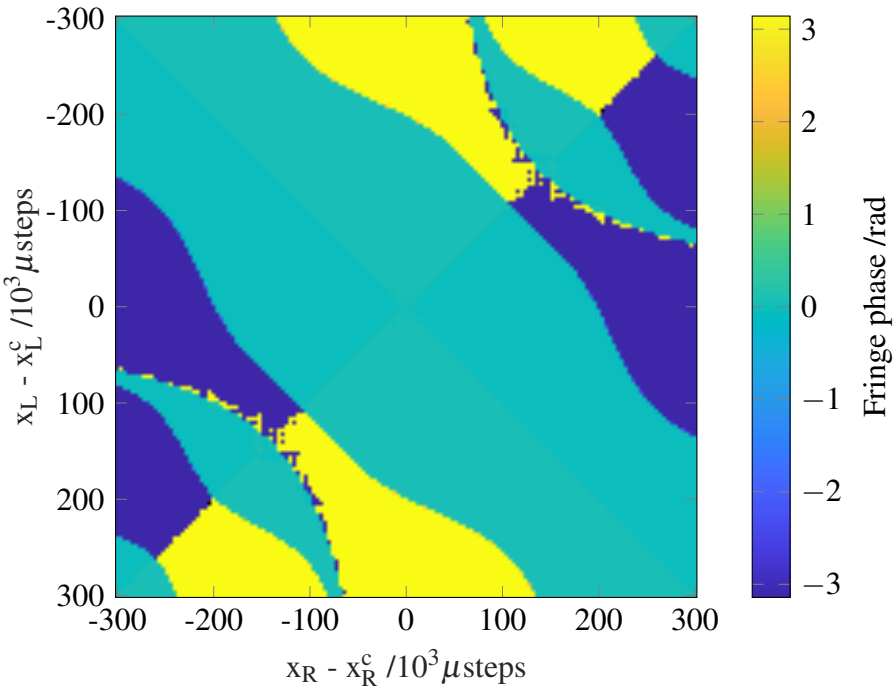

Fig. 7.21 Simulated fringe phase for a four-mode system, built from the LG_{00}, LG_{01}, LG_{10} and LG_{11} modes, corrected with the phase of a two-mode system, built from the LG_{00} and LG_{01} modes.

7.5 Conclusion

We have described several experimental methods that allow us to correct for the drift in the fringe phase recorded by the device under test in an EAI experiment. Two broad categories were considered, the first of which relies on creating Lissajous figures from two signals, separated either by time-domain splitting of the output of the device under test or by routing a small fraction of the output power from the phase modulators into beamcoupler-based systems to obtain a real-time phase reference. The second method uses a second photodetector forming a phase reference channel, placed spatially close to the device under test: its output also displays a fringe as the relative phase between the sources is modulated, and the phase component of its complex amplitude can be subtracted from the fringe phase of the signal channel.

This category of phase correction methods was selected, as it subtracts the environmental phase drift fully and reliably. It also has the important advantage of subtracting a significant fraction of the phase wrapping that appears in the fringe phase as either or both sources are scanned over a plane. We have further investigated the effects of such a phase-referenced system on the measured DRF. We have proven theoretically that the phase correction using

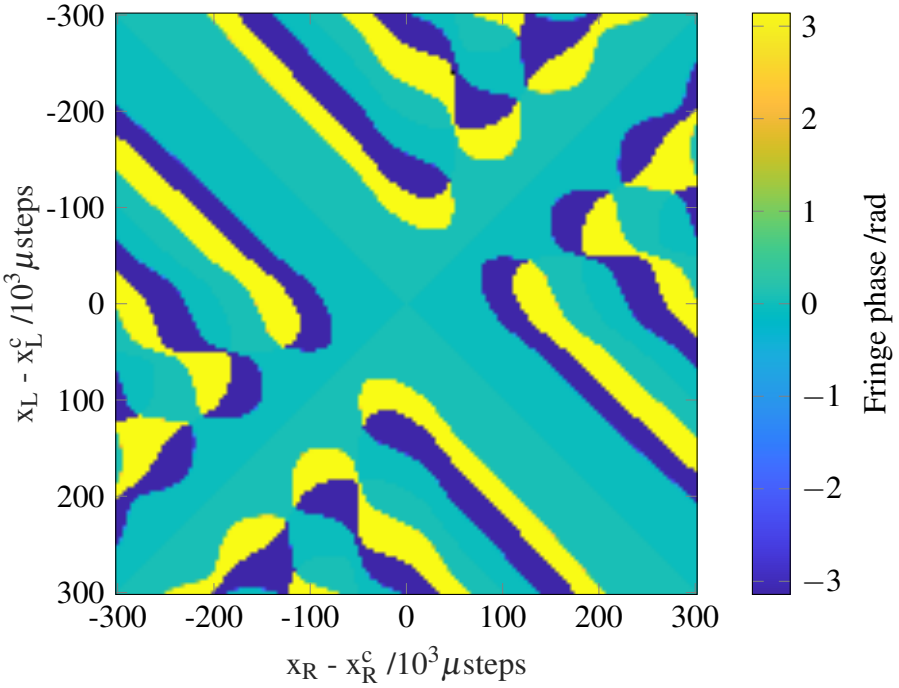

(a) Equal relative sensitivities

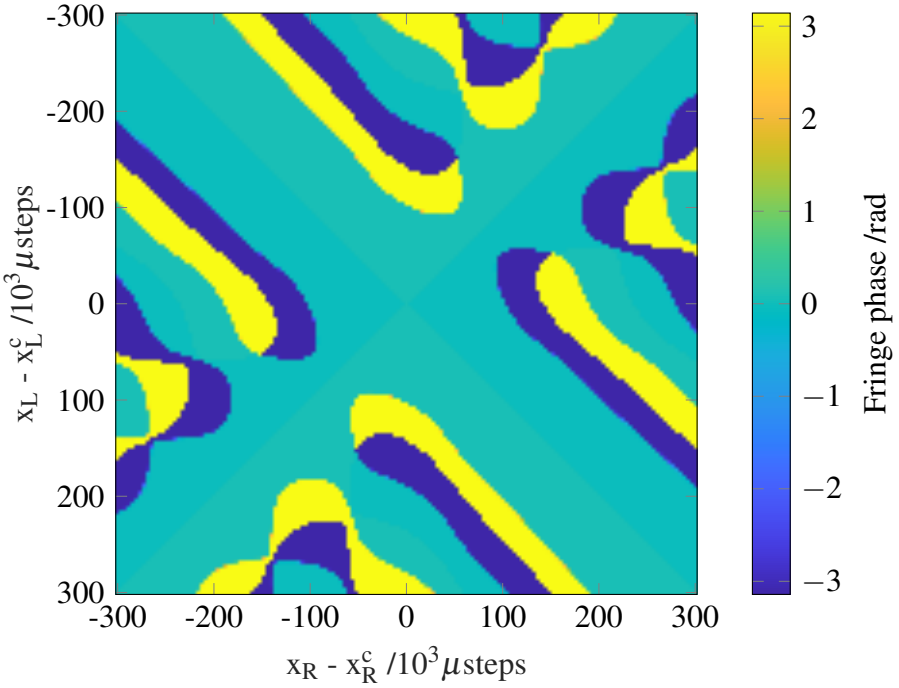

(b) Sensitivities defined by logistic function, with center index 60 and 0.1 inverse width

Fig. 7.22 Simulated fringe phase for a 121-mode system, built from the 121 first LG modes, corrected with the phase of a single-mode system, built from the LG_{00} mode.

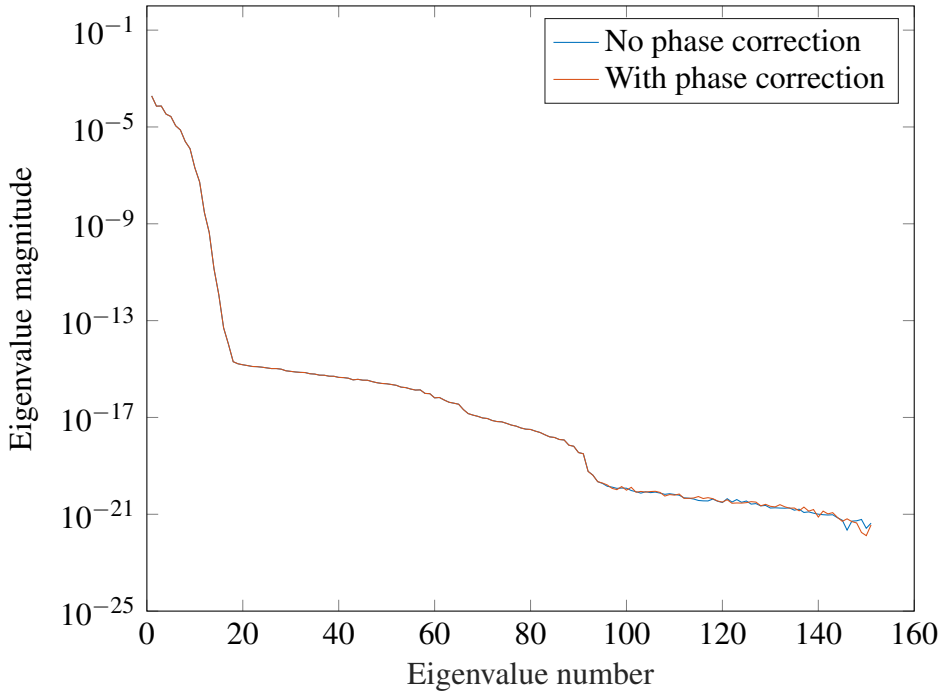

Fig. 7.23 Comparison of the eigenspectrum of simulated single-mode DRFs, built from the 121 first LG modes, without and with phase correction.

a nearby phase reference channel only changes the phase pattern of the eigenvectors of the signal channel's detector response, while its eigenspectrum remains unchanged. Numerical studies showed this phenomenon in a large number of simulated systems, and the effect of finite distance between the two channels was explored.

These investigations have provided important insights into how such a scheme should be implemented experimentally. In particular, the relative position of the two channels should be orthogonal to the direction of the source scans. Moreover, the distance between the two channels significantly influences the magnitude of the residual geometric phase difference that appears in the fringe phase pattern as the sources are scanned. Finally, choosing a single-mode system to serve as the reference channel significantly simplifies post-measurement analysis.

Additionally, we have repurposed the simulation framework built in Chapter 3, based on the projection of an incident field produced by two scanned single-mode sources onto the assumed reception pattern of a detector system. By subtracting element-wise the DRF phase of a reference detector from the device under test's DRF, we obtain a DRF with corrected phase. In particular, we repeated the simulations of single-mode, few-mode and multi-mode detectors to obtain characteristic DRF phase patterns for these different modal regimes, in

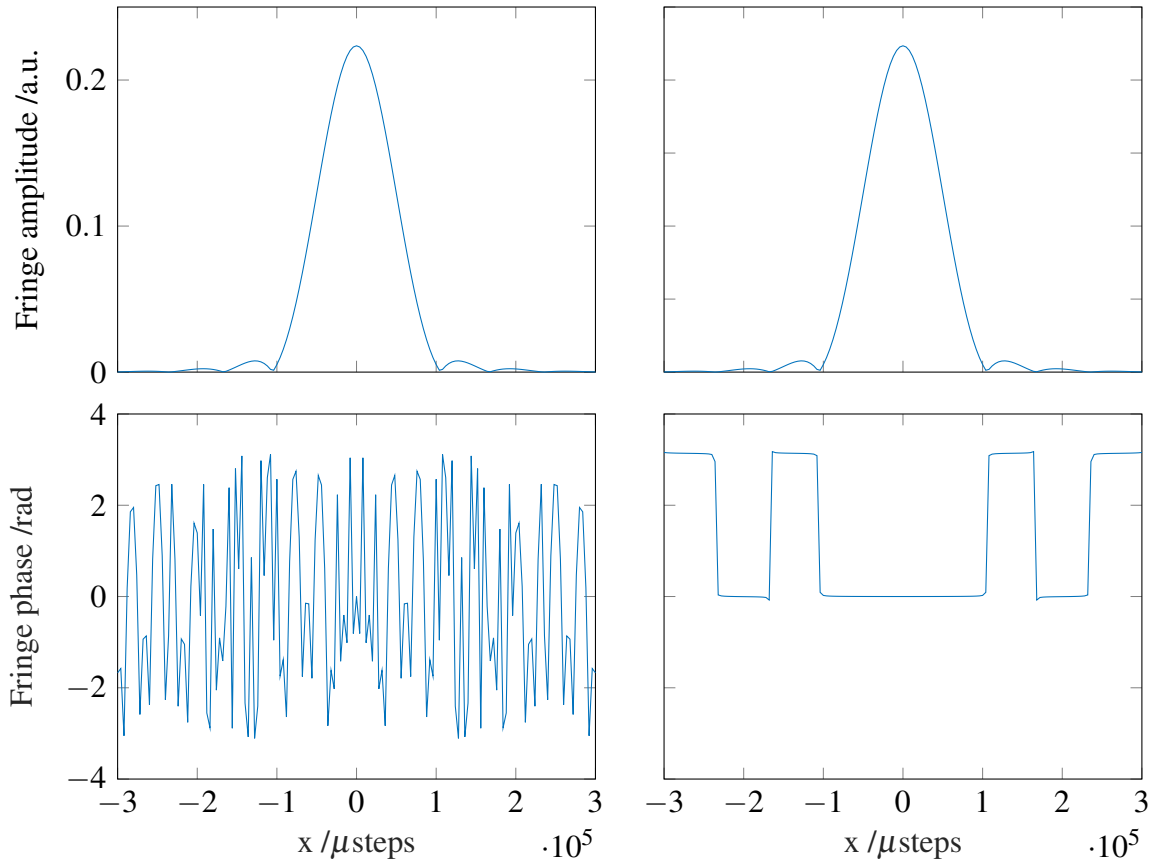

Fig. 7.24 Comparison of the first eigenmode of simulated single-mode DRFs, built from the 121 first LG modes, without and with phase correction.

addition to the characteristic DRF amplitude patterns simulated in Chapter 3 and measured experimentally in Chapter 6.

In the next chapter, we will use the insights gained to implement this phase reference correction scheme, with the goal of stabilizing the measured fringe phase up to a level that will allow us to perform a full EAI of several hours with a reliable phase reference. Deep understanding of the system's behavior can be gained by carefully comparing the experimental results obtained and the numerical results presented in this chapter. In particular, we will wish to confirm the scheme's strong ability for differentiating between single-mode, few-mode and multi-mode regimes.

Chapter 8

Phase-Sensitive Experimental Characterization

8.1 Introduction

In the previous chapter, we have investigated several schemes to stabilize the measured fringe phase and chosen a method based on correcting the phase data in the device under test with that obtained in a nearby reference channel. In particular, numerical studies have revealed that this scheme has two main consequences: (i) the correction of the phase drift caused by environmental instabilities, and (ii) the near-perfect cancellation of the geometric phase shift accumulated as the sources are scanned.

In this chapter, we will present the experimental realization of this scheme and the results obtained with the new two-detector phase correction system. In particular, we will pay special attention to the effects predicted by numerical simulations and to the large improvement in phase coherence time obtained with this extension to the experimental system. More generally, the work described in this chapter culminates in the measurement of the DRF phase, in addition to the measurement of the DRF amplitude performed in Chapter 6. In other words, we describe a major achievement: the complete measurement of the DRF of infrared detectors over a wide range of modal behaviors. As we discussed in Chapter 2, such measurements of the DRF complex amplitude allows us to fully characterize the optical response of the device under test.

The first objective for this chapter is to describe our implementation of this experimental system extension, and to discuss what improvements were achieved with the extended experimental system. Once fulfilled, the main goal is to perform the first measurements of the DRF's phase, for a wide range of behavior for single-mode, few-mode and multi-

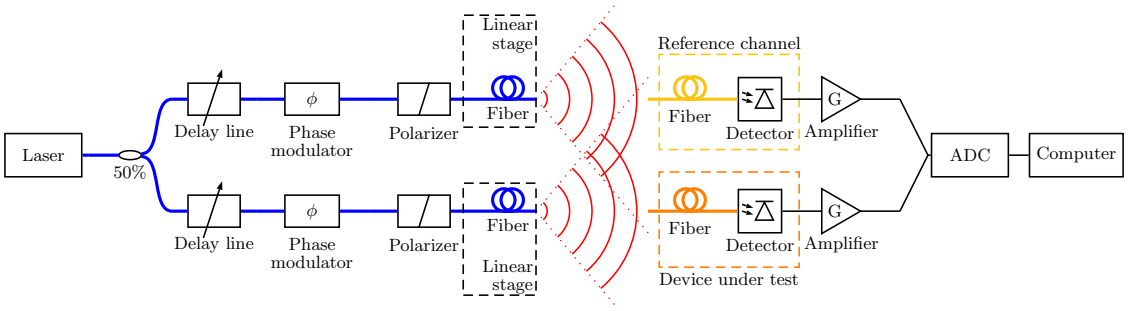

Fig. 8.1 Schematic drawing of extended experimental system, with a reference channel constructed using a reference fiber and amplified detector (yellow).

mode systems. We will seek to leverage simple numerical simulations, as well as those presented in Chapter 7, to gain valuable insights into the strengths and limitations of the phase stabilization system, for instance any remaining variability in the phase measurements. Further improvements to the experimental system can then be discussed, two of which we will implement: reducing the distance between the signal and reference channel fibers, and varying the distance between the source and detector planes.

Section 8.2 describes the extension of the experimental system in detail, from the specifications of the reference channel detector to the custom parts required for the realization of the scheme. In Section 8.3, we present a first set of experimental results, including a characterization of the hours-long phase coherence time obtained and its robustness against vibrations of the optical table. In Section 8.4, we numerically investigate the planar phase slope observed experimentally, and whether it originates as part of the geometric phase factor that the two-detector phase correction method does not rectify. Section 8.5 describes a further improvement of the phase correction scheme, based on the use of fiber arrays where neighboring fibers are densely packed. The repeatability of fringe phase measurements is discussed in Section 8.6; in particular, we explore the effects of variability in the source height. In Section 8.7, we investigate the effect of changing the distance between the source and detector planes, and how the amount of useful information in the DRF can be maximized by choosing an optimal distance.

8.2 Extension of Experimental System

Figure 8.1 shows the extended experimental system, and can be compared to the diagram of the single detector system in Figure 4.2 in Chapter 4. A second detector is added and coupled to an open-ended length of optical fiber; its signal is amplified and converted into a digital signal by an ADC. This extension clearly leaves a significant majority of the experimental

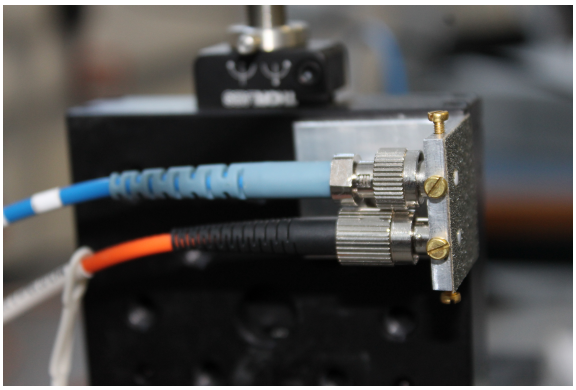

Fig. 8.2 Two-detector holder mounted on the manual stage, with two optical fiber patch cables' connector ferrules secured.

system unaltered, and the fringe phase correction will be obtained from post-measurement analysis of the two channels. In this section, we present the technical details of this extension.

A Thorlabs PDA20CS-EC variable-gain amplified InGaAs photodetector was added to serve as the reference channel detector. As it contains a transimpedance amplifier with gain factor up to 70 dB, an external amplifier is not required, contrary to the DET01CFC photodetector that will be used for the signal channel. On the other hand, their responsivity at 1550 nm wavelength is nearly identical, as the photodiode is based on a similar InGaAs architecture. While the detector is coupled to free-space using a flat glass window, an adapter can be used to mount flat-faced FC/PC and angled FC/APC fiber connectors. This adapter is designed such that the photodiode diameter is larger than the size of the divergent input beam from the coupled optical fiber. The distance between the optical fiber end and the photodetector is less than 4.1 mm, such that the e^{-2}-power diameter of the beam is at most 0.8 mm, smaller than the 2 mm diameter of the photodiode: we conclude the power exiting the coupled fiber is entirely incident on the photodiode surface.

In order to properly secure the two optical fibers coupled to the two detectors, we designed and manufactured a new holder, shown in Figure 8.2. The structure is essentially shaped as an L, with 25 mm side length. One side was placed against the manual stage's vertical slide and secured to it using a single screw for convenient vertical alignment. The other side was placed vertically, normal to the sources' propagation direction, and contains two holes of diameter equal to 2.5 mm fitting standard connectors ferrules, aligned vertically at a distance of 10 mm, corresponding to the diameter a standard FC/PC connector. The vertical arrangement of the two fibers is in line with the optimal configuration studied numerically in Chapter 7. The two detector fibers' connector ferrules were inserted in the holes, and each secured using two orthogonal fastening screws (one vertical and one horizontal) in the width of the side. We remark that an initial design with one fastening screw was rejected,

because the detector fibers' ferrules were found to be able to rotate by several degrees, both during the tightening of the screws and afterwards, depending on the tension applied to the connectorized optical fiber. A known issue with such configurations where beams propagate between large reflective surfaces is optical standing waves [101]. Although none were measured with our system, some scattering wet-and-dry paper was added on the mounting structure's surface to minimize this risk. In this configuration, the only reflective surfaces facing each other are those of the polished fiber ferrules of the two source fibers and two detector fibers; each is approximately 1 mm in diameter.

In order to use the two-detector system, we designed and manufactured a custom three-input ADC adapter card, an extension of the two-input adapter described in Section 5.4.2. This PCB contains two analog inputs, connected to the relevant pins of the ADC's input cable, and one digital input, for the synchronization of the measurements on the two analog inputs. The ADC chosen in Chapter 5 and used in Chapter 6 was retained: its 250 kS/s maximum sampling frequency is cumulative over analog inputs, such that in our two-detector configuration, each channel can be sampled at 125 kS/s. This means that 2.5 kHz-frequency fringes are measured at a rate of 50 points per fringe period in each channel, far above the Nyquist sampling requirement.

Our LabVIEW measurement program was straightforwardly extended. The ADC's measurement VI was modified to measure the two channels; the synchronization output signal from waveform generator remains used as the digital trigger for the multi-channel measurement. The individual waveforms are saved consecutively, the real-time FFT fringe amplitude and phase extraction process was extended to accept two-channel waveforms, and the extracted parameters are saved as a concatenated vector. Additionally, comparative tests were successfully run to confirm that the fringe parameter extraction procedure outputs results identical to our benchmark post-processing Matlab script applied to each waveform individually.

8.3 Measuring a Stable Fringe Phase

8.3.1 System Characterization

We recall that the reason for the system extension was the drift in the relative phase between the experimental system's two arms, which was measured to be approximately π rad every 3 s, as first observed in Chapter 5 and described in Chapter 7. The metric to evaluate the improvement obtained with our extended system should be the time stability on the difference of phases extracted from fringes recorded in the outputs of the two detectors, when the two

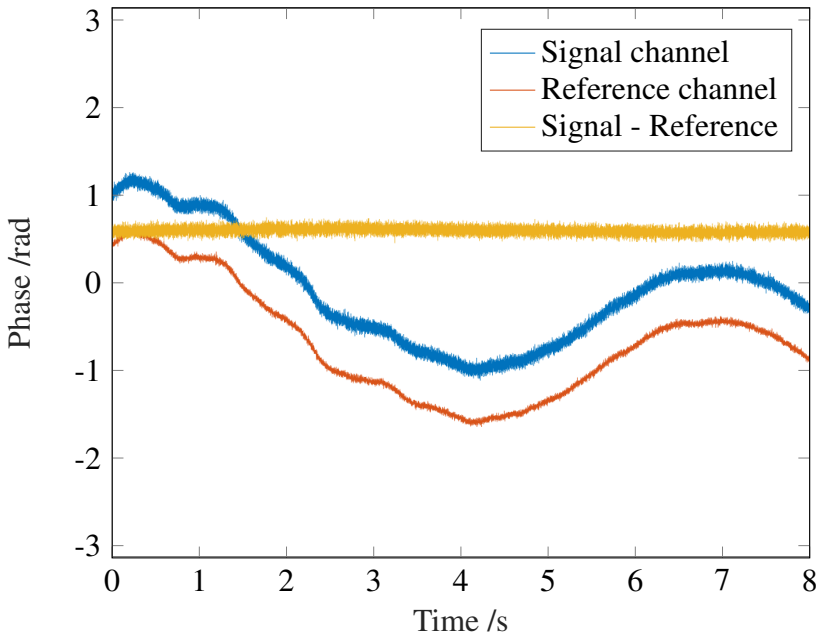

Fig. 8.3 Extracted fringe phase of the signal channel (blue) and reference channel (orange), and their difference (yellow), for a measurement of 1 MS at 125 kS/s sampling frequency for each channel, 2.5 kHz phase modulation frequency.

sources are held at a fixed set of positions. In other words, the key characteristic of our extended experimental system we wish to measure is the coherence time of the fringe phase after applying the phase correction scheme.

In order to perform this, we can first straightforwardly use the LabVIEW code executed in Chapter 5 for the characterization of the detector system: it consisted of one continuous measurement of the detector output, for instance over 8 s to simultaneously record 1 MS at 125 kS/s sampling frequency for each channel. In Figure 8.3, we present such an 8 s-long simultaneous measurement of the signal and reference channels' fringe phase, as well as their difference, which corresponds to the instantaneous corrected phase. The fringe phase was extracted for blocks of 50 datapoints, corresponding to a 0.4 ms-long phase modulation period. While each channel's phase drifts over several radians, the corrected phase is extremely stable: our phase correction method provides a fringe phase coherence time in excess of 8 s.

We recall that performing such measurements required full utilization of the control computer's performance, particularly its RAM. In order to accomplish similar measurements for longer time periods, we need to find a measurement scheme that is feasible with the computing resources available. The solution we chose was to perform shorter, 40 ms-long measurements (i.e. 100 periods of the 2.5 kHz fringe) repeated at fixed time intervals. Note that LabVIEW contains a particular VI, `Wait (ms)`, that ensures the precise timing between

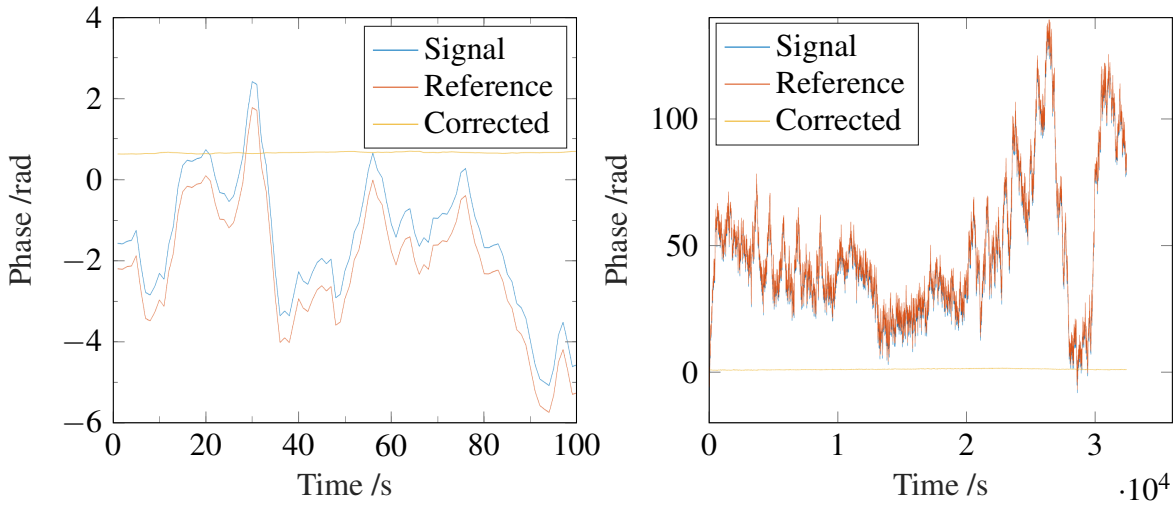

(a) 100 measurements

(b) 36 000 measurements

Fig. 8.4 Extracted fringe phase of the signal channel (blue) and reference channel (orange), and their difference (yellow), for measurements separated by 1 s of 5 kS at 125 kS/s sampling frequency for each channel, 2.5 kHz phase modulation frequency.

the repeated runs, with a 1 ms resolution. Each 40 ms-long measurement is then analyzed independently, producing one datapoint consisting of the fringe amplitude, phase and offset. In Figure 8.4a, 100 such measurements are performed at 1 s intervals to obtain the fringe stability over 100 s; in Figure 8.4b, this procedure was repeated with 36 000 measurements separated by 1 s. These effectively provide the fringe phase stability respectively for 100 s and 36 000 s (i.e. 10 hours) with a time resolution of 1 s. Figure 8.4b presents a fringe stability better than 1 rad over 10 hours. This result shows that our fringe phase correction scheme provides an enormous improvement over the 3 s observed in Chapter 5. Recalling that the operating wavelength is $\lambda = 1550$ nm, this time stability corresponds to an effective spatial stability of 250 nm over a period of 10 hours.

Additionally, we repeated the measurements we had performed with the single-detector system in Section 5.6.1, to assess the impact of environmental disturbances. In particular, we are interested in quantifying how the two-detector phase correction method responds to these perturbations. We simultaneously measured the two channels' output over 8 s at the maximum sampling frequency, meaning 1 MS at 125 kS/s for each channel. As in Section 5.6.1, the data was analyzed by extracting the fringe amplitude and phase for blocks of data lasting 1 fringe period, i.e. 0.4 ms. The results are presented in Figure 8.5: the fringe phase for each channel is very disturbed, but the corrected phase is much more stable, with a variability reduced by a factor 5 for all types of perturbations. This proves that the phase correction system significantly reduces the effect of environmental perturbations around

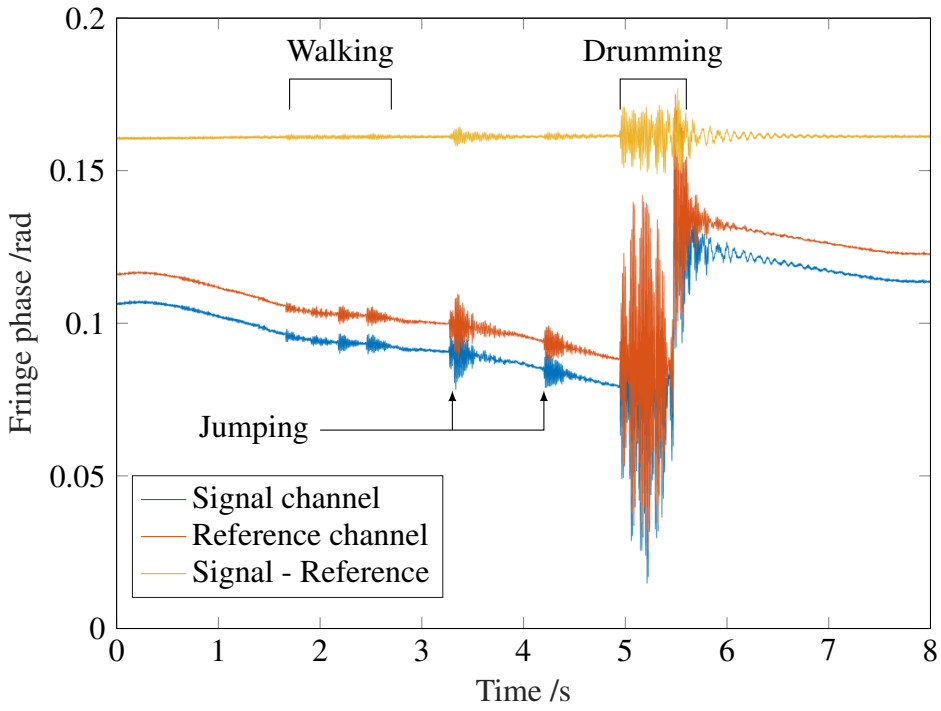

Fig. 8.5 Extracted fringe phase of the signal channel (blue) and reference channel (orange), and their difference (yellow), for a measurement of 1 MS at 125 kS/s sampling frequency for each channel; the environment was perturbed by walking around the optical table, jumping next to it and drumming on it for 1 s.

and on the optical table that could result from human activity. We also remark that we can quantify the sensitivity of the measured fringe phase to perturbations in the individual source and detector fibers by applying a small vibration to each successively. Perturbations of either of the detector fibers has no noticeable effect; on the other hand, perturbations of the source fibers produces variations in the fringe phase, approximately 2 rad in magnitude for both channels, which are reduced to 0.2 rad variations in the corrected fringe phase.

8.3.2 Experimental Results: Single-Mode Systems

We perform two-source one-dimensional scans using the same procedure as for amplitude-only measurement sets, in Section 6.2.3. Table 8.1 summarizes the key properties of the various optical fiber patch cables we will use; those with single-moded behavior will be investigated in this section, while the few-mode and multi-mode optical fibers will be studied in Section 8.3.3.

The 2 m-long, single-mode Thorlabs 1550BHP patch cable is used for the signal channel with the DET01CFC detector and its transimpedance amplifier; the 2 m-long, single-mode,

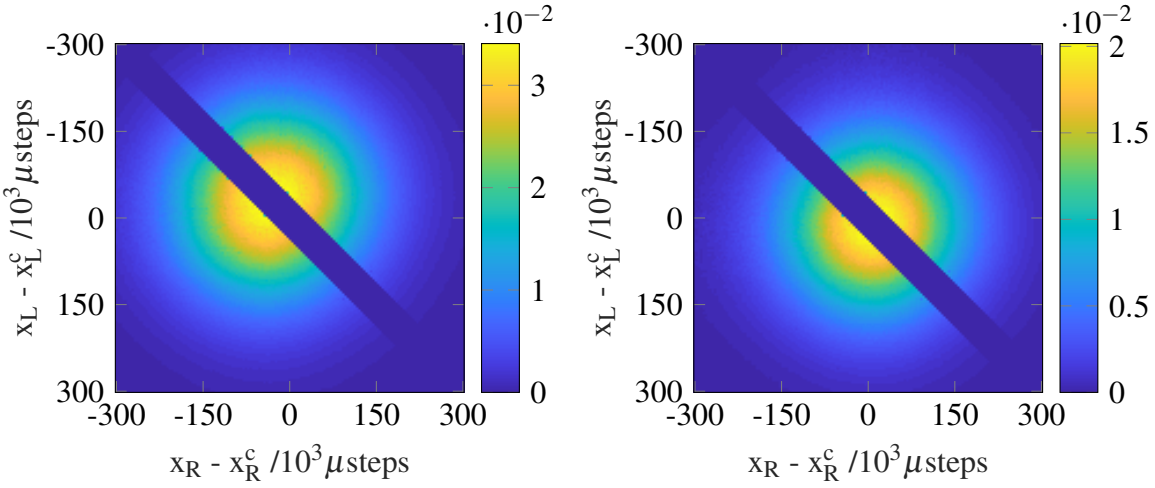

(a) Signal channel

(b) Reference channel

Fig. 8.6 Extracted DRF amplitude for single-mode signal and reference channels.

Fiber name	Core diameter /µm	Numerical aperture	Number of modes at $\lambda = 1550$ nm	Polarization maintaining
Thorlabs 1550BHP	9	0.13	1	No
Thorlabs PM1550-XP	8.5	0.125	1	Yes
Thorlabs SM2000	11	0.12	2	No
Thorlabs P1-23Z	9	0.19	2	No
Thorlabs P1-32F	9	0.26	4	No
Thorlabs FG050LGA	125	50	0.22	No

Table 8.1 Properties of the various 2 m optical fiber patch cables used as interchangeable mode filters for the photodetector

polarization-maintaining Throlabs PM1550-XP patch cable is used for the reference channel with the PDA20CS-EC amplified detector. The fringe amplitude patterns are measured for the signal and reference channels simultaneously, and shown in Figures 8.6a and 8.6b respectively, as functions of the right and left source positions, x_R and x_L, relative to their on-axis positions, x_R^c and x_L^c. The results are qualitatively identical to those obtained in Section 6.4.1, but with some quantitative differences because the vertical alignment with the sources is not identical, as the sources' scanned position set is approximately midway between signal and reference channel heights.

Figures 8.7a and 8.7b show the phase data extracted from the fringes recorded by the signal and reference detectors, respectively. These extracted fringe phase datapoints are not individually true DRF phase values, as the fringe phase drifts randomly for approximately 0.75 s between each measurement, corresponding to an estimated 0.5 rad average angular drift.

Figure 8.7c shows the element-wise subtraction of the extracted fringe phase of the reference channel from the signal channel: we obtain the so-called corrected fringe phase, with an obvious structure. Figure 8.7d shows the corrected phase after a 2π-period phase unwrapping procedure, based on applying Matlab's `unwrap` function, consecutively along x_R and x_L. We obtain a near-perfect plane, with a phase difference of approximately 60 rad between adjacent corners of the triangular DRF matrix. In Figure 8.7e, we perform a least-square fit on the same unwrapped, corrected fringe phase data with a planar functional form

$$\phi = p_{00} + p_{10}(x_R - x_R^c) + p_{01}(x_L - x_L^c), \tag{8.1}$$

where we retrieve the slope coefficients p_{10} and p_{01} along x_R and x_L, and the phase offset p_{00} at $(x_R, x_L) = (x_R^c, x_L^c)$ µsteps. The fitted slope coefficients are similar but not identical; the origin of this fringe phase plane and its small asymmetry will be discussed in Section 8.4. After having fitted the planar functional form, it can be subtracted from the fitted corrected phase data. This procedure reveals an underlying structure, which is nearly constant, as shown in Figure 8.7f. Further investigation is needed to confirm whether this remaining pattern is the true phase structure of the device's DRF (or more precisely, the difference of phase patterns of the signal and reference channel detector systems), or if it is due to additional non-planar contributions that were not cancelled by our plane fitting procedure. This study is performed with simulations in Section 8.4.

8.3.3 Experimental Results: Few-Mode and Multi-Mode Systems

We repeat the same measurement set with the 2 m-long Thorlabs P1-23Z few-mode fiber patch cable ($\lambda_c \approx 2.3$ µm cut-off wavelength) on the signal channel; the reference channel fiber remains the Thorlabs PM1550-XP polarization-maintaining optical fiber. The signal channel's amplitude is approximately identical to the results obtained with the single-detector system, in Section 6.4.2. The DRF's phase component is best represented for the two-dimensionally unwrapped, corrected fringe phase with the planar fit subtracted, shown in Figure 8.8: we observe a π rad phase difference between the nearly constant regions in the center and the anti-diagonal corners. In Figure 8.8, we plot the lines where the x_R- and x_L-gradients of the signal channel fringe amplitude are equal to zero: the circular lines in the anti-diagonal corners correspond perfectly with the boundary of the phase-reversal. This is a clear characteristic of few-mode behavior. It is important here to note that we use the x_R- and x_L-gradients as proxies for finding the zero-amplitude lines, which correspond to where both gradients are zero simultaneously.

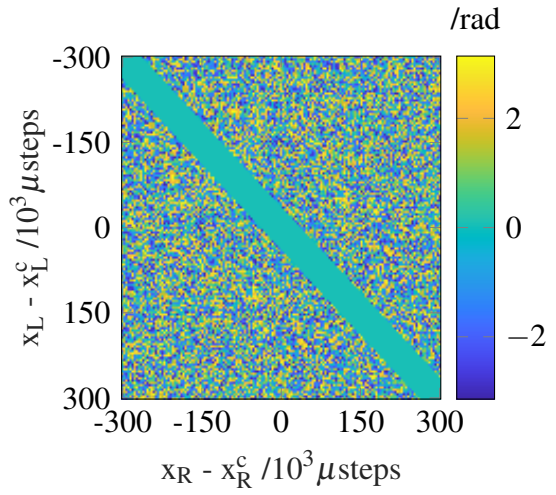

(a) Signal channel phase

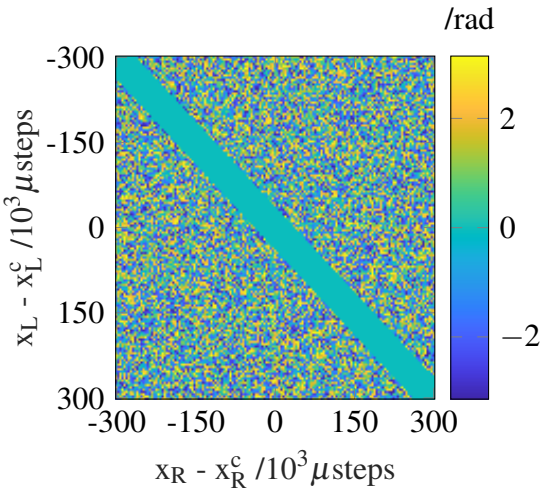

(b) Reference channel phase

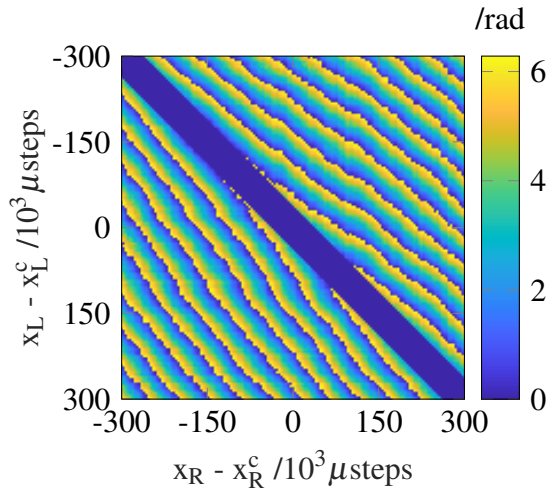

(c) Corrected phase: Signal - Reference

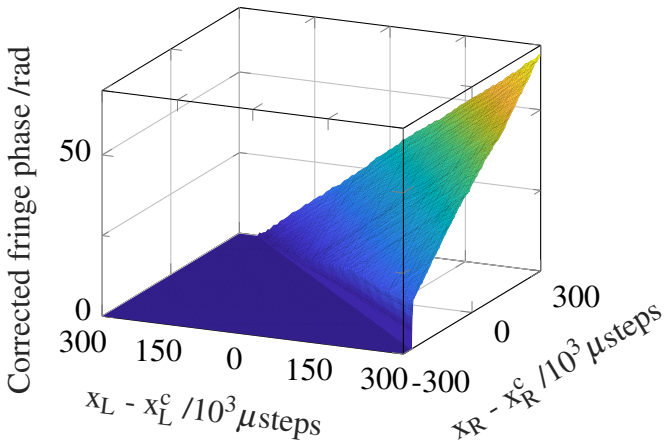

(d) 2-D unwrapped phase

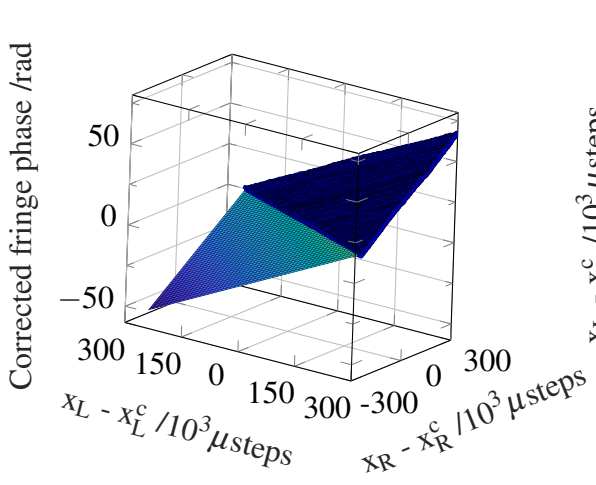

(e) Planar fit of the 2-D unwrapped corrected fringe phase

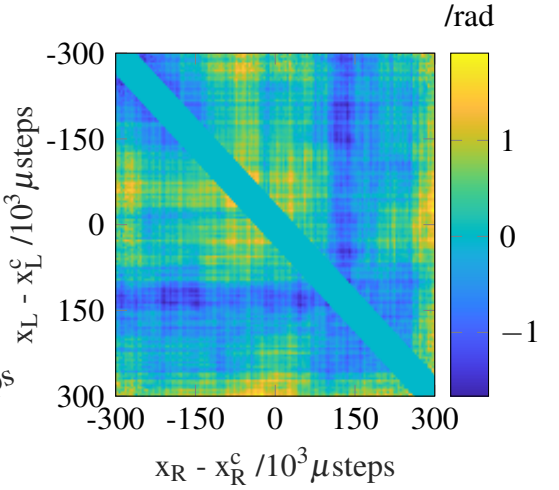

(f) 2-D unwrapped corrected fringe phase with planar fit subtracted

Fig. 8.7 Extracted DRF phase for single-mode signal and reference channels.

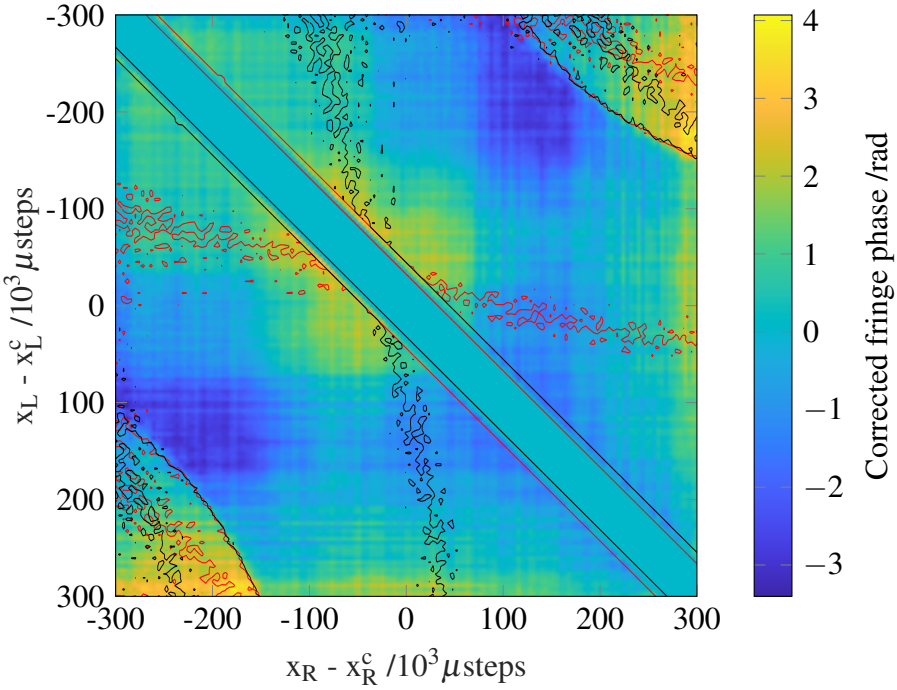

Fig. 8.8 Corrected DRF phase for few-mode signal fiber; the black/red lines correspond to the zeros in the x_R- and x_L-gradients of the signal channel fringe amplitude.

Lower variability over the regions of nearly constant phase can be obtained when, instead of subtracting the planar fit from the signal channel's unwrapped corrected fringe phase, we directly subtract the two-dimensionally unwrapped, corrected phase matrix measured with the single-mode optical fiber (i.e. the data represented in Figure 8.7f). The resulting matrix is shown in Figure 8.9. The fact that lower variability over the quasi-constant regions is achieved, which we view as a metric for the quality of the DRF's measurement, also implies that the phase slope is very stable over time. Indeed, given that the measurements with the few-mode and single-mode fibers, presented in this section and Section 8.3.2 respectively, were performed one week apart, we can infer that the phase slope is stable over at least this amount of time.

The same measurement procedure is repeated with the signal channel detector coupled to a 2 m-long Thorlabs FG050LGA step-index multi-mode optical fiber patch cable, with core radius $a = 25\,\mu$m and numerical aperture NA $= 0.22$. This optical fiber was used in Section 6.4.3; the amplitude pattern obtained with our two-detector system is qualitatively identical. Using Matlab's `unwrap` method twice on the corrected fringe phase, consecutively along the horizontal and vertical axes, generates poor results with horizontal bands that differ from the neighboring bands by 2π rad multiples, as shown in Figure 8.10. A more complex method is needed to deal with the combination of the planar phase slope and the underlying phase

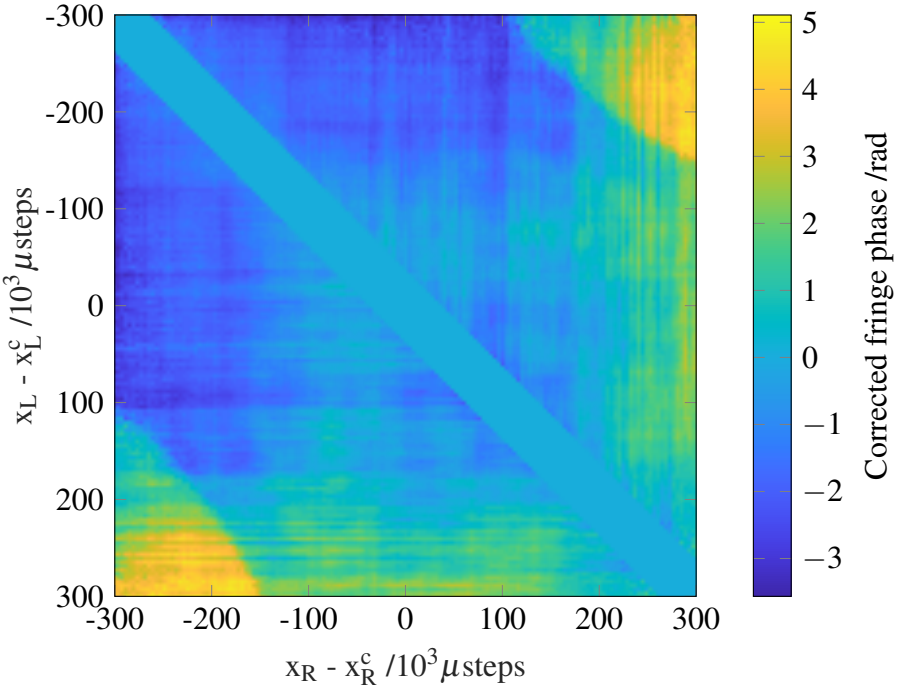

Fig. 8.9 Two-dimensionally unwrapped, corrected DRF phase for few-mode signal fiber; the single-mode two-dimensionally unwrapped corrected DRF phase has been subtracted.

structure, which appears to be structured in diagonal bands of roughly constant width. We use the `unwrap_phase` method [116] that relies on a quality-guided path unwrapping algorithm, in which the two-dimensional path is allowed to be discontinuous [117]. The results obtained when applying this unwrapping function to the multi-mode phase data corrected with the single-mode phase data clearly show diagonal bands with π rad phase jumps between these regions, without the artificial horizontal bands that plagued our initial method. Rather than performing a least-squares fit for a planar function, which would be limited by the fringe phase's diagonal structure, we subtracted the unwrapped corrected fringe phase obtained with the single-mode signal channel in Section 8.3.2. Figure 8.11 shows the output of this method for the same dataset as in Figure 8.10, after the some additional manual 2π rad modifications. The dataset is shown with superimposed lines representing the locations where the x_R- and x_L-gradients of the signal channel fringe amplitude are equal to zero. This result is much more convincing than Figure 8.10, devoid of artificial horizontal bands, and clearly illustrates how the regions of near-constant phase are delimited by lines where the fringe amplitude is equal to zero. This behavior observed in the diagonal amplitude and phase structure is a distinctive feature of a system's multi-mode behavior, demonstrating that our experimental system has the capacity to characterize highly multi-mode devices.

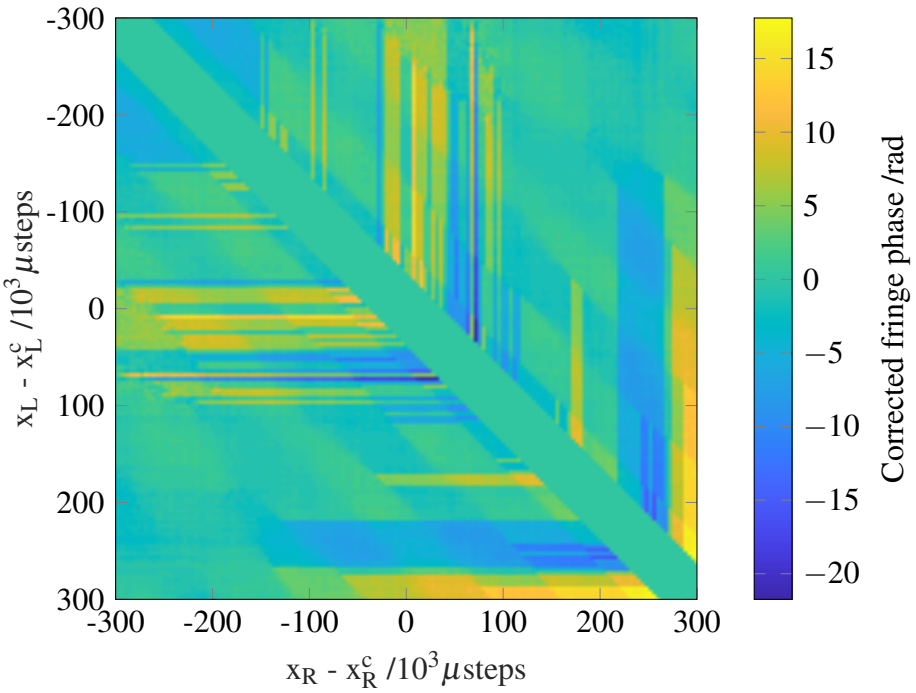

Fig. 8.10 Corrected DRF phase for multi-mode signal fiber; two-dimensionally unwrapped and planar least-squares fit subtracted.

8.4 Numerical Study of the Phase Slope

While we have found post-measurement tools to subtract the large phase slope observed in the measured DRF as sources are scanned, its origin needs to be investigated. We suggest several possible mechanisms:

1. Imperfect definition of source beampattern centers: the assumed values for the on-axis position (x^c, y^c) of each of the sources are inaccurate;

2. Misalignment of one or both sources: the small misalignment of the sources characterized in Section 6.3.2 contributes to the phase slope, individually or collectively or both;

3. Difference in position between detectors: the known position difference between the two detector fibers produces a contribution to the phase slope;

4. Misalignment of one or both detectors: the experimental imperfections of the two-detector system means that either or both of the detector fibers are slightly misaligned;

5. Misalignment of one or both source scanning planes: the experimental imperfections of the sources' respective scanning systems imply that the plane over which they are

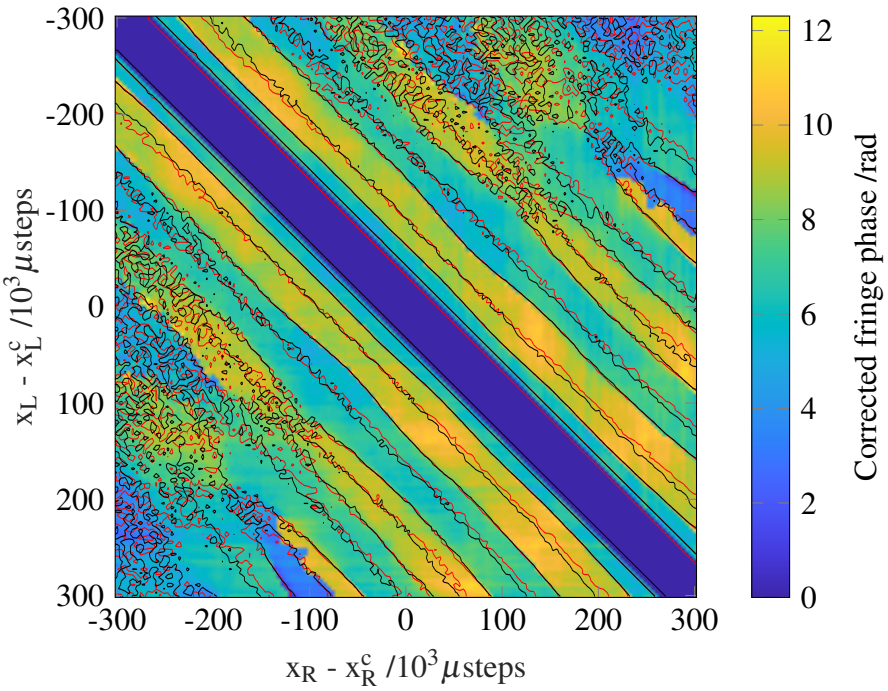

Fig. 8.11 Corrected DRF phase for multi-mode signal fiber; the corrected SM phase is subtracted, and the result is 2D-unwrapped (using unwrap_phase) and improved manually; the black/red lines correspond to the zeros in the x- and y-gradients of the signal channel fringe amplitude.

scanned (for a fixed z value) are not identical, and slightly rotated with respect to the detector plane.

We can use the simplified simulation framework developed in Chapter 7, which assumed the detectors and sources as point-like objects with spherical phasefronts, in order to simulate the corrected fringe phase patterns as the sources are scanned. This simplification means that a translation of the source or detector position is equivalent to an angular misalignment. In the enumeration at the beginning of this section, cases 2 and 4 can therefore be identified with cases 1 and 3. Three classes of imperfections are tested, namely the cases 1, 3 and 5 in the list. In Section 7.3.2, we had obtained the following form for the difference of measured phases between two detectors, labeled A and B:

$$\begin{aligned}\phi_{AB} &= arg(D^A_{mn}) - arg(D^B_{mn}) \\ &= [k|\boldsymbol{r}_n - \boldsymbol{r}_A| - k|\boldsymbol{r}_m - \boldsymbol{r}_A|] - [k|\boldsymbol{r}_n - \boldsymbol{r}_B| - k|\boldsymbol{r}_m - \boldsymbol{r}_B|]\,. \end{aligned} \tag{8.2}$$

Using this formalism, we can simulate the effect of various misalignment types. For simplicity, we consider cases where only a single imperfection is applied. The base configuration is:

- The detectors, labeled A and B, are placed at positions defined by the vectors $\boldsymbol{r}_{A/B} = (x_{A/B}, y_{A/B}, z_{A/B}) = (0, \mp 5, 100)$ mm;
- The right and left sources, labeled R and L, are placed at positions defined by the vectors $\boldsymbol{r}^c_{R/L} = (x_{R/L}, y_{R/L}, z_{R/L}) = (0,0,0)$ mm;
- The right and left sources are scanned in the directions $\hat{\boldsymbol{s}}_{R/L} = (1,0,0)$, i.e. along the x-axis, with a step size equal to 2 mm.

The latter two statements imply that the right and left sources are scanned over the position pairs $(x_R, x_L) \in \{-15\,\text{mm}, -14.8\,\text{mm}, ..., 15\,\text{mm}\}^2$, with $y_R = y_L = z_R = z_L = 0$ mm. In this configuration, the corrected fringe phase is 0 at all source position pairs. Note that these values are again chosen to replicate the configuration of the experimental system.

We can then investigate the various imperfections relative to the base configuration: a change of detector A and/or B's position $\boldsymbol{r}_{A/B}$, a change of source R and/or L's center position $\boldsymbol{r}^c_{R/L}$, or a rotation of source R and/or L's scanning direction $\hat{\boldsymbol{s}}_{R/L}$. In Figure 8.12a, we show the corrected fringe phase pattern when detector A is displaced by 0.05 mm along the x-axis: it forms a plane with equal and positive slopes along x_R and x_L, with a 60 rad difference between the corrected fringe phases at $(x_R, x_L) = (0,0)$ µsteps and $(x_R, x_L) = (300\,000, 300\,000)$ µsteps. In Figure 8.12b, the detector A is displaced by 1 mm along the z-axis: the corrected fringe phase pattern has the form of a saddle, with a 40 rad difference between the corrected fringe phases at $(x_R, x_L) = (0,0)$ µsteps and $(x_R, x_L) = (\pm 300\,000, 0)$ µsteps, and -40 rad difference with $(x_R, x_L) = (0, \pm 300\,000)$ µsteps. Using the same procedure for all possible unique imperfections, we summarize our results in Table 8.2.

These observations provide a large range of behaviors, even from unique imperfections. Some combinations would lead to the observed plane with slightly different slopes along x_R and x_L, such as an increase in x_A and a small rotation of $\hat{\boldsymbol{s}}_R$ about $\hat{\boldsymbol{z}}$. The orders of magnitude of the example cases are also sufficient to explain the measured experimental phase slopes. We therefore conclude that the observed phase slope is of geometric origin.

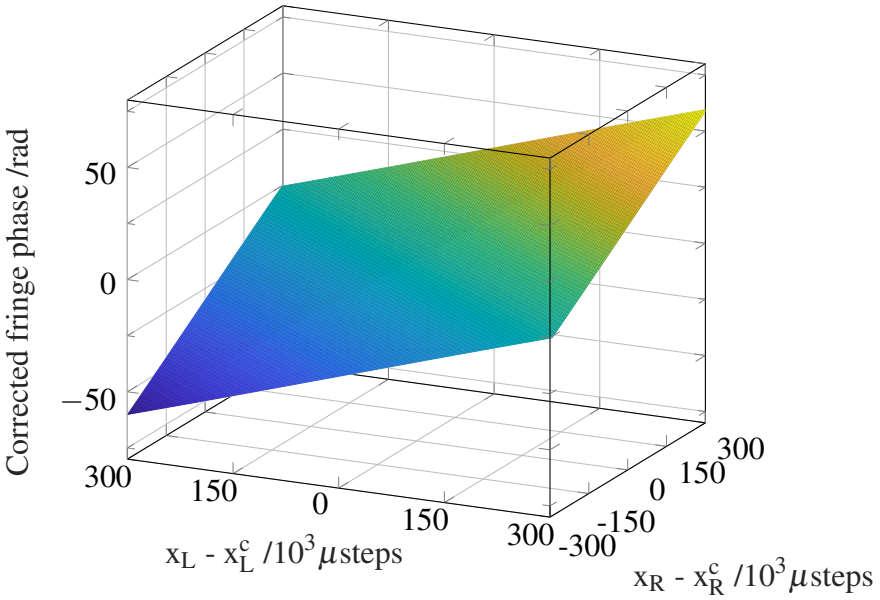

(a) Detector A's position along the x-axis is $x_A = 0.05$ mm, instead of $x_A = 0$ mm

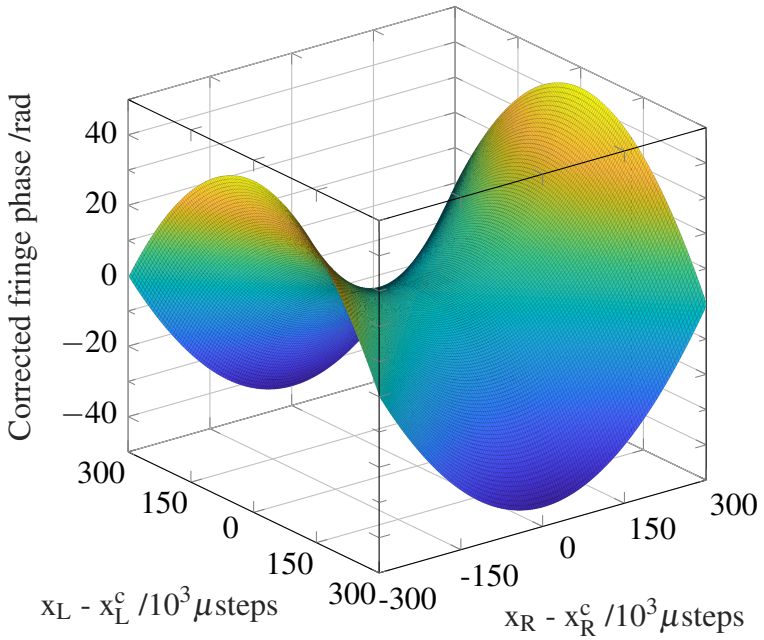

(b) Detector A's position along the z-axis is $z_A = 101$ mm, instead of $z_A = 100$ mm

Fig. 8.12 Simulated corrected DRF phase pattern for point-like sources and detectors, with small deviations from the base configuration.

Table 8.2 Simulated effect of deviations from the reference configuration on the corrected fringe phase, with numerical examples.

Type	Mechanism	Qualitative Effect	Numerical Examples	
			Change Magnitude	Maximum Effect Magnitude
1	Offset x_R^c and/or x_L^c	no effect		
	Increase y_R^c	negative U-shape along x_L, constant along x_R	1 mm	.5 rad along x_L
	Increase y_L^c	positive U-shape along x_R, constant along x_L	1 mm	.5 rad along x_R
	Increase y_R^c and y_L^c	saddle	1 mm	+/-.5 rad along x_R / x_L
	Offset z_R^c and/or z_L^c	no effect		
3	Increase x_A	plane with equal positive slopes along x_R and x_L	0.05 mm	60 rad along x_R and x_L
	Increase x_B	plane with equal negative slopes along x_R and x_L	0.05 mm	-60 rad along x_R and x_L
	Offset x_A and/or x_B	no effect		
	Increase y_A and/or y_B	saddle	+.1 mm to y_A and y_B	-/+ 0.05 rad along x_R / x_L
	Increase z_A	saddle	1 mm	+/- 50 rad along x_R / x_L
	Increase z_B	saddle	1 mm	-/+ 50 rad along x_R / x_L
	Offset z_A and z_B	no effect		
5	Rotate $\hat{\boldsymbol{s}}_{R/L}$ about $\hat{\boldsymbol{x}}$	no effect		
	Rotate $\hat{\boldsymbol{s}}_{R/L}$ about $\hat{\boldsymbol{y}}$	no effect		
	Rotate $\hat{\boldsymbol{s}}_R$ about $\hat{\boldsymbol{z}}$	linear slope along x_L constant along x_R	$\pi/1000$ rad	-40 rad along x_L
	Rotate $\hat{\boldsymbol{s}}_L$ about $\hat{\boldsymbol{z}}$	linear slope along x_R constant along x_L	$\pi/1000$ rad	-40 rad along x_R

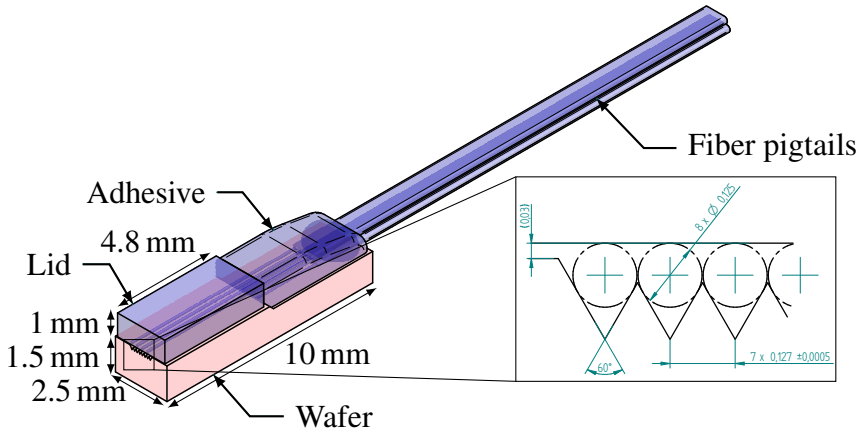

Fig. 8.13 Diagram of an 8-channel fiber array, modified from manufacturer's documentation.

8.5 Fiber Arrays

8.5.1 Characteristics of Fiber Arrays

In previous sections, we have successfully implemented a phase stabilization method based on a second optical fiber and detection system constituting a reference channel, placed near the original fiber-coupled detector system, which can be viewed as the signal channel. While this has allowed us to measure the phase of the DRF with a good accuracy, these results remained limited by the large geometric phase slope observed, which needs to be subtracted. In addition, we will investigate variability in the measured corrected fringe phase in Section 8.6, and show that it is highly dependent on the distance between the signal and reference fiber channels. The goal of this present section is to describe further improvements obtained by using fiber arrays, in which the distance between neighboring fibers is substantially reduced.

The main insight is that, by reducing distance between channels by a given factor, we expect to obtain a decrease in the geometric phase slope by the same factor. Indeed, using the simulation framework introduced in Section 8.4 and repeating it with the base configuration of the detectors labeled A and B at positions $\boldsymbol{r}_{A/B} = (0, \mp 0.065, 100)$mm respectively, rather than $\boldsymbol{r}_{A/B} = (0, \mp 5, 100)$mm, we observe an 80-fold decrease in the effects summarized in Table 8.2.

We chose to use custom-made fiber arrays, with densely packed optical fibers placed at 127 µm distance [118]. The fiber arrays are built from a borosillicate glass wafer with a structure of "v"-shaped grooves in which the coating-stripped optical fibers with 125 µm diameter are slotted; a glass lid placed on top of the fibers firmly secures them in the v-

grooves. The entire structure has a width of 2.5 mm, a length of 10 mm and a height of 2.5 mm; the dimensions of the various components are described in further detail in Figure 8.13. The pitch between the neighboring fibers' cores is 127 µm with accuracy better than 1 µm; it is limited by the concentricity of individual fibers' core with their cladding, rather than the v-groove structure precision. The angular precision, i.e. the angular misalignment of each individual fiber beam with respect to the target direction, is better than 1°.

Two fiber arrays were used. The first has 8 identical Corning SMF-28e single-mode fibers, with 9 µm core diameter and 125 µm cladding diameter, identical to the Thorlabs 1550BHP used in Section 8.3. The 8 individual pigtails are numbered 54 through 61. The second array has 4 fibers, in following order: a single-mode Corning SMF-28e, a few-mode Thorlabs SM2000, another single-mode Corning SMF-28e, and a multi-mode Thorlabs FG050LGA. In this second array, with few-mode and multi-mode fibers, we chose the few-mode Thorlabs SM2000 fiber rather than the fluoride-based ZrF4 and InF3 fibers, which were also investigated in Section 8.3.3. This choice is made for manufacturing purposes: fluoride fibers are significantly more fragile, and arrays incorporating such fibers have not been produced in the past and would have required a long study phase by the manufacturer. This would have applied even to unstripped, 250 µm-diameter fibers, as well as the fiber stripped down to the cladding with 125 µm diameter. As previous results in Chapter 6 did not show a significant qualitative difference between the Thorlabs SM2000 and the fluoride-based fibers, we chose the former.

Several alternatives to fiber arrays were considered but ultimately rejected. One of these was a fiber bundle, produced by various companies: several optical fiber cores are embedded into a single large-diameter cladding layer, and split after several centimeters into individual connectorized pigtails. These fan-out fiber bundles have many applications in spectrometry. The main motivations for rejecting these are:

- the lack of customization possibilities: the available fiber cores did not have the same behavior as the fiber patch cables used in Chapter 6 and Section 8.3, meaning that results would not be directly comparable;
- the lower manufacturing precision: the pitch between fiber cores is specified to within 10 µm only, and manufacturers are not able to provide specifications on the potential misalignment between the fiber cores.

An additional custom part is needed to reliably mount the fiber array to the manual stage. We designed and manufactured this structure based on a rectangular bloc of aluminum with a rectangular groove; its dimensions are chosen precisely such that it is just large enough to fit the array. Two plastic strips are used to clamp the fiber array in the rectangular groove.

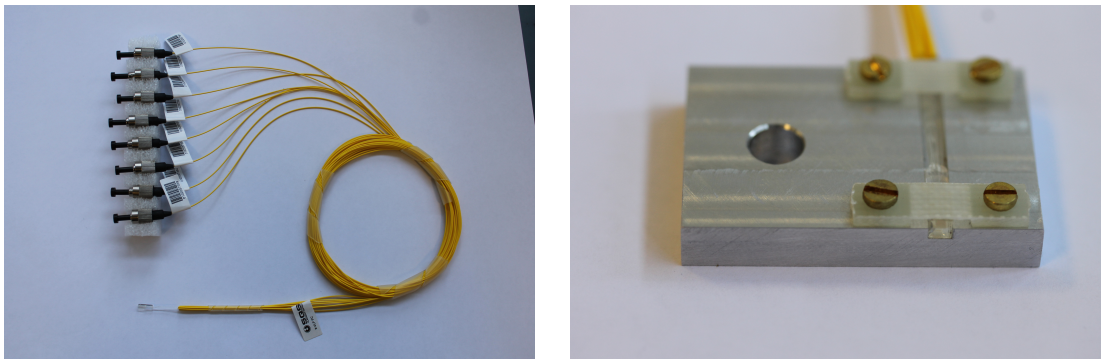

(a) Bare array (b) Array in holder

Fig. 8.14 8-channel, single-mode fiber array and its custom holder.

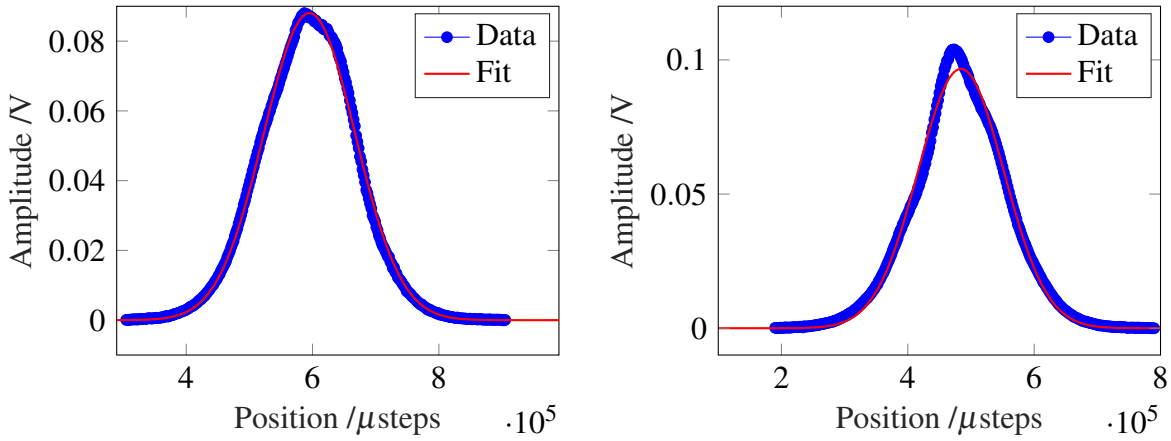

(a) Left source scanned (b) Right source scanned

Fig. 8.15 Single-source beampattern measurement of a single-mode fiber in the fiber array, with least-squares fit of Gaussian function.

Each is secured with two small screws to the aluminum structure: one to clamp down the lid of the array, the other to secure the set of individual fiber leads inside the groove. The dimensions of the aluminum bloc and plastic strips were chosen precisely to secure the array without damaging it. Figure 8.14 shows the fiber array with 8 identical single-mode fibers and the custom holder we fabricated. The small lines visible in the middle of the array wafer in Figure 8.14b are fibers in the v-groove structures. The fiber array is placed inside the rectangular groove such that the fibers are aligned vertically, in line with the vertical configuration of Section 8.2.

8.5.2 Experimental Results: Single-Mode Systems

We aligned the fiber array using a set square, by ensuring the top surface of the holder is orthogonal to the vertical surface of the manual stage. The precision of this arrangement is expected to be better than 1°. Two fibers from the array are selected and used for the signal and reference channels respectively; we later found that these fibers are neighbors, meaning that their core-to-core distance is 127 µm. The first is used for the signal channel with the PDA20CS amplified photodetector at 70 dB amplification; the other is chosen for the reference channel and fed into the DET01CFC photodetector, with its amplifier set to $G = 10^7$ V/A gain factor. Apart from this change of detectors used for the two channels, all other settings are identical to Section 8.3.2.

We first proceeded with single-source beampattern measurements, in part to calibrate the sources' on-axis positions, as the new holder secures the optical fibers at a different position with respect to the manual stage's vertical plate, compared to the former holder with 10 mm distance between fiber cores. The beampatterns observed deviate from their expected Gaussian shape, mostly for the source positions at which the signal is greater than the beampattern's half maximum. Figures 8.15a and 8.15b show these small distortions for scans of the left and right source, respectively. Wrapping the fiber tightly around a mandrel, such as the 40 mm-diameter cylinder used to suppress the few-mode Thorlabs SM2000 fiber's second mode in Section 6.4.2, does not reduce the distortions observed. The way we understand the distortions to the expected Gaussian shape is that the electromagnetic behavior of the optical fiber's surface has been changed by the borosilicate v-groove structure in which it is set, compared to the concentric 127 µm bore size ceramic ferrule it was epoxied into in the case of connectorized optical fiber patch cables, such as those used in Section 8.3. In the v-groove, the surface of the stripped fiber's cladding layer is exposed: small sections are in contact with the borosilicate glass v-groove and lid structures, while the majority is in direct contact with air from the v-groove's gap. In an FC/PC connector, the entirety of the stripped fiber's cladding outer boundary is covered with high refractive index epoxy with a maximum thickness of 2 µm and tightly fitted inside the optically opaque ceramic ferrule. Not only does the fiber array allow for additional radiation input through the air-cladding boundary, the circular symmetry of the medium outside the cladding layer is also broken. However, we conclude that the beampattern distortions are an intrinsic part of the system's optical response, which EAI is fully capable of measuring.

Figure 8.16a shows the DRF amplitude for a two-source fringe scan, measured with the same settings as in Section 8.3.2. It displays an amplitude pattern almost identical to that measured with the single-mode fiber patch cable, in Section 8.3.2, and in line with the results presented with the same optical fiber in the single-detector system in Section 6.4.1.

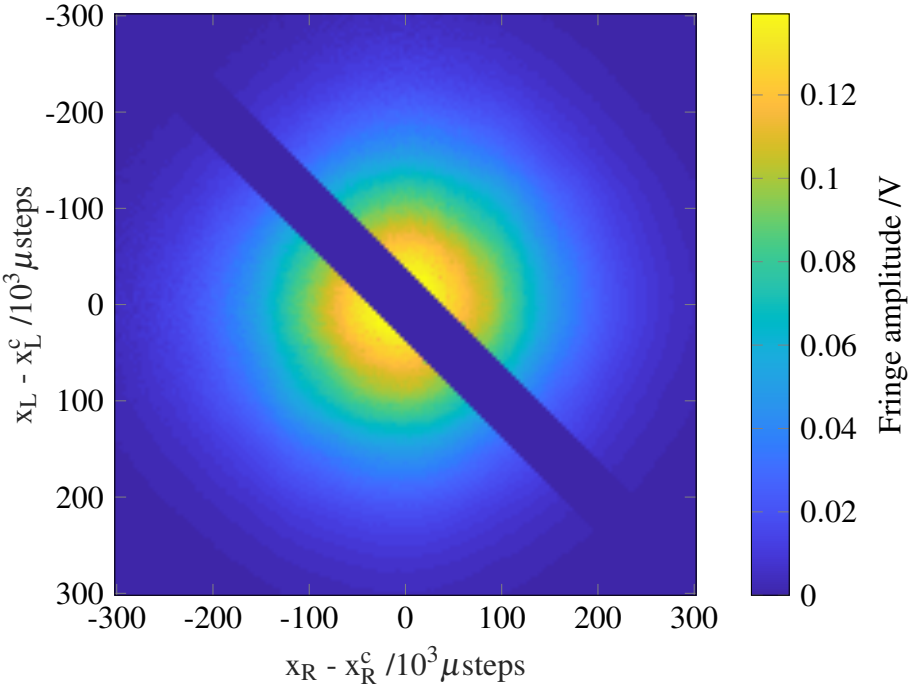

(a) DRF amplitude

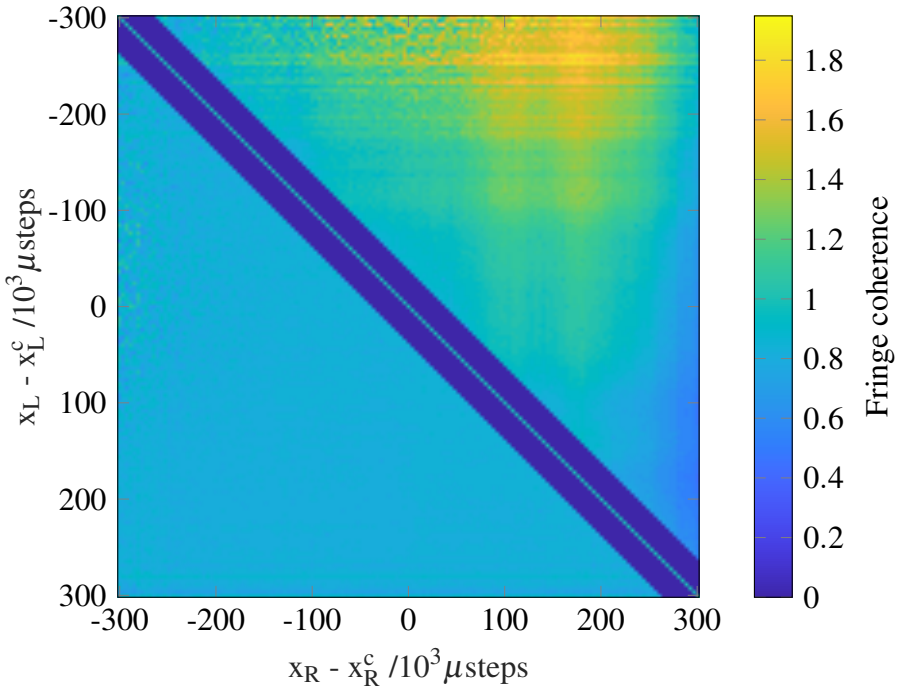

(b) DRF coherence

Fig. 8.16 Measured DRF fringe amplitude and coherence of single-mode fiber in array.

Fiber number	p_{10} ($\times 10^{-6}$)	p_{01} ($\times 10^{-6}$)
59	7.193	-6.510
61	-6.885	6.036
58	35.00	-31.92
57	13.73	-12.44
56	27.95	-25.49
55	20.95	-19.07
54	41.89	-38.38

Table 8.3 Fitted corrected fringe phase parameters for 8-channel single-mode fiber array, with fitting function $\phi = p_{00} + p_{10}(x_R - x_R^c) + p_{01}(x_L - x_L^c)$ defined in Equation (8.1)

The measured reference channel's DRF is qualitatively similar. The signal channel DRF's coherence matrix is presented in Figure 8.16b. We observe a constant pattern, characteristic of single-mode devices. This confirms that, while the single-source beampattern measurements produced distorted Gaussian shapes, the behavior of the detector under test remains single-mode.

Figure 8.17a shows the near-planar phase pattern. Performing a least-squares fit to a planar functional form in Equation (8.1), we obtain the linear coefficients of the plane, $p_{10} = 7.193 \times 10^{-6}$ rad/µsteps and $p_{01} = -6.510 \times 10^{-6}$ rad/µsteps. These are smaller than those measured in Section 8.3.2 using the two-detector system at $d = 10$ mm distance, $p_{10} = 9.092 \times 10^{-5}$ rad/µsteps and $p_{01} = -1.199 \times 10^{-4}$ rad/µsteps. This reduction is however not by the factor 80 that we had expected. We also remark that the slope coefficients along x_R and x_L again have different magnitude, but their comparison has changed. Figure 8.17b is similar to Figure 8.17a, but the plane obtained by a least-squares fit on the data is subtracted. We clearly see that the fringe phase pattern is almost flat, and that the largest deviations of magnitude approximately 0.5 rad correspond to datapoints obtained with low-SNR measurements. Some small structure of magnitude within ± 0.1 rad can be observed. It has strong qualitative similarities with the structure observed when using the two-detector system with 10 mm core-to-core pitch in Section 8.3.2, for instance in Figure 8.7f. This observation strongly suggests that the structure observed is a nonlinear remnant of the geometric phase slope, after the linear contribution has been subtracted.

By repeating these two-detector measurements using various fibers for the signal channel, while keeping the reference channel fiber identical, we can obtain a table of least-squares fitting parameters to the planar model in Equation (8.1), presented in Table 8.3. In the two-fiber system described in Section 8.3.2, we had seen that a positive slope in x_R, i.e. $p_{10} > 0$, and a negative slope in x_L, i.e. $p_{01} < 0$, corresponded to the signal channel fiber being below the reference channel fiber. From this information, we observe that the slope

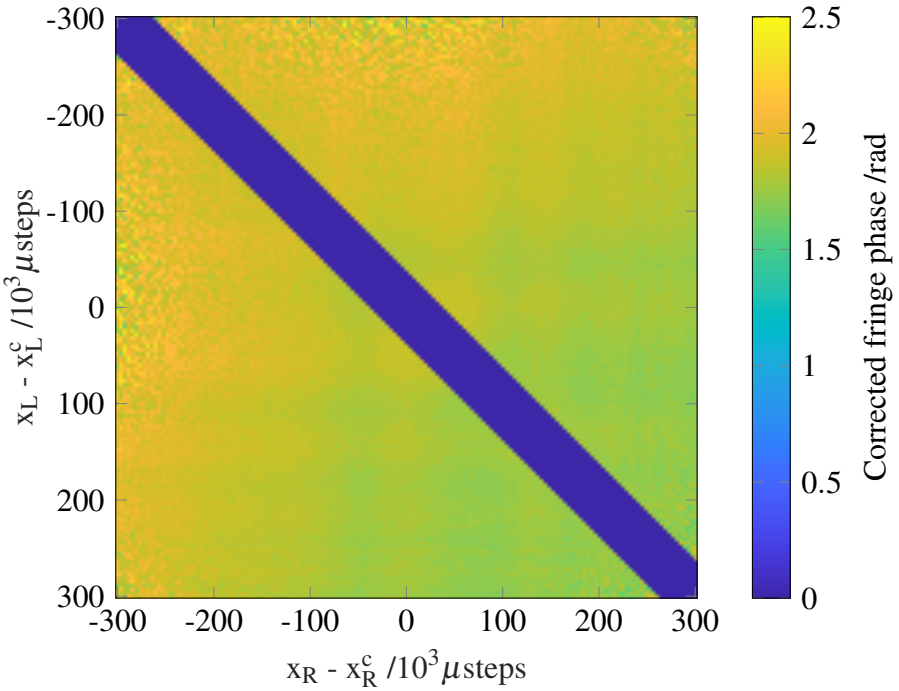

(a) DRF phase, corrected with phase of neighboring single-mode fiber

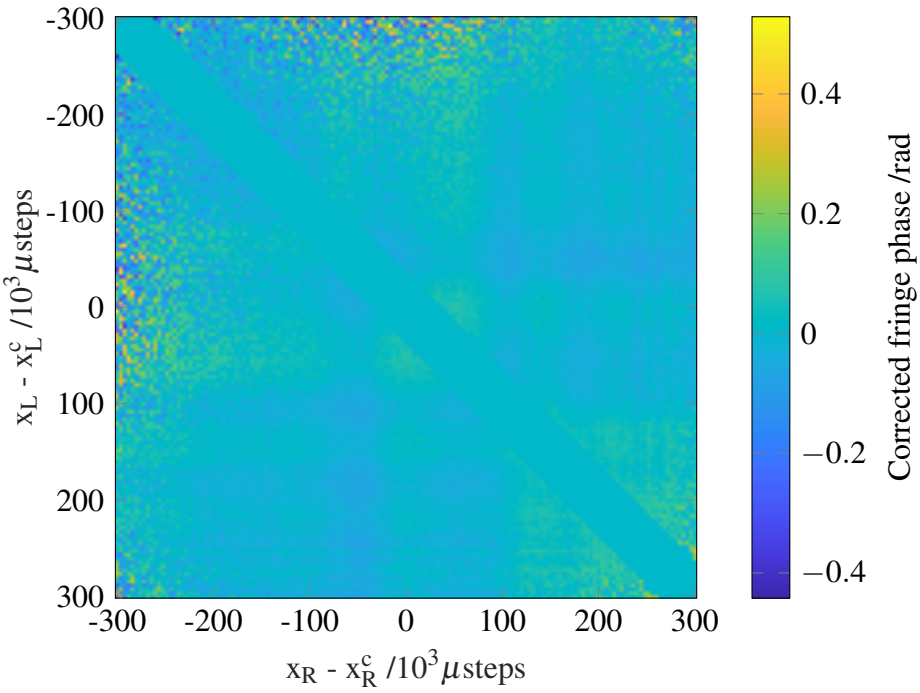

(b) Corrected DRF phase with planar least-squares fit subtracted

Fig. 8.17 Measured DRF phase of single-mode fiber in fiber array.

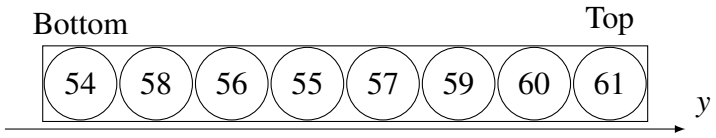

Fig. 8.18 Order of labeled fibers in array.

parameters are proportional to the distance between the chosen channels' fiber cores, and we deduce the vertical order of the 8 single-mode fibers in the array. Figure 8.18 shows the inferred configuration of the fiber array. More generally, we remark that the phase slope's proportionality to the distance between channels' fibers further confirms that the phase slope is geometric, as suggested by the simulations performed in Section 8.4.

8.5.3 Experimental Results: Few-Mode and Multi-Mode Systems

We can repeat the same measurement procedure using the fiber array containing the few-mode and multi-mode fibers, starting with the few-mode Thorlabs SM2000 fiber, which has a cutoff wavelength of $\lambda_c \approx 1.7\,\mu$m. Finding which of the single-mode fibers is located between the few-mode and multi-mode fibers can be done by comparing the phase slope fit coefficients as in Section 8.5.2, or by straightforwardly following the fiber to the corresponding connector. This center single-mode fiber is used for the reference channel, while the few-mode fiber is used for the signal channel; all other settings are identical to Section 8.5.2. Figure 8.19a shows the measured DRF's amplitude, which has a slightly oval shape, characteristic of few-mode behavior; the DRF's coherence matrix also decreases from a value close to 1 along the diagonal towards 0 at the anti-diagonal corners. In Figure 8.19b, we present the corrected fringe phase. We again observe a clear reduction in the phase slope, compared to those obtained with the same fibers in patch cables at 10 mm core-to-core pitch, in Section 8.3.3. Contrary to this latter case, we do not observe the phase-reversed region nor the corresponding zero-amplitude line. However, the fringe amplitude pattern is slightly ellipsoidal and the fringe coherence decreases to values close to zero at the anti-diagonal corners. Together, these observations indicate that a second mode is present in the measured DRF, but that its relative responsivity is lower than in Section 8.5.3.

We then turn to using the multi-mode fiber for the signal channel, and keep the center single-mode fiber for the reference channel. We perform the same measurement set under otherwise identical conditions. Figure 8.20a presents the measured DRF's amplitude: its diagonal structure is characteristic of multi-mode behavior. Its coherence matrix has the same structure: the band closest to the center reaches a value of 0.37, constant along its entire length, and the local maxima decrease towards the antidiagonal corners. In Figure

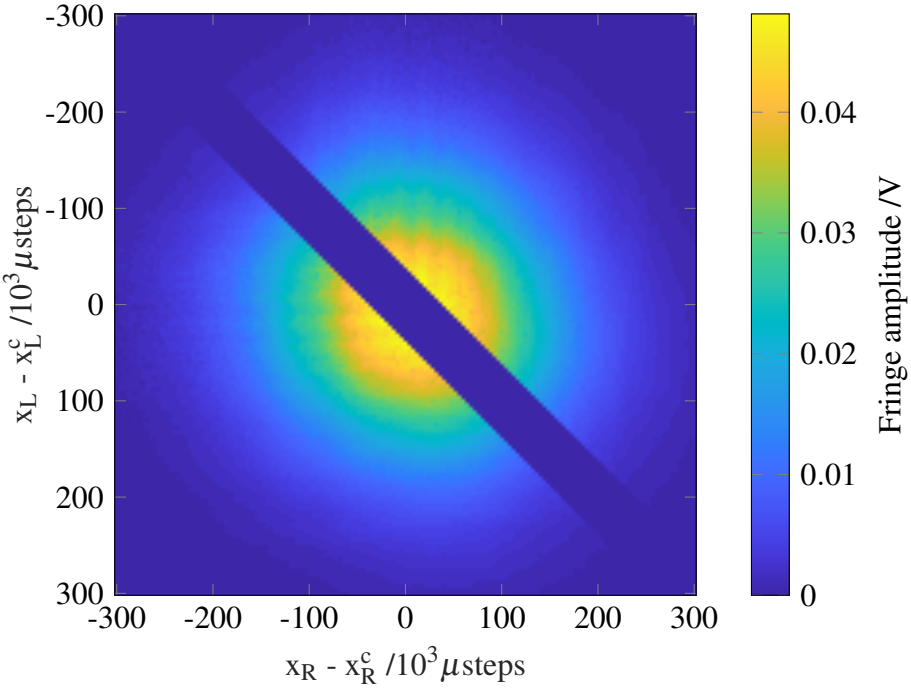

(a) DRF amplitude

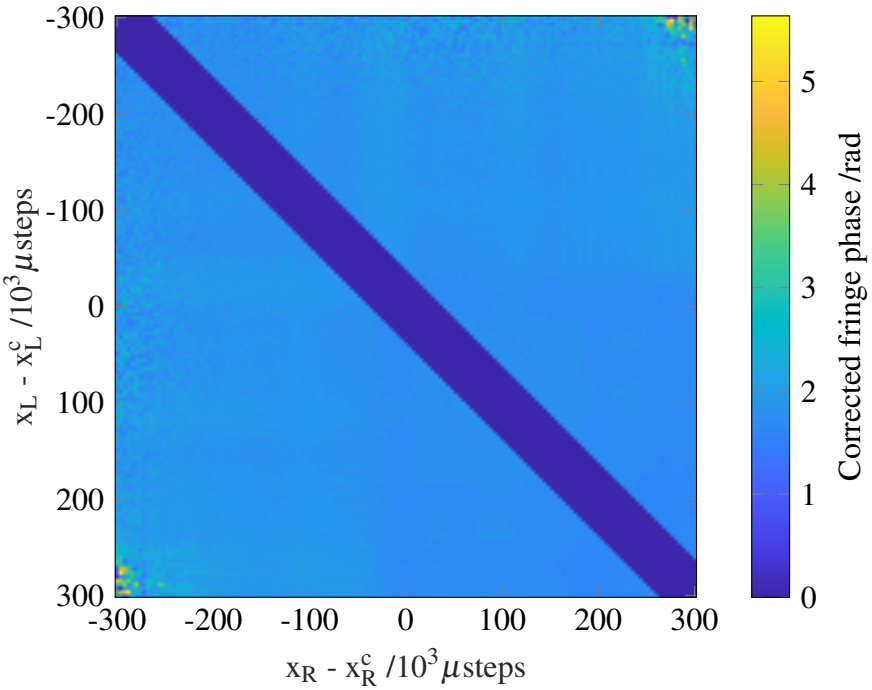

(b) DRF phase, corrected with phase of neighboring single-mode fiber

Fig. 8.19 Measured DRF amplitude and phase of few-mode fiber in fiber array.

8.20b, we present the corrected fringe phase; using the `unwrap_phase` method discussed in Section 8.3.3 was not necessary here, as the geometric phase slope is small and does not interfere with Matlab's standard `unwrap` method. We again observe diagonal bands of quasi-constant phase, with π rad differences between neighboring bands; their boundary correspond to zero-amplitude lines, as in Section 8.3.3.

Our observations in both few-mode and multi-mode cases confirm our expectation that reducing the distance between the optical fibers corresponding to the signal and reference channels has greatly reduced the geometric phase slope. We argue that this amounts to an improvement to the quality of the measured fringe phase patterns, as it relies less on accuracy of post-measurement operations. More importantly, they confirm the insights discussed in Section 8.3 into the differences between the single-mode, few-mode and multi-mode behavior of fiber-coupled photodetector's modal behavior.

8.5.4 Synthesizing DRFs by Summing Measured DRFs

We can now ask whether summing the DRFs from two separate detectors synthesizes a multi-mode DRF. Our intuition starts from recalling that multi-mode DRFs can be diagonalized as incoherent sums of fully-coherent modes. If we add two or more DRFs, it remains an incoherent sum of fully-coherent modes. By carrying out this technique with experimentally acquired DRFs, we may be able to synthesize DRFs with a larger number of modes than the summed DRFs individually.

In order to avoid using one channel as its own reference, we can extend our experimental system to a three detector configuration. One detector serves as the reference channel, and the two others corresponds to independent signal channels. A third detector is required to realize this arrangement; we chose a Thorlabs PDA20CS amplified PIN photodiode detector: its photodiode and amplification electronics are strictly identical to the Thorlabs PDA20CS-EC detector, and we assume their equal performances are as characterized in Section 8.3.1. We also require a new multi-input ADC adapter card, in order to measure the three detectors' outputs simultaneously. We designed and manufactured a custom PCB board that allows the connection of our ADC's relevant connector pins to ten BNC cables. Eight are connected to analog inputs and two to digital inputs, for the synchronization of measurements on analog inputs. We continue to use the same National Instruments PCIe-6321 ADC, with a 250 kS/s maximum cumulative sampling frequency: we can therefore set the sampling rate to 80 kS/s for each channel, producing 32 points per fringe period at a phase modulation frequency of 2.5 kHz.

Using this extended experimental system, we can proceed with the simultaneous measurement of three fiber-coupled detectors. In practice, we use the DET01CFC detector

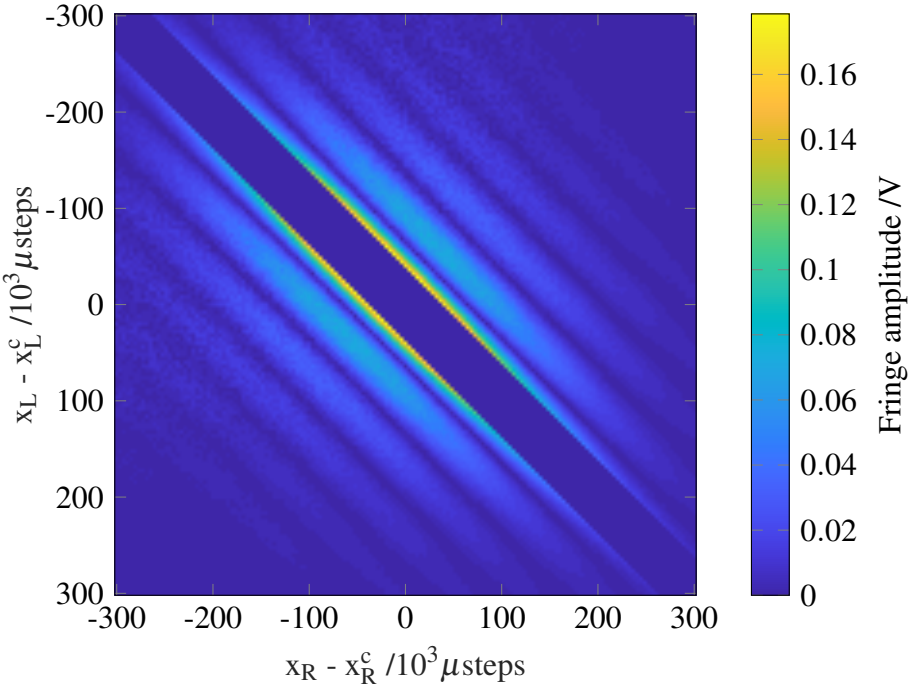

(a) DRF amplitude

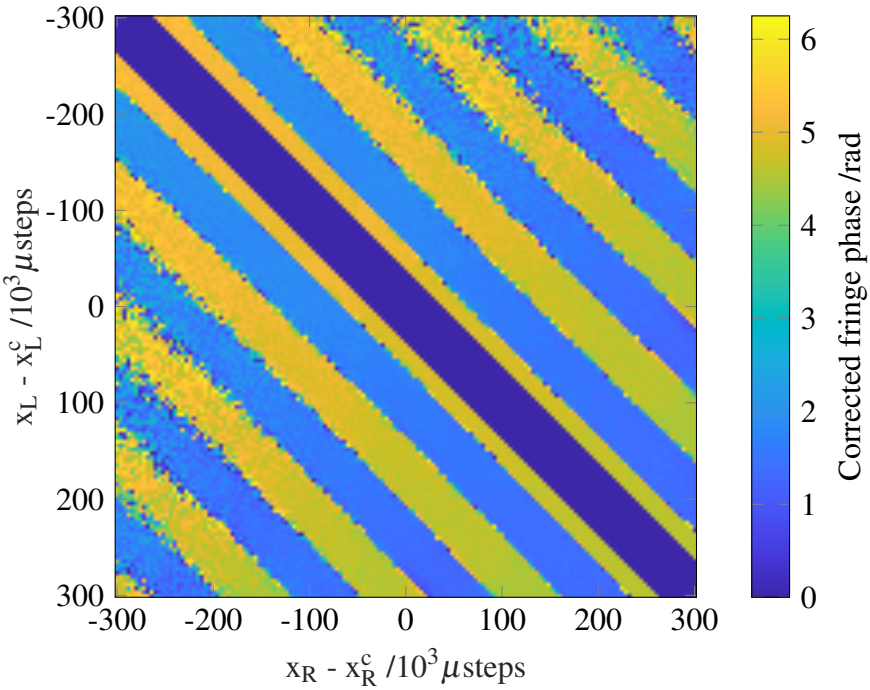

(b) DRF phase, corrected with phase of neighboring single-mode fiber

Fig. 8.20 Measured DRF amplitude and phase of multi-mode fiber in fiber array.

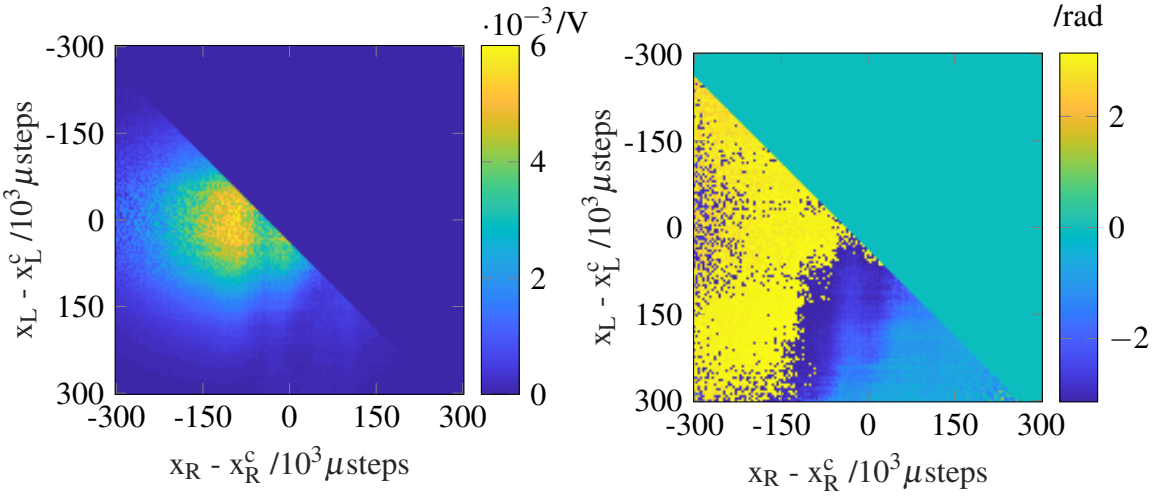

(a) DRF amplitude

(b) DRF phase

Fig. 8.21 DRF synthesized from addition of two single-mode DRFs.

(and its transimpedance amplifier) as the reference channel detector and the two identical PDA20CS(-EC) amplified detectors for the two signal channels. In order to obtain the best results, these detectors are coupled to three optical fibers from the fiber arrays, either the full single-mode or the few- and multi-mode designs. Figure 8.21 presents the amplitude and phase of the DRF obtained by adding two single-mode DRFs, with their phase corrected by a third, single-mode reference channel. There is some ambiguity regarding whether we should add one DRF to the other without modification or after applying the complex conjugation operator. Figure 8.22 shows the amplitude and phase of the DRF obtained by adding two single-mode DRFs, with the second complex conjugated. By adding the unconjugated or conjugated DRF, we obtain the symmetric and anti-symmetric parts of the DRF sum with respect to the reference detector. This can be understood by considering how the geometric phase slope is added without and with complex conjugation: in this configuration where the phase reference is placed between the two summed channels, complex conjugation inverts the phase slope. In effect, complex conjugation maps the geometric phase difference to the other signal channel, such that both signal channels have the same geometric phase contribution with respect to the reference channel.

We perform a similar measurement set using both few- and multi-mode fibers in the fiber array as signal channels. In Figures 8.23 and 8.24, we present the amplitude and phase of the two DRFs obtained by adding a few-mode and multi-mode DRF, with the latter without and with complex conjugation respectively. Again, the case with the complex conjugation is qualitatively most resemblant to the original multi-mode DRF, as the maximum amplitude is attained in the centermost diagonal band. The DRFs' corrected phase shows nearly diagonal

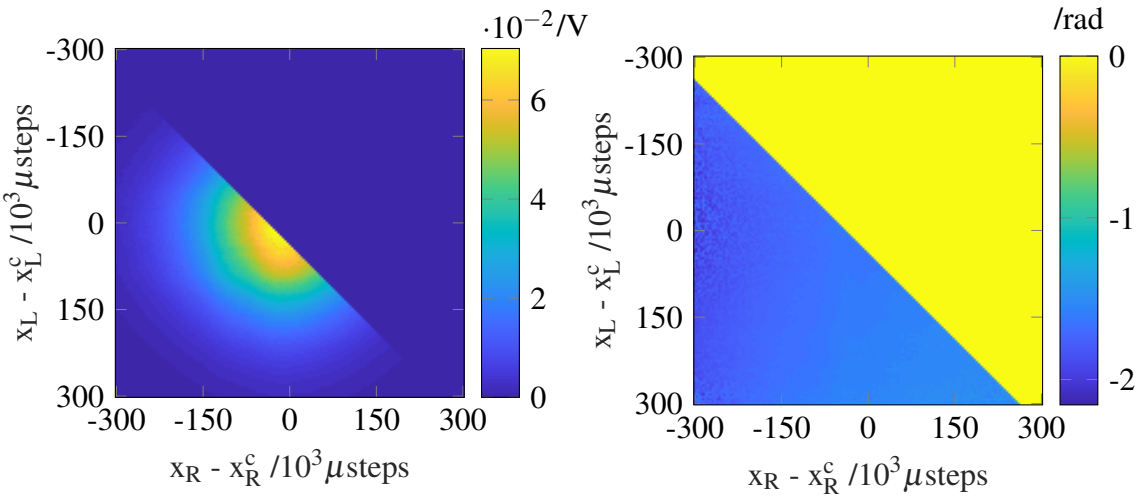

(a) DRF amplitude

(b) DRF phase

Fig. 8.22 DRF synthesized from addition of two single-mode DRFs, after complex conjugation of the second.

features, but slightly circular towards the extreme x_R and x_L values. We also remark that the phase pattern of the conjugated and unconjugated addition cases are different, and do not have the same boundaries. These are again understood to be the symmetric and anti-symmetric parts of the DRF sum with respect to the center reference channel.

8.6 Repeatability

8.6.1 Limited Fringe Phase Repeatability

We have demonstrated that the extension to our phase correction scheme has provided an improvement of the phase stability over time from a few seconds to several hours. This has allowed us to successfully perform simultaneous measurements of fringe amplitude and phase for two-source one-dimensional scans lasting up to four hours. In particular, being able to subtract the corrected fringe phase pattern obtained with single-mode signal and reference channels from that obtained with a few-mode or multi-mode fiber on the signal channel has shown that the results have good repeatability, even for datasets recorded several days apart. However, we also observe that the repeatability is limited not by time, but rather by the reiteration of the measurement process. For instance, when we repeat the same scanning strategy of moving the sources at a fixed distance of 10 positions, equivalent to 40 000 µsteps, with a 10 mm core-to-core pitch, the comparison in Figure 8.25 shows differences in the corrected fringe phase between scans of up to 1 rad. We may then ask

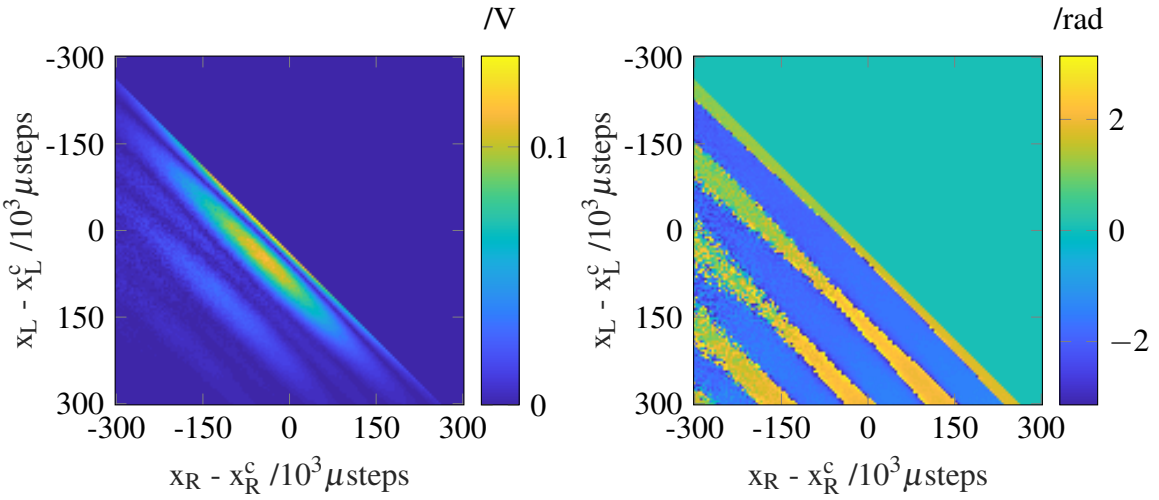

(a) DRF amplitude

(b) DRF phase

Fig. 8.23 DRF synthesized from addition of a few-mode and a multi-mode DRF.

whether this observation is caused by a variability mechanism in the measured corrected fringe phase, or by some underlying structure that requires finer spatial sampling. In either case, the goal of the work presented in this section will be to locate the origin of this lack of repeatability, understand the mechanism causing it and address it to reduce the variability on our experimental results.

In order to further investigate a potential spatial dependence of the corrected fringe phase, rather than the temporal stability studied in Section 8.2, we perform a first measurement run, that will serve as the benchmark when the procedure is reiterated under different settings. We move the sources to the target position $(x_R, y_R, x_L, y_L) = (470\,000, 360\,000, 585\,000, 360\,000)$ µsteps where they are next to each other and closest to their respective center values, perform a fringe measurement of 50 kS at 125 kS/s sampling frequency per channel, move the sources back to some reference position such as $(x_R, y_R, x_L, y_L) = (0, 360\,000, 0, 360\,000)$ µsteps, i.e. move the right and left sources by $\Delta x_R = 470\,000$ µsteps and $\Delta x_L = 585\,000$ µsteps respectively, and repeat this procedure a number of times, chosen to be 50. Doing so with the Thorlabs 1550BHP single-mode optical fiber on the signal channel and the Thorlabs PM1550-XP polarization-maintaining fiber on the reference channel, the 50 corrected fringe phase values are distributed randomly over a range of approximately 1 rad, as shown in Figure 8.26. This indicates that the variability observed in Figure 8.25 is not temporal, but appears as a measurement is repeated identically. In order to compare different measurement runs, the fringe phase dataset's range, standard deviation and mean absolute difference (i.e. the mean of the absolute values of the difference between successive fringe phase datapoints) are computed; larger values in these metrics imply larger variability.

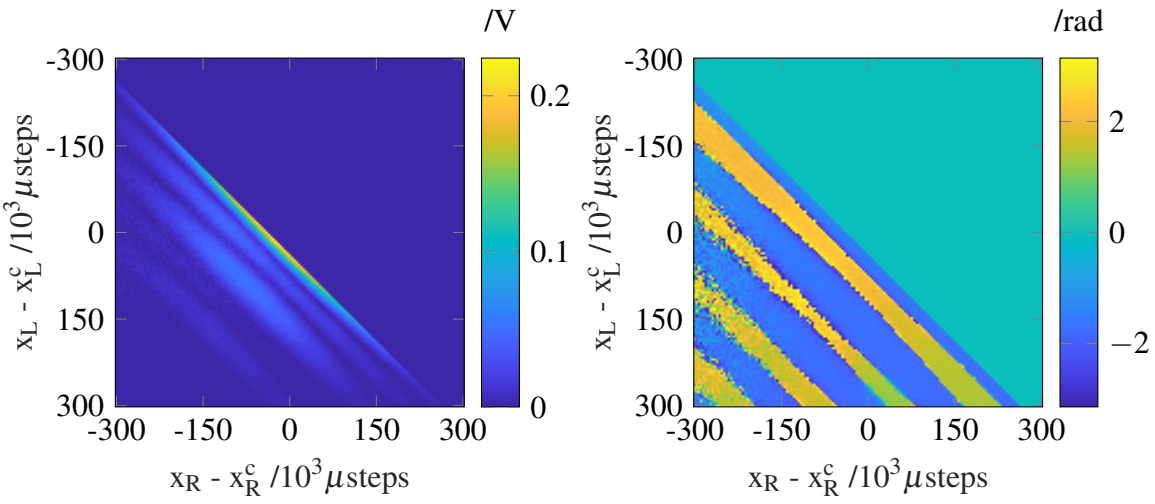

(a) DRF amplitude

(b) DRF phase

Fig. 8.24 DRF synthesized from addition of a few-mode and a multi-mode DRF, after complex conjugation of the latter.

This same experimental procedure can be slightly modified by choosing different scanning parameters. Various attempts are made:

- Scanning the right or left source only: the corrected fringe phase variability statistics are slightly decreased, by approximately 30%;
- Changing the delay time after the movements: the phase variability is considerably increased for delay times shorter than 0.3 s, in line with the stages' settling time of 0.2 s, but constant for longer delay times, tested up to 5 s;
- Adding a delay time once the probes have been moved back: the phase variability is independent of the time spent by the stages at their reference position;
- Changing the number of samples per measurement: between 50 S and 50 kS measured at 125 kS/s for each channel, the phase variability is independent of the number of samples recorded;
- Changing the magnitude of the back-and-forth movement $\Delta x_{R/L}$: the phase variability increases with the magnitude of the sources' movement between their target and reference positions, as shown in Figure 8.27.

We conclude that the fringe phase variability is linked to the movement of the motorized scanning stages.

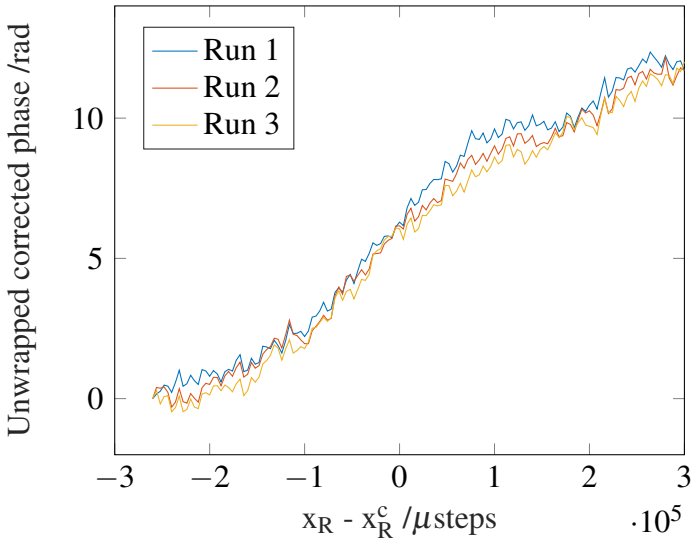

Fig. 8.25 Repeatability of unwrapped corrected fringe phase over three identical scans, during which the sources scanned at fixed distance of 10 sampled positions.

8.6.2 System Verifications

We continue our investigation by performing various troubleshooting tests. The first of these is to verify the performance of the motorized slides in their current configuration. This includes the loads from mounting the three linear stages together, torque from the extender arm and optical fiber holder, the weight from the fiber patch cable that extends for approximately 20 cm in length until it rests onto the optical table, as well as any tension resulting from the fiber being moved as the sources are scanned. Two main aspects of the slide performance are verified:

- The motorized slides' positioning precision: The stage plate's position is measured, using a mechanical dial gauge with a graduated scale of 1/10 000", i.e. 2.5 µm, as movements are repeated to the same target position. The repeatability is measured to be within 1 µm, which corresponds to the manufacturer's specifications, and is in agreement with the repeatability measured in Chapter 5.

- The motorized slides' angular precision: The angle of the slide plate with respect to the $\hat{z}$ direction is measured using a red Helium-Neon (632.8 nm wavelength) collimated free-space laser illuminating a 45°-angle mirror placed on the horizontal slide's plate next to the mounted vertical slide. The laser beam is reflected onto a screen placed at a distance of 2 m, as movements are repeated to the same target position; the variability of the reflected dot on the screen is smaller than 1 mm, implying an angular precision

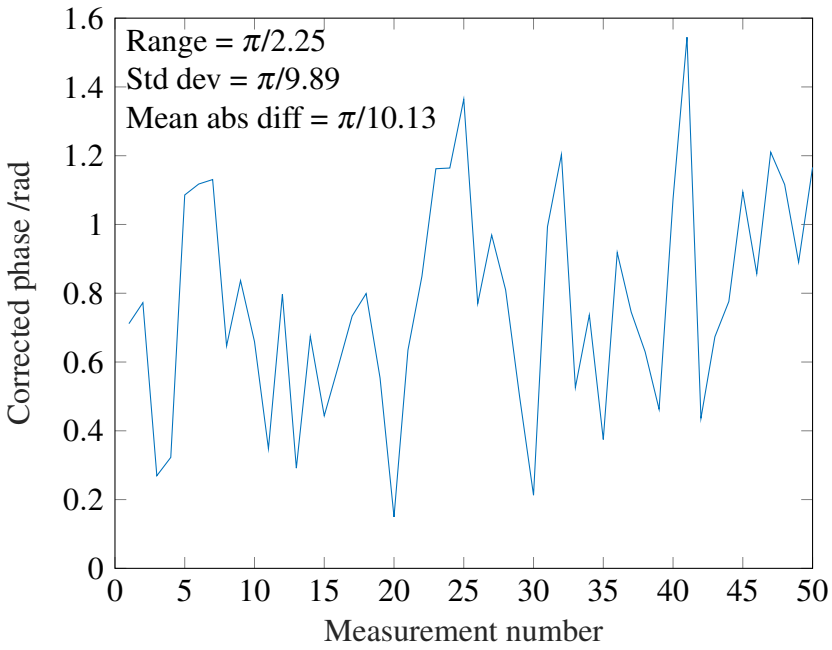

Fig. 8.26 Corrected fringe phase as the two sources are moved back and forth to their target position from $(x_R, x_L) = (0,0)$ µsteps, i.e. $\Delta x_R = 470\,000$ µsteps and $\Delta x_L = 585\,000$ µsteps.

better than $\tan^{-1}(1\text{mm}/2\text{m}) = 0.5$ mrad. This is in line the manufacturer's maximal specifications of 0.349 mrad pitch, 0.08 mrad roll and 0.349 mrad yaw.

Another factor that could contribute to the fringe phase variability is perturbations in the refractive index of the air between the sources and each of the detector fibers. The refractive index of air is dependent on the medium temperature t, relative humidity RH and pressure p [119], so this investigation covers a large variety of phenomena, such as local temperature fluctuations or air flows. Note that this is not straightforward in the current experimental configuration, as we are considering the corrected phase, i.e. the fringe phase difference between the signal and reference channels, for which the optical path of the radiation from the sources is quite similar. In the case of a single source and detector, the phase change on the source's phasefront at a point some distance d away is given by

$$\Delta\phi = k\Delta l = \frac{2\pi}{\lambda} d\Delta n, \tag{8.3}$$

where $\Delta l = d\Delta n$ is the optical path length variation over the distance d caused by a variation in refractive index $\Delta n = n_f - n_i$, and $n_{i/f}$ are the refractive indices of the initial and disturbed environment respectively. To compute the refractive indices $n_{i/f}$, we use the modified Edlen equation [120, 121].

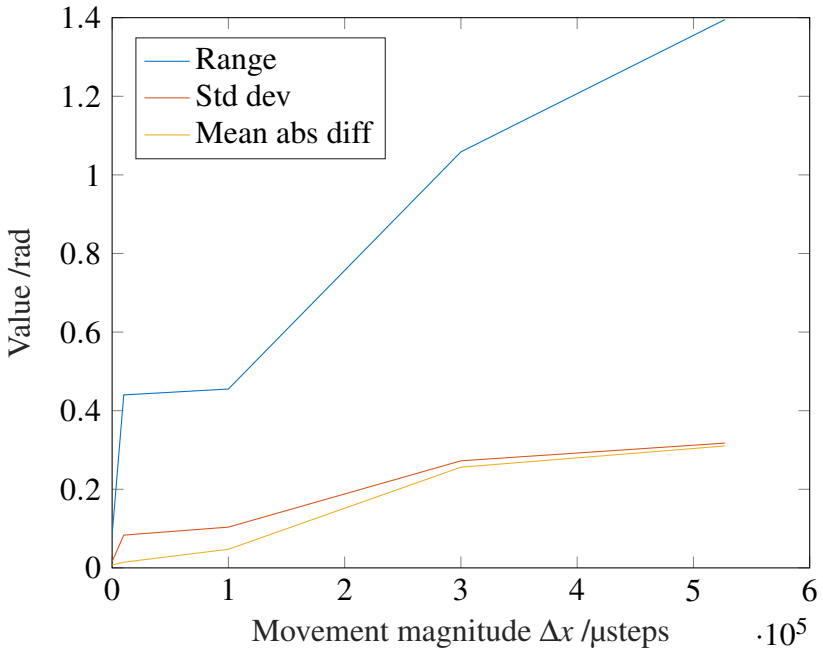

Fig. 8.27 Corrected fringe phase statistics over 50 repeated measurement, for different movement magnitudes.

Considering our initial configuration as $(t_0, RH_0, p_0) = (20\,^\circ\text{C}, 30\,\%, 101.325\,\text{kPa})$, we can compute the phase change caused by perturbations in either of the temperature, relative humidity or pressure parameters. For $(t = 21\,^\circ\text{C}, RH_0, p_0)$, $\Delta\phi = -0.378 \approx -\pi/83$ rad; for $(t_0, 40\%, p_0)$, $\Delta\phi = -0.0352 \approx -\pi/90$ rad; for $(t_0, RH_0, 100\,\text{kPa})$, $\Delta\phi = -1.42 \approx -\pi/2.2$ rad. While the $\Delta\phi$ values obtained with reasonable changes in temperature and pressure are of the order of magnitude required in the naive case of a single source and detector, this cannot be extended to the two-source, two-detector measurement of the corrected fringe phase. As the paths from one source to the two detector fibers are nearly identical, such temperature or pressure differences would imply very large gradients, which are unlikely to occur in a laboratory environment. For instance, considering the example of a pressure perturbation from 101.325 kPa to 100 kPa, having such a difference between the detector locations would imply a pressure gradient of 132.5 kPa/m, whereas pressure gradients responsible for wind are of the order of 0.1 Pa/m. We therefore conclude that variations in the refractive index of air in the free-space section of our experimental system are not the origin of the corrected fringe phase variability.

8.6.3 Source Height Variability

In order to further investigate the limited repeatability of the fringe phase as the sources are scanned back and forth to the same position, we want to devise an experimental method to simultaneously measure the corrected fringe phase and the source height. While repeating the back and forth movements between a reference and a target position, as described in Section 8.6.1, we can use a confocal sensor that measures the distance to some surface, which we choose to be the flat surface of the left source's extender arm. Confocal sensors function by focusing polychromatic white light onto a target surface using an optical system with multiple lenses; by controlling the chromatic aberration, a single wavelength of the dispersed white light corresponding to a calibrated distance is focused on the surface and reflected onto a sensor. The confocal sensor used is a Micro-Epsilon confocalDT IFS2401-1, which is controlled by and feeds back a signal to a Micro-Epsilon IFC2451 controller. Key specifications of this system include its 10 mm minimum distance to surface, 1 mm range between the minimum and maximum measured distance, 40 nm resolution and 27° acceptance angle, which is the maximum angle of the beam to the target surface. The controller provides integrated software via Ethernet communication to a computer, which allows the user to start and end measurements as well as control measurement settings. The two most important are the measurement bandwidth, which we choose to be fixed at a fixed value of 3.33 kHz rather than an adaptative value dependent on the signal strength, and the low-signal rejection threshold, which we set to 5%. The confocal sensor is held by a clamp secured on a retort stand; we choose to place the sensor vertically above the left source's extender arm when it is in its target position, $x_L = 585\,000$ µsteps. Figure 8.28 shows the experimental arrangement. It is important to note that, while the placement of the confocal sensor in the clamp has a settling time of several tens of minutes after installing the confocal sensor, it is considered stable after this period of time.

All experiments use the same procedure: the sources are controlled by our LabVIEW script with displacement instructions requesting 50 back and forth movements to the same target position, and the height measurement is manually started on the confocal sensor's console as soon as the scan begins. The measurement and analysis of the fringes in the detectors' outputs is performed as described in Sections 8.6.1 and 8.6.2. The height measurement dataset corresponds to a list of time and height datapoints, uniformly spaced for analysis simplicity by 300 ms at the chosen fixed sampling rate of 3.33 kHz, recorded as a text file and which can easily be read into a Matlab script. This dataset is first cleaned by deleting all elements where the height is out of range, corresponding to time periods when the source has moved back from the center position, and is associated with a recorded value of 2147. We then further clean and split the remaining data by considering only the time periods during

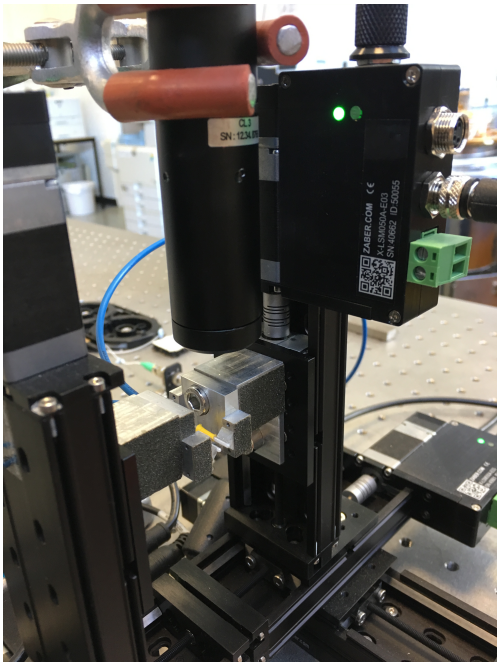

Fig. 8.28 Experimental arrangement with confocal sensor measuring its distance to the surface of the left source's extender; the small bright dot on the extender is the confocal sensor's focused beam.

which the time-derivative of the height data is small; an appropriate threshold is set manually in our data analysis script, and generally has a value of 0.2 nm/µs. Thus, we obtain 50 time segments, over which the height data is averaged to produce a single datapoint, in one-on-one correspondance with the 50 extracted fringe phase values. Similarly to Section 8.6.2 with fringe phase datasets, we can obtain important insight from the measured height variability datasets by using the range, standard deviation and mean absolute difference of these 50 height values.

Using this system, we obtain three main products: (i) the corrected fringe phase versus the measurement number, and the statistics of this dataset, (ii) the target surface's height versus the measurement number, and the statistics of this dataset, and (iii) the corrected fringe phase versus the source height, for which we can compute a linear regression to obtain a correlation measure. We perform a first measurement run using the multi-mode Thorlabs FG050LGA and polarization-maintaining single-mode Thorlabs PM1550-XP fiber patch cables respectively as the signal and reference channels, in the two-fiber system with 10 mm pitch. The sources are placed at their center positions $x_R = 470\,000$ µsteps and $x_L = 585\,000$ µsteps, and the left source is scanned to its home position $x_L = 0$ between each measurement. Figure 8.29a presents the corrected fringe phase, while the measurements of

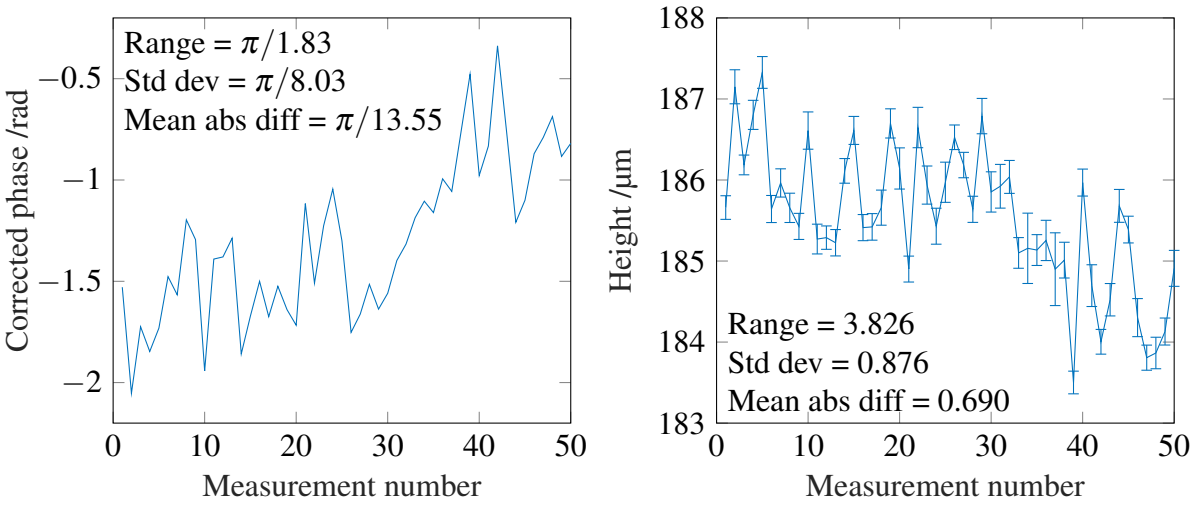

(a) Corrected phase

(b) Source height

Fig. 8.29 Simultaneous corrected phase and surface height measurement, for 50 consecutive measurements, with left source moved back to $x_L = 0$ between each. Multi-mode signal and single-mode reference channels, 10 mm separation.

the confocal sensor height with respect to the left source's extender arm are shown in Figure 8.29b. The source height range over the 50 measurements is approximately 3 µm, and the standard deviation and mean absolute difference statistics are similar to those obtained for the fringe phase, in relative terms. In Figure 8.30a, we show the corresponding corrected fringe phase and height measurements. We observe a clear correlation between the source height and the corrected fringe phase.

The same procedure is repeated with the left source is moved to and from the reference position $x_L = 485\,000$ µsteps, i.e. $\Delta x_L = 100\,000$ µsteps, rather than $x_L = 0$ µsteps. In Figure 8.30b, we observe that the range of height measurements is reduced to approximately 1 µm, outside of one outlier datapoint that corresponds to the first measurement; the range of corrected phase values is also reduced to approximately 0.4 rad, and the correlation between the two quantities is less visible than in Figure 8.30a. This same process can be repeated with both sources moved rather than only the left, in which case the fringe phase statistics are increased by roughly a factor 2 and the goodness of fit of the linear regression is worsened. When scanning only the right source and leaving the left source fixed, the corrected fringe phase shows similar variability while the left source height is constant. We therefore conclude that the limited corrected phase reproducibility is caused by variability in the source height.

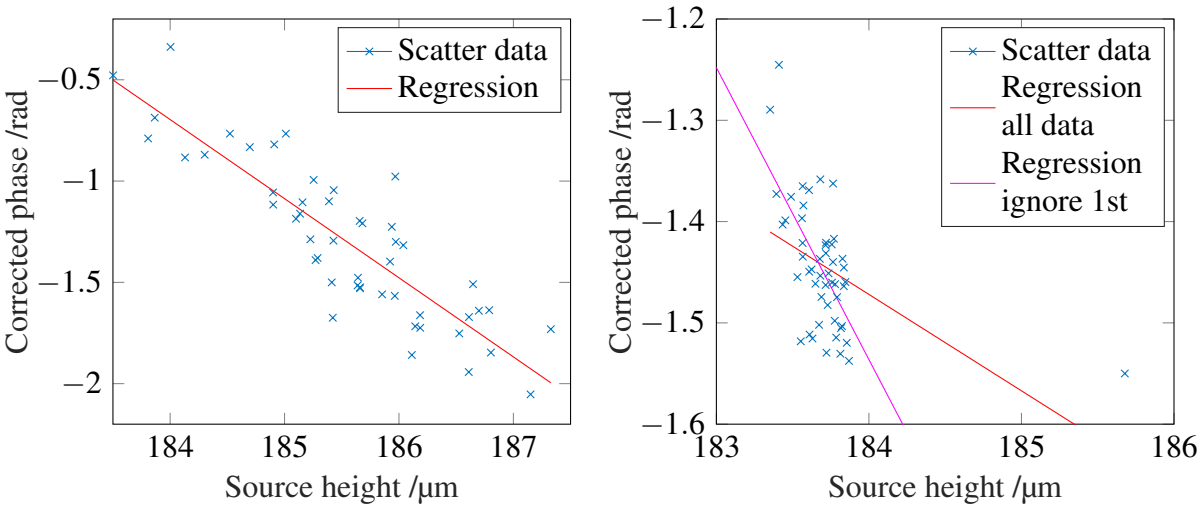

(a) $\Delta x_L = 585\,000$ µsteps (b) $\Delta x_L = 100\,000$ µsteps

Fig. 8.30 Scatter plot of corrected fringe phase against confocal sensor distance. Multi-mode signal and single-mode reference, 10 mm separation. 50 measurements, with back and forth movement to reference position between each. Line: linear regression of scatter.

8.6.4 Effect of Reduced Two-Detector Pitch

We can now perform the same investigation using the fiber arrays, in which the distance between the signal and reference channel optical fibers is reduced by factor 80, from 10 mm to 127 µm. First, we numerically investigate the effect of reducing the core-to-core pitch on the measured corrected fringe phase, when one source's location along the y-axis is imperfect. Assuming point-like sources and detectors at fixed positions, as in Section 8.4, we can compute the corrected fringe phase when the position of a source along the y-axis is changed. In Figure 8.31, we show the corrected fringe phase when varying the height of the left source, $y_L \in [0;0.1]$ mm, for core-to-core pitches of 10 mm and 130 µm. In both cases, the evolution of the corrected fringe phase is linear with y_L; the range of the corrected fringe phase is decreased 80-fold, from 40 rad for a 10 mm core-to-core pitch to 0.5 rad for a 130 µm pitch.

In order to perform similar experiments to those described in Section 8.6.3, we install the fiber array with 8 single-mode fibers in its dedicated holder as in Section 8.5.1. We choose two neighboring fibers to serve as signal and reference channels, numbered 59 and 60 respectively as studied in Section 8.5.2, and couple them to the DET01CFC detector (and its transimpedance amplifier) and the PDA20CS amplified detector respectively. Again, we perform 50 simultaneous measurements of the corrected fringe phase and sensor height with respect to the left source's extender surface. Figure 8.32a shows the corrected fringe phase

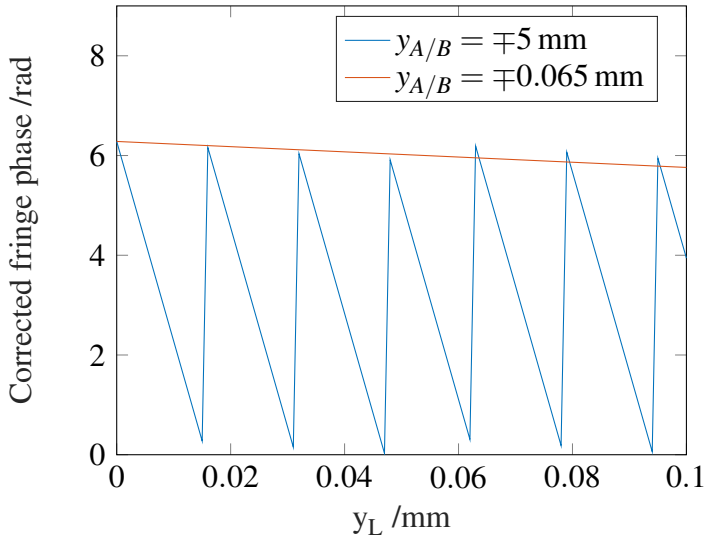

Fig. 8.31 Simulated corrected fringe phase for y_L displacements, for 10 mm and 130 µm pitch between the signal and reference channel fibers.

repeatability as the left source only is scanned back from $x_L = 585\,000$ µsteps to $x_L = 0$ µsteps between measurements and the right source remains fixed. Its range is reduced by a factor 30, its standard deviation by a factor 40, and its mean absolute difference by 20 compared to the same measurement with a 10 mm pitch presented in Figure 8.29a. Importantly, these statistics are identical in datasets obtained when the left source is moved only to $x_L = 485\,000$ µsteps, i.e. with a movement of $\Delta x_L = 100\,000$ µsteps, indicating that the dominating factor is now caused by a different mechanism, potentially limited by the detectors' noise. In Figure 8.32b, we observe that the dataset shown in Figure 8.32a no longer has a correlation with the recorded height variability, even though the latter is similar to what was observed in Section 8.6.3.

Figure 8.33 compares the fringe phase for 3 repeated scans of the two sources at a fixed distance of 40 000 µsteps, corresponding to an interval of 10 sampled positions, similarly to the results presented in Figure 8.25. We observe a significantly smaller phase slope of 0.3 rad over the scanning range, instead of 12 rad, and the repeatability is improved to within ± 0.05 rad over the high-SNR central region and within ± 0.5 rad over the entire range. The latter corresponds to a greater repeatability than even in high-SNR section of the dataset obtained with a 10 mm core-to-core pitch. Figure 8.34 shows the fringe phase as the sources are scanned in opposite directions, symmetrically from their center positions. The observations are identical: the repeatability has been greatly improved by the change from the 10 mm pitch system to the fiber array with 127 µm pitch.

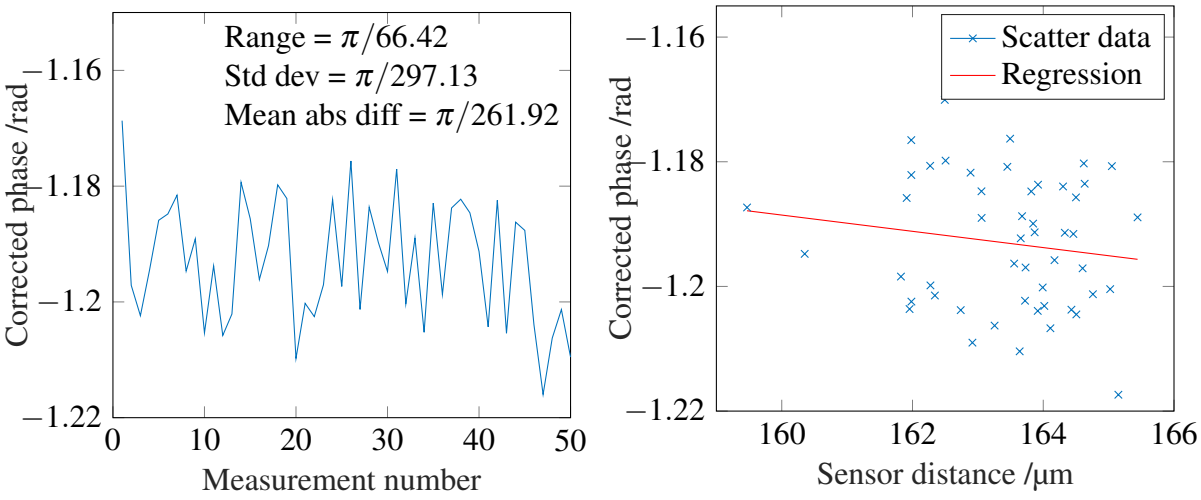

(a) Corrected phase

(b) Scatter of phase versus height

Fig. 8.32 Simultaneous corrected phase and surface height measurement, for 50 consecutive measurements, with left source moved back to $x_L = 0$ between each. Single-mode signal and reference channels, 127 µm separation.

While the use of the fiber array has allowed us to overcome the phase variability, further investigation is still necessary to find the origin of the mechanical variability in order to attempt to solve it. This would allow us to extend the areas of use of the phase correction method, as placing a reference channel closer than several millimeters may not be feasible in all applications. We repeated the measurements of height variability using the confocal sensor, first by comparing the cases when the left source was placed at a height of $y_L = 0$ µsteps and $y_L = 1\,000\,000$ µsteps, corresponding to the extreme top and bottom of its vertical scanning range. The height variability was significantly better in the latter case, by approximately a factor 2. In order to further test its dependence on y_L, we proceeded with other rounds of height measurements, but this time with respect to the plate of the horizontal stage. We observe sub-micron variations, significantly smaller than those measured with respect to the source extender surface. Together, these observations strongly indicate that, the higher the surface probed by the confocal sensor, the larger the height variability measured. We also remark that, during measurements of the height variability with respect to top of encoder-motor stack, i.e. the highest point in the source scanning system, this conclusion seemed further confirmed but our observations were limited by a slow monotonic drift in the height measurement, which we did not attempt to resolve.

In order to test whether this height variability comes from the flexing of the vertical stage structure with respect to the horizontal stage plate onto which it is bolted, we added custom-

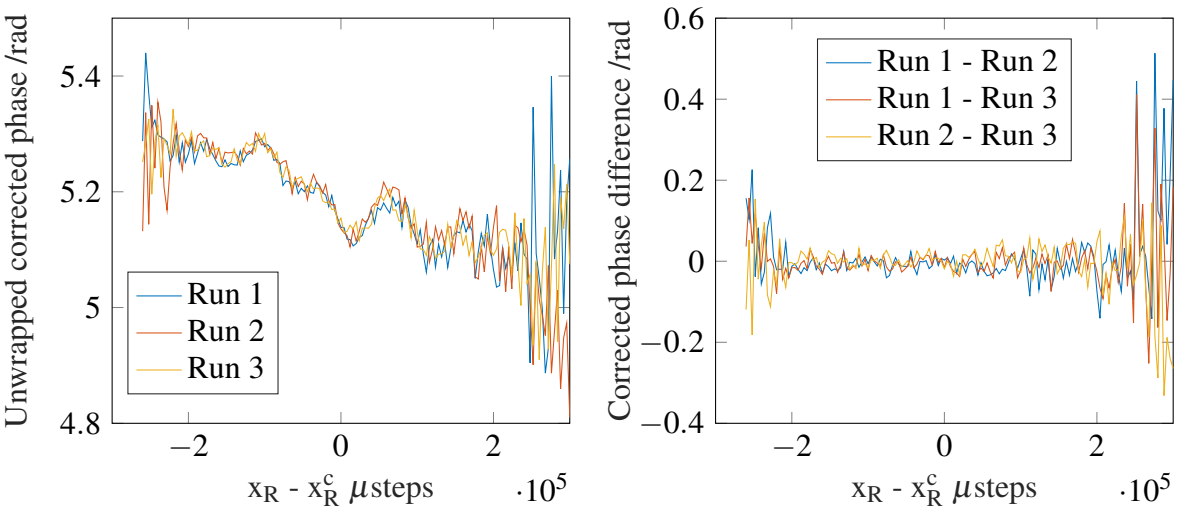

(a) Corrected fringe phase

(b) Differences of runs

Fig. 8.33 Repeatability over three identical runs, sources scanned at fixed distance; corrected fringe phase from two single-mode fibers in fiber array.

made stiffening square brackets. These produced no clear improvement of the repeatability of height measurements.

Having ruled out all other degrees of freedom, the last possibility is a small rotation of the horizontal stage's plate, with the vertical stage firmly secured to it. Under this hypothesis, the rotation's effect would be amplified by the distance of the source to the horizontal stage's plate; to produce a height offset of 3 µm over a distance of 105 mm, the rotation angle would have to be 0.03 mrad. There is no straightforward way of checking this more precisely with our current apparatus than in Section 8.6.2, which gave an upper bound of 0.5 mrad. One hypothetical arrangement would be to use at least two confocal sensors at different corners of stage plate, in order to measure much more precisely its height variability.

In conclusion, we have completed our primary objective for this study: the mechanism causing the variability in the measured corrected fringe phase between scans was found to be micron-size errors in vertical position. While it was not possible to precisely pinpoint the origin of this position variability, we have reduced the possibilities to one highly likely mechanism, sub-degree rotations of the horizontal stage's plate. Using our two-detector phase correction method with 127 µm-pitch fiber arrays, we have obtained reduced fringe phase variability, in line with expectations and results from numerical simulations.

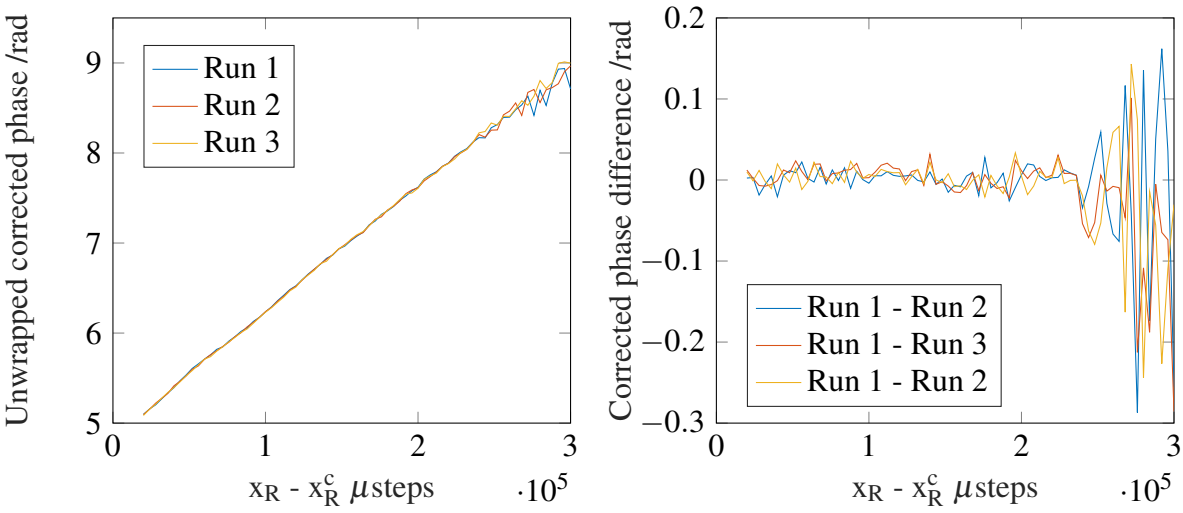

(a) Corrected fringe phase

(b) Differences of runs

Fig. 8.34 Repeatability over three identical runs, sources scanned in opposite directions; corrected fringe phase from two single-mode fibers in fiber array.

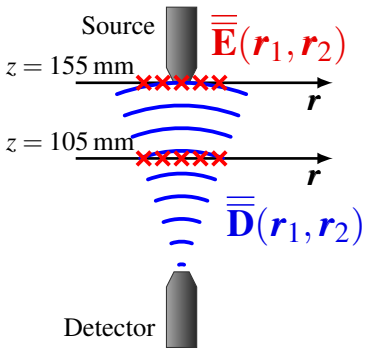

Fig. 8.35 Illustration of the experimental configuration when the distance between the source and detector planes z is changed, as the sources' scanning positions (red crosses) are fixed.

8.7 Changing source-to-detector distance

8.7.1 Experimental Results: Single-Mode Array

Up to this point, all of our experimental measurement sets have been performed at a single distance between the source and detector planes, $d = 105$ mm. In this section, we investigate whether the measured DRF is qualitatively and quantitatively different for other distances, using the same position sets for scanning the sources.

We choose a new distance between the source and detector planes of $d = 155$ mm, by moving the detector system and the manual stage it is mounted on back by 50 mm. This is achieved straightforwardly by securing the manual stage onto the optical table two additional

mounting holes away from the sources' motorized stages. The main intuition is that, by keeping the same scanning range and spatial resolution, we effectively zoom in on the pattern obtained at $d = 105\,\text{mm}$ distance. This reasoning is best visualized when considering the projection of the virtual detector response beam onto the plane of source locations. This configuration is represented schematically in Figure 8.35, and is valid because the surface on which the projection of the incident field correlation dyadic with the detector response correlation dyadic occurs is generic, and its specific choice is left to the user, as discussed in Section 2.2.2. If the sources' scanning locations are kept identical and the distance between the source and detector planes is increased, we effectively probe the detector response over a conic section with a smaller angle.

We need to carefully recalibrate the virtual source centers, as we know from Section 6.3.2 that the sources have a small angular misalignment: they point slightly inwards horizontally. The resulting effect is that the virtual centers are further out, i.e. at smaller $x_{R/L}$ values for the right and left sources respectively. In particular, this implies that more of the scanning locations can be reached before being prohibited by the physical size of the probes. In scans with step size $\Delta x = 10\,000\,\mu\text{steps}$, only the center diagonal element is missing; for $\Delta x = 4\,000\,\mu\text{steps}$, such as presented in Figure 8.36a, the number of missing elements along the diagonal is brought down from 10 to 3.

We perform single-source beampattern scans using the same settings as in Section 8.7.1, with the right and left sources successively, which clearly show that we are now focusing on the center of the beampattern. The measured signal at the outermost positions of the scan range now has non-zero amplitude. Note that this will also reduce the effect of noise around zero amplitude, with a direct effect on the measured fringe coherence matrices, where near-zero single-source amplitude values had led to very large peaks in Sections 6.4.1 and 8.3.2.

Figure 8.36a shows the fringe amplitude pattern, where elements with significant magnitude indeed fill a much larger portion of the recorded DRF matrix. In effect, we have significantly increased the amount of useful information acquired for a given scanning convention. We also remark that the smaller missing diagonal band allows us to reach many more position pairs and fill a significantly larger portion of the triangular matrix. Figure 8.36b shows the corrected fringe phase pattern, after subtracting the plane obtained by a least-squares fit. The pattern is nearly constant, as had been observed in Figure 8.17b, and is qualitatively similar to the latter with small-amplitude structure along the x_R and x_L axes. This indicates that the measured pattern is not qualitatively dependent on the distance d between the source and detector planes.

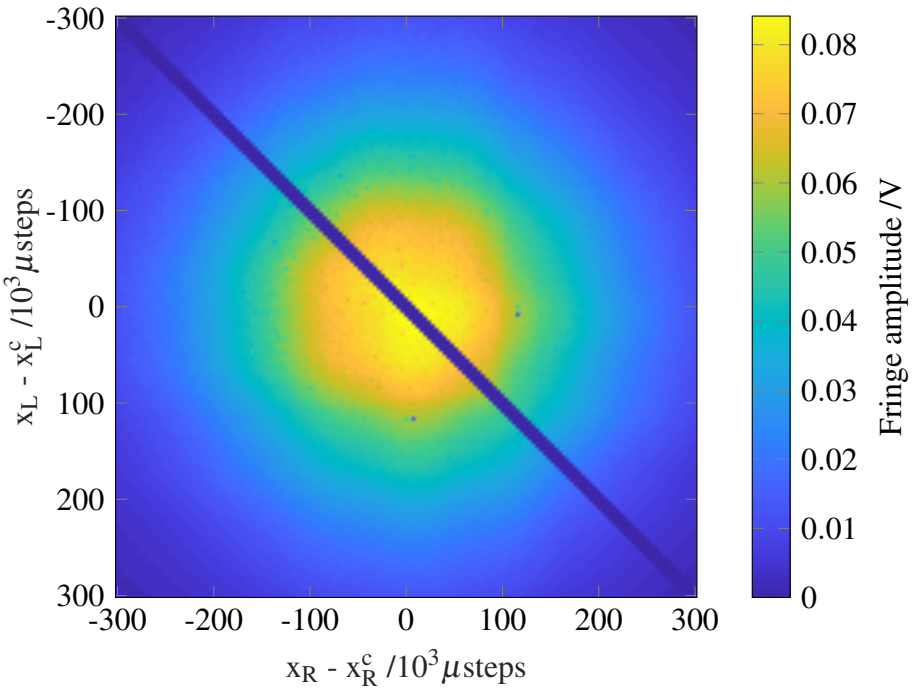

(a) DRF amplitude

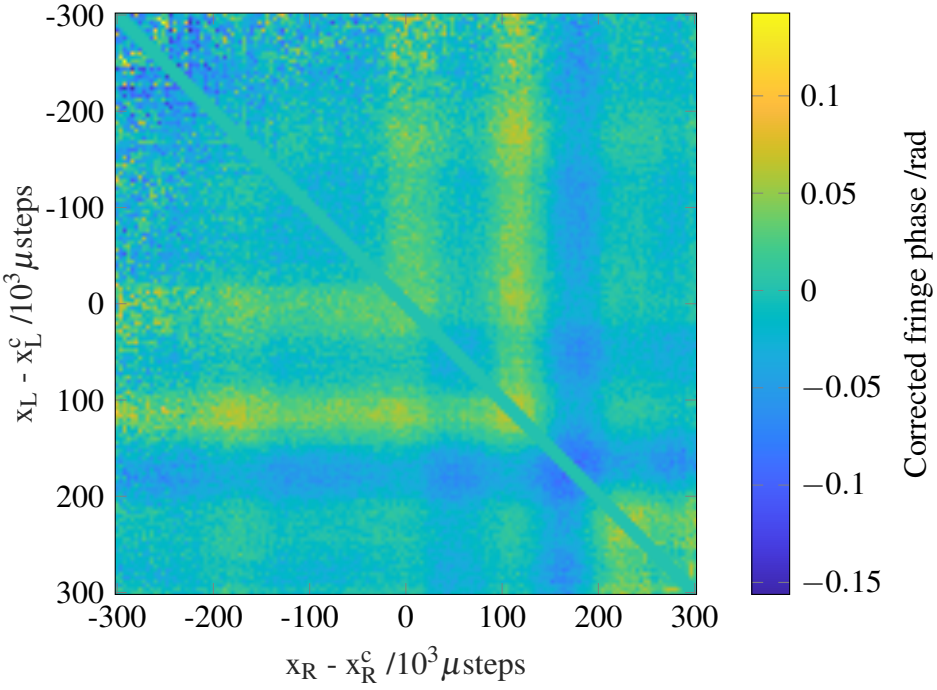

(b) DRF phase, corrected with phase of neighboring single-mode fiber

Fig. 8.36 Measured DRF amplitude and phase of single-mode detector in single-mode array, at $d = 155$mm distance.

8.7.2 Experimental Results: Few-Mode and Multi-Mode Array

We then turn to the case of the fiber arrary containing the few-mode and multi-mode fibers. We first reproduce the same measurement set at a distance between the source and detector planes of $d = 85$ mm, by setting the z-axis position of the sources to $z = 20$ mm, using either the few-mode or multi-mode fiber for the signal channel, and the center single-mode fiber for the reference channel. The results are qualitatively similar to those presented in Section 8.3.3. In particular, the expected zoom-in effect onto the central section of the measured DRF is not observed. The way to understand this observation is to recall that the few-mode and multi-mode fibers used have larger numerical apertures than the sources; in effect, the sources' numerical aperture are the limiting factor.

The same measurement set is repeated under identical settings, except for a distance between the source and detector planes of $d = 155$ mm; this is achieved by moving the detector's manual stage back by 50 mm, as in Section 8.7.1. By keeping the same scanning range and resolution, we again effectively reduce the portion of the beampattern that is scanned, i.e. zoom into the DRF measured for $d = 105$ mm. In this manner, we have again reduced the importance of the center missing diagonal band and recorded more useful information.

The fringe amplitude pattern of the few-mode fiber is shown in Figure 8.37a. The pattern is significantly more oval than the few-mode case at $d = 105$ mm. The slightly concave nature of the pattern is interpreted as being caused by the non-Gaussian single-source beampatterns, rather than a true effect of the few-mode behavior. Figure 8.37b shows the fringe phase pattern for the few-mode signal channel, corrected using single-mode reference channel. In particular, there is a clear presence of phase jumps with π rad magnitude at the anti-diagonal corners. This observation is contrary to our intuition of zooming into the pattern obtained at $d = 105$ mm distance by moving to $d = 155$ mm. The phenomenon is therefore more complex than can be understood with the simplified view of point-like sources probing the detectors' virtual beams: the detector response is a two-point correlation function with points in two-dimensional space, and sources have finite width.

The DRF amplitude pattern of the multi-mode fiber is shown in Figure 8.38a. It is qualitatively similar to the results obtained in the $d = 105$ mm case, but is indeed "zoomed in". This is particularly visible in the width of the diagonal features. The same is true for the DRF phase pattern for the multi-mode signal channel, corrected using the single-mode reference channel, as Figure 8.38b shows. We remark again that we use the single-mode fiber used for the reference is the one between the few-mode and multi-mode fibers; the subtracted phase plane therefore has opposite slope coefficients. The results are similar to the center region of those presented in Figure 8.20b in the case where $d = 105$ mm. We also

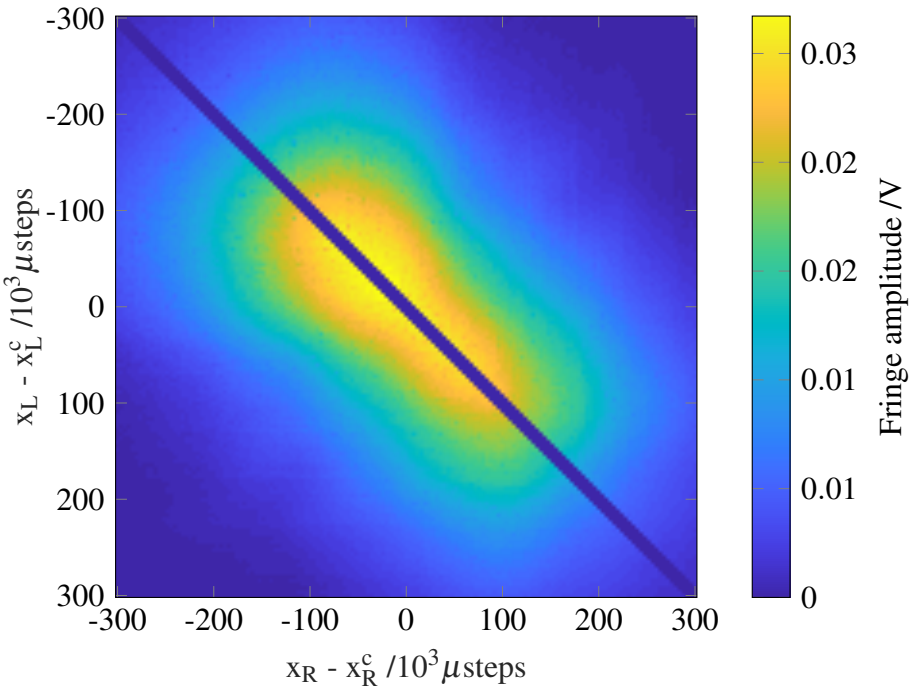

(a) DRF amplitude

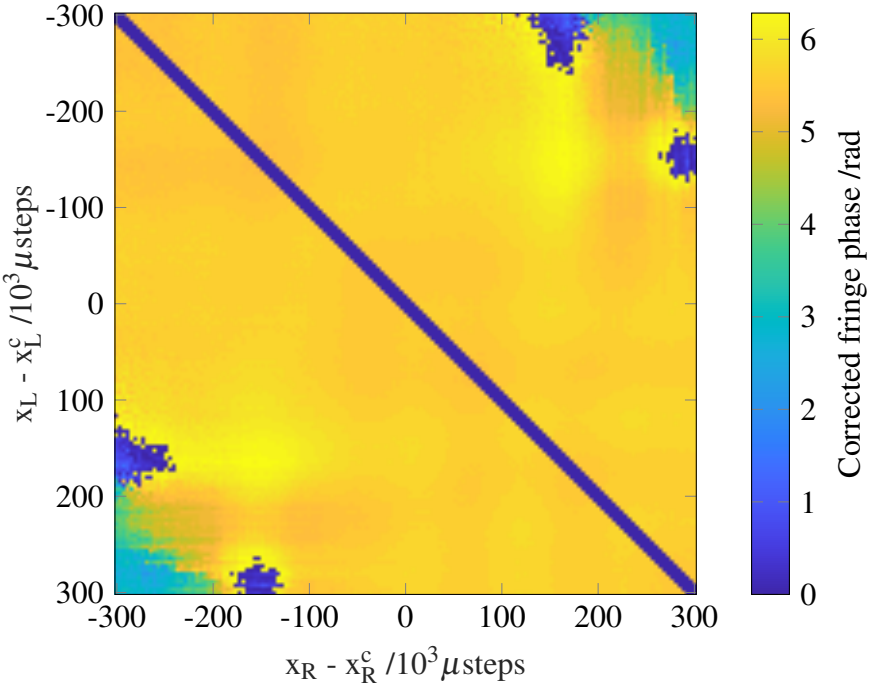

(b) DRF phase, corrected with phase of neighboring single-mode fiber

Fig. 8.37 Measured DRF amplitude and phase of few-mode detector in few-mode/multi-mode array, at $d = 155$mm distance.

remark that the centermost diagonal band, in light blue in Figure 8.38b, has a smaller width compared to the other bands, by approximately a factor $\sqrt{2}$; this indicates that the center band is qualitatively different from the others.

8.8 Conclusion

We have demonstrated the experimental realization of a robust method for correcting the drift in fringe phase caused by environmental fluctuations, based on the addition of a reference channel constructed from a single-mode fiber near the signal channel fiber and coupled to an amplified detector. We have effectively obtained a fringe phase that is spatially stable to within 300 nm deviations over several hours, long enough to accurately measure the fringe phase pattern as the two sources are scanned over finely sampled one-dimensional grids. By repeating the experimental process described in Chapter 6 with our extended experimental system, we performed fringe measurements for one-dimensional scans of the two sources and extracted both the amplitude and phase of the measured detector response. These results were obtained using single-mode, few-mode and multi-mode detector systems, and confirm our capacity to differentiate their behavior. In doing so, we have fulfilled the major objective set out in Chapter 1: we have measured the complex-valued DRF of devices under test, which fully characterizes their optical response, in a way that is independent of their modal behavior.

These investigations also brought us to ask whether incoherently summing the extracted fringe parameters of multiple fiber-coupled detectors measured simultaneously was equivalent to synthesizing a single detector system with the sum of their modal behaviors. The answer is yes, but with an important subtlety linked to the fact that the phase correction method effectively moves the plane of reference of the recorded phase from the plane of sources to the surface of the reference channel optical fiber. An extended three-detector system, using one fiber-coupled detector as the reference for two others placed on either side of it, further confirmed this understanding.

In this chapter, we have also investigated the limit on the repeatability of the fringe phase measurements. While we were not able to reduce the observed variability, our study rejected many potential origins and determined that it is most likely caused by small angular imperfections of the motorized slides' stages, in particular the horizontal stage commanding the x-axis.

Finally, increasing the distance between the source and detector planes, we focused on the substantive part of the DRF pattern. We also used the slight misalignment of our sources to our advantage, by realizing that the virtual centers of the source scans were divergent and

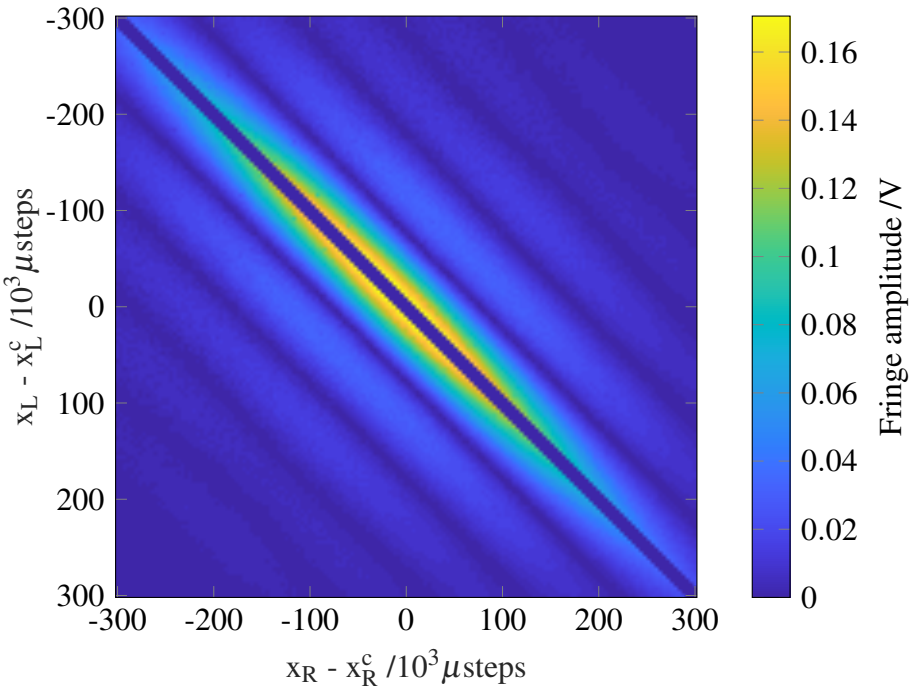

(a) DRF amplitude

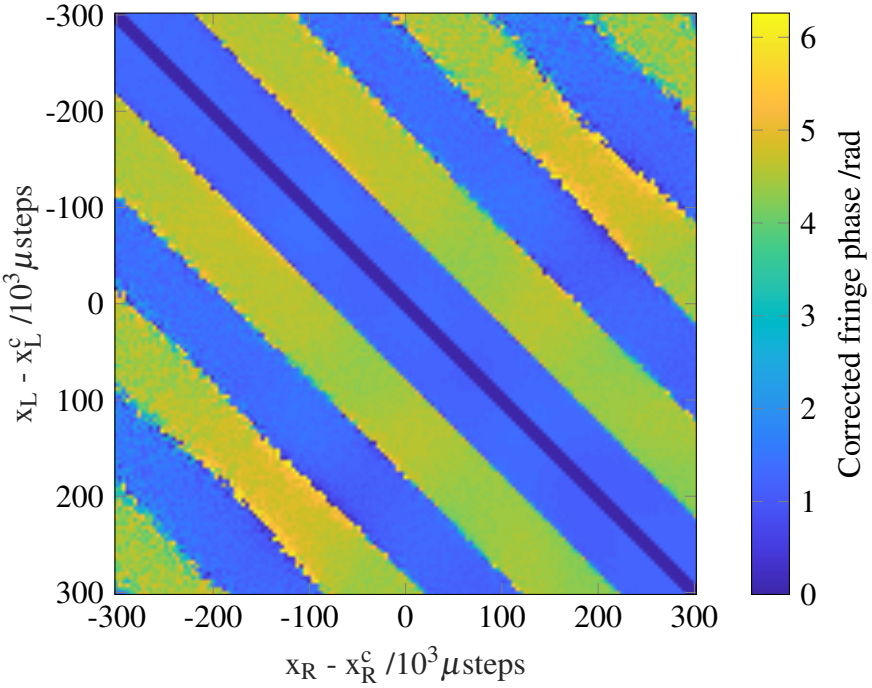

(b) DRF phase, corrected with phase of neighboring single-mode fiber

Fig. 8.38 Measured DRF amplitude and phase of multi-mode detector in few-mode/multi-mode array, at $d = 155$mm distance.

that more positions could be attained without having the probes collide. In practice, this means that the diagonal band of missing data is reduced by at least 60%, and up to the single center diagonal elements for medium spatial resolution scans.

Chapter 9

Full DRF Reconstruction and Mode Recovery

9.1 Introduction

In Chapter 8, we made significant progress towards completing our goal of measuring the DRF of various detector systems. The main limit to the experimental datasets recorded is the presence of a diagonal band of missing data, caused by the finite size of the probes. The presence of this diagonal band of unknown elements is not a fundamental flaw of EAI, but rather a feature of the experimental system; in this chapter, we seek to find numerical methods to circumvent this issue. Its significance can be reduced by moving further into the far-field, for instance, with a trade-off between an improved angular resolution and a decreased signal-to-noise ratio. Moreover, the missing diagonal band means that we are lacking access to potentially valuable information and prohibits the proper diagonalization of the DRF to recover its constituent modes, i.e. the spatial patterns of the modes through which the device under test absorbs incident optical power. These modes are obtained in the basis of the sampled source positions, but can also be represented in the spatial basis of the detector surface, as discussed in Chapter 2.

The goal of this chapter is to fully use the datasets produced during numerical simulations and experimental measurements, in order to attain two objectives sequentially: reconstructing the DRF to fill the missing diagonal band, and recovering the DRF modes. While several different missing-band reconstruction schemes were implemented, we discuss in this chapter the implementation of the most successful method and its application to simulated and experimental datasets. Other classes of reconstruction methods also exist, such as Maximum Entropy Methods [122, 123], used among other fields in Aperture Synthesis Interferometry

[124]. We chose to develop application-specific methods, to fully exploit the structure of missing elements along the diagonal, rather than spread throughout the DRF matrix.

In Section 9.2, we derive the theory behind this technique, based on partitioning the measured DRF into 9 rectangular submatrices: two are fully known off-diagonal square matrices, one corresponds to the fully unknown center square matrix, and the six remaining contain some unknown elements. Using the singular vectors obtained from the SVD of the former, we can find the unknown elements in all other submatrices. In Section 9.3, we investigate the effect of our diagonal filling scheme on the reconstruction of the device under test's natural modes, i.e. the reception field patterns through which the device absorbs the incident optical power. In particular, using simulated DRFs with a large variety of modal behaviors, we find that the recovered modes are not the projections of the LG modes onto the set of sampled source positions. The same mode recovery method is then applied to reconstructed experimental DRF datasets, to extract the modes of the device under test.

9.2 Filling in the Missing Diagonal

9.2.1 SVD-based Scheme

Let D be the measured detector response matrix. D is Hermitian by construction, assuming symmetry under exchange of the sources, and positive definite in the absence of noise. D admits an eigenvector decomposition

$$\mathsf{D} = \mathsf{E} \cdot \mathsf{S} \cdot \mathsf{E}^{\dagger}. \tag{9.1}$$

Assume D is an $N \times N$ matrix. We will assume that Equation (9.1) is the reduced eigenvector decomposition, so if D has M non-zeros eigenvalues, S is an $M \times M$ diagonal matrix with the eigenvalues on the diagonal. E is then an $N \times M$ matrix, and

$$\mathsf{E}^{\dagger} \cdot \mathsf{E} = \mathsf{I}_{M \times M} \neq \mathsf{E} \cdot \mathsf{E}^{\dagger}. \tag{9.2}$$

We will ignore the effects of measurement error and noise for now.

We partition D into submatrices using the elements we can and cannot measure, as in Figure 9.1. All elements of D_{31} and D_{13} are known, while all elements of D_{22} are unknown. We define k as the number of elements along the half-width of the missing diagonal band, and we wish to find l, the length of the largest square matrix that can be formed with no missing elements, labeled D_{13}. The number of elements along the antidiagonal of D_{22} is at least $k-1$ and at most k. Considering the number of elements along the antidiagonal of the

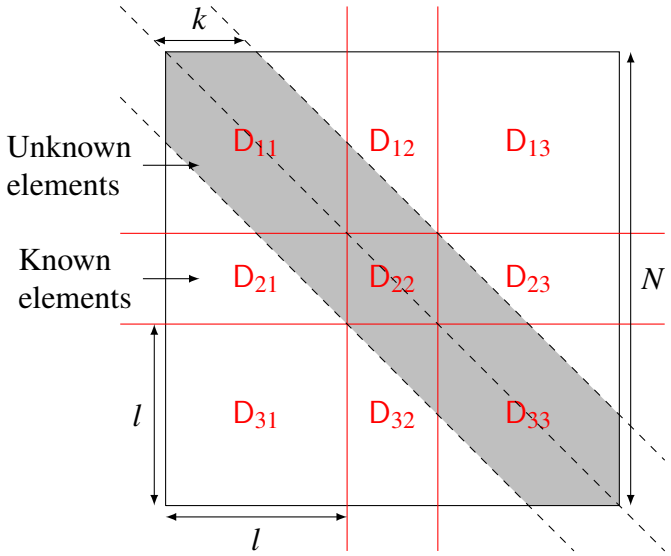

Fig. 9.1 Partitioning of the D matrix.

matrix D of sidelength N, we must therefore have

$$\begin{aligned}
&(k-1) \leq N-2l \leq k \\
&\implies \frac{N-k+1}{2} \geq l \geq \frac{N-k}{2} \\
&\implies l = \left\lfloor \frac{N-k+1}{2} \right\rfloor = \left\lceil \frac{N-k}{2} \right\rceil .
\end{aligned} \tag{9.3}$$

We can also partition E in Equation (9.1) with the same divisions:

$$E = \left(\begin{array}{c} E_1 \\ \hline E_2 \\ \hline E_3 \end{array} \right) \tag{9.4}$$

$$\mathsf{D} = \begin{pmatrix} \mathsf{D}_{11} & \mathsf{D}_{12} & \mathsf{D}_{13} \\ \mathsf{D}_{21} & \mathsf{D}_{22} & \mathsf{D}_{23} \\ \mathsf{D}_{31} & \mathsf{D}_{32} & \mathsf{D}_{33} \end{pmatrix} = \begin{pmatrix} E_1 S E_1^\dagger & E_1 S E_2^\dagger & E_1 S E_3^\dagger \\ E_2 S E_1^\dagger & E_2 S E_2^\dagger & E_2 S E_3^\dagger \\ E_3 S E_1^\dagger & E_3 S E_2^\dagger & E_3 S E_3^\dagger \end{pmatrix} . \tag{9.5}$$

Similarly, Equation (9.2) implies

$$\mathsf{E}_1^\dagger \cdot \mathsf{E}_1 + \mathsf{E}_2^\dagger \cdot \mathsf{E}_2 + \mathsf{E}_3^\dagger \cdot \mathsf{E}_3 = \mathsf{I}_{N \times N}. \tag{9.6}$$

We now look at the decomposition of D_{13}, which we obtain from Equation (9.5):

$$\mathsf{D}_{13} = \mathsf{E}_1 \cdot \mathsf{S} \cdot \mathsf{E}_3^{\dagger}. \tag{9.7}$$

However, since we have all the elements of D_{13}, we can also find its reduced Singular Value Decomposition:

$$\mathsf{D}_{13} = U\lambda V^{\dagger}, \tag{9.8}$$

where $UU^{\dagger} = I$, $V^{\dagger}V = I$. Critically, the set of vectors formed from the columns of U spans the same space as the set of vectors formed from the columns of E_1. The same is true for the columns of V and E_3.

We now turn to reconstructing D_{11}. We start by showing the structure of U and E_1, obtained above:

$$U = \left(\begin{array}{c|c|c|c} \boldsymbol{u}_1 & \boldsymbol{u}_2 & \ldots & \boldsymbol{u}_K \end{array} \right) \tag{9.9}$$

$$\mathsf{E}_1 = \left(\begin{array}{c|c|c|c} \boldsymbol{e}_1 & \boldsymbol{e}_2 & \ldots & \boldsymbol{e}_M \end{array} \right). \tag{9.10}$$

Using the fact that vectors formed from the columns of U and E_1 span the same space, we obtain that

$$\boldsymbol{e}_m = \sum_{n=1}^{K} T_{mn}\boldsymbol{u}_n, \tag{9.11}$$

and from Equation (9.5),

$$\mathsf{D}_{11} = \sum_{p=1}^{M} S_p \boldsymbol{e}_p \boldsymbol{e}_p^{\dagger} \tag{9.12}$$

$$= \sum_{m=1}^{K}\sum_{n=1}^{K}\sum_{p=1}^{M} S_p T_{pm}\boldsymbol{u}_p T_{pn}^{*}\boldsymbol{u}_p^{\dagger}. \tag{9.13}$$

But D_{11} is Hermitian, so we can simplify this result to

$$\mathsf{D}_{11} = \sum_{m=1}^{l}\sum_{n=m}^{l} d_{mn}E_{mn}, \tag{9.14}$$

where l is the sidelength of D_{11}, as illustrated in Figure 9.1,

$$E_{mn} = \boldsymbol{u}_m\boldsymbol{u}_n^{\dagger} + \boldsymbol{u}_n\boldsymbol{u}_m^{\dagger}, \tag{9.15}$$

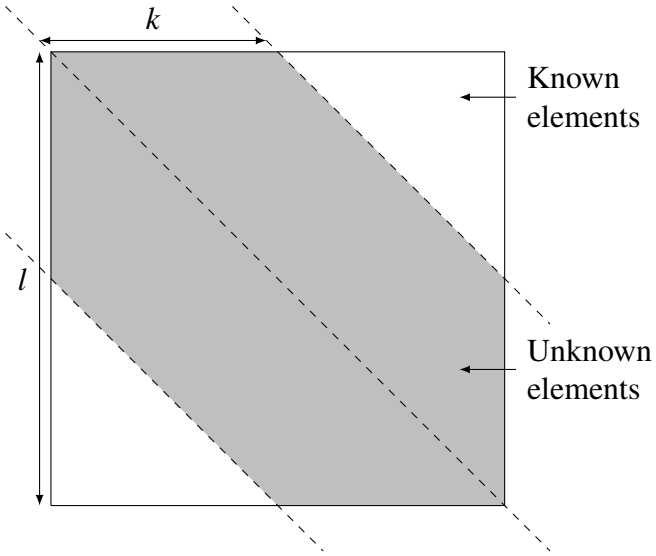

Fig. 9.2 Partitioning of the D_{11} matrix.

and

$$d_{mn} = \sum_{p=1}^{M} S_p T_{pm} T_{pn}^{*}. \tag{9.16}$$

So we use U to generate the basis for expanding D_{11}.

D_{11} is an $l \times l$ complex Hermitian matrix. Let H_N be the set of all $N \times N$ complex Hermitian matrices. It can be shown that H_N is a real inner product space with respect to the inner product [125]

$$\langle A, B \rangle = \mathrm{Tr}\left[A^{\dagger} \cdot B\right] = \sum_{m=1}^{N} \sum_{n=1}^{N} A_{mn}^{*} B_{mn}. \tag{9.17}$$

D_{11} can be split into known and unknown parts, as illustrated in Figure 9.2. The two subsets of H_N with either all of the unknown elements set to zero, or all of the known elements set to zero, form two disjoint subspaces of H_N: the inner product, as defined by Equation (9.17), of a member from the former with a member from the latter is always zero. Let D'_{11} equal D_{11} with all unknown elements set to zero; then we can treat D'_{11} s a projection of D_{11} into a subspace. Further, let f be a function that sets unknown elements to zero, so

$$\mathsf{D}'_{11} = f(\mathsf{D}_{11}). \tag{9.18}$$

For notational convenience, we order the E_{mn} so

$$\{E_{11}, E_{12}, ..., E_{ll}\} = \{E_1, E_2, ..., E_K\} \tag{9.19}$$

where K is the total number of E_{mn} elements. Then

$$\mathsf{D}_{11} = \sum_{p=1}^{K} \alpha_p E_p, \tag{9.20}$$

and

$$\mathsf{D}'_{11} = \sum_{p=1}^{K} \alpha_p f(E_p) \tag{9.21}$$

Then taking the inner product of D'_{11} with each of the E_i, we obtain the matrix equation

$$\boldsymbol{p} = \underline{\underline{\boldsymbol{C}}} \cdot \boldsymbol{\alpha} \tag{9.22}$$

where

$$\{\boldsymbol{p}\}_i = \langle E_i, \mathsf{D}'_{11} \rangle \tag{9.23}$$

$$C_{ij} = \langle E_i, f(E_j) \rangle \tag{9.24}$$

$$\{\boldsymbol{\alpha}\}_j = \alpha_j. \tag{9.25}$$

We can then use the pseudo-inverse of $\underline{\underline{\boldsymbol{C}}}$ to find

$$\boldsymbol{\alpha} = \underline{\underline{\boldsymbol{C}}}^{-1} \cdot \boldsymbol{p}, \tag{9.26}$$

effectively obtaining the best fit of the matrix D_{11} with unknown elements using the basis set of singular vectors of D_{13}. This lets us reconstruct D_{11}. The same procedure with V and E_3 can be used to reconstruct D_{33}.

We now wish to reconstruct D_{12}.

$$\mathsf{D}_{12} = E_1 S E_2^{\dagger} = \sum_m S_m \boldsymbol{e}_m^{(1)} \boldsymbol{e}_m^{(2)\dagger}. \tag{9.27}$$

So the columns of D_{12} can be expressed as

$$\mathsf{D}_{12} = \left(\sum_m c_{1m} \boldsymbol{u}_m \;\middle|\; \sum_m c_{2m} \boldsymbol{u}_m \;\middle|\; \ldots \;\middle|\; \sum_m c_{Km} \boldsymbol{u}_m \right). \tag{9.28}$$

Therefore, we can treat each column as a separate vector and reconstruct any missing values by working out the decomposition coefficients c_{im} from the values we have. The same can be done for D_{23}.

We now only have D_{22} left to reconstruct. At this point, we have D_{11}, D_{12} and D_{13}. We can use this to make a full sub-block D_S of the matrix D:

$$\mathsf{D}_S = \left(\begin{array}{c} \mathsf{D}_{11}^\dagger \\ \hline \mathsf{D}_{12}^\dagger \\ \hline \mathsf{D}_{13}^\dagger \end{array} \right). \tag{9.29}$$

Then, we can take the SVD of D_S,

$$\mathsf{D}_S = U_S \lambda_S V_S^\dagger, \tag{9.30}$$

where λ_S is the diagonal matrix containing the singular values of D_S and the columns of U_S and V_S are respectively the corresponding left- and right-singular vectors. We use the column vectors of U_S to reconstruct D in full using the method previously utilized for D_{11}.

9.2.2 Algorithm

We have written a Matlab implementation of the algorithm described in Section 9.2.1.

1. Initialization: load the DRF, choose or find the width of the missing diagonal band k, compute the sidelength l of the largest submatrix with all elements known, and select a threshold for small singular value rejection;

2. Partitioning: divide the measured matrix D into 9 submatrices, as in Figure 9.1, and its matrix of eigenvectors E into 3 corresponding blocks;

3. Creating a basis: perform an SVD on the fully known matrix D_{13}, and keep only large singular values above the selected threshold;

4. Reconstructing D_{11}: perform the on-diagonal reconstruction method, using the singular vectors of D_{13} to fill in the missing diagonal band elements of D_{11};

5. Reconstructing D_{12}: perform the off-diagonal reconstruction method, using the singular vectors of D_{13} to fill in the missing off-diagonal elements of D_{12};

6. Creating a second basis: create the D_S matrix using the construction in Equation 9.29, perform an SVD on it, and select the left-singular vectors with singular values above the selected threshold;

7. Reconstructing D: perform the on-diagonal reconstruction method, using the singular vectors of D_S to fill in the missing elements of D.

We remark that the algorithm described maximizes the information used from the known elements of the measured D matrix by construction. Contrary to many other schemes, it does not rely on an iterative process and is therefore immune to convergence issues.

An important step is the suppression of small singular values, obtained in the SVD of D_{13} and in the SVD of D_S. Many possibilities are available for the choice of a threshold, in particular the choice between an absolute or a relative tolerance, the value of the chosen tolerance, and whether to apply the same condition to the SVDs of both D_{13} and D_S. Assuming that the signal-to-noise ratio of the DRF to be reconstructed is high, the singular value spectrum of the matrices D_{13} and D_S displays two distinct regions with different slopes. The first region contains relatively large singular values, whose corresponding singular vectors account for the DRF's behavior; the second region contains relatively small singular values, whose corresponding singular vectors account for the noise contributions to the DRF, including numerical or experimental imperfections in the DRF computation or measurement. Ideally, the selected threshold suppresses the singular values of the latter category to avoid creating a basis that partially accounts for noise contributions. As we will see in applications of this algorithm, the distinction between the two categories becomes harder as the signal-to-noise ratio decreases.

9.2.3 Application to Simulated DRFs

We first consider the application of our SVD-based missing diagonal reconstruction method to simulated data. The main reason is that the DRF datasets obtained using simulations are not contaminated by noise and experimental errors; the only limitation is numerical, but we have already seen that the machine precision of 10^{-16} utilized is more than sufficient. We can study the effect of the additional reconstruction algorithm step, by comparing the eigenvectors obtained from the (near-)perfect simulated matrix and the reconstructed matrix. We use simulated datasets presented in Chapters 3 and 7, which assumed a distance of 100 mm between the source and detector planes, and sources scanned over 151 positions along the x-axis, distributed uniformly over the range $x = [-15, 15]$ mm; the sources are considered to be on-axis along the y-axis, i.e. $y = 0$ mm.

Figure 9.3a shows simulated DRF using two identical sources, the assumed detector response is fully-coherent, with $\overline{\overline{\mathbf{D}}}(\mathbf{r}_i, \mathbf{r}_j) = \mathrm{LG}_{00}(\mathbf{r}_i)\mathrm{LG}^*_{00}(\mathbf{r}_j)$. The measured DRF simulated is a 151×151 matrix; we apply a phase correction with itself, meaning that the corrected DRF phase is zero throughout. We apply a diagonal mask with width equal to 10 elements, in order to replicate the diagonal band of missing data in equivalent experimental datasets. This partially masked DRF is the original data that is fed into the algorithm, and accurately represents the configuration we would have in experimental measurement sets, such as those

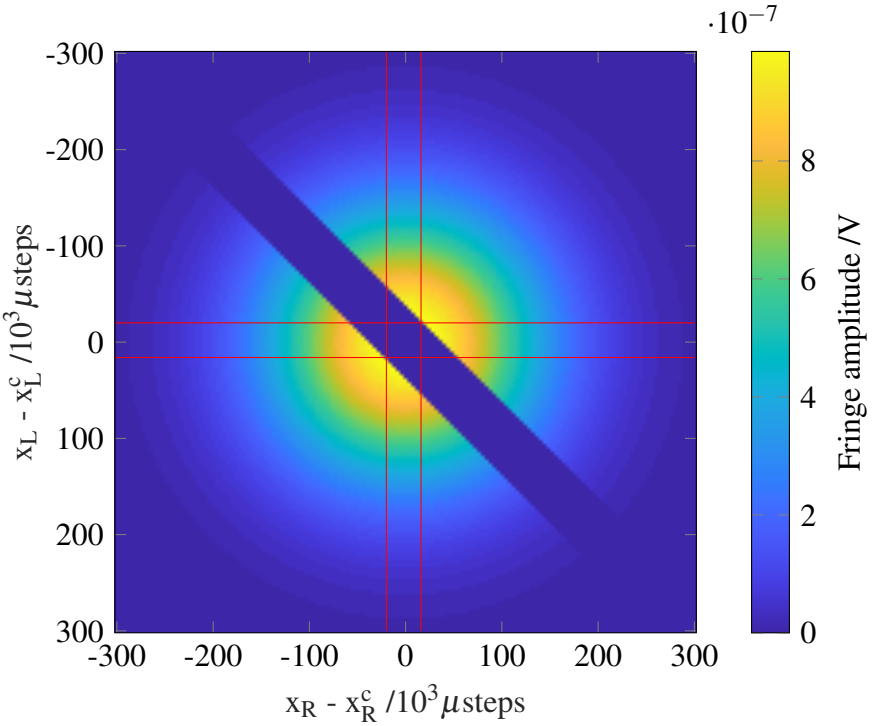

(a) Simulated DRF amplitude, with applied diagonal band mask of width equal to 10 elements; the red lines indicate the boundaries between the 9 partitioned submatrices.

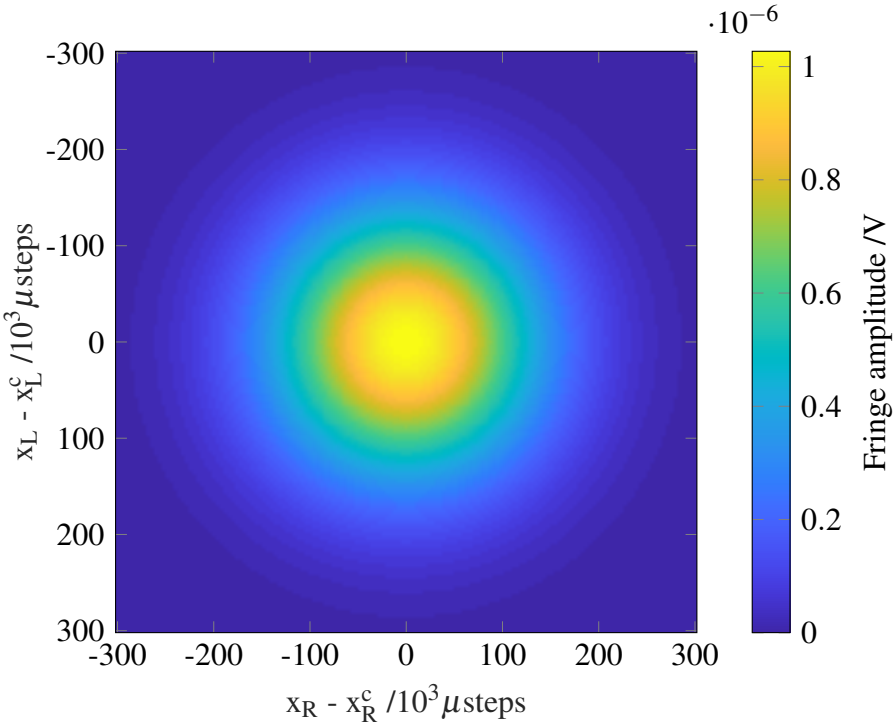

(b) Reconstructed DRF amplitude.

Fig. 9.3 DRF amplitude of simulated single-mode system, built from LG_{00} mode.

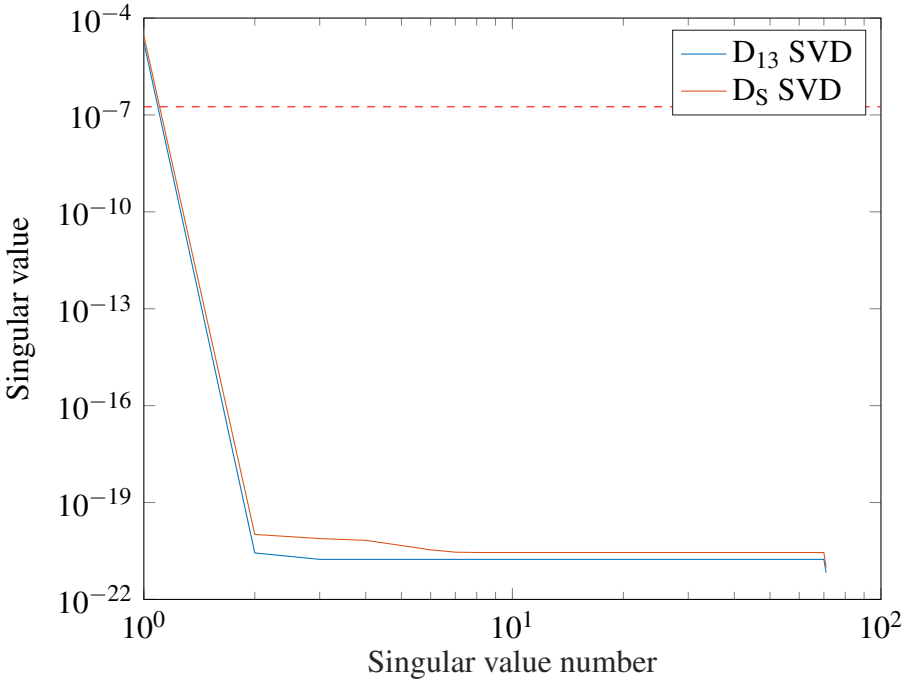

Fig. 9.4 Singular Value Decompositions of the D_{13} and D_S matrices, obtained in the reconstruction algorithm applied to the simulated single-mode DRF built from the LG_{00} mode; the red line shows the 0.01 relative threshold selected.

used in Chapters 6 and 8. We obtain an excellent reconstruction, with all features of the original dataset recovered, as shown in Figure 9.3b. The relative reconstruction error matrix, defined as

$$\varepsilon_{mn} = \left| \frac{D_{mn}^{\text{reconstructed}} - D_{mn}^{\text{original}}}{D_{mn}^{\text{original}}} \right|, \tag{9.31}$$

was computed and found to be smaller than 10^{-10} for all elements of the DRF matrix. For this DRF, the choice of the threshold for discarding small singular values (and their corresponding singular vectors) in the SVDs of the D_{13} and D_S matrices is simple. Figure 9.4 shows the singular value spectrum of these two matrices: only one singular value is non-negligible, and can be selected with an appropriate threshold, for instance the 0.01 relative threshold shown in the figure.

Figure 9.5 shows the simulated DRF in the same configuration, but using a two-moded detector response, obtained using an incoherent sum of the LG_{00} and LG_{01} modes: $\overline{\overline{\mathbf{D}}}(\mathbf{r}_i, \mathbf{r}_j) = LG_{00}(\mathbf{r}_i)LG_{00}^*(\mathbf{r}_j) + LG_{01}(\mathbf{r}_i)LG_{01}^*(\mathbf{r}_j)$. The original DRF amplitude pattern was presented in Figure 3.7a while the original phase, corrected with the single-mode phase, was presented in Figure 7.15. Again, we can apply a diagonal mask of width equal to 10 elements, as shown for the DRF amplitude in Figure 9.5a, and proceed with the reconstruction algorithm, using a

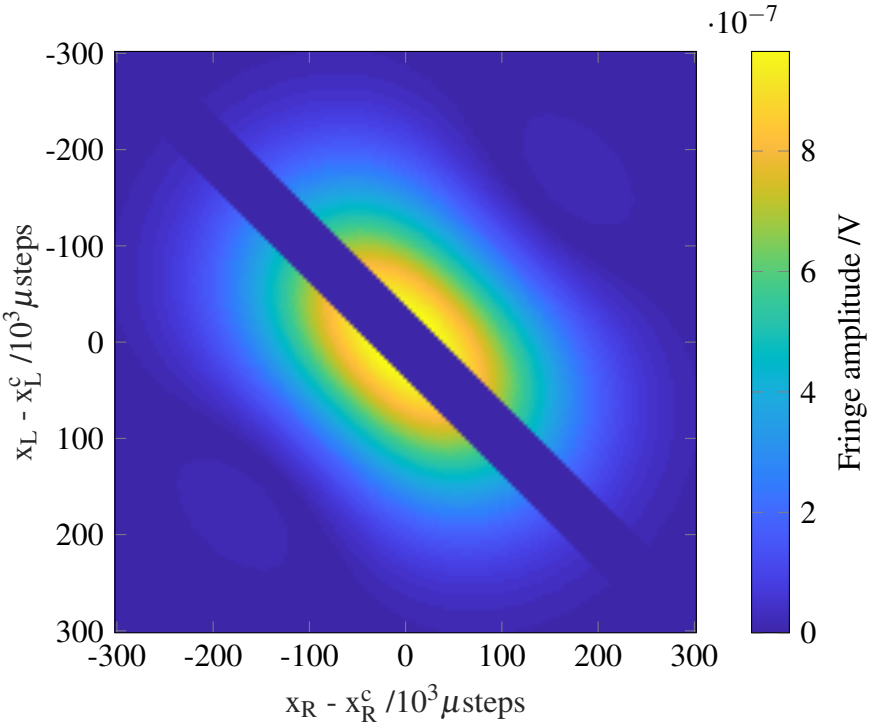

(a) Simulated DRF amplitude, with applied diagonal band mask of width equal to 10 elements

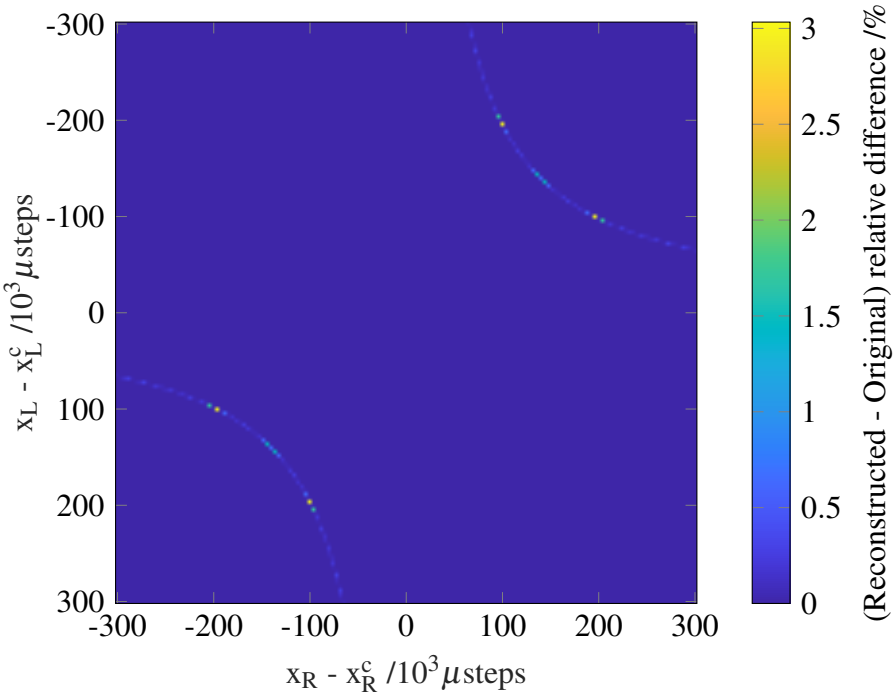

(b) Reconstruction error

Fig. 9.5 Reconstruction of simulated two-mode DRF, built from the LG_{00} and LG_{01} modes.

relative threshold of 0.01 to discard all negligible singular values. The reconstruction quality is still excellent, with errors smaller than 3%, as shown in Figure 9.5b; the largest errors are found along the zero-amplitude lines corresponding to the π rad jump in phase. This was to be expected because of their near-zero amplitude, where the machine precision is the limiting factor. Indeed, the simulated DRFs are computed with a 10^{-10} absolute precision and saved in files with 5 significant digits; we understand that the large singular vectors therefore pick up the large-amplitude behavior, while numerical errors on these as well as small-amplitude elements are bundled into the high-order singular vectors, which are suppressed in our algorithm when selecting only large singular values. On a more general note, compared to the single-mode case, the reconstruction quality is not degraded for elements of similar amplitude.

We repeated the same procedure with a four-moded detector response, simulated using $\overline{\overline{\mathbf{D}}}(\mathbf{r}_i,\mathbf{r}_j) = \mathrm{LG}_{00}(\mathbf{r}_i)\mathrm{LG}^*_{00}(\mathbf{r}_j)+\mathrm{LG}_{01}(\mathbf{r}_i)\mathrm{LG}^*_{01}(\mathbf{r}_j)+\mathrm{LG}_{10}(\mathbf{r}_i)\mathrm{LG}^*_{10}(\mathbf{r}_j)+\mathrm{LG}_{11}(\mathbf{r}_i)\mathrm{LG}^*_{11}(\mathbf{r}_j)$. The corrected DRF phase pattern was shown in Figure 7.20. The reconstructed DRF amplitude is in excellent agreement with the original's, while the reconstructed DRF phase presented in Figure 9.6a displays a very slight broadening of the boundary between the regions of constant phase, compared to the original corrected DRF phase pattern. This causes the reconstruction error to increase sharply along the zero-amplitude lines, as shown in Figure 9.6b, while remaining significantly below 1% for all large-amplitude elements. Figure 9.7 presents the singular value spectra computed during the reconstruction algorithm: only four singular value are non-negligible, and can be selected with an appropriate threshold, for instance the 10^{-4} relative threshold shown in the figure. The small, quasi-constant offset factor between the first four singular values of the two SVDs can be explained by the presence of larger amplitude values in the D_S matrix, in which the missing diagonal band is partially reconstructed.

Finally, we used the same reconstruction algorithm on a simulated highly multi-mode detector response, namely with 121 modes. While we use the LG modes here, their order of simulation is the same as that of LP modes, as discussed in Chapter 3. Figure 9.8 shows the amplitude and phase patterns of the reconstructed 121-mode DRF, whose original amplitude and phase patterns were presented in Figures 3.10a and 7.22 respectively, when a diagonal mask of width equal to 10 elements is applied. Important qualitative features of the original DRF are reconstructed, but significant differences arise, including the appearance of discontinuities at the boundaries between the matrix partitions.

We investigated the nature of the discontinuities at the matrix partition boundaries observed in Figure 9.8 by considering the sub-block matrix D_S, built from the reconstructed D_{11}, D_{12} and D_{13} matrices, as defined in Equation (9.29). We found that the boundary

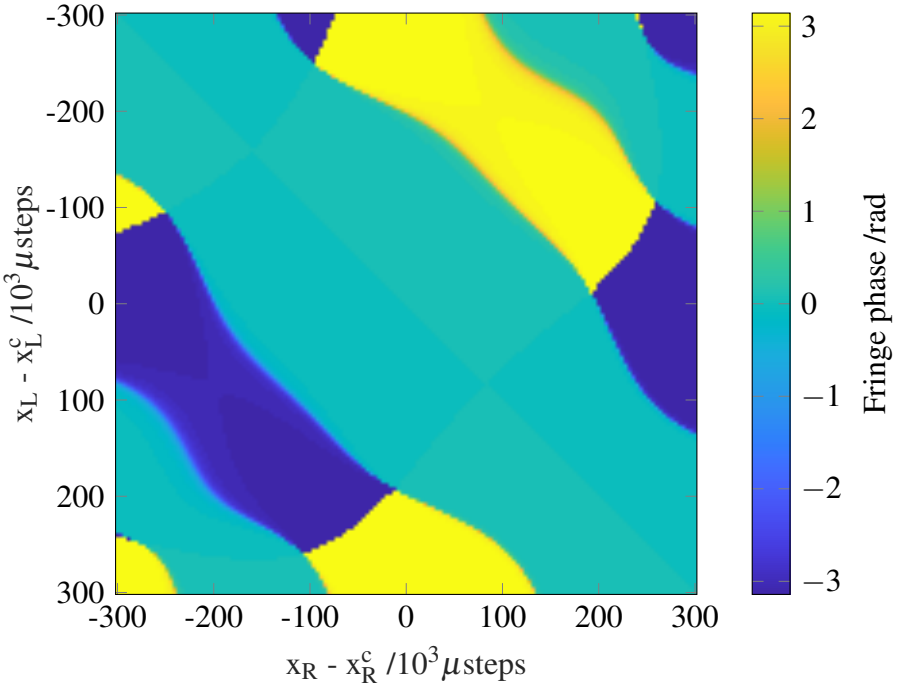

(a) Reconstructed DRF phase

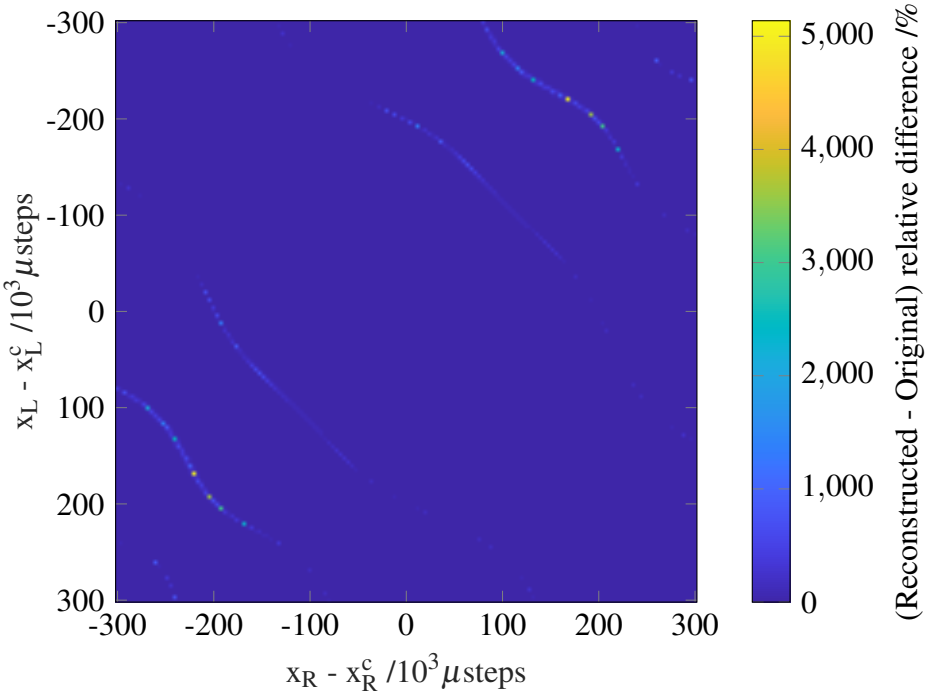

(b) Reconstruction error

Fig. 9.6 Reconstruction of a simulated four-mode DRF, built from the LG_{00}, LG_{01}, LG_{10} and LG_{11} modes with equal sensitivities, with applied diagonal band mask of width equal to 10 elements.

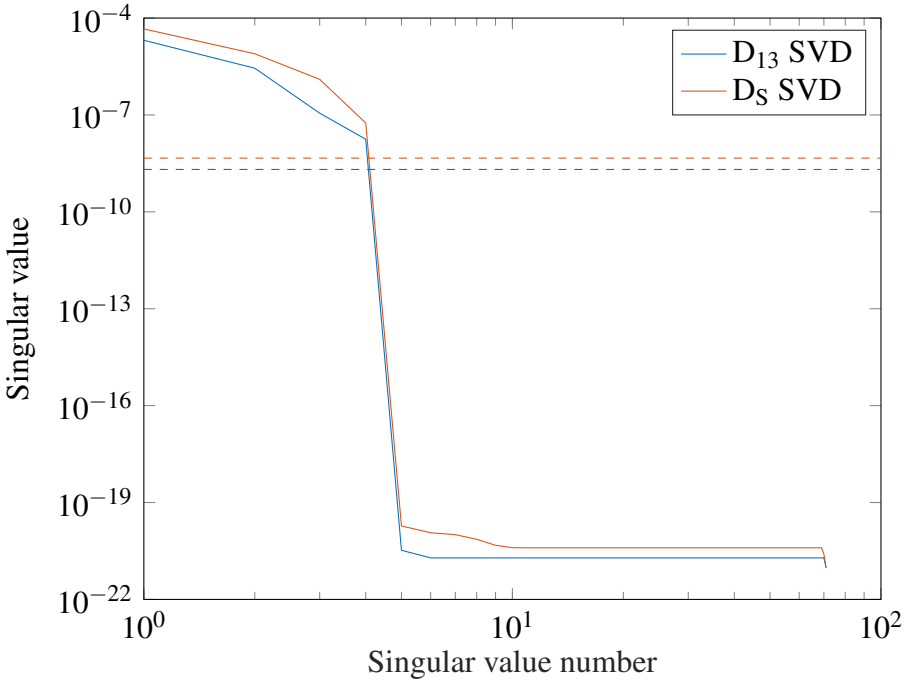

Fig. 9.7 Singular Value Decompositions of the D_{13} and D_S matrices, obtained in the reconstruction algorithm applied to the simulated single-mode DRF built from the LG_{00}, LG_{01}, LG_{10} and LG_{11} modes; the dashed lines show the 10^{-4} relative threshold selected.

between the former pair displays a discontinuity, not the latter pair, as illustrated in Figure 9.9 at $x_R - x_R^c = 20\,000$ µsteps. We understand this to be caused by the on-diagonal reconstruction method for D_{11}, which relies on the projection of small-magnitude elements onto the column vectors of the matrix U containing the largest amplitude elements of the matrix D Additionally, the D_{11} submatrix has the largest proportion of missing elements, and consequently that many elements need to be filled in using the limited information contained in the known elements. The number of missing elements in D_{11} is particularly dependent on the missing diagonal width k, increasing linearly from 1% for $k = 1$ to 50% for $k = 20$, whereas this effect is much less pronounced for D_{12}, hence its relative ease of reconstruction: this explains why the boundary between D_{11} and D_{12}, rather than D_{12} and D_{13}, displays a discontinuity in the case of multi-mode DRFs. Note also that the algorithm's behavior is analogous if we reconstruct $\mathsf{D}_{13/23/33}$ instead of $\mathsf{D}_{11/12/13}$: the submatrix D_{33} then is the one displaying such reconstruction artefacts.

Figure 9.10 presents the singular value spectra computed during the reconstruction algorithm. We found that we obtained optimal reconstruction results using a relative threshold of 10^{-8}, for which the 9 largest singular values are selected. Note that this number is significantly smaller than the 121 input modes, because the latter are modes over the two-

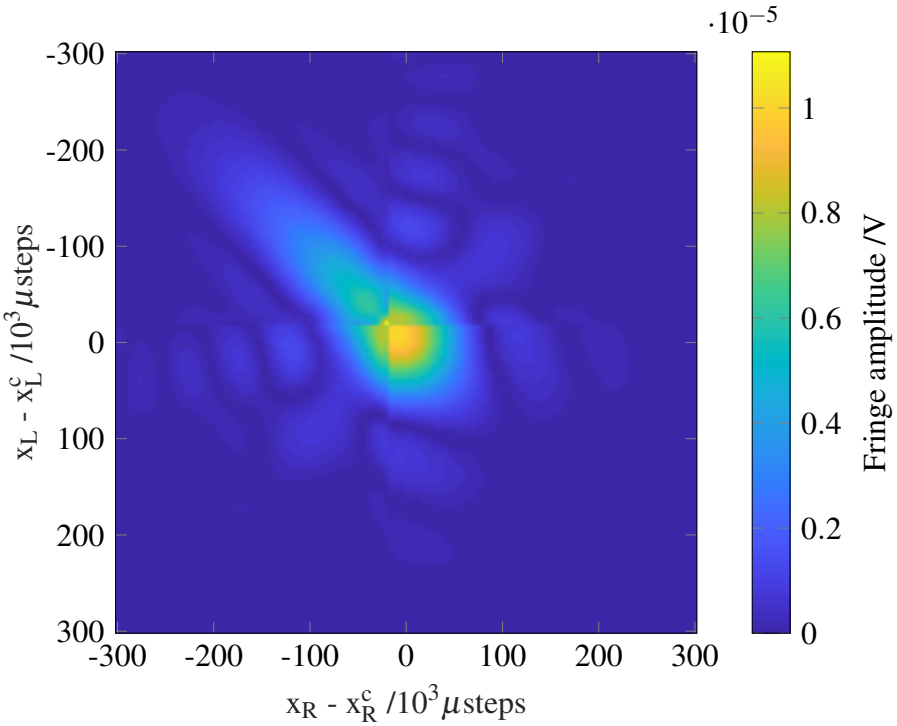

(a) Reconstructed DRF amplitude

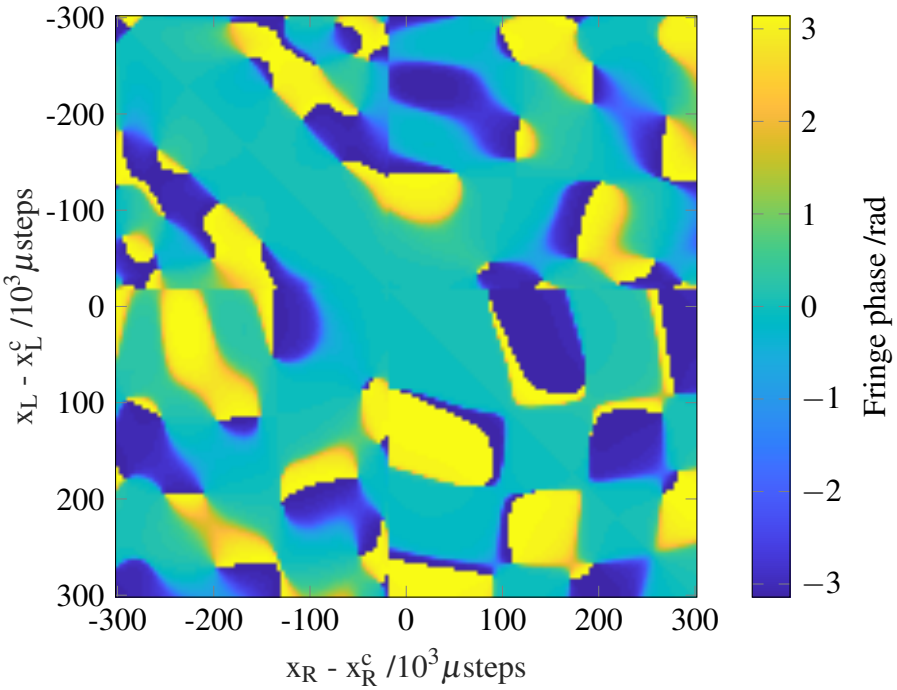

(b) Reconstructed DRF phase

Fig. 9.8 Reconstructed DRF complex amplitude components of simulated 121-mode system, built from LG modes, with applied diagonal band mask of width equal to 10 elements.

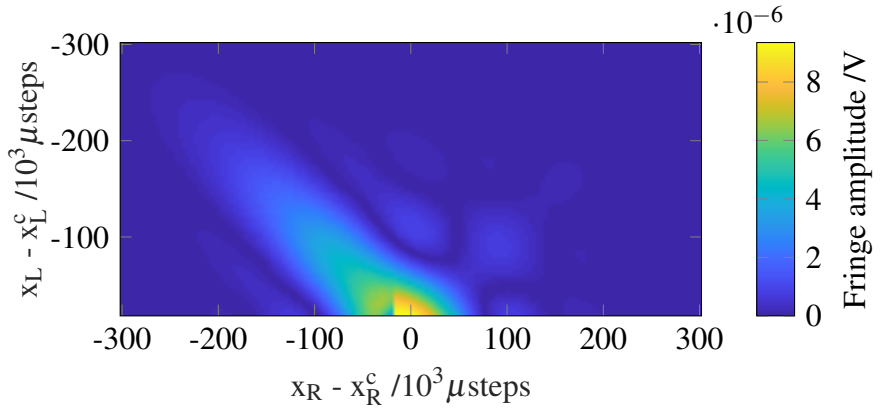

(a) Reconstructed DRF amplitude

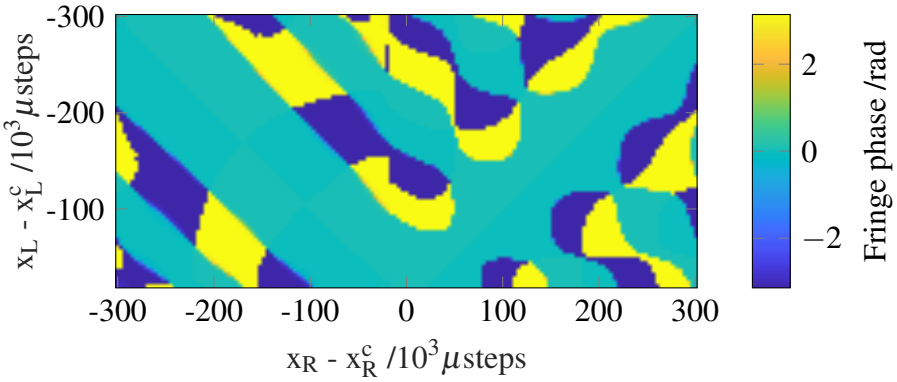

(b) Reconstructed DRF phase

Fig. 9.9 Sub-block matrix D_S, defined in Equation (9.29) and built from the reconstructed D_{11}, D_{12} and D_{13}, during the reconstruction of a simulated 121-mode system's DRF, built from LG modes, with applied diagonal band mask of width equal to 10 elements.

dimensional spatial basis of the detector surface, but not in the basis of sampled source positions, as discussed in Section 3.4.3.

When the width of the missing diagonal band is reduced to 3 elements, as is the case in experimental datasets presented in Section 8.7, where the distance between the source and detector planes is 155 mm, the reconstructed DRF is very good agreement with the original DRF. For instance, the DRF amplitude and phase presented Figure 9.11 are obtained with the same reconstruction parameters as Figure 9.8, and no longer display discontinuities at the matrix partitioning boundaries. Small additional improvements can be obtained with finer tuning of the tolerance parameters used to reject small singular values of D_{13} and D_S: this clearly indicates that our algorithm is limited when the proportion of missing elements in D_{11} is high, rather than by an intrinsic inability to deal with the reconstruction of multi-mode

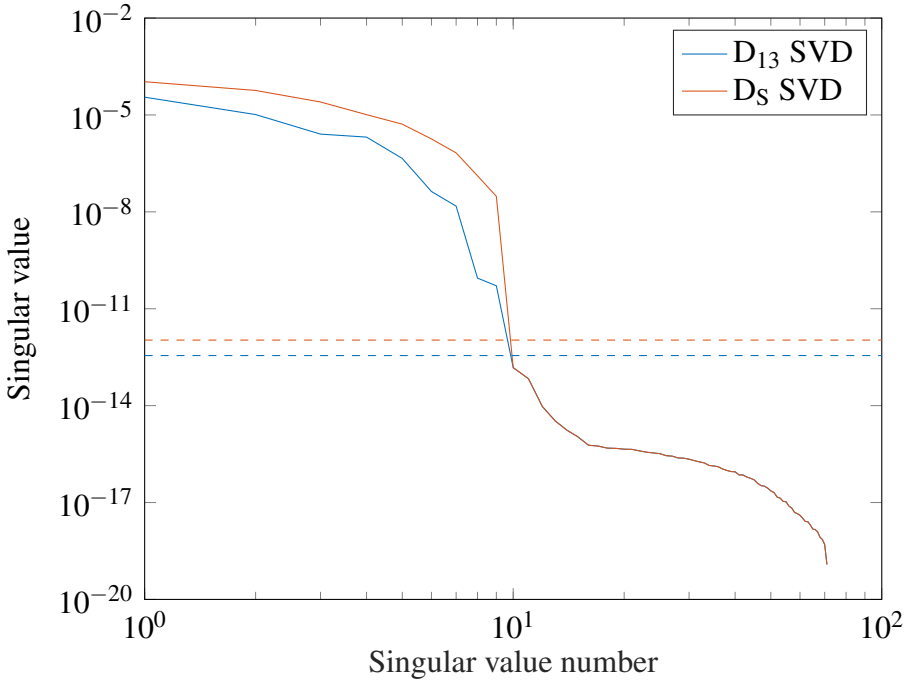

Fig. 9.10 Singular Value Decompositions of the D_{13} and D_S matrices, obtained in the reconstruction algorithm applied to the simulated single-mode DRF built from the first 121 LG modes; the dashed lines show the 10^{-8} relative threshold selected.

DRFs. We conclude that our reconstruction scheme is less accurate as both the number of missing element and the number of modes increase, i.e. when we attempt to reconstruct a larger number of unknown elements while having less information available from the known elements. While the scheme's performance is degraded for such highly multi-mode DRFs, it performs very well for the few-mode DRFs, its main target.

9.2.4 Application to Experimental DRFs

We used the same algorithm on DRFs obtained from experimental measurements of the device under test. In particular, we chose to work with the DRF measurements obtained with the fiber arrays, presented in Section 8.5. As this data already contains the missing diagonal band, the diagonal mask is not applied; instead, its width is recovered from the number of missing elements along the diagonal.

Figure 9.12 shows the result of the reconstruction method on a single-mode dataset, obtained with the SM fiber array, which was displayed in Figure 8.16a; the measured DRF phase is corrected with itself, meaning that it is zero throughout. The DRF reconstruction is very good, with some artificial structure is visible, linked to partitioning of the matrix for

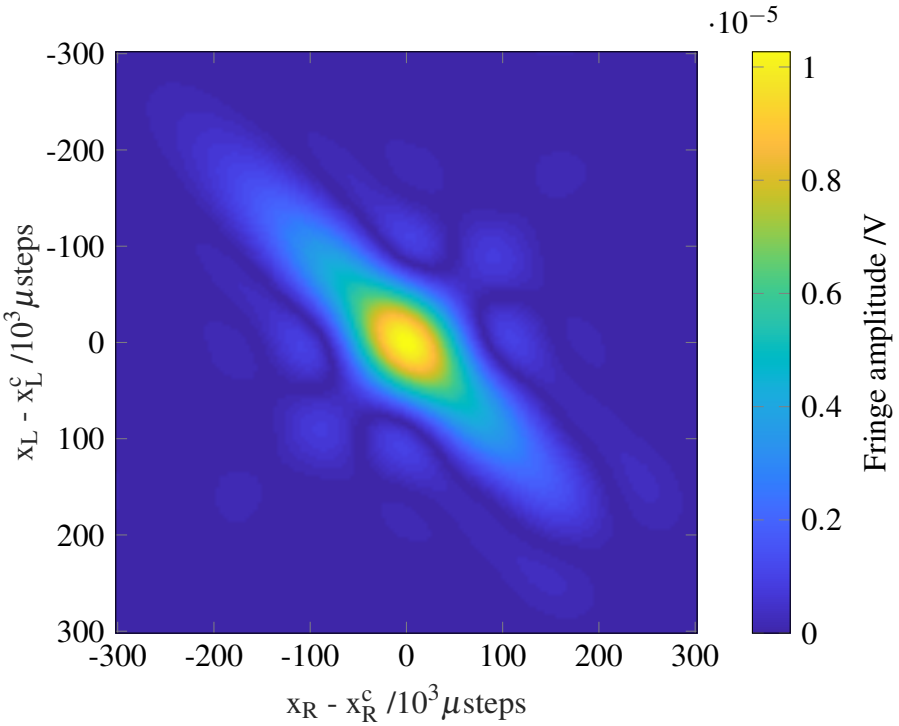

(a) Reconstructed DRF amplitude

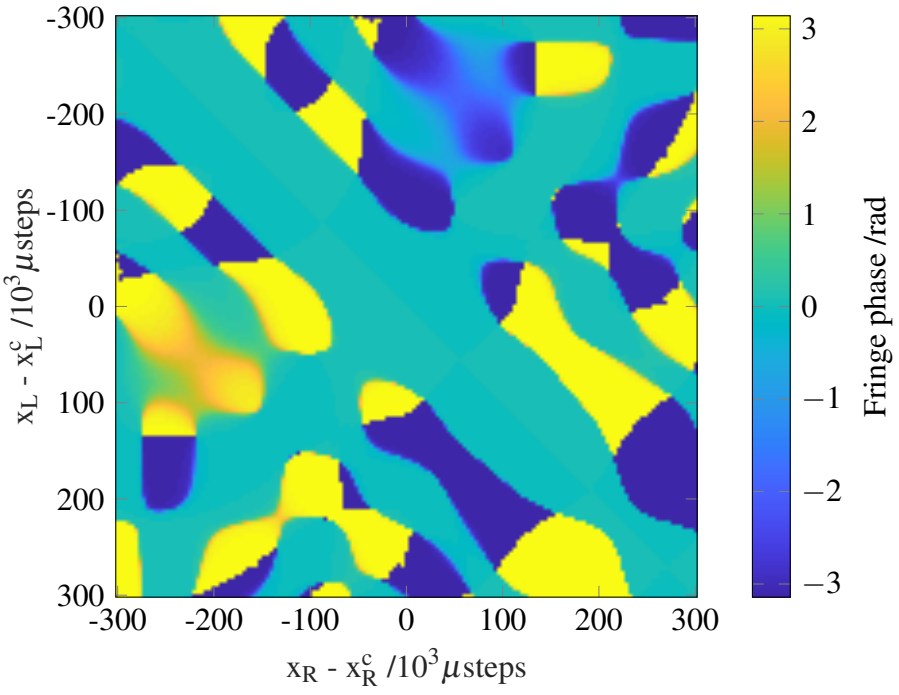

(b) Reconstructed DRF phase

Fig. 9.11 Reconstructed DRF amplitude of simulated 121-mode system, built from LG modes, with applied diagonal band mask of width equal to 3 elements.

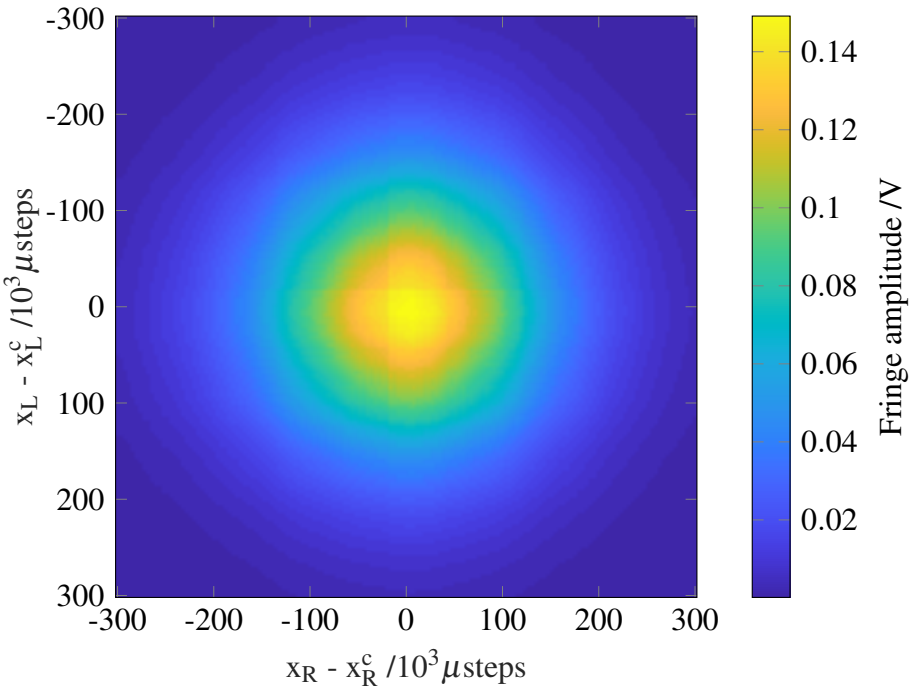

(a) DRF amplitude

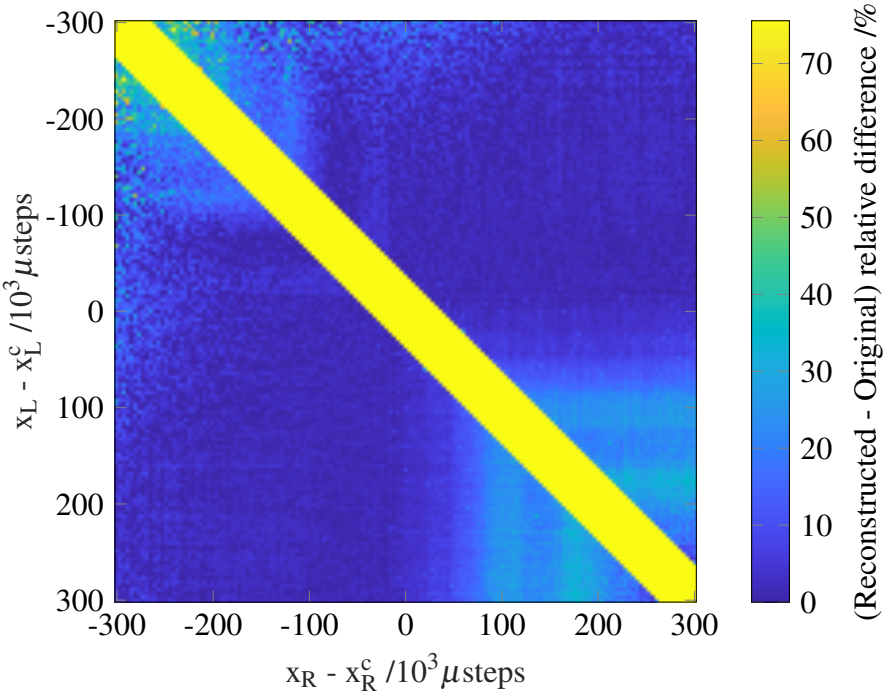

(b) Reconstruction error

Fig. 9.12 Reconstructed DRF amplitude of single-mode system, measured experimentally, with missing diagonal band of width equal to 10 elements.

the various reconstruction steps. We remark that this artefact appears in only a fraction of reconstructed single-mode datasets; for instance, reconstructing the DRF amplitude of the reference channel measured simultaneously to the signal channel presented in Figure 9.12a does not produce this feature. The reconstruction error, presented in Figure 9.12b, is low. Note also that a point with lower amplitude, on the centermost diagonal, has disappeared with the reconstruction method, indicating that it is robust against discrete experimental imperfections.

We repeat the same procedure with the same dataset, but using the corrected phase with respect to the neighboring fiber, as shown in Figure 8.17a. The missing diagonal band is again successfully filled: the DRF amplitude is very similar to that shown in Figure 9.12a, while the DRF phase is presented in Figure 9.13a. The reconstruction quality is similar to that of the self-corrected DRF case, presented in Figure 9.12b, showing that our reconstruction method is able to deal simultaneously with the amplitude and phase of experimental datasets. Note that the phase slope on the mirrored upper triangle section of the matrix is the transpose of the phase slope from the original. After the reconstruction, however, this phase slope has largely disappeared, at the cost of relatively large variations in the DRF phase patterns, up to 0.5 rad. We also note the presence of a discontinuity at the same boundary between the matrix partitions that displayed a discontinuity in amplitude in Figure 9.12a. We also investigated the effect of subtracting the plane-like geometric phase prior to the reconstruction, using the dataset presented in Figure 8.17b. The reconstructed DRF phase is shown in Figure 9.13b, and is almost constant, with a small structure up to 0.1 rad in magnitude that is similar to the structure observed before the reconstruction. This quasi-constant pattern is in agreement with the expected behavior of single-mode systems, and is well reconstructed by our diagonal filling algorithm. As discussed in Chapter 8, the remaining phase structure has potentially two contributions: non-planar geometric phase terms that are not subtracted by our planar fit, and true structure from the device under test's optical behavior.

We also considered the reconstruction of datasets taken at a distance between the source and detector planes equal to 155 mm, rather than 105 mm, which were discussed in Section 8.7. For scans using a small step size of 4000 µsteps, the width of the missing diagonal band is reduced to 3 elements, because of the small converging misalignment of the sources, discussed in Section 8.7. In Figure 9.14, we present the reconstructed DRF amplitude and phase patterns for the experimental DRF shown in Figure 8.36a: these are qualitatively similar to those shown in Figures 9.12a and 9.13b. While we may have expected a higher reconstruction quality than with datasets having a larger missing diagonal band, we found that the main contribution to the discontinuities between matrix partitions comes from the on-diagonal filling of D_{11}, which is only mildly influenced by the change in the missing

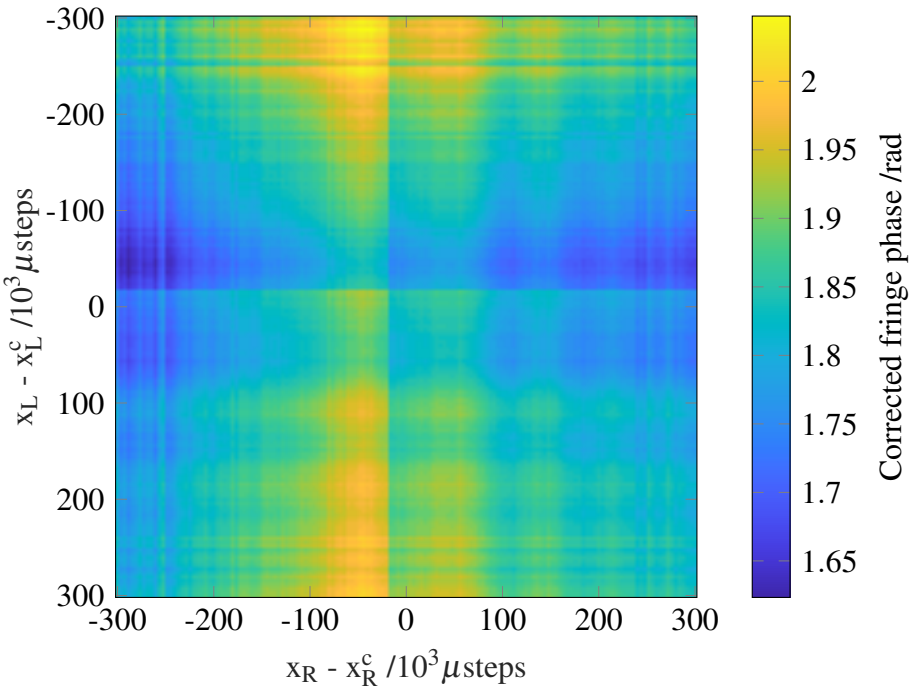

(a) Without phase slope subtraction

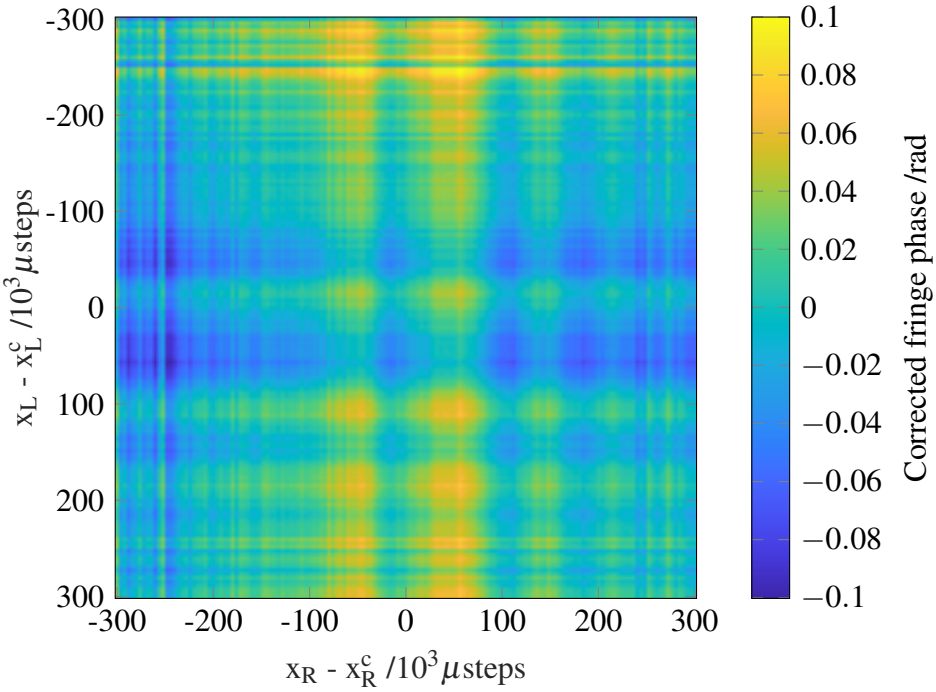

(b) With phase slope subtraction, prior to reconstruction

Fig. 9.13 Reconstructed DRF phase of single-mode system, measured experimentally, with missing diagonal band of width equal to 10 elements.

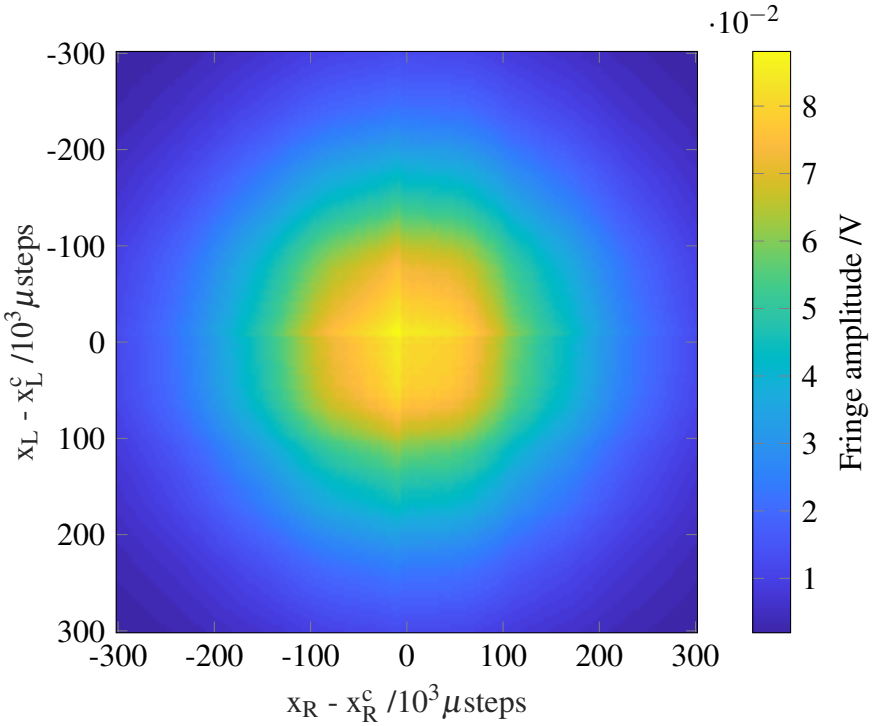

(a) Reconstructed DRF amplitude

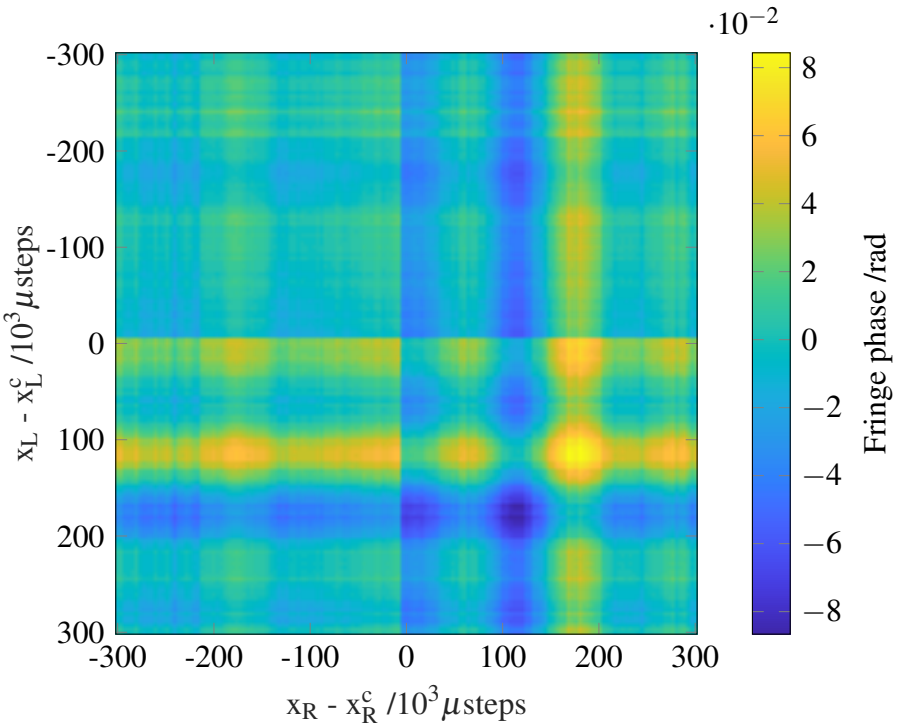

(b) Reconstructed DRF phase

Fig. 9.14 Reconstructed DRF phase of single-mode system, measured experimentally at 155 mm distance between the source and detector planes, with missing diagonal band of width equal to 3 elements; planar fit of phase pattern subtracted before reconstruction.

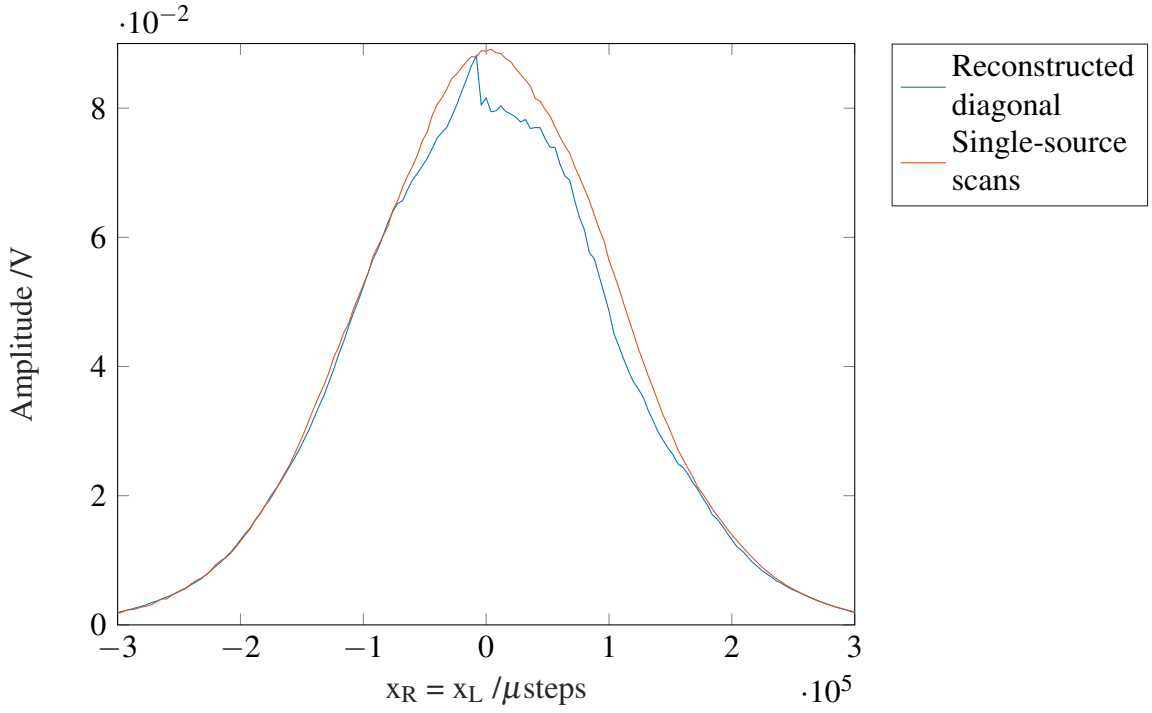

Fig. 9.15 Comparison of the reconstructed DRF matrix's diagonal with the geometric mean of corresponding single-source scans, measured experimentally with single-mode signal and reference channels.

diagonal band's width from 10 to 3 elements. More generally, the reconstructed DRF is in excellent agreement with the expected behavior of single-mode systems.

It is interesting at this stage to compare the results of the reconstruction of the single center diagonal elements with those that could be expected with the geometric mean of single-source measurements. Figure 9.15 clearly shows that the expected diagonal, based solely on single-source measurements, has its center elements approximately 10% larger than the reconstructed DRF values. This is in line with the 10% difference between the measured DRF coherence value for a single-mode system, approximately 0.9, and the expected value of 1. Calibrating for this discrepancy, we could appropriately scale the geometric mean of single-source measurements and include it as the center diagonal of the DRF matrix to be reconstructed: as it potentially contains additional information, it may produce an improved DRF reconstruction.

We then repeated the same procedure with DRFs measured experimentally using the fiber array comprising a few-mode and a multi-mode fiber. In both cases, we find that the reconstruction quality is slightly improved when considering the DRFs measured at 155 mm distance between the source and detector planes. Figure 9.16 shows the reconstructed DRF amplitude and phase patterns for the experimental DRF shown in Figure 8.37b. The DRF

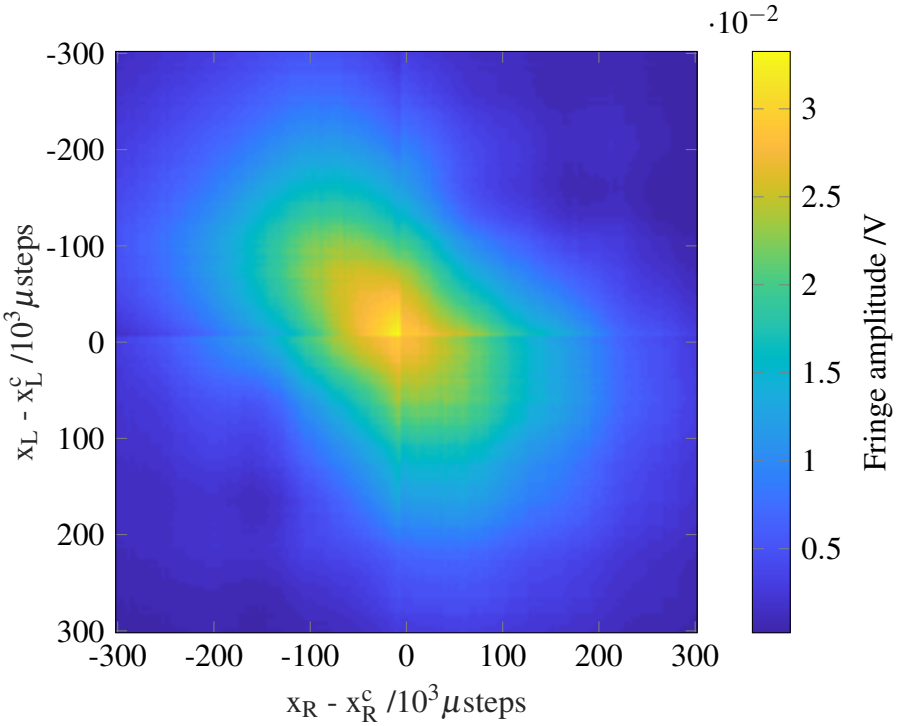

(a) Reconstructed DRF amplitude

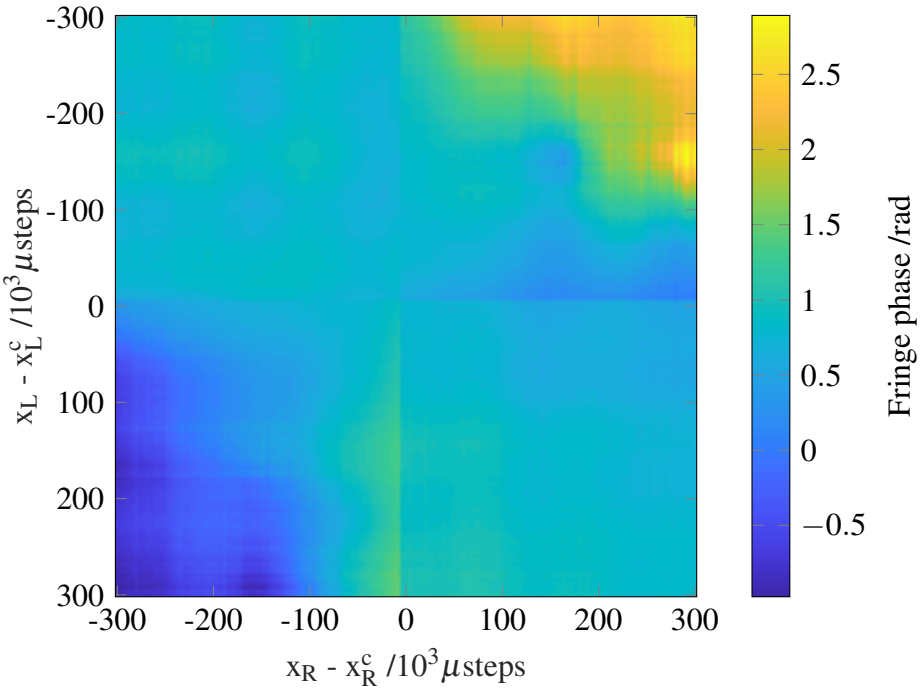

(b) Reconstructed DRF phase

Fig. 9.16 Reconstructed DRF complex amplitude of the few-mode system, measured experimentally at 155 mm distance between the source and detector planes, with missing diagonal band of width equal to 3 elements; planar fit of phase pattern subtracted before reconstruction.

amplitude is well reconstructed, and the phase pattern displays a relatively wide transition between the center region of constant phase and regions in the off-diagonal corners. In practice, we found that the on-diagonal matrix filling, used first for the submatrix D_{11} and later the entire matrix D, is the main contributor to the discontinuities seen between the reconstructed matrix partitions. There are indications that DRF asymmetries about the antidiagonal participate strongly to the appearance of these discontinuities. In particular, important information is lost when selecting the left-singular vectors from the SVD of D_{11} and D_S, and ignoring the right-singular vectors.

Lastly, we used the reconstruction scheme on the DRF measured experimentally using the multi-mode fiber in the relevant fiber array, at 155 mm distance between the source and detector planes. The DRF with the missing diagonal band was presented in Figure 8.38b. Figure 9.17 shows the reconstructed DRF, using a relative threshold of 1/40 to select the four largest singular values; we found that this threshold produced optimal reconstruction results, and the corresponding SVDs are shown in Figure 9.18. As with the experimental few-mode DRF, the reconstructed DRF has a good reconstruction quality for each partitioned submatrix, although the full reconstruction is distorted by differences between submatrices. While the DRF phase in Figure 9.17 retains a clear diagonal pattern with a structure width identical to that of the un-reconstructed case, the representation of the DRF amplitude is particularly prejudiced by the presence of a few high-amplitude reconstructed elements along the diagonal. However, we note that the total power absorbed during the scan, measured as the two-dimensional integral of the DRF surface, remains unaltered; this behavior will be explained in the following section as we consider the individual modes of the reconstructed DRF.

9.3 Recovering DRF modes

9.3.1 Mode Recovery Method

Now that we are able to reconstruct DRF matrices with missing diagonal bands, we turn to recovering the DRF's modes from these reconstructed matrices. In Chapter 7, we had investigated the effect of the two-detector phase-correction scheme on the measured DRF's recovered modes. In particular, we had concluded that only the DRF modes' phase patterns were affected by the phase correction step, while their amplitude patterns and sensitivity spectrum were unaltered. In much the same way, we want to understand the effect of the missing diagonal band reconstruction technique on the reconstructed DRF's modes

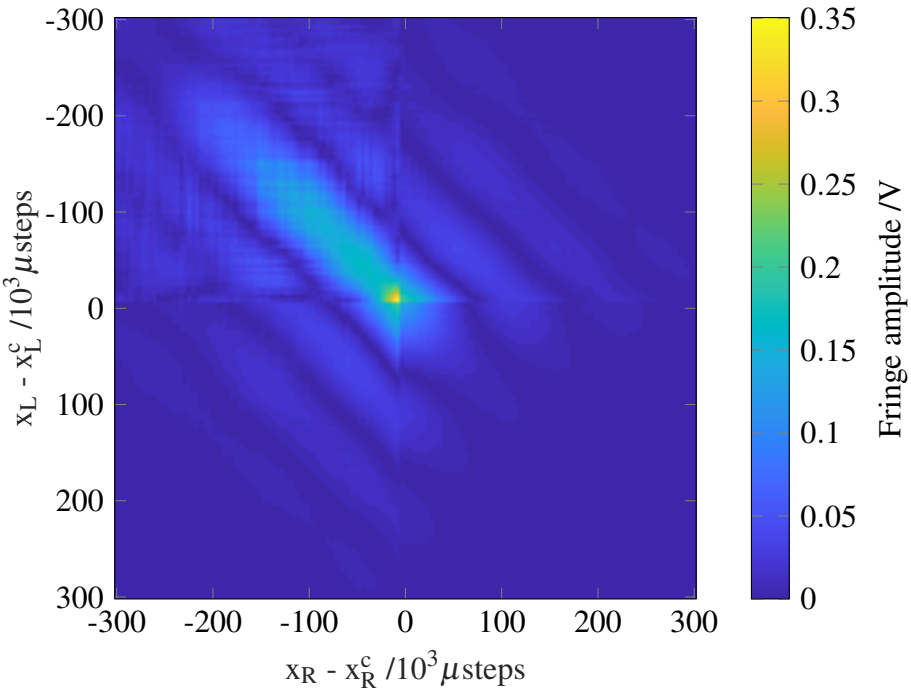

(a) Reconstructed DRF amplitude

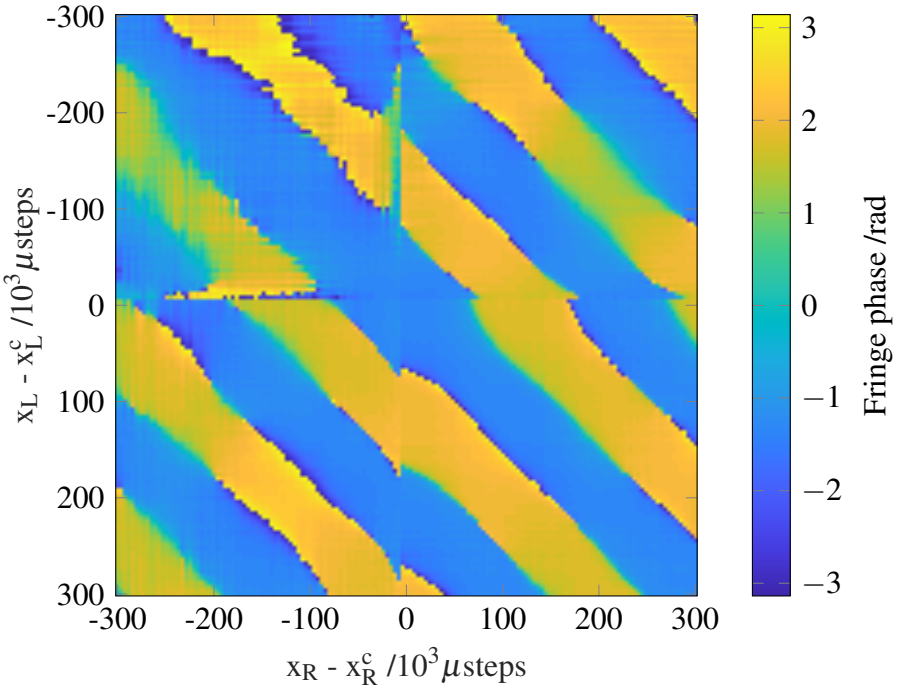

(b) Reconstructed DRF phase

Fig. 9.17 Reconstructed DRF complex amplitude of the multi-mode system, measured experimentally at 155 mm distance between the source and detector planes, with missing diagonal band of width equal to 3 elements.

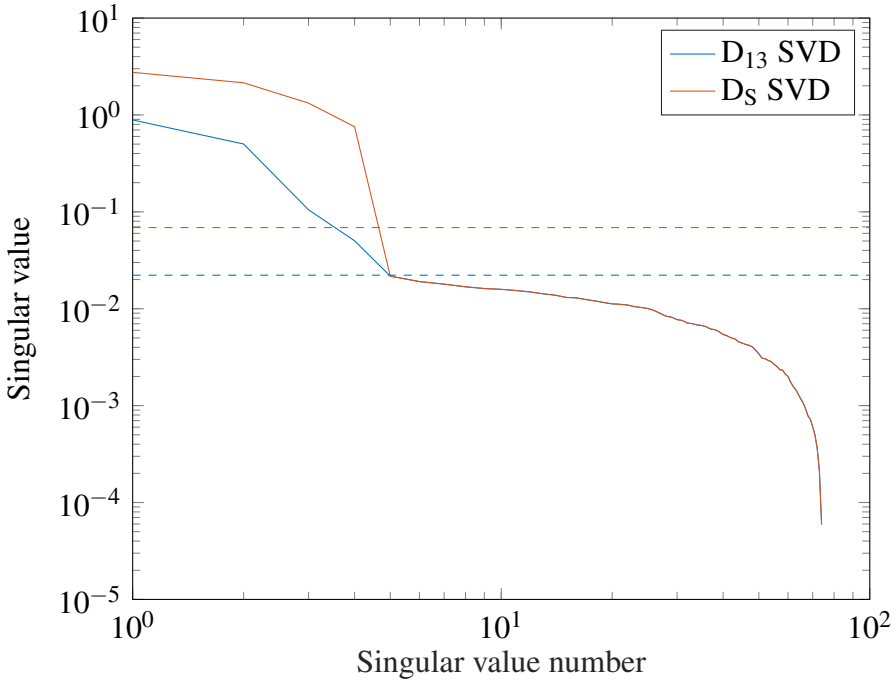

Fig. 9.18 Singular Value Decompositions of the D_{13} and D_S matrices, obtained in the reconstruction algorithm applied to the experimental multi-mode DRF, measured at 155 mm distance between the source and detector planes; the dashed lines show the 1/40 relative threshold selected.

and sensitivity spectrum, using simulated DRFs, before moving on to its application to experimentally measured DRFs.

The general method is to diagonalize the DRF matrix of interest, and straightforwardly plot the outer product of the selected eigenvector. In practice, this is performed using Matlab's eigenvalue decomposition methods: selecting the n^{th} column of the matrix of eigenvectors, we compute its outer product with its conjugate transpose to obtain the n^{th} mode. It is important here to recall that this computation of each mode of the measured DRF corresponds to the goal of EAI. Indeed, this method is the final step to recover the modes through which the detector system absorbs power from its environment; the eigenspectrum obtained from the decomposition is the spectrum of mode sensitivies. In Chapter 2, we had discussed the diagonalization of the DRF, in particular in Equation (2.59).

As we discussed in Chapter 3, as well as in Section 9.2.2 in the context of suppressing low, the eigenspectrum will display two distinct regions corresponding to two types of modes: In practice,

- Natural modes of the detector: modes with large eigenvalues indicating high sensitivity of the detector to these modes;

- Background noise modes: modes with significantly lower eigenvalues, potentially by several orders of magnitude, are dominated by background noise.

Assuming the signal-to-noise ratio is high, these two types of modes can be distinguished by a large difference in eigenspectrum slope.

9.3.2 Application to Simulated DRFs

Just as we first investigated the missing diagonal band reconstruction scheme using simulated DRFs in 9.2.3, we initially considered the recovery of DRF modes using reconstructed simulated DRFs. As previously, the data obtained using simulations is not distorted by noise and experimental errors. More importantly, we can study the effect of the additional reconstruction algorithm step, by comparing the eigenvectors obtained from the quasi-perfect simulated matrix and the reconstructed matrix.

We make a first attempt with a simulated DRF based on a single-mode response, namely the LG_{00} mode, and 151 positions distributed uniformly over the scanning range $x = [-15, 15]$ mm, as in Section 9.3.2. Phase correction with the first mode of the incoherent sum is performed to obtain the DRF, which is here the single-mode DRF itself. In Figure 9.19a, we present the eigenspectrum of the original and reconstructed DRFs with 10 missing elements: both display a single element with non-negligible magnitude, while other elements amount to contributions from the imperfections in the simulation method, i.e. the finite machine precision used. The sensitivity spectra are nearly identical; in particular, the magnitude of the first eigenvalue is identical within 10^{-23}. Figure 9.19b shows the amplitude of the first mode of the reconstructed DRF. We see that it is in excellent agreement with the original single-mode DRF; the scale difference is equal to the first eigenvalue.

The same procedure was repeated for a two-moded system, effectively the simplest model of a few-mode behavior. We chose the simulated dataset obtained from an assumed DRF built from the LG_{00} and LG_{01} modes, where reconstruction with a missing diagonal band 10 elements in width was presented in Figure 7.15. In Figure 9.20, we present the nearly-identical eigenspectrum of the original and reconstructed DRFs with 10 missing elements. As we had noted in Section 7.4 in the context of investigating the effect of the phase-correction method on simulated DRF eigenspectra, the normalization of the recovered eigenmodes induces a difference in the recovered sensitivities, even though the sensitivities used to create the simulated two-mode DRF are equal. The first and second modes are in excellent agreement with the original modes, showing that the phase reconstruction method does not impact the recovery of the simulated two-mode DRF's modes.

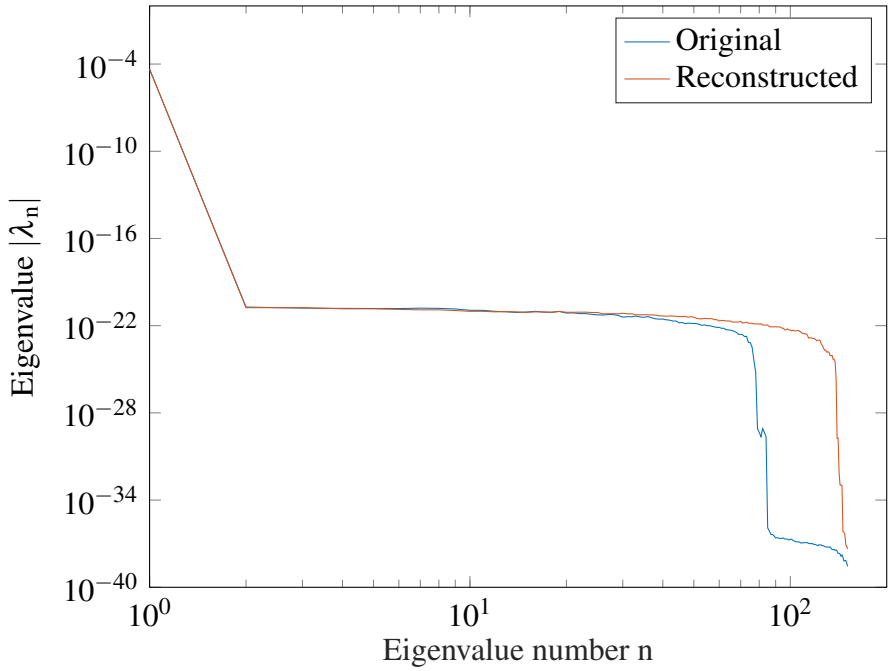

(a) DRF eigenspectrum, before and after the reconstruction of the missing diagonal band.

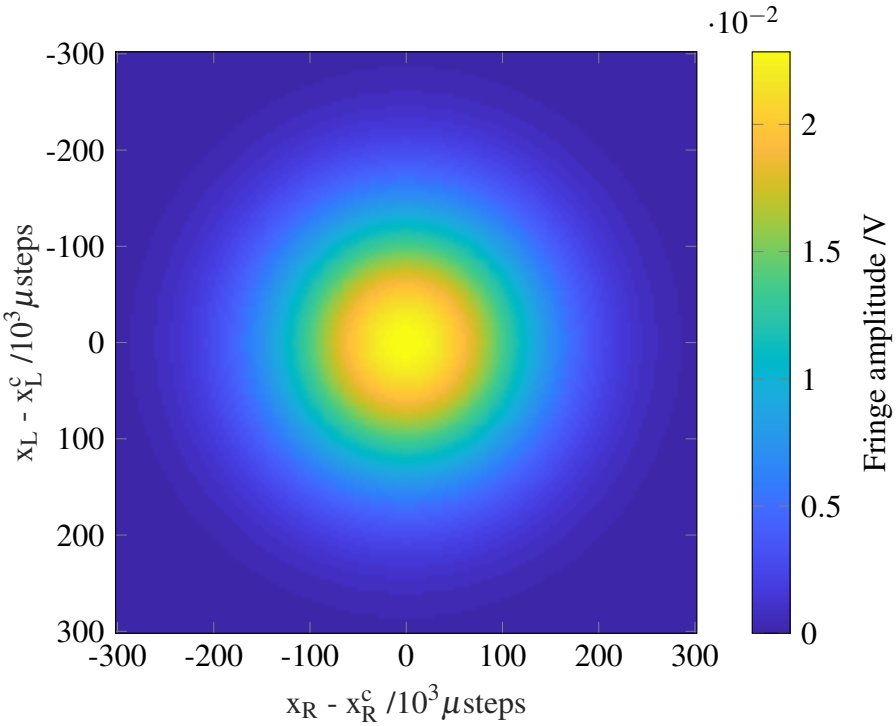

(b) Amplitude pattern of reconstructed 1st mode

Fig. 9.19 Simulated DRF amplitude built from the LG_{00} mode; the missing diagonal band is obtained by applying diagonal band mask of width equal to 10 elements.

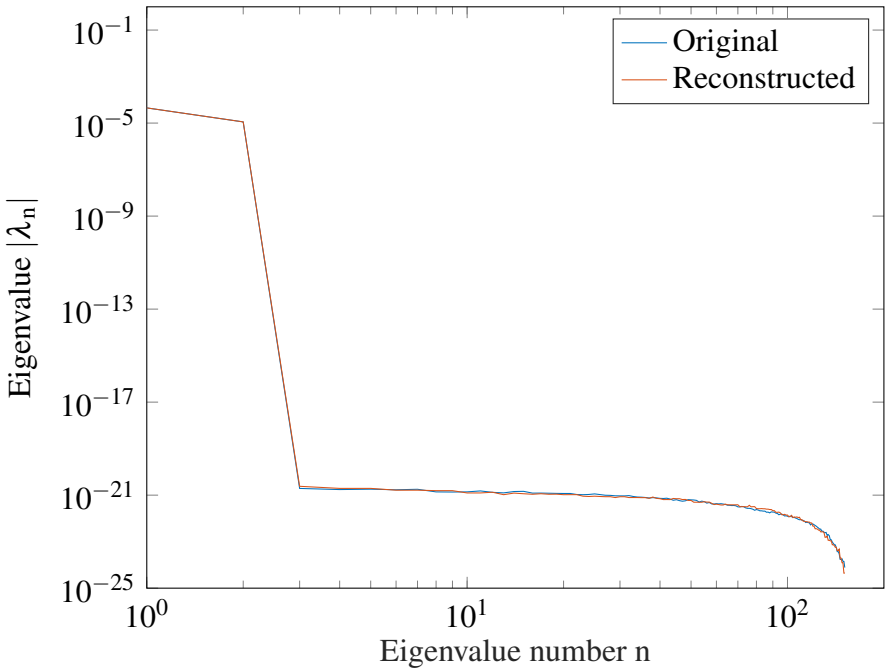

Fig. 9.20 Eigenspectrum of simulated DRF built from the LG_{00} and LG_{01} modes, before and after the reconstruction of the missing diagonal band obtained by applying diagonal band mask of width equal to 10 elements.

We also compared the mode recovery accuracy for various mode sensitivity profiles in few-mode systems. Indeed, there are indications that the missing diagonal band reconstruction may be more efficient for single- and few-mode systems, but the definition of the number of modes is quite loose. We therefore wanted to understand whether a constant or a decreasing eigenspectrum yielded different results. We investigated the existence of this phenomenon a four-mode system, built from the LG_{00}, LG_{01}, LG_{10} and LG_{11} modes , either with equal sensitivity, as in Figure 9.6, or with decreasing sensitivities (namely 1, 0.8, 0.8, and 0.3 respectively). In Figure 9.21, we compare the reconstruction qualities of these two cases, and observe that the reconstruction is indeed more accurate with the tapered sensitivity spectrum, i.e. with a lower effective number of modes. The eigenspectra obtained from the diagonalization of the two simulated DRFs also reflect this difference: the difference between the eigenspectra of the original and reconstructed DRFs is smaller for the case with tapered sensitivities than for the case with equal sensitivities.

It is also worth at this point to study the patterns of the recovered modes of the reconstructed DRF, in particular in comparison (i) to the individual Laguerre-Gaussian modes used to build the assumed DRF in the spatial basis and (ii) to the original DRF without the application of a diagonal mask and its subsequent missing diagonal reconstruction. The recovered

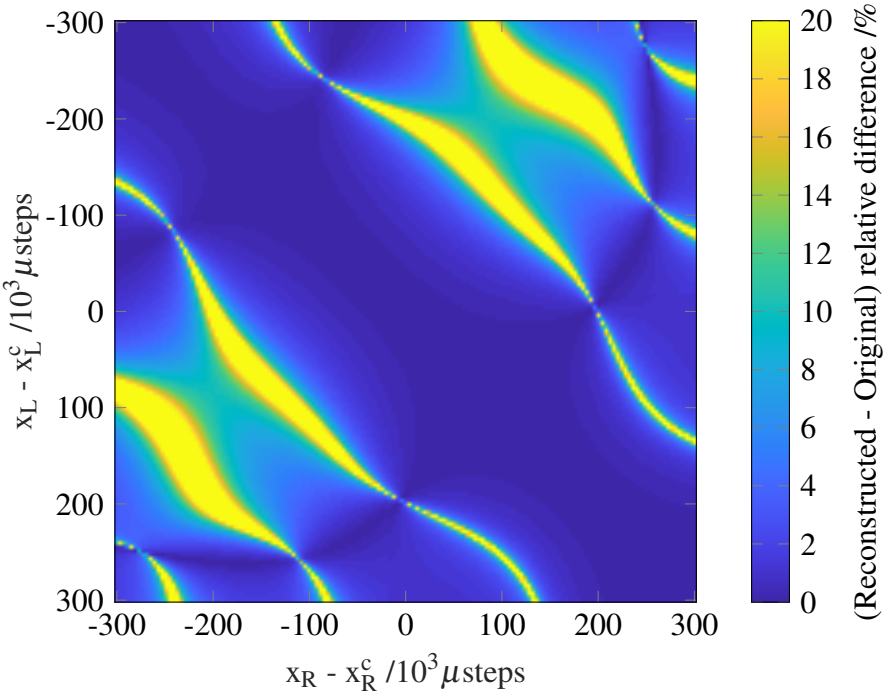

(a) Equal sensitivities

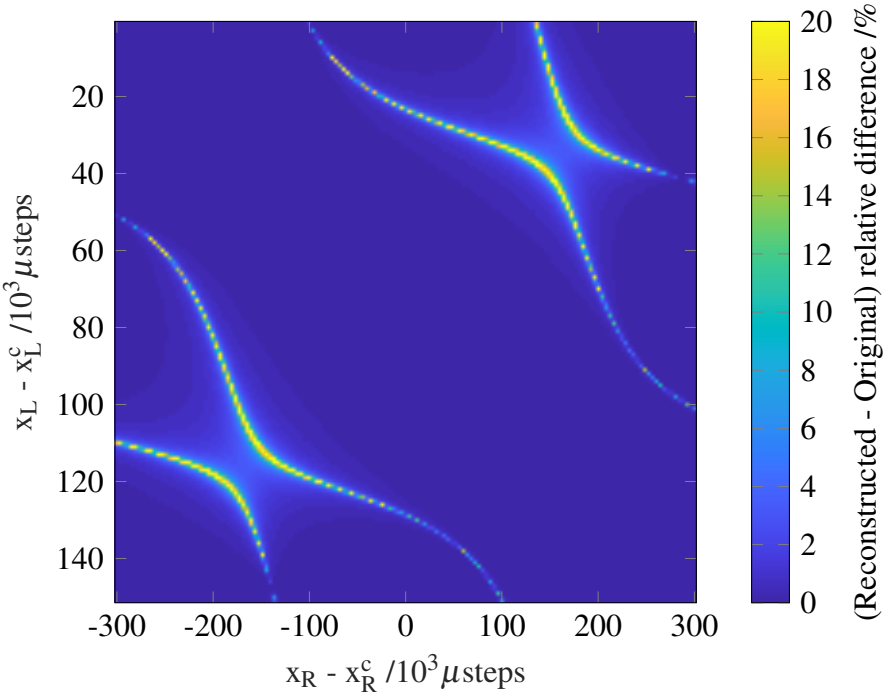

(b) Decreasing sensitivities

Fig. 9.21 Reconstruction quality for the simulated DRF with LG_{00}, LG_{01}, LG_{10} and LG_{11} modes, with missing diagonal band obtained by applying diagonal band mask of width equal to 10 elements; the color scale is selected to be identical, and smaller than in Figure 9.6b.

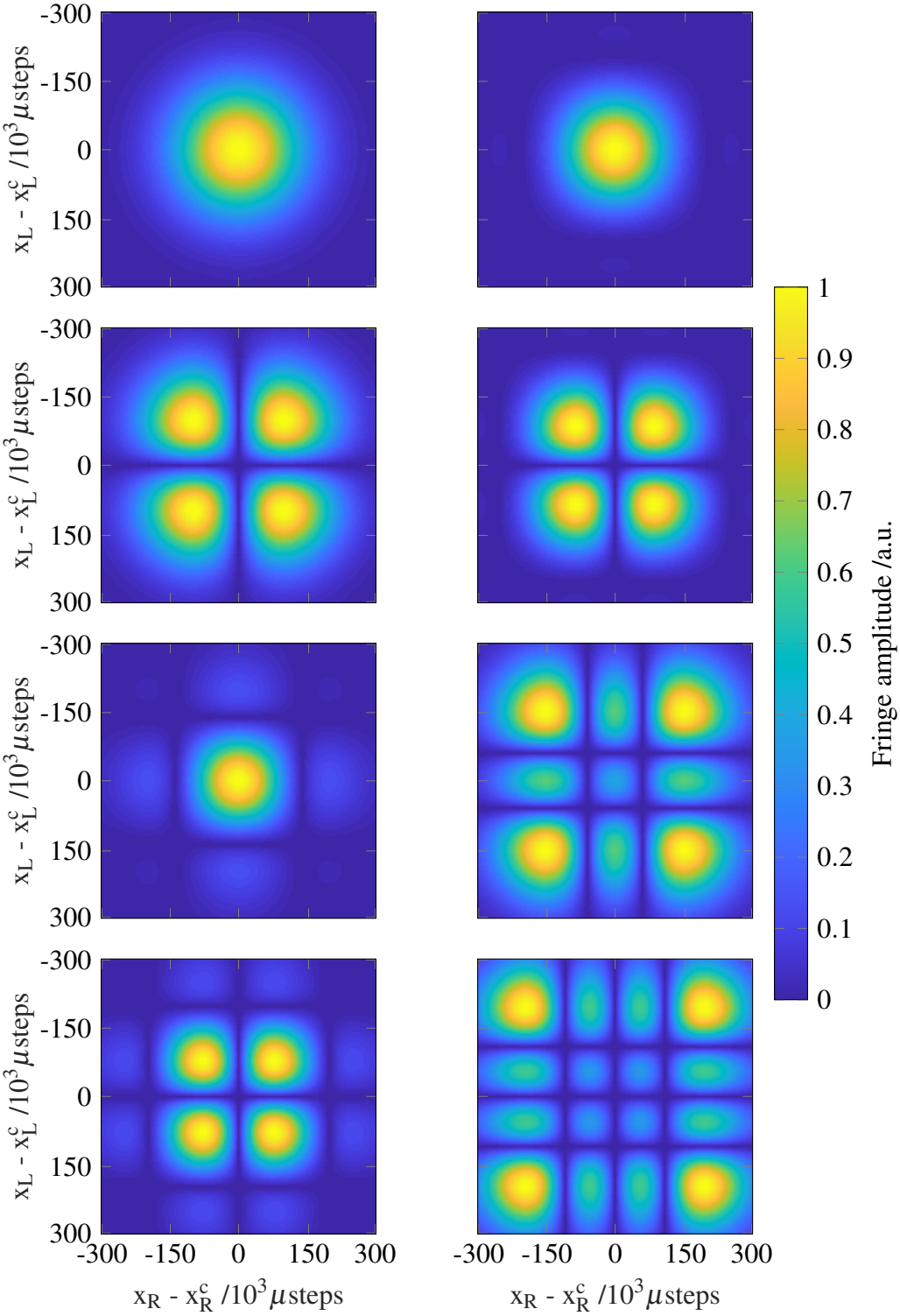

Fig. 9.22 Comparison of the normalized amplitude patterns of the four single-mode DRFs obtained from the LG_{00}, LG_{01}, LG_{10} and LG_{11} modes (left), and of the modes of the simulated DRF built from the incoherent sum of these four modes, after reconstruction of the DRF's missing diagonal band obtained by applying diagonal band mask of width equal to 10 elements (right).

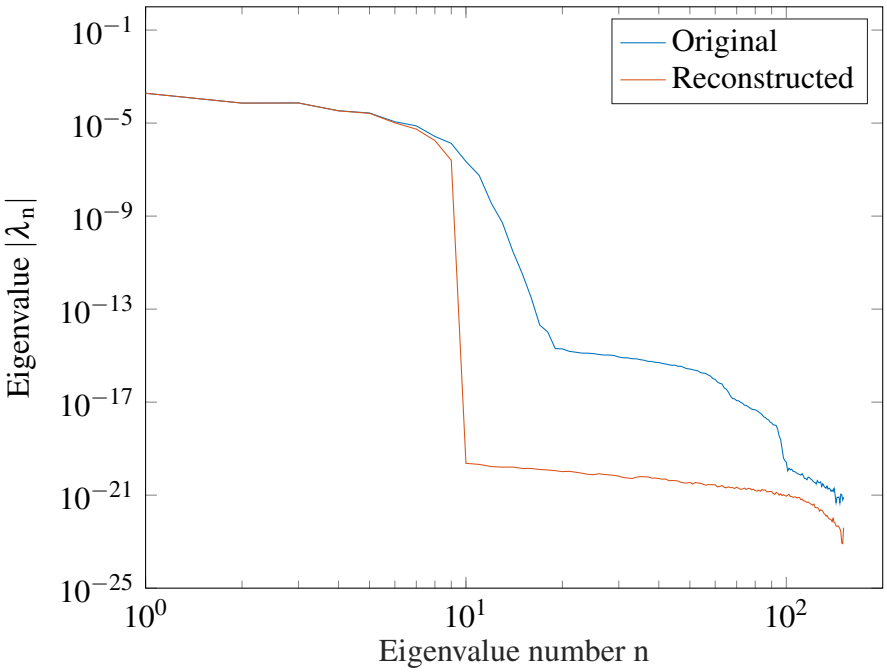

Fig. 9.23 Eigenspectrum of simulated DRF built from the first 121 LG modes, before and after the reconstruction of the missing diagonal band obtained by applying diagonal band mask of width equal to 3 elements.

modes of the reconstructed matrix are qualitatively different from those used to created the four-mode simulated DRF, as shown in Figure 9.22; however, they are identical to the four modes recovered from the total simulated DRF. This can be understood by considering the effect of projecting a two-dimensional basis set onto a one-dimensional representation: the LG modes used to create the four-mode simulated DRF are two-dimensional in the spatial basis on the reference surface used for the numerical integration (here, the detector surface), but are no longer a basis set once projected onto the sampled source positions. This did not occur in the two-mode case because the LG_{00} and LG_{01} modes are still orthogonal in the one-dimensional basis of sampled source positions.

We repeated the same mode recovery procedure using the simulated 121-mode DRF, after applying the reconstruction algorithm to fill a missing diagonal band of width equal to 3 elements, which was presented in Figure 9.11. The DRF's eigenspectrum, shown in Figure 9.20, displays how the reconstructed DRF's largest eigenvalues are well recovered compared to the original DRF: 9 modes have non-negligible eigenvalues, 8 of which are almost identical to that of the original DRF. We note that lowering the threshold for singular value suppression in the reconstruction algorithm allows us to have a greater number of identical eigenvalues, but the overall reconstruction quality is not improved. Part of the

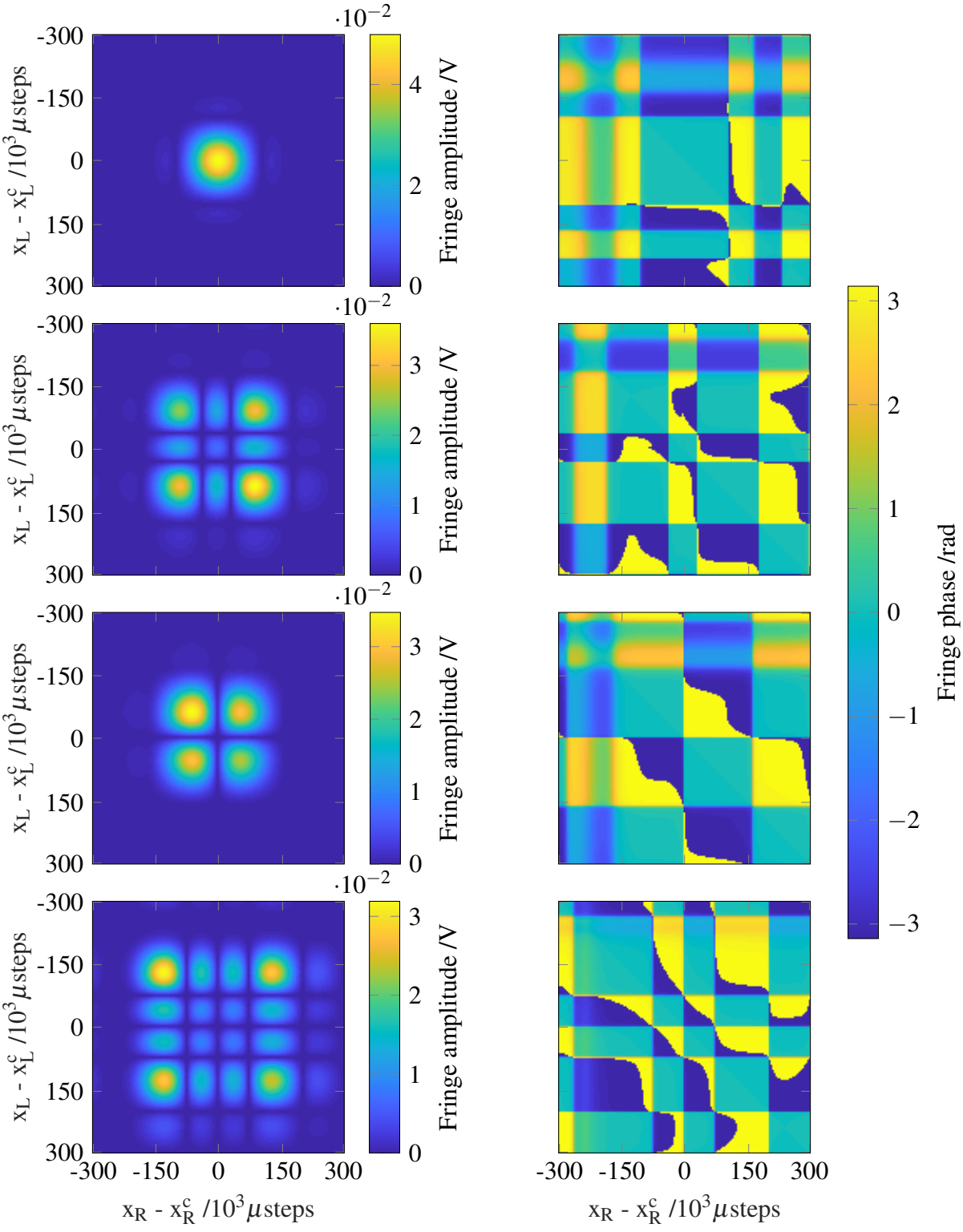

Fig. 9.24 Amplitude and phase patterns of the four first modes of the simulated 121-mode DRF, built from the from the LG_{00}, LG_{01}, LG_{10} and LG_{11} modes, after reconstruction of the missing diagonal band of width equal to 3 elements.

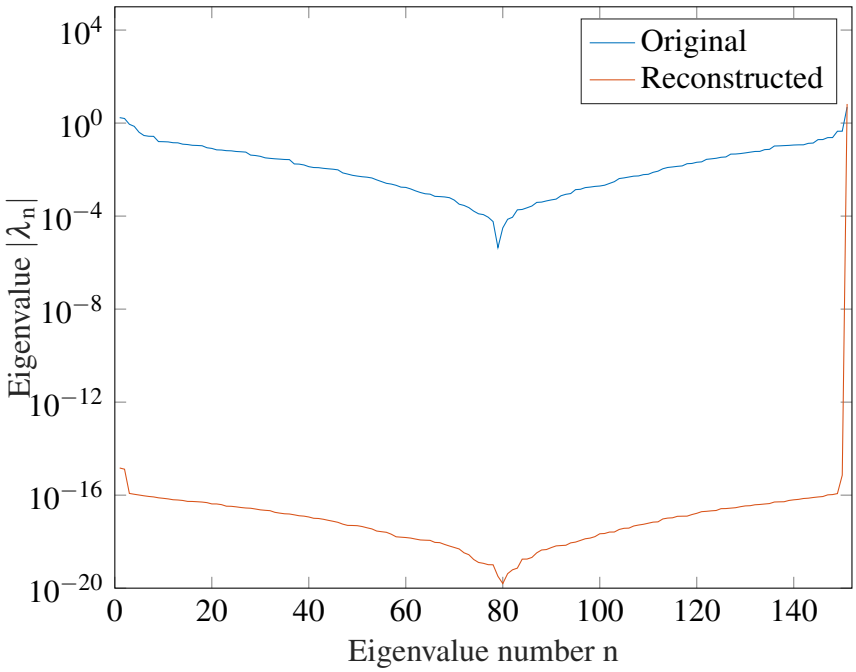

Fig. 9.25 Eigenspectrum of single-mode DRF amplitude measured experimentally, before and after the reconstruction of the missing diagonal band of width equal to 3 elements.

reason can be seen in Figure 9.24, which presents the amplitude and phase patterns of the first four modes recovered from the reconstructed DRF: contrary to the case of the simulated four-mode system shown in Figure 9.22, we observe that the modes with largest eigenvalues have several zero-amplitude lines and corresponding quasi-constant phase regions. This is a qualitative feature of multi-mode systems.

9.3.3 Application to Experimental DRFs

Having investigated the effect of our missing diagonal filling algorithm on the modes and sensitivities of simulated DRFs, we applied the diagonalization procedure to experimentally measured DRFs after their reconstruction, to retrieve the natural modes of the device under test. We diagonalized the matrix obtained with the reconstructed single-mode dataset, presented in Figures 9.12a and 9.13b. Figure 9.25 shows the eigenspectrum of the reconstruction, which clearly displays that a single mode is present. The spatial form of the mode is identical to that of the DRF, presented in Figures 9.12a and 9.13, because the mode is the only one with non-negligible eigenvalue.

Similarly, we show in Figure 9.26 the eigenspectra of the DRF before and after the reconstruction of the missing diagonal band of the DRF obtained with the few-mode fiber in the fiber array, at a distance between the source and detector planes equal to 155 mm,

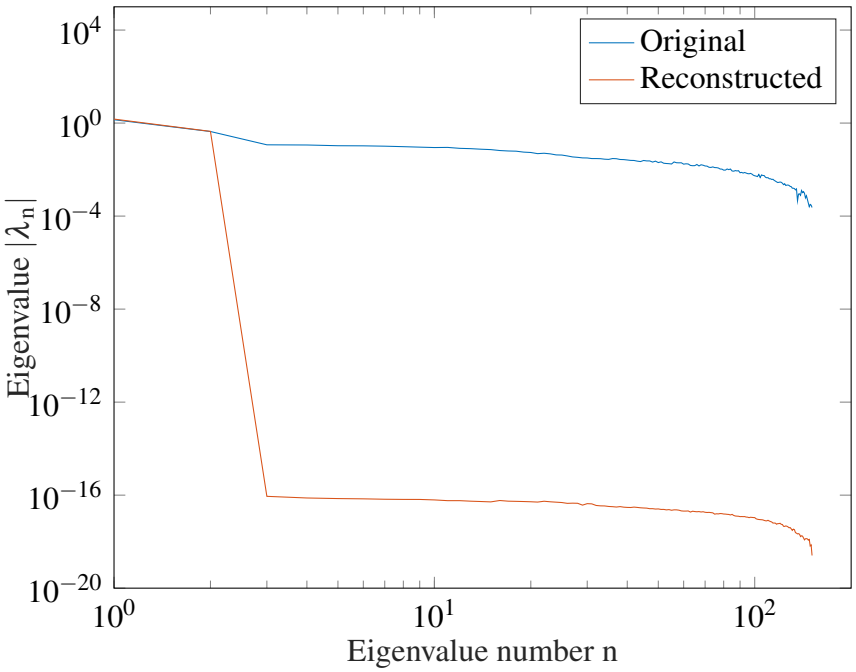

Fig. 9.26 Eigenspectrum of few-mode DRF amplitude measured experimentally, before and after the reconstruction of the missing diagonal band of width equal to 3 elements.

presented in Figure 9.16. Two large eigenvalues form a sharp slope, while the following eigenvalues decrease more slowly: the former are associated with the two natural modes of the device under test, while others account largely for noise and experimental imperfections.

Figure 9.27 shows the amplitude and phase patterns of the first two modes after reconstruction. We find that the two modes are in very good agreement with the recovered modes of the simulated two-mode system: the first mode is similar to that of a single-mode system, with an approximately Gaussian amplitude pattern and constant phase pattern, while the second mode has four-fold symmetry in amplitude with a π rad phase difference between neighboring quadrants. We remark that the irregularities in the shape of the recovered experimental modes are caused by the artefacts of the reconstruction method, rather than the diagonalization of the reconstructed DRF: refinements of the missing diagonal filling methods would therefore have a direct positive impact on the quality of the recovered modes.

We repeated this procedure with the reconstructed experimental multi-mode DRF presented in Figure 9.17. We found that its eigenvalue decomposition contains four modes with non-negligible eigenvalues; their amplitude and phase patterns are shown in Figure 9.28. We observe that these modes contain many zero-amplitude lines and corresponding quasi-constant phase regions: this is very different from the two recovered modes in the few-mode system, and indicative of highly multi-mode behavior in the device under test.

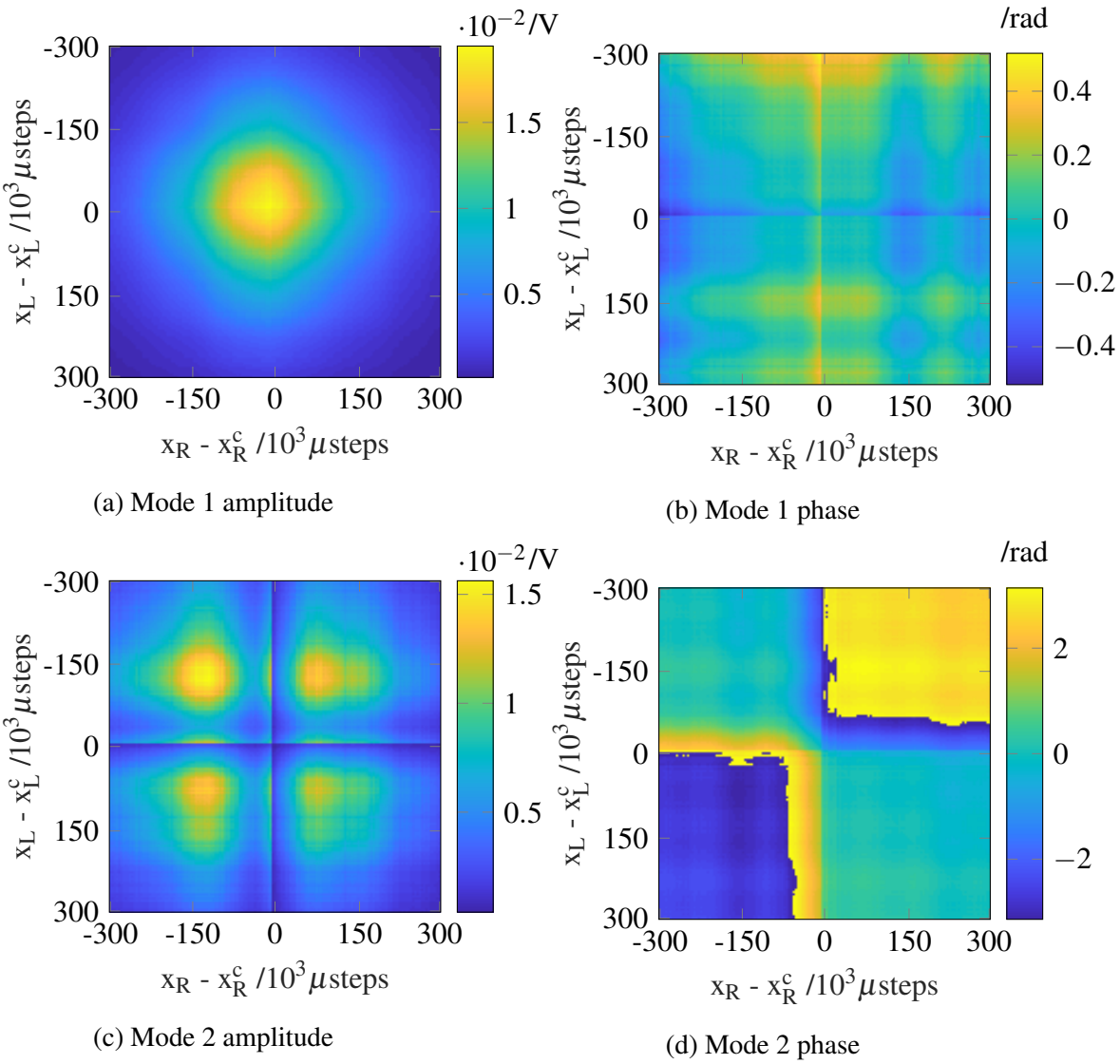

(a) Mode 1 amplitude

(b) Mode 1 phase

(c) Mode 2 amplitude

(d) Mode 2 phase

Fig. 9.27 Amplitude and phase patterns of the first and second modes recovered from the few-mode DRF, after reconstruction of the missing diagonal band of width equal to 3 elements.

It also indicates that the device under test has many more modes than the 121 studied in the simulated DRF presented in Figure 9.11, and whose recovered modes were presented in Figure 9.24. In relation to the elements with large amplitude observed in Figure 9.17 in the corner of the D_{11} submatrix, we see from the mode decomposition that several modes constructively contribute. In particular, the corresponding elements in each mode have large magnitudes with respect to the rest of the mode pattern, even though each mode displayed is normalized (i.e. its two-dimensional integration is equal to 1); its contribution to the total DRF is then weighted only by its corresponding eigenvalue. More generally, we conclude

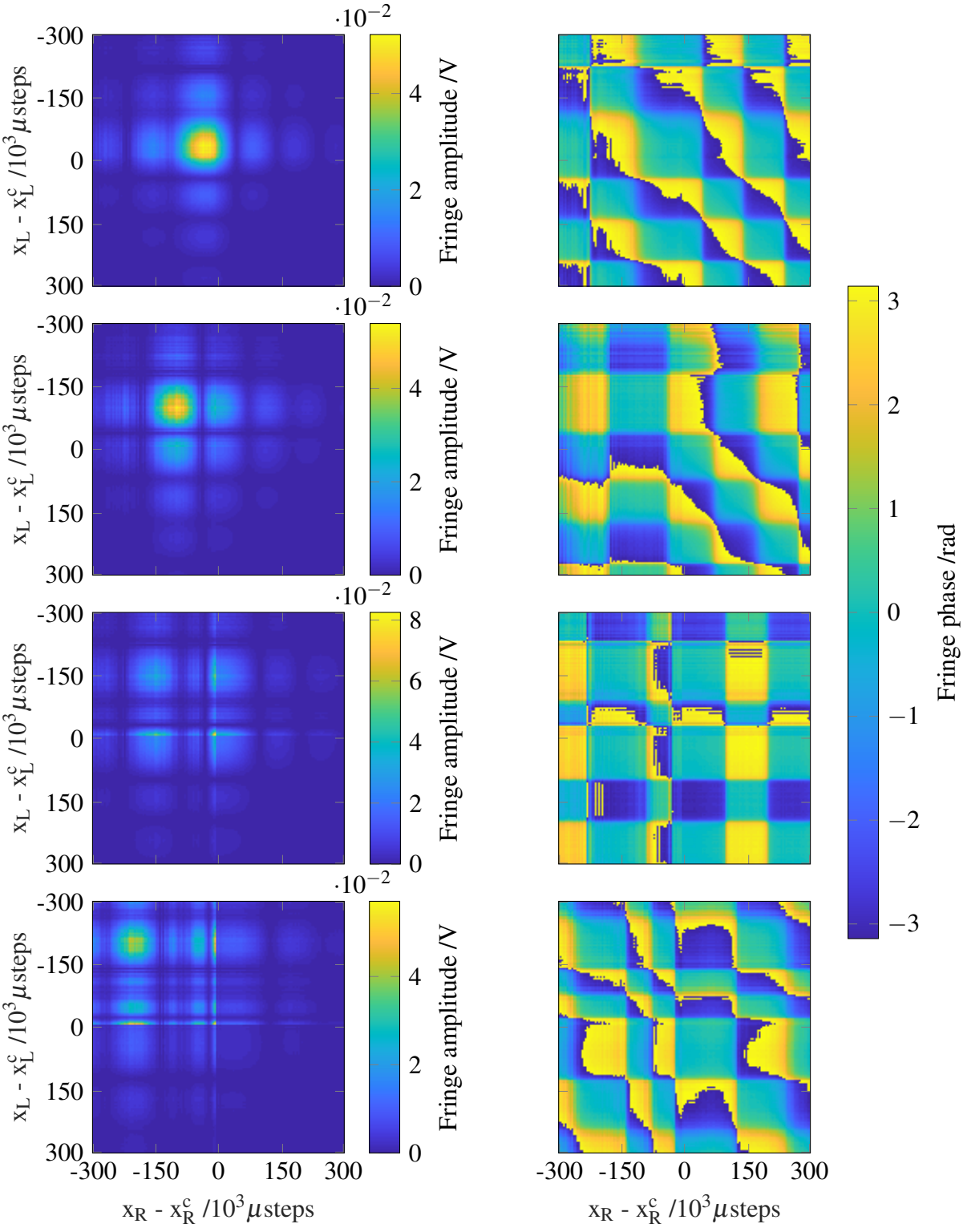

Fig. 9.28 Amplitude and phase patterns of the four modes of the experimental DRF measured with the multi-mode fiber system, after reconstruction of the missing diagonal band of width equal to 3 elements.

that such large-magnitude elements are artifacts caused by the trade-off in the reconstruction threshold, and hence the number of available modes, between intentionally discarding noise modes and unwillingly losing some valid information. The amplitude and phase patterns of higher-order modes, which are not displayed here and have significantly smaller eigenvalues, are much more erratic and readily attributed to noise and experimental imperfections.

9.4 Conclusion

We started this chapter with a large collection of experimental complex fringe amplitude datasets, obtained with a large variety of modal behaviors of the device under test. The use of these datasets was limited by the absence of data along a diagonal band, caused by the physical restrictions on the scanned source positions due to the probes' finite size. In particular, this missing diagonal prohibited the diagonalization of the measured DRF to obtain its constituent natural modes, the key product of performing EAI on the devices under test.

We have demonstrated a numerical method used to fill in the missing diagonal band data, based on partitioning the DRF matrix into 9 submatrices, and using the singular-vectors of the fully known submatrices to sequentially reconstruct those with missing elements. We found that this technique produced good results, using both simulated DRF matrices presented in Chapter 3 and experimentally acquired datasets described in Chapter 8. Two other methods were implemented, but not discussed here as they were generally less successful. Further progress still needs to be made on datasets obtained with highly multi-mode systems, where the combination of noise and number of missing elements degrades the reconstruction quality. However, this limitation is mainly a computational challenge rather than one related to the physics of EAI. More generally, the difficulties encountered do not fundamentally negate the strong results obtained with EAI, and the reconstructed DRFs that fully characterize the device under test's optical behavior.

Finally, we have used these reconstructed DRFs to successfully recover the natural modes of the device under test. In particular, in Section 9.3.3, we recovered the modes of experimental datasets of single-mode, few-mode and multi-mode systems, built from a fiber-coupled photodetector. This achievement is the realization of the objective we had initially set out for ourselves, in Chapter 1. We recall that our goal was to reconstruct the natural modes of the detector response for a wide variety infrared detector systems. This has now been achieved successfully for single-mode, few-mode and multi-mode systems.

As we had discussed in Chapter 2, the recovered modes are in the basis of sampled positions. For the chosen one-dimensional sampling grid, these modes do not have the

same forms as the original LG modes, because the latter are not orthogonal in the basis of sampled source positions. All of the methods presented in this chapter are directly applicable to simulated and experimental datasets obtained for sources scanned instead over two-dimensional sampling grids. In that case, the recovered modes would be those of the DRF in the basis of selected source positions.

Chapter 10

Conclusion

10.1 Review of Key Achievements

In Chapter 1, we set out the ambitious goal of demonstrating Energy Absorption Interferometry at infrared wavelengths, an experimental method to fully characterize the optical response of detectors using only power measurements. This work involved showing the technique's feasibility at infrared wavelengths using fiber-coupled near-infrared detectors, designing and constructing an experimental system to carry out such studies, and performing these measurements on a range of systems with single-mode, few-mode and multi-mode behaviors in order to ultimately recover their natural modes.

Throughout this thesis, we have systematically carried out this plan and have successfully measured the optical response correlation functions of a variety of detectors and reconstructed their natural modes:

- In Chapter 2, we summarized the theoretical description of power-absorbing structures, which states that their optical response can be written in the form of a two-point Detector Response Function (DRF) [61]. We further described an experimental method to fully recover a device under test's DRF solely using power measurements, from the fringe displayed in the detector output when the relative phase between two highly-coherent sources is modulated.

- In Chapter 3, we created and implemented a simulation framework to numerically investigate EAI for any functional form of the two-point DRF. In particular, we first studied simulated DRFs under the assumption of point-like sources and detectors, then assuming finite-sized sources and detectors based on Laguerre-Gaussian free-space modes, Linearly Polarized fiber modes, and even using a non-modal finite-coherence functional form.

- In Chapter 4, we qualtiatively and quantitatively explored the feasibility of an experimental system to perform EAI on near-infrared detectors. A fiber-based architecture was designed, which includes a detector coupled to an interchangeable optical fiber, whose properties set the modal behavior of the device under test. Functional forms for performance requirements were proposed, and applied to our conceptual system for all components, including the minimum linewidth of the laser source, an upper bound on the step size of the motorized stage system used to position the probes, and the required sensitivity and noise characteristics of the detector system.

- In Chapter 5, we discussed the choice of specific components for the construction of the experimental system, including the fabrication of several custom-made items. Their performance was tested at each stage of the construction, and found to fulfill all specified requirements. Fringes in the detector output for sources at fixed position pairs were measured, demonstrating the operation of the experimental system and allowing additional tests with increased sensitivity. These results, along with those of Chapter 4, were presented and published as a conference proceeding [126].

- In Chapter 6, we devised a standardized experimental procedure to perform EAI on a wide range of fiber-coupled detection systems, consisting of two single-source measurements of the detector beampattern and a two-source measurement of fringes in the detector output, as the sources are scanned over a finely-sampled one-dimensional grid. The first measurements of the DRF amplitude of infrared detectors were thus performed for single-mode, few-mode and multi-mode devices, and differentiating characteristics were observed. We additionally derived that the amplitude-only measurements could produce a lower bound for the number of modes with non-negligible sensitivity, and an upper bound for the number of modes with quasi-constant sensitivity. This relationship was successfully applied to estimate the number of modes of DRFs measured experimentally.

- In Chapter 7, we described several classes of phase-correction schemes, allowing either offline or real-time suppression of the observed phase instabilities caused by temperature variations and mechanical vibrations. We chose to further study a scheme where a reference detector is added to the experimental system near the device under test: subtracting the reference's fringe phase from that of the device under test produces a corrected fringe phase. This technique fully removes the phase drift up to the probe tips, and partially up to the detector surfaces; additionally, it subtracts a significant fraction of the fast geometric phase wrapping which occurs when scanning the sources.

- In Chapter 8, we implemented this real-time phase-correction scheme by adding a reference channel spatially close to the device under test, and obtained a significant improvement of the phase stability time from a few seconds to several hours. We found that the phase-correction method is extremely robust against environmental differential phase drift and mechanical vibrations. The first simultaneous EAI measurement of the DRF amplitude and phase components was performed on a large variety of devices; these included tightly-packed fiber arrays, which allowed us to decrease the distance between the measurement channels.
- In Chapter 9, we presented the most successful of several reconstruction schemes we implemented to fill the diagonal band of missing data, caused by the finite size of the probes. We investigated the strengths and limits of the technique on simulated DRFs, and successfully applied it to a large number of experimentally-measured DRFs. These reconstructed DRFs were then decomposed to recover their natural modes.

10.2 Overall Conclusions

This work produced the following scientific advances:

- A bespoke simulation framework numerically explored EAI at infrared wavelengths, for a variety of assumptions and models for the source and detector beams.
- The feasibility of EAI at infrared wavelengths was theoretically investigated, and an experimental architecture was created and implemented.
- The first EAI study of fiber-coupled infrared detector systems was performed to recover their DRF amplitude pattern; the DRF amplitude, visibility and coherence of single-mode, few-mode and multi-mode systems were shown to have clear differentiating characteristics.
- The DRF of few-mode fiber-coupled systems was shown to be in agreement with simulations using Laguerre-Gaussian modes, indicating that the latter is a suitable basis to describe the far-field optical response of optical fibers.
- The DRF amplitude pattern was shown to contain sufficient information to estimate the number of modes of the device under test, without the need for phase information.
- Hour-long phase stability times were reproducibly obtained using a purpose-built phase reference scheme, to correct for the relative phase drift between the two probes caused by environmental variations.

- The simultaneous measurement of the DRF amplitude and phase patterns of single-mode, few-mode and multi-mode fiber-coupled near-infrared photodetectors was performed; this unique work demonstrated that EAI can be applied at near-infrared wavelengths.
- An algorithm to fill missing elements of the DRF was successfully implemented and applied to simulated and experimental DRFs.
- The modes of experimental DRFs were recovered, producing the individually fully coherent, mutually independent field patterns through which the device under test absorbs incident optical power.

10.3 Improvements and Extensions

10.3.1 Numerical Studies

Having successfully demonstrated EAI in the context of near-infrared fiber-coupled photodetectors, a large number of opportunities become available. First, simple additions can be made to the simulation framework implemented in Chapters 3 and 7, in order to study the effects of particular phenomena:

- The large square integration surface used in Chapter 3 can be replaced by a form, shape and size corresponding to different kinds of physical realizations, for instance an absorber wrapped on a sphere. This would be performed by directly changing the surface of integration, or by applying an appropriate two-dimensional top hat function to the integrand.
- In the same way that we investigated the impact of experimental imperfections in the sources' positioning on the phase correction scheme, in Chapter 7, imperfections can be added to source and detector positions and directions in the non-simplified DRF simulations; for instance, their impact on the recovery of DRF modes could be studied.
- Noise could be introduced to simulated DRFs, including those produced by fitting simulated fringes for each source position pair, to study its effect on the recovery of DRF modes, including their quality and the rate of convergence as source positions are sampled. In effect, this would imitate the presence of a finite measurement SNR.

Other numerical investigations would require significant extensions or modifications to the simulation framework presented in this manuscript:

- In extending our study of the convergence towards a complete basis of sampled source positions, the implementation of incremental SVD could be used on numerical DRFs [70] to study its impact on EAI performance. This would provide important experience in order to add iSVD to the real-time processing of experimental data, for instance using intelligent source scanning methods to minimize the total number of source sampling positions required.

- A more detailed understanding of the electromagnetic behavior of step-index fibers is required to precisely simulate high-order modes, beyond assuming a single value of the Gaussian beam waist for all simulated modes. In particular, this would provide the ability to simulate the behavior of fluoride-based fibers more precisely. Extensions to account for fibers with graded refractive index profiles are also conceivable [127].

- While our simulation framework has allowed us to study a broad variety of assumed DRF functional forms, full electromagnetic simulations are necessary to account for complex processes. For instance, Thomas et. al studied the application of EAI to sets of electric dipoles to reveal long-range coherent phenomena [128], while Thion et. al investigated nanoparticle-based periodic structures [129, 64]. In the case of infrared devices, the study of polarization-dependent behavior would be of particular interest, in analogy with simulations performed for submillimeter systems [59].

10.3.2 Experimental Studies

The experimental system in the configuration described can be used for several further investigations:

- Having realized two-source scans over a uniformly sampled scanned, a straightforward extension is to perform scans over two-dimensional grids. In fact, a demonstration of fringe measurements for uniformly sampled source positions on a circle was successfully achieved; the step size considered was large and the on-axis position not known with sufficient accuracy, rendering the data interpretation difficult. For two-dimensional Cartesian grids, a critical choice would be the choice of a graphical representation of the data, in what can be viewed as a four-dimensional dataset; all of the technical capabilities to perform such scans are available.

- A more speculative study would be to perform z-axis scans in order to measure coherence volumes. The DRF measurement and mode reconstruction would then effectively become a six-dimensional problem: while choosing an appropriate representation is non-trivial, the EAI theory described in this manuscript is fully applicable.

- Other detector systems can be investigated. Replacing the flat-faced detector fiber by one with a shaped tip would offer further insights into the coupling of incident radiation and fiber modes [90]. A detection system based on a PIN photodiode array [130] with $25 \times 25\,\mu m^2$ pixels has been planned, but a custom transimpedance amplifier array would be required. The investigation of solar cells is feasible with our experimental architecture, but choosing an appropriate operation wavelength below 1000 nm: an optical-wavelength analogue of the experimental system would be suitable.

- Further improvements on current experimental imperfections coud be made, such as the angular misalignment of the sources, their polarization misalignment, and the physical size of the probes. In particular, we hypothesized that the former two could contribute to non-unity coherence values in the measured single-mode DRFs: under this assumption, improvements to the experimental system would directly translate into increased fringe visibility and coherence.

- An experimental system has been built by Hall et. al for the measurement of the effective position of pixels in CCD arrays, used for exoplanet-searching spectrographs [49]: comparing the recorded fringe pattern over the CCD array surface, deviations from the ideal configuration produce estimates of the true position of each pixel [131]. Our experimental system should be able to reproduce these results, in addition to measuring each pixel's DRF.

Other further experimental studies would require small to significant extensions of the experimental system:

- By increasing the optical power output of the laser, we would improve the SNR of measured fringes. This could be particularly helpful at far off-axis source positions, where we observed that low SNR had led to variability in the measured fringe amplitude and phase. Such an extension may have important safety implications, beyond those discussed in Section 4.4.

- Improved SNR could also be achieved using a lock-in system on the two-detector sytem's outputs, using the fact that we are modulating the relative phase of sources illuminating all detectors equally [79]. The experimental system's dynamic range for detecting fringes would then be increased.

- A custom tightly-packed fiber array could be built to obtain good phase correction capability without the observed electromagnetic modification caused by the borosilicate v-groove structures of fiber arrays used in Chapter 8.

- We have created a conceptual design for a dual-polarization system, in which an optical switch would select either of two channels to each probe, built from a dual fiber ferrule assembly with orthogonal polarizations [132]. Its implementation would allow the study of polarization-depedent DRF behavior.
- Other phase correction methods, such as those presented in Chapter 7, could be implemented to investigate experimentally the effect of phase drift correction without geometric phase cancellation.

10.4 Future Research Outlook

As part of the broader study of the optical behavior of low-temperature devices, the work described in this manuscript presents important lessons towards the possible application of EAI to superconducting detectors such as KIDs and TESs. Many of the design choices for the room-temperature experimental system can be translated to a low-temperature system: a fiber-based architecture would retain many of its room-temperature advantages, and the list of required components would be similar. The fiber-based scheme described here lends itself exceptionally well to applications at low-temperature: the two source fibers, and possibly a reference fiber, would simply need to be fed into the cryostat and onto the cold stage where the low-temperature detector is mounted. Additional considerations are necessary, starting with the mechanical constraints of placing a large part of the experimental system on a cryostat's cold stage, whose size is limited and where the distance to the detector may be smaller [133]. Solving these would also open new opportunities, such as near-field characterization of the device under test; for instance, cryogenic motorized stages are available in the form of piezo-activated stages, with position resolutions as small as 100 nm [134]. Additionally, the phase correction scheme introduced in Chapter 7 could suppress the effect of large temperature gradients along the optical fibers fed into the cryostat. Finally, the broad spectral sensitivities of superconducting detectors provide the opportunity to investigate their wavelength-dependent DRFs, by repeating EAI for different operating wavelengths [27].

The work presented in this dissertation can also influence the realization of EAI using sources acting on the device under test with other forces. For instance, numerical investigations have been produced in the case of two magnetic sources, to recover the spatial, spectral and polarimetric forms of collective dissipative modes of correlated spin systems [135]. The classical and quantum correlation functions of chains of electric dipoles were also studied through computational spectroscopy followed by EAI [136]. The theoretical application of EAI to two sources acting through generalized forces of possibly different natures, was

proven by Withington [137] and implemented numerically in the case of an elasto-electric source pair applied to amorphous materials incorporating coupled two-level systems [138]. There is significant potential for such studies to be extended to other examples, and for experimental realizations of EAI on such systems: these would continue to demonstrate the power and versatility of Energy Absorption Interferometry.

References

[1] Ken Ichi Kitayama and Nikolaos Panteleimon Diamantopoulos. Few-Mode Optical Fibers: Original Motivation and Recent Progress. *IEEE Communications Magazine*, 55(8):163–169, 2017.

[2] James R. Janesick. *Scientific Charge-Coupled Devices*. SPIE, jan 2001.

[3] Mary Diakides, Joseph D. Bronzino, and Donald R. Peterson, editors. *Medical Infrared Imaging*. CRC Press, dec 2012.

[4] M Esposito, T Anaxagoras, A C Konstantinidis, Y Zheng, R D Speller, P M Evans, N M Allinson, and K Wells. Performance of a novel wafer scale CMOS active pixel sensor for bio-medical imaging. *Physics in Medicine and Biology*, 59(13):3533–3554, jul 2014.

[5] O. Cohen, G. Zohar, M. Brumer, G. Gershon, O. Ofer, N. Ben-Ari, I. Nevo, N. Shiloah, and E. Kahanov. Backside illuminated CMOS-TDI line scanner for space applications. In Nikos Karafolas, Bruno Cugny, and Zoran Sodnik, editors, *International Conference on Space Optics — ICSO 2016*, page 140. SPIE, sep 2017.

[6] George Joseph. *Building Earth Observation Cameras*. CRC Press, jan 2015.

[7] Wei Wang, Jiasen Zhang, Xiaozhou Che, and Guogang Qin. Large Absorption Enhancement in Ultrathin Solar Cells Patterned by Metallic Nanocavity Arrays. *Scientific Reports*, 6(1):34219, dec 2016.

[8] K. Franze, J. Grosche, S. N. Skatchkov, S. Schinkinger, C. Foja, D. Schild, O. Uckermann, K. Travis, A. Reichenbach, and J. Guck. Muller cells are living optical fibers in the vertebrate retina. *Proceedings of the National Academy of Sciences*, 104(20):8287–8292, may 2007.

[9] Leonard Mandel and Emil Wolf. *Optical coherence and quantum optics*. Cambridge University Press, Cambridge, 1995.

[10] Bahaa E. A. Saleh and Malvin Carl Teich. *Fundamentals of Photonics*. Wiley Series in Pure and Applied Optics. John Wiley & Sons, Inc., New York, USA, aug 1991.

[11] Rene Daendliker. Concept of modes in optics and photonics. In *Proc. SPIE*, volume 3831, page 193, jun 2000.

[12] E. L. Dereniak and D.G. Crowe. *Optical Radiation Detectors*. John Wiley & Sons, Inc, 1984.

[13] E. L. Dereniak and G. D. Boreman. *Infrared Detectors and Systems*. John Wiley & Sons, Inc, 1996.

[14] John David Vincent, Steven E. Hodges, John Vampola, Mark Stegall, and Greg Pierce. *Fundamentals of Infrared and Visible Detector Operation and Testing*. John Wiley & Sons, Inc, Hoboken, NJ, USA, oct 2015.

[15] J. Bennett, A. Anderson, P. McInnes, and A. Whitaker. Microwave holographic metrology of large reflector antennas. *IEEE Transactions on Antennas and Propagation*, 24(3):295–303, may 1976.

[16] A. Yaghjian. An overview of near-field antenna measurements. *IEEE Transactions on Antennas and Propagation*, 34(1):30–45, jan 1986.

[17] Brian E. Vyhnalek, Sarah A. Tedder, Evan J. Katz, and Jennifer M. Nappier. Few-mode fiber coupled superconducting nanowire single-photon detectors for photon efficient optical communications. In Hamid Hemmati and Don M. Boroson, editors, *Free-Space Laser Communications XXXI*, number February, page 11. SPIE, feb 2019.

[18] Allan W. Snyder and John D. Love. *Optical Waveguide Theory*. Springer US, Boston, MA, 1984.

[19] An Li, Yifei Wang, Qian Hu, and William Shieh. Few-mode fiber based optical sensors. *Optics Express*, 23(2):1139, jan 2015.

[20] O. Muliar, M. A. Usuga, K. Rottwitt, and J. Lægsgaard. Interferometric characterization of few-mode fibers (FMF) for mode-division multiplexing (MDM). *Photonic Instrumentation Engineering II*, 9369(Mdm):936909, 2015.

[21] Michael Lesser. A Summary of Charge-Coupled Devices for Astronomy. *Publications of the Astronomical Society of the Pacific*, 127(957):1097–1104, nov 2015.

[22] M. D. Eisaman, J. Fan, A. Migdall, and S. V. Polyakov. Invited Review Article: Single-photon sources and detectors. *Review of Scientific Instruments*, 82(7):071101, jul 2011.

[23] Mary J. Hewitt, John L. Vampola, Stephen H. Black, and Carolyn J. Nielsen. Infrared readout electronics: a historical perspective. In Eric R. Fossum, editor, *Proc. SPIE 2226, Infrared Readout Electronics II*, pages 108–119, jun 1994.

[24] Horst Zimmermann. *Integrated Silicon Optoelectronics*, volume 3 of *Springer Series in Photonics*. Springer Berlin Heidelberg, Berlin, Heidelberg, 2000.

[25] S.M. Sze and Kwok K. Ng. *Physics of Semiconductor Devices*. John Wiley & Sons, Inc., Hoboken, NJ, USA, oct 2006.

[26] Da-Wen Sun. *Infrared Spectroscopy for Food Quality Analysis and Control*. Elsevier, 2009.

[27] Frank Eisenhauer and Walfried Raab. Visible/Infrared Imaging Spectroscopy and Energy-Resolving Detectors. *Annual Review of Astronomy and Astrophysics*, 53(1):155–197, 2015.

[28] K. D. Irwin and K. W. Lehnert. Microwave SQUID multiplexer. *Applied Physics Letters*, 85(11):2107–2109, sep 2004.

[29] Aaron J Miller, Adriana E Lita, Brice Calkins, Igor Vayshenker, Steven M Gruber, and Sae Woo Nam. Compact cryogenic self-aligning fiber-to-detector coupling with losses below one percent. *Optics express*, 19(10):9102–9110, 2011.

[30] Jiansong Gao. *The Physics of Superconducting Microwave Resonators*. PhD thesis, California Institute of Technology, 2008.

[31] A. Megrant, C. Neill, R. Barends, B. Chiaro, Yu Chen, L. Feigl, J. Kelly, Erik Lucero, Matteo Mariantoni, P. J J O'Malley, D. Sank, A. Vainsencher, J. Wenner, T. C. White, Y. Yin, J. Zhao, C. J. Palmstr??m, John M. Martinis, and A. N. Cleland. Planar superconducting resonators with internal quality factors above one million. *Applied Physics Letters*, 100(11):113510, mar 2012.

[32] Andrey Baryshev, Jochem J A Baselmans, Angelo Freni, Giampiero Gerini, Henk Hoevers, Annalisa Iacono, and Andrea Neto. Progress in antenna coupled kinetic inductance detectors. *IEEE Transactions on Terahertz Science and Technology*, 1(1):112–123, 2011.

[33] Ajoy Ghatak and K. Thyagarajan. *Introduction to fiber optics*. Cambridge University Press, Cambridge, 1998.

[34] Anthony Dandridge, Alan B. Tventen, R. O. Miles, and T. G. Giallorenzi. Fiber Optic Interferometric Sensor Development at NRL. In *First International Conference on Optical Fibre Sensors, The Institution of Electrical Engineers*, number April 1983, 1983.

[35] Ma. Del Rosario Bautista-Morales, R. Martínez-Manuel, and C.A. Pineda-Arellano. Overlapped fiber-optic Michelson interferometers for simultaneous refractive index measurement at two sensing points. *Applied Optics*, 56(34):1–5, 2017.

[36] U. Roland, C. P. Renschen, D. Lippik, F. Stallmach, and F. Holzer. A New Fiber Optical Thermometer and Its Application for Process Control in Strong Electric, Magnetic, and Electromagnetic Fields. *Sensor Letters*, 1(1):93–98, dec 2003.

[37] Yousef Fazea and Vitaliy Mezhuyev. Selective mode excitation techniques for mode-division multiplexing: A critical review. *Optical Fiber Technology*, 45:280–288, nov 2018.

[38] Philippe Genevaux, Christian Simonneau, Guillaume Le Cocq, Yves Quiquempois, Laurent Bigot, Aurelien Boutin, and Gabriel Charlet. A Five-Mode Erbium-Doped Fiber Amplifier for Mode-Division Multiplexing Transmission. *Journal of Lightwave Technology*, 34(2):456–462, jan 2016.

[39] John M. Dudley, Goëry Genty, and Stéphane Coen. Supercontinuum generation in photonic crystal fiber. *Reviews of Modern Physics*, 78(4):1135–1184, oct 2006.

[40] Emil Wolf. New theory of partial coherence in the space–frequency domain Part I: spectra and cross spectra of steady-state sources. *Journal of the Optical Society of America*, 72(3):343, mar 1982.

[41] Emil Wolf. New theory of partial coherence in the space-frequency domain Part II: Steady-state fields and higher-order correlations. *Journal of the Optical Society of America A*, 3(1):76, jan 1986.

[42] Christopher N. Thomas and Stafford Withington. Optical modeling techniques for multimode horn-coupled power detectors for submillimeter and far-infrared astronomy. *Journal of the Optical Society of America A*, 30(8):1703, aug 2013.

[43] J. Chen, S. Withington, C. N. Thomas, D. J. Goldie, and O. Quaranta. Modal optical modelling of a test system for ultra-low-noise transition edge sensors for space science. In *2015 8th UK, Europe, China Millimeter Waves and THz Technology Workshop (UCMMT)*, pages 1–4. IEEE, sep 2015.

[44] Rémi Carminati, Manuel Nieto-Vesperinas, and Jean-Jacques Greffet. Reciprocity of evanescent electromagnetic waves. *Journal of the Optical Society of America A*, 15(3):706, 1998.

[45] R. Carminati, J. J. Sáenz, J. J. Greffet, and M. Nieto-Vesperinas. Reciprocity, unitarity, and time-reversal symmetry of the S matrix of fields containing evanescent components. *Physical Review A - Atomic, Molecular, and Optical Physics*, 62(1):7, 2000.

[46] Arthur Babuty, Karl Joulain, Pierre Olivier Chapuis, Jean Jacques Greffet, and Yannick De Wilde. Blackbody spectrum revisited in the near field. *Physical Review Letters*, 110(14):1–5, 2013.

[47] David T. Chuss, Edward J. Wollack, S. Harvey Moseley, Stafford Withington, and George Saklatvala. Diffraction Considerations for Planar Detectors in the Few-Mode Limit. *Publications of the Astronomical Society of the Pacific*, 120(866):430–438, apr 2008.

[48] Christopher N. Thomas, Stafford Withington, David T. Chuss, Edward J. Wollack, and S. Harvey Moseley. Modeling the intensity and polarization response of planar bolometric detectors. *Journal of the Optical Society of America A*, 27(5):1219, may 2010.

[49] Richard D. Hall, Samantha Thompson, and Didier Queloz. Measuring the effective pixel positions for the HARPS3 CCD. In Andrew D. Holland and James Beletic, editors, *Proc. SPIE 9915, High Energy, Optical, and Infrared Detectors for Astronomy VII, 99152*, page 991525, aug 2016.

[50] F. Pont, S. Zucker, and D. Queloz. The effect of red noise on planetary transit detection. *Monthly Notices of the Royal Astronomical Society*, 373(1):231–242, nov 2006.

[51] S. Withington, C. N. Thomas, and D. J. Goldie. Probing quantum correlation functions through energy-absorption interferometry. *Physical Review A*, 96(2):022131, aug 2017.

[52] S Withington and G Saklatvala. Characterizing the behaviour of partially coherent detectors through spatio-temporal modes. *Journal of Optics A: Pure and Applied Optics*, 9(7):626–633, jul 2007.

[53] George Saklatvala, Stafford Withington, and Michael P. Hobson. Coupled-mode theory for infrared and submillimeter wave detectors. *Journal of the Optical Society of America A*, 24(3):764, 2007.

[54] A. Richard Thompson, James M. Moran, and George W. Swenson. *Interferometry and Synthesis in Radio Astronomy*. Astronomy and Astrophysics Library. Springer International Publishing, Cham, 2017.

[55] Ramesh Narayan and Rajaram Nityananda. Maximum Entropy Image Restoration in Astronomy. *Annual Review of Astronomy and Astrophysics*, 24(1):127–170, sep 1986.

[56] R. C. Jennison. A Phase Sensitive Interferometer Technique for the Measurement of the Fourier Transforms of Spatial Brightness Distributions of Small Angular Extent. *Monthly Notices of the Royal Astronomical Society*, 118(3):276–284, jun 1958.

[57] John D Monnier. Optical interferometry in astronomy. *Reports on Progress in Physics*, 66(5):789–857, may 2003.

[58] Christopher N. Thomas and Stafford Withington. Experimental Demonstration of an Interferometric Technique for Characterizing the Full Optical Behavior of Multi-Mode Power Detectors. *IEEE Transactions on Terahertz Science and Technology*, 2(1):50–60, jan 2012.

[59] Christopher N Thomas. *Theoretical , Numerical and Experimental Studies of the Optical Behaviour of Few-Mode Power Detectors for Submillimetre and Far-Infrared Astronomy*. PhD thesis, University of Cambridge, 2012.

[60] S. Drabowitch, A. Papiernik, H. D. Griffiths, J. Encinas, and B. L. Smith. *Modern Antennas*. Springer US, Boston, MA, 2005.

[61] George Saklatvala, Stafford Withington, and Michael P Hobson. A coupled-mode theory for infrared and submillimeter wave detectors, jun 2006.

[62] Philip E. Sarachik. *Principles of linear systems*. Cambridge University Press, Cambridge, 1997.

[63] K Cahill. *Physical Mathematics*. Cambridge University Press, 2013.

[64] Denis Tihon, Stafford Withington, Christopher N. Thomas, and Christophe Craeye. Identification of the absorption processes in periodic plasmonic structures using energy absorption interferometry. *Journal of the Optical Society of America A*, 36(1):12, jan 2019.

[65] R B Ash. *Information Theory*. Dover books on advanced mathematics. Dover Publications, 1990.

[66] Anirban Pathak. *Elements of Quantum Computation and Quantum Communication*. CRC Press, jun 2013.

[67] Rachel H. Berry, Michael P. Hobson, and Stafford Withington. General approach for representing and propagating partially coherent terahertz fields with application to Gabor basis sets. *Journal of the Optical Society of America A*, 21(5):786, 2004.

[68] R. H. Berry, M. P. Hobson, and S. Withington. Modal decomposition of astronomical images with application to shapelets. *Monthly Notices of the Royal Astronomical Society*, 354(1):199–211, 2004.

[69] Max Born, Emil Wolf, A. B. Bhatia, P. C. Clemmow, D. Gabor, A. R. Stokes, A. M. Taylor, P. A. Wayman, and W. L. Wilcock. *Principles of Optics*. Cambridge University Press, Cambridge, 1999.

[70] Matthew Brand. Incremental Singular Value Decomposition of Uncertain Data with Missing Values. In *Lecture Notes in Computer Science*, volume 2350, pages 707–720. Springer, Berlin, Heidelberg, 2002.

[71] Badrul Sarwar, George Karypis, Joseph Konstan, and John Riedl. Incremental Singular Value Decomposition Algorithms for Highly Scalable Recommender Systems. *Proceedings of the Fifth International Conference on Computer and Information Technology (ICCIT)*, pages 1–6, 2002.

[72] A E Siegman. *Lasers*. University Science Books, 1986.

[73] M.W. Beijersbergen, L. Allen, H.E.L.O. van der Veen, and J.P. Woerdman. Astigmatic laser mode converters and transfer of orbital angular momentum. *Optics Communications*, 96(1-3):123–132, feb 1993.

[74] Atsushi Wada, Takumi Ohtani, Yoko Miyamoto, and Mitsuo Takeda. Propagation analysis of the Laguerre–Gaussian beam with astigmatism. *Journal of the Optical Society of America A*, 22(12):2746, dec 2005.

[75] B. Jacot and S. Withington. Private communication, 2019.

[76] David J. Griffiths. *Introduction to Electrodynamics*. Cambridge University Press, fourth edi edition, 2017.

[77] Francesco Pampaloni and Joerg Enderlein. Gaussian, Hermite-Gaussian, and Laguerre-Gaussian beams: A primer. oct 2004.

[78] Koichi Shimoda. *Introduction to Laser Physics*, volume 44 of *Springer Series in Optical Sciences*. Springer Berlin Heidelberg, Berlin, Heidelberg, 1984.

[79] F. Yu, S. (Ed.) Yin, P. (Ed.) Ruffin, B. Thompson, L. Zhang, P. Chu, I. Bennion, Y. Jeong, C. Kim, B. Lee, W. Zhang, and C. Zhan. *Fiber Optic Sensors, Second Edition*, volume 20085244 of *Optical Science and Engineering*. CRC Press, second edi edition, mar 2008.

[80] Robert Brüning, Yingwen Zhang, Melanie McLaren, Michael Duparré, and Andrew Forbes. Overlap relation between free-space Laguerre Gaussian modes and step-index fiber modes. *Journal of the Optical Society of America A*, 32(9):1678, sep 2015.

[81] Nicolas Bourbaki. *Topological Vector Spaces*. Springer Berlin Heidelberg, Berlin, Heidelberg, 1987.

[82] Michael Hosea. integralN.m - File Exchange - Matlab Central, 2014.

[83] E Cheney and D Kincaid. *Numerical Mathematics and Computing*. International student edition. Cengage Learning, sixth edit edition, 2007.

[84] K Stephan. *Analog and Mixed-Signal Electronics*. Wiley, 2015.

[85] Eugene Hecht. *Optics*. Pearson Education Limited, fifth edit edition, 2017.

[86] H. Nyquist. Certain Topics in Telegraph Transmission Theory. *Transactions of the American Institute of Electrical Engineers*, 47(2):617–644, apr 1928.

[87] C.E. Shannon. Communication in the Presence of Noise. *Proceedings of the IRE*, 37(1):10–21, jan 1949.

[88] Orazio Svelto. *Principles of Lasers*. Springer US, Boston, MA, 2010.

[89] Jay N Damask. *Polarization Optics in Telecommunications*, volume 101 of *Springer Series in Optical Sciences*. Springer-Verlag, New York, 2005.

[90] Fiberguide Industries. White Paper: Shaped Tip Fibers, 2014.

[91] D. Marcuse. Loss Analysis of Single-Mode Fiber Splices. *Bell System Technical Journal*, 56(5):703–718, may 1977.

[92] M. Artiglia, G. Coppa, P. Di Vita, M. Potenza, and A. Sharma. Mode field diameter measurements in single-mode optical fibers. *Journal of Lightwave Technology*, 7(8):1139–1152, 1989.

[93] K. Petermann. Constraints for fundamental-mode spot size for broadband dispersion-compensated single-mode fibres. *Electronics Letters*, 19(18):712, 1983.

[94] University of Cambridge. Safe Use of Lasers, 2018.

[95] Thorlabs Ltd. FN96A Manual - Guide to Connectorization and Polishing Optical Fibers, 2016.

[96] V. Ossenkopf. The stability of spectroscopic instruments: a unified Allan variance computation scheme. *Astronomy & Astrophysics*, 479(3):915–926, mar 2008.

[97] R. Schieder and C. Kramer. Optimization of heterodyne observations using Allan variance measurements. *Astronomy & Astrophysics*, 373(2):746–756, jul 2001.

[98] D.W. Allan. Statistics of atomic frequency standards. *Proceedings of the IEEE*, 54(2):221–230, may 1966.

[99] Freescale. Allan Variance: Noise Analysis for Gyroscopes. Technical report, Freescale Semiconductor, 2015.

[100] J. W. Kooi, G. Chattopadhyay, M. Thielman, T. G. Phillips, and R. Schieder. Noise stability of SIS receivers. *International Journal of Infrared and Millimeter Waves*, 21(5):689–716, 2000.

[101] N. Trappe, J.A. Murphy, S. Withington, and W. Jellema. Gaussian beam mode analysis of standing waves between two coupled corrugated horns. *IEEE Transactions on Antennas and Propagation*, 53(5):1755–1761, may 2005.

[102] Oleg V. Ivanov, Sergei A. Nikitov, and Yurii V. Gulyaev. Cladding modes of optical fibers: properties and applications. *Physics-Uspekhi*, 49(2):167, 2006.

[103] G. E. Chamberlain, B. L. Danielson, G. W. Day, D. L. Franzen, R. L. Galawa, E. M. Kim, and M. Young. *Optical Fiber Characterization*. National Bureau of Standards, Gaithersburg, MD, nbs specia edition, 1982.

[104] G H Hardy, J E Littlewood, and G Pólya. *Inequalities*. Cambridge Mathematical Library. Cambridge University Press, 1988.

[105] K. E. Atkinson. *An Introduction To Numerical Analysis*. Wiley India Pvt. Limited, 2nd editio edition, 2008.

[106] Roger Balian. Entropy, a Protean Concept. In *Poincaré Seminar 2003*, pages 119–144. Birkhäuser Basel, Basel, 2004.

[107] Fukai Zhang, Fajie Duan, Changrong Lv, Xiaojie Duan, En Bo, and Fan Feng. Fiber-optic project-fringe interferometry with sinusoidal phase modulating system. *Optical Engineering*, 52(6):065601, jun 2013.

[108] D A Jackson, A Dandridge, and S. K. Sheem. Measurement of small phase shifts using a single-mode optical-fiber interferometer. *Optics Letters*, 5(4):139, apr 1980.

[109] Andrew J Moore, Roy McBride, James S Barton, and Julian D C Jones. Closed-loop phase stepping in a calibrated fiber-optic fringe projector for shape measurement. *Applied Optics*, 41(16):3348–3354, 2002.

[110] Xiaojun Fang, Richard O. Claus, and Guy Indebetouw. Interferometric model for phase analysis in fiber couplers. *Applied Optics*, 35(22):4510, aug 1996.

[111] Hisham A. H. Al-Khazali. Geometrical and Graphical Representations Analysis of Lissajous Figures in Rotor Dynamic System. *IOSR Journal of Engineering*, 02(05):971–978, may 2012.

[112] D. Stowe and Tsung-Yuan Hsu. Demodulation of interferometric sensors using a fiber-optic passive quadrature demodulator. *Journal of Lightwave Technology*, 1(3):519–523, 1983.

[113] Eric Udd and William B. Spillman, editors. *Fiber Optic Sensors*. John Wiley & Sons, Inc., Hoboken, NJ, USA, jul 2011.

[114] K. P. Koo, A. B. Tveten, and A. Dandridge. Passive stabilization scheme for fiber interferometers using (3×3) fiber directional couplers. *Applied Physics Letters*, 41(7):616–618, oct 1982.

[115] Sang K. Sheem. Optical fiber interferometers with [3x3] directional couplers: Analysis. *Journal of Applied Physics*, 52(6):3865–3872, jun 1981.

[116] Miguel Arevallilo Herráez, David R. Burton, Michael J. Lalor, and Munther A. Gdeisat. Fast two-dimensional phase-unwrapping algorithm based on sorting by reliability following a noncontinuous path. *Applied Optics*, 41(35):7437, dec 2002.

[117] M. F. Kasim. Fast 2D phase unwrapping implementation in MATLAB, 2017.

[118] SQS Vlaknova Optika. V-Grooves & Fiber Arrays, 2019.

[119] Philip E. Ciddor. Refractive index of air: new equations for the visible and near infrared. *Applied Optics*, 35(9):1566, mar 1996.

[120] Bengt Edlén. The Refractive Index of Air. *Metrologia*, 2(2):71–80, apr 1966.

[121] K P Birch and M J Downs. Correction to the Updated Edlén Equation for the Refractive Index of Air. *Metrologia*, 31(4):315–316, jan 1994.

[122] S.F. Gull and J. Skilling. Maximum entropy method in image processing. *IEE Proceedings F Communications, Radar and Signal Processing*, 131(6):646, 1984.

[123] Anisa T. Bajkova. The generalization of maximum entropy method for reconstruction of complex functions. *Astronomical & Astrophysical Transactions*, 1(4):313–320, mar 1992.

[124] H. Junklewitz, M. R. Bell, M. Selig, and T. A. Enßlin. RESOLVE: A new algorithm for aperture synthesis imaging of extended emission in radio astronomy. *Astronomy & Astrophysics*, 586:A76, feb 2016.

[125] Nicholas Young. *An introduction to Hilbert space*. Cambridge University Press, Cambridge, 1988.

[126] Dan Moinard, Stafford Withington, and Christopher N. Thomas. Probing infrared detectors through energy-absorption interferometry. In Paul D. LeVan, Ashok K. Sood, Priyalal Wijewarnasuriya, and Arvind I. D'Souza, editors, *Infrared Sensors, Devices, and Applications VII*, volume 44, page 22. SPIE, aug 2017.

[127] M. D. Feit and J. A. Fleck. Light propagation in graded-index optical fibers. *Applied Optics*, 17(24):3990, dec 1978.

[128] S. Withington and C. N. Thomas. Probing the dynamical behavior of surface dipoles through energy-absorption interferometry. *Physical Review A*, 86(4):043835, oct 2012.

[129] Denis Tihon, Stafford Withington, Christopher N. Thomas, and Christophe Craeye. Characterization of power absorption response of periodic three-dimensional structures to partially coherent fields. *Journal of the Optical Society of America A*, 33(12):2459, dec 2016.

[130] Wei Gao. *Precision Nanometrology*. Springer Series in Advanced Manufacturing. Springer London, London, 2010.

[131] S Shaklan, M C Sharman, and S H Pravdo. High-precision measurement of pixel positions in a charge-coupled device. *Applied optics*, 34(29):6672–81, 1995.

[132] OzOptics Limited. Polarization Maintaining Fiber Patchcords and Connectors, 2019.

[133] J.G. Weisend II, editor. *Cryostat Design*. International Cryogenics Monograph Series. Springer International Publishing, Cham, 2016.

[134] Oliver Kahl, Simone Ferrari, Vadim Kovalyuk, Gregory N. Goltsman, Alexander Korneev, and Wolfram H. P. Pernice. Waveguide integrated superconducting single-photon detectors with high internal quantum efficiency at telecom wavelengths. *Scientific Reports*, 5(1):10941, sep 2015.

[135] Benjamin Jacot. *Probing magnetic excitations through Energy Absorption Interferometry*. Master thesis, ETH Zürich, 2018.

[136] Andrea Muni. *Computational spectroscopy on quantum dipoles*. Master thesis, École Polytechnique Fédérale de Lausanne, 2018.

[137] S Withington, C N Thomas, and D J Goldie. Probing Quantum Correlation Functions Through Energy Absorption Interferometry. *arXiv preprint arXiv:1609.03174*, sep 2016.

[138] Ronan Gautier and Stafford Withington. Coupling of electromagnetic and elastic interactions in two-level systems. *Manuscript in preparation*, 2019.